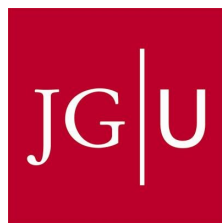

MAINZTPC:
—
DETECTOR COMMISSIONING AND
STUDY OF THE LOW-ENERGY RESPONSE
OF ELECTRONIC RECOILS IN LIQUID XENON
FOR DARK MATTER APPLICATIONS

DISSERTATION ZUR ERLANGUNG DES GRADES
“DOKTOR DER NATURWISSENSCHAFTEN”
AM FACHBEREICH PHYSIK, MATHEMATIK UND INFORMATIK
DER JOHANNES GUTENBERG-UNIVERSITÄT MAINZ

Pierre Dominik Sissol

geboren am 11. April 1986 in Wiesbaden



Tag der mündlichen Prüfung: 03.12.2019

D77: Dissertation Johannes Gutenberg-Universität Mainz

Erklärung

Hiermit versichere ich gemäß § 12 Abs. 3e der Promotionsordnung des Fachbereichs 08, Physik, Mathematik und Informatik der Johannes Gutenberg-Universität Mainz vom 02.12.2013:

- dass ich die vorgelegte Arbeit selbständig verfasst habe. Es wurden ausschließlich die angegebenen Quellen und Hilfsmittel verwendet. Von der Ordnung zur Sicherung guter wissenschaftlicher Praxis in Forschung und Lehre und vom Verfahren zum Umgang mit wissenschaftlichem Fehlverhalten habe ich Kenntnis genommen.
- dass ich die vorliegende Dissertation nicht als Prüfungsarbeit für eine andere Prüfung eingereicht habe.
- dass ich die vorliegende Abhandlung oder Teile davon noch nicht als Dissertation bei einer anderen Fakultät oder einem anderen Fachbereich eingereicht habe.

Mainz, 28 April 2019

Pierre Sissol

To my parents.

PS

Abstract

Direct Dark Matter detection is an ongoing and quickly developing field in astroparticle physics, aiming to measure the scattering of Dark Matter particles with Standard Model particles. With detectors searching for predicted Dark Matter particles and narrowing the parameter space over the last three decades, the technological approach becomes more and more challenging. Today the best limits on Dark Matter mass and cross-section are set by dual-phase xenon time projection chambers (TPC). To increase their sensitivity, a deeper understanding of the physical processes in xenon with respect to the energy deposit by impinging particles is crucial.

The MainzTPC is a small dual-phase xenon time projection chamber which was co-developed and commissioned in the course of this thesis. Its main goal is to study the scintillation $S1$ and ionization response of liquid xenon from low-energy electronic and nuclear recoils. Two signals are measured: The primary signal $S1$ originates from prompt scintillation after the scattering interaction. The secondary signal $S2$ is the charge signal created in the gas phase. It is proportional to the number of extracted electrons. The MainzTPC also provides a 3D position reconstruction which allows the definition of a fiducialized volume inside the TPC.

The charge-to-light ratio for electronic recoils generally is larger than for nuclear recoils which leads to a discrimination method for background events undergoing interactions with the electronic shell of the xenon atoms, such as gamma-rays or electrons. Like neutrons, Dark Matter is expected to scatter on a xenon nucleus. For the low-energy region, this distinction becomes less reliable. The measurement of light and charge yields for liquid xenon for energy deposits down to only a few keV is necessary to improve on this discrimination tool.

The experimental part of this dissertation describes the MainzTPC detector as well as its surrounding subsystems which are necessary for operation. The emphasis is set on the data acquisition system, which was developed in the course of this thesis and was used to record the data from Compton scattering as well as neutron scattering. The data presented here are Compton measurements conducted at the nELBE facility at the HZDR.

In the analysis part the MainzTPC as a prototype is characterized and examined for its various properties, such as the 3D position reconstruction employing avalanche photodiodes, the determination of the liquid level inside the TPC, signal corrections for $S1$ and $S2$ as well as several other parameters (electron drift velocity, electric field strengths in the gas phase, and so on).

The light and charge yields of the MainzTPC were measured and show qualitatively similar results as simulations from [1] and previous measurements from [2]. The performance of the MainzTPC is limited by a series of factors, which are described in detail in the analysis part. Examples are a high noise level on the photomultipliers limiting the low-signal detection and the non-feasible TPC calibration data.

For future measurements, necessary improvements are discussed.

Zusammenfassung

Die direkte Suche nach Dunkler Materie (DM) ist ein sich ständig weiterentwickelndes Feld der Astroteilchenphysik mit dem Ziel, die Streuung von DM-Teilchen mit Teilchen des Standardmodells zu messen. Die fortlaufende Einschränkung des Parameterraums bei der Suche nach den vorhergesagten DM-Teilchen während der letzten drei Dekaden führt zu immer größeren technologischen Herausforderungen. Heutzutage werden die besten Limits für die Masse und den Wirkungsquerschnitt von Dunkler Materie mithilfe von Zweiphasen-Xenon-Zeitprojektionskammern (TPC) bestimmt. Um deren Sensitivität zu verbessern, ist ein tieferes Verständnis der physikalischen Prozesse bezüglich Streuung von Teilchen in Xenon ausschlaggebend.

Die MainzTPC ist eine kleine Zweiphasen-Xenon-Zeitprojektionskammer, die im Verlauf dieser Arbeit mitentwickelt und aufgebaut wurde. Ihre Hauptaufgabe ist die Untersuchung der Szintillation $S1$ und der Ionisation in flüssigem Xenon, die durch niederenergetische elektronische und nukleare Rückstöße erzeugt werden. Zwei Signale werden gemessen: Bei der Streuung im flüssigen Xenon entsteht Szintillationslicht, das primäre Signal $S1$. Das sekundäre Signal $S2$ ist das in der Gasphase generierte Ladungssignal und ist proportional zur Anzahl der extrahierten Elektronen. Eine 3D-Positionsrekonstruktion erlaubt außerdem die Definition eines Vertrauensvolumens innerhalb der TPC.

Für elektronische Rückstöße wird generell ein größeres Verhältnis von Ladung zu Licht als für Kernrückstöße gemessen. Dies kann als Diskriminationsmethode für Hintergrundereignisse verwendet werden, die mit der Elektronenhülle der Xenonatome wechselwirken. Ähnlich wie bei Neutronen erwartet man für Dunkle Materie eine Streuung am Kern. Im niederenergetischen Bereich ist diese Methode nicht mehr eindeutig. Die Messung von Licht- und Ladungsausbeute für flüssiges Xenon bei deponierten Energien im Bereich weniger keV ist notwendig, um dieses Diskriminationswerkzeug zu verbessern.

Der experimentelle Teil dieser Dissertation beschreibt den Detektor MainzTPC sowie seine Subsysteme, die für Betrieb und Experiment notwendig sind. Der Schwerpunkt wurde auf das Datennahmesystem gelegt, welches als Teil dieser Arbeit entwickelt wurde und sowohl für Comptonstreuung als auch für Neutronenstreuung zum Einsatz kam. Die hier präsentierten Daten von Comptonmessungen wurden am HZDR durchgeführt.

Im Analyseteil wird die MainzTPC bezüglich ihrer unterschiedlichen Eigenschaften charakterisiert und untersucht. Beispiele sind die 3D-Positionsrekonstruktion mithilfe von Avalanche-Photodioden, die Bestimmung des Flüssigkeitslevels innerhalb der TPC, Signalkorrekturen für $S1$ und $S2$ usw.

Die Licht- und Ladungsausbeute der MainzTPC wurden gemessen und qualitativ mit Simulationen von [1] und früheren Messungen von [2] verglichen. Sie zeigen ähnliche Ergebnisse. Die Leistungsfähigkeit der MainzTPC ist durch eine Reihe von Faktoren beschränkt, wie beispielsweise einem hohen Rauschpegel, der die Detektion kleinster Signale verhindert, und die nicht verwendbaren Kalibrationsdaten für die TPC.

Notwendige Verbesserungen für zukünftige Messungen werden dargelegt.

Contents

Abbreviations, Symbols and Units	VII
Introduction	1
I THEORETICAL FRAMEWORK	5
1 Dark Matter and Direct Searches	7
1.1 Evidences for Dark Matter	8
1.1.1 Rotational Curves - Galactic Scale	8
1.1.2 Cluster Dynamics & Gravitational Lensing - Galaxy Cluster Scale	9
1.1.3 Cosmic Microwave Background - Universal Scale	10
1.2 WIMPs as Dark Matter Candidates	12
1.3 Direct Search for Dark Matter	14
1.3.1 Backgrounds and Interactions in Dark Matter Detectors	14
1.3.2 Overview on Direct Search Experiments	14
1.3.3 Principle of a Dual-Phase Xenon Time Projection Chamber	17
1.3.4 Current Status of Direct Dark Matter Searches and Outlook	20
2 Liquid Xenon as Detection Medium	23
2.1 Xenon as a Detection Medium	24
2.2 Scattering of Particles in Liquid Xenon	26
2.2.1 Interactions of Photons with Xenon	26
2.2.2 Compton Scattering in Liquid Xenon - Electronic Recoil in the Free Electron Approximation	27
2.2.3 Compton Scattering off Bound Electrons	28
2.2.4 Neutron Scattering in Liquid Xenon - Nuclear Recoil	30
2.2.5 Energy Measurement in Scatter Experiments	30
2.3 Liquid Xenon Scintillation and Ionization	31
2.3.1 Underlying signal processes	31
2.3.2 Anti-Correlation of Light and Charge Signal	32
2.4 $S1$ Pulse Shape in Liquid Xenon	34
2.5 Results of Low-Energy Electronic Recoil Measurements	36

II	THE MAINZTPC EXPERIMENT	39
3	MainzTPC - Experimental Setup	41
3.1	Goals and Motivation	42
3.2	MainzTPC Specifications	43
3.2.1	The Time Projection Chamber	43
3.2.2	Technical Constraints	46
3.2.3	Electric Fields and Electrodes Structures	47
3.2.4	Levelmeters	48
3.2.5	Optical Fibers	51
3.3	From Physics to Data - Hardware Infrastructure	51
3.3.1	MainzTPC in the Setup	52
3.3.2	Cryogenic System	53
3.3.3	Gas System	56
3.3.4	Slow Control System (SCS)	57
3.3.5	Data Acquisition System	58
3.4	Signal Readout	58
3.4.1	PMTs	58
3.4.2	APDs	59
3.4.3	Germanium detector - Compton Mode	60
3.4.4	Plastic scintillators - Neutron Mode	60
3.5	Operating the MainzTPC	62
3.5.1	Setup 1 (Mainz) - Compton Setup	62
3.5.2	Setup 2 (HZDR) - Compton and Neutron Setup	62
3.5.3	Gamma-ray Sources	65
3.5.4	Neutron Source nELBE	66
3.5.5	Gamma-ray Data	67
3.5.6	Raw Data Processing	67
4	MainzTPC - Data Acquisition	71
4.1	Events and Signals	72
4.2	Hardware Components	75
4.2.1	Signal Measurement	76
4.2.2	Timing and Trigger Signals	78
4.2.3	High Voltage Modules	80
4.3	Event Trigger	81
4.3.1	DAQ version 1: Internal Trigger Generation on SIS3316	81
4.3.2	DAQ version 2: Trigger Generation with CAEN V1495	84
4.4	DAQ Program Functionality Overview	95
4.5	Communication in VME Electronics	95
4.6	DAQ Program Initialization and Configuration	96
4.6.1	SIS3316 Initialization and Configuration	97
4.6.2	SIS3305 Initialization and Configuration	98
4.6.3	CAEN VX1290 Configuration	101

4.6.4	Additional Boards	103
4.7	Data Acquisition	104
4.7.1	The Acquisition Stage	104
4.7.2	Event Consistency	106
4.7.3	High-Frequency Mode	108
4.8	Data Readout and Data Format	110
4.9	SIS3820 VME scaler	114
4.10	Controlling the High Voltage Modules	115
4.11	Improvements & Summary	117
III	ANALYSIS & RESULTS	119
5	Sensor Calibration	121
5.1	Gain Determination for the PMTs	122
5.1.1	PMT Calibration at the HZDR	122
5.1.2	Calculation of the PMT Gains for the HZDR Measurements	124
5.2	Germanium Detector Calibration	126
5.2.1	Energy Calibration using Gamma-Ray Sources	126
5.2.2	Energy Resolution of the Germanium detector	129
5.3	APD Calibration	133
6	Position Reconstruction	139
6.1	3D Position Reconstruction in the MainzTPC	140
6.2	Determination of the x - y Position	140
6.2.1	The Centroid Method	140
6.2.2	Position Reconstruction in x - y with Data	142
6.2.3	Improvement of the Shape of the Reconstruction Pattern	145
6.2.4	Discrimination Ability	146
6.3	Status and Next Steps	148
7	Liquid Level Determination	151
7.1	Levelmeter Calibration	152
7.1.1	Calibration of the Levelmeters with Data from July 2015	152
7.1.2	Calibration of the Levelmeters with Data from July 2017	155
7.1.3	Capillarity	157
7.1.4	Comparison of the Calibration Results	159
7.2	Determination of the Liquid Level during Operation	160
7.2.1	Level during Run HZDR 2016	161
7.2.2	Level during Run July 2017	162
7.3	Tilt in the Liquid Level	164
7.3.1	Level Tilt at the HZDR in April 2016	165
7.3.2	Level Tilt in Mainz in July 2017	167
7.4	Electric Field between Gate and Anode Mesh	169

7.5	Examination of the measured $S2$ Width	171
8	Electron Drift and Signal Corrections	173
8.1	Electron Drift Velocity	174
8.2	Drift Time and Interaction Depth	178
8.3	$S1$ z -correction	179
8.4	Electron Lifetime and $S2$ z -correction	187
8.5	$S2$ Signal Saturation	192
9	Compton Scattering	197
9.1	Introductory Remarks	198
9.2	Conducted Measurements	199
9.2.1	Overview of TPC Calibration Measurements	199
9.2.2	Overview of Compton Measurements	200
9.3	Event Selection	202
9.3.1	Fiducialization of the Active LXe Volume	202
9.3.2	$S1$ as Trigger Signal	203
9.3.3	$S1$ in Dependence of E_{TPC} for the Compton Measurements	204
9.3.4	$S1$ Top-Bottom Asymmetry in z	207
9.3.5	Multiple $S2$ Signals per Waveform	209
9.3.6	Spatial Resolution of Double Scatters in z	212
9.3.7	Width of the $S2$ Signal as Selection Tool	213
9.4	TPC Calibration	218
9.4.1	Observed Calibration Data	218
9.4.2	Estimation of the Energy Resolution in $S1$	223
9.4.3	Examining the $S2$ Signal using the APDs	225
9.4.4	Improvements of the TPC Calibration	227
9.5	Trigger Efficiency	228
9.5.1	Effect and Measurement of the $S1$ Trigger Efficiency	228
9.5.2	Determination of the Trigger Efficiency	229
9.5.3	Further Steps to improve the Trigger Efficiency	236
9.6	Primary Scintillation $cS1$	237
9.6.1	Light Yield for $cS1$	237
9.6.2	Field Quenching	244
9.6.3	Impact of the $S1$ z -correction	249
9.7	Secondary Scintillation $cS2$	251
9.7.1	Event distribution for $cS2$	251
9.7.2	Charge Yield Calibration using Single $S2$ signals	255
9.7.3	Charge Yield QY for $cS2$	255
9.7.4	Impact of the $S2$ z -correction	259
9.8	Compton $S2$ and $S1$ as calibration signals	262

10 Summary & Outlook	265
10.1 Summary	266
10.2 Outlook	267
IV APPENDICES	269
A Formula derivations and Schematics	271
A.1 Derivation of the electric fields in the $S2$ region	272
A.2 Derivation of the capillarity effect	273
A.3 Tilt angle for the liquid level fit plane	275
A.4 TPC PMT base circuit - Schematic	276
B Tables and Graphs	277
B.1 Germanium calibration	278
B.2 APD calibration	281
B.3 Determination of maximum drift time	292
B.4 $S1$ z -correction	294
B.5 $S2$ z -correction	296
B.6 $S1$ Asymmetry	301
B.7 $S2$ Width	302
B.8 TPC Calibration	303
B.9 Trigger Efficiency	305
B.10 Light Yield	309
C Data sheets	317
List of Tables	321
List of Figures	327
Bibliography	339

Abbreviations, Symbols and Units

List of Abbreviations

ADC	Analog-to-Digital Converter
APD	Avalanche Photodiode
CAD	Computer-Aided Design
CFD	Constant Fraction Discriminator
C.L.	Confidence Level
CMB	Cosmic Microwave Background
CSP	Charge-Sensitive Preamplifier
DAC	Digital-to-Analog Converter
DAQ	Data Acquisition (program or system)
DM	Dark Matter
ECL	Emitter Coupled Logic
EEprom	(Electrically Erasable programmable read-only memory)
ER	Electronic Recoil
FADC	Flash Analog-to-Digital Converter
FPGA	Field Programmable Gate Array
FWHM	Full Width at Half Maximum
G & D	Gate & Delay
GXe	Gaseous Xenon
HDM	Hot Dark Matter
HF	High-Frequency (mode)

HZDR	Helmholtz-Zentrum Dresden-Rossendorf
HPGe	High-Purity Germanium
HV	High Voltage
IOB	Input/Output Block (in FPGAs)
ΛCDM	Λ Cold Dark Matter (model)
KPH	Kernphysik
LaBr	Lanthanum Bromide
LCE	Light Collection Efficiency
LE	Leading Edge
LED	Light Emitting Diode
LNGS	Laboratori Nazionali del Gran Sasso
LVDS	Low Voltage Differential Signaling
LXe	Liquid Xenon
MACHO	Massive Astrophysical Compact Halo Object
MAW	Moving Average Window
MaxNbEvts	Maximum number of events (to be acquired)
MOND	MOdified Newtonian Dynamics (model)
NaI, NaI(Tl)	Sodium Iodide, doped with Thallium
nELBE	neutron facility at the electron accelerator ELBE (Electron Linac for beams with high Brilliance and low Emittance)
NIM	Nuclear Instrument Module:
NR	Nuclear Recoil
PCB	Printed Circuit Board
PEEK	Polyether ether ketone
PID	Proportional-Integral-Derivative controller
PMT	Photomultiplier Tube
PL	Plastic (scintillator, for neutron detection)
PTFE	Polytetrafluoroethylene
PTR	Pulse-Tube Refrigerator
QE	Quantum Efficiency
SCS	Slow Control System
SM	Standard Model (of Particle Physics)
SPE	Single Photoelectron

SPI	Serial Peripheral Interface
TDC	Time-to-Digital Converter
TeVS	Tensor-Vector-Scalar (model)
TI	Trigger In
TOF	Time-of-Flight
TO	Trigger Out
TPC	Time Projection Chamber
UTI	Universal Transducer Interface
UO	User Out
VME	Versa Module Europa (bus system)
VUV	Vacuum Ultra-Violet
WIMP	Weakly Interacting Massive Particle

List of Symbols

a_x	gain factors (capacitance measurement theory)
A_x	amplitudes
α	angle
α -particle	nucleus of ${}^4\text{He}$
c	speed of light
C	capacitance
$cS1, cS2$	scintillation signals corrected for the interaction depth z
γ	relativistic factor, photon/gamma-ray
d	distance
e	electron
E	energy
$\vec{E}, \vec{E} = E$	electric field strength
ϵ_0	vacuum permittivity
$\epsilon_{\text{LXe}}, \epsilon_{\text{GXe}}$	relative permittivity
ϵ_{Ge}	energy gap between valence and conduction band in germanium
$f, f_{\text{amplifier } x}$	fill factor between gate and anode, amplification factor
$f_{\text{Gaussian}}, f_{\text{Lorentzian}}$..	Gaussian or Lorentzian function

f_{S1}, f_{S2}	correction factor for $S1, S2$
F_{Ge}	Fano factor for germanium
g	gravitational acceleration
g_x	gain factors (PMT calibration)
h	Planck's constant; height
$k\alpha/k\beta$	X-ray lines from K-shell in atom
λ	wavelength, mean free path
l	length
m	mass, calibration slope (levelmeters)
μ	mean value (Gaussian)
ν	gamma-ray frequency
p	pressure
Q	charge
$r / R, R_x$	radius, relative capacitance C_x/C_{ref}
Res	residual
ρ	density
$S1$	prompt scintillation signal
$S2$	proportional scintillation signal
σ	cross-section, Gaussian standard deviation, surface tension
Σ	excimer states of xenon: singlet $^1\Sigma^+$ and triplet $^3\Sigma^+$
T	temperature; time constants
t	time
θ	scattering angle
τ	lifetime
U	voltage
v	velocity
W_E	electronic noise (energy)
Z	proton number
z	interaction depth

List of Units

b	barn
eV	electronvolt
ly	light year
MS/s	Megasamples per second
pc	parsec; 1 parsec \approx 3.26 ly.
p.e.	photoelectrons
u	atomic mass unit: $1 \text{ u} = 1.66 \cdot 10^{-27} \text{ kg}$
yr	year

Introduction

One of the yet unsolved mysteries of modern astroparticle physics is the nature of the so-called Dark Matter. It accounts for 26.6 % of the energy content of the universe and is therefore about five times more abundant than the “normal” matter stars, planets and we ourselves are made of.

Experiments to detect Dark Matter have been performed for several decades now, but so far it was only possible to set limits and constraints to Dark Matter particle properties. The most promising candidate for a Dark Matter particle is the WIMP (Weakly Interacting Massive Particle), that is searched for with a variety of experimental setups of which experiments with dual-phase xenon time projection chambers (TPC) currently set the best constraints on WIMP mass and cross-section, respectively.

Basically, the search for Dark Matter is a counting experiment: The signals detected in a TPC such as XENON1T are counted and categorized either as Dark Matter signals or background signals. For WIMPs, the expected rate is extremely low, therefore it is crucial to suppress or at least identify and discriminate unwanted background signals. In xenon TPCs, the ratio of light and charge signals from the energy deposit are used to discriminate impinging particle types: Gamma-rays and electrons interact with the atomic electron shells, which leads to a high charge-over-light ratio (electronic recoil), while a neutral particle such as a neutron or WIMP scatters off the atomic nucleus with a more constraint release of electrons (nuclear recoil).

Although the ratio is used successfully for large energy deposits, electronic and nuclear recoils in the low-energy regime can not be easily distinguished.

The MainzTPC is a small dual-phase TPC designed to study the low-energy response of liquid xenon for both electronic and nuclear recoil. A second goal is to test an alternative method to discriminate between the two interaction types by measuring the scintillation pulse-shape.

The cornerstones of my PhD thesis are three-fold:

The development and commissioning of the MainzTPC was done in cooperation with [3] and embody the foundation of this thesis. Therefore part II describes the experimental setup of the MainzTPC which employs specific features such as the use of avalanche photodiodes (APDs) for the position reconstruction, a very fine electronic mesh configuration, a custom-built electric field cage and a customized detector design which distinguish this TPC from other dual-phase xenon TPCs in the field. Although this thesis concentrates on the signal analysis from electronic recoils, the measurement specifications for both Compton scattering with gamma-rays and neutron scattering (nuclear recoils) are presented.

The data acquisition system (DAQ) is an integral part of this work, as I was the responsible developer for the system. The DAQ consists of a variety of electronics gathering the signals from different sensors in the TPC and eventually recording the measurement data. The trigger setup used to decide whether an event has occurred and has to be recorded is one of the key aspects for the DAQ system, which has been utilized successfully in several theses in the XENON Mainz group up to now [3, 4, 5].

As a second cornerstone, the tooling equipment to analyze the electronic recoil data

and to understand the performance of the MainzTPC was developed. These include the determination of the liquid level in the TPC, the test of the x - y -position reconstruction, the examination of the electron drift, signal corrections and calibration tools. The results are found in chapters 5.3 to 8.

Last but not least, the results of the experimental run from April 2016, including TPC calibration, trigger efficiency and Compton scattering measurements are presented and discussed in chapter 9. The results for the light and charge yield measurements are compared to previous simulations and measurements.

Encountering limits of the MainzTPC performance, the thesis addresses the required experimental improvements for future studies.

Part I

THEORETICAL FRAMEWORK

Dark Matter and Direct Searches

Chapter 1

1.1 | Evidences for Dark Matter

From the beginning of the twentieth century, technological advancement allowed physicists and astronomers to look deeper into space and time than ever imagined before. But the enhanced precision of their instruments led them to the astonishing conclusion that their astronomical models built on Newton's law of gravity were incomplete, if not wrong. What they encountered was the existence of celestial objects that did not show the expected behaviour.

The problem became even more serious when measurements for different scales showed the same abnormality: Many objects move through space as if there was more matter present than what is observed. Several theoretical attempts to solve this mystery were proposed and some of them are still examined. One of them is the prominent theory of a new kind of non-visible matter: Dark Matter (DM).

1.1.1 | Rotational Curves - Galactic Scale

Applying Newton's law of gravity to the visible mass distribution of a galaxy (which can be estimated by astrophysical means, such as the mass-luminosity relation), one expects a decrease in star velocity for larger distances from the center. This is illustrated in figure 1.1 as a dashed line labeled "disk". Otherwise the velocities of the stars would exceed the escape velocity of the galaxy and the galaxy would diverge.

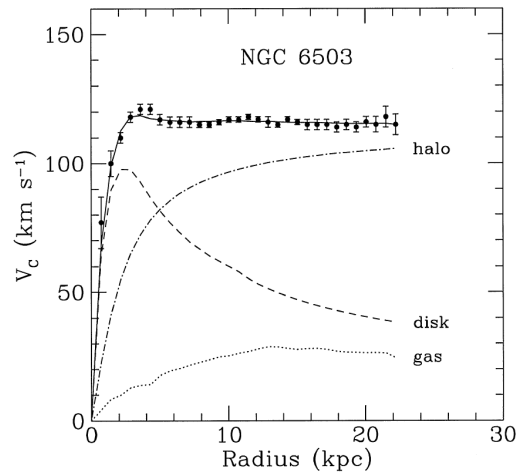


Figure 1.1: Star velocities in a spiral galaxy depending on their distance to the galactic center. The theoretical prediction is indicated by the dashed line labeled "disk" and shows a strong discrepancy to the measured values on the rotational curve (solid line). To account for the deviation, additional mass contributions from gas (dotted line) and a DM halo (dashed-dotted line) are also shown [6].

In 1939, Horace Babcock published his measurements of the rotation curve of the Andromeda galaxy. He reported that the outer parts of the galaxy rotated too fast [7]. But it was not until the 1970's that Vera Rubin, together with Kent Ford, found that most of the stars in spiral galaxies orbit their galactic centers with a roughly constant velocity and suggested that the mass distribution of the galaxies therefore should be considered as linearly increasing [8], which stands in contradiction to the observed matter distribution.

As can be seen exemplarily in figure 1.1, the star velocity in spiral galaxies increases with radial distance from the galactic center and then remains approximately constant even for large distances. For the galaxies to remain stable, there has to be some additional effect, such as a non-visible kind of matter which is responsible for holding the stars on their trajectories, apart from the gravitational pull of the visible matter. The amount of visible matter - compared to the very first measurements - was corrected using improved astronomical techniques. Gamma-ray astronomy for example revealed that a large amount of matter in galaxies is present in the form of hot gas, emitting photons in the X-ray and gamma-ray regime instead of the visible range.

But finally the amount of additional mass to provide a sufficient gravitational potential was estimated to be 4-5 times larger than the (visible) matter of the galaxies. A possible explanation is that each galaxy is embedded in a much larger Dark Matter halo that exceeds the size of the galaxy and leads to a linear increase of mass for larger radii.

1.1.2 | Cluster Dynamics & Gravitational Lensing - Galaxy Cluster Scale

In 1933 Swiss astronomer Fritz Zwicky examined the dynamics of the COMA galaxy cluster. Back then, the COMA cluster was known as a system of around 800 "nebulae", while today, a total of around 2000 galaxies has been observed, of which 650 galaxies are confirmed to belong to the COMA cluster [9].

Zwicky used the virial theorem to compare the kinetic energy of the galaxies according to their velocities with the potential energy of the COMA cluster which corresponds to its visible mass. He found that the galaxy velocities exceeded the escape velocity of the COMA cluster and estimated that the mass of the COMA cluster was about a factor of 400 smaller than the value necessary to keep the galaxies on their paths [10]. This factor was reduced by X-ray and gamma astronomy, but a discrepancy of a factor of 4-5 still remains.

Zwicky suggested the existence of a new kind of matter not interacting with the electromagnetic force, since it seemed neither to emit nor to absorb radiation, and labeled it "Dunkle Materie" – Dark Matter (the original article was actually published in German).

Another evidence for Dark Matter on the scale of galaxy clusters is found using gravitational lensing. According to this effect, predicted by Einstein's General Theory of Relativity, large masses in space bend space-time so that the light emitted from behind the mass distribution is deflected comparable to an optical lense. In reverse, observing light deflections allows to determine the mass and its distribution inside the structure

responsible for the lensing effect.

Figure 1.2 shows an X-ray image of the 1E 0657-558 galaxy cluster. In fact, this structure is made up of two galaxy clusters which collided, and the interstellar medium of the two clusters emits X-rays due to the collision pressure. The overlaid green contours depict the mass distribution determined with gravitational lensing and show two distinct mass concentrations which can be identified as the centers of mass for each of the two galaxy clusters after the collision. This means that most of the mass of the two clusters passed through each other without noteworthy effect. Furthermore, interstellar plasma makes up the major mass contribution to a galaxy cluster when only normal matter is considered. Thus, finding the centers of mass dislocated from the plasma points to the existence of non-luminous Dark Matter.

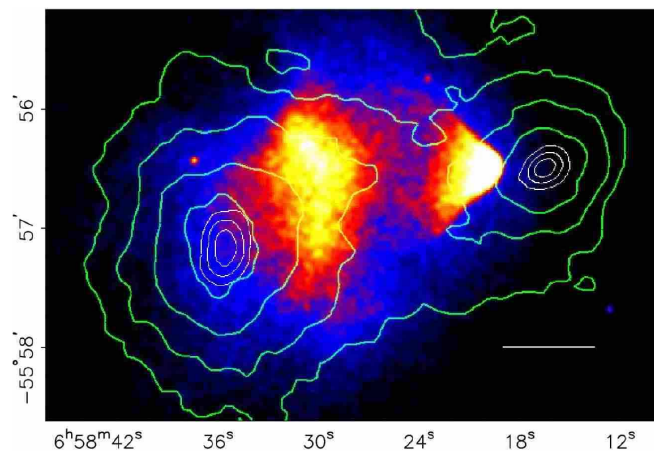


Figure 1.2: X-ray image of the 1E 0657-558 galaxy cluster, also called “Bullet Cluster”. Two clouds of hot interstellar medium emitting X-rays are visible. In green contours, the mass distribution according to gravitational lensing is overlaid. The centers of mass for the two colliding galaxy clusters are clearly distinguishable from the hot gas. The bar at the lower left indicates a scale of 200 kpc = 652,000 ly. [11]

1.1.3 | Cosmic Microwave Background - Universal Scale

The cosmic microwave background (CMB) probably provides the most prominent evidence for Dark Matter.

In the 1940s, theorists claimed that a cosmic background radiation would be present in the universe for a Big Bang scenario. By accident, this radiation was discovered in 1964. It is an isotropic radiation in the microwave range and its spectrum corresponds to a black body at a temperature of (2.725 ± 0.002) K [12]. The CMB was measured with experiments like the satellite missions COBE, WMAP and Planck. The latter gathered data for the most recent results in 2015, which are shown in figure 1.3.

In figure 1.3a, a temperature map of the sky is shown. The radiation measurement of the Planck satellite allows to determine the temperature corresponding to the energies

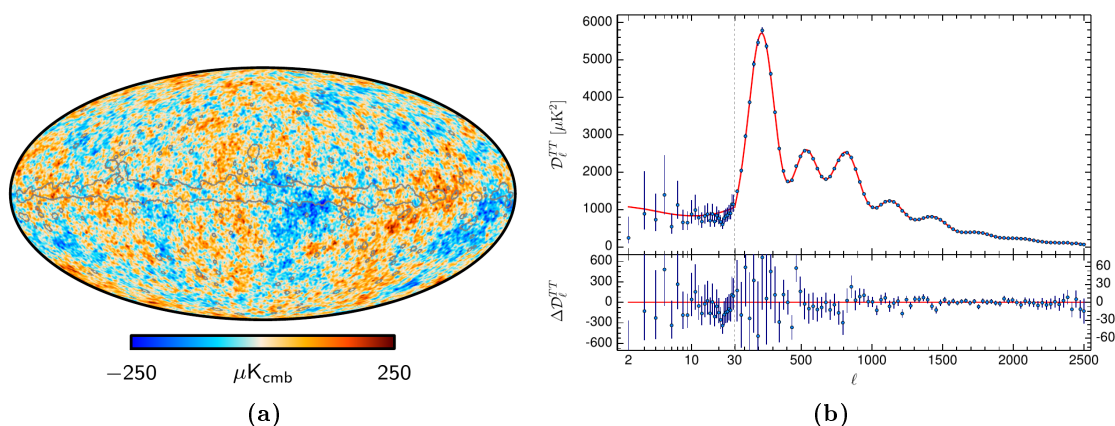


Figure 1.3: Left (a): Sky map of the temperature differences in the CMB after removing known sources of cosmic rays. As can be seen, the temperature differences are very small in the order of 10^{-4} K. The contours of the Milky Way band are overlaid. Right (b): CMB power spectrum. The spectrum shows the measured power (which is connected to the temperature) in dependence of the multipole moment l which corresponds to the angular size of the structure in the sky. The applied fit function arises from the Λ CDM-model. [13].

of the detected photons. Measuring different wavelength ranges allows to subtract radiation sources from the temperature map until only the background radiation is left. The contours of the band of the Milky Way are drawn in this figure. The background radiation with its approximately 2.7 K is very uniform in temperature. In fact, the temperature map shown in figure 1.3a shows the relative temperature differences in the CMB according to the position in the sky. As can be seen, the differences are in the order of μ K which is also evidence for the universe starting in thermal equilibrium.

Figure 1.3b depicts the power spectrum of the temperature map. Basically, it shows the CMB intensity (which corresponds to a temperature) depending on the angular size of the temperature structures on the sky map. The temperature map was developed as a series of multipoles and the power spectrum is depending on the multipole moment l corresponding to the angular size of the respective structures. The power spectrum contains three prominent peaks, along with some minor peaks to the right side of the spectrum.

The data points are fitted with a function that represents a cosmological model called Λ CDM, which is the prevailing cosmological model nowadays. Λ stands for the cosmological constant and “CDM” means “Cold Dark Matter”. This model describes our universe using a variety of parameters which include fundamental physical constants as well as measured or estimated quantities such as the Hubble constant or the amount of Dark Matter and Dark Energy in the universe. Hereby, Dark Matter is a crucial element involved in the structure formation in the early universe. To fit the data from the Planck satellite, the model parameters have to be fine-tuned.

According to the latest values from the Λ CDM-model, our universe consists of 4.9 % matter, 26.6 % Dark Matter and 68.5 % Dark Energy (from table 21 in [13]).

1.2 | WIMPs as Dark Matter Candidates

More than 80 years after the first evidences, the true nature of Dark Matter still remains a secret. A number of different approaches was tested to find an explanation for the astronomical phenomena.

The Modified Newtonian Dynamics (MOND) theory, for example, was developed to explain the unexpected star and galaxy motions with a change in the gravitational force for large scales. Later, even relativistic models as the tensor-vector-scalar gravity (TeVeS) were introduced to circumvent the necessity of a Dark Matter particle. To date, none of these theories can account for all observed phenomena, as e.g. the matter distribution measured by gravitational lensing of galaxy clusters [14].

Using gravitational microlensing, scientists searched for non-luminous objects that could constitute enough “dark” matter to account for the observations. These objects called MACHOs (Massive Astrophysical Compact Halo Objects) could be gas planets, brown dwarfs, neutron stars or black holes. Today, this scenario is excluded as far as possible since the number of MACHOs found is too small.

Also, MACHOs consist of baryonic matter. From primordial nucleosynthesis, it is possible to extract the ratio between photons and baryons. Furthermore, this can be translated to a contribution of the baryons to the total energy of the universe which is about 4% [15]. This number is in good agreement with the expected matter in the universe from the CMB. Consequently, Dark Matter is not expected to be baryonic matter and this contradicts the MACHO theory.

So far, the search for Dark Matter only allows to list criteria of exclusion for the particles we know from the Standard Model of Particle Physics (SM). A Dark Matter candidate would need to be a non-baryonic massive particle with no charge. Electromagnetic interactions are forbidden as well as strong interactions.

This constraints the available particles so that only the neutrinos remain. But since they have a very low mass and high velocities, they are not suitable for the structure formation in the early universe. In some models, neutrinos play a role as so-called Hot Dark Matter. Conclusively, the Standard Model does not contain a Dark Matter candidate.

Extension theories for the Standard Model include new types of particles, such as axions or WIMPs. The WIMP – Weakly Interacting Massive Particle – is one of the most prominent Dark Matter candidates today. It naturally emerges from different SM extensions, as for example the neutralino from supersymmetric models.

From the astronomical observations it is clear that Dark Matter interacts via the gravitational force which is why the WIMPs are supposed to have a large mass. Although there is no direct evidence for a “weak interaction” of Dark Matter so far, many experiments are based on the assumption that Dark Matter is weakly interacting, due to a phenomenon called the “WIMP miracle”.

In the early universe Dark Matter (and other particles) pair production and annihilation was in equilibrium. At a certain point in time, the expanding universe became too large and too cold to sustain the pair production so that the overall amount of Dark Matter particles would decrease and eventually vanish. This is illustrated in figure 1.4a. To prevent the total annihilation and to explain the presence of Dark Matter in our universe today, something has to suppress the annihilation process. The continued expansion of the universe leads to a freeze-out of the amount of Dark Matter. The figure shows a stop in DM annihilation at different amounts of Dark Matter in the universe which are directly connected to the annihilation cross-section σ_A . It turns out, that σ_A has to be of the order of a weak interaction to maintain the observed amount of Dark Matter.

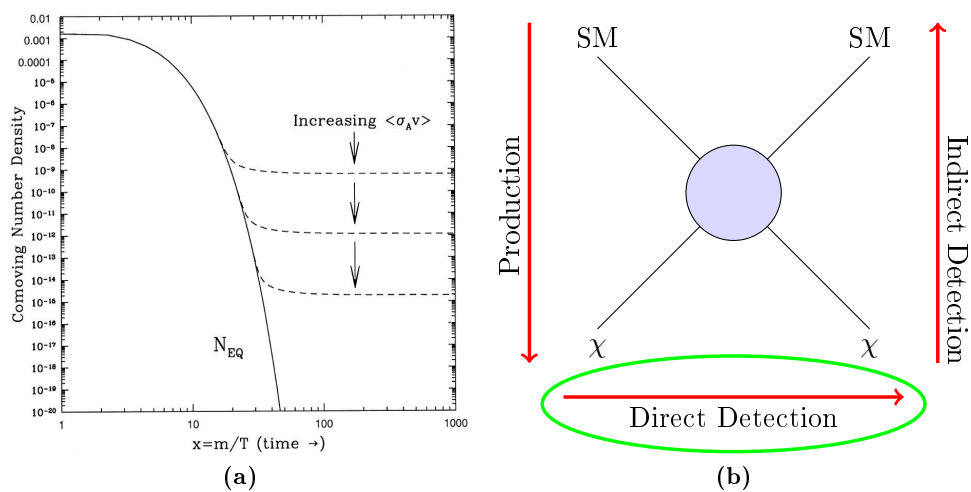


Figure 1.4: (a) WIMP miracle [6]: With time the universe expands and cools down until the thermal equilibrium for DM production and annihilation can not be further sustained and DM only annihilates. The decrease in DM is stopped at a certain size depending on the annihilation cross-section σ_A of the DM. Considering the estimated amount of DM in our universe, σ_A is of the order of a weak interaction cross-section. Figure (b) shows possible detection modes for DM: Production of DM particles at accelerators, indirect detection of DM annihilation products and the direct detection of a DM particle interacting with normal matter.

The WIMP theory allows to search for Dark Matter from different perspectives as is indicated in figure 1.4b. The figure shows a Feynman diagram with a non-specific interaction between four particles. The red arrows are the respective time lines for a certain interaction. A first approach shown on the left downwards is the collision of two SM particles in an accelerator experiment to create DM particles (“Production”). The second approach “Indirect Detection” is the reverse on the right upwards, searching for the SM particles like gamma-rays from DM annihilations. Indirect searches are conducted using large earthbound gamma-ray telescopes or satellites examining cosmic rays.

The third approach called “Direct Detection” is drawn from left to right and shows the

scattering of a DM particle on a SM particle via a weak interaction process. The different methods to examine this scattering process are discussed in the following section.

1.3 | Direct Search for Dark Matter

1.3.1 | Backgrounds and Interactions in Dark Matter Detectors

Direct Dark Matter detection is based on the weak interaction of a Dark Matter particle with normal matter from the Standard Model. To detect such an interaction with a very small expected cross-section, other interactions have to be avoided or at least identified as background events. Therefore experiments for direct Dark Matter searches are preferably installed in underground laboratories, as for instance the LNGS in Italy, where, amongst others, the XENON1T experiment is located. The placement beneath mountains or in deep mines ensures a natural shielding of the cosmic radiation. For XENON1T, the muon flux at the experimental site is reduced to a total flux of less than $3 \cdot 10^{-8} \text{ cm}^{-2}\text{s}^{-1}$ [16].

Other sources of background radiation have also to be taken into account: Natural radioactivity from elements, such as uranium, can induce background signals in Dark Matter detectors. To minimize the amount of these background events, Dark Matter detectors are surrounded by different kinds of shielding materials, such as copper, polyethylene, lead and water. In XENON1T, for example, a large water tank equipped with photomultipliers even allows to discriminate signals from muon-induced neutrons in the detector itself, by detecting the responsible muon from its Cherenkov radiation in the watertank.

Discrimination is a key word for Dark Matter detection. Since WIMPs (and also other Dark Matter candidates) do not interact via the electromagnetic force, only interactions with the detection medium nuclei are possible. These are so-called “nuclear recoils” (NR), that can also be caused by neutrons (which therefore have to be either vetoed or shielded). The counterpart interaction is the “electronic recoil” (ER) from particles interacting with the detection medium shell electrons. This interaction is via the electromagnetic force and thus only occurs if the incident particle is a charged particle such as an electron or if it is a photon itself. Being able to distinguish between electronic and nuclear recoils provides the means to discriminate a large part of background signals and increases the detector sensitivity.

1.3.2 | Overview on Direct Search Experiments

The methods used in direct detection experiments can be very different, as quantities such as scintillation light, ionization charge and heat or phonons, respectively, can be measured. Some experiments even measure several of these quantities simultaneously. Figure 1.5 relates a selection of direct Dark Matter detectors to their specific

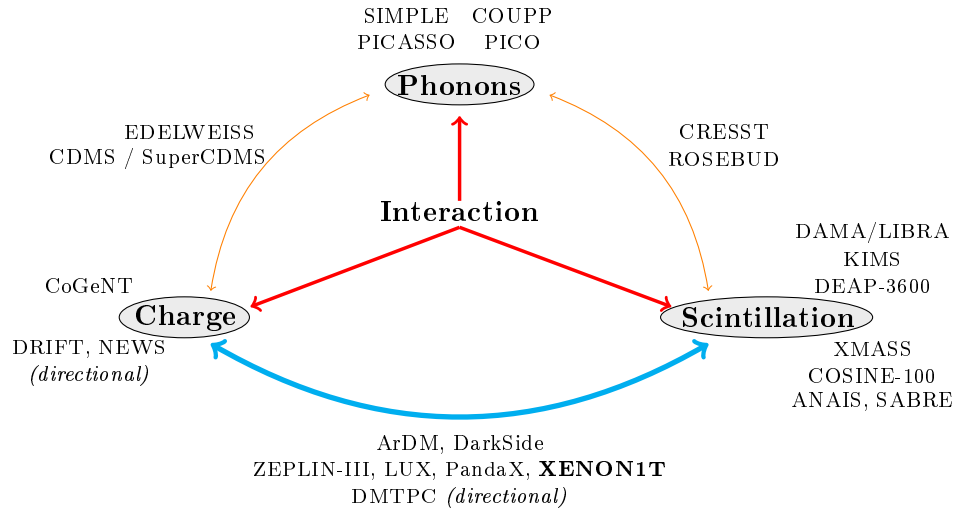


Figure 1.5: Different experiments for direct Dark Matter search, sorted by the physical quantity used for the detection of the interaction. Basically, each experiment detects either a charge signal, scintillation light or phonons in the detection medium. Many detectors are designed to measure a combination of two signals, as for instance the dual-phase xenon time projection chambers which can detect scintillation light as well as charge from the interaction.

measurement channels. In the following, the different types of experiments are briefly introduced.

Scintillation-only detectors Two of the prominent experiments searching for scintillation signals from Dark Matter particles are the DAMA/LIBRA [17], employing NaI(Tl) crystals, and KIMS [18], using CsI(Tl). The DAMA/LIBRA collaboration, former DAMA/NaI, is the first experiment to have claimed the discovery of a Dark Matter signal, namely a predicted annual modulation of the measured detector signal which arises from the Earth’s motion through the galactic Dark Matter halo. The discovery has not been verified by any other experiment up to today, although CoGeNT found a similar annual modulation signal. Instead, other experiments (e.g. CDMS, XENON) measured the parameter space with a higher sensitivity without finding a signal, rejecting the interpretation of the signal as a light WIMP.

Cryogenic detectors The CoGeNT experiment uses a single germanium crystal at liquid nitrogen temperature to measure ionization signals. It measured a similar annual modulation signal as DAMA/LIBRA [19].

SuperCDMS (former CDMS) [20] and EDELWEISS [21] measure both the ionization signal and the deposited heat in their experiments. Both use germanium detectors at a few mK to minimize the vibrations of the crystal lattice and measure the ionization with electrodes attached to the crystals. The phonon detection for SuperCDMS

is done with the help of tungsten transition edge sensors and for EDELWEISS-III, the latest experimental stage, with germanium thermistors. The combined ionization and phonon measurement allows discrimination between nuclear and electronic recoil events. Cryogenic experiments such as CRESST [22], using CaWO_4 crystals, and ROSEBUD [23] which uses several different scintillating bolometers, employ photosensors for the scintillation signals and superconductors at the transition temperature to measure the deposited heat as a change of resistance. The ratio of light to phonons allows electronic recoil discrimination.

Superheated liquid detectors use materials such as C_2ClF_5 or C_4F_{10} to create unstable droplets that undergo a transition to the gas phase when a scattering particle causes a critical increase in temperature. The resulting phonons are measured with microphones. Experiments using this type of detector are SIMPLE [24], PICASSO [25] and COUPP [26], the latter two eventually merged to construct the PICO detector [27].

Directional Dark Matter detectors aim not only to identify a Dark Matter signal but also to measure the origin direction of the incoming particle.

Experiments such as DMTPC [28] or DRIFT [29] use low pressure gas time projection chambers with CF_4 gas or a CF_4 and CS_2 gas mixture, respectively. The ionization trail from a recoil event can be used to reconstruct the scattering particle trajectory.

A planned detector called NEWS will consist of solid detectors made of a nuclear emulsion. In comparison the low pressure gas experiments, the ionization trajectories will be much shorter, in the order of hundreds of nanometers [30].

Noble gas detectors The noble gas detectors can be divided in two large groups dependent on the detection medium: argon and xenon. This type of experiments represents the most sensitive direct Dark Matter detectors to date.

The DEAP experiment uses a single-phase liquid argon detector to measure the scintillation light. Electronic recoils discrimination is done by analyzing the signal pulse shape. Other experiments are constructed to run in a dual-phase mode, these include the ArDM detector (which was operated in single-phase liquid mode only up to now) [31] and the DarkSide-50 detector [32].

Representatives for xenon-based experiments are XMASS [33], ZEPLIN-III [34], LUX [35], PandaX [36] and XENON1T [37]. With the exception of the liquid xenon detector XMASS, all of these employ dual-phase time projection chambers.

The technique of dual-phase xenon time projection chambers is discussed in the next section.

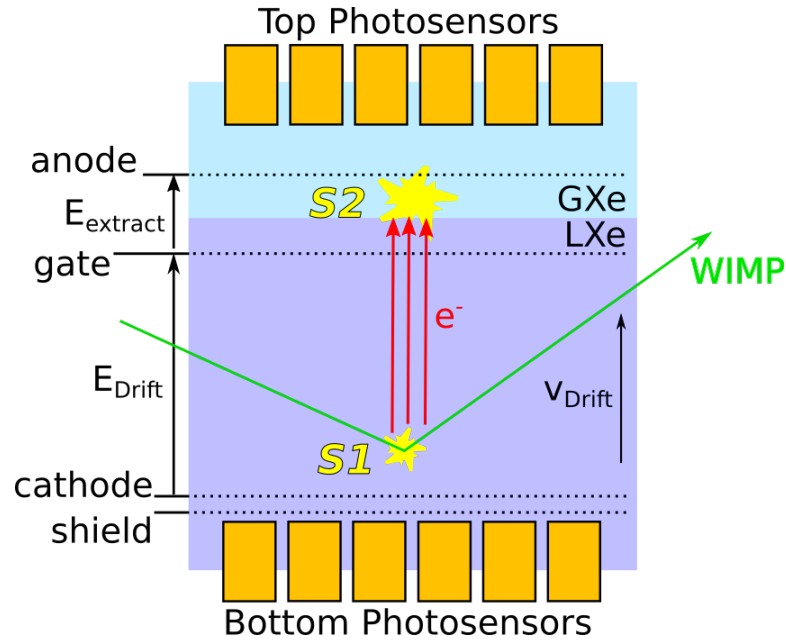


Figure 1.6: Sketch of the TPC principle: A dual-phase TPC consists of a liquid phase and a gaseous phase above. Photosensors at the top and at the bottom allow the detection of scintillation signals. A particle (here: WIMP) scatters in the liquid xenon phase and deposits energy in form of prompt scintillation light $S1$ and ionization. The released electrons are drifted upwards and extracted to the gas phase with applied electric fields and generate a secondary scintillation signal $S2$, proportional to the number of electrons. The electric fields are generated using a series of meshes on different electric potentials, labeled “anode”, “gate” and “cathode”, according to their respective function. A “shield” mesh is added here, which protects the bottom photosensors from the high voltage of the cathode.

1.3.3 Principle of a Dual-Phase Xenon Time Projection Chamber

The basic structure of a dual-phase xenon time projection chamber (TPC) is sketched in figure 1.6. It consists of a volume that is partially filled with liquid xenon (LXe), the upper part contains gaseous xenon (GXe). From the top and the bottom, arrays of photosensors, as for example photomultiplier tubes (PMTs), can detect light signals from particle scatter interactions.

A particle, e.g. a WIMP, scattering in the liquid xenon deposits energy in the form of a prompt scintillation signal which is called $S1$. Additionally, the interaction leads to ionization and free electrons. The physical processes of LXe scintillation and ionization are discussed in detail in section 2.3.1.

The $S1$ scintillation signal is measured with the photosensors. To collect the charge information, the electrons are extracted to the gas phase and are accelerated in an electric field to create a secondary scintillation signal $S2$ proportional to the charge released in the scatter interaction. For this, the TPC is equipped with three metallic electrode meshes called the cathode, gate and anode mesh which are set on different

potentials, as indicated in figure 1.6. In some setups, a fourth mesh acting as a shield is placed below the cathode mesh.

Between the cathode and the gate mesh a homogeneous electric drift field is generated that drifts the electrons from the interaction point upwards. The electrons reach drift velocities in the order of 10^3 m/s in liquid xenon depending on the field strength [38]. The drift velocities achieved with the MainzTPC are discussed in section 8.1.

The second “stage” is the field between the gate and the anode mesh which is called the extraction field. This field has two responsibilities: First, it extracts the drifted electrons from the liquid phase to the gaseous phase. Second, the electrons in the gaseous phase are accelerated by the field and create proportional scintillation, the $S2$ signal. For a complete electron extraction, the field needs to exceed a field strength of ~ 5 V/cm [39]. The generation of the $S2$ signal also requires a minimum field strength E at a given pressure p : $\frac{E}{p} \sim 1.315 \text{ kV cm}^{-1} \text{ bar}^{-1}$ [40].

To achieve a sufficiently large field strength, the gate and anode mesh are placed at a smaller distance. Also, the relative electric permittivities of xenon are $\varepsilon_{\text{GXe}} \approx 1$ in the gas phase [41] and $\varepsilon_{\text{LXe}} = 1.95$ in the liquid phase, respectively [42]. Therefore, the transition to the gaseous xenon leads to a field strength increased by a factor of 1.95 compared to the value in liquid.

The shielding mesh below the cathode mesh is grounded and shields the lower PMT array from the high negative voltage on the cathode. Actually, the anode mesh acts similarly for the upper PMT array, being also set to ground. (In case of a positive potential being used for the anode mesh, an additional shielding mesh above the anode should be considered.)

In general, only the cathode and gate mesh are set to high voltages.

In conclusion, a dual-phase xenon TPC can measure the scintillation response as well as the charge response of the interaction. The readout of the two signals $S1$ and $S2$ is useful in several aspects:

Depending on the interaction, different ratios of light and charge can be expected. As illustrated in figure 1.7a, a particle scattering on the electron shell of a xenon atom leads to more ionization and released electrons – and hence a larger $S2$ signal in comparison to the $S1$ signal – than a particle depositing the same amount of energy scattering off a xenon nucleus. The charge-to-light ratio $\frac{S2}{S1}$ therefore can be used as a discrimination tool which is shown in figure 1.7b.

Furthermore, the signals can be used to reconstruct the interaction position in the TPC volume. This ability is powerful since it allows to define a fiducial volume inside the TPC or to examine where certain event populations in the detector are located. The reconstruction is done in two steps:

1. The interaction depth z can be calculated with the time between the signals $S1$ and $S2$, taking into account the electron drift velocity corresponding to the applied electric field.
2. For the x - y -position, an array of multiple photosensors at the top of the TPC is needed to obtain a spatial distribution of the $S2$ signal.

Calculation of the electric fields in the TPC

The strength of the drift field can be calculated using the formula

$$|\vec{E}_{\text{drift}}| = \frac{U_{\text{drift}}}{d_{\text{drift}}} \quad (1.1)$$

with U_{drift} being the potential difference between cathode and gate mesh and d_{drift} the distance.

The determination of the electric field between the gate and the anode mesh is complicated since the transition from the liquid to the gas phase has to be taken into account. The liquid level between the two meshes has a large influence on the electric field strength.

Figure 1.8 shows schematically the region between anode and gate mesh, with the liquid-gas surface dividing the volume in between. The electric field strength of the extraction field between the two meshes in vacuum is $|\vec{E}_{\text{vac}}| = \frac{U_{\text{ext}}}{d}$, with U_{ext} being the applied potential difference between the gate voltage U_G and the anode voltage U_A . Since the anode mesh was set to ground ($U_A = 0$), it is $U_{\text{ext}} = U_G$. For the calculation of the electric field strengths in each medium, that means $|\vec{E}_{\text{liquid}}|$ between gate and liquid-gas

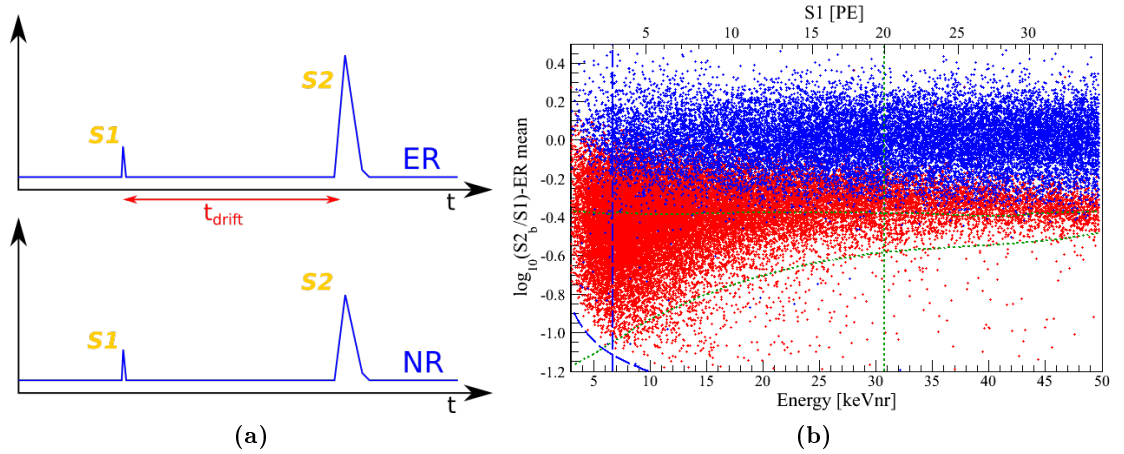


Figure 1.7: Particle discrimination: Depending on the type of interaction of a particle with xenon, a different ratio between initial scintillation $S1$ and proportional scintillation $S2$ is produced. The respective signals are sketched for electronic (ER) and nuclear recoil (NR) in (a). Using calibration sources in XENON100 [43], the ratio of $S2/S1$ (here the logarithm of the ratio) can be used to distinguish ER and NR (b): The blue data points represent the ER, the NR data is shown in red. The vertical dashed blue and dotted green lines mark the benchmark limits in energy for the WIMP search, with a more constricted benchmark window marked by the vertical green dotted line. The horizontal green dotted line indicates the cut in $S2/S1$, excluding 99.75 % of the ER background. The rising dotted green line depicts the 97 % quantile for the NR. These for lines enclose the signal region used for the WIMP search. The blue line in the lower left edge shows the minimum signal cut in $S2$.

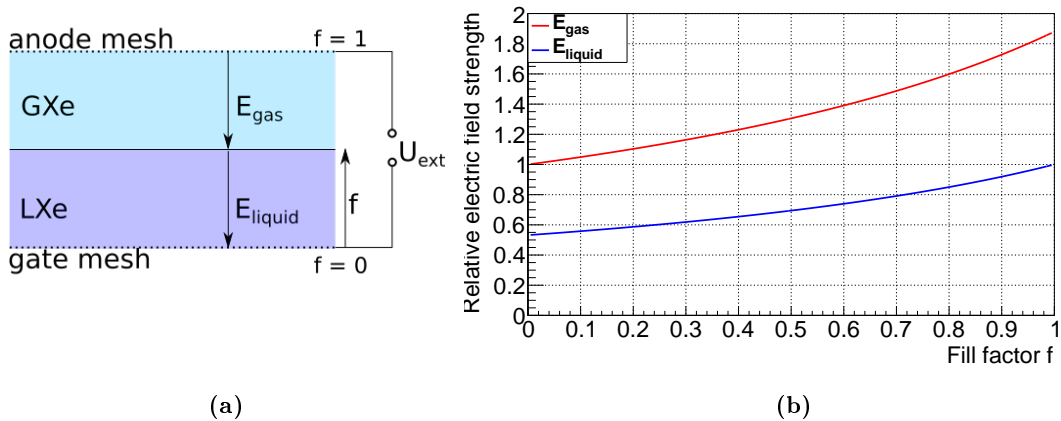


Figure 1.8: The electric field between the gate mesh and the anode mesh is dependent on the liquid level. (a) shows a sketch of the region between the meshes. The factor $0 \leq f \leq 1$ denotes the filled share of the gap between the meshes. In (b), the relative electric field strength as compared to the field in vacuum is shown for both the liquid and gaseous phase in dependency of the fill factor f .

interface as well as $|\vec{E}_{\text{gas}}|$ between the liquid surface and the anode mesh, the following formulae¹ apply:

$$|\vec{E}_{\text{liquid}}| = \frac{\varepsilon_{\text{GXe}} \cdot |\vec{E}_{\text{vac}}|}{\varepsilon_{\text{GXe}} \cdot f + \varepsilon_{\text{LXe}} \cdot (1 - f)} \quad |\vec{E}_{\text{gas}}| = \frac{\varepsilon_{\text{LXe}} \cdot |\vec{E}_{\text{vac}}|}{\varepsilon_{\text{GXe}} \cdot f + \varepsilon_{\text{LXe}} \cdot (1 - f)} \quad (1.2)$$

Here, ε_{LXe} and ε_{GXe} are the relative permittivities of liquid and gaseous xenon as mentioned above. The factor f is the fill factor as depicted in figure 1.8a, which can vary between 0 and 1 and refers to the liquid fraction between the gate and the anode mesh. As can be seen in figure 1.8b, the change in liquid level has an impact on the electric fields in both the liquid and the gaseous phase.

1.3.4 Current Status of Direct Dark Matter Searches and Outlook

Figure 1.9 shows the exclusion curves for the WIMP cross-section dependent on the WIMP mass. WIMP models with parameters above this curve are rejected with a 90% confidence level (C.L.). In addition, the estimated exclusion limits of upcoming direct Dark Matter detectors employing xenon as detector material are shown. The most sensitive detectors will eventually be limited by the neutrino background [44].

The experiments setting the most stringent limits to date are LUX [35], PandaX [36] and XENON1T [45], which are all xenon dual-phase time projection chambers. The latter currently provides the lowest limit for a WIMP cross-section of $4.1 \cdot 10^{-47} \text{ cm}^2$ at $30 \text{ GeV}/c^2$ after an exposure time of 278.8 days and will improve in sensitivity during its continued operation.

¹See section A.1 for the formula derivation.

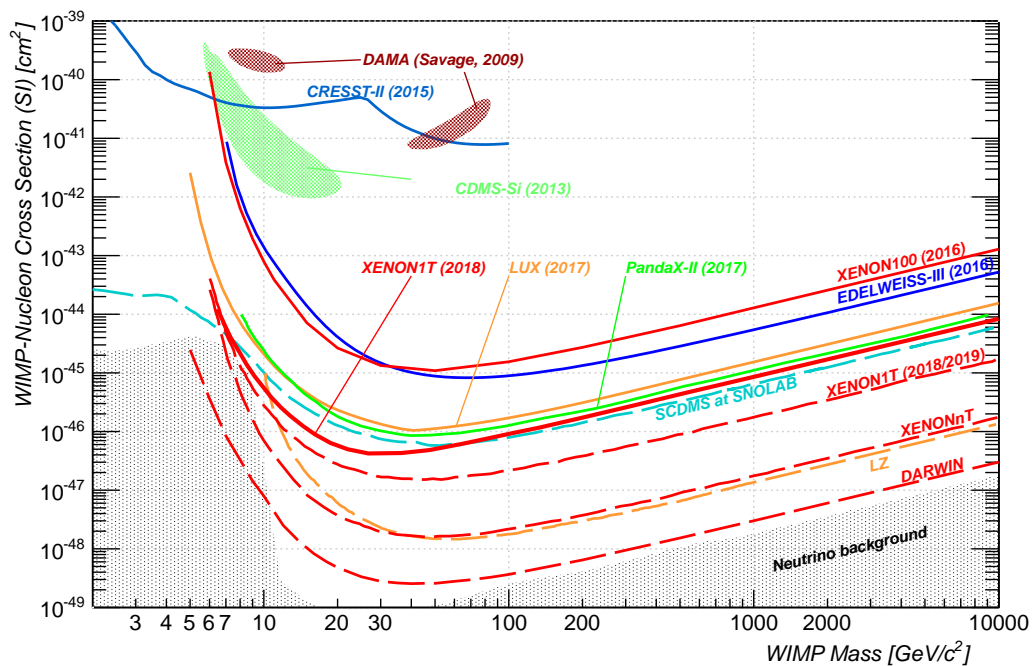


Figure 1.9: Experimental sensitivity (90 % C.L.) to spin-independent WIMP-nucleon interaction for different direct Dark Matter experiments: The lowest limits in sensitivity are currently set by XENON1T in 2018 [45]. The results of LUX (2017) [35] and PandaX-II (2017) [36] show similar sensitivities. Also shown are the latest results from XENON100, EDELWEISS-II, CRESST-II and the discovery contours of DAMA/LIBRA and CDMS-Si, which were taken from [46]. The estimated exclusion limits of upcoming xenon-based experiments are depicted with dashed lines: XENON1T [37], LZ [47], XENONnT [48] and DARWIN [49]. In black, the neutrino background limiting the WIMP detection is shown [44].

At present, four experiments have been started to test DAMA/LIBRA’s claim of a Dark Matter signal. The experiments ANAIS [50], SABRE [51] and COSINE-100 [52], which is a collaboration of the groups of KIMS-NaI [53] and DM-Ice [54], employ NaI(Tl) detectors, as did DAMA/LIBRA, to have a model-independent cross-check of their findings. These measurements will not push the limits of direct Dark Matter search to smaller WIMP cross-sections, but aim to support or reject the Dark Matter signal controversy.

The DarkSide collaboration plans a successor of their dual-phase argon TPC DarkSide-50 to a 20 ton-scale. The new detector, labeled DarkSide-20k, is estimated to reach a sensitivity of $7.4 \cdot 10^{-48} \text{ cm}^2$ ($6.9 \cdot 10^{-47} \text{ cm}^2$) for a $1 \text{ TeV}/c^2$ ($10 \text{ TeV}/c^2$) WIMP, given a 10 year exposure time [55].

For the xenon-based Dark Matter detectors, the groups of ZEPLIN and LUX plan a joint detector called LZ [47], which aims to achieve a maximum sensitivity of $3 \cdot 10^{-48} \text{ cm}^2$ for WIMP masses of $100 \text{ GeV}/c^2$ in its final stage with 20 tons of target material.

Compared to this, XENON1T will reach a sensitivity of around $2 \cdot 10^{-47} \text{ cm}^2$, before it is upgraded to XENONnT with a target mass up to 7 tons [56]. XENONnT is estimated

to improve the sensitivity by one order of magnitude down to $1.6 \cdot 10^{-48} \text{ cm}^2$ for WIMP masses of $x \text{ GeV}/c^2$ [48].

A successor of XENONnT is the planned DARWIN detector, aiming for examining cross-sections of a few 10^{-49} cm^2 for WIMP masses of $50 \text{ GeV}/c^2$ and also small WIMP masses down to $5 \text{ GeV}/c^2$. DARWIN is foreseen to employ a total of 50 tons of xenon, with 40 tons being active target material [49].

Liquid Xenon as Detection Medium

Chapter 2

2.1 | Xenon as a Detection Medium

Xenon is the heaviest stable noble gas, with a standard atomic mass of 131.293(6) u [57] and an atomic number of 54. It is a rare element, with an abundance in the Earth's atmosphere of 86 ppb by volume [58] and is mostly obtained by fractional distillation.

Isotope	Abundance (by mass)	half-life
^{124}Xe	0.095 %	$> 4.8 \cdot 10^{16}$ yr
^{126}Xe	0.089 %	-
^{128}Xe	1.910 %	-
^{129}Xe	26.401 %	-
^{130}Xe	4.071 %	-
^{131}Xe	21.232 %	-
^{132}Xe	26.909 %	-
^{134}Xe	10.436 %	$> 1.1 \cdot 10^{16}$ yr
^{136}Xe	8.857 %	$2.165 \cdot 10^{21}$ yr

Table 2.1: Xenon isotopes, natural abundance and half-life decay times [59].

Natural xenon consists of a variety of isotopes, which are either stable or very long-lived, as shown in table 2.1. Synthetic isotopes have half-lives in the order of hours or days at the most [60], therefore they can be neglected in the long run. This leads to a very low natural radioactivity of xenon. Additionally, as xenon is a noble gas, it also has a very low chemical reactivity. Together, this means that intrinsic signals have a small probability to occur, which is an advantage in low-background experiments.

Since the intrinsic radioactivity of xenon is very low, background signals emerge primarily from noble gas impurities in the detection medium, such as ^{85}Kr , which represents one crucial background source in xenon detectors [61].

From table 2.1 one can also extract that natural xenon consists of even and odd nuclei in almost equal proportions, specifically 52.4 % isotopes with even number of nucleons. These atoms have nuclei in which all nucleons are paired and the resulting spin is zero. On the other side, approximately 47.6 % have an odd number of nucleons and therefore an unpaired nucleon. Those atomic nuclei have a resulting spin. This property of xenon allows to probe spin-dependent as well as spin-independent interactions with the same detection medium.

Considering the macroscopic properties of xenon, at standard conditions of 0°C and 1 bar it is a gas with a density of $\rho_{\text{Xe,gas}} = 0.005897 \frac{\text{g}}{\text{cm}^3}$ [62]. However, the density of liquid xenon is $\rho_{\text{Xe,liquid}} \approx 2.943 \frac{\text{g}}{\text{cm}^3}$ at $T = 165$ K, decreasing slightly with temperature, as is shown in figure 2.1a [63]. The advantage of this large density value, together with the large atomic number $Z = 54$, is a self-shielding effect of liquid xenon detectors, such that particles from the outside interact in the peripheral regions of the xenon volume,

while only particles with small interaction cross-sections can reach the center. This allows the definition of a fiducial volume, if the detector provides an event position reconstruction. Also, using a liquid instead of a cryogenic solid detector medium is greatly superior when scaling to large detector masses.

To use xenon in its liquefied form as a detection medium, it is necessary to control its pressure and its temperature while cooling it. At standard pressure, the melting point lies at $T_{\text{melt}} = 161.4 \text{ K}$, while the boiling point is found at $T_{\text{boil}} = 165.051 \text{ K}$ [58]. Compared to other noble gases such as argon, which have lower melting and boiling temperatures, less cooling power is necessary. Therefore, liquid xenon detectors are typically operated in the range of about 1.5 to 2.5 bar. Still, the small temperature range for liquid xenon requires a stable cryogenic system.

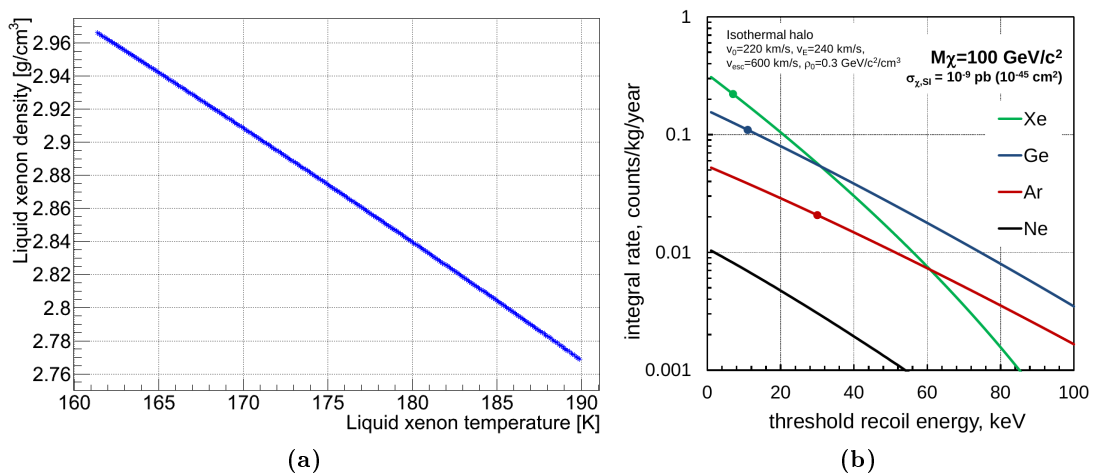


Figure 2.1: Left: Liquid xenon density in dependence of the xenon temperature. Data taken from NIST ([63]). Right: Expected WIMP rates in different mediums for WIMPs with a mass of $100 \text{ GeV}/c^2$ and a spin-independent cross-section of $\sigma_{\chi, \text{SI}} = 10^{-9} \text{ pb}$ [39].

Another reason to use xenon as a detection medium is the expected event rate in dependency of the recoil energy. Figure 2.1b shows the total event rate for WIMPs for different target materials, with xenon having the highest expected event rate for low-energy recoils.

The calculation of the expected WIMP rate can be done using the following equation, giving the differential event rate in events/keV/day [64]:

$$\frac{dR}{dE_r} = \frac{\rho_0}{m_N m_\chi} \int_{v_{\text{min}}}^{\infty} v f(v) \frac{d\sigma_{WN}}{dE_R}(v, E_R) dv \quad (2.1)$$

with E_r being the recoil energy of the target nucleus, ρ_0 the local WIMP density, m_N and m_χ the masses of the nucleus and the WIMP, respectively, $f(v)$ the velocity distribution for the WIMPs and $\frac{d\sigma_{WN}}{dE_R}(v, E_R)$ the differential cross-section for the scattering process between a WIMP and a nucleus. Since most of these quantities are yet unknown, the event rate for the scattering of WIMPs can only be estimated to a certain extent.

2.2 | Scattering of Particles in Liquid Xenon

As a dense medium, liquid xenon can be used as a target material for various scattering processes depending on the incident particle type. Charged particles such as electrons interact via the electromagnetic force, as do gamma-rays. Neutral particles on the other hand only interact via the nuclear forces.

2.2.1 | Interactions of Photons with Xenon

Depending on their energy, photons interact differently with xenon. This can be seen in figure 2.2 which shows the cross-sections for different interactions for an energy range between 1 keV and 10 MeV. The total cross-section is the sum of the different interaction types of photoabsorption, the Compton effect and pair production.

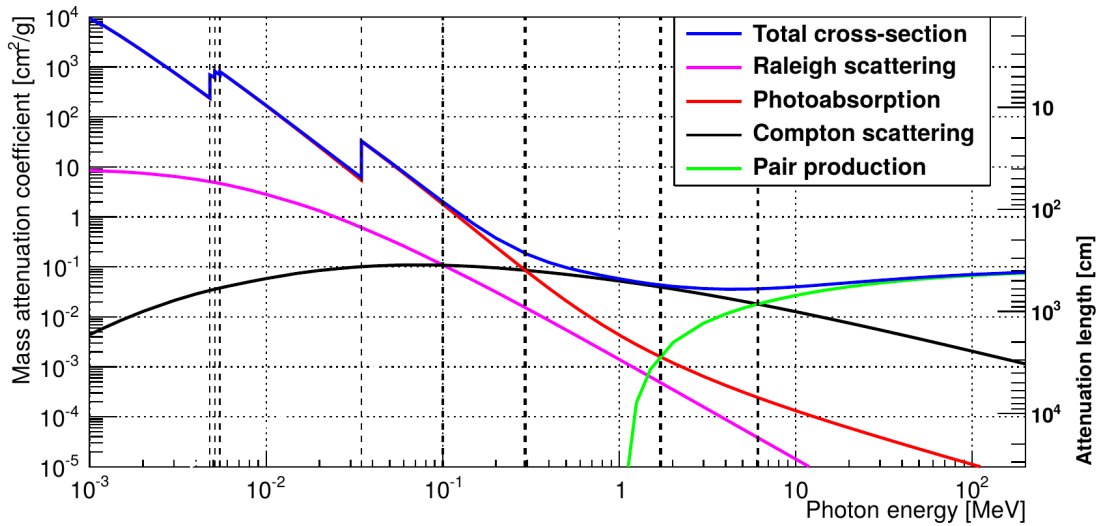


Figure 2.2: Cross-sections for different photon interactions with xenon: For low energies, photoabsorption (as well as Raleigh scattering) is the dominant interaction. On the left of the graph, the absorption edges for the individual atomic shells are visible. Above 300 keV, Compton scattering is the most probable process, eventually surpassed by pair production for energies higher than ca. 6.1 MeV [65].

In the total cross-section, which is equivalent to the photoabsorption cross-section for lower energies, the different electronic shells are prominently visible as steps. While the L-shell has energies of 4.78 keV, 5.11 keV and 5.45 keV (L_3 , L_2 , L_1), the K-shell is at 34.56 keV [66]. If the energy of the incident photon is above the K-shell, 86 % will be absorbed by K-shell electrons. Of these interactions, 87.5 % result in characteristic X-ray emission and 12.5 % in the release of K-Auger electrons. The remaining 14 % of incident photons interacting with the higher atomic shells will also cause characteristic line emissions and low-energy Auger electrons, but since the respective energies are very low, the emitted fluorescence is reabsorbed in close vicinity of the interaction point,

which makes these processes quasi “radiationless” [67].

Low-energy photons can be absorbed completely by shell electrons in atoms, which results in the ionization of the atom. This mechanism is called the photoelectric effect. Also Raleigh scattering plays an important role for energies below about 100 keV.

On the other side, at photon energies above 1.022 MeV, which is twice the rest mass of the electron, a photon near an atomic nucleus can produce an electron-positron pair. For even higher energies, this particle-antiparticle pair receives additional kinetic energy. Pair production becomes the dominant photon interaction process in xenon above energies of approximately 6.1 MeV.

The interaction which is most interesting in this experiment is the Compton effect. It primarily occurs at medium photon energies between 300 keV and several tens of MeV. This information is important, as it influences the choice of radioactive source that is used in the measurements. The photon scatters off a shell electron which is kicked out of the shell and gains kinetic energy from the energy deposit ΔE . For large energy deposits $\Delta E \gg E_b$, which is the binding energy, Compton scattering can be approximated as elastic scattering off a free electron. The latter is discussed in section 2.2.2. The case of small energy deposits is addressed in section 2.2.3. The photon loses this energy and therefore has a larger wavelength after the scattering.

2.2.2 Compton Scattering in Liquid Xenon - Electronic Recoil in the Free Electron Approximation

Electrons and gamma-rays scatter on the electron shell of the xenon atoms, which is sketched in figure 2.3a. Here, we want to concentrate on the gamma-ray scattering off electrons which is called Compton scattering. The interaction with the electronic shell is predestined to excite and even ionize the atom, for larger energy deposits this can lead to a cascade of excited and ionized atoms with a cloud of free electrons.

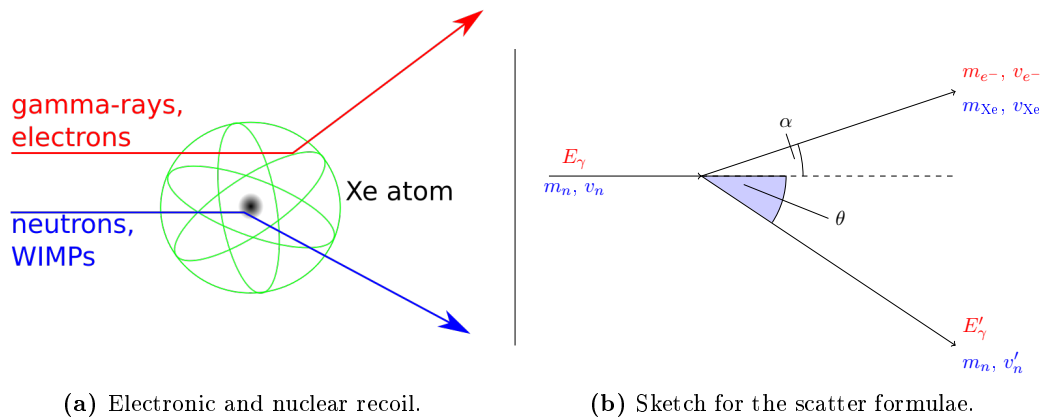


Figure 2.3: (a) Sketch of particles scattering on xenon, indicating electronic and nuclear recoil. (b) Sketch for the derivation of the Compton and neutron scattering formulae in the laboratory frame.

Using the quantities provided in figure 2.3b, one can derive the Compton formula from the laws of energy and momentum conservation:

$$E' = \frac{E_0}{1 + \frac{E_0}{m_0 c^2} (1 - \cos \theta)} \quad (2.2)$$

This formula is only valid for a free electron at rest [68], with E_0 being the incident photon energy, E' the scattered photon energy, m_0 the electron mass and θ the scattering angle between incident and scattered photon. The difference between incident and scattered photon energy can be used to calculate the energy deposit:

$$\Delta E = E_0 - E' = E_0 \left(1 - \frac{1}{1 + \frac{E_0}{m_0 c^2} (1 - \cos \theta)} \right). \quad (2.3)$$

Using a germanium detector allows the direct measurement of the scattered photon energy with a better energy resolution than from the scatter angle measurement. In conclusion, the measurement of the scattering angle is only used as an orientation. More information on this can be found in the author's diploma thesis [69].

The incident photon energy E_0 is known from the gamma-ray source spectrum. Thus, with the scattered photon energy E' measured by a germanium detector, the deposited energy is obtained simply by the energy difference:

$$\Delta E = E_0 - E' \quad (2.4)$$

2.2.3 | Compton Scattering off Bound Electrons

As mentioned in the previous section, the description of Compton scattering is different for free electrons compared to strongly bound electrons. The impact of the nuclear potential on shell electrons depends on the number of protons in the nucleus as well as the electronic shell in the atom: For electrons in atoms with a low number of protons Z or electrons in the outer shells of high- Z atoms, the free electron approximation can be considered to be valid, since the atomic binding energy E_b in these cases is much less than the kinetic energy transferred to the struck electron by the Compton interaction [70].

Equation (2.5) includes the binding energy term in the calculation of the deposited energy. The formula shows that for low-energy deposits $E_0 - E'$ this term can have a significant impact.

$$\Delta E = E_0 - E' - |E_b| \quad (2.5)$$

For xenon, the binding energies for the different electron shells are listed in table 2.2. The K-shell electrons are most tightly bound with an energy $E_b = 34.561$ keV. In comparison, the electrons in the M shells or higher already have binding energies below 1 keV.

Compton scattering on K-shell electrons leads to a recombination signal which is of the

State	Energy [keV]
K 1s	34.561
L ₁ 2s	5.453
L ₂ 2p _{1/2}	5.107
L ₂ 2p _{3/2}	4.786
M ₁ 3s	1.149
M ₂ 2p _{1/2}	1.002
M ₃ 2p _{3/2}	0.941
M ₄ 3d _{3/2}	0.689
M ₅ 3d _{5/2}	0.676
N ₁ 4s	0.213
N ₂ 4p _{1/2}	0.147
N ₃ 4p _{3/2}	0.146

Table 2.2: Atomic binding energies for electrons in ${}_{54}\text{Xe}$ [66].

order of the binding energy E_b . The place in the K-shell where the electron has been struck and released is filled up with an outer shell electron. Depending on the origin of the recombinating electron, the resulting energy line can have slightly different values: The $k\alpha$ X-ray lines are at energies of 29.461 keV and 29.782 keV, the $k\beta$ X-ray energies show the values 33.562 keV, 33.624 keV and 34.419 keV. Alternatively, an Auger electron can be released with an energy of 24.6 keV [60].

These lines were used in [70], [71] and other experiments for measuring the Compton scattering off bound electrons in different target materials. By triggering on a coincidence between the X-ray signal and the scattered photon one can make sure that the scattering involved a bound electron.

For the Compton scattering with outer shell electrons, the value for the deposited energy ΔE is not affected to the same extent. Still, the electron being bound in a potential and having a certain momentum plays a role when applying the Compton formula (2.2). The unknown direction of the bound electron momentum leads to an uncertainty in the angular measurement of the deposited energy. To account for this uncertainty, the electron momentum distribution has to be added to the Compton formula [72]:

$$p_z = -m_0c \frac{E_0 - E' - E_0E'(1 - \cos\theta)/m_0c^2}{\sqrt{E_0^2 + E'^2 - 2E_0E' \cos\theta}} \quad (2.6)$$

The quantity p_z is referred to as ‘‘Compton profile’’. It leads to an effect called ‘‘Doppler broadening’’ when measuring the deposited energy using the Compton scattering angle (see also [69]).

2.2.4 | Neutron Scattering in Liquid Xenon - Nuclear Recoil

A neutral particle such as a neutron (or a WIMP) does not interact with the electrons in the atomic shell, but only scatters off the nucleus (see also figure 2.3a). This means that less free electrons can be expected from such a scattering process. Since the nucleus has a higher mass than electrons, also the impact on the surrounding atoms is limited to a smaller region in the liquid.

The scattering process of WIMPs should be similar to the one of neutrons, therefore neutron scatterings in liquid xenon are of great interest for calibration. The kinematics can be derived with the quantities shown in figure 2.3b, with E_n being the energy of the incident neutron, m_n the neutron mass and m_{Xe} the mass of the xenon nucleus.

The energy deposit ΔE for neutron scattering in xenon depending on the scattering angle θ is:

$$\begin{aligned} \Delta E &= E_n \frac{2m_n^2}{(m_n + m_{\text{Xe}})^2} \left(\frac{m_{\text{Xe}}}{m_n} + \sin^2 \theta - \cos \theta \sqrt{\frac{m_{\text{Xe}}^2}{m_n^2} - \sin^2 \theta} \right) \\ \Rightarrow \Delta E &\approx E_n \frac{2m_n m_{\text{Xe}}}{(m_n + m_{\text{Xe}})^2} (1 - \cos \theta) \quad \text{for } m_{\text{Xe}} \gg m_n \\ &\approx 1.5 \cdot 10^{-2} E_n (1 - \cos \theta) \quad \text{with } m_{\text{Xe}} = 131.293 \text{ u}, m_n = 1 \text{ u} \end{aligned} \quad (2.7)$$

The derivation of this formula can be found in detail in [69].

2.2.5 | Energy Measurement in Scatter Experiments

In section 2.2.2, two different ways to measure the energy deposit in the xenon for Compton scattering are described. In both cases the scattering photon is emitted by a gamma-ray source, scatters in the xenon and is then measured in a secondary detector.

- In an ideal direct measurement, the scattered photon is absorbed completely in a secondary detector with very good energy resolution, for example a germanium detector. The deposited energy is calculated using formula (2.4).
- Since the energy resolution of many detectors is quite poor, it is also possible to measure the energy deposit from the scattering angle, using formula (2.3).

The uncertainty of the second method is highly dependent on the setup conditions, especially the position resolution of the secondary detector. In general, a good angular resolution leads to a significant loss in solid angle for the experiment, which in turn limits the event rate. Therefore, a direct measurement is favored if the energy resolution is sufficient.

For the neutron scattering, formula (2.7) provides a measure for the energy deposit also

depending on the scattering angle. Also, a direct energy measurement is possible but even more costly for neutron detectors than for photon detectors. As an alternative, the neutron energy can be determined with a third method: Time-of-Flight (TOF). To determine the energy of the scattered neutron, the time difference between the scattering interaction and the detection in the secondary detector is measured. Together with the distance between the two interaction positions one can calculate the mean velocity of the neutron. The energy is determined with the following formula:

$$E'_{\text{neutron}} = (\gamma - 1)m_n c^2 \quad \text{with} \quad \gamma = \frac{1}{\sqrt{1 - \frac{v^2}{c^2}}} \quad (2.8)$$

For the TOF method, the neutron energy has to be measured before and after the scattering process. The difference in energy corresponds to the energy deposit ΔE in the liquid xenon.

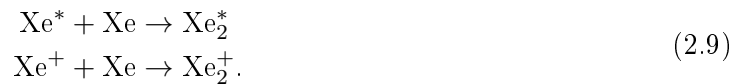
2.3 | Liquid Xenon Scintillation and Ionization

2.3.1 | Underlying signal processes

Although the scatterings of particles off the electronic shell or the atomic nucleus are quite different from each other, none of these interactions is limited to only one xenon atom. The energy that is deposited by the scattering particle usually results in a cascade of xenon atoms that are affected.

Energy deposits from interactions of particles in liquid xenon lead to either excited or ionized states of the respective xenon atom. In the latter case, shell electrons are freed. Since each interaction involves multiple atoms, both atom states will be present, their abundance being dependent on the interaction type.

Both the excited and the ionized xenon atom can bond with a ground state xenon atom, forming excimers Xe_2^* ("excited dimers") or ionized dimers Xe_2^+ .



Ionized dimers can recombine with the free electrons, forming additional excimers and releasing heat:



The excimers deexcite to the ground state of 2 xenon atoms by emission of a photon with a wavelength of 178 nm (VUV radiation).



Since this radiation comes from an excimer energy level which is not present in normal xenon atoms, the xenon is transparent for these photons. The information on the

processes is taken from [73].

Figure 2.4 summarizes the scintillation and ionization processes in a schematic and shows that each branch finally leads to a scintillation signal. The signal resulting from the deexciting excimers is a prompt signal which occurs directly after the interaction. That is why it is labelled “primary scintillation” or $S1$.

The scintillation signal from the free electrons in liquid xenon does not occur naturally like the $S1$ signal. Instead, an electric field is needed to extract the electrons from the liquid xenon to the gas phase. Since the gaseous xenon has a lower relative permittivity, which leads to a higher electric field, the extracted electrons are accelerated and induce scintillation in the gaseous xenon. The signal is delayed in time due to the electron drift time in the liquid, that is why it is called “secondary scintillation” or $S2$.

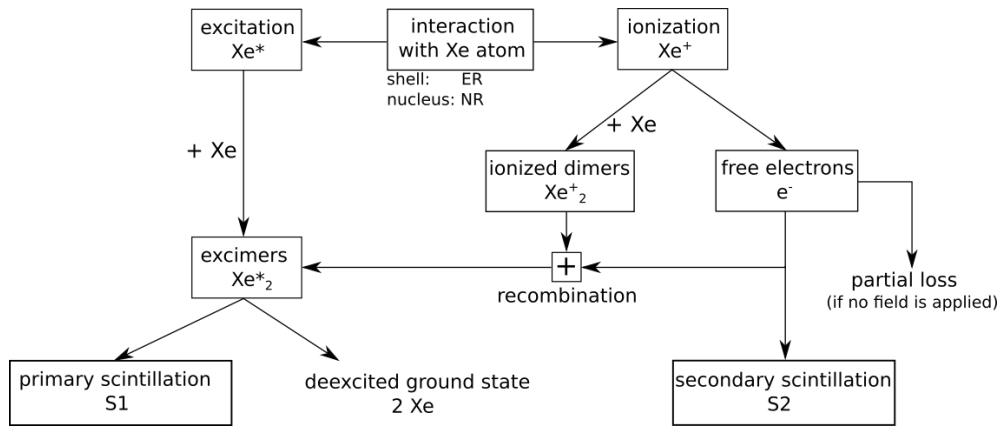


Figure 2.4: Scheme of the scintillation and ionization processes in LXe after an energy deposit by a scattering particle.

In the absence of an electric field, the electrons from the ionization process remain at the interaction point as a charge cloud and can recombine with the ionized dimers. In case an electric field is applied, this situation changes. If the electrons are drifted away from their ionized partners, less $S1$ light is produced eventually. On the other side, the electric field is necessary to generate an $S2$ in the first place. That means that both scintillation signals are anti-correlated.

The loss in $S1$ light due to an applied electric field is called “field quenching”.

2.3.2 | Anti-Correlation of Light and Charge Signal

In the scattering interaction in LXe, the energy deposit E_{deposit} is distributed partly to scintillation light and to free charge in form of released electrons. The theoretical model sketched in the following can be found in detail in [74].

The energy deposit in liquid xenon can be described by a simple Platzman equation:

$$E_{\text{deposit}} = N_{ex}W_{ex} + N_iW_i = N_i(\alpha W_{ex} + W_i) \quad \alpha = \frac{N_{ex}}{N_i} \quad (2.12)$$

N_{ex} and N_i are the number of excitons and ions, respectively, which are created by the interaction. The values W_{ex} and W_i are the work functions or the energy necessary to create an exciton or ion. Depending on the ratio α , the energy deposit leads to different amounts of excitons and ions relative to each other. For liquid xenon, α was experimentally determined to be 0.06. The total number of quanta can be assumed to be roughly constant for a given energy. The numbers of excitons and ions, N_{ex} and N_i , are linked to the number of photons N_{ph} and the number of electrons N_e released in the interaction:

$$N_{ph} = N_{ex} + r \cdot N_i \quad N_e = N_i(1 - r) \quad (2.13)$$

The parameter r is the probability for electrons to recombine with the ions. The recombining electron-ion pairs contribute to the number of photons. From this it is obvious that the light and charge signals in a dual-phase xenon TPC are anti-correlated. The more electrons are released, the less energy is available for the generation of scintillation photons and vice versa.

Plotting the $S2$ signals in dependence of their corresponding $S1$ signals should result in bar-shaped, slightly elliptical event distributions for the individual energy lines of the gamma-ray source, situated between high $S2$ values for low $S1$ and low $S2$ values for high $S1$. Figure 2.5a gives an example of the anti-correlated event distribution for a TPC measurement with ^{133}Ba , conducted by the MiX experiment [75]. The event structures corresponding to the individual energy lines are marked and can be identified as tilted, elliptical distributions. Especially the distribution for the 356 keV line is prominently visible. Considering the width in either $S1$ or $S2$, the energy resolution for this gamma-ray line is quite poor, as the value of $S1$ for example ranges between 2000 and 3500 p.e. Furthermore, only taking into account the spectrum of the $S1$ or $S2$ signal makes the identification of individual lines impossible for gamma-ray sources with more than one distinct energy line, since the event distributions overlap in the $S1$ spectrum (see also section 9.4.1).

Figure 2.5b is a sketch from [76] illustrating the mathematical approach to measure the energy deposit in the TPC by combining the charge and light signal. In the sketch, the energy deposit is labelled ε_0 and can be found on both axes, the abscissa being the energy ε_s measured from scintillation light ($S1$) and the ordinate being the energy ε_q from the charge signal ($S2$). The energy distribution compared to the actual energy deposit ε_0 leads to a large uncertainty in energy with regard for both axes. The anti-correlation of the charge and light signal can be used to calculate the energy deposit from the combined signal by projecting the combined signal to a new energy axis ε'_c , according to equation (2.14). The combined signal has a smaller uncertainty, as indicated in the sketch. The angle θ has to be determined with a fit to the event distribution.

$$\varepsilon_c = \frac{\sin \theta \varepsilon_s + \cos \theta \varepsilon_q}{\sin \theta + \cos \theta} = \frac{\varepsilon'_c}{\sin \theta + \cos \theta} \quad (2.14)$$

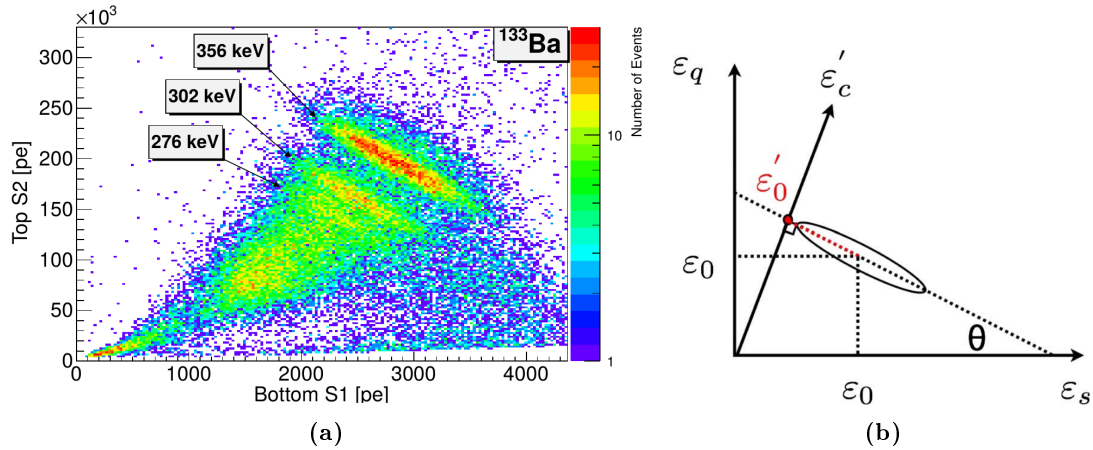


Figure 2.5: Example plot of the charge signal $S2$ versus scintillation signal $S1$ of a calibration measurement with ^{133}Ba conducted in [75] with the MiX TPC (a). The different gamma-ray lines can be identified as tilted, elliptical event distributions. The sketch in (b) shows how the event distributions can be used to determine the energy deposit with a very good energy resolution using a combination of both signals [76].

As a conclusion, the measurement of gamma-ray sources with only one distinct energy line would be necessary to avoid the stacking of event distributions in the $S1$ spectrum, allowing to identify the peak structure corresponding to the energy line. In any case, to get a reasonable energy resolution for the TPC calibration, the combined signals from scintillation and charge should be used instead of the broad distribution in only one of the signal spectra to account for the charge-to-light anti-correlation.

2.4 | $S1$ Pulse Shape in Liquid Xenon

Equation (2.11) describes the radiative decay of the Xe_2^* excimer to an unstable ground state. Depending on the energy involved, the excimer Xe_2^* can be present in different states of excitation. The two lowest excimer states are the singlet $^1\Sigma^+$ and the triplet $^3\Sigma^+$. The emitted scintillation light of both states can not be distinguished, but the respective lifetimes of singlet and triplet excimer differ by about an order of magnitude:

$$\tau_s = (2.2 \pm 0.3) \text{ ns} \quad \tau_t = (27 \pm 1) \text{ ns} \quad (2.15)$$

with the lowercase s and t referring to the singlet and triplet state, respectively. The lifetimes stated in equation (2.15) are taken from [77] and were measured using electrons to excite the xenon. As can be seen in figure 2.6a, the photon signal from the deexcitation is dependent on the time after the excitation. The light signal decreases rapidly in the beginning which corresponds to the singlet state decay, before the signal

shape becomes dominated by a slower decay constant from the triplet state. The values for τ_s and τ_t have been measured in various experiments, such as e.g. [78], but many findings do not agree with each other ($\tau_t = 45$ ns in [78]). A list of the conducted measurements and the discrepancies is found in [3].

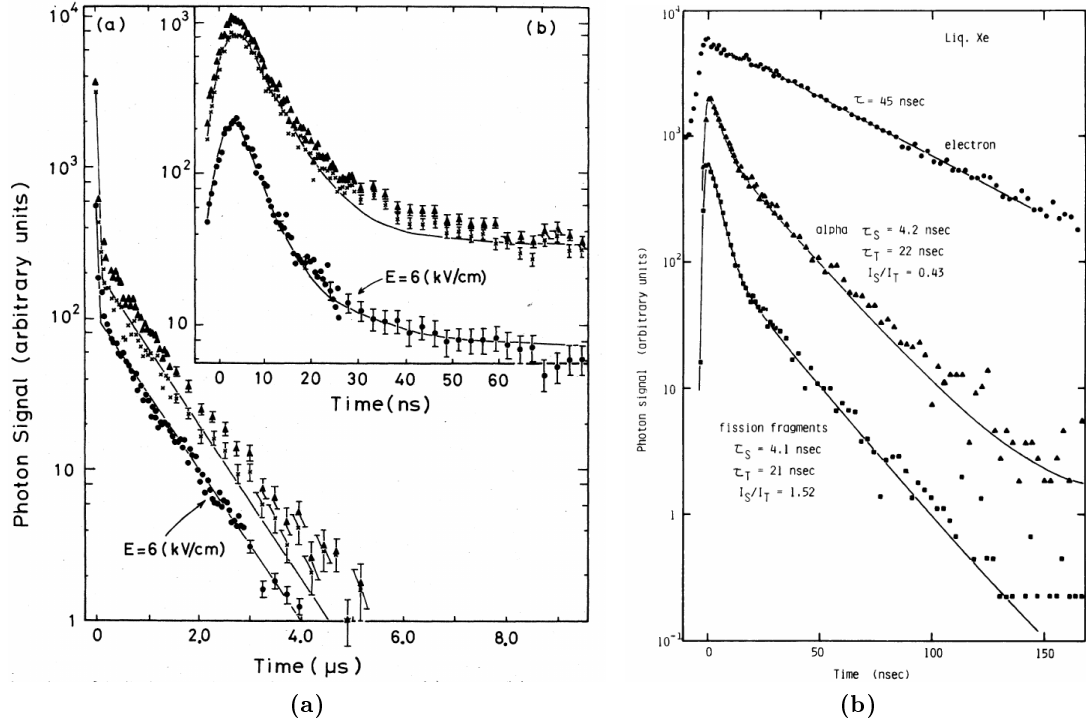


Figure 2.6: S1 pulse shape: (a) shows the deexcitation of liquid xenon after excitation with electrons for no applied field (upper graph) and an electric field of 6 kV. The change in photon signal due to suppressed electron recombination is visible, as well as the rapid signal decay in the beginning and the slower decay for longer measurement times. The graph is taken from [77]. (b) shows the photon signal decay for excitation by different particles (electrons, α -particles and fission fragments from ^{252}Cf). While the rapid decay is quite small for the electron data (upper line), the signal shape of the α -particle and fission fragment measurements is quite different. The graph is taken from [78].

Figure 2.6b depicts the pulse shape of signals caused by different particles. The shape of the uppermost signal emerging from scattering electrons differs significantly from the two lower signals, which are associated with α -particle and fission fragment scattering. This means that the type of interaction - electronic recoil from electrons or nuclear recoil from e.g. α -particles - has an impact on the signal shape.

For direct Dark Matter detectors employing xenon the measurement of the scintillation pulse shape therefore can be studied as a means of particle discrimination, since the latter is an important tool to increase the detector sensitivity (see section 1.3.1).

2.5 | Results of Low-Energy Electronic Recoil Measurements

The study of low-energy nuclear and electronic recoils in LXe has led to a series of experiments similar to the MainzTPC. The MiX experiment [75] in Michigan and the neriX experiment [2] in New York both used small dual-phase xenon TPCs to measure the light and charge response. The first was already mentioned in section 2.3.2 and has been used to measure the energy deposit from electronic recoils with high precision using both charge and light signal. The second one was dedicated to measure the light and charge yield of liquid xenon in dependence of the energy deposit and its results will be presented in this section. Complementary simulations were developed to predict the experimental results. The NEST model (Noble Element Simulation Technique) is an extension to the simulation software *Geant4*. Implementing the physical processes described in section 2.3.1 and taking into account the anti-correlation of the primary scintillation and the charge signal led to a theoretical model of the light and charge yield for nuclear and electronic recoils in LXe. This model is used as a comparison for the measured values from neriX and the MainzTPC (see section 9.6.1).

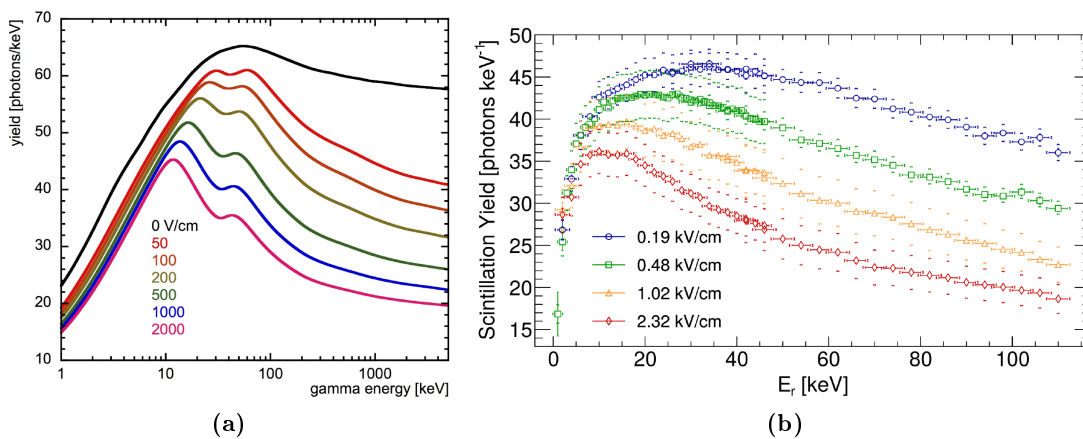


Figure 2.7: Light yield from (a) simulations with NEST [1] and (b) measurements with neriX [2], for comparison with the light yield determined with the MainzTPC. The literature light yield data is presented in scintillation photons per keV. Both simulation and measurement show similar shapes for the light yield curves. The light yield curves are discussed in the text.

The NEST simulation in figure 2.7a shows a steep rise of the light yield for energies below roughly 20 keV. The light yield then reaches a maximum in the case of no applied drift field (black) and then smoothly declines for higher energies. If a drift field is applied, the light yield shows a maximum around 20–30 keV which shifts to lower energies and a lower maximum light yield for increasing drift field. Subsequently, the light yield first decreases before exhibiting a second, smaller maximum between 100 and 50 keV, depending on the applied drift field, before declining. The light yield decreases stronger

with increasing drift field for high energies.

The measured light yield from the neriX experiment in figure 2.7b has a similar shape as the simulation by NEST. The steep rise of the light yield for low energies can be observed as well as the decrease of the light yield for higher energies, after a maximum situated around 20–30 keV of energy deposit. The overall decrease of light yield with increasing drift field is also visible. Contrary to the simulation, the double peak structures for the non-zero drift field curves are not prominent in the measured light yield data.

For the charge yield, both NEST and neriX also provide similar graphs, as shown in figure 2.8. Since primary scintillation and the charge signal are anti-correlated, the shape of the charge yield has an inverse shape as the light yield curves.

A steep decline in charge yield for small energy deposits is followed by the double peak structure in case of the NEST simulations, before the charge yield increases again. The minimum value can be found at the same positions as the light yield maxima described above. For higher drift fields, the charge yield shows larger values, as is expected since the applied electric field suppresses the electron recombination and leads to more electrons contributing to the charge signal.

The measured charge yield from neriX shows a similar shape, with a decline for the low energy regime, a minimum around 20 keV and a rising charge yield for larger energy deposits.

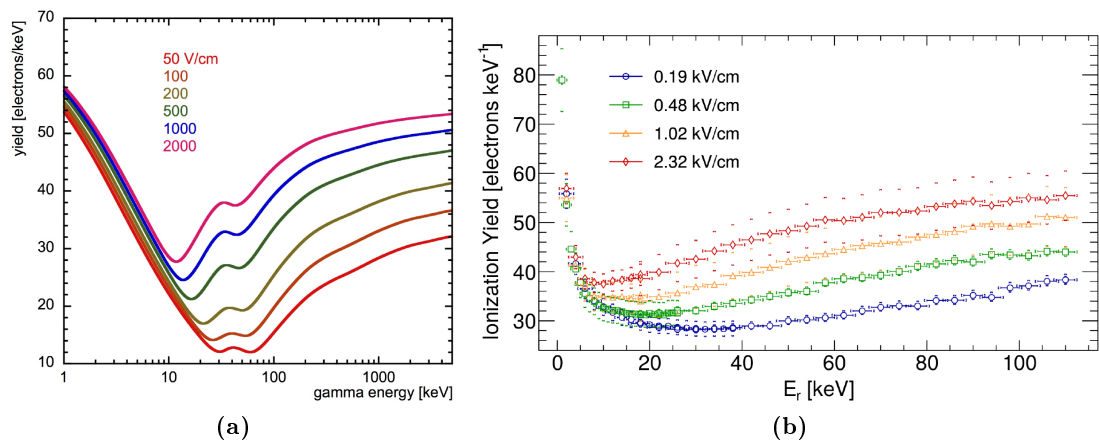


Figure 2.8: Charge yield from (a) simulations with NEST [1] and (b) measurements with neriX [2], for comparison with the charge yield determined with the MainzTPC. The literature charge yield data is presented in electrons per keV. Both simulation and measurement show similar shapes for the charge yield curves. The charge yield curves are discussed in the text.

Part II

THE MAINZTPC EXPERIMENT

MainzTPC - Experimental Setup

Chapter 3

The MainzTPC is an experiment which was designed and constructed in the course of two doctoral theses and several diploma and bachelor theses so far. Detector and infrastructure designs, the selection of suitable materials, key aspects in simulations and other programs were topics discussed in smaller or larger project groups to obtain optimal solutions and results.

This chapter will present the experimental setup which was designed, commissioned and used for measurements during my doctorate.

The design of the TPC itself and the surrounding cryogenic system are explained in more detail in [3]. Simulations for the Compton scattering as well as the realization of a Kapton-PCB based field cage [69] provided input for the TPC design. The gas system was designed and built during a diploma thesis [79], as well as the collimator and the rotatable stand for the germanium detector [80]. The bachelor theses [81] and [82] were focussed on the properties of the Avalanche Photodiodes (APDs) and Photo Multiplier Tubes (PMTs), respectively. Also, the slow control system programmed in [83] was extended and used as a monitoring tool in every test and measurement (see also section 3.3.4).

The main focus of my thesis concerning the setup is the data acquisition system, which will be presented in detail in chapter 4.

3.1 | Goals and Motivation

As described in section 1.3, direct Dark Matter searches with liquid xenon use the ratio between charge and light signal to distinguish between electronic and nuclear recoil. Measured events can be assigned to either type of signal for energy deposits above 5 keV, but for low-energy recoils, especially down to only a few keV, the distinction of these two types of interaction only by $\frac{S_2}{S_1}$ becomes more difficult. Figure 1.7b in section 1.3.3 shows that the bands for the two different interactions overlap for low energy deposits. The study of this effect with the Dark Matter detectors at hand is difficult due to the self-shielding property of xenon (section 2.1), since the liquid xenon is dense enough to stop low-energy particles already in the detector periphery.

The MainzTPC is designed to measure low-energy recoils down to an energy deposit of 1 keV in liquid xenon. It is optimized for Compton scattering, i.e. electronic recoil measurements, but can also be used to examine nuclear recoils from neutron scattering. The setup is predestined not only to study the difference between electronic and nuclear recoil for low-energy deposits, but also the response of charge and light signals for these low-energy events with high accuracy. To achieve this goal, several physics requirements have to be met which are discussed in section 3.2.

A second goal of the MainzTPC is the study of an alternative way to distinguish electronic from nuclear recoil, using the S_1 signal shape. For this, the S_1 signal is measured additionally with a fast FADC (Flash Analog-to-Digital Converter). The requirements

necessary for this measurement are discussed in chapter 4 in more detail especially when the data acquisition system is concerned.

3.2 | MainzTPC Specifications

The MainzTPC detector was designed from scratch with the goal to fulfill the physics requirements of the planned measurement. The working principle of a dual-phase xenon TPC is described in section 1.3.3. The MainzTPC has the same functionality as its larger counterparts XENON100 or XENON1T, but due to its smaller size, the detector setup has some distinctive differences. The materials and the shape of the detector structures had to be evaluated with regard to purity, low passive material mass, reduction of multiple scatterings etc. Details on the physical constraints are discussed in section 3.2.2.

3.2.1 | The Time Projection Chamber

The detector structure shown in figure 3.1 has a total height of 148.8 mm. The sensitive volume used for the measurement is located inside the brown cylinder in the lower center. The brown Kapton foil [84] is the back side of the electric field cage. This active volume has a height of 50.5 mm and a diameter of 52 mm. Compared to Dark Matter detectors, the MainzTPC is significantly smaller, which reduces its self-shielding properties drastically. This effect is intended, since it allows to study even low-energy deposits very closely in the center of the TPC. The small size is optimized for a single Compton scatter of gamma-rays in the active volume: For Compton scattering with ^{137}Cs with a gamma energy of 661.6 keV the scattering cross-section is $\sigma = 7.351 \cdot 10^{-2} \text{ cm}^2/\text{g}$ [65], which leads to a mean free path¹ of the photons of

$$\lambda_{\text{free}} = \frac{1}{\sigma \rho} \approx 4.72 \text{ cm.} \quad (3.1)$$

The exact value for the TPC diameter emerges from the diameter of the PMTs used in the experiment.

The detector structure is very filigree, which is also visible in the figures in the following sections. The idea behind this is that material surrounding the TPC can lead to particle scattering either before or after the interaction in the detector volume which means that the event is either lost or the inferred energy deposit is different from the real value. Therefore the amount of passive materials is minimized and the needed parts, such as the cryostat walls for example, are chosen as thin as possible.

As can be seen in figure 3.1, a large part of the detector consists of a white plastic material, which is polytetrafluoroethylene (PTFE). This material has a very good reflectivity

¹calculated for a xenon density of $\rho = 2.88 \text{ g/cm}^3$ at a temperature of 174 K (see figure 2.1a).

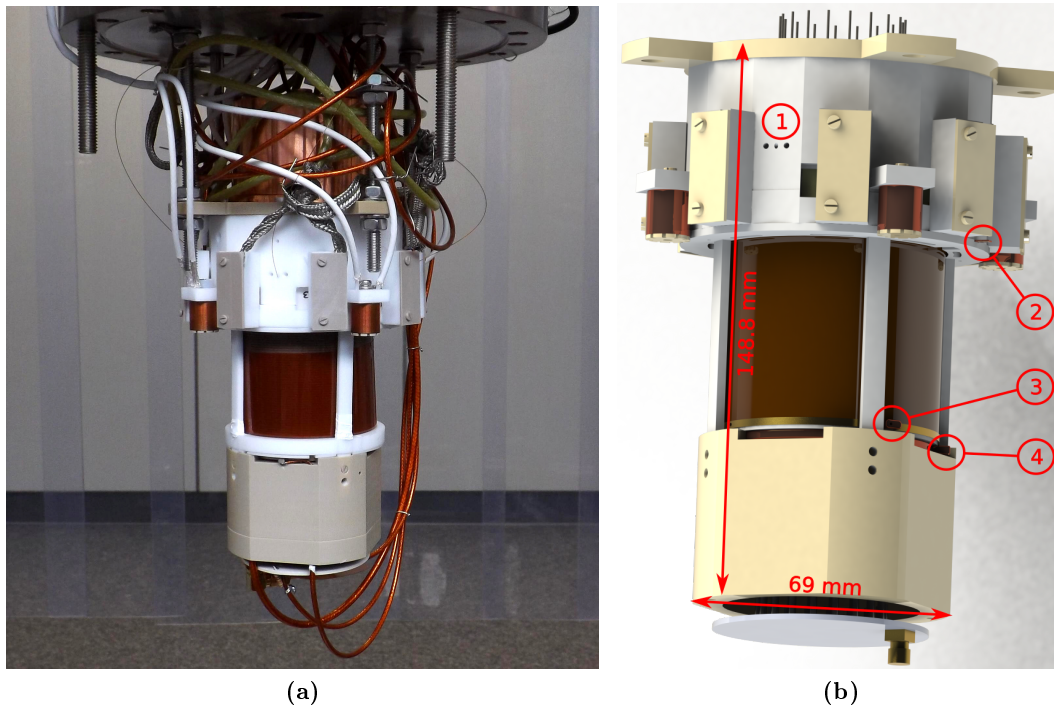


Figure 3.1: The MainzTPC detector: Figure (a) shows the detector during assembly in a clean room. All cables are conducted through an opening in the upper flange. Besides the cables, four thin optical fibers are installed in the MainzTPC structure, two of which are visible in this photograph. Figure (b) is a rendered CAD model which shows several of the APD connectors, three out of four levelmeters, the PTFE pillars to connect the holding structures of the two PMTs and the holes to insert the optical fibers for the photo-detector calibration (1). Furthermore the back side of the field cage can be seen as well as the connectors for the gate (2), the cathode (3) and the shield mesh (4). The connector for the anode mesh is situated on the other side of the TPC to avoid sparking between the anode and gate mesh connectors.

for VUV light and hence also for the xenon scintillation light. Therefore, the active volume is surrounded by a PTFE cylinder ((13) in figure 3.2) which itself is surrounded by the field cage. From a mechanical point of view, other materials are more suited for the detector structure, but the high reflectivity of PTFE is the crucial property. The reflection of the scintillation light enhances the Light Collection Efficiency (LCE) of the detector, and makes it more uniform. This leads to a higher energy resolution and a lower energy threshold.

Figure 3.2 shows a cut view of the MainzTPC as a rendered CAD model. Compared to larger xenon TPCs, the MainzTPC has only one PMT at the top (1) and the bottom (2), facing the active volume (4). While this maximizes the photo-detection area, these two PMTs cannot provide the information about the signal position in the x - y -plane. Instead, an array of eight APDs is placed around the detector region where the $S2$ is created (3). The relative signal strength measured with each APD provides the x - y

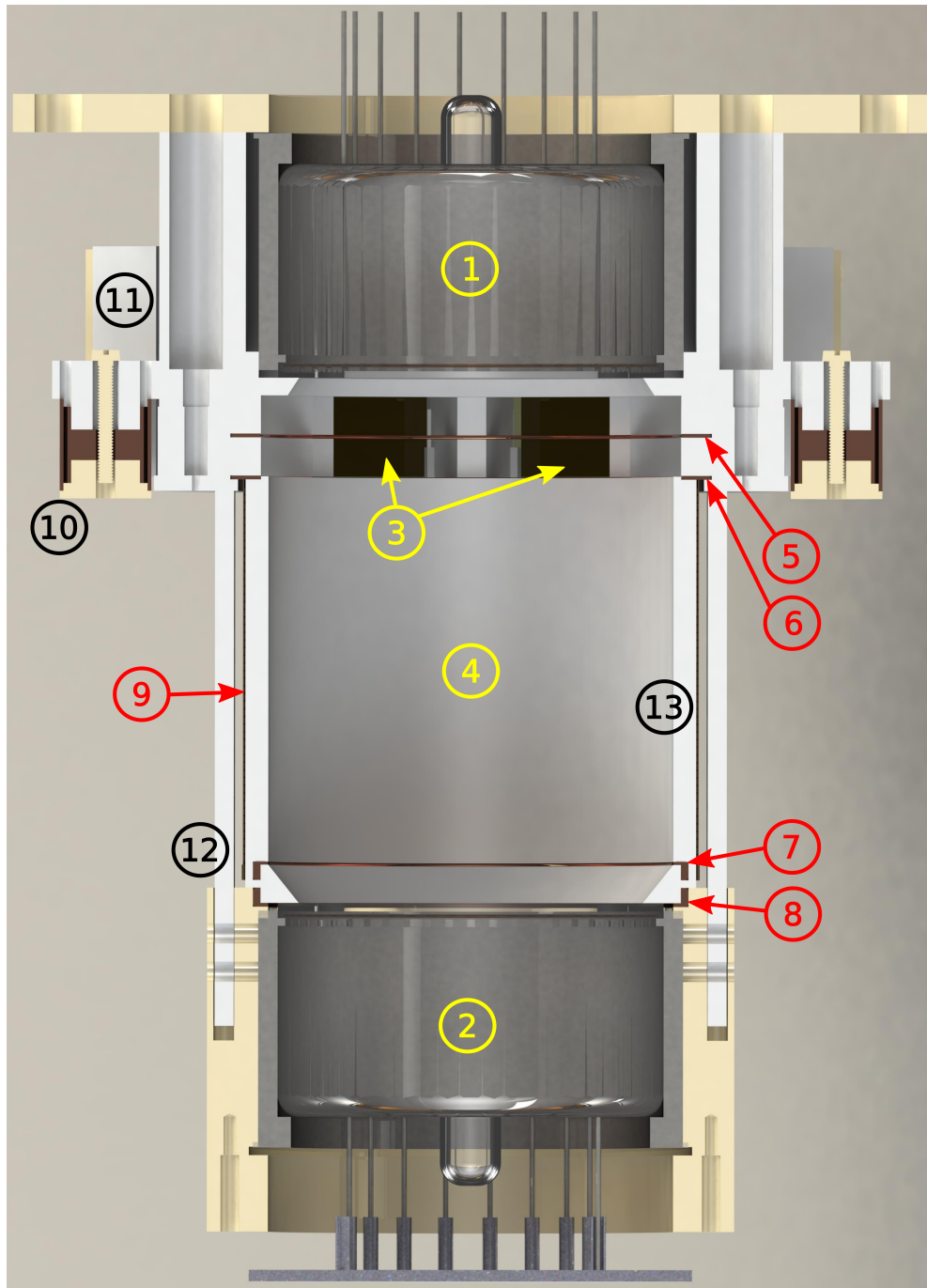


Figure 3.2: The MainzTPC - rendered cut view of a CAD model. The individual parts are marked with numbers: (1) Top PMT, (2) Bottom PMT (with base on its pins), (3) two of the eight APDs, (4) the active detector volume surrounded by a PTFE cylinder (13), (5) anode mesh, (6) gate mesh, (7) cathode mesh, (8) shield mesh, (9) field cage (on a very thin flexible printed circuit board around the PTFE cylinder), (10) levelmeter, (11) APD cable connector, (12) PTFE pillar as mechanical connection between the PMT holding structures. The color code was chosen to group the parts for the light collection in the TPC (yellow), the electric field generation (red) and outer parts (black). As for the materials, brown depicts copper, white PTFE and beige PEEK.

position. The PMTs and APDs are discussed in section 3.4.

To generate the electric drift field in the MainzTPC, copper meshes are installed (5-8). An innovation of this detector is the field cage (9) made of a flexible printed circuit board (PCB) which provides uniformity of the electric drift field. Optical fibers are inserted to the detector volume for photo-detector calibration (see figure 3.1). Levelmeters (10) made of two concentric cylinders measure the height of the liquid level between anode and gate mesh via capacitance. All these parts are explained in more detail in the following sections.

3.2.2 | Technical Constraints

The technical constraints for this experiment are manifold:

- The materials used inside the TPC, i.e. in direct contact with the xenon, have to be chemically pure. Otherwise, the detector elements might contaminate the xenon by outgassing, which can lead to light and charge loss, and hence a reduction of the detector performance (see also section 8.4).
- The photosensors used in the setup have to be functional at liquid xenon temperatures, which is around 165-185 K depending on the chamber pressure. Also, the materials of the detector structure must be chosen such that they withstand repeated cooling and rewarming cycles, and their thermal expansion coefficients must not differ too much from each other. The latter would lead to a distortion of the detector and the measured signals could not be interpreted properly since the reference of the detector dimensions would be missing.
- To restrict the choice of materials even further, one has to take into account that the photodetectors and especially the electric drift field are operated at high voltages. The detector structure must therefore also be electrically nonconducting to avoid shortcuts or sparks. This eliminates metallic materials for most of the detector structure.
- Ultimately, the detector structure also has to be mechanically stable enough to support all the detectors, electric meshes and the field cage. Additional constraints are imposed by accessibility, such that mounting and dismounting of the complete structure remains technically feasible.

In summary, the choice of passive and active elements composing the TPC is limited not only by their performance but also by their applicability in the liquid xenon environment. The physical demands on the detector structure and its materials constrict the number of possible materials even further.

3.2.3 Electric Fields and Electrodes Structures

As described in section 1.3.3, the electric fields in the TPC are mandatory for the creation of a secondary scintillation signal S_2 proportional to the released charge. The four metal meshes used for this in the MainzTPC, from top to bottom, are named anode, gate, cathode and shield mesh, according to their function. Their position inside the detector structure can be seen in figure 3.2.

The meshes consist of oxygen-free copper and have a diameter of 27.5 mm, not including their frames. They were electroformed and electropolished to achieve very fine wire structures. The individual wires have a thickness of 14 μm and are 268 μm apart from each other. This results in an optical transparency of 88 %, as stated by the manufacturer Precision Eforming [85] (mesh type MC20).

The distance between the cathode mesh and the gate mesh, which generate the electric drift field, is 50.5 mm. To get an impression of the different voltages applied and the resulting electric fields, table 3.1 lists the drift field configurations used in the measurements that are discussed in the analysis chapter of this thesis.

U_C [V]	U_G [V]	ΔU [V]	E_{drift} [$\frac{\text{V}}{\text{cm}}$]	$E_{\text{drift}}^{\text{nom}}$ [$\frac{\text{V}}{\text{cm}}$]
4000	3000	1000	198.02	198
5000	3000	2000	396.04	396
6000	3000	3000	594.06	594
7000	3000	4000	792.08	792

Table 3.1: Voltage values applied during the measurements for this thesis and resulting values for the electric drift field between the cathode and the gate mesh. The distance between the two meshes is 50.5 mm. The supply voltages were very stable with fluctuations of about 5 V. The uncertainty of the drift field for a voltage error of $\Delta U_x = 5$ V is approximately 1 V/cm. For the remaining thesis, the drift field values from the last column, without the decimals, will be stated to account for the uncertainty.

Since the extraction field at the transition between the liquid and the gaseous phase has to be distinctively higher than the drift field, the gap between gate mesh and anode mesh has a width of only 5 mm. In general, only the cathode and gate mesh are set to high voltages, while the anode is set to ground potential. For the measurements examined in this thesis, the gate mesh voltage was always held constant at 3 kV. After determination of the liquid level and using equations (1.2), it is possible to calculate the strength of the extraction field in the liquid ($|\vec{E}_{\text{liquid}}|$) and the gaseous phase ($|\vec{E}_{\text{gas}}|$). The resulting field strengths are shown in section 7.4 in the analysis part.

Figure 3.3 shows photographs of the copper meshes that are mounted in the MainzTPC. The field meshes were chosen to be manufactured very thoroughly, not only in matters of material choice and the fineness of their granularity but also with regard to achieving and maintaining their shape such that the electric drift field is as uniform as possible. To improve this condition, a field cage for the drift field between the cathode and the gate mesh was designed and manufactured in [69] according to simulations from [3].

The field cage basically consists of a flexible printed circuit board (PCB) with 49 paral-

lel conduction lines. This flexible PCB is wrapped in the shape of a cylinder so that the conduction lines form complete circles which are only connected via $100\text{ M}\Omega$ resistors. Figure 3.4 shows a photograph of the PCB before wrapping it. The conduction lines are placed on the inside of the cylindrical field cage.

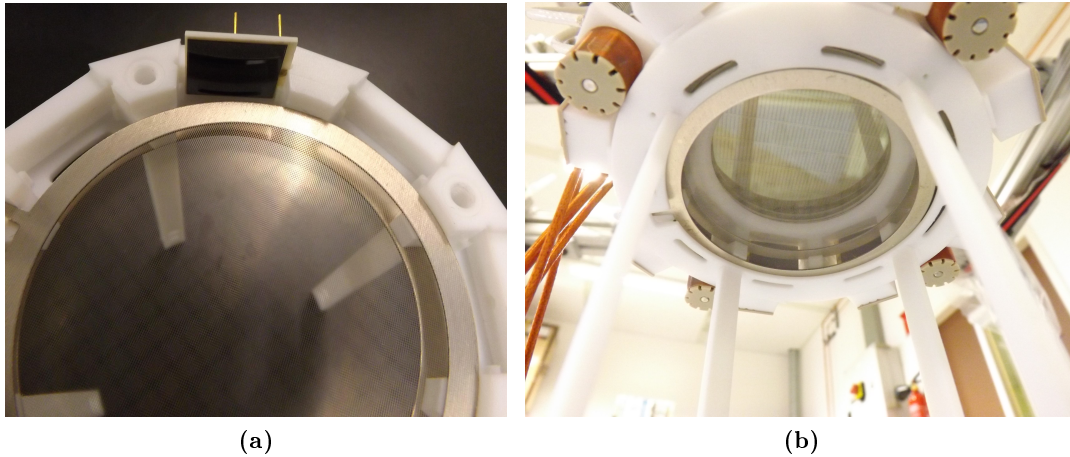


Figure 3.3: Meshes for the generation of the electric field in the MainzTPC: The electroformed and electropolished meshes were manufactured with a wire thickness of $14\text{ }\mu\text{m}$ and a wire pitch of $268\text{ }\mu\text{m}$. This leads to an optical transparency of 88% as stated in the specifications in [85] (mesh type MC20). The figures show the gate and the anode mesh, in (a) from above in the PTFE frame next to an APD, in (b) during the mounting process from below. Here, the upper PMT as well as the surrounding APDs in their slots can be seen through the transparent meshes.

3.2.4 | Levelmeters

Figure 3.5a depicts two of the four detector levelmeters of the MainzTPC. They are crucial to determine the liquid level in the TPC during operation. Measuring the liquid level in the TPC is important during the preparations for the experiment, particularly after the filling process.

The liquid-gas interface has to be at a stable height between the gate and the anode mesh, otherwise the electric field and therefore also the charge signal $S2$ are considerably affected. The choice of the liquid level can be used to tune the $S2$ amplification, keeping in mind the dynamic range of the detector before signal saturation.

Furthermore, a possible detector tilt can be recognized to avoid a varying liquid-to-gas ratio for different x - y -positions between gate and anode mesh. $S2$ signals from a tilted TPC would provide different signals for the same charge depending on the event position.

The four levelmeters of the MainzTPC are cylindrical capacitors. As can be seen in the CAD drawing in figure 3.5b, the levelmeters consist of two concentric copper cylinders.

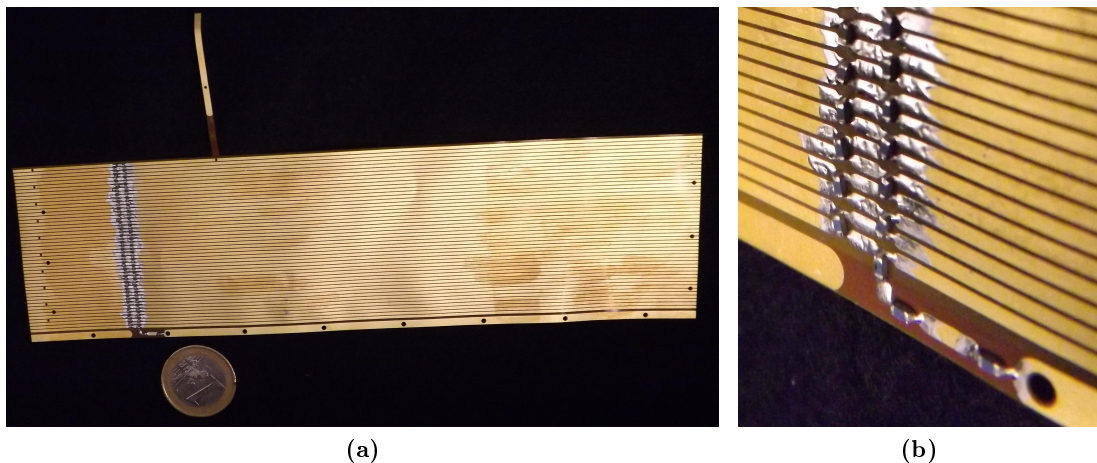


Figure 3.4: Electric field cage: A flexible PCB with parallel conduction lines as displayed in (a) is wrapped to a cylindrical shape. In this picture, a broader, lower conduction line can be seen at the lower edge of the PCB. This line provides the connection to the cathode mesh. The latch on the upper end is connected to the gate mesh voltage supply. The potential difference between the conduction lines is provided with resistors shown in (b). The field cage layout was developed in [69]. The resistor configuration, especially in the lower part visible in (b), is according to simulations from [3].

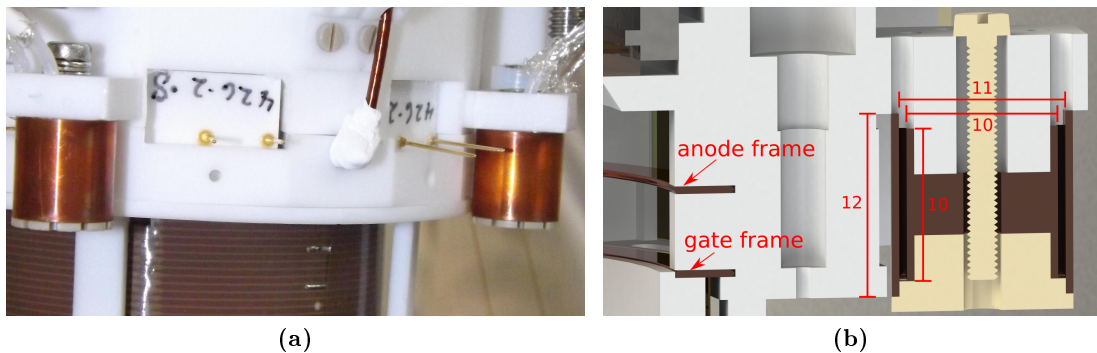


Figure 3.5: MainzTPC levelmeters: Two of the four levelmeters to measure the liquid level in the MainzTPC are displayed on the photograph in (a), which was taken during one of the detector assemblies. Between the two copper cylinders, the back sides of two APDs with their pin connectors are shown as well as the (isolated) connection to the anode mesh in the center. In (b), a cut view of a levelmeter from the MainzTPC CAD model is shown. The cut view includes the frames of the anode and gate mesh on the left. This demonstrates that the levelmeter range covers not only the distance between the meshes, but that it also starts a bit below the gate and ends above the anode.

The outer cylinder has an inner radius of $R_o = 5.5$ mm, while the inner cylinder has an outer radius of $R_i = 5.0$ mm. The height of the cylinders is $h = 10$ mm. The capacitance

C of a cylindrical capacitor is calculated as

$$C = 2\pi\epsilon_0\epsilon_r \frac{h}{\ln\left(\frac{R_i}{R_a}\right)} \quad (3.2)$$

with $\epsilon_0 = 8.854 \cdot 10^{-3} \frac{\text{pF}}{\text{mm}}$ the vacuum permittivity which is a physical constant and ϵ_r the permittivity of the medium between the cylinder walls of the capacitor. Knowing the permittivities of gaseous xenon $\epsilon_{\text{GXe}} = 1$ and of liquid xenon $\epsilon_{\text{LXe}} = 1.95$ (see section 1.3.3), one can calculate the values for a levelmeter filled with xenon gas (or basically “empty”) and with liquid xenon to find that the capacitance increases for the filled levelmeter.

The levelmeters were designed in [3] to be in a range of 5.84 - 11.44 pF for the empty and filled state, respectively, which is equivalent to a capacitance difference of $\Delta C = 0.560 \text{ pF/mm}$. This capacitance range can be measured with two readout boards called “Universal Transducer Interface” (UTI) boards, by Smartec [86]. Each of these boards is able to measure up to three capacitances in a range up to 12 pF without changing the setup. Since the MainzTPC has four levelmeters on the detector only, two UTI boards are included in the setup.

A fifth levelmeter is placed in the buffer volume of the cryogenic setup (see section 3.3.1), which has different dimensions than the TPC detector levelmeters to account for its purpose. It is also read out by one of the UTI boards. Since it is primarily used as a control sensor when filling the setup with xenon and not used in the analysis, it will not be discussed and is only mentioned for the sake of completeness. Further information can be found in [3].

Furthermore, it is possible to monitor the liquid level by using the gate and anode meshes as “plates” of a capacitor. This allows an additional measurement of the liquid xenon level between these two meshes.

Determination of the levelmeter capacitances

The measurement of the capacitances with the UTI boards is done using the three-signal technique explained in [87]. The UTI boards do not actually measure the capacitance values per se but the time T_x in clock cycles necessary to charge and discharge each capacitance. Therefore each measured value can be represented as

$$T_x = a_0 + a_1 \cdot C_x \quad (3.3)$$

Since the offset a_0 and a possible gain factor a_1 for a capacitance C_x are unknown, these two values have to be quantified and included in the determination of the unknown capacitance. This means that to obtain all required values, three measurements are necessary:

1. In a first measurement with $C_0 = 0$, the offset value $T_0 = a_0$ is determined.

2. Using a known capacitance C_{ref} as reference, a second measurement results in a time constant $T_{\text{ref}} = a_0 + a_1 C_{\text{ref}}$, which includes the unknown gain factor.
3. In the third measurement the time constant T_x for the unknown capacitance is found as stated in equation 3.3.

These three measurements put together allow the computation of the unknown capacitance relative to the reference capacitance:

$$\frac{T_x - T_{\text{off}}}{T_{\text{ref}} - T_{\text{off}}} = \frac{a_0 + a_1 C_x - a_0}{a_0 + a_1 C_{\text{ref}} - a_0} = \frac{a_1 C_x}{a_1 C_{\text{ref}}} = \frac{C_x}{C_{\text{ref}}} \quad (3.4)$$

$$C_x = \frac{T_x - T_{\text{off}}}{T_{\text{ref}} - T_{\text{off}}} C_{\text{ref}}$$

Each UTI chip has the ability to measure the time constant of five different capacitances². To use the three-signal technique, two of these five capacitances have to act as an offset capacitance and a reference capacitance, respectively.

3.2.5 | Optical Fibers

Four optical fibers are inserted to the MainzTPC detector structure, as shown in figure 3.2. Via an optical feed-through, which feeds all four fibers simultaneously, a light signal can be sent into the TPC inner volume. During the experimental run, a blue LED driven by a pulse generator is used to calibrate the PMTs and APDs inside the MainzTPC.

It is worth noting that the fibers do not actually enter the active volume inside the TPC. In fact, their inlet holes through the PTFE structure are closed to the inside. This is because it is very difficult to direct the light from the fibers to a certain point in the TPC, also taking into account that the ends of the fibers could not be perfectly smooth so that the light exits in an unexpected angle to the fiber direction. In the current setup, a 0.5 mm thick PTFE wall that separates the fibers from the TPC inner volume is illuminated by the light of the fibers. The light is scattered in the PTFE resulting in a more diffuse and spreaded illumination in the inner volume of the MainzTPC.

3.3 | From Physics to Data - Hardware Infrastructure

To operate the MainzTPC detector, a surrounding setup of equipment is necessary. Besides voltage supplies and readout electronics for the sensors in the detector itself, a

²Actually, the UTI boards are multifunctional and can be operated in different modes. For this thesis, the focus is set to the mode that is most suitable for the experimental setup (mode 2 in [86]).

gas system and a cryogenic system need to be at hand. The gas system is used to fill and recuperate the xenon to and from the setup as well as recirculating the xenon during the MainzTPC operation to clean the xenon continuously. The cryogenic system is needed to reach and maintain the physical requirements for a dual-phase xenon experiment. These systems in turn also have to be controlled, so that the measured data can be evaluated with respect to the experimental conditions. This is done with a slow control system.

3.3.1 MainzTPC in the Setup

The MainzTPC is situated in a stainless steel vessel which then is filled with the detection medium xenon. Figure 3.6 shows a photograph of this vessel along with a CAD drawing of this cryostat and the TPC inside.

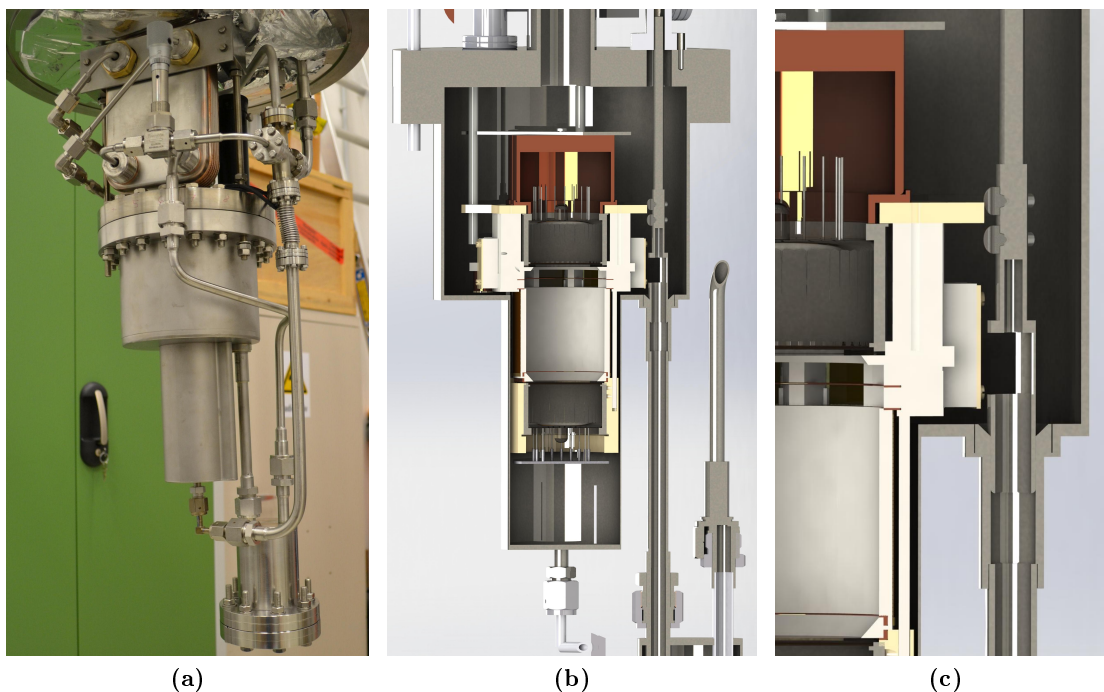


Figure 3.6: MainzTPC in the xenon cryostat: The photograph in (a) shows the inner cryostat which is filled with liquid xenon up to the desired level, along with the buffer volume in the lower left and the heat exchanger above the vessel. The form of the cryostat is chosen to minimize passive liquid xenon around the active volume. The CAD drawing in (b) illustrates the position of the MainzTPC inside the vessel. The liquid xenon surplus spills over an adjustable weir into the buffer volume. The weir is shown in a zoomed-in image section in (c).

As mentioned before, the setup is designed to have a minimum of passive material,

therefore the vessel has its peculiar shape: The inner diameter of the upper part is 15 cm and contains the detector part down to the gate mesh, including the upper PMT, the APDs, the anode and gate mesh and the levelmeters. Since the APDs and the levelmeters have to be placed around the $S2$ region, the TPC is broader there. Furthermore, the connectors for these devices need to be installed as well. The cabling for all sensors (supply voltage, signals) and the optical fibers in the TPC are guided to the outside via the large pipe in the upper flange.

The part of the detector below the gate mesh is placed in the narrower part of the vessel. This is reasonable with respect to the self-shielding properties of xenon (see section 2.1). With this design the amount of passive liquid xenon around the active area inside the TPC is minimized.

In figure 3.6c the levelling mechanism is shown. Using a linear feed-through on top of the TPC cryostat, one can change the height of a weir with clearance fit. The liquid xenon enters the TPC vessel from the bottom, floats upwards through the TPC and reaches the desired level. During measurements, the xenon in the setup is recirculated (see section 3.3.2) which means that a constant flow of liquid xenon is introduced to the TPC chamber. The excess of liquid xenon spills through the weir into a buffer volume.

3.3.2 | Cryogenic System

Operating the MainzTPC at stable thermodynamical conditions is crucial. For instance, changes in pressure or temperature can lead to level fluctuations which corrupt the measurement of the $S2$ signal. Also, the freezing of the xenon should be avoided to protect the sensitive parts such as the light sensors from damage.

The cooling device applied in the setup is a pulse-tube refrigerator (PTR), which uses electric power to cool down a so-called cold finger. The cold finger is placed in a funnel-shaped vessel above the TPC cryostat, which is shown in figure 3.7a. As a backup or support cooling system, liquid nitrogen can be flowed through a helical copper pipe which is also placed in this cooling vessel. Through a pipe, the gaseous xenon can float upwards while the liquid can run downwards into the TPC inlet at the bottom of the TPC chamber.

To maintain stable conditions in the TPC chamber, a gas connection from its top to the pipe towards the cooling system allows gas exchange. The performance of the cryosystem is monitored by the slow control system (see section 3.3.4) using multiple sensors for pressure and temperature at different positions of the system.

As usual for cryogenic systems, the MainzTPC is placed completely in an insulation vacuum. In figure 3.7b one can see the outer cryostat for the cooling system at the top of the structure with the connection pipe inside an insulation pipe leading to the outer top flange of the MainzTPC cryostat. Here, the outer cryostat of the MainzTPC is removed and the TPC chamber vessel and the buffer volume are visible.

The recirculation process for continuous purification of the xenon in the MainzTPC can be described as follows using figure 3.8:

After the gas purifier in the gas system, the gaseous xenon, pumped by the recirculation pump, reaches the heat exchanger. During operation and with stable conditions, the heat exchanger is cold enough to liquefy the gaseous xenon.

At a cross connection after the heat exchanger, the part of the xenon that is still in the gas state can float forward to the cooling system to be cooled down or upwards to the gas phase of the TPC chamber, while the liquid xenon drops down and reaches the bottom of the TPC chamber.

Because of the constant flow of new liquid xenon, the liquid xenon in the chamber slowly ascends inside the TPC chamber and eventually spills over the weir into the buffer volume. From there, the liquid xenon is withdrawn upwards by suction (by the recirculation pump) into the heat exchanger and heats up to the gaseous state again. Reaching the gas system, it passes the flow meter and the gas purifier to commence the cycle once again.

For further details see also [3].

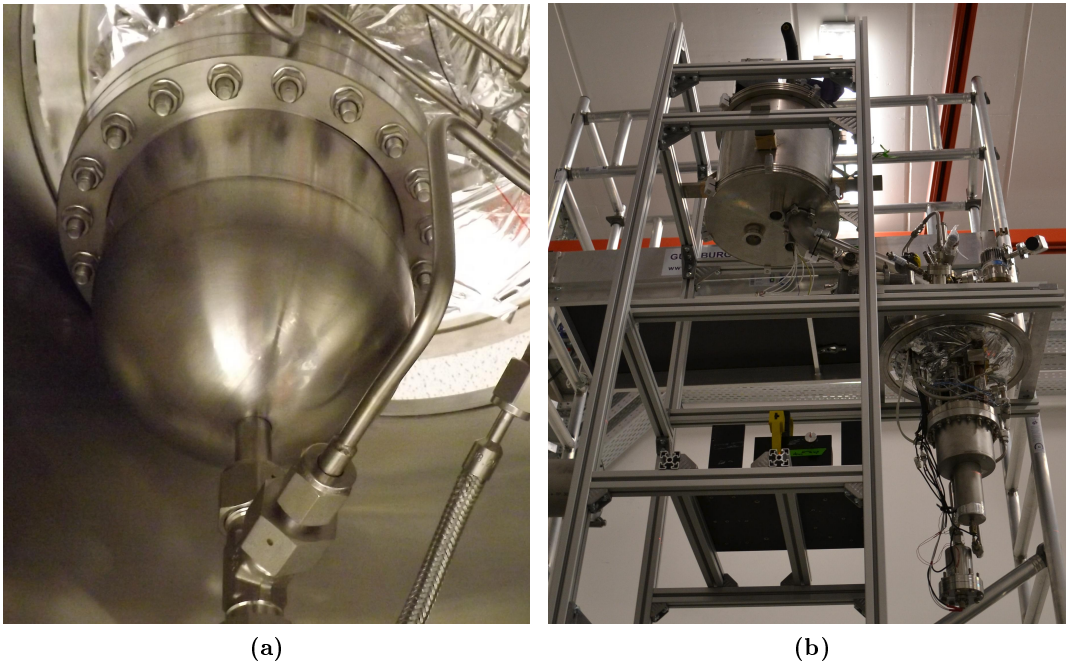


Figure 3.7: Cooling system of the MainzTPC. In (a), the funnel-shaped vessel containing the PTR cold finger is shown. In (b), this vessel is enclosed in the cryostat at the top of the depicted structure, with a pipe connection to the MainzTPC at the lower right side. The MainzTPC is shown here without the cryostat for the insulation vacuum.

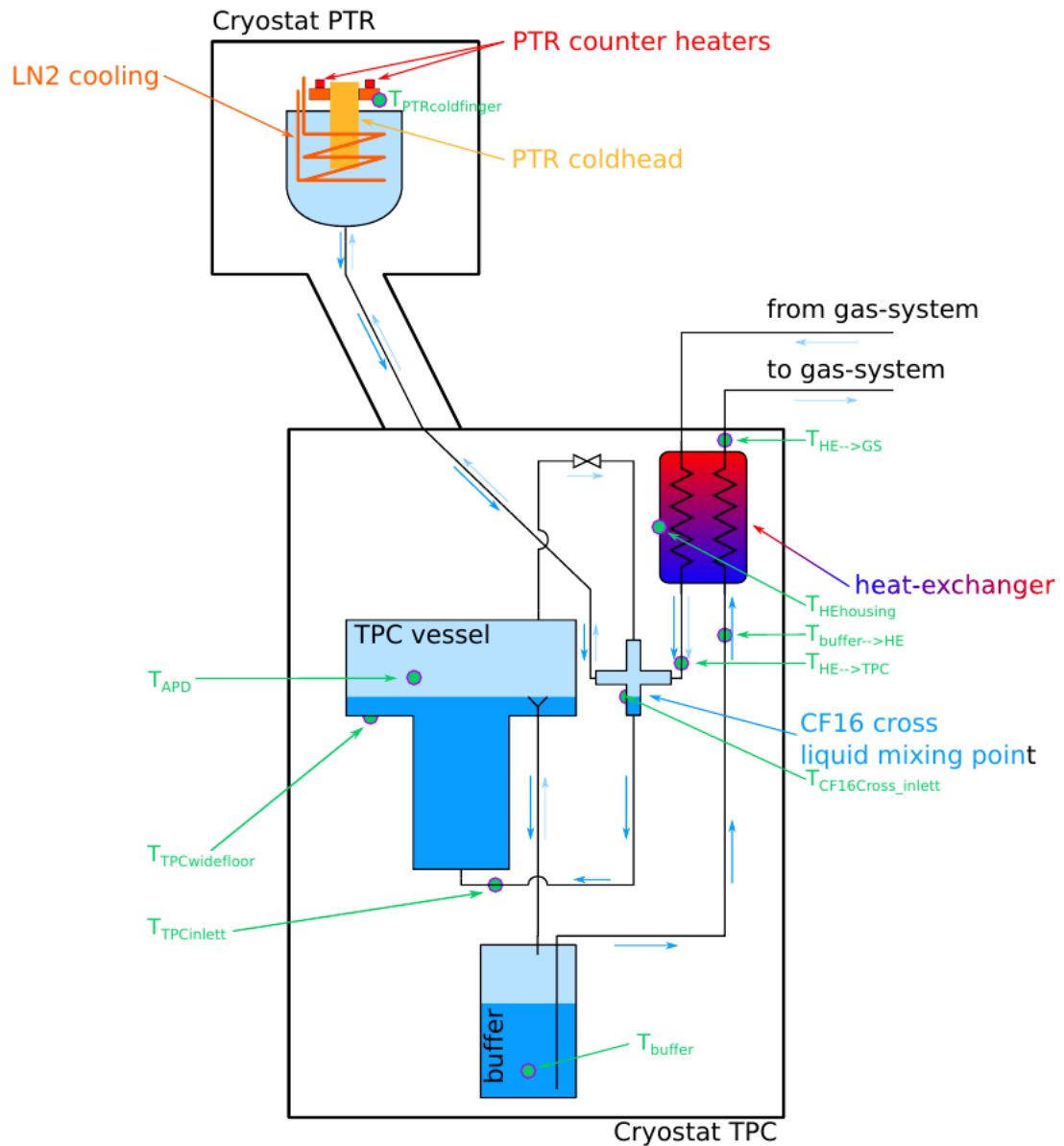


Figure 3.8: Sketch of the cryocooling system: Gaseous xenon condensates at the PTR on the upper right and flows down to the bottom of the TPC. When adding liquid xenon or recirculating the xenon during operation, the LXe ascends inside the TPC until it spills into the buffer volume. A heat exchanger is used to warm up the xenon pumped into the gas system for cleaning while cooling down the clean xenon entering the system. Dark blue arrows indicate the LXe flow directions, light blue stands for GXe. The temperature sensors used to monitor the thermodynamics of the system are marked in turquoise. The image is taken from [3].

3.3.3 Gas System

The gas system was designed and constructed in [79] for the MainzTPC setup. It is necessary to transfer the xenon from its high-pressure bottles to the MainzTPC system and vice versa after the end of the experiment, i.e. the filling and the recuperation process. Furthermore, the gas system includes a double-diaphragm pump and a gas purifier which allow the recirculation of the xenon during the operation of the MainzTPC. The purifier is used to reduce the amount of molecules such as H_2O , O_2 , CO , CO_2 , N_2 , CH_4 and H_2 which are mostly residuals from air in the TPC, to less than 1 ppb. These impurities in the xenon can reduce the detector performance with respect to the $S2$ signal, as free electrons from the interaction point can be absorbed by impurity atoms and molecules. This effect is studied in section 8.4 within the analysis part.



Figure 3.9: The gas system is the large structure on the lefthand side, which can be seen as two connected parts. The left is the holding structure for the xenon bottles with two bottles (colored in green) connected. They can be seen hanging from the structure, with the left one being partly inserted to a dewar for liquid nitrogen. This is for the cryopumping during the recuperation process. The right part of the gas system is the recirculation part, including the gas purifier in the grey box and the pump in the metal box in the lower center of the picture. The flowmeter as well as displays for pressure sensors are installed at eye height. The device on the right is a pumping station which is evacuating and therefore cleaning the gas system before operating with xenon gas.

The gas system is shown in figure 3.9, being evacuated with a pumping system connected on the right side. On the left, the xenon can be stored in high-pressure bottles to

be introduced or recuperated from the MainzTPC. The latter process is done with cryocooling the xenon bottle with liquid nitrogen to create a depression in the respective bottle, the dewar for the liquid nitrogen can be seen placed beneath the left bottle. The right part of the gas system (center of the picture) is designated for the recirculation with a recirculation pump (in the box) and a gas purifier. A flowmeter allows to control the xenon flux through the system. This is useful to ensure that the performance of the gas purifier is not reduced because of a flow rate too large. Also, it is used to estimate the total amount of xenon during the filling and recuperation process. The flowmeter as well as pressure sensors of the gas system are monitored continuously during the experiment by the slow control system (see section 3.3.4). More information on the gas system can be found in [79].

3.3.4 | Slow Control System (SCS)

It follows from the previous section that the MainzTPC infrastructure has to be controlled and monitored with regard to many different physical quantities. The slow control system developed in [83] provides a monitoring and logging tool for a variety of quantities. The program itself has been debugged and slightly improved after the end of the bachelor thesis and has been extended to handle additional hardware in the setup.

Basically, the slow control system as a monitoring tool consists of a software that logs data from a variety of sensors to a server which can be accessed to observe the parameters live via a web interface. Also, the data as such can be extracted for analysis from the server.

The software uses drivers to communicate with the measurement devices. As for now, the SCS software is merely a monitoring tool. The controlling is realized using the hardware devices connected to the SCS, such as a SRS CTC100 (Stanford Research Systems Cryogenic Temperature Controller). It possesses four inputs for temperature sensors, four analog inputs/outputs and two power outputs, which allows the measurement of sensors but also the control of other devices, such as the cooling power by varying the cold finger temperature with a PID³ controller or define a liquid nitrogen flow for supportive cooling.

Beyond that, several other devices are connected to this system to form the slow control system in its entirety. The list includes temperature and pressure measuring devices, the UTI boards for the capacitance measurement for the levelmeters (see section 3.2.4), voltage supplies (see section 4.2.3), and signal and trigger rates from the data acquisition system (see section 4.2.2).

For the experimental run examined in this thesis, the SCS recorded a total of 110 different parameters per second.

³A PID (Proportional-Integral-Derivative) controller is a mechanism that uses a fixed setpoint (e.g. for a temperature) and its measured value to continuously evaluate the difference. According to this feedback and the PID settings, the controller reacts slower or faster to balance the system at the defined setpoint.

3.3.5 | Data Acquisition System

The data acquisition system is mentioned here only for the sake of completeness. This system is responsible for recognizing an event in the MainzTPC and triggering the recording and storage of the signals from the individual sensors. The system is explained in detail in chapter 4.

3.4 | Signal Readout

This section concentrates on the sensors measuring the actual events in the MainzTPC experiment. Four different sensor types are represented: Photomultiplier tubes (PMTs) and avalanche photodiodes (APDs) situated inside the TPC, a germanium detector for the Compton setup and plastic scintillators for the neutron setup.

3.4.1 | PMTs

The PMTs are the main light sensors in the MainzTPC. They are required to be working in liquid xenon and to be sensitive to its scintillation light, which has a wavelength of 178 nm (see section 2.3.1). Eventually the model Hamamatsu R6041 PMT was chosen. The ordered PMTs have a quantum efficiency (QE) of more than 30 % for light with 178 nm wavelength. This relatively high QE is desired since higher quantum efficiencies lead to a more precise light measurement and therefore a better energy resolution in the detector.

Additionally, the PMTs were chosen for their time response, which is crucial for the pulse shape analysis of the $S1$ signals. In order to examine the scintillation pulse shape, the response time should be equal or less than the decay time of the xenon excimer singlet state, which is about of 2.2 ns (see section 2.4). According to the data sheet in figure C.1, the PMTs have a rise time of 2.3 ns for the anode pulse and a transit time spread of 0.75 ns at 25 degrees Celcius.

Figure 3.10a shows one of the installed PMTs. It is cylindrically built with a metal housing, with a diameter of 2 inches. With the MainzTPC built according to this size, the probability for multiple scatterings of gamma-rays with an energy of 662 keV, as from a ^{137}Cs source, is kept very small. The decision to use only one PMT on top and one at the bottom of the TPC was made to avoid areas that are not photo-sensitive.

Amplifiers for the PMTs The PMT signals were amplified using two different types of custom-made amplifiers. The KPH amplifier has a amplification factor of 5 and a bandwidth of 2 GHz, while the DetectorLab amplifier amplifies with a factor of 10.5 but provides a smaller signal bandwidth. Both types split the incoming signal such that two amplified output signals can be measured simultaneously. The amplifiers are described in detail in [3].

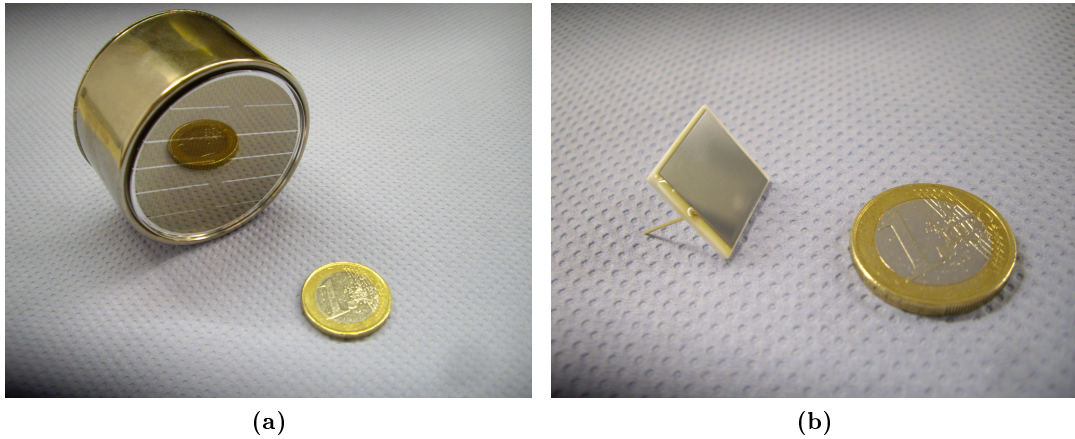


Figure 3.10: Light sensors in the MainzTPC: (a) The Hamamatsu R6041 PMT is cylindrical with a diameter of 2 inches and a metal housing. During operation, a positive bias voltage was used so that the photocathode effectively is on ground potential to avoid sparking to the nearby electric field meshes. (b) The RMD S1315 APD is a very filigree device without a housing. This prevents gas traps in the setup.

3.4.2 | APDs

The S1315 large area avalanche photodiodes (APDs) manufactured by RMD have an active area of $14 \times 14 \text{ mm}^2$. One of the APDs mounted in the MainzTPC is displayed in figure 3.10b. As can be seen, it basically consists only of the active area on a ceramic plate with two thin connectors at the back (one is visible). The APDs were chosen without housing to avoid gas traps in the setup.

An array of eight APDs is installed around the MainzTPC at the height of the gate-anode mesh gap with the liquid-gas interface. In this area, the S_2 signal is created. Measuring the S_2 signal with the APDs allows for the reconstruction of the signal position in x - y .

The APDs were chosen because of their high gains of up to 2000 (according to the data sheet in figure C.2) and previous experience with this detector model [88]. Then, quantum efficiencies of $34 \pm 5\%$ were measured which is a reasonable value for the use in the MainzTPC setup.

The APDs are very temperature-sensitive. In order to measure with a stable gain the APDs have to be operated with non-changing thermal conditions.

APD Preamplifiers The APDs are not read out directly. Instead, a charge-sensitive preamplifier (CSP) is placed between the APD on the one side and the high voltage supply and the data readout board on the other side. The CSP used here is a commercial model from CAEN with the number A1422 [89]. Two four-channel CSPs are used to operate and read out the eight APDs.

The CSP collects the charge generated from a signal in the APD and stores it on a capacitor. The signal that is measured then is the voltage on the capacitor, which by the formula $Q = C \cdot U$ is equivalent to the charge.

3.4.3 | Germanium detector - Compton Mode

For the Compton scatter experiment, a secondary detector is necessary to measure the energy of scattered photon. This energy measurement can be done using the scattering angle or by directly measuring the energy deposit in a secondary detector. Simulations from [69] showed that the direct energy measurement with a germanium detector has a better energy resolution than using the scattering angle which could also be done with a cheaper and faster NaI detector that only provides a mediocre energy resolution.

Starting from this, several types of germanium detectors from different suppliers were taken into consideration. Finally, the GEM-F5930-S HPGe detector from Ortec was chosen [90], which can be seen in figure 3.11 (labeled “3”). This detector is a coaxial p-type (p-doped). Measures are provided in the datasheet in figure C.3. According to the performance specifications, Ortec measured a full width at half maximum (FWHM) energy resolution of 1.7 keV for the ^{60}Co line at 1.33 MeV, as well as a FWHM resolution of 626 eV for the 122 keV line in ^{57}Co . For these resolutions, an additional shaping amplifier was used.

The good energy resolution is essential for the experiment since the energy deposit in the MainzTPC ΔE is directly calculated from the energy measured in the germanium: $\Delta E = E_\gamma - E'_\gamma$, with E_γ being the photon energy at its source and E'_γ the measured photon energy after the Compton scattering.

The output signal of the germanium detector comes from a built-in CSP. Analogous to the APD preamplifiers, the resulting signal is a voltage peak that is equivalent to the collected charge from the detector signal.

The germanium detector at hand provides two signal outputs. To increase the signal resolution, one of the output signals is amplified using a device similar to the DetectorLab amplifier discussed in section 3.4.1, but with no signal split, since two outputs are available. This one-channel amplifier (“germanium DetectorLab amplifier”) increases the signal also by a factor of 10.5. The choice not to use a shaping amplifier as was used to measure the energy resolution mentioned above was made to preserve the raw waveform in the stored data to be able to identify multiple events in the germanium detector.

3.4.4 | Plastic scintillators - Neutron Mode

Neutron detectors consist of different materials than photon detectors. Our collaborators at the Helmholtz-Zentrum Dresden-Rossendorf (HZDR) provided us with plastic scintillators (“plastics”) to detect scattered neutrons. The plastics are shown in figure 3.11, labeled as “5”.

The scintillator material is EJ-200, an organic scintillator in crystalline form. The plastics each have a scintillator crystal of 1 m length and a section area of 1.1 cm thickness \times 4.2 cm width. The thickness is chosen to avoid multiple scatterings of neutrons in the crystal. The width along with the detector distance to the MainzTPC of 1 m is used to calculate the angular resolution.

The scintillation signal is read out with two PMTs (Hamamatsu R2059-01) which are installed on each end of the 1 m long crystal. The complete crystal is wrapped with reflective foil to minimize signal losses and is covered with black plastic tape to make the plastics light-tight. Instead of using the amount of scintillation light to measure the neutron energy, it was decided to measure the neutron velocity via the time-of-flight to determine its energy. Alternatively, the scattering angle can be used as well.

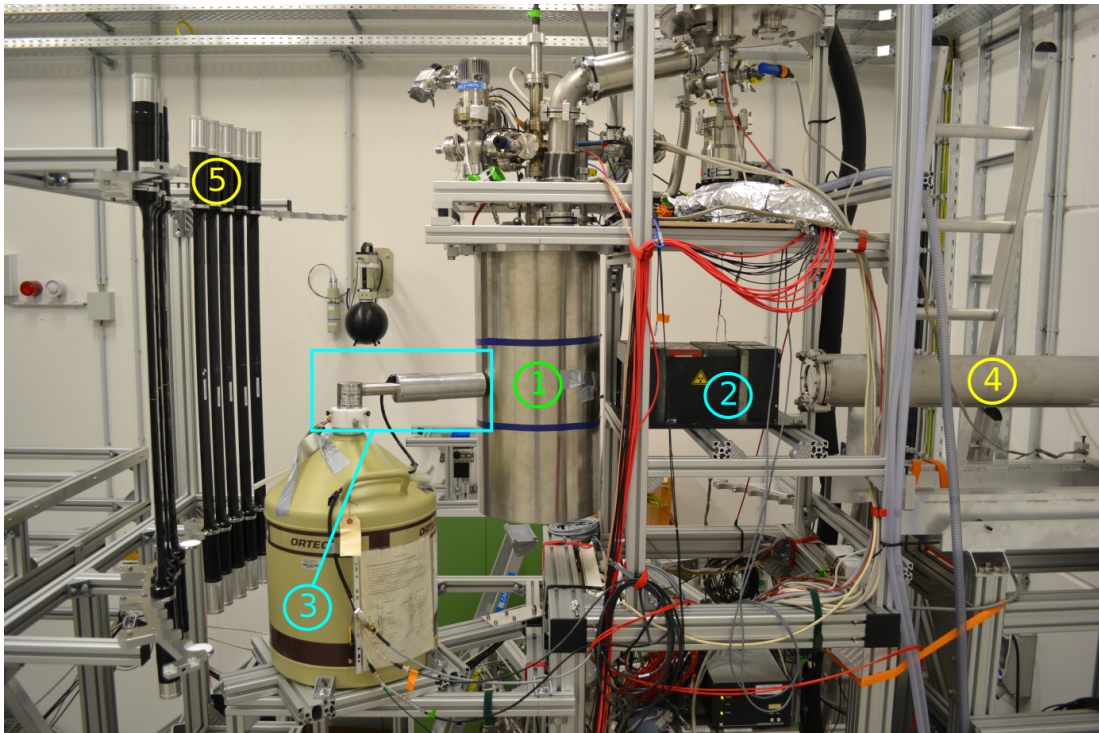


Figure 3.11: The MainzTPC setup for both Compton and neutron scattering at the HZDR. In the center, the green (1) marks the TPC position inside the cryostat for the insulation vacuum. In this picture a Compton measurement is conducted. For this, a gamma-ray source is placed in the lead collimator (2) and the scattered photons are measured with the ORTEC GEM-F5930-S HPGe detector (3). This detector is constantly cooled with liquid nitrogen, for this it is connected to the dark-yellow dewar beneath the marked area. For the measurement of neutron scattering both the collimator and the germanium detector are removed from the setup. Then neutrons can enter the measurement hall through the pipe visible on the right (4). The scattered neutrons are then detected by one of the plastic scintillators (5) that are positioned at different angles to cover a range of neutron energies. At both ends of the plastic scintillators, the rear ends of the PMTs can be seen that are used to detect the scintillation light.

3.5 | Operating the MainzTPC

The experimental setup for the MainzTPC was developed, constructed and tested at the institute of Physics in Mainz. At this location, only the Compton measurement was possible. For the neutron scattering measurement, the setup was transferred to the Helmholtz-Zentrum Dresden-Rossendorf (HZDR) and adjusted to measure the time-of-flight. Figure 3.11 shows the setup for the Compton scattering at the HZDR, with the detectors necessary for the neutron scattering measurement already under commission. In both Compton and neutron scattering measurement, the liquid phase of the MainzTPC serves as scattering target. Apart from this, the data acquisition of the two experimental setups is quite different. To account for the different setup configurations in Mainz and at the HZDR, which are explained considering the data acquisition in chapter 4, the Compton setup in Mainz is denoted as “setup 1”, while the setup configuration used at the HZDR for both Compton and neutron scattering will be referred to as “setup 2”. The connections of the different sensors to the respective readout electronics are discussed in detail in section 4.3.

3.5.1 | Setup 1 (Mainz) - Compton Setup

For the Compton measurement in Mainz, the gamma-rays from a ^{137}Cs source placed in the lead collimator are scattered in the TPC and absorbed in the germanium detector which is placed on a rotatable stand so that the Compton scattering can be measured at different scatter angles. The rotatable setup is described in detail in [80]. In setup 1, the energy of the scattered photon is directly measured by the germanium detector. This leads to a very good energy resolution, which is determined in section 5.2.2. In this setup, one of the germanium detector outputs is amplified using the germanium DetectorLab amplifier as mentioned in section 3.4.3, while the other output is measured with the preamplification from the built-in CSP only.

3.5.2 | Setup 2 (HZDR) - Compton and Neutron Setup

At the HZDR Compton measurements as well as neutron measurements were conducted using the same setup.

For the Compton measurements, the germanium detector had to be placed at the same height as the MainzTPC with the possibility of being rotated to different scatter angles. The structure for this is can be seen in figure 3.11.

The germanium detector was positioned at different nominal angles α_{nom} to cover a range of deposited energies for the Compton measurements. The term nominal refers to the fact that this angle is measured geometrically for a gamma-ray scattering in the center of the TPC and being absorbed in the center of the germanium detector, as sketched in figure 3.12. The actual scattering angles can differ from α_{nom} (see also [69]).

Table 3.2 contains a list of the nominal angles used for Compton measurements at the HZDR and the respective nominal energy deposits, ranging from 0.35 – 144.54 keV. The nominal energy deposit ΔE_{nom} is calculated with equation (2.3) using the gamma-ray energy of 661.6 keV for ^{137}Cs and the nominal angle, while the minimum and maximum values are calculated by adding and subtracting $\Delta\alpha_{\text{nom}} = 8.36^\circ$ to the nominal angle which corresponds to the theoretical angular uncertainty due to the solid angle covered by the germanium detector. Since the gamma-rays that will hit the germanium detector for $\alpha_{\text{nom}} \pm \Delta\alpha_{\text{nom}}$ scatter in the detector periphery, they most likely will not be absorbed completely and therefore the measured energy is too small. Also the probability of the gamma-rays to pass through the germanium detector edges is larger than for gamma-rays hitting the center of the germanium detector, therefore the major contribution of the measured gamma-rays will be close to the nominal energy deposit ΔE_{nom} .

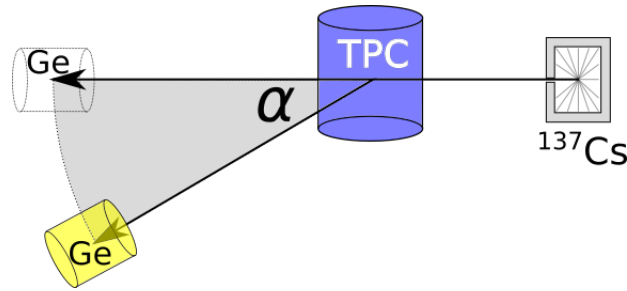


Figure 3.12: Sketch of the nominal angle in the Compton scattering setup: Ideally, the scattered photon is completely absorbed by the germanium detector and the angle can be determined exactly. The finite detector dimensions and effects such as the Doppler broadening introduce uncertainties to the scattering angle, therefore it is used to only estimate the scattering energy when positioning the germanium detector.

$\alpha_{\text{nom}} [^\circ]$	$\Delta E_{\text{nom}} [\text{keV}]$	$E_{\text{nom,min}} - E_{\text{nom,max}} [\text{keV}]$	$E_{\text{TPC,min}} - E_{\text{TPC,max}} [\text{keV}]$
10	12.76	0.35 - 40.92	0 - 40
15	27.95	5.69 - 63.49	4 - 55
22.5	59.35	24.96 - 102.50	9 - 90
30	97.80	55.31 - 144.54	29 - 140

Table 3.2: Nominal scatter angles for the Compton measurements conducted at the HZDR in April 2016, with calculated deposited energy in the MainzTPC for ^{137}Cs . Using the solid angle covered by the germanium detector, also the minimum and maximum energy deposits with respect to the nominal angle were calculated. The last column lists the actual intervals for the energy deposit determined with the germanium detector during the experimental run in April 2016.

The energy deposit in the MainzTPC for the Compton measurement in setup 2 is determined by measuring the energy deposit in the germanium detector, as is the case for setup 1. The nominal energy deposits listed in table 3.2 are used to choose an energy

range but do not influence the final energy measurement.

As a comparison, the energy intervals measured with the germanium detector at the respective nominal angles are listed in the last column. The approximate minimum and maximum energy values are taken from the energy distributions of the germanium detector shown in figure 3.13.

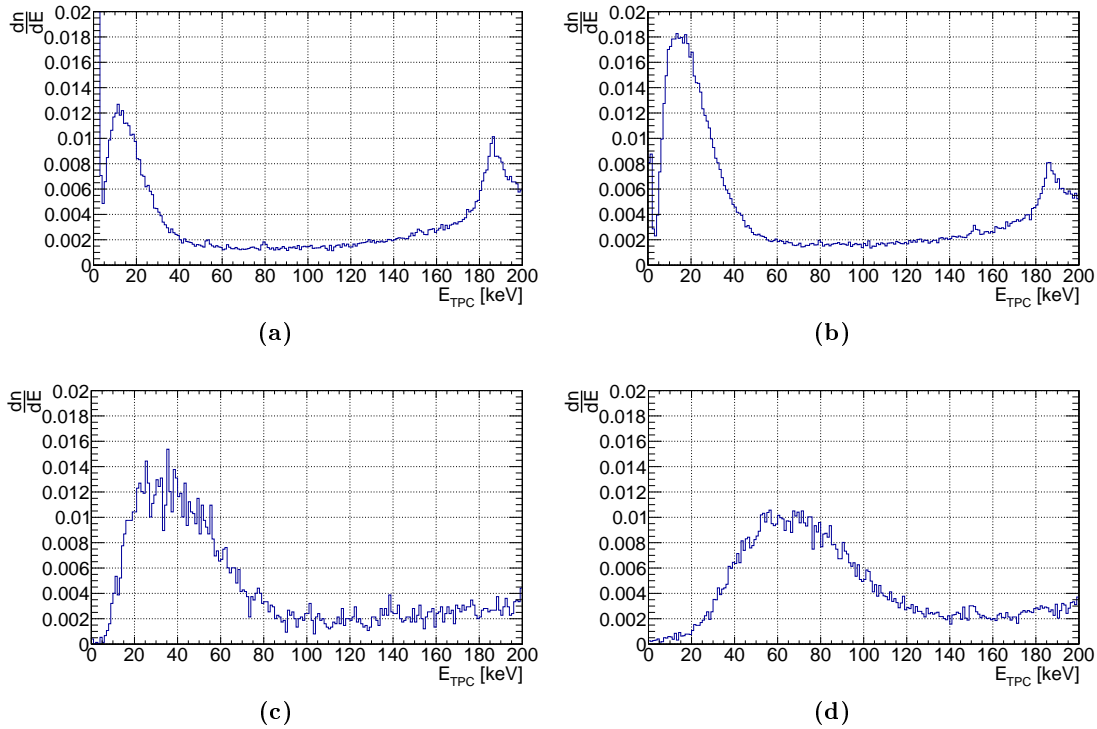


Figure 3.13: Distributions of the energy deposit in the TPC for the Compton scattering, measured with the germanium detector, for the nominal angles of (a) 10° , (b) 15° , (c) 22.5° and (d) 30° . With increasing angle, the distribution of the scattering energy E_{TPC} becomes broader and is shifted to larger values. For the two smaller nominal angles, events at zero energy and at the Compton edge are visible, indicating that the germanium detector is at least partially located in the gamma-ray beam of the ^{137}Cs source.

The depicted energy spectra for the energy deposit E_{TPC} are obtained using equation (2.4), subtracting the measured energy in the germanium detector from the initial gamma-ray energy $E_0 = 661.6 \text{ keV}$ for ^{137}Cs . The measured energy intervals range to lower values than the calculated minimum energy values, while the maximum values are comparable. This behaviour indicates that there could be a systematic error determining the nominal angular position of the germanium detector during the experiment, shifting the nominal angles to larger values. Since the energy measurement is independent of the scattering angle, this has no influence on the subsequent analysis.

For the two smaller nominal angles, additional events are found for an energy around zero, which can be linked to gamma-rays being completely absorbed in the germanium

detector without previous interactions (with a chance coincidence with the TPC). A second peak structure for the two smaller angles located at approximately 184 keV is the Compton edge for the 661.6 keV gamma-ray line. These two features are not present for larger angles since the collimated gamma-ray beam from the ^{137}Cs can not reach the germanium detector in these cases.

In the Compton setup 2 at the HZDR, the two outputs of the germanium detector are both fed into amplifiers: The first output is connected to the germanium DetectorLab amplifier as before, while the second one is led through a Fast Filter amplifier which additionally inverts the signal. The resulting negative pulse is split, with one of the outputs used for the trigger via a constant fraction discriminator (see section 4.2.2) and the other one being measured.

For the neutron scattering measurement, the germanium detector is not suitable as a secondary detector. It is replaced by the so-called “plastics”, which have been introduced in section 3.4.4 and are labeled (5) in figure 3.11. The energy resolution of these organic scintillators is not sufficient enough for our purpose, therefore the energy deposit in the MainzTPC was determined by measuring the neutron velocity before and after the scattering process to determine the difference in kinetic energy (see section 2.2.5). To calculate the energy deposit, the kinetic energy of the scattering neutron is calculated using the timing information of the MainzTPC and the plastics. A first time-of-flight (TOF) is measured between the neutron generation and the signal from the scattering of the neutron inside the liquid xenon of the TPC, which is called TOF1. Since the distance between the neutron source and the TPC is 5.9 m, TOF1 is approximately 350 ns for a 1.5 MeV neutron, according to equation 2.8. After the scattering, the neutron is detected by a plastic scintillator. The distance between TPC and plastics is 1 m from center to center, which corresponds to a TOF of around 59 ns for 1.5 MeV neutrons (the energy deposit was neglected here). This second time difference is called TOF2.

Neutron scattering data was not studied in this thesis, but the data acquisition system was developed and successfully used also with regard to neutron measurements. First results concerning neutron scattering in the MainzTPC are found in [3].

3.5.3 | Gamma-ray Sources

For the study of electronic recoils the MainzTPC was irradiated using a range of different gamma-ray sources. Depending on the type of measurement, the sources can be divided into two groups:

- The MainzTPC was planned for Compton scattering measurements with a ^{137}Cs source. To achieve reasonable coincidence rates between the TPC and the germanium detector, a strong source with an activity of 37 MBq was purchased which is placed inside the lead collimator (labeled (2) in figure 3.11). The collimator opening leads to a narrow gamma-ray beam directed to the TPC center. The

beam diameter can be adjusted using aluminum pipes inserted to the collimator opening. The rate in the TPC alone is of the order of some kilohertz, while the coincidence rate of the TPC with the germanium detector is only in the order of a few hertz due to the solid angle of the germanium.

- To examine the MainzTPC response to different gamma-ray energies, a set of calibration sources with significantly smaller activities was used. For the measurement of these sources the system was triggered on the response of the TPC only, meaning a coincidence between the two PMTs inside the TPC. The rates for these measurements are, depending on the respective source energies and activities, in the order of hundreds to thousands of Hertz. The calibration sources included ^{60}Co , ^{22}Na , ^{152}Eu and ^{133}Ba .

3.5.4 | Neutron Source nELBE

Although the analysis of the neutron scattering measurements is not part of the thesis, some basic information are necessary to understand the specifications applied in the data acquisition for this measurement mode. For a more detailed overview about nELBE see for example [3], [91] or the website at the HZDR [92].

The neutron generation at nELBE is realized by using the electron accelerator ELBE (Electron Linac for beams with high Brilliance and low Emittance) in pulsed mode and directing the electron bunches onto a liquid lead target. The electrons produce bremsstrahlung, which in turn generates free neutrons by (γ, n) -reactions. The kinetic energy of the resulting neutrons ranges from 50 keV up to 10 MeV, with 1.5 MeV being the peak value of the neutron spectrum.

The energy range for the neutrons is suitable for neutron scattering measurements with the MainzTPC. However, the neutron generation process leads to a gamma-to-neutron ratio of about 1000. For a pure time-of-flight measurement this does not have any impact, since the gamma-rays arrive in the MainzTPC 200 ns before the fastest neutrons. But an event in the MainzTPC consists of the measurement of both $S1$ and $S2$ signal which can have a time difference of up to 32 μs . While the $S1$ signals for a gamma-ray photon and a neutron from the same beam pulse could be associated with the respective particle, this is not true for the $S2$ signals. Hence, for the neutron scattering only events with one neutron scattering in the TPC and no gamma-rays are accepted as viable events.

To improve the gamma-to-neutron ratio, a lead absorber is placed in the beginning of the neutron flight path. Although it also attenuates the neutron spectrum, the lead has a much larger impact on the number of photons reaching the MainzTPC. The gamma-to-neutron ratio was examined in simulations in [93].

3.5.5 | Gamma-ray Data

The gamma-ray data which is analyzed in this thesis was taken during the experimental run of 18-28 April, 2016. This run was designated for Compton measurements and sensor calibration.

During the run, six different types of measurements were carried out, in detail:

- PMT calibration: Measurement of the single photoelectron response of the PMTs with blue LED light. The data acquisition system was triggered by the pulse generator which also created the LED pulses.
- Germanium calibration: The spectra of several gamma-ray sources were recorded with the germanium detector. The measurements were triggered by the germanium detector itself, with a chosen signal threshold.
- APD calibration: To measure the relative gain of the APDs, data was taken with blue LED light for different APD bias voltages to obtain gain curves for each APD. An external trigger by the pulse generator driving the LED was applied.
- TPC calibration: Similar to the germanium calibration, different gamma-ray sources were used to measure the TPC response for different drift field strengths. The data recording was triggered by the Top PMT and Bottom PMT coincidence.
- Trigger efficiency: For this measurement, a NaI(Tl) scintillator provided by our colleagues at the HZDR was placed in front of the MainzTPC. The scintillator was shaped like a well and a ^{60}Co calibration source was inserted into the well such that the gamma-rays of the ^{60}Co could either reach the MainzTPC or be absorbed in the NaI(Tl) scintillator. To measure the trigger efficiency, the system recorded not only all signals detected in the scintillator but also the time stamps of the signals inside the TPC. Comparing the time stamps with the triggered signals one can check whether the TPC would have triggered on a certain signal or not.
- Compton measurement: With a strong, collimated ^{137}Cs source, the TPC was targeted and the scattered photon was measured in the germanium detector. The trigger mechanism was a coincidence between the TPC PMTs and the germanium detector.

All measurements were conducted with the Compton setup 2 which was commissioned at the HZDR. The analysis methods for these measurements are described in part III.

3.5.6 | Raw Data Processing

The Raw Data Analysis tool is an analysis framework written in *C++* to process the raw data which is stored as binary files, to find key information such as signals in waveforms

and store the respective values such as peak heights, integrals etc. in a *ROOT* file for more specific analysis. The framework is described in detail in [3], here only a short overview of the basic features is given, as far as it is necessary to understand how the values in the processed data is obtained.

The Raw Data Analysis was developed at the same time as the MainzTPC data format which is elaborated in section 4.8.

Fixed Window Integral Analyzing data from LED calibration measurements (for the PMTs or the trigger efficiency) is done using the Fixed Window Integral method. Since the trigger is provided by the LED pulser, all signals are found at roughly the same time in the waveform. The Fixed Window Integral method measures the peak integral in two different ways: Using a fixed start and end sample, the integral over a fixed interval in the waveform can be determined. Alternatively, the sample with the maximum value is searched in a chosen fixed window, and a number of samples before and after this maximum sample are used as the integration window. In both cases, the integral is calculated for the baseline-corrected waveform, taking into account a possible signal offset.

PeakFinder The PeakFinder identifies peak-like structures in a waveform and stores the information in a class called “XeRawPeak”. This routine is used for signals measured with the PMTs, but can be applied to any sensor measurement with peak-like signals. The peak features that are determined by the PeakFinder are, amongst others, the peak amplitude, integral, position in the waveform (time in samples), the sample number of the peak edges and the peak width. Some of these properties are measured in the raw and the filtered waveform and both values are stored for subsequent data analysis. Peaks identified by the PeakFinder are classified either as *S1* or *S2* peaks. This depends on their respective properties, i.e. the signal requires a minimum width to be regarded as *S2*. The waveform is first scanned for the large *S2* signals. In a second step, the waveform is scanned for *S1* peaks excluding the regions that are “occupied” by a found *S2* peak.

StepFinder and StepFitter Signals from sensors such as the germanium detector and the APDs, which both are amplified by CSPs, show a step-like shape. The signal height corresponds to the charge collected in the CSP. Therefore, the signal analysis has to be different from the peak-like signals discussed before.

The step properties of interest are the position of the maximum of the step in the waveform, the amplitude of the raw waveform (at the determined position), the “peakAmplitude”, which is determined by using a Moving Average Window (MAW) filter on the waveform and the decay constant of the falling flank of the step.

There are two routines to determine the step properties:

The StepFinder was implemented first and is used to find the peak position of the

step. This is done by applying a MAW filter to the waveform, which transforms the step-shaped signal into a peak-like structure. By normalizing the filtering process, the amplitude of this filtered waveform (“peakAmplitude”) becomes identical with the raw data amplitude.

The StepFitter was introduced as an improvement of the StepFinder routine. Using the found position and amplitude of the step, a fit function is applied to the raw data waveform to get more precise values for the amplitude, the rise time or the decay time of the step.

DataViewer The DataViewer is a subprogram of the Raw Data Analysis tool. It allows to access the acquired data and to browse through the individual signal waveforms. Its main purpose is to check the data during the experiment and before the processing to make sure that the desired signals are recorded in their respective measurement time window. Also, one can find problems with individual detectors by checking the detector response.

Furthermore, the DataViewer provides the possibility to do some on-the-fly analysis, by using the PeakFinder or StepFinder/StepFitter routines on individual waveforms. This can be used to cross-check parameters for the raw data processing.

So far, the DataViewer is designed to work with FADC data only.

The Raw Data Analysis tool is – as mentioned – only the first step in the analysis process. The second-level analysis methods for the individual measurements were developed in the course of this thesis (if not mentioned otherwise) and are explained in detail in the respective analysis sections in part III.

MainzTPC - Data Acquisition

Chapter 4

The measurement of scatter processes in the MainzTPC is a complex operation because of the various different sensors involved. In total, the Compton setup measures 11 sensors, the neutron setup even 30 sensors. The information obtained from these sensors is recorded by the data acquisition system `mainztpc_DAQ` (DAQ), which uses a setup-specific trigger logic to decide whether an event has occurred or not.

The DAQ ensures the selection and recording of desirable events in the MainzTPC.

The *MainzTPC DAQ* program (DAQ program) is designed to control the signal readout electronics. Its purpose is to recognize if a signal fulfills the trigger requirements for an event and to measure and store the event signals.

The structure of the program is based on *Xespec*, a data acquisition program by U. Oberlack which was also designed to control VME boards from the company Struck. Its C-based structure was used as a scaffold for *MainzTPC DAQ*, that is why the latter is also written in C.

Note: DAQ program versions

This thesis presents two subsequent versions of the MainzTPC data acquisition system. The first version (DAQ version 1) was developed for Compton scattering only and involves only a part of the hardware described in this chapter. It is still in use in Mainz to date.

The second version (DAQ version 2) is an extension to version 1. For the neutron scattering measurement at the HZDR in 2015/2016, the DAQ program had to be adapted to handle the additional electronics that were included, such as the TDC (Time-to-Digital Converter) and the General Purpose board for the external triggering, for example. The noteworthy differences between the first version used in Mainz for Compton scattering and the second version developed for the measurements at the HZDR are emphasized.

4.1 | Events and Signals

The definition of an event is dependent on the measurement mode of the experiment. In general, several sensors provide different signals, which in sum make up the event structure.

A typical event in the MainzTPC contains signals from the PMTs and the APDs. These detect the two scintillation signals:

- *S1* signal: This signal is measured with the two PMTs. Since it is crucial to measure the energy as well as the pulse shape with good resolution, this signal is recorded with two different FADCs (Flash Analog-to-Digital Converters), a slow one with high signal resolution and a fast one with high time resolution.

- *S2* signal: This signal is measured with the PMTs as well as with the APDs. The PMTs provide a good energy measurement. The APD signals are used to determine the x - y -position of the *S2* signal. Both APDs and PMTs are read out with the slow FADC with high signal resolution.

Figure 4.1 shows an event in the MainzTPC recorded with the 125 MS/s FADC SIS3316 during a Compton measurement. The waveform is taken exemplarily from the Top PMT for a drift field of 198 V/cm. The PMT signals are fast-rising peaks with rise times of 2.3 ns [94]. The *S1* signal, which is also shown in a zoomed plot in figure 4.2a, is very short with a signal width in the order of a hundred nanoseconds, while the *S2* signal can be broader up to the microsecond scale.

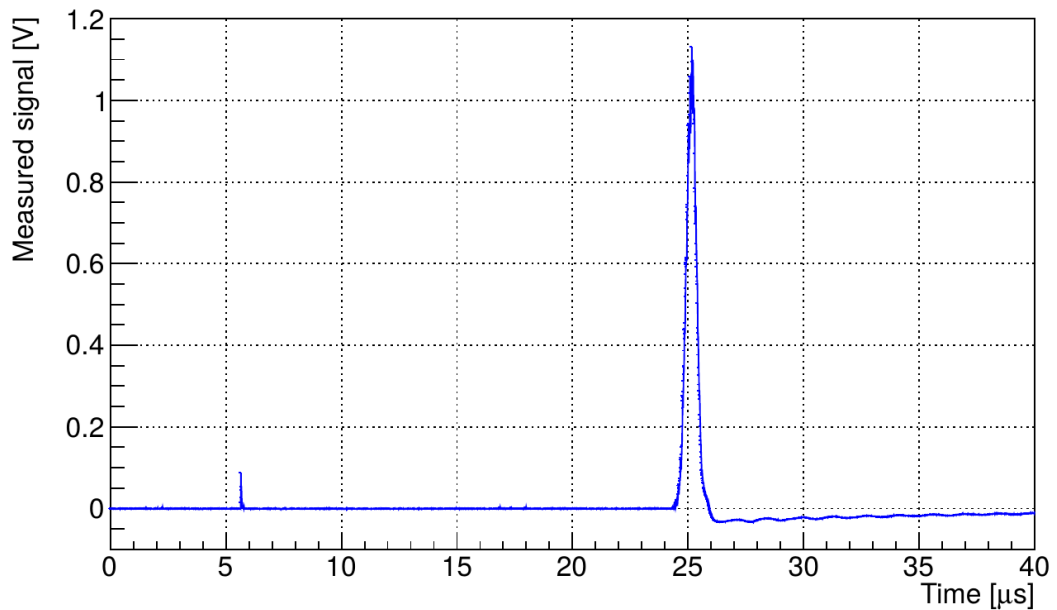


Figure 4.1: *S1* and *S2* signals measured on the Top PMT during a Compton measurement. The *S2* signal exceeds the *S1* signal by about a factor of 12.5 for the amplitude and by a factor of 210 for the signal integral and occurs after the time the electrons need to drift from the scattering point in the liquid phase to the gas phase. The signals are recorded with the 125 MS/s FADC SIS3316.

To get an impression of the typical relative signal strength of *S1* and *S2*, the ratio $\frac{S2}{S1}$ is characterized in table 4.1 for a Compton measurement at a drift field strength of 198 V/cm, for both the signal integral and amplitude. As can be seen, the ratios for the Top PMT exceed the ones of the Bottom PMT by far. This is due to the higher bias voltage applied to the Top PMT and the resulting higher PMT gain. With increasing drift field, the ratio will also change to larger values.

The time difference between the two signals is dependent on the interaction depth in the MainzTPC as well as the strength of the electric drift field.

As described in section 2.3.1, the *S1* pulse shape is different for electronic and nuclear

	$\frac{S_2}{S_1}$ (integral)	$\frac{S_2}{S_1}$ (amplitude)
Top	280 ± 200	11 ± 5
Bottom	40 ± 20	2 ± 1

Table 4.1: Typical signal ratios $\frac{S_2}{S_1}$ with respect to the integral and amplitude of the signals. The listed values are estimated values from the integral and amplitude distributions from a Compton measurement at a drift field strength of 198 V/cm. The Top PMT was operated with a higher gain.

recoils in the xenon. To examine the S_1 pulse shape, the time resolution of the slower FADC with 125 MS/s (8 ns per sample) is not sufficient. Using the SIS3305 with a sampling rate of 5 MS/s, it is possible to record the same signal with a time resolution of 0.2 ns. For comparison, figure 4.2 shows waveforms the S_1 signal recorded by each FADC board.

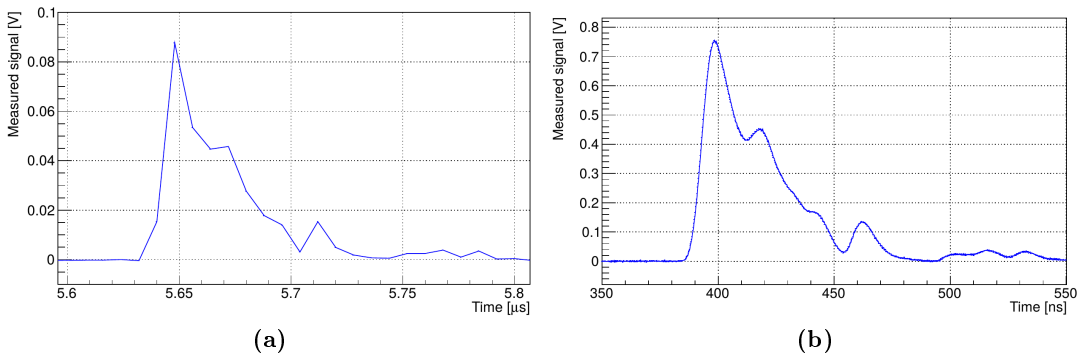


Figure 4.2: Comparison of the S_1 signal recorded (a) on the SIS3316 with 16 bit and 8 ns time resolution and (b) on the SIS3305 with 10 bit and 0.2 ns time resolution. Although both panels show an identical signal, the signal in (b) was amplified using the DetectorLab amplifier with an amplification factor of 10.5.

The APD signals are not directly read out from the sensors, but from a charge-sensitive preamplifier (CSP) of the model CAEN A1422, which collects the measured charge so that the resulting signal is step-shaped, as exemplarily shown in figure 4.3a. As stated before, the height of the step corresponds to the collected charge. The APD signals are not involved in the trigger process.

In scatter mode, secondary detectors provide additional signals to the event structure. Each scatter mode, Compton and neutron, requires a different measurement approach and an adapted DAQ structure.

For the Compton scatter mode, the secondary detector is a germanium detector. As stated in section 3.4.3, it was specifically chosen for a direct energy measurement. The signal is recorded with the slow FADC also used for the PMTs and the APDs to have a maximum energy resolution. Optionally, the energy can be calculated from the angular position of the germanium detector. Figure 4.3b shows a typical germanium signal. A built-in CSP leads to a similar signal shape as in the APD measurement.

An event is classified as a Compton event for a coincidence of the S_1 signal in the

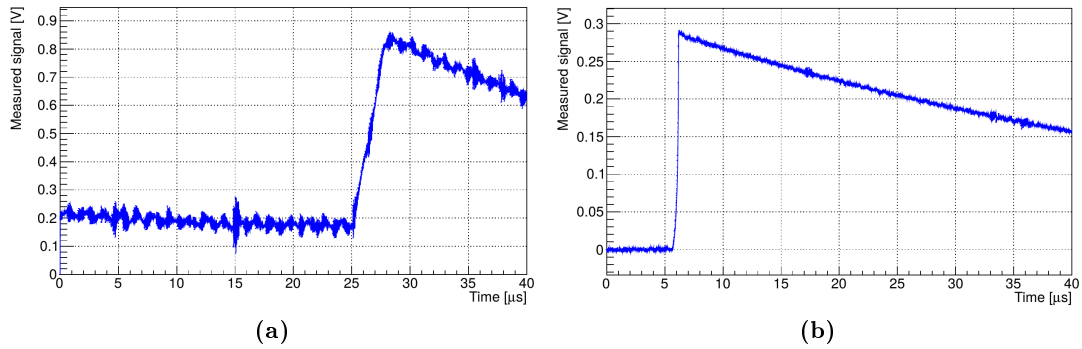


Figure 4.3: (a) APD signal shaped by the CSP CAEN A1422 and (b) germanium signal shaped by the customized DetectorLab amplifier as examples for “step”-like signals.

MainzTPC and the germanium signal of the scattered gamma-ray.

For the neutron scatter mode, a direct energy measurement is not applicable, since neutrons are not absorbed but only scatter in plastic scintillators. Instead, a time-of-flight measurement is used to determine the velocity and hence the energy of the neutrons before and after the scatter interaction in the TPC. The DAQ had to be extended to also include time measurements, using a TDC.

A neutron scatter event is defined as a coincidence between the $S1$ signal in the MainzTPC and a neutron scintillation signal of one of the plastic scintillators. Due to the slow neutron velocities, the assignment of sensor signals to the coincidence signal that generates the trigger is more complicated than for the Compton scatter mode. The trigger conditions and the requirements for the trigger generation are discussed in section 4.3.

4.2 | Hardware Components

The DAQ system is located in a VME crate shown in figure 4.4 and consists of two FADCs (Flash Analog-to-Digital Converter), a TDC (Time-to-Digital Converter), a programmable logic board for the event trigger generation and three high voltage modules. Beside this, a NIM crate (Nuclear Instrument Module) is used to power a series of constant fraction discriminators¹ (CFD), which provide the signals for the trigger generation, as well as gate & delay modules and shaping amplifiers.

Since the PMT signals have to be split to be measured in both FADCs simultaneously, the signals are led through amplifiers to maintain signal strength. An amplifier is also used for the germanium detector, since the built-in CSP does not provide the required signal resolution.

¹The CFDs were designed and manufactured at the HZDR and we were provided with them for the duration of the experiment.

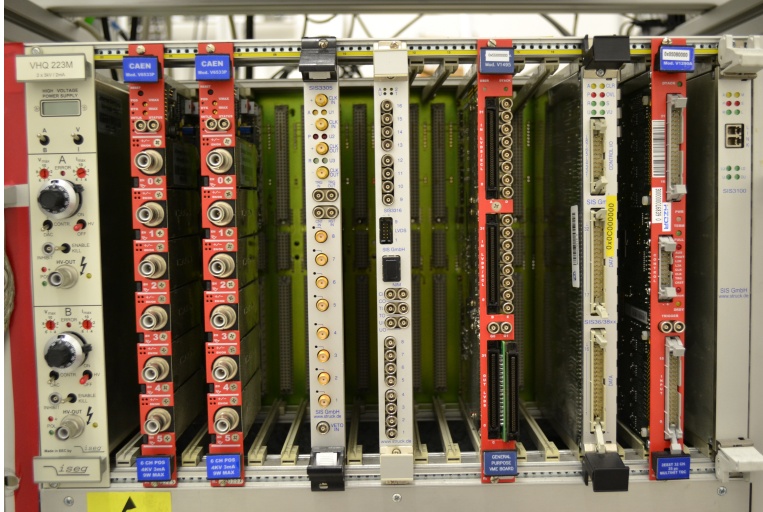


Figure 4.4: VME crate with DAQ and HV boards. From left to the right one can see three HV boards, the fast and the slow FADC board, the logic board, the scaler and the TDC board. The last board on the right is the SIS3100 controller.

For the APDs a commercial CSP box is used, which is connected to both the high voltage supply and the FADC.

The DAQ system is controlled from a computer with a SIS1100 PCI board. Via an optical link cable, this PCI board communicates with a SIS3100 VME controller in the VME crate. From the controller, the individual boards can be addressed to configure settings, control operations and readout data. The SIS3100 also provides a library containing the VME commands that are used in the DAQ software [95].

4.2.1 | Signal Measurement

The SIS3316 [96] is a 16-channel digitizer VME board with 125 MS/s per channel and an analog bandwidth of 62.5 MHz from Struck Innovative Systems. That yields a time resolution of 8 ns per sample. This FADC has a 16 bit resolution for the signal measurement, which means that it can register voltage differences down to $\approx 30.5 \mu\text{V}$. With this excellent resolution, this FADC is the essential measurement device of the DAQ system. It records the waveforms of the 2 PMTs and the 8 APDs of the MainzTPC as well as the germanium detector signal. With the five remaining channels, additional detectors can be read out (such as a second germanium detector or similar).

For each channel, the voltage range can be chosen to be either $\pm 1 \text{ V}$ or $\pm 2.5 \text{ V}$. Also, the signal polarity can be set according to the connected detector and the baseline offset is adjustable over the full range.

The recording time for each event can be adapted, for all measurements it was chosen to be equal or longer than $34 \mu\text{s}$ to take into account the electron drift time in the TPC.

As the FADC has a ring buffer, also samples before the trigger time can be stored to the data. To ensure that all signals are recorded completely and to have an initial baseline for each waveform, a pretrigger window was used.

The SIS3305 [97] is the second digitizer in the DAQ system. Compared to the SIS3316 this 8-channel VME board has a smaller signal resolution of 10 bit, but each channel has a sampling rate of 1.25 GS/s. Using several channels in a multiplexed connection, a maximum sampling rate of 5 GS/s is achieved. In this mode, only two channels can be used, since the sampling rate of 4 channels each are combined. This time resolution is necessary for the pulse shape measurement, since the decay time of the singlett excimer is about 2 ns and therefore it is not resolvable with the SIS3316 FADC (see also section 2.4).

As each sample is only 0.2 ns long, even a large waveform with 4800 samples only corresponds to a short time window of 960 ns. That is why this digitizer is only used to measure the $S1$ signal and not the complete waveform. Also, with a voltage range of 0 V to -1 V, the dynamic range is too small for many of the $S2$ signals. The range was chosen deliberately, since the positive part of the standard input range of ± 1 V is not used with negative PMT signals. By asking Struck for the adapted voltage range, the effective resolution was doubled. The use of SMA connectors provides an analog bandwidth of 2 GHz. Similar to the SIS3316, a part of the recorded waveform is contributed by the pretrigger window to obtain a baseline.

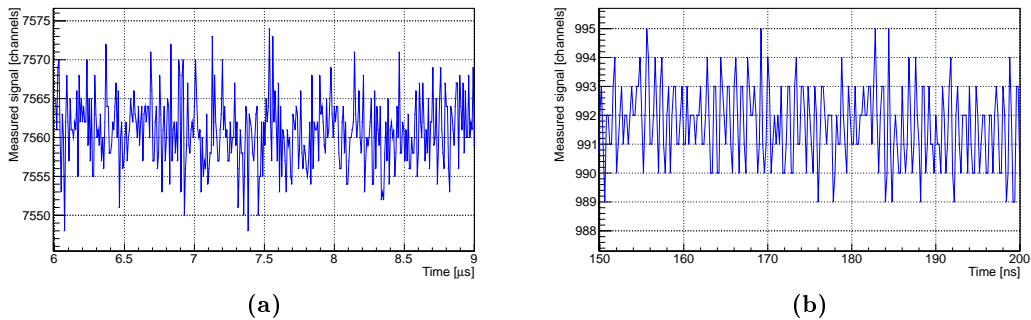


Figure 4.5: Baselines on (a) SIS3316 and (b) SIS3305, exemplarily for a measurement with a PMT. The FADC data is presented in measured channels to simplify the determination of the effective resolution. The respective offsets are chosen such that the baseline and possible signal-induced baseline shifts can be observed.

Figure 4.5 shows the baselines of the two digitizers. The baseline data is presented in measured FADC channels without a conversion using a voltage range. With a 16 bit resolution, the SIS3316 possesses $2^{16} = 65536$ channels. The respective baseline in figure 4.5a is positioned at a mean value 7560 channels. This large offset was chosen to take into account dips of the baseline after large signals. The signals on the SIS3316 are

recorded as positive pulses. With a standard deviation of 4.52 for the signal baseline, the effective resolution is about 13.82 bits.

For the SIS3305, the signals from the PMTs are not inverted to positive pulses and therefore negative pulses are recorded. With its 10 bit resolution, the number of channels of this FADC is 1024. Considering the baseline in figure 4.5b, the values are close to the maximum of the FADC. For the expected negative PMT signals, this means that almost the complete FADC dynamic range can be utilized. An internal offset shifting the baseline to the observed values ensures that the baseline as well as small signal features can be measured. The standard deviation of the baseline is calculated to 1.37, which leads to an effective resolution of approximately 9.55 bits.

4.2.2 | Timing and Trigger Signals

In the DAQ version 1, the generation of the event trigger is done internally by the SIS3316 FADC. This is explained in detail in section 4.3.

For the setup at the HZDR which includes the neutron detectors (DAQ version 2), the information about the signal timing is more crucial because of the TOF measurement for the neutrons. The DAQ system was changed and extended for the neutron setup, with the possibility to use the new features also for Compton measurements.

The constant fraction discriminators (CFDs) which were provided by the HZDR play the keyrole for the time measurement as well as the signal production for the trigger

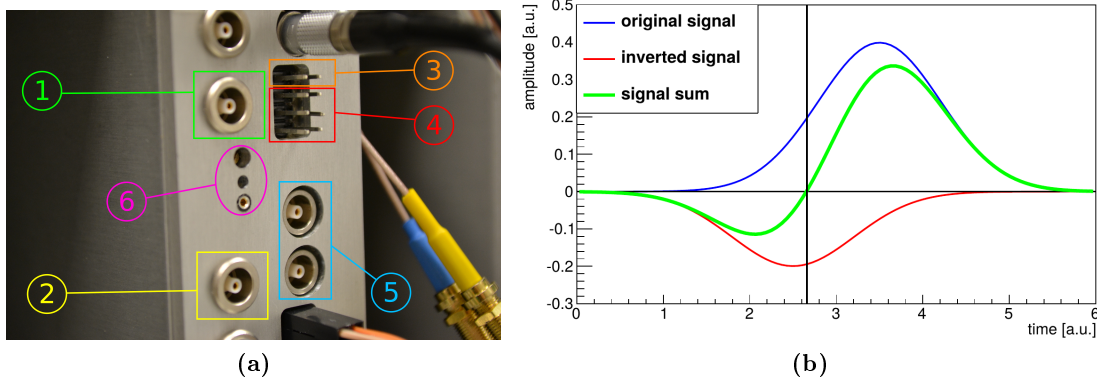


Figure 4.6: Constant Fraction Discriminator (CFD): The photograph in (a) shows the front panel of a CFD manufactured at the HZDR. The analog signal is fed in via the LEMO input (1), the resulting digital signals can be retrieved from LEMO outputs (2) (and on the rear side), an LE output (3) and three ECL/LVDS outputs (4). (5) marks the connectors for the delay cable and (6) is an adjusting screw to set the discriminator threshold. The CFD principle is sketched in (b): The incoming analog signal is split into one delayed (and amplified) signal (blue) and an inverted signal (red). The zero-crossing point of the signal sum is used as timing information.

generation. Figure 4.6a shows a photograph of the CFD front panel for one channel. The purpose of a constant fraction discriminator is to determine the time position of signals with a constant rise time independently from their signal amplitudes. To work with the time information, the analog signal from the detectors has to be converted to a digital signal.

In the CFD, the incoming signal is split. One of the signals is delayed by a delay time which is smaller or equal to the signal rise time. Furthermore the signal might be amplified by a small factor. The other split signal is directly inverted. Both the inverted and the delayed signal are summed which results in a pulse that begins with a negative amplitude but crosses the baseline at a fixed fraction of the signal rising edge. Because of this it is called “constant fraction” discriminator. Figure 4.6b illustrates the signal processes in the CFD.

The NIM modules we used have five channels which each have one LEMO input for analog signals and 6 outputs for digital, standardized signal pulses. Two LEMO outputs (one at the front panel, the other on the rear side) provide NIM pulses, one output a differential Leading Edge (LE) pulse and the three remaining outputs deliver a differential ECL/LVDS (Emitter Coupled Logic/Low Voltage Differential Signaling) pulse. The pulse has a length of 30 ns and is started when the CFD signal reaches the zero-crossing point in the summed input signal.

Two additional LEMO connectors on the front panel for each channel are connected via a delay cable. The length of the cable depends on the necessary delay and varies for the different detectors.

Of the 6 outputs the NIM pulse was used to adjust the CFD threshold (e.g. at which fraction of the rising edge does the zero-crossing occur), while the three ECL outputs were connected to a TDC for time measurement, to a logic board for the trigger generation and to a scaler to get an information about the signal rates on the detectors.

The Time-to-Digital Converter (TDC) used in our setup is a CAEN VX1290 VME board with 32 ECL/LVDS input channels [98]. The resolution is 21 bit, which corresponds to an effective precision of 25 ps for the timing measurement. Due to jitter effects in the signal generation of the CFDs, each signal itself can only be measured with a 25 ns precision, but by subtracting the timestamps from a reference point (for the neutron setup: the accelerator clock), the maximum precision can be achieved.

The TDC measures the CFD signals from the MainzTPC (PMTs and APDs), from the germanium detector in case of the Compton measurement at HZDR and from the plastic detectors for the neutron detection. Besides this, additional signals were measured: the nELBE accelerator clock and different coincidence signals from the logic board which indicated for example a coincidence between the two MainzTPC PMTs or a coincidence in a plastic scintillator.

The CAEN V1495 General Purpose VME board is a programmable logic board [99]. It is used to identify different event structures from the CFD signals of all detectors and to send out a trigger signal if the event conditions are met (the trigger generation is discussed in more detail in section 4.3).

The number of channels for the board is variable, since it can be equipped with 6 different input/output stages. For the experiment, the inputs and outputs were chosen to be ECL/LVDS connectors. One stage of 8 LEMO outputs was used to cross-check signals live with an oscilloscope for test purposes.

The logic board is fed with all signals that are also measured at the TDC. With a program that was developed together with our collaborators at HZDR, it is possible to choose different conditions for the generation of an output trigger signal which in turn activates the data taking on the FADCs and the TDC.

Since the internal gate&delay programming is limited for this board, an external gate&delay generator NIM module (ORTEC octal gate generator GG8010) was employed to create signal gates or delays for signals, since this was necessary for several event trigger conditions. The trigger conditions will be elaborated in section 4.3.

The last VME board that is fed with the CFD signals is a 32-channel SIS3820 VME Scaler with ECL connectors [100]. All signals mentioned in this section are also led into this board. The scaler is used to monitor the signal rates which are recorded with the SCS system (see also section 4.9).

4.2.3 High Voltage Modules

Two different types of VME high voltage modules are used in the MainzTPC setup:

- The CAEN V6533P is a 6-channel VME board with positive polarity up to 4 kV and 3 mA [101]. For our setup, two of these boards are required to provide the high voltage of the eight APDs and the two TPC PMTs.
- For the germanium detector, which needs a positive bias voltage of 1.5 kV, the iseg VHQ 223M [102] was implemented. This 2-channel board with a maximum of 3 kV (with selectable polarity) and 2 mA was chosen for its low-ripple voltage output of typically less than 1 mV (maximum 2 mV). This ensures a stable signal measurement with the germanium detector.

The VME modules are read out during the data acquisition process.

Further high voltage supply modules which are not integrated to the DAQ system directly but are crucial for the measurement are the following:

- The Bertan 225 Series provides the negative high voltage for the cathode mesh. It has only one output channel and can reach voltages of -30 kV.
- With a NIM module of type iseg NHQ 226L, the gate mesh is set to a negative potential. The 2-channel board can reach up to 6 kV with selectable polarity and has a maximum current of 1 mA.

4.3 | Event Trigger

The decision whether the measured signals in the various photosensors of the setup constitute an "event" as defined in section 4.1 has to be made during the acquisition to obtain clean data. This makes the trigger generation stage one of the most important parts of the DAQ system.

The trigger generation for DAQ version 1 and 2 are quite different, since version 2 includes a lot more hardware and required a rethinking of the triggering mechanism to account for the TOF measurement of the neutrons. In the second version, both trigger generation mechanisms are implemented as described below.

The measurement data examined in this thesis was taken with DAQ version 2.

4.3.1 | DAQ version 1: Internal Trigger Generation on SIS3316

In the DAQ version 1 for the Compton setup, the DAQ program only included the two FADC boards SIS3316 and SIS3305. Each of these boards is able to detect a signal and to generate an internal trigger. The choice of using the SIS3316 for the overall trigger generation is founded on its ability to record the complete event time interval of up to more than 40 μ s. This allows to trigger on the $S1$ signal as the first occurring light signal of the event and recording the subsequent $S2$ signal in the same waveform. This also simplifies the measurement of the time difference between the two signals.

Recording the complete event with the SIS3305 would lead to a huge amount of data, considering the sample length of 0.2 ns. Therefore only a window of 960 ns is measured with the SIS3305, which still corresponds to 4800 samples per event. Triggering on the SIS3305 with its smaller event length would imply the necessity to trigger on both $S1$ and $S2$ separately. Possible associations between the signals would have to be examined in the analysis. Also, having a smaller input range of only 1 V compared to 5 V for the SIS3316, the $S2$ signals exceed the SIS3305 dynamic range.

To operate the SIS3316 with internal trigger generation, several registers on the VME board have to be configured accordingly:

- The expected signal polarity has to be set so that the trigger threshold can be applied.
- The internal trigger threshold has to be set. In addition, even a so-called High Energy Suppress Trigger threshold can be chosen, which prevents the recording of signals that exceed this threshold. Furthermore, a CFD feature can be used to measure the signal in time more precisely. (The working principle of a CFD is described in section 4.2.2.)
- The trigger threshold is not applied to the signal itself but to a Moving Average Window (MAW). The parameters of this MAW, the peak time and the gap time, can be set compatible to the expected signals (see also [96]).

The board offers the choice between external and internal triggering. For external triggers, a NIM input is provided.

The SIS3316 firmware includes a Trigger Coincidence Lookup Table² that allows to set up a coincidence pattern for different channels. For example, a coincidence mode for the Compton measurement would yield a trigger signal if the following condition was fulfilled:

$$\text{CH}(\text{Top PMT}) \wedge \text{CH}(\text{Bottom PMT}) \wedge \text{CH}(\text{Ge})$$

Similarly, another lookup table could yield a trigger signal if at least one of the PMTs would see a signal coincident with the germanium detector:

$$\begin{aligned} & (\text{CH}(\text{Top PMT}) \vee \text{CH}(\text{Bottom PMT})) \wedge \text{CH}(\text{Ge}) \\ = & (\text{CH}(\text{Top PMT}) \wedge \text{CH}(\text{Ge})) \vee (\text{CH}(\text{Bottom PMT}) \wedge \text{CH}(\text{Ge})) \end{aligned}$$

In the first example, the lookup table would consist of one entry activating a logic `True` if all of the three named channels would detect a signal, while in the second example, two entries are necessary, since now the trigger can be activated by two different conditions. The present DAQ system has a series of implemented lookup tables that can be chosen from the `hardware.xml` file:

- MainzTPC coincidence: The trigger is generated for a signal detected in both TPC PMTs. This mode is used for the measurement of radioactive sources for a direct TPC calibration. Since both PMTs detect the *S1* signal almost simultaneously, the coincidence window length can be set to a very small value.
- Compton coincidence: To measure clean Compton events, a coincidence between the *S1* signal on the MainzTPC PMTs and the germanium signal from the scattered photon is required (triple coincidence). Considering the time-of-flight of the photon, the time difference between the two interactions is almost negligible with only a few nanoseconds. But the signal generation inside the germanium detector introduces a time delay. First, the time for the charge collection inside the germanium crystal can differ in the order of hundreds of nanoseconds, depending on the location of the interaction in the crystal. Second, the built-in CSP adds an additional delay. The first effect leads to a range of time intervals between the *S1* and germanium signal. To compensate for this range with the SIS3316, the length of the coincidence window has to be in the order of 1 – 2 μs , which increases the risk of chance coincidences.
- Trigger efficiency mode: With the internal trigger generation, the measurement of the trigger efficiency is done in two steps. First, a radioactive source such as ^{22}Na is installed between the MainzTPC and a secondary detector, for instance a NaI(Tl) or LaBr scintillator. The decay process of ^{22}Na releases two 511 keV

²The Lookup Table, as well as the Internal Feedback feature and the Trigger Hold-Off, was implemented to the firmware by Struck after our feedback on the required trigger options for the SIS3316 and is available from revision 1.10 (February 2015) and higher.

gamma-rays with opposite directions. Then a coincidence between MainzTPC and the secondary detector is measured. In the second step, the same setup is used but triggered only on the secondary detector. Since the second measurement can include also events where the signal in the MainzTPC was too small to generate a trigger, the combination of both measurements can be used to determine the trigger efficiency.

- External trigger: For photosensor calibration, a pulse generator is used to create LED pulses. The trigger signal of the pulse then is used to trigger the DAQ system. In this case, an external trigger is led to the NIM Trigger In input.

Apart from these trigger modes, the internal triggering using a single channel is also possible.

In all cases, the LEMO Trigger Out or LEMO User Out signal have to be configured so that the outgoing signal triggers the SIS3305. The SIS3316 provides the common trigger source for the data acquisition. The trigger pulse generated by the Lookup Table is used as the output signal as well as the internal trigger signal for the SIS3316 itself (Internal Feedback Select register).

The "External Trigger Disable with internal Busy" bit in the acquisition control register ensures that no external trigger signals are generated while the SIS3316 is busy, even if the incoming signals match the trigger conditions.

Figure 4.7 illustrates the connections between the MainzTPC sensors and the DAQ electronics for a Compton scattering measurement with DAQ version 1. The TPC

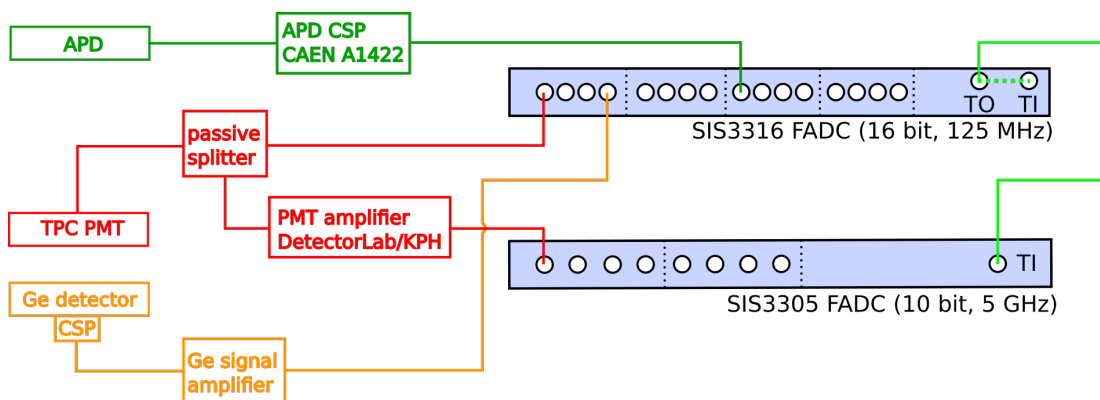


Figure 4.7: DAQ setup version 1: The DAQ records the signals of the APDs, the TPC PMTs and the germanium detector. For convenience, only one device of each kind is depicted. The APDs are amplified using a commercial CSP and are recorded by the SIS3316. The PMT output signal is passively split, with the unamplified signal being measured by the SIS3316 and the amplified signal fed to the fast FADC SIS3305. The germanium signal is amplified using the built-in CSP and the custom-made germanium amplifier and is recorded by the SIS3316 for the good energy resolution. The signals of the TPC PMTs and the Ge detector on the SIS3316 are internally processed to generate the DAQ system trigger pulse, triggering both SIS3316 (internally) and SIS3305.

PMT signals are measured on both FADC boards, while the APDs and the germanium detector only provide signals for the SIS3316. The internal trigger generation on the SIS3316 forces the recording of both FADCs.

4.3.2 | DAQ version 2: Trigger Generation with CAEN V1495

For the neutron scattering setup the DAQ program was upgraded to the second program version which includes also the TDC for the Time-Of-Flight (TOF) measurement. Consequently the two ADCs as well as the TDC have to be triggered simultaneously, and especially for the TDC the trigger timing is crucial to ensure a good energy resolution for the neutrons.

As described in section 4.2.2, CFDs are used to transform the analog signal from each sensor into a standardized digital signal which is evaluated for the trigger generation and measured by the TDC, providing a precise timing information.

The CAEN V1495 General Purpose board is used as a trigger logic processing the CFD signals to externally trigger both FADCs and the TDC. Figure 4.8 illustrates the electronic setup. Similar to the DAQ setup for version 1, the APDs do not contribute to the trigger generation and are measured by the SIS3316 only. The TPC PMTs are measured on the SIS3316 without amplification and on the SIS3305 with amplification. A second amplified signal is fed to a CFD channel. Also the germanium detector now has two amplified signals being measured; after the built-in CSP, one output signal is amplified by the germanium DetectorLab amplifier (for the SIS3316) while the second output signal goes into a Fast Filter amplifier which shapes and inverts the positive signal such that it can be measured by the CFD. The plastic PMTs of the neutron scintillators only provide a timing information in this setup, therefore their single output signal is directly fed to the respective CFD channel.

The CFDs have three ECL outputs (not counting the one marked LE – leading edge). The first output is connected to the CAEN V1495, sending the digital signals to the logic board, which in turn decides whether the trigger conditions are fulfilled or not. The second output provides the signals for the TDC board. By directly measuring the CFD signal, the timing resolution is limited by the individual sensor response. The third ECL output is connected to the scaler board (not drawn in the schematic, see also section 4.9). These signals are not crucial for the measurements.

If the trigger conditions are fulfilled, the CAEN V1495 sends out a trigger signal that simultaneously activates the data recording on both FADCs and the TDC board.

Logic board firmware

To use the logic board, not only VME registers have to be set. Instead, a customized firmware has to be written for the User FPGA on the board, because the required functionality for specific applications can differ extremely. The board offers large amounts

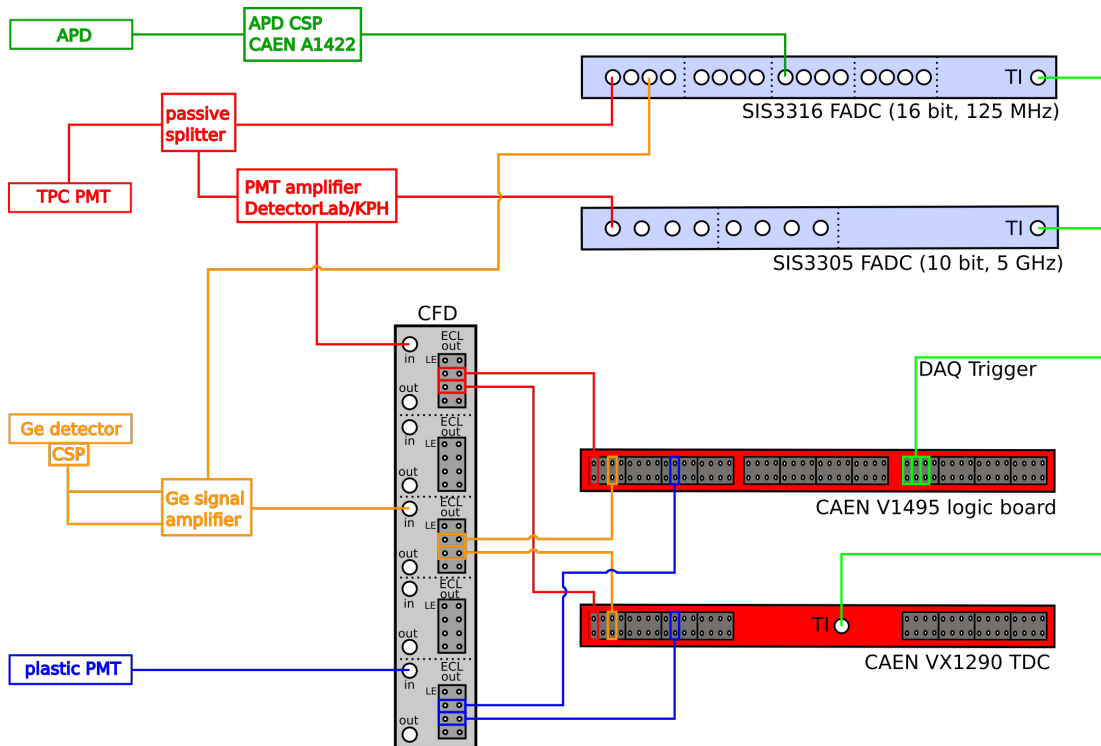


Figure 4.8: DAQ setup version 2: In comparison to the first version shown in figure 4.7, additional electronics and connections are necessary for the TDC measurement and trigger generation. Besides the APDs, the TPC PMTs and the Ge detector, the plastic PMTs for the neutron measurement are a new class of sensors included in the DAQ system. For the first three sensor types, the signals are measured as before with the FADC boards. Furthermore, the amplified TPC PMT signal, the Ge CSP signal amplified and inverted by a Fast Filter amplifier and the plastic PMT signals are fed to a CFD each, which generates a logic signal for each of the sensor signals surpassing a fixed threshold. The logic signals are fed to both a TDC to measure the signal time and the logic board CAEN V1495. The latter (together with a gate & delay generator, see text) processes the logic signals and eventually generates the DAQ trigger signal, which forces the FADC boards and the TDC to record the respective signals.

of input/output channels which can be adjusted to the respective purpose.

In the firmware a series of in-/outputs is declared as inputs, and the interconnection between the incoming signals is defined. Figure 4.9 shows the logic scheme for the firmware developed at the HZDR. The firmware allows the user to access customized VME registers to configure the logic board for the individual measurement.

To understand the logic scheme, it is helpful to explain the function of the different configuration bits in the control register. It holds the values for the bits `tpc_logic`, `plastics_logic`, `gate_signal` and `trig_sel`.

tpc logic: As can be seen on the left side of the logic scheme, the CFD signals of the sensors are paired, taking into account the respective combination possibilities. The

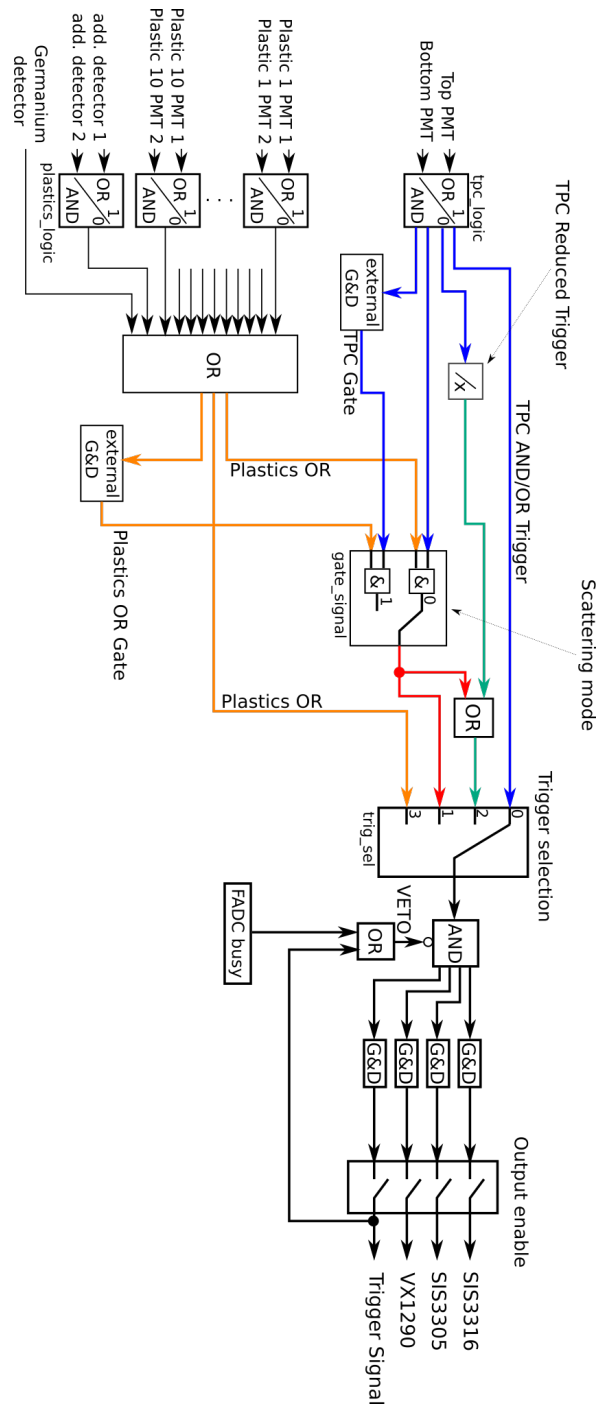


Figure 4.9: Logic scheme for the trigger generation with CAEN V1495: In a first step, the CFD signals of grouped sensors (such as the TPC PMTs) can be merged by a logic AND or passed on individually by an OR. The TPC AND/OR Trigger (blue) is the basic TPC trigger, either by the coincidence of both TPC PMTs or the individual CFD signals. It can be reduced by a factor x , which allows to downsize the trigger rate in the TPC. Both of these triggers can be combined with the signal of the secondary detectors, either the germanium detector or the plastics for neutron detection. Even additional detectors such as a NaI(Tl) or LaBr detectors can be used as secondaries. The combined signal (red) is the common mode for Compton or neutron measurements. For calibrations, the Plastics OR trigger (orange) is useful, allowing the secondary detector(s) to act as the trigger source(s). Both TPC Trigger and Plastics Trigger are usually delayed and elongated with an external gate & delay generator (see text). The generated DAQ trigger creates a gate signal which is sent to the DAQ electronics. A veto input is used to improve data quality (see text). The scheme was developed with R. Beyer.

value for bit `tpc_logic` decides whether both TPC PMT signals are processed as TPC Trigger (OR) in the logic board or only the coincidence of both TPC PMTs (AND). In the latter case single PMT signals surpassing the threshold would not lead to a TPC Trigger.

plastics logic: For the secondary detectors, which include the plastics for the neutron detection, the germanium detector for the Compton scattering as well as additional detectors, such as LaBr or NaI(Tl) detectors for trigger efficiency measurements, the logical interconnection is defined using the `plastics_logic` bit. In case of the germanium detector, a coincidence between secondary detectors is not necessary. For neutron detection, a coincidence of the two PMTs connected to the individual plastic scintillators is mandatory to regard the signal as a neutron detection³.

gate signal: The resulting internal trigger signals from the TPC (marked blue) and the secondary detectors (marked orange and labeled Plastics OR, since all secondary detectors or detector pairs are interconnected by a logic OR) can then either be used as a trigger output signal or they can be processed further to improve the resulting trigger. Both signals can be combined in a coincidence stage. The output is marked in red and represents the Compton scattering or neutron scattering mode. More exactly, the coincidence stage can be used either with the raw TPC Trigger and Plastics OR signals or with a gated version of the two, which is the common procedure and is explained in more detail below in this section. The latter is activated using the `gate_signal` bit.

trig sel: Regarding the logic scheme, all signals on the left of the "Trigger selection" box are internal logic signals. In part, they are sent to the scaler board or can be accessed at LEMO outputs for cross-checks with an oscilloscope, but for the final output trigger that is responsible for the DAQ to record an event, the signal has to pass the Trigger selection box. Four choices are available for the `trig_sel` parameter: For "0", the TPC Trigger is used as DAQ trigger. This mode is used for the TPC calibration measurements with radioactive sources. The mode "1" is used for the scattering measurements, since it passes the Coincidence trigger. The trigger setting "2" is a special case (marked cyan), combining the TPC Trigger and the Coincidence trigger, but suppressing the TPC trigger by a factor x . This mode was not applied during the measurements, it can be useful to measure Compton scattering with a low coincidence rate and simultaneously take advantage of the high event rate in the TPC to measure the TPC response with high statistics. Setting `trig_sel` to "3" eventually allows to trigger on the secondary detectors only, which is necessary to calibrate these detectors.

³The scheme lists up to ten plastics with two PMTs each. Actually, 15 neutron detectors were installed in the setup (ten in front of the TPC to measure forward direction at angles between 8 and 35°, five at angles of about 130 to 152° to account for backward scattering), but only ten could be operated simultaneously due to the limited number of CFD and TDC channels.

For a better overview, the control register bits and their functionalities are summarized in table 4.2.

bit value	0	1	2	3
tpc logic	TPC OR	TPC AND	–	–
plastics logic	plastics OR	plastics AND	–	–
gate signal	direct CFD signal	CFD signal processed by gate & delay generator	–	–
trig sel	TPC Trigger	Coincidence Trigger	Combination of Coincidence and Reduced TPC Trigger	Plastics Trigger

Table 4.2: Control register for the logic board: The individual bits are used to configure the logical connection of the two TPC PMTs (tpc logic), of the secondary detectors (plastics logic), whether the raw CFD signals or processed signals are used for the trigger generation (gate signal) and to select the DAQ Trigger signal for the specific measurement.

The selected logic trigger signal is gated and sent to the output connectors if two additional conditions are met: First, the output has to be enabled. During the readout and storage of the data the DAQ trigger is disabled to ensure that data can only be acquired if all boards are ready for recording. Second, while recording events in the course of the data acquisition (see section 4.7) the SIS3316 sends a busy signal "FADC busy" to the logic board vetoing the DAQ trigger. Equivalently to the "External Trigger Disable with internal Busy" bit for DAQ version 1 described in the previous subsection the FADC busy signal blocks outgoing DAQ triggers until the recording on the SIS3316 with the longest acquisition window is complete and all boards are ready for recording. The logic board firmware also includes a module reset register which is executed at startup and it enables the user to specify the input channels used in the specific measurement. Table 4.3 gives an overview of all ECL and LEMO inputs and outputs with the respective purpose of the output signals. Output channels without a specified purpose are not used for the trigger generation, but for testing and as scaler inputs, to monitor the signal rates.

The signals for input A are CFD signals from the respective sensors, except for channels 30 and 31, which are the TPC Trigger and Plastics OR signals after passing the gate & delay generators (see below). For the plastics, the PMT at the top of each scintillator is denoted with the ending "-1" and the PMT on the bottom end with "-2". For a Compton scattering measurement, most of the input channels are not useful and should therefore be deactivated before taking data. Also, if one of the neutron detectors would be so noisy that the neutron scattering measurement could not be conducted properly, excluding this particular neutron detector from the list of possible signal providers would clean up the data.

Trigger Generation with Gate & Delay generator and Veto Conditions

As described in section 4.3.1, the germanium detector introduces a time delay for the signal generation itself. The charge collection in the crystal as well as the internal

ECL connectors					
Ch	Input A	Output F	used for		
0	TPC Top PMT	TPC AND/OR trigger	gate & delay		
1	TPC Bottom PMT	PL OR trigger	gate & delay		
2	germanium detector	Trigger Out	TDC input		
3	additional detector	PL OR trigger	TDC input		
4	additional detector	TPC AND/OR trigger	TDC input		
5	plastic PMT 1-1	Coincidence trigger	TDC input		
6	plastic PMT 1-2	Red. Coincidence trigger	TDC input		
7	plastic PMT 2-1	-			
8	plastic PMT 2-2	TPC Top trigger			
9	plastic PMT 3-1	TPC Bottom trigger			
10	plastic PMT 3-2	TPC AND/OR trigger			
11	plastic PMT 4-1	TPC Reduced trigger			
12	plastic PMT 4-2	TPC AND/OR gate & delay			
13	plastic PMT 5-1	PL X-1 PMT signal			
14	plastic PMT 5-2	PL X-2 PMT signal			
15	plastic PMT 6-1	PL X-X PMT signal			
16	plastic PMT 6-2	PL OR trigger			
17	plastic PMT 7-1	PL OR gate & delay			
18	plastic PMT 7-2	PL OR trigger			
19	plastic PMT 8-1	TPC AND/OR trigger			
20	plastic PMT 8-2	Coincidence trigger			
21	plastic PMT 9-1	TPC Reduced trigger			
22	plastic PMT 9-2	Trigger Out (no veto)			
23	plastic PMT 10-1	Trigger Out			
24	plastic PMT 10-2	Trigger Out			
25		FADC busy			
26		Veto			
27		Trigger Out			
28		Trigger Out			
29		Trigger Out			
30	TPC AND/OR gate & delay				
31	PL OR gate & delay				

LEMO (NIM) connectors					
Ch	Input D	Output E	used for	Output G	used for
0	FADC busy	Trigger Out	TDC Trigger	Trigger Out	
1		Trigger Out	SIS3316 Trigger	Veto	
2		Trigger Out	SIS3316 Trigger		
3		TPC AND/OR trigger			
4		PL X-X PMT signal			
5		PL OR trigger			
6		Coincidence trigger			
7		TPC Reduced trigger			

Table 4.3: Input and output assignments for the CAEN V1495 logic board: The top part of the table shows the signal in-/outputs with ECL connectors. The input signals are mostly provided by the CFD channels of the respective sensors, except for the inputs 30 and 31, which are the TPC Trigger and Plastics Trigger (PL) from the gate & delay generator, which were sent out as raw trigger signals on channels 0 and 1 of output F. The other ECL outputs are used for the TDC. If nothing is specified in the "used for" column, these signals were used to be monitored in the scaler or to check if the board functions as required. In the lower part of the table, the in-/outputs with LEMO connectors are listed. The only input is the FADC busy from the SIS3316, inhibiting the trigger output during data taking. The LEMO outputs were used to trigger the FADCs and the TDC as well as a convenient possibility to access various raw trigger signals.

CSP add an analog delay, therefore the germanium signal, already being the second "scattering" process of the incoming gamma-ray, is always delayed with respect to the TPC signal. Since the interaction in the crystal can happen in different spots, the introduced pulse shape and therefore the time delay can vary substantially. The time difference of up to about $1\ \mu\text{s}$ between the $S1$ and the germanium detector are shown in figure 4.10.

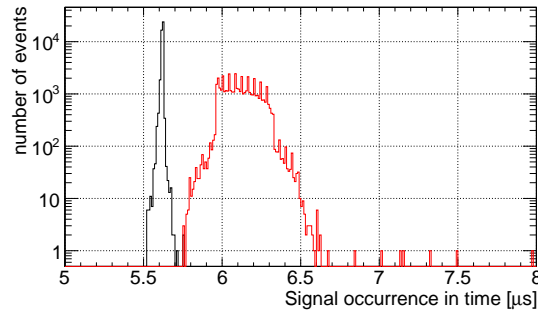


Figure 4.10: Occurrence time of $S1$ signal and germanium signal from Compton scattering measurements. Due to the charge collection in the germanium detector, the corresponding signal is created between hundreds of nanoseconds up to the microsecond scale after the $S1$ signal is observed.

For the Compton scattering coincidence mode, this would mean that the signal of the TPC would start the coincidence window and the germanium signal would then trigger the recording at a non-specified time. Therefore the trigger should be associated with the TPC signal. If the TPC signal is activating the trigger, the triggering $S1$ can be found in the same timing position in all FADC waveforms, which simplifies the analysis. To realize this trigger, a gate & delay generator is employed for both the germanium (Plastics OR) and TPC logic signals. Figure 4.11a indicates the generation of the DAQ trigger using the gated signals.

The CFD signals from the TPC PMTs (here assumed to be in coincidence) and the germanium detector arrive with different delays. These are caused in part by the cable length, but also by the detectors themselves. The PMTs are very fast performing and their intrinsic delay is small compared to the delay introduced by the germanium detector. Depending on the spatial position of the interaction in the germanium crystal, the time required for the light collection can differ between events. This is indicated with different positions of the germanium CFD signals in time. It also has an influence on the shape of the germanium signal rising edge. Also, the built-in CSP adds to the analog delay.

The germanium signal is transformed into a long gate signal of $537.4\ \mu\text{s}$ and delayed by a total $120\ \text{ns}$. A delay of approximately $54\ \text{ns}$ caused by the gate & delay generator itself affects both the germanium and TPC signal, constituting a minimum additional time offset. The gate & delay generator introduces its intrinsic offset twice for the germanium logic signal, because it passes through the module two times. First, the incoming signal is gated with $754.4\ \text{ns}$ which is longer than the actual germanium gate length and the

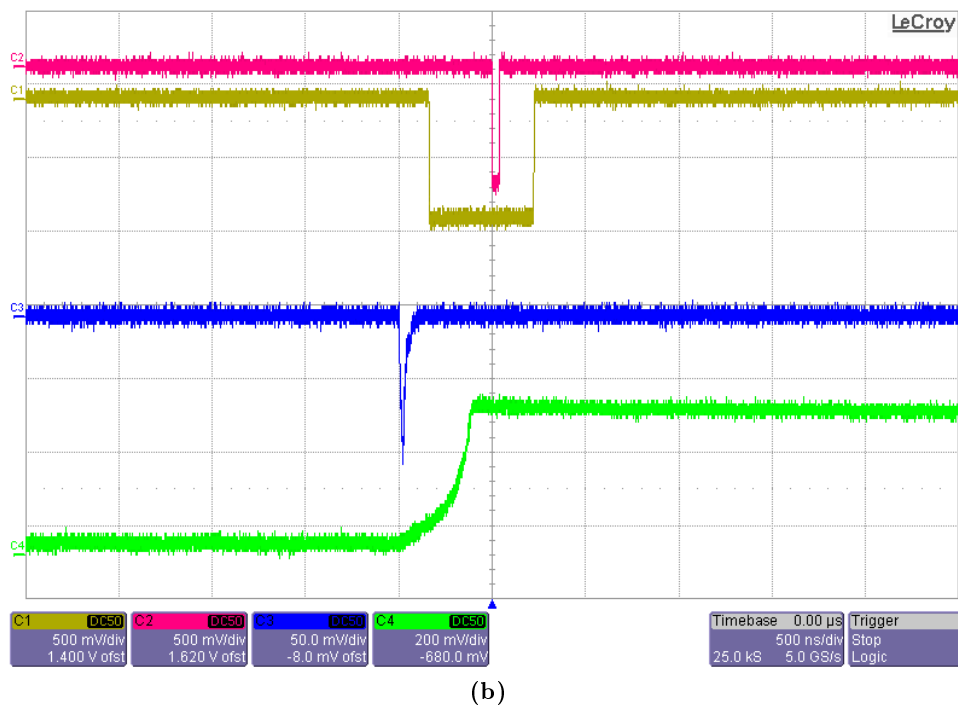
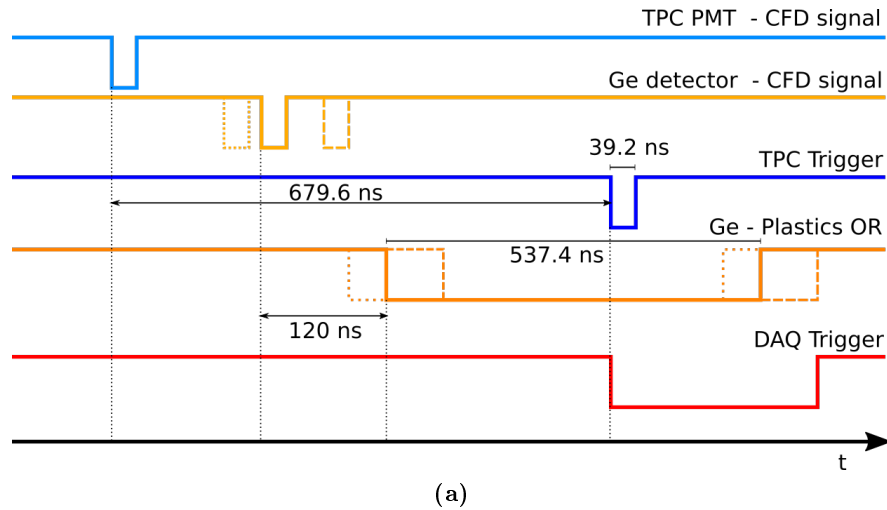


Figure 4.11: Compton event trigger generation with DAQ version 2: (a) The CFD signals of the TPC PMTs and the germanium detector occur with an analog delay. For the latter, the signal collection in the crystal can lead to different delay times, as indicated. The germanium signal is elongated and delayed by 120 ns, which is less than the delay for the TPC PMT CFD signal. Therefore, the germanium gate becomes active first and opens the coincidence window, which also can shift in time according to the analog germanium signal delay. The TPC Trigger occurring during this gate complements the coincidence trigger condition and leads to the generation of the DAQ Trigger with a fixed delay with respect to the signal in the TPC. The signal times are not to scale. (b) The signal of one of the TPC PMTs, which are in coincidence mode, is shown in blue, the germanium signal of the scattered gamma-ray in green. Both signals surpass their CFD thresholds and the logic board processes the CFD signals, sending them to a gate & delay generator. The resulting gate of the germanium signal (yellow) has a length of 537.4 ns, while the delayed TPC gate (pink), being not elongated, defines the trigger timing with its fixed delay time of 500 ns in this test (which was increased to 679.6 ns for the measurements). The result is the DAQ trigger for the Compton measurements. The picture was taken with an oscilloscope at the HZDR during preparation for the Compton measurement.

resulting gate is fed to a second input of the gate & delay generator. The second channel produces the output gate with the required gate length (537.4 ns) and delay. Using two channels for one signal and gating the incoming signal prevents signal pile-up: A second logic signal would not affect the length of the second channel as the input is only sensitive to a falling edge of a logic signal. Hence the germanium gate length is fixed to the chosen value.

Meanwhile, the TPC signal gate is relatively short with 39.2 ns but delayed by 679.6 μ s. This very long delay is necessary to account for the large analog delay of the germanium signal. Consequently, the germanium gate signal occurs first and opens the coincidence window, and the delayed TPC signal completes the coincidence when occurring during the germanium gate time. Using the TPC Trigger to set the timing of the overall DAQ Trigger fixes the *S1* position in the waveforms and TDC data.

Figure 4.11b depicts an oscilloscope screenshot of an event in a Compton measurement together with its logic gate signals that generate the DAQ trigger. It shows the signal of one of the TPC PMTs in blue (which are in coincidence mode) and the germanium signal in green. It can be seen that the germanium signal occurs after the TPC signal, as expected. In yellow, the long gate signal from the germanium logic pulse is shown. The pink signal is the gate pulse from the TPC Trigger, which is delayed and therefore occurs after the germanium gate. The falling edge of the pink signal in the center of the picture marks the trigger time because at this point both TPC and germanium signal are in coincidence.

Using the gate & delay generator allows to define different coincidence window lengths for each involved logic signal as well as the triggering signal and its timing with respect to the interaction in the TPC. All these features make this trigger generation setup superior to the one implemented in DAQ version 1.

Contrary to the Compton measurements, an additional veto condition is introduced for the DAQ trigger in the neutron scattering configuration. As described in section 3.5.4, at the nELBE neutron source both gamma-rays and neutrons are produced by the ELBE accelerator, and since the MainzTPC is sensitive to both particle types, the probability to detect both particle types in one event has to be maximally suppressed. While a lead absorber is used to block most of the gamma-rays already at the production site, a trigger veto was introduced which inhibits the DAQ trigger with the exception of a 3 μ s gate window per beam clock cycle. This veto suppresses chance coincidences and helps to clean up the neutron data significantly. The beam clock occurs 9.7 μ s before the neutron production. This offset explains the necessity of a large TDC measurement window (see section 4.6.3). The beam clock gate length of 3 μ s is chosen to allow neutrons with energies between 30 keV and 1.5 MeV to reach the neutron detectors.

Figure 4.12 shows the measured trigger generation for a neutron event. Since the plastics signals are directly converted to logic pulses in the CFD, only the logic gate signals are shown here. The figure depicts the accelerator beam gate in yellow. The Plastics OR gate (green) from the neutron detector opens the coincidence window and the TPC Trigger gate (blue) triggers the coincidence. Here, the actual DAQ trigger signal is also measured (pink).

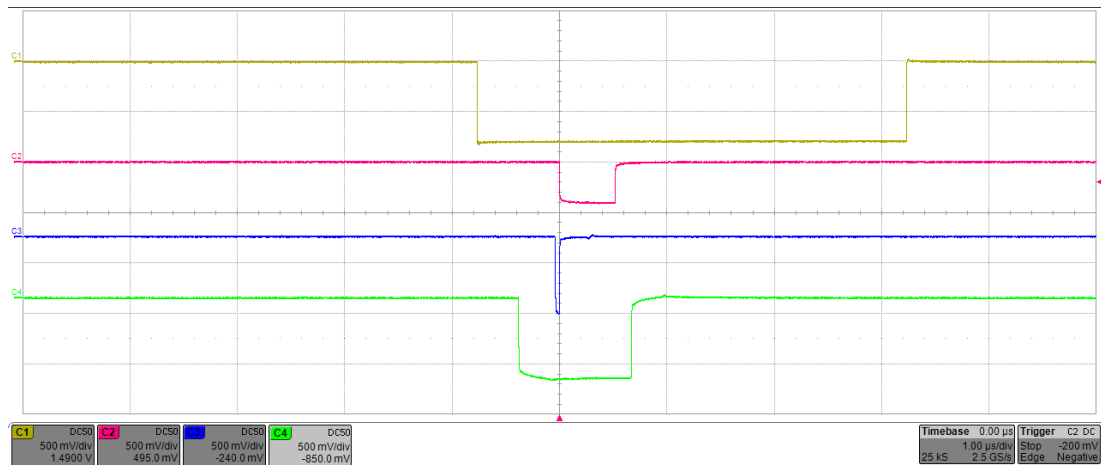


Figure 4.12: Neutron event trigger generation with DAQ version 2 - oscilloscope measurement: The large gate drawn in yellow shows the measurement window defined by the beam trigger veto (see text). Since the analog signal of the plastics is not recorded, the figure shows the gate generated by the plastic that detected a neutron (green), the delayed TPC PMT trigger signal (blue), and the resulting DAQ trigger (pink) which leads to the recording of the event. The picture was taken with an oscilloscope at the HZDR during the neutron measurement run.

The signal processing of the raw CFD signals to the gated signals of the TPC Trigger and the Plastics OR is illustrated in figure 4.13. Here, the more complicated case of neutron scattering is shown. Both PMTs as well as all PMTs of the plastics are connected to their respective CFD channels. The resulting digital signals are sent to the CAEN V1495 logic board and the coincidence signals TPC Trigger (red) and Plastics (blue) are created. These raw logic signals are fed to an external gate & delay module which elongates the Plastics signal (here for the neutron detectors, but in Compton mode also for the germanium detector) and delays the TPC Trigger signal which then serves as the timing trigger pulse in the coincidence window. The numerical values given in the figure were used in the neutron scattering measurements at the HZDR.

The beam clock with a rate of approximately 25.4 kHz is used as a DAQ trigger veto as explained above. The relatively low beam rate is linked to the length of the acquisition window in the MainzTPC. For an acquisition window of 41.6 μs used on the SIS3316, a higher beam rate would only lead to superposed events.

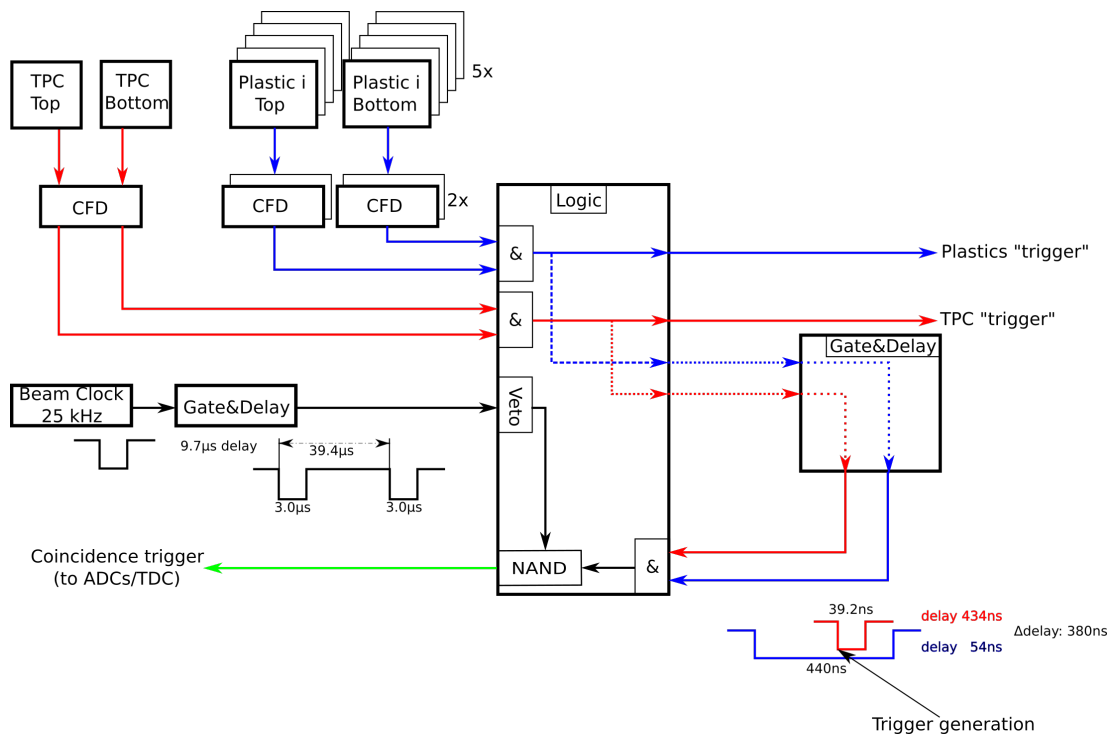


Figure 4.13: Trigger logic for DAQ version 2: The sketch shows the trigger generation in the CAEN V1495 with the help of an external gate & delay module for the neutron scattering measurements (analogous for Compton scattering with only one Plastic input and no Beam Clock Veto). The signals from the TPC PMTs (red, the amplifiers are not drawn here) and the signals from the PMTs of the "plastics" (blue) are fed to their respective CFD channels. For signals surpassing the CFD threshold, logic signals are generated which reach the input of the logic board CAEN V1495. For the cleanest neutron scattering events, a coincidence between the TPC PMTs as well as between the two PMTs of one plastic is required for the signal to be passed on. The respective coincidence logic signals can be checked on the logic board outputs as "plastics trigger" and "TPC trigger", and are also fed to the scaler board. The logic signals are furthermore sent to the gate & delay module, which opens a large gate for the plastics signal and a short, delayed gate for the TPC signal. This ensures that the TPC signal triggers the coincidence, which is generated back in the logic board. The resulting coincidence logic signal is vetoed by the beam trigger veto if required (see text), otherwise a NIM trigger signal for the DAQ system is created.

4.4 | DAQ Program Functionality Overview

The program operation can be divided into three subparts:

1. At startup, the program needs to be initialized and configured. For this, two `xml`-files are read. The first one, labeled “hardware”, contains basic configuration parameters which are supposed to be left unchanged for the experiment. The second one, “settings”, can be changed by the operator so that the program is configured for the specific measurement at the time (for example sensor calibrations or Compton scattering).
The parameters are then transferred to the respective electronics board to set the internal registers.
2. After the system is configured, the data acquisition routine is started. This is done by activating the trigger generation. In this state, the DAQ system acquires event data for every trigger signal until the termination condition is fulfilled and the trigger is deactivated.
3. In the third part, the acquired data is read out from the VME electronics and stored to binary files using the MainzTPC data format (see section 4.8) The data is also checked for consistency, that means that all FADCs have to have measured the same number of events. This is necessary to ensure that the stored events do not contain signals from multiple measured events in different channels.

Since the memory on the FADC boards is limited, steps 2 and 3 are repeated alternately until the requested number of events is acquired.

4.5 | Communication in VME Electronics

The different VME boards of the DAQ system are controlled via the VME controller SIS3100, which itself is linked to the SIS1100 PCI board in the DAQ computer. The Linux driver for the SIS1100/3100 PCI to VME interface provides routines to read and write data from and to the individual VME boards in the VME crate.

The following line of code depicts a read routine:

```
vme_A32D32_read(vme_stream, vme_addr, &data)
```

Here, `vme_stream` stands for the connection to the SIS3100 driver, `vme_addr` is the address of the datum to be read and `data` is providing a variable to store the required datum in.

The nomenclature `vme_A32D32_read` indicates that the address as well as the datum is

a 32-bit word. Depending on the VME board firmware, also other addressing and data standards can occur. For the DAQ program, the standards A32D32 (Struck boards and CAEN V1495) and A32D16 (CAEN VX1290) were encountered. The high voltage supply boards use A32D16 (CAEN V6533) and A16D16 (iseg VHQ 223M).

When addressing a specific register in a VME board, the upper 16 bit of the 32-bit word identify the board. For example, the base address of the SIS3316 is 0x30000000, the register address for the Raw Data Buffer Configuration register is 0x1020, that means to read out this register the value for `vme_addr` should be 0x30001020.

The VME registers hold their information also in form of hexadecimal values. Decoding the hexadecimal number to binary code allows to decrypt the status or configuration of the respective register. For example, the Control/Status register of the SIS3316 allows to control three LEDs on the board front panel with the three lowest bits. So if `data` contains the value 0x7 after reading this register, which in binary means 0 1 1 1 (lowest bin on the right), then all three LEDs are switched on.

To configure the VME boards the complementary write routine is used:

```
vme_A32D32_write(vme_stream, vme_addr, data)
```

In this case, the word `data` is not filled with information from the board, but instead provides the binary configuration of the addressed register.

One has to keep in mind, that not all registers allow for writing. Also, some registers do not contain a reading information. An example for this are module reset registers, which restore the factory settings when an arbitrary `data` word is written to them.

4.6 | DAQ Program Initialization and Configuration

During the initialization process, the DAQ program accesses two `xml`-files which provide input parameters. The decision to use two different files called `hardware.xml` and `settings.xml` was taken to distinguish between configuration parameters for the electronics that should not be changed for the duration of the complete experiment and settings parameters that might be adjusted for the respective measurements by the respective operator. The settings file therefore contains parameters which can be changed without deeper knowledge of the DAQ program code.

The initialization starts with loading the VME driver and checking the response of the SIS3100, the VME controller.

After that, the DAQ program reads the information from the two `xml`-files for each VME board and then initializes and configures the respective board. The initialization is always preceded by a check of the board response by accessing the module identification register and a subsequent module reset command.

4.6.1 | SIS3316 Initialization and Configuration

After resetting the SIS3316, it also gets a disarm command, which means that it can not acquire data. Furthermore, two initialization steps are carried out:

1. Configuration of the Sample Clock: For this, an ADC clock reset command is issued for the complete board. Afterwards, each ADC FPGA input logic has to be calibrated for the resetted clock, to adjust the data strobe timing. An IOB delay value of half a sample clock periode is added for each ADC channel using the Tap Delay registers (IOB: Input/Output Block in FPGAs).
2. Reset and configuration of the four ADCs: After the global board reset command, the output of the four ADCs should be disabled. For safety, a disarm command is issued for each individual ADC before resetting it. Afterwards, the input span (reference voltage) is set as described in the SIS3316 User Manual, the ADC registers are updated and the outputs are enabled again. For this initialization step, the ADC FPGAs are addressed directly using the Serial Peripheral Interface (SPI) of the ADC chips.

The initializations are necessary after each power up. Since it does no harm, they were implemented to be executed for each program startup.

The SIS3316 allows to configure a large variety of parameters. Some of them can be set for each individual channel, while others affect groups of four channels (each four neighboring channels are connected to one ADC) or have an effect on the complete board. For the MainzTPC, the following parameters and features are implemented:

- The gain, which is equivalent to the voltage input range, and the termination of each group of four channels can be adjusted. For each group of four channels the input range can be set to be 2 V or 5 V, which has an influence on the measurement resolution. For example, with a 5 V range, the minimal voltage difference that can be measured is $5\text{ V}/2^{16} \approx 76.3\text{ }\mu\text{V}$.
- The DAC (Digital-to-Analog Converter) offsets allow to shift the chosen voltage range from a total of -5 V to $+5\text{ V}$, that means expecting a negative signal from a PMT, the 5 V range would be shifted to cover values from -5 V to 0 V .
- The information about the signal polarity can be set. It is necessary when using the trigger ability of the SIS3316.
- The End Address Threshold is a parameter that contains the number of samples that are recorded for each channel before the board changes a bit in the acquisition control register. This “Memory Address Threshold Flag“ signals that the required amount of data is reached (or that the available memory is filled up). The value applies for all channels and should be set so that the acquisition can be stopped before a memory overload occurs and data is lost (see also section 4.7.2).

- Setting the Raw Data Buffer register determines the number of samples stored per event. With a sampling rate of 125 MHz, each sample has a width of 8 ns. For the measurements with the MainzTPC, the usual event length accounts for 35-40 μs , which is due to the maximum electron drift time expected in the liquid xenon. For a Compton measurement, for example, an event length of 41.6 μs was chosen, equivalent to 5200 samples (the event length also includes the pretrigger window, which was 800 samples or 6.4 μs).
- It is possible to choose one of several modes for the event header that is written to the memory for each waveform in each channel. The setting applies for all channels.
- When configuring the internal trigger of the SIS3316, the Active Gate Trigger Window Length has to be set. A trigger signal that does not occur within this gate window is ignored.
- Since it is useful to get an information about the baseline of a waveform, a pretrigger window length can be set. It is possible to set the pretrigger for each channel group individually, but for better comparison of all channels the DAQ program only allows to set a global pretrigger value.

In the first version of the DAQ program, the SIS3316 is responsible for the trigger generation, which is not mentioned in the list above. It uses its ability to internally measure signals and to use trigger conditions to identify an event. In the first DAQ version, the complete DAQ system is provided with a trigger signal from the SIS3316 User Out output. The trigger generation and the different possibilities implemented are described in section 4.3, where also the trigger generation for the second DAQ program version is discussed.

4.6.2 | SIS3305 Initialization and Configuration

The SIS3305 also needs to be initialized after each power up. After the board reset three initialization steps have to be executed:

1. Reset and calibrate the sample clock: By default, the internal 2.5 GHz clock is used (it is possible to also use an external clock). A synchronization pulse forces the clock out signals of the two ADCs to synchronize. The success of this procedure is checked for each ADC. The sample clock has to be calibrated not only at power up, but also when changing the sampling mode (1.25 Ghz on 8 channels / 2.5 Ghz on 4 channels / 5 Ghz on 2 channels).
2. The SIS3305 has an onboard EEprom (Electrically Erasable programmable read-only memory) which contains initialization parameters which are provided by the

manufacturer Struck. The parameters for the Tap Delay registers are read out to adjust the data strobe timing. Also, the ADCs are configured using the parameters for ADC gains, phases and offsets. The configuration is controlled by the choice of the sampling mode of the FADC, since the ADC can support 1, 2 or 4 different channels depending on the applied mode.

3. Although the sample clock is resetted in the first step of the initialization, the ADC clocks can have an offset from the sample clock. In fact, the ADCs use a smaller frequency of $\frac{1}{12}$ of the sampling frequency, which here is 208.33 MHz. This means that for an external trigger occurring at a random time, the start of the sampling period of the board ADCs is dependent on the ADC being in an active clock phase, and therefore it is possible to have a time difference between trigger signal and start of sampling of up to ~ 5 ns, corresponding to the ADC clock frequencies (see also the manual in [97], p. 11). An internal TDC has to be configured to measure the time difference between the external trigger signal and the start of the ADC sampling to account for this effect.

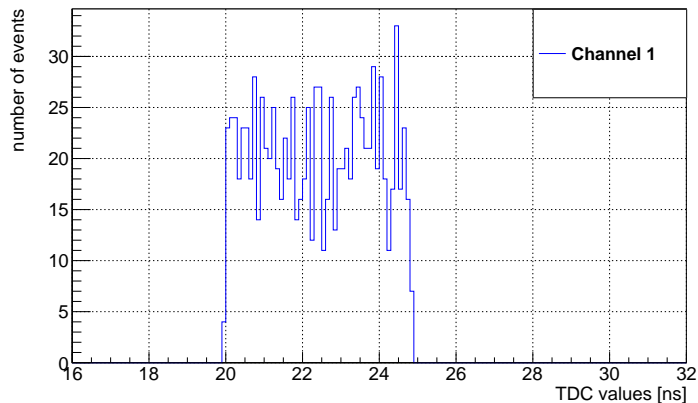


Figure 4.14: Measured time difference between external trigger signal and start of data sampling on the SIS3305 board, using the internal TDC feature.

The SIS3305 claims a time measurement accuracy of up to 0.2 ns, hence it is necessary to determine the time difference between the incoming trigger pulse and the beginning of the sampling period. Figure 4.14 shows the measured time differences between external trigger signal and the start of the data sampling. For this test, a test pulse was used as the signal as well as the external trigger. As can be seen, the measured value ranges between approximately 20 and 25 ns. This interval also shows the maximum deviation caused by the length of an ADC clock cycle.

Figure 4.15a shows the peak position of a test pulse. In blue, the uncorrected peak positions are shown, distributed over a range of time samples. In red, two sharp peaks are visible, showing the corrected peak positions applying the information from the TDC

measurement.

As obviously only one peak position can be the correct one, an additional correction has to be included: The TDC measurement for each channel is independent from the corresponding ADC measurement. This means that an external trigger first leads to the sampling of the waveform and storing the information as an ADC event, and subsequently reading out the TDC information and storing this as a TDC event. Both types of event have individual time stamps, which therefore can differ from each other and cause a discrete offset as observed in figure 4.15a. This offset corresponds to 24 samples = 4.8 ns per differing time stamp count.

Taking into account the respective time stamps, the corrected peak positions are all found in the same position, as can be seen in figure 4.15b. Note that also this peak has a width of 4 samples, which emerges from the fact that each ADC is sampling four different channels.

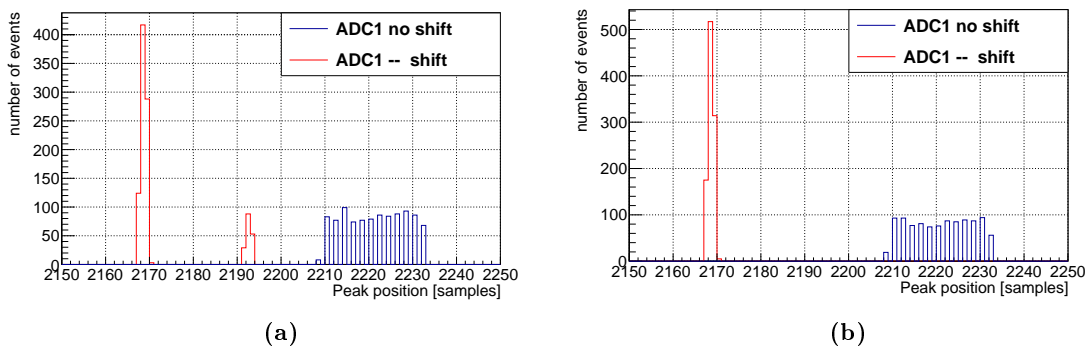


Figure 4.15: Peak position of a test pulse measured with the SIS3305 (blue) and corrected using the TDC feature (red). Figure (a) shows the resulting peak position without time stamp correction and (b) with time stamp correction.

The configuration of the SIS3305 comprises the following parameters:

- The choice of the sampling mode was implemented in the code to be 5 GHz on 2 channels. For future applications, this could be added to the parameters that are read in from the `hardware.xml`.
- It is possible to trigger the data acquisition on this board with internal or external trigger signals. For the DAQ program, an external trigger signal was chosen (see section 4.3).
- Similar to the SIS3316, an End Address Threshold value is set to be alerted when the required amount of data for the respective acquisition period is collected.
- The number of samples per events has to be set. For a sampling rate of 5 GHz, each sample corresponds to a time interval of 0.2 ns. Since this results in a large amount

of data for long time windows, the event length was fixed to be 4800 samples which corresponds to 960 ns. This time window is very short compared to the event length of the SIS3316, but sufficient for the measurement of $S1$ signals which have widths in the order of tens of nanoseconds.

- A pretrigger window length is set to get information about the signal baseline prior to the signal
- The threshold for the internal trigger can be adjusted. This parameter has no influence on the operation of the SIS3305 in the DAQ program, since the board is always controlled by an external trigger signal.

Aside from the implemented parameters, the SIS3305 is capable of an even wider range of possible configurations.

4.6.3 | CAEN VX1290 Configuration

The CAEN VX1290 is the TDC board which is required for the time-of-flight measurement in the neutron scattering experiment. In the first DAQ program version this board was not implemented. In the second one, it was used for both Compton and neutron scattering measurements.

The TDC board does not require an initialization. Its configuration however is done in a different way as for the other boards.

The basic registers can be read and configured using the VME commands described in section 4.5, but most of the configuration is done by a microcontroller chip using so-called OPCODE words, which are a list of 16-bit words that are assigned to specific operations.

To read and write information via the microcontroller, first a "handshake" register has to be read out to check if the microcontroller is ready for a read or write command. For a read procedure, first the handshake register is checked so that the "write ok" bit is set to 1. Then the specific opcode is written to the microcontroller address. Afterwards, the microcontroller is checked if now the "read ok" bit is set to 1, before the data is read from the microcontroller address.

The write-procedure is implemented in a similar way. The commands to read and write from and to the microcontroller address are A32D16 VME commands.

The CAEN VX1290 requires a series of configuration parameters:

- The operation mode of choice is the Trigger Matching mode, which means that the time window for the measurement is started by an external trigger. Another option would be a continuous operation mode, which is not useful for our setup. The Trigger Matching Mode has four parameters that have to be set according to the measurement requirements:

- The matching window width describes the length of the time window, which was set to $15\ \mu\text{s}$ for the DAQ. This long time period was chosen because the ELBE accelerator clock was used as a reference time signal, and the time difference between the accelerator clock and the first gamma-rays or neutrons from the neutron source was $9.7\ \mu\text{s}$. Taking into account that neutrons with different energies were created, the maximum time-of-flight for the slowest neutrons in the neutron spectrum was calculated to be $2\ \mu\text{s}$. A TDC window of $15\ \mu\text{s}$ is able to cover the necessary time interval.
 - An offset value for the matching window is used to record signals that occurred before the external trigger signal activates the acquisition on the TDC. Similar to the pretrigger window of the FADCs, the offset value of $13\ \mu\text{s}$ shifts the time window so that only a time interval of $2\ \mu\text{s}$ is stored after the trigger time, as described in the previous bullet point.
 - The Extra Search Margin, set to a value of $200\ \text{ns}$ (default minimum), is an extended search window at the end of the matching window. It is necessary to ensure that all hits for a specific matching window are found, even if they were stored to the buffer memory at a later time.
 - A Reject Margin of $100\ \text{ns}$ (default minimum) is used to reject older hits in the buffer before the matching window to avoid buffer overflows.
- Enable subtraction trigger time: In this configuration, the time information stored in the TDC is the time difference between the signal itself and the beginning of the matching window. This mode was chosen, because the resulting time informations can be interpreted very intuitively for each single event.
 - The TDC is set on Edge Detection mode, that means that an incoming signal (ECL standard from the CFD modules) is recognized by its leading edge. The timing resolution is set to the maximum achievable value of $25\ \text{ps}$. The dead time between triggers for each channel is set to the minimum value of $5\ \text{ns}$.
 - For the readout of the TDC, several parameters concerning the TDC data format are set as follows:
 - Most importantly, the correct input channels have to be chosen. This is done using a hexadecimal mask which is sent to the microcontroller using the respective opcode.
 - To save memory, the automatic TDC header / trailer information for each event is disabled, since it is inserted to the stored data by the DAQ program.
 - For each event, the maximum number of hits can be chosen. For our application the number is set to "unlimited" so that all signals during the matching window are recorded. For other applications it is possible to only measure the first one, two, four, ... hits.

- The TDC readout FIFO size denotes the memory used to store the hits for each event during acquisition in trigger matching mode. Otherwise it is used for data readout during continuous storage mode.
- Similar to the the end address thresholds of the FADCs, the TDC also uses an “almost full level register”.
- Since the neutron setup involves ten neutron detectors which itself consist of two PMTs each, it is expected that for each event most of the channels do not contain a signal. Enabling the option “empty event” ensures that the automatic header information of the TDC is written to the buffer in the same way every time, and this simplifies the data readout to our data format.

Regardless of the chosen number of hits per event, which affects the necessary memory size, the TDC is only able to store up to 1024 events at a time. As the events of both FADCs and TDC have to be synchronized, the complete acquisition has to be stopped to read out the data from each board after the mentioned 1024 events. Otherwise the FADCs might measure additional events so that the assignment of the data chunks from each board to a specific event becomes impossible. This topic is discussed in section 4.7.2.

4.6.4 | Additional Boards

Apart from the FADCs and TDCs, three different kinds of VME boards are present in the DAQ system:

The **CAEN V1495 General Purpose board** is a programmable logic board. It is implemented in the second version of the DAQ program and serves as the trigger logic. The configuration for this board is explained in detail in section 4.3.2.

For a better overview of the individual signal rates for each detector, a VME scaler board of type **SIS3820** (see section 4.9) was used in the second DAQ program version. Furthermore, three **VME High Voltage modules** were read out during the data acquisition to control the bias voltages for the photosensors in the setup. Their configuration and operation is discussed in section 4.10.

4.7 | Data Acquisition

4.7.1 | The Acquisition Stage

After the program start and the board initializations and configurations, the actual data acquisition is started. The two DAQ versions basically use the same program structure for the acquisition itself, but they differ with respect to the start and stop conditions of the program.

DAQ version 1 only includes the two FADC boards, of which the SIS3316 is responsible for the DAQ Trigger generation. Figure 4.16 gives an overview on the DAQ program for version 1. To acquire data in the first place, the FADC boards have to be armed. This means that an incoming trigger – depending on the configuration this trigger can be external or internal – leads to the recording of the respective event data. As the SIS3316 is configured to generate the DAQ Trigger by internally evaluating the measured signals, the SIS3305 has to be armed first. This way, it is ready to receive the DAQ Trigger which can be produced by the SIS3316 directly after the latter is armed.

During the acquisition, the boards are checked periodically with a time interval of approximately 100 μ s. About every five seconds a text output is produced stating the number of acquired events, which is the trigger counter. With the same periodicity, the VME high voltage boards are checked and written to a file which is then accessed by the SCS system. This is crucial to monitor the performance of the high voltage and to control that there are no problems with the individual sensors in the experiment (voltage trips, high currents, etc.).

A series of break conditions can become active during the acquisition loop: Either of the FADC boards can reach their respective memory limit (SIS3305 FULL or SIS3316 FULL), the required number of events for the ongoing measurement can be reached (MaxNbEvts) or the operator can send a termination signal to the program (terminate DAQ) to interrupt the measurement.

If the memory limit of the SIS3316 is reached, this VME board has the possibility to switch to a second memory bank and perform a data readout during the data acquisition (see also section 4.7.3). The SIS3316 FULL condition is resetted and the acquisition loop continues. This procedure is marked in red in figure 4.16 and is called the “inner cycle”. If the SIS3305 signals that its memory limit is reached, the data acquisition has to be stopped, because this board does not support data readout during operation. For this the two boards are disarmed in the reverse order as for the arming process, first the trigger-generating SIS3316 and afterwards the SIS3305. Subsequently, the two boards are read out. If the measurement is not finished yet, the program cycles back to arming both FADCs. This is marked in green and denoted “outer cycle”. One outer cycle is equivalent with an acquisition period (see section 4.8) and for each new outer cycle, a new data file is created.

The acquisition can also be stopped if the required number of events is reached or if the user terminates the data acquisition manually. In both cases, the FADCs are disarmed and read out, but afterwards the DAQ program is terminated.

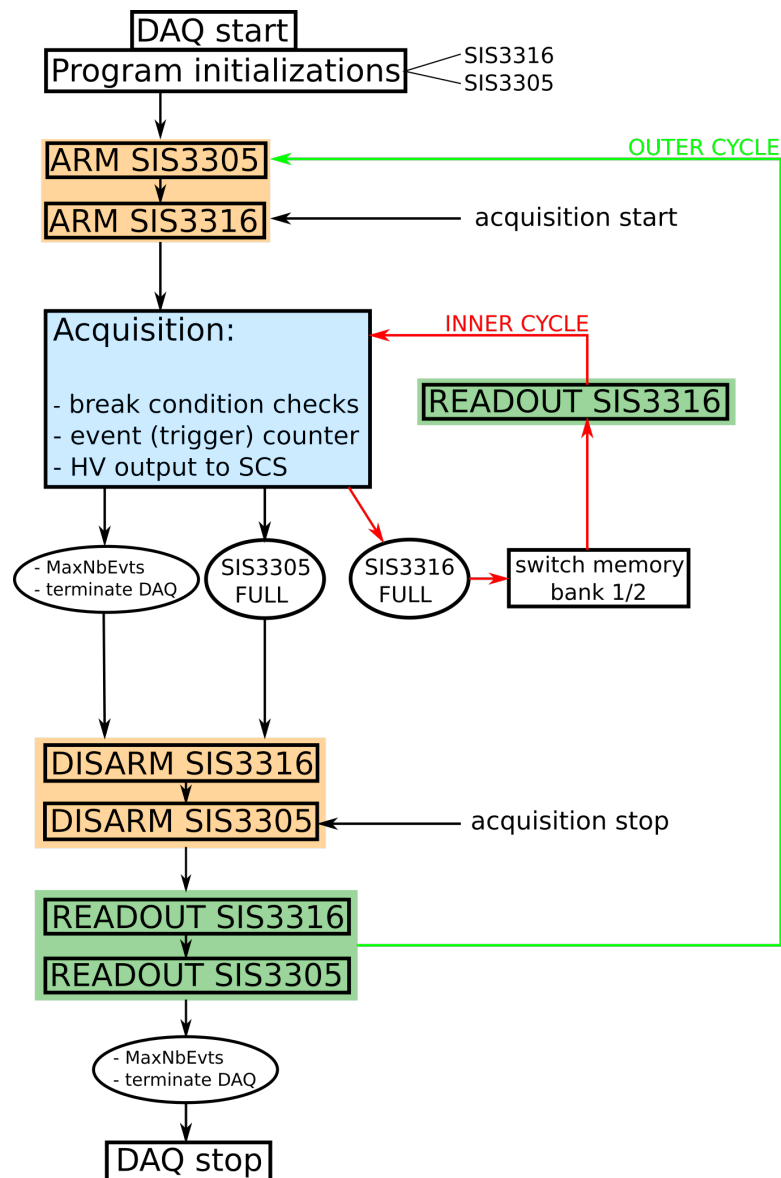


Figure 4.16: MainzTPC DAQ version 1 acquisition scheme: The centerpiece of the DAQ program starts with the arming of the FADCs. Since the SIS3316 produces the DAQ trigger, the acquisition begins when the board is armed. During the acquisition, the boards are checked periodically if the conditions to stop the acquisition are fulfilled. Also the number of acquired events and the performance of the VME HV boards are checked, with the latter being monitored by the SCS system. If the memory of the SIS3316 is full, the board is able to switch between two memory banks and perform a readout during the acquisition process (inner cycle). If the SIS3305 memory limit is reached, the acquisition has to be stopped. The boards are disarmed to prevent additional triggers and both boards are read out. If the required maximum number of events for the measurement is not reached yet or the termination command is not given, the boards are armed again after the readout (outer cycle), otherwise the program is terminated.

DAQ version 2 has a similar structure concerning the acquisition stage, but the implementation of the logic board and the TDC board has an influence both on the triggering and the break conditions. Figure 4.17 shows the scheme for the respective acquisition stage. With the TDC board CAEN VX1290, the logic board CAEN V1495 and the scaler SIS3820, the program initializations now include three additional boards.

The DAQ trigger is generated by the logic board in DAQ version 2. The firmware of this board allows the user to activate and deactivate the DAQ trigger, which controls the acquisition start and stop. Consequently, the two FADCs and the TDC, expecting an external trigger signal, have to be armed before the DAQ trigger output on the CAEN V1495 is activated and disarmed after the trigger is deactivated. The sequence of arming and disarming is irrelevant. In doing so, all boards are ready for incoming trigger signals at the same time, while arming the boards after activating the DAQ trigger could lead to different numbers of received triggers on each board.

The acquisition loop includes the same functionalities as described for DAQ version 1 and an additional break condition introduced by the TDC board. Both the SIS3305 and the TDC can only be read out if the acquisition is stopped. Therefore both of them can lead to the outer cycle loop.

4.7.2 | Event Consistency

The event structure of the MainzTPC is a combination of signals from different sensors, such as PMTs and APDs inside the TPC and secondary detectors as germanium or neutron detectors. Moreover, for each event one has to combine not only the signals from different channels on one VME board, but the according data from the FADCs and – for DAQ version 2 – the TDC.

As the boards have very different properties, one has to make sure that the data stored for event number 1234 from each board is in fact the required information. For example, if the signal waveforms for *S1* on the fast FADC SIS3305 were actually from event number 1235, the according signals on the SIS3316 or the time information of the TDC would not match.

In the first program version, only the two FADCs were implemented. Normally it is possible to feed the FADC clock of one board to another one to synchronize the board clocks and therefore the timestamps, which will allow for a distinct event identification. In our case, the input and output ranges for both FADCs differ from each other in a way that the SIS3305 clock is too fast for the SIS3316, while the SIS3316 clock is too slow in return, which denies the synchronization using a clock.

As a solution, the boards were not only triggered so that both boards would acquire the same amount of data, but also the number of events for each acquisition is checked to ensure that the data is consistent. That means also that the board with the smallest amount of memory is the limiting device for the number of events per acquisition cycle. The SIS3316 provides the possibility of switching between two memory bank during runtime and reading out the inactive bank during the acquisition. The SIS3305 instead has

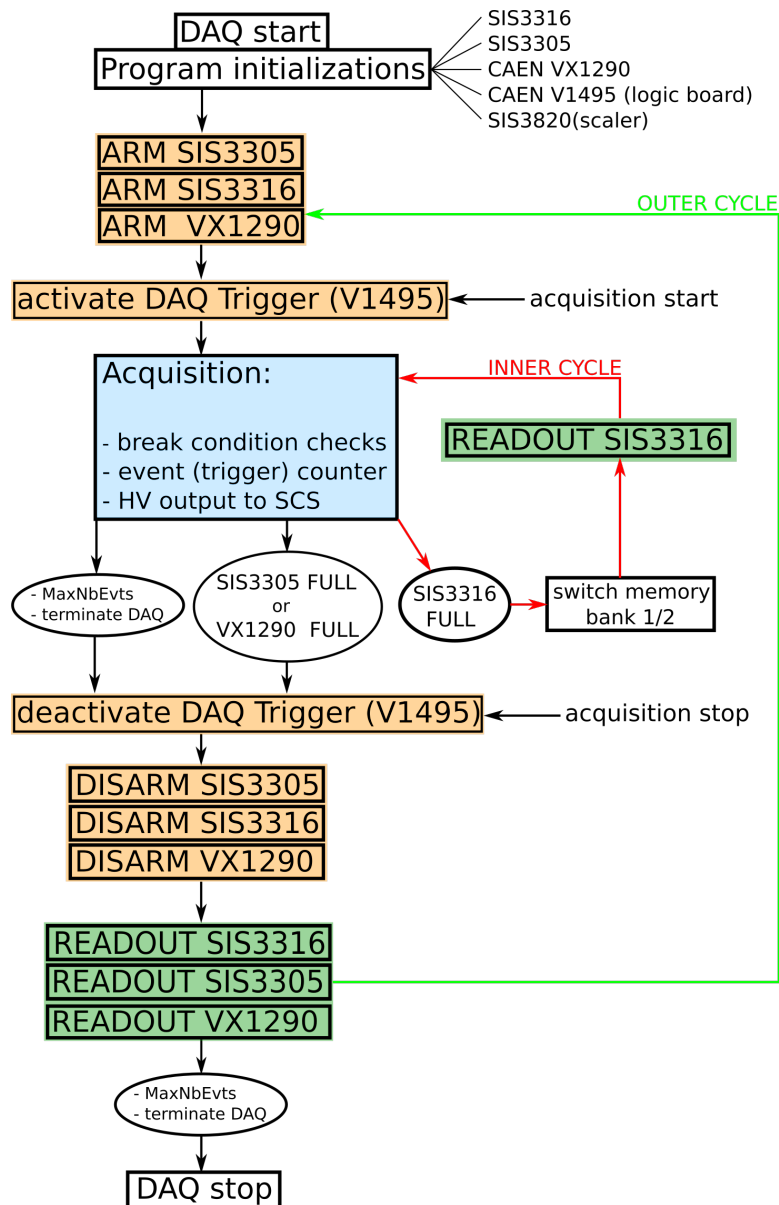


Figure 4.17: MainzTPC DAQ version 2 acquisition scheme: In this program version the arming of the FADC and TDC boards does not lead to the acquisition start. For this, the DAQ Trigger output from the logic board has to be activated. Likewise, the acquisition is stopped by deactivating the DAQ Trigger output, before disarming the individual boards. Controlling the DAQ trigger with the logic board ensures that all boards receive the same triggers. Compared to DAQ version 1, the TDC board introduces a new breaking condition for the acquisition cycle.

to be stopped for data readout. From this follows that the data acquisition has to be paused from time to time to read out the SIS3305, because continuing the data taking on the SIS3316 during this period would result in an inconsistency of the events. Including the CAEN VX1290 TDC to the DAQ program led to the necessity to read out the acquired data after a maximum of 1024 events, since this is the limit for the TDC.

Each of the VME boards has a different amount of dead time due to the data acquisition process, where the board stores the incoming data on its respective internal memory (before the readout). For example, since the SIS3305 only records a time window of 960 ns while the SIS3316 is busy for the complete duration of the event ($> 35 \mu\text{s}$, dependent on the chosen event length in the `hardware.xml`), the SIS3305 could record several waveforms before the SIS3316 has recorded the first. In such a case the individual waveforms can not be associated with the waveforms or TDC information that belong to the same event and therefore the event information is lost.

As a solution, all boards have one common trigger source, which is inhibited for the time one or more of the boards are busy during the acquisition.

4.7.3 | High-Frequency Mode

As mentioned in section 4.7.1, the SIS3316 allows to read out data during the data acquisition by switching between two memory banks. This process is sketched in figure 4.18. As can be seen, the acquisition has to be stopped eventually to also read out the SIS3305 and the TDC. An additional DAQ program feature called the “High-Frequency mode” (HF mode) was implemented to prevent the bank-switching of the SIS3316 and to force an acquisition stop and complete readout also if the memory limit of the SIS3316 is reached. Using the HF mode, the inner cycle of the acquisition stage is skipped. The HF mode was implemented because for high event rates the readout of the inactive memory bank of the SIS3316 during acquisition takes too much time compared to the number of events recorded on the active memory bank. This is outlined by the following example:

1. For a high event rate, the SIS3316 switches the memory banks after 200 events have been acquired. Subsequently, these events are read out and stored, while the acquisition continues.
2. During the data storage from bank one, the SIS3316 acquired 400 events in its second memory bank due to the high event rate. Since the program was busy with the data storage, the “end address threshold“ flag which would have caused the SIS3316 to switch banks again could not be checked before.
3. The readout of these 400 events from the second stage will take even longer than the first readout sequence, because more data has to be stored. The problem with

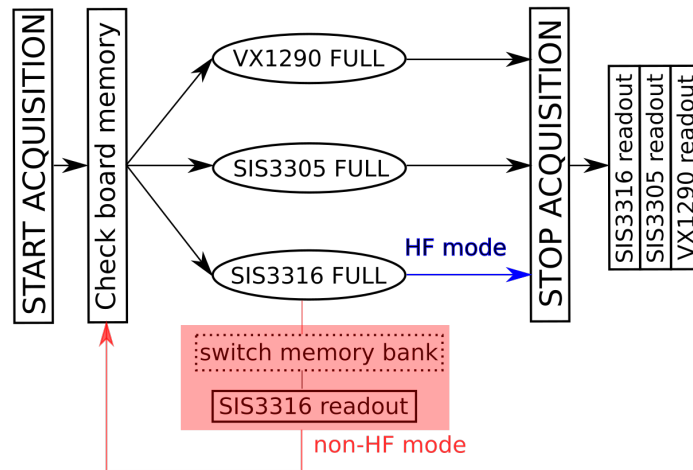


Figure 4.18: Illustration of the data acquisition and readout procedure for the HF and the non-HF mode. In the HF mode, the acquisition is stopped if either a FADC or the TDC reaches their memory limit for data readout. In the non-HF mode, the SIS3316 memory can be read out during the ongoing data acquisition.

this behaviour is that the data acquisition is not stopped before the maximum number of events for an acquisition cycle is reached (for the TDC this is 1024 events), the event consistency is lost because the SIS3316 recorded too many events.

When enabling the HF mode, the bank-switching for the SIS3316 is disabled. In our setup, this does not affect the memory performance because one bank is already sufficient to store more than 1024 events. For the measurements conducted with the MainzTPC, the HF mode was used permanently.

However, in a setup without the TDC and with low event rates, the non-HF mode can reduce the data acquisition dead time. Figure 4.19a shows the time measured for acquiring 10^5 events with the SIS3316 only, with event rates between 500 Hz and 6 kHz, for either non-HF or HF mode. For this, a test pulse with a constant frequency (equally spaced pulses) was used. As can be seen, for low event rates, the non-HF mode yields smaller run-time values, while for higher rates, the HF mode acquires the same amount of events in a smaller total measurement time, making it the more efficient mode. Also shown are the DAQ run times in a system test mode, which includes the readout of the SIS3316 board but does not write the data to the hard drive. As expected, the run times for both HF mode and non-HF mode are smaller than with the writing procedure. The HF mode, being slower for low event rates, converges to the run time of the non-HF mode for higher event rates. This indicates that the writing procedure plays a crucial role for the run time.

In figure 4.19b, the actual live time for both acquisition modes is plotted against the event rate. For low event rates up to ~ 2 kHz, the live times for the data taking in both modes are quite similar and correspond to the theoretical minimum, plotted as a

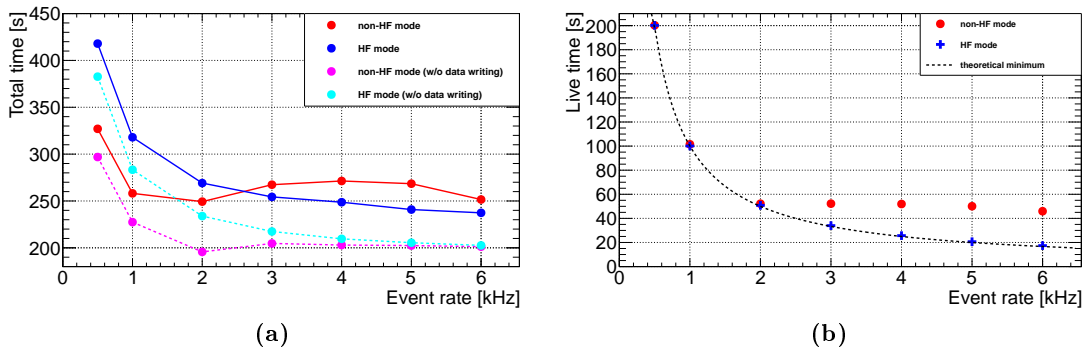


Figure 4.19: Measurement of test events with the SIS3316 for different event rates with non-HF mode and HF mode: The plot in (a) shows the total measurement time, which for low event rates is smaller in the non-HF mode since the data can be read out on-the-fly, but for high event rates shows a better result for the HF mode. In (b), the live time fraction for these measurements are shown together with the theoretical minimum value of the live time data acquisition. For higher event rates, the non-HF mode live times are larger than the HF mode live times, which correspond to the expected minimum values.

dashed line. For higher event rates, only the HF mode yields live times as expected, while the non-HF mode live time is artificially extended due to the fact that only a part of this live time is used to acquire data until the FADC board memory limit is reached and the board is idle during the data readout. The latter situation will then cause a problem in the event consistency as described in the previous section.

As explained above, a part of the live time measured for the non-HF mode at high event rates does not contribute to the data acquisition, since it emerges only from the fact that the readout of the memory bank postpones the acknowledgement of the "end address threshold" flag. That means that figure 4.19b is infeasible to provide conclusive information about the real live time fraction from the data. The precise measurement would require extensive changes in the data acquisition stage of the DAQ program.

To improve the generally low live time fraction of the DAQ system, one aspect could be a different way to readout the data from the VME boards. While using the VME readout only one task at a time can be handled. The data from the SIS3316 could be collected via LVDS or an optical cable connection to the module, minimizing the time for the VME crate being occupied during the readout and writing stage.

4.8 | Data Readout and Data Format

The last step of the data acquisition is the readout of the data and its storage. The VME boards provide a block transfer routine which copies the complete acquired data to a memory array. This approach is much faster than copying event-by-event.

After stopping the acquisition, first the SIS3316 is readout and the data is written to

the respective files. Subsequently, the SIS3305 and the TDC CAEN VX1290 are also readout.

To be able to work with the acquired data from the DAQ system, a suitable data format was developed. It is foreseen to hold all information of interest for data analysis in a redundancy-free way. Also it is easily extendable.

The current data format (version 002) was developed in 2015 before moving the MainzTPC to the HZDR. At the same time, the ground structure of the raw data analysis tool was created. The analysis tool uses the same data format structure to read in the stored data.

All data acquired with the MainzTPC DAQ system is stored in the form of binary files with the customized file extension `.mtd`. To minimize redundant information, the data is organized in a three-level file hierarchy, which is sketched in figure 4.20.

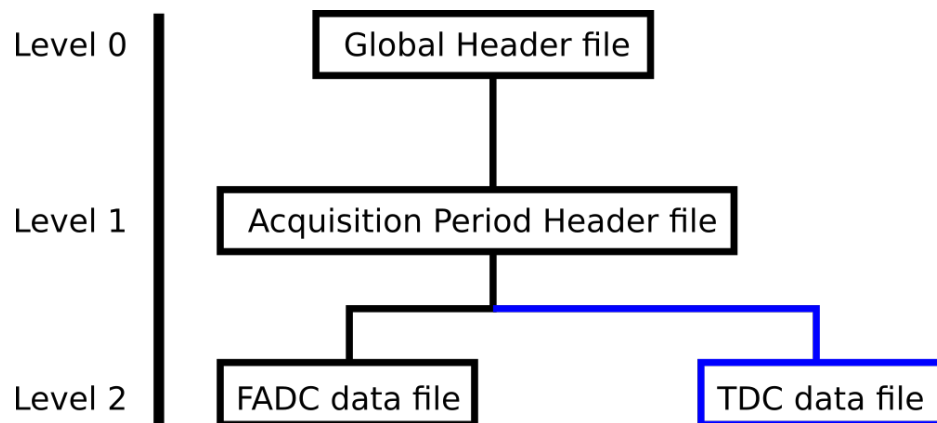


Figure 4.20: Three-level file hierarchy of the MainzTPC data format: Each measurement with the MainzTPC DAQ system leads to the generation of a series of data files. On the highest level (0), one file is created containing the global information about the measurement. On the level (1), the header information concerning a data acquisition period for each readout cycle is stored. The actual data is written to the files on level 2. While DAQ version 1 only collects data from the FADCs, DAQ version 2 additionally acquires TDC data (marked in blue).

Each file starts with a file header that is used to identify the file level in the hierarchy as well as the content of the respective file. Apart from the file header, the files at each hierarchy level contain different data. Figure 4.21 gives an overview of the file contents for each level.

The global header file on level 0 holds the general information which does not change during this individual measurement. This includes for example specifics about the different boards used during the measurement, the channel and sensor information, as well as the global run time. For each measurement, there exists only one global header file. For convenience, a human-readable version of this file is created automatically, allowing the user to cross-check the applied settings.

The files on level 1 of the data format hierarchy hold the acquisition period header information. Every acquisition cycle of the DAQ system is stored in a separate data file.

This ensures that data is saved regularly and in case of a program failure, only a small fraction is lost. It also leads to data files with a manageable size considering memory and number of events, respectively. The acquisition period header contains the start and end time of the acquisition cycle and the number of acquired events. Additionally, the event headers for the respective events are stored in this file, since they apply to a number of different waveforms and data chunks on different boards and channels.

Level 2 of the hierarchy are the data files actually containing the measured signals. There are two types of data files on this level:

Type A files contain waveform data from the FADCs. After the file header the structure of the file is basically an alternation of waveform headers, specifying the event and the channel of the waveform as well as the trigger timestamp, and the respective waveform data.

Type B files consist of the data from the TDC measurement. The structure is similar to the files of type A, but since the TDC does not measure waveforms with a fixed number of samples, the acquired timestamps in the measurement interval are stored as data chunks of variable length. Since each timestamp includes the channel ID, the TDC data header in figure 4.21 holds the number of timestamps ("nbSamples") instead of the channel ID. Files of type B are only created with the DAQ version 2.

To distinguish the different files, the hierarchy level and type are already included to the file name: `prefix_hierarchyLevel_idWithinLevel.mtd`. The prefix reads as `mainztpcYYYYMMDDThhmm`, stating the date and the time of the measurement. The hierarchy level has the form `00xT`, where `x` can be 0, 1 or 2 for the level and `T` is A for all files except for the TDC data files, which are marked with B.

Exemplarily, the file `mainztpc20171110T1550_002A_00001.mtd` is the first data file containing waveforms from the FADCs from the measurement started at 15:50 on 10 November, 2017.

The idea of the hierarchy structure – besides minimizing the amount of stored data – is to ensure that reading any data file leads to the information to analyze the data. To illustrate this, assume a user wants to access a specific waveform in a level 2 file of type A:

The user will instantly know that this is a level 2 file from the file ID, while the parent ID in the file header points to the level 1 file belonging to this data. Furthermore, finding the waveform of interest, the event ID as well as the channel ID become known. With this information the user can access the parent file, gathering the information about the acquisition period and knowing which level 0 file is belonging to this measurement. In the level 0 file, additional information about the number of samples for the respective channel, the sampling frequency, the identity of the sensor which was measured and so on can be found.

As mentioned above, the measured waveforms and TDC timestamps are read out using standard routines to fill them into memory arrays. Filling the data to the data format requires customized functions, which also collect the respective information needed for the individual headers, such as the trigger time in the waveform header or TDC data header.

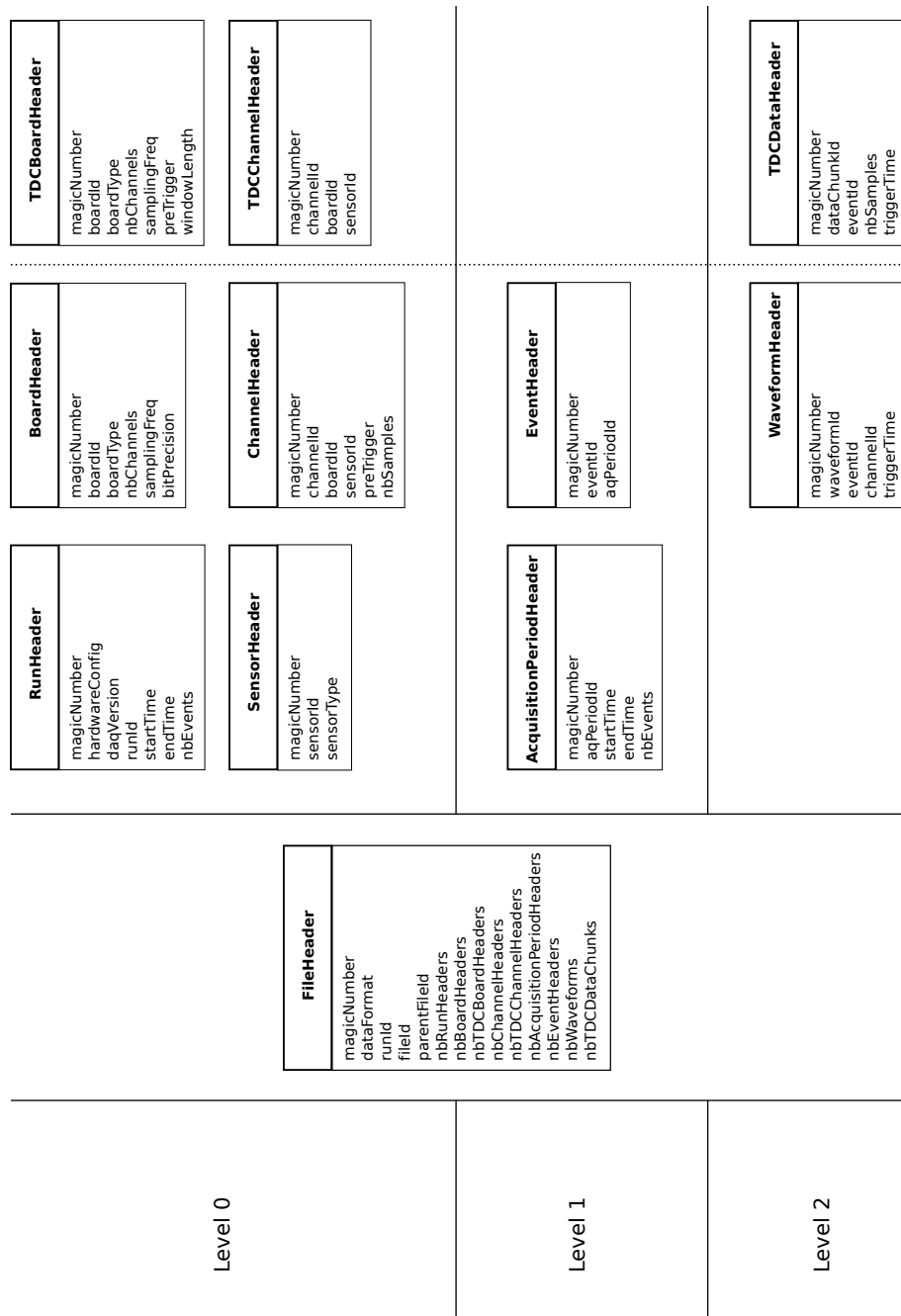


Figure 4.21: Overview of all headers for the MainzTPC data format, organized in the respective hierarchy level: All files contain a file header which clarifies the file identity and level as well as the data stored in this file. For level 0, a number of headers with global information is found in the file. Level 1 files also contain header information only, but specific for each acquisition period. The physical data – signal waveforms and TDC timestamps – are stored in the level 2 files. The vertical dashed line on the right marks the difference between data format 1 and 2, the latter including the TDC data.

4.9 | SIS3820 VME scaler

The scaler SIS3820 was predominantly added to the DAQ version 2 to monitor the rates on the MainzTPC PMTs as well as the PMT rates of the plastics. The board is fed by the CFD signals directly, therefore the measured rate is dependent on the CFD threshold and reflects the rate of the signals which can induce a trigger in the DAQ system. The scaler was eventually also used in the Compton measurements at the HZDR.

The VME scaler has 32 ECTL inputs. The input signal assignment is listed in table 4.4. As a timing reference an internal 10 MHz signal is recorded on channel 1. The remaining signals can be divided by the channel 1-value to obtain a rate instead of a signal count.

Ch	Signal	Ch	Signal
1	10 MHz counter (ref.)	17	plastic PMT 6-1
2	Top PMT	18	plastic PMT 6-2
3	Bottom PMT	19	plastic PMT 7-1
4	germanium detector	20	plastic PMT 7-2
5	additional detector	21	plastic PMT 8-1
6	additional detector	22	plastic PMT 8-2
7	plastic PMT 1-1	23	plastic PMT 9-1
8	plastic PMT 1-2	24	plastic PMT 9-2
9	plastic PMT 2-1	25	plastic PMT 10-1
10	plastic PMT 2-2	26	plastic PMT 10-2
11	plastic PMT 3-1	27	secondary detector trigger
12	plastic PMT 3-2	28	TPC trigger
13	plastic PMT 4-1	29	Coincidence Trigger
14	plastic PMT 4-2	30	Event Trigger
15	plastic PMT 5-1	31	live-time counter
16	plastic PMT 5-2	32	real-time counter

Table 4.4: Signal assignment to the SIS3820 VME scaler. Most of the input signals come from the CFDs of the respective sensors, while others represent processed logic signals. The signal counts on channels 2–30 are converted to rates using the 10 MHz pulser recorded on channel 1. The channels 31 and 32 provide information of the total run time and the live-time of the run.

The signals of the Top and Bottom PMTs, the germanium detector and the individual plastic PMTs are recorded. In total, ten plastics with two PMTs each can be recorded by the scaler during the same measurement.

The channels 5 and 6, labeled "additional detector", serve as input for different sensors depending on the measurement type. These sensors include a NaI(Tl) detector for a trigger efficiency measurement, two LaBr detectors for a different trigger efficiency measurement (which was conducted in March 2016 and is not discussed in this thesis) and a second germanium detector in a Compton measurement.

Besides the reference signal and the sensors a third group of input signals are the four channels 27 – 30. These signals come from the CAEN V1495 logic board and represent the logic signals for different trigger conditions: Channel 27 is fed the logic trigger for the secondary detectors, channel 28 records the TPC logic trigger signal and channel 29 receives the coincidence trigger. The actual Event Trigger signal, which is the logic board trigger output that leads to the recording of an event in the DAQ system, is recorded on channel 30.

The last two channels are used for a live-time measurement of the DAQ program. Both channels are fed with the signal of an 10 MHz pulser. The CAEN V1495 logic board provides a logic veto signal which is active while the FADC boards are not armed. This is the case when the DAQ program is not running and during the readout of the data, for which the boards have to be switched off (see section 4.7.2). The logic veto signal is used to inhibit the recording on a part of the scaler channels (27 – 32), with the exception of channel 32. This means that channel 32 records the complete run-time of the DAQ program, while channel 31 only records the live-time, which is the time fraction of the total measurement which is used to acquire data. The respective total measurement time and the live-time are calculated in the DAQ program.

The scaler, as a part of the DAQ system, is read out by the DAQ program in regular time intervals of roughly 5 s during operation. In addition of measuring the live-time, the rates of the different sensors are calculated for each interval and are written to a text file, which in turn is evaluated by the slow control system⁴.

4.10 | Controlling the High Voltage Modules

Compared to the FADC boards, the handling of the VME voltage supply boards is much simpler. The control program `VME_HVcontrol` (HVcontrol program) was designed in the course of this thesis to operate the two CAEN V6533p boards as well as the iseg VHQ 223M board.

The program structure is the same as for the DAQ program, but very simplified. It also reads in parameters from a `HV_hardware.xml` and a `HV_settings.xml` file (the prefix `HV_` is added here to avoid confusion with the `xml`-files for the DAQ program). A board initialization is not necessary. The input parameters from the respective `xml`-files are used to configure the boards.

Similar as in the DAQ program, the parameters of the `HV_hardware.xml` are meant to be unchanged by the program user, since they determine the software voltage and current limits of the boards. The software limits can be set with more accuracy than the hardware limits, which are adjusted using a screwdriver on the front panel of the respective board. In the `HV_hardware.xml` also the availability of the individual channels for the HVcontrol program can be chosen. If a channel is deactivated here, it can

⁴This means that sensor rates can only be monitored during data taking. For testing purposes, the DAQ program can be executed in a non-saving mode, providing the possibility to examine the sensor rates without storing unwanted data.

not be switched on.

The `HV_settings.xml` holds the information of the voltage for each channel. It furthermore has an "On/Off" option for each channel. Only if a channel is activated in both `xml`-files, it is ramped up to the chosen voltage settings.

The HVcontrol program has four functionalities after the startup:

- **on**: Choosing this function loads the `HV_settings.xml`. The program checks whether all parameters are in their allowed ranges and if there are no activation conflicts for the channels. Then it shows the loaded configuration for the high voltage boards with all settings and requests a confirmation to proceed. If the user declines, the program exits and the settings can be changed. If everything is correct and the user accepts, the program ramps the individual channels to the chosen settings.
- **off**: This function ramps down all channels to zero voltage.
- **c (check)**: With this function all voltages and currents on each channel of all three boards are measured and written to the terminal.
- **q (quit)**: This function ends the HVcontrol program without changing anything on the status of the HV boards.

The difference between the functions "off" and "q (quit)" is important: With the HVcontrol program the voltages for the sensors in the MainzTPC are set on the HV boards. Shutting down the HVcontrol program must not affect the status of the board outputs. The HVcontrol program uses the VME controller SIS3100 to communicate with the HV boards, but it is only possible for one program at the time to employ the VME controller. As a consequence, the HVcontrol program has to be shut down in order to use the DAQ program.

A similar program exists to control the Bertan 225 series, which is responsible for the cathode voltage. Since this is no VME board, it is independent from the DAQ program.

During the data acquisition, the voltage and current values for each sensor have to be monitored, in case of a voltage trip or similar. The VME voltage supply boards of type CAEN V6533p or iseg VHQ 223M are read out by the DAQ program. For this, the DAQ program addresses the individual boards and executes a function equivalent to the "c (check)"-function in the HVcontrol program. The measured voltages and currents are written to a text file which in turn is accessed by a so-called "file watcher" program. The file watcher reads the text file and sends the information to the SCS monitoring system.

Likewise, the Bertan 225 series device can be monitored using a file watcher.

4.11 | Improvements & Summary

The DAQ program developed in the course of this thesis has been operated successfully for Compton measurements both at the institute of physics in Mainz and at the HZDR, with either program version 1 or 2 being applied to the respective setups. The elaborated version 2 installed at the HZDR was also used to measure neutron scattering with an extended trigger setup.

The program structure is built in a versatile way, allowing to choose different channel patterns and properties such as signal polarity, range, offset, pretrigger and more as well as to adapt the trigger mode for multiple different types of measurements. The possibilities provided by the implemented FADC boards have not been completely exploited yet, leaving room for program extensions in this area.

The DAQ collects and processes data to fit into a customized data format, suitable for the Raw Data Analysis tool also developed in the XENON Mainz group. The readout and data storage time is the limiting factor for the DAQ live time during data acquisition with high event rates. Still, storing the data in a different format would only shift the necessity of sorting the acquired data into a usable format for data analysis.

To further enhance the DAQ performance, several features of the system can be revised:

- To ensure the event consistency of the different FADC boards (and additionally the TDC), an external clock could be used to synchronize the different boards.
- Instead of checking the board status information, for example the memory limits indicated by internal board flags, via VME, the use of the VME interrupts could be implemented. The interrupt functions of the boards interject information even while other VME processes are ongoing, and can force a new command according to their respective VME priority. Using the VME interrupts would control the acquisition cycle with more accuracy regarding the number of events.
- Since all information exchange from and towards the VME boards is carried out via the optical link to the SIS3100 and the VME crate backplane, the data transfer rate is limited and also blocks further communication between the computer and the boards. Using an ethernet or optical link cable to read out the data from the SIS3316, the slow FADC collecting the largest part of the event data, for the transfer to the DAQ computer, could lead to faster download speed and therefore a reduced measurement dead time due to the readout process

Concerning the data taking, as will be discussed in the analysis part III, the signal thresholds can be improved in future experimental runs. Due to noise or background signals, especially the thresholds on the TPC PMTs for the $S1$ signals could not be set as low as planned (see section 9.5).

DAQ version 1 is currently employed in Mainz for measurements of electronic recoils (TPC calibration and Compton scattering). Although a TDC is not necessary for this

measurement, the trigger generation using CFDs and the logic board would be preferable to the internal trigger generation of the SIS3316. Using a CFD allows the experimenter to cross-check the exact waveforms that surpass the analog signal thresholds in the CFDs and lead to the logic signals that are processed in the logic board, while it is more difficult to reconstruct the trigger generation inside the SIS3316, as it uses a filtered waveform which is not accessible for comparison with a threshold value.

For future measurements, DAQ version 2 is the recommended system configuration. It is a refined upgrade of version 1 and provides a much better trigger setup with the implementation of the logic board CAEN V1495. As discussed, the external triggering of all boards ensures synchronization for the events, which is particularly important for the fast FADC SIS3305: In DAQ version 1, the internal trigger generation on the SIS3316 can cause the resulting trigger signal for the SIS3305 to jitter such that the timing measurement discussed in section 4.6.2 becomes ineffective. The external trigger from the logic board in DAQ version 2 leads to a fixed pretrigger value for all events.

Part III

ANALYSIS & RESULTS

Sensor Calibration

Chapter 5

The calibration of the photo-sensors in the MainzTPC is crucial for the data analysis. All photo-sensors are recorded with the FADC boards, which store the data in time samples. Each sample contains a voltage value. The signal waveforms have to be scaled correctly, i.e. the recorded voltage values have to be assigned to the amount of detected light (for example in the units of photoelectrons, p.e.) or directly to an energy value, if possible.

That means that the calibration of the individual sensors allows the conversion of the measured voltages of the FADCs to the actual light signal in physical units. This is used to determine the energy of the interaction in the TPC.

All calibration measurements were conducted during the experimental run 18-28 April, 2016.

5.1 | Gain Determination for the PMTs

5.1.1 | PMT Calibration at the HZDR

The PMT calibration is used to determine the number of photoelectrons (p.e.) on the photocathode of the PMT corresponding to the signal voltage.

This calibration is done measuring the single-photon response of the PMT. A single photon detected by a PMT leads to a single photoelectron (SPE) being emitted by the PMT photocathode. Experimentally, light pulses from a blue LED were guided through optical fibers to calibrate the PMTs in the MainzTPC. The voltage pulses of the pulse generator were adjusted (by browsing the waveforms by eye on an oscilloscope) so that only $\sim 5\%$ of all pulses resulted in a PMT signal. The measurement itself was triggered by the pulse generator.

According to Poisson statistics, the probability of the number of detected photons can be linked to the average number of signals measured. Equation (5.1) denotes the Poisson distribution with the parameters n for the number of photons and λ for the mean number of signals per event.

$$\text{Poi}(n, \lambda) = \frac{\lambda^n}{n!} \cdot e^{-\lambda} \quad (5.1)$$

For a value of $\lambda = 0.05$, the values of the Poisson distribution are calculated:

$$\begin{aligned} \text{Poi}(0, 0.05) &= 0.95123 & \text{Poi}(1, 0.05) &= 0.04756 \\ \text{Poi}(n > 1, 0.05) &= 1.209 \cdot 10^{-3} & \frac{\text{Poi}(1, 0.05)}{\text{Poi}(n > 1, 0.05)} &= 39.34 \end{aligned}$$

The probability of measuring events with two or more photons differs from the case of a SPE by a factor of 39.34, and the fraction of events containing more than one photon can be quantified as only 1.209‰, which can be neglected.

To generate the SPE spectra, the signal waveforms were integrated over a fixed range

around the signal peak position. The obtained integral value was then divided by the channel impedance to get a measured charge:

$$Q = \sum_i \frac{U_i}{R} \cdot \Delta t \quad \left[\frac{\text{V} \cdot \text{s}}{\Omega} \right] = [C]$$

Here, Q is the charge, U_i denotes the measured voltage in FADC sample i , R is the impedance and Δt is the time resolution, which is $\Delta t = 8$ ns per sample for the SIS3316. The resulting SPE spectra, as shown exemplarily in figure 5.1 for the Top and Bottom PMT at different bias voltages, consist of a large pedestal which contains the integral values from the empty waveforms and a smaller peak from the SPE signals. The single photoelectron peak position yields a measured charge value Q_0 . Since this charge value is a multiple of the actual electron charge, the ratio

$$G_{\text{PMT}} = \frac{Q_0}{e} \quad (5.2)$$

is the PMT gain that arises from the charge multiplication in the PMT dynode system. It is used to scale the charge response in subsequent data analysis as multiples of photoelectrons. By dividing the measured signal charge by the charge Q_0 , the influence of the PMT gain is cancelled out.

The pedestals observed for the PMTs reflect the noise on the respective sensors. As can be seen, for lower bias voltages, the pedestals and the SPE peaks overlap to a point where a distinction is not possible.

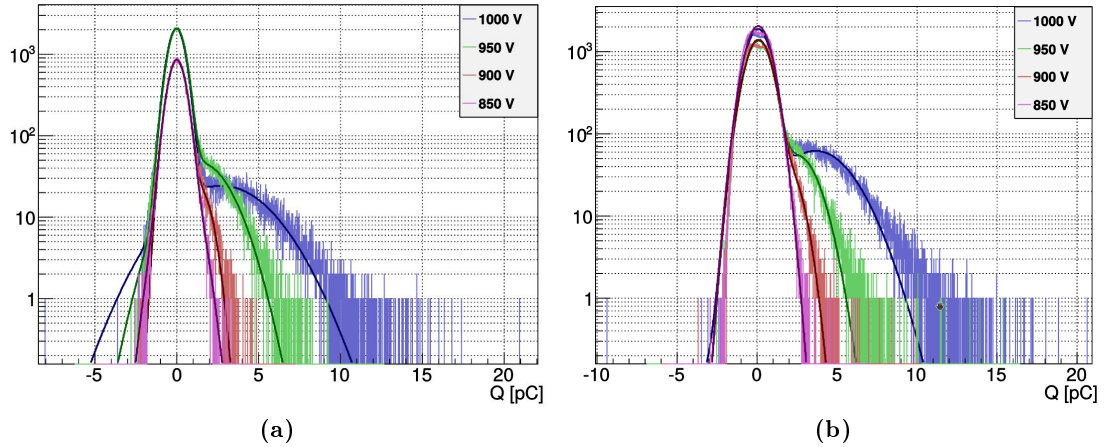


Figure 5.1: SPE spectra of Top (a) and Bottom PMT (b) for different bias voltages between 850 V and 1000 V. The plots are taken from [3]. The pedestal around 0 pC is clearly visible and comparable for all voltages. The SPE peak differs for each measurement, for 1000 V it is quite prominent, while it merges with the pedestal for lower bias voltages. Because of this, the PMT calibration for lower bias voltages was done with a relative gain measurement (see text). For the Bottom PMT, a dip can be spotted for the pedestal peak which is investigated further in [3].

The calibration procedure for the MainzTPC PMTs was split into two steps: For the maximum bias voltage of $U_{\text{bias}} = 1000 \text{ V}$, the absolute PMT gains were measured from the respective SPE spectra for each PMT. In these measurements, the PMT signals were additionally amplified by the DetectorLab amplifier with a gain of 10.5 which was also used in the actual measurements. The measured charge values Q_0 of the single photoelectron peaks are:

$$\begin{aligned} \text{Top: } Q_{0,T}(1 \text{ kV}) &= (2.735 \pm 0.032) \text{ pC} & \sigma_T(1 \text{ kV}) &= (0.4627 \pm 0.0008) \text{ pC} \\ \text{Bottom: } Q_{0,B}(1 \text{ kV}) &= (3.659 \pm 0.018) \text{ pC} & \sigma_B(1 \text{ kV}) &= (0.6573 \pm 0.0007) \text{ pC} \end{aligned} \quad (5.3)$$

In the second step, the gains of the PMTs at different bias voltages were determined using large light signals and comparing the PMT responses at different bias voltages. This step was necessary since the SPE peak for lower bias voltages was indistinguishable from the pedestal and therefore the direct gain measurement was not possible in this case.

This procedure led to the derivation of the following analytical functions to describe the average PMT gains in dependence of the bias voltage relative to the absolute gain for $U_{\text{bias}} = 1000 \text{ V}$:

$$\begin{aligned} \text{Top PMT: } \quad \bar{g}_T(U) &= \exp(12.53 \cdot [U/U_{\text{bias}} - 1]) \\ \text{Bottom PMT: } \quad \bar{g}_B(U) &= \exp(12.19 \cdot [U/U_{\text{bias}} - 1]) \end{aligned} \quad (5.4)$$

The complete PMT calibration procedure was done and is explained in detail in [3]. Based on this, the PMT gains can be calculated for different measurement conditions.

5.1.2 | Calculation of the PMT Gains for the HZDR Measurements

For all measurements that were conducted for this thesis, the PMTs were set to constant bias voltages and therefore their (relative) gains can be directly calculated to:

$$\begin{aligned} \text{Top PMT: } \quad \bar{g}_T(1000 \text{ V}) &= 1 \\ \text{Bottom PMT: } \quad \bar{g}_B(950 \text{ V}) &= 0.544 \end{aligned}$$

During the measurements, the Top PMT was always operated with the DetectorLab amplifier with a gain of 10.5, while the Bottom PMT was connected to the KPH amplifier with a gain of 5 (information about the different amplifiers can be found in section 3.4.1). The different amplifier gains have to be taken into account when calculating the actual single photoelectron peak value (using the value from (5.4)):

$$Q_{0,B}(950 \text{ V, KPH amp}) = 3.659 \text{ pC} \cdot \bar{g}_B(950 \text{ V}) \cdot \frac{5}{10.5} = (0.94786 \pm 0.00466) \text{ pC} \quad (5.5)$$

The uncertainty arises from error propagation.

The conversion from PMT signals to values in photoelectrons can therefore be described

according to equation (5.6), here for the sum of the signals from both Top PMT and Bottom PMT:

$$Sx = \frac{\sum_i \frac{U_{T,i}}{R} \cdot \Delta t}{Q_{0,T}(1000 \text{ V})} + \frac{\sum_i \frac{U_{B,i}}{R} \cdot \Delta t}{Q_{0,B}(950 \text{ V, KPH amp})} \quad [\text{p.e}] \quad (5.6)$$

Here, Sx stands for either $S1$ or $S2$. Of course, it is possible to examine the signals from Top PMT and Bottom PMT individually, in this case, the according term from equation (5.6) is used, for example for the Bottom PMT:

$$Sx_B = \frac{\sum_i \frac{U_{B,i}}{R} \cdot \Delta t}{Q_{0,B}(950 \text{ V, KPH amp})}$$

The PMT gains for the applied settings can be calculated using equation (5.2):

$$G_{\text{Top PMT,1000 V}} = \frac{Q_{0,T}(1000 \text{ V})}{e \cdot f_{\text{DetectorLab amp}}} = 1.397 \cdot 10^6$$

$$G_{\text{Bottom PMT,950 V}} = \frac{Q_{0,B}(950 \text{ V, KPH amp})}{e \cdot f_{\text{KPH amp}}} = 1.242 \cdot 10^6$$

Here, $f_{\text{DetectorLab amp}} = 10.5$ and $f_{\text{KPH amp}} = 5$ denote the amplification factors of the DetectorLab and KPH amplifiers, respectively. e is the electron charge. The found gain values exceed the nominal value of $1 \cdot 10^6$ stated in the data sheet (see figure C.1). This effect can be associated with the difference in the voltage divider chain on the PMT base. A non-standard voltage distribution for the PMT dynodes was applied to improve the SPE performance.

5.2 | Germanium Detector Calibration

5.2.1 | Energy Calibration using Gamma-Ray Sources

The calibration of the germanium detector is crucial for the Compton measurements, since the energy deposit in the TPC is calculated as the energy difference $E_{\text{deposit}} = E_0 - E_{\text{Ge}}$ between the gamma-ray source energy and the detected energy in the germanium detector. The chosen bias voltage for all measurements was $U_{\text{bias}} = 1500 \text{ V}$. As described in section 4.3, the positive detector signal was fed to a Fast Filter Amplifier and the resulting inverted and amplified signal was then split, leading to the FADC SIS3316 on the one hand and via a NIM discriminator to a CFD (for the trigger generation).

The germanium signal is a step, resulting from a built-in CSP, which collects the signal charge and provides a “charge sum” as a voltage step signal. That means that only the step height has to be measured.

To calibrate the germanium detector, different gamma-ray sources were installed in front of the detector and for each source a measurement of 10^5 events was conducted. The gamma-ray sources used here were ^{137}Cs , ^{22}Na and ^{133}Ba . By identifying the peaks in the respective spectra one can assign energies to the measured voltage at each peak.

Figure 5.2 shows the calibration spectra for the gamma-ray sources ^{137}Cs , ^{22}Na and ^{133}Ba , respectively. The peak shape in the respective spectra is not exactly Gaussian-shaped, especially in case of the ^{133}Ba . That is why each peak of interest was fitted with two different fit functions, a Gaussian and a Lorentzian function, to examine whether this leads to a significant change in the determination of the peak position:

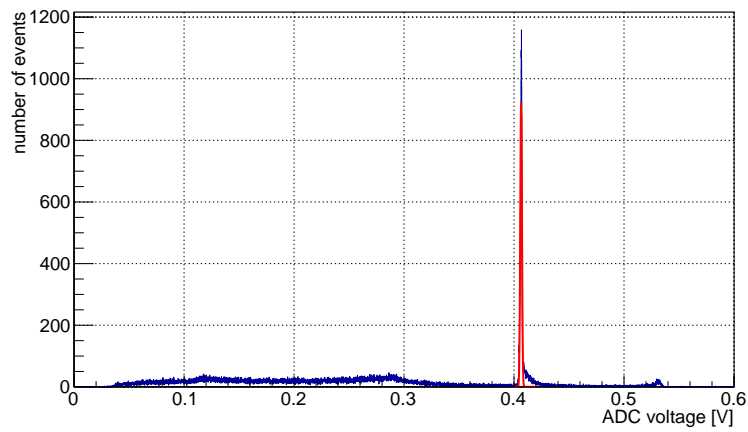
$$\begin{aligned}
 f_{\text{Gaussian}}(U_{\text{signal}}) &= \frac{A}{\sigma\sqrt{2\pi}} \cdot e^{-\frac{1}{2}\left(\frac{U_{\text{signal}} - \mu_{\text{peak}}}{\sigma}\right)^2} \\
 f_{\text{Lorentzian}}(U_{\text{signal}}) &= \frac{A_L}{\pi} \cdot \frac{1}{s^2 + (U_{\text{signal}} - t)^2}
 \end{aligned} \tag{5.7}$$

Here, A and A_L are generic amplitudes, μ_{peak} is the mean value of the Gaussian and σ its standard deviation. For the Lorentzian, there is no mean value per se, the quantity t denominates the center of the function, while s is a parameter for the width. The fit values of some of these parameters are listed in table 5.1. To get an impression of the deviations between the two fit approaches, the parameters t and μ_{peak} are compared. The plots with the fits can be found in B.1, for clarity only the measured spectra are shown here.

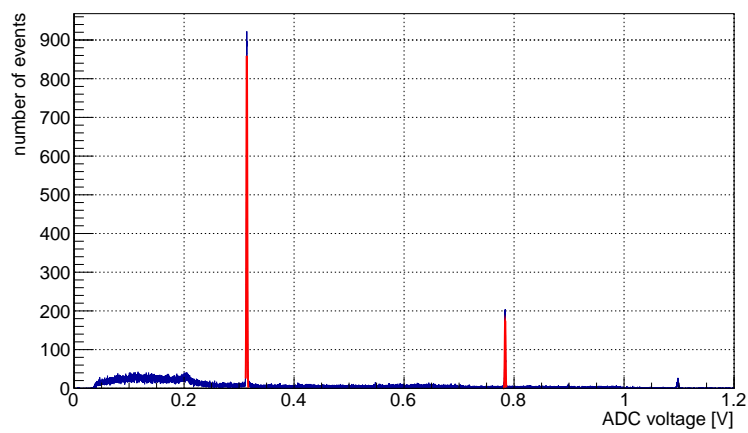
The ^{137}Cs spectrum only contains one peak and the ^{22}Na has two major peaks from the β^+ -decay. Each of these peaks was fitted individually.

The spectrum of ^{133}Ba on the other hand shows a number of photon peaks, of which the most prominent is the 356 keV line. This energy was used as calibration line.

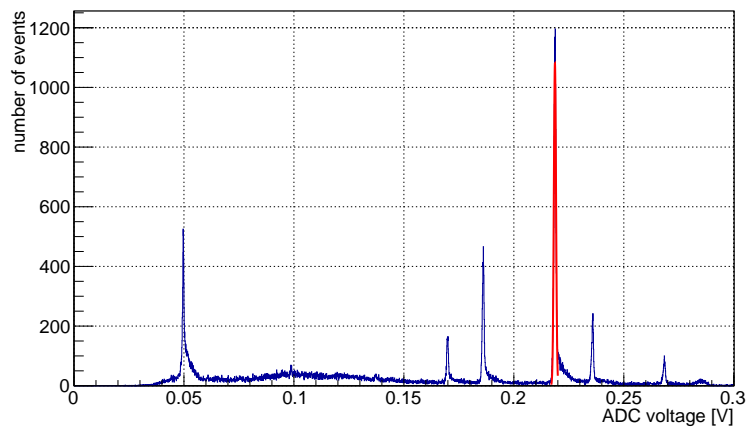
Comparing the center value t from the Lorentzian fits with the mean value μ_{peak} from the Gaussian fits leads to the observation that they agree within the uncertainty $\Delta\mu_{\text{peak}}$ of the Gaussian mean value. Since it is complicated to calculate an uncertainty for



(a)



(b)



(c)

Figure 5.2: Germanium calibration spectra: (a) ^{137}Cs spectrum with its distinct peak at 661.6 keV, (b) ^{22}Na spectrum with the 511 keV and 1274 keV peak, (c) ^{133}Ba spectrum with a variety of peaks. The first five peaks from the left correspond to the photon energies of 81 keV, 276.4 keV, 302.9 keV, 356 keV and 383.8 keV. The peaks are not ideally Gaussian-shaped, therefore they were examined using Gaussian fits as well as Lorentzian fits, of which only the former are shown here. The fitted peaks are plotted separately in the appendix section B.1.

the Lorentzian and since the fit results do not deviate noteworthy, the calibration is continued using the values from the Gaussian fits.

source	E_γ (keV)	t (V)	μ_{peak} (V)	$\Delta\mu_{\text{peak}}$ (μV)
^{137}Cs	661.6	0.406576	0.406547	0.26
^{22}Na	511	0.314128	0.314125	0.38
^{22}Na	1274	0.783915	0.783892	1.50
^{133}Ba	356	0.218706	0.218703	0.18

Table 5.1: Photon energies for three gamma-ray sources and corresponding mean values from Lorentzian and Gaussian fits of the respective source spectra for the germanium calibration. The center value t for the Lorentzian fits is in agreement with the mean value μ_{peak} from the Gaussian fits within its uncertainty $\Delta\mu_{\text{peak}}$.

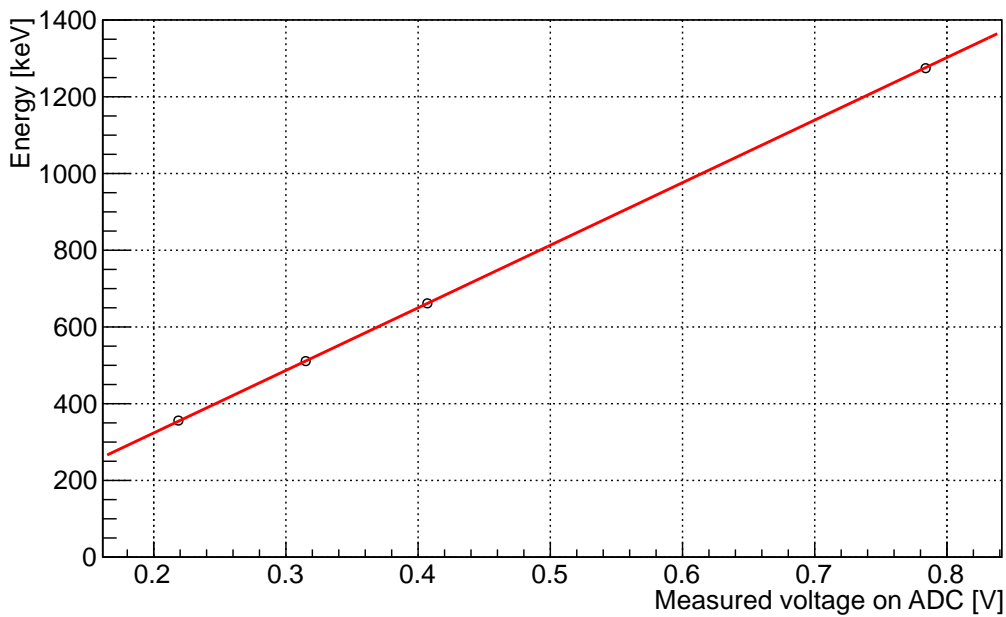


Figure 5.3: Linear fit of the photon peak voltage values from the gamma-ray source spectra. The errors of the data points are too small to be visible (see table 5.1). Data and fit show a good agreement. The residuals calculated are each equal or less than $|0.4 \cdot 10^{-3}|$.

The fit mean values μ_{peak} are plotted in figure 5.3 with respect to their assigned energies. The data point errors are too small to be visible in the plot. A linear fit was applied, resulting into the following calibration function:

$$\begin{aligned}
 U_{\text{signal}}(E_{\text{Ge}}) &= 0.61489 \frac{\text{mV}}{\text{keV}} \cdot E_{\text{Ge}} - 0.191857 \text{ mV} \\
 \Rightarrow E_{\text{Ge}}(U_{\text{signal}}) &= 1626.318 \frac{\text{keV}}{\text{V}} \cdot U_{\text{signal}} + 0.318 \text{ keV}
 \end{aligned}
 \tag{5.8}$$

With this one can directly link the voltage signal from the FADC to a gamma-ray energy from the calibration, no additional conversion is needed.

To quantify the deviation between the fit function and the data points, one can calculate the residuals:

$$\text{Res} = \frac{\mu_{\text{peak}} - U_{\text{signal}}(E_{\text{Ge}})}{\mu_{\text{peak}}} \quad \Delta\text{Res} = \frac{\Delta\mu_{\text{peak}}}{\mu_{\text{peak}}}$$

The residuals corresponding to the examined photon energies are summarized in table 5.2. The observed deviations between the calibration function and the measured mean values are quite small, as the residuals each are equal or less than $|0.4 \cdot 10^{-3}|$.

source	E_{γ} (keV)	Res (‰)	ΔRes (‰)
^{137}Cs	661.6	-0.382	0.002
^{22}Na	511	0.277	0.003
^{22}Na	1274	0.092	0.002
^{133}Ba	356	0.167	0.004

Table 5.2: Calculated residuals showing the relative deviation of the germanium calibration function from the measured data for each data point.

5.2.2 Energy Resolution of the Germanium detector

Since the germanium detector is responsible for the determination of the deposited energy in the MainzTPC during Compton scattering measurements, it is vital to know its energy resolution as a measure of the systematic error. For this, the calibration source spectra in figure 5.2 are replotted using the germanium calibration obtained in the previous section. The source spectra depending on the energy are shown in figures 5.4 to 5.6.

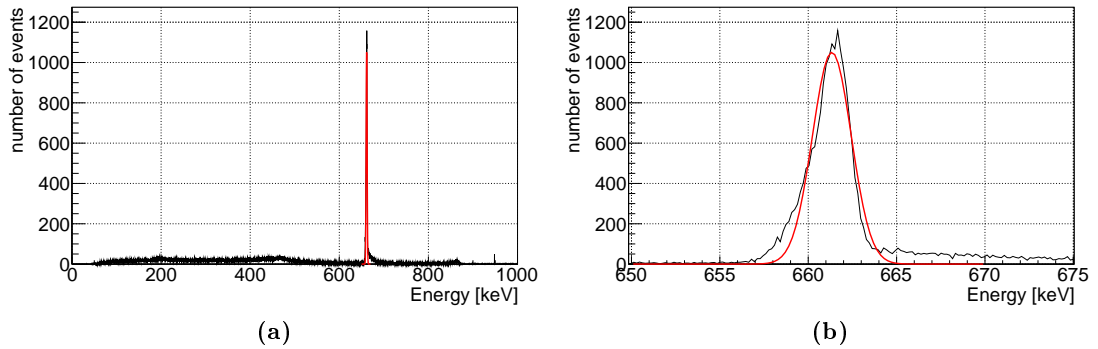


Figure 5.4: ^{137}Cs spectra measured with the germanium detector. Using the germanium calibration, the spectra are plotted in dependence of the energy and the main energy peaks are fitted with a Gaussian. The plots show (a) the complete ^{137}Cs spectrum and (b) a zoom to its distinct peak at 661.6 keV.

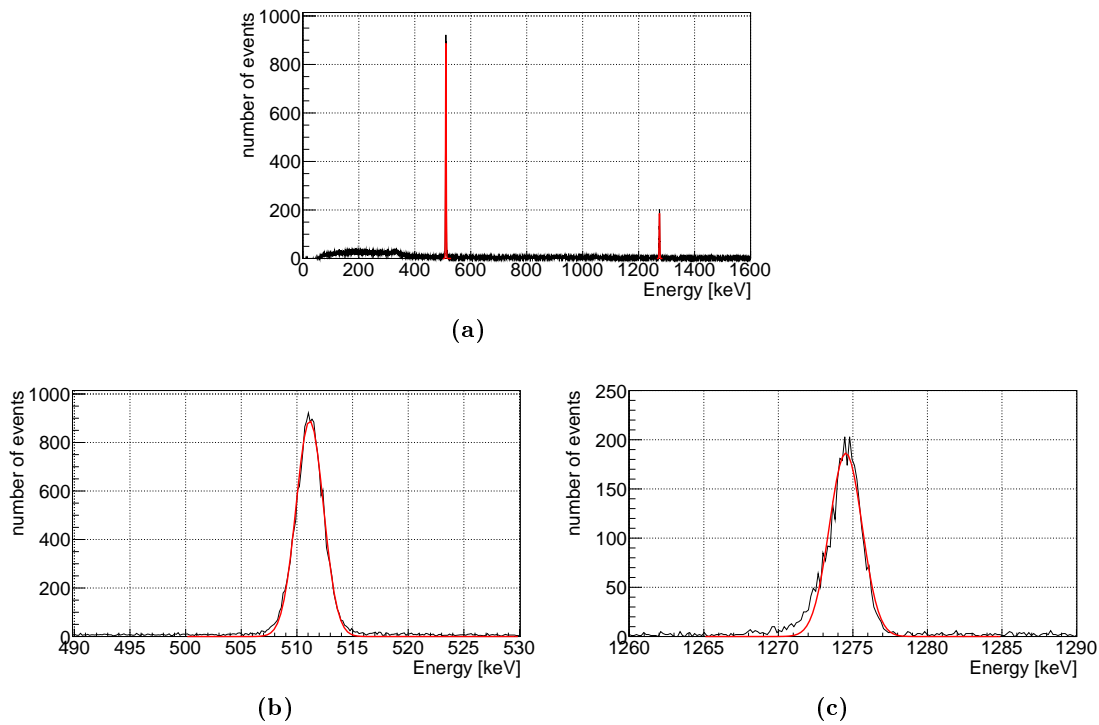


Figure 5.5: ^{22}Na spectra measured with the germanium detector. Using the germanium calibration, the spectra are plotted in dependence of the energy and the main energy peaks are fitted with a Gaussian. The plots show (a) the complete ^{22}Na spectrum and a zoom to its distinct peaks at 511 keV in (b) and at 1274 keV in (c).

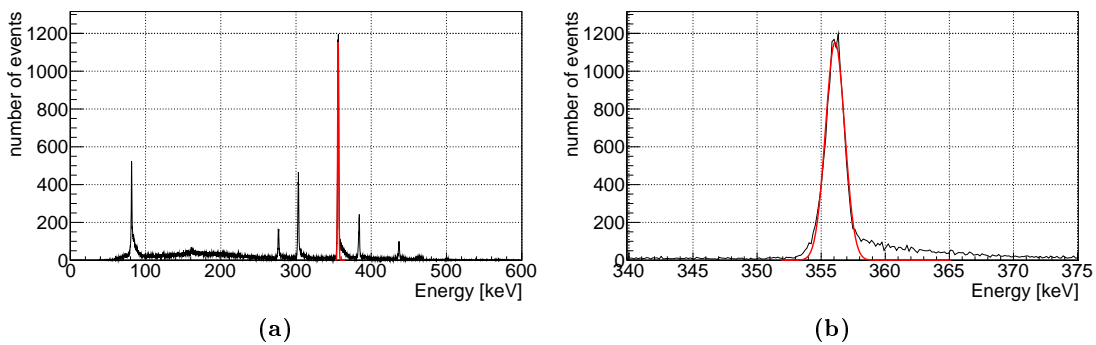


Figure 5.6: ^{133}Ba spectra measured with the germanium detector. Using the germanium calibration, the spectra are plotted in dependence of the energy and the main energy peaks are fitted with a Gaussian. The plots show (a) the complete ^{133}Ba spectrum and (b) a zoom to its most prominent peak at 356 keV. The remaining peak fits can be found in appendix B.1.

The main gamma-ray peaks are fitted using a Gaussian to determine the standard deviation σ_{E_γ} and from this the full width at half maximum (FWHM) for the respective peaks in units of keV. The two quantities are connected:

$$\text{FWHM} = 2 \sqrt{2 \ln(2)} \sigma_{E_\gamma} \quad (5.9)$$

The fit values for σ_{E_γ} are listed in table 5.3, along with the calculated FWHM values. The peak fits are plotted in the figures above and in case of the remaining ^{133}Ba peaks in appendix B.1.

	E_γ [keV]	σ_{E_γ} [keV]	$\Delta\sigma_{E_\gamma}$ [keV]	FWHM [keV]	ΔFWHM [keV]
^{137}Cs	661.6	1.10	0.03	2.59	0.07
^{22}Na	511	1.23	0.01	2.90	0.02
^{22}Na	1274	1.10	0.02	2.59	0.05
^{133}Ba	80.8	0.72	0.06	1.70	0.14
^{133}Ba	276.6	0.70	0.03	1.65	0.07
^{133}Ba	302.8	0.72	0.02	1.70	0.05
^{133}Ba	356	0.74	0.02	1.74	0.05
^{133}Ba	381.6	0.77	0.04	1.81	0.09
^{133}Ba	436	0.92	0.05	2.17	0.12

Table 5.3: Germanium detector energy resolution measured as the standard deviation for the gamma-ray peaks in energy-dependent calibration source spectra and calculation of the respective FWHM values.

The FWHM values are plotted in dependence of the peak energy in figure 5.7. A fit of the form of equation (5.10) is shown in red.

$$\text{FWHM}_{\text{fit}}(E) = 2\sqrt{2 \ln(2)} \cdot \sqrt{F_{\text{Ge}} \epsilon_{\text{Ge}} \cdot E + W_E^2} \quad (5.10)$$

F_{Ge} stands for the Fano factor and ϵ_{Ge} is the energy gap between valence and conduction band in germanium. For the fit, these quantities are fixed to $F_{\text{Ge}} = 0.132 \pm 0.08$ and $\epsilon_{\text{Ge}} = 2.9 \text{ eV}$ (values taken from [80]). The third unknown in equation (5.10) is the electronic noise W_E , which is kept as a free fit parameter.

Fitting the data (red line in figure 5.7) yields an electronic noise of $W_E = 0.777 \pm 0.062 \text{ keV}$. Considering the data points for energies below 500 keV, the fit exhibits too high values. This is caused by the outlying value for the 511 keV line. Cross-checks for the peak width confirm the found value, its large width compared to the ones from the other peaks can not be explained.

As a comparison, the energy resolution found by [80] for the same germanium detector is plotted as a dashed green line in the same figure, finding a value for the electronic noise of $0.545 \pm 0.007 \text{ keV}$. The electronic noise can be explained by the fact that instead of the germanium DetectorLab amplifier, a shaping amplifier of model Ortec 671 was used for the measurements in [80].

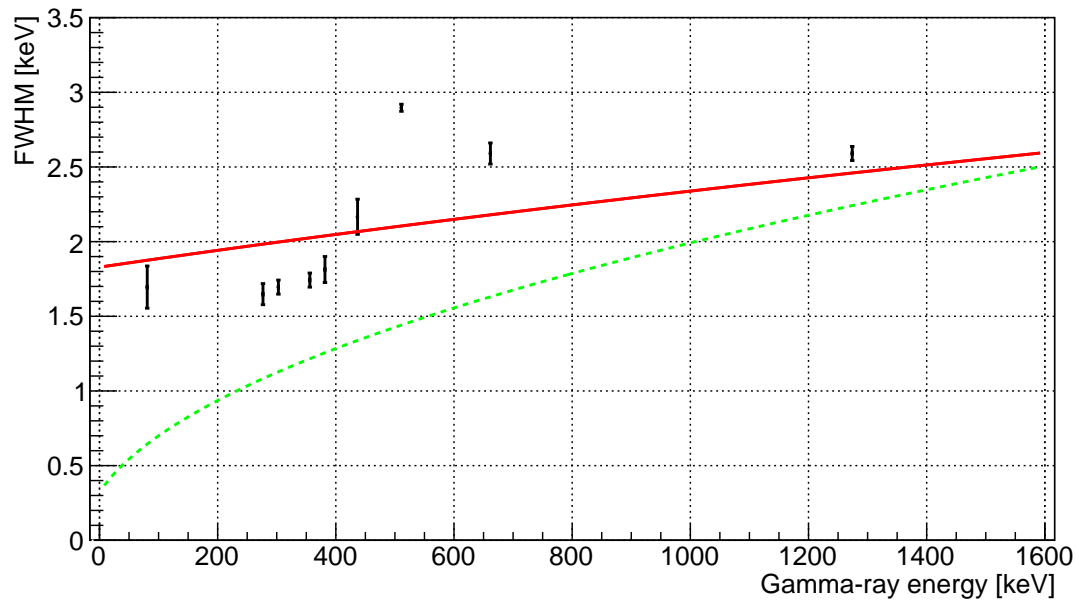


Figure 5.7: FWHM of the germanium detector for different energies measured. The red line is a fit depicting the energy resolution using equation (5.10). The dashed green line marks the energy resolution for the same germanium detector measured by [80], with a different setup as explained in the text.

5.3 | APD Calibration

The eight APDs installed in the MainzTPC are used to reconstruct the position of the interaction in the x - y -plane, by measuring the $S2$ signal. For the reconstruction, which is explained in detail in chapter 6, the APD gains have to be determined first.

It is not necessary to know the exact amount of light measured by each APD but rather the relative gain differences between the APDs. With this information, all APD signals can be rescaled relative to each other to define the impact of each APD on the reconstructed position.

A relative gain calibration for the APDs can be achieved by measuring the APD response to blue LED light pulses at different APD bias voltages. Since the APDs have a temperature-dependent gain, it is crucial to calibrate them during the experimental run, when the TPC is filled with xenon at the operation temperature.

The APD calibration was conducted during the experimental run at HZDR on 21 April 2016. Several technical difficulties affect the quality of the calibration data:

- The APDs seemed to have quite different performances, although the same bias voltages were applied. This can be traced back to the fact that at least one of the four optical fibers, which are used for LED calibration, is broken inside the setup. Since the APDs need a larger amount of light for the calibration than the PMTs, this might affect the APDs which are placed at the positions mostly illuminated by the broken fiber(s). Figure 5.8 gives an example of the different signal heights measured with the APDs. As can be seen, APDs with a strong response are neighbored, as are the APDs showing weak signals.
- Additionally one expects a slightly different performance for each APD, especially for APD 8, which was manufactured from another wafer than the other APDs. In a previous test at Mainz it was measured to have a significantly lower gain. In this calibration, it was not possible to calibrate APD 8, as it was one of the less illuminated sensors and the signals for lower bias voltages were not visible.
- The pulse generator originally foreseen to drive the LED was non-functional, which is why a replacement pulse generator was used which could not generate sufficiently short pulses. This leads to very long calibration signals, which distorts the result of the gain calibration, but since the calibration is only used for a relative gain measurement, this effect was neglected.

For the calibration, the APD signal for a given LED pulse is measured at different bias voltages. For higher bias voltages, the APD gain increases exponentially, therefore the LED driving pulse is reduced using a voltage attenuator. The employment of an attenuator also leads to a reproducibility of the original light signal.

At a given LED pulse strength and APD bias voltage, $5 \cdot 10^4$ events are recorded using the pulse generator as an external trigger. The APD signals are read out via a CSP and

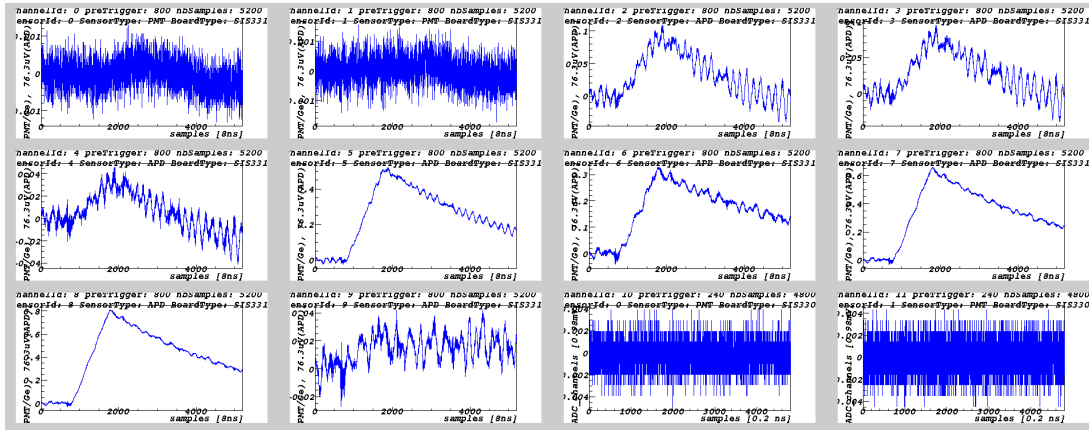


Figure 5.8: APD calibration signals for a bias voltage of 1000 V. The figure shows a screenshot of the DataView program. The individual channels visible are the two PMT signals on the SIS3316 (first two graphs, top left) and on the SIS3305 (last two plots, bottom right), which were recorded without a signal. The APDs are visible with APD 1 and 2 in the top row, APD 3 – 6 in the center row from left to right and APD 7 and 8 in the bottom row. Since all APDs should have a similar amplification at the same bias voltage, it is clearly visible that some APDs (4 – 7) are exposed to more light than others (8, 1 – 3). This effect is occurring to neighbored APDs, which is due to the fact that at least one of the optical fibers inside the TPC is broken.

therefore have the characteristic step-form. As explained in section 5.2, the step height in voltage is equivalent to the collected charge signal from the APD. The step height can be determined using either the StepFinder or StepFitter functionality of the raw data analysis tool (see section 3.5.6).

As the APD signals recorded for this calibration are very broad, the StepFitter routine is not working properly. Therefore, the StepFinder routine is used to get the APD step height. For comparison, figure 5.9 shows the height spectra obtained by the StepFitter and StepFinder routines for APD 4 at a bias voltage of 1000 V.

The StepFitter routine on the left shows two different peak-shaped distributions, a narrow peak at low heights and a broad peak at larger heights. The latter are still smaller than the mean height found by the StepFinder routine, which yields a Gaussian-shaped peak as can be seen on the right. The height distribution of the StepFinder routine is consistent with the signal heights observed when browsing the raw data waveforms.

The calibration consists of 65 measurements at five different LED voltages for each APD. Fitting the respective APD height spectrum with a Gaussian as shown exemplarily in figure 5.9 yields the corresponding data points for the raw data gain curves. The results of the Gaussian fits are summarized in the appendix section B.2.

Figure 5.10a shows the Gaussian fit values plotted against the respective bias voltages. For higher bias voltages, the LED pulse voltage was attenuated to account for the exponential APD gain increase. The different curves are fitted using the following exponential function:

$$A(U) = \exp(m \cdot U + b) \quad (5.11)$$

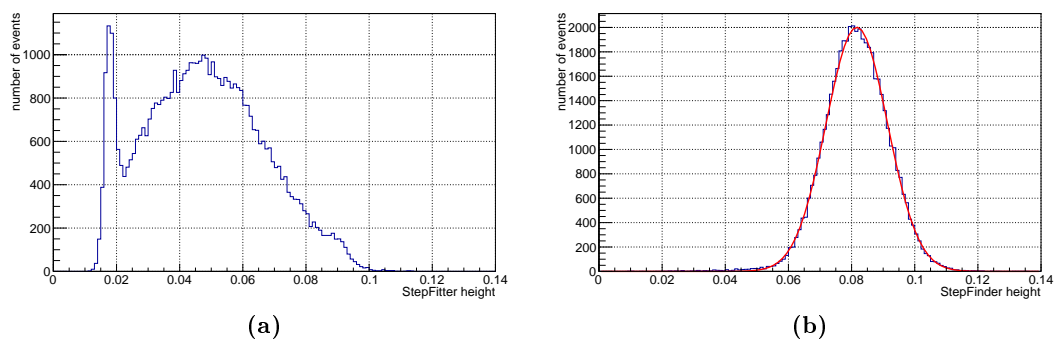


Figure 5.9: APD signal height distributions for APD 4 at a bias voltage of 1000 V, obtained from raw data processing using (a) the StepFitter routine and (b) the StepFinder routine. The heights observed in the raw data waveforms agree much better with the StepFinder distribution, therefore this distribution is used for the further calibration. As can be seen, the StepFinder distribution in (b) can be fitted with a Gaussian.

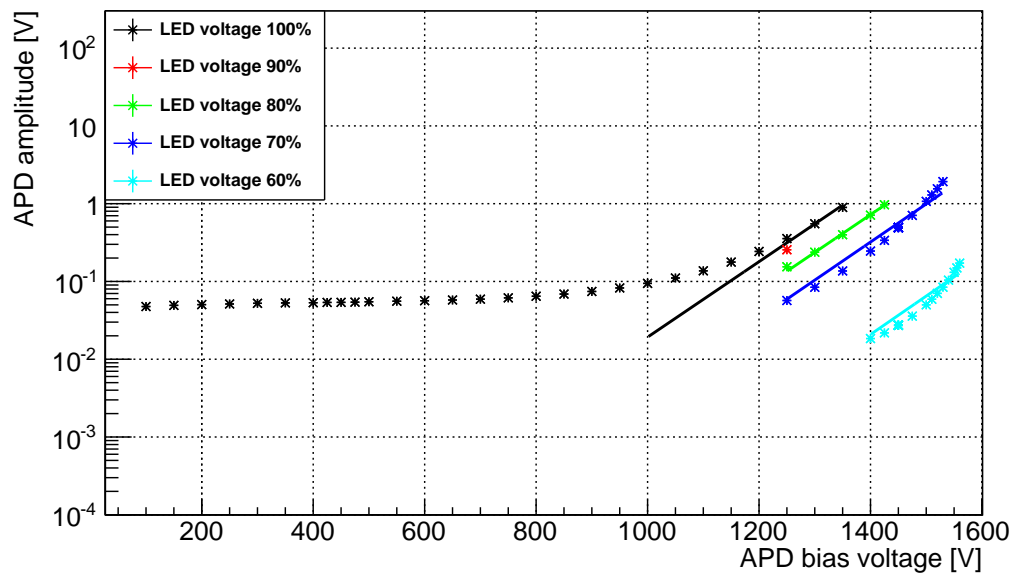
The exponential behaviour for higher bias voltages should be equivalent for the different LED voltages, since the amplification is not dependent on the amount of measured light. Therefore, the slope m for the respective fits is fixed to the value of the LED voltage fit at 80 %, to have a mean slope. The fit values are listed in table 5.4.

APD	$m [\times 10^{-3}]$	b_{100} [V]	b_{80} [V]	b_{70} [V]	b_{60} [V]
1	11.17	-15.12	-15.96	-16.91	-19.79
2	11.73	-15.94	-16.78	-17.73	-20.58
3	11.19	-16.10	-17.00	-17.93	-20.72
4	11.31	-13.63	-14.42	-15.58	-18.53
5	11.90	-14.67	-15.58	-16.72	-19.75
6	10.12	-11.70	-12.63	-13.57	-16.58
7	8.23	-9.13	-10.00	-10.97	-13.62
8	-	-	-	-	-

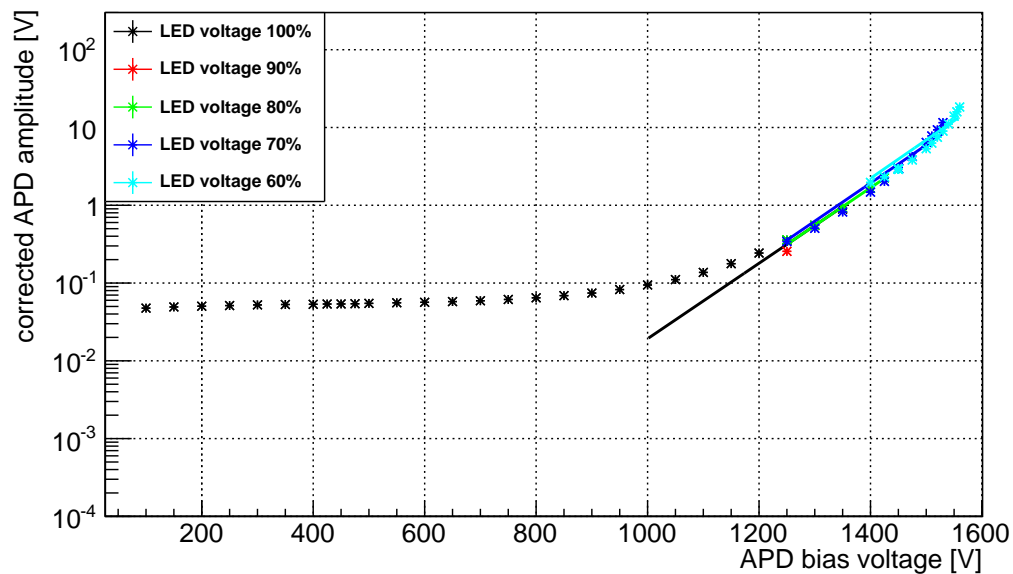
Table 5.4: Parameters of the exponential fits to the raw data points in the respective LED voltage ranges. The lowercase numbers on the offset parameters b_x correspond to the respective part of the data set which is fitted, as shown exemplarily in figure 5.10a.

With this, the fit value for the offset b can be used to adjust the data points with respect to the LED voltage of 100 %, since the measurements for different LED voltages were taken with overlaps concerning the bias voltage. The resulting data curve is shown in figure 5.10b, where the data points for the different LED voltages are partly overlapping, as do the respective exponential fits.

To determine the relative APD gain for a given bias voltage, the data points shown in figure 5.10b are normalized such that the amplitude value for a bias voltage of 400 V corresponds to a gain of 1, since the curve is almost constant in this region. This normalization yields the APD gain curve, which is shown in figure 5.11.



(a)



(b)

Figure 5.10: APD calibration signal amplitudes for different LED pulse voltages in dependency of the APD bias voltage (APD 1). For higher bias voltages, the APD gain increases exponentially. To account for this, the LED pulse voltage was decreased to calibrate also for higher gains. Using an overlap in the bias voltage for different LED voltages, the data points can be normalized. Exponential fits are used to determine the offset between the different LED voltage measurements. (a) shows the mean values from the Gaussian fits as obtained from the raw data, in (b) the data points for the lower LED voltages are normalized with respect to the the LED voltage at 100%.

Note that this gain curve only represents a relative gain. For an absolute gain, a calibration using a well-defined energy deposit in the APDs is necessary to create a reference point.

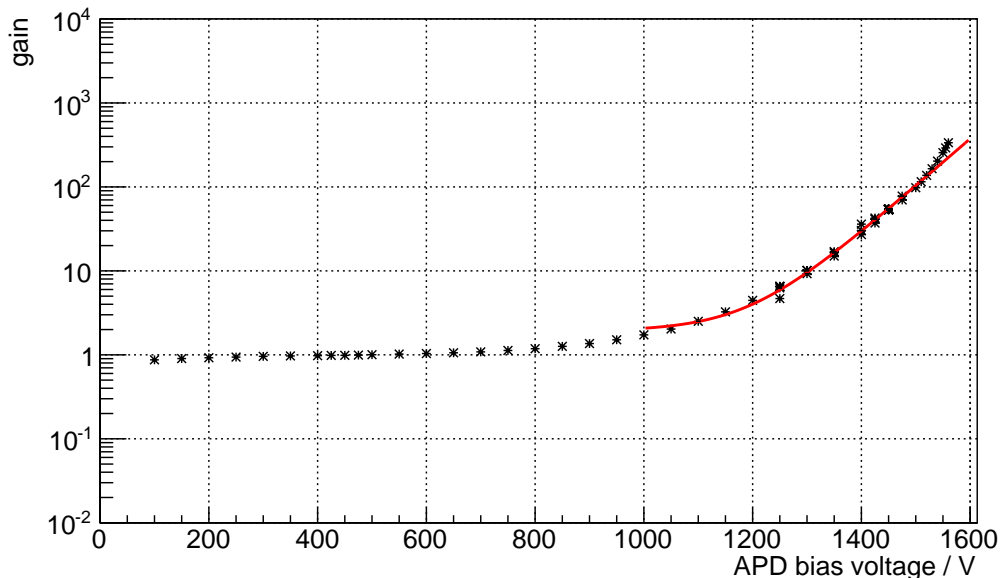


Figure 5.11: APD gain curve for APD 1. The APD amplitudes from the calibration are normalized to a gain of 1 at a bias voltage of 400 V. An exponential fit for the higher bias voltages allows to determine the gain for the APD during operation in the experiment.

$$g(U) = g_0 \cdot \exp(m_g \cdot (U - U_0)) \quad (5.12)$$

Using a fit of the form given in equation (5.12), the APD gains for each APD at the bias voltage during the experimental operation can be determined. The gain values are summarized in table 5.5. The plots of the raw data points with the respective exponential fits as well as the resulting gain curves for the remaining APDs can be found in the appendix B.2.

As stated before, the calibration for APD 8 was not possible, since only calibration signals for high bias voltages could be measured. APD 8 is also the only APD operated at a different, higher bias voltage to counteract its weaker performance.

The gains found for the APDs are significantly smaller than the expected gains of $1 - 2 \cdot 10^3$, which is probably due to the measurement problems that are mentioned in the beginning of this section.

To achieve better results in a future APD gain calibration, it is crucial to replace the broken optical fibers inside the MainzTPC and to use a better-suited pulse generator. One has to make sure that each APD is illuminated sufficiently so that calibration signals are visible even at low bias voltages.

APD	U_{bias}	m_g [V^{-1}]	b_0	g_0	g
1	1500	13.11	1147.11	2.17654	104.25
2	1500	13.60	1147.18	2.33551	123.74
3	1500	13.07	1142.29	1.86688	109.21
4	1500	14.24	1178.42	3.87553	101.24
5	1500	15.08	1138.59	3.65954	236.73
6	1500	16.58	1208.27	4.75269	130.71
7	1500	16.00	1212.84	5.23991	104.10
8	1540	-	-	-	-

Table 5.5: Fit parameters for the APD gain curve for each APD at its bias voltage U_{bias} during operation in the MainzTPC experiment. The fit errors can be found in the appendix B.2.

Position Reconstruction

Chapter 6

6.1 | 3D Position Reconstruction in the MainzTPC

The ability of the MainzTPC to reconstruct the position of the scattering interaction in the liquid xenon is a useful tool for event discrimination but also helpful in terms of understanding the measured signals. By knowing the interaction point of an event one can fiducialize the active volume. This can improve analysis results, since edge effects in the TPC periphery from e.g. electric drift field nonuniformities can be cancelled out by discriminating events in the outer regions of the active volume.

The MainzTPC measures the drift time of the electrons by examining the time difference between the $S1$ and the $S2$ signal to determine the interaction depth z in the liquid. This technique is discussed in detail in chapter 8 about the electron drift in the MainzTPC. The x - y -position of an event is reconstructed by the light distribution of the $S2$ signal, which will be examined further in this chapter.

Large-scale experiments such as XENON1T use the same technique as the MainzTPC to determine the interaction depth z . To measure the x - y -position, the small scale of the MainzTPC required a revision of the TPC design compared to its larger counterparts, as explained in chapter 3. While large-scale experiments use an array of PMTs to examine the $S2$ distribution, there are only two single PMTs installed in the MainzTPC, one at the top and one at the bottom. Consequently, using only the PMTs, the MainzTPC is non-sensitive to the x - y -position.

An array of eight APDs is incorporated to the TPC in a circle around the liquid-gas interface, where the $S2$ signal is generated. The decision not to use an array of smaller PMTs instead of a single PMT was made to maximize the photo-sensitive area for optimal light collection. Other small-scale xenon TPCs such as MIX [75] or neriX [2] use small PMT arrays. To the best of the author's knowledge the employment of APDs for the position reconstruction in a xenon dual-phase TPC has not been tested yet.

6.2 | Determination of the x - y Position using the Centroid Method

6.2.1 | The Centroid Method

Ideally, the $S2$ signal is detected by all eight APDs simultaneously. Depending on the position of the $S2$ in the x - y -plane, the amount of light shining on each APD differs by a large factor. Figure 6.1a illustrates a non-centered $S2$ signal and the difference in illumination for the APDs nearby and further away.

An intuitive way to reconstruct the x - y -position is the centroid method. It is known from the calculation of the center-of-mass of an object, where the positions of the individual mass points are weighted with their mass and then averaged. With the APDs, the signal amplitude A_i is the weighting factor. To account for the different APD gains,

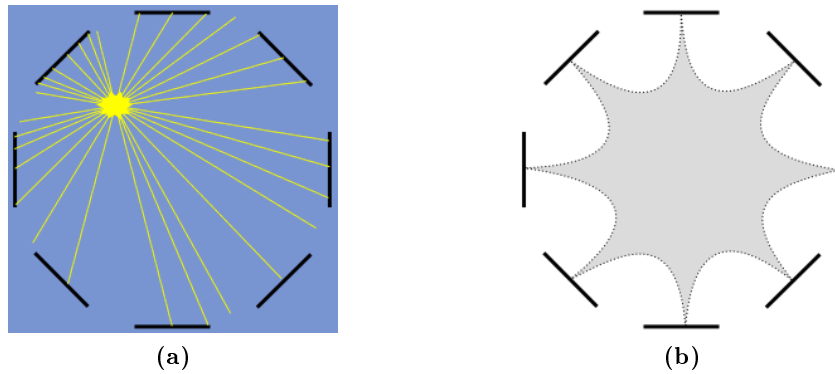


Figure 6.1: Illustration of the centroid method: The change in illumination of the APDs depending on the position of the $S2$ is sketched in (a). Using the centroid method leads to a distortion of the reconstructed position distribution, which is indicated by the grey area in (b). The degree to which the distribution is distorted is influenced by the detector geometry and measurement thresholds.

the amplitude of each APD is divided by the product of the respective APD gain g_i and its quantum efficiency η_i .

The reconstructed coordinates \bar{x} and \bar{y} are determined according to equation (6.1). The weighted sum of the APD positions in the numerator is divided by the sum of the weights, which are the gain-corrected amplitudes.

$$\bar{x} = \frac{\sum x_i \cdot \frac{A_i}{g_i \eta_i}}{\sum \frac{A_i}{g_i \eta_i}} \quad \bar{y} = \frac{\sum y_i \cdot \frac{A_i}{g_i \eta_i}}{\sum \frac{A_i}{g_i \eta_i}} \quad (6.1)$$

The centroid method allows an examination of the $S2$ position only depending on measurement data, which makes it a good candidate for a first-order reconstruction tool.

However, the method introduces a reconstruction uncertainty which has to be taken into account. The APD coordinates x_i and y_i are the centers of the APDs and do not reflect the finite detection areas. In the reconstruction this results in a distortion of the position distribution in x - y . This effect is sketched in figure 6.1b.

The distortion is due to the way this reconstruction method works: Assume only two neighboring APDs detect a light signal, then the reconstructed position is found on a straight line connecting the two APD centers. In case of three APDs, the position can not lie on the same connection line anymore, since the third APD “pulls” the reconstructed position more to the TPC center.

For optimal reconstruction, all eight APDs should be evaluated. The reconstruction of events in the outer region between two APDs is therefore shifted towards the center of the TPC, which leads to the distorted shape of the reconstruction pattern sketched in 6.1b.

An alternative reconstruction method that avoids the distortion in the distribution of the reconstructed positions is presented in section 6.3. Due to time reasons only the centroid method was applied in the course of this thesis.

6.2.2 | Position Reconstruction in x - y with Data

For the reconstruction, the gains and the quantum efficiencies of the APDs have to be known. Since APD 8 could not be calibrated, there is no gain information for this sensor. The reconstruction pattern as sketched in figure 6.1b is supposed to be symmetric after taking into account all APD signals. Without gain information, the signal measured by APD 8 can not be used for the reconstruction. Since the APDs are identical in construction and the expected gain value of APD 8 should not deviate significantly from the other APD gains, this gain was assumed to be the mean value of the gains from APD 1 to 7. The APD gain values are listed in table 6.1.

This approach is preferable considering the alternative: If the APD on the opposing side of the MainzTPC, APD 4, is evaluated for the position reconstruction without the signal information provided by APD 8, the distribution shape is distorted towards APD 4, since the “counterweight” of APD 8 is missing. For symmetry reasons, APD 4 would thus have to be excluded for the position reconstruction as well.

Since the exact quantum efficiencies of the APDs are unknown, their value was set to 1. Previous experiments found quantum efficiencies for this type of APD of approximately $(34 \pm 5) \%$ [88].

APD i	g_i (blue LED)	η_i	$g_{\text{rel}} = \frac{g_i \cdot \eta_i}{g_5 \cdot \eta_5}$
1	104.25	1	0.44
2	123.74	1	0.52
3	109.21	1	0.46
4	101.24	1	0.43
5	236.73	1	1.00
6	130.71	1	0.55
7	104.10	1	0.44
8	130.00	1	0.55

Table 6.1: APD gain values from calibration. The value for the APD 8 gain is the mean of the other APD gains. The quantum efficiency is unknown and therefore set to 1 for all APDs. For the relative factor g_{rel} the highest measured gain of APD 5 was chosen as standard gain value.

To test the position reconstruction in x - y , a ^{152}Eu source was placed in three different positions around the TPC vessel. The distance between the TPC center and the source positions on the outer wall of the cryostat adds up to 17.5 cm. The positions relative to the TPC and the collimator for the ^{137}Cs source used in Compton scattering measurements are sketched in figure 6.2a. With respect to the orientation of the APDs inside, the deviation of the source position from the ideal placement as sketched is estimated to be approximately 0.5 cm. Also, the x - y plane orientation is indicated. The positions of the APDs relative to the x - y plane are shown in figure 6.2b. The beam direction for Compton measurements is always the positive x -direction.

Using the TPC PMT coincidence as DAQ Trigger, data were taken for the three source

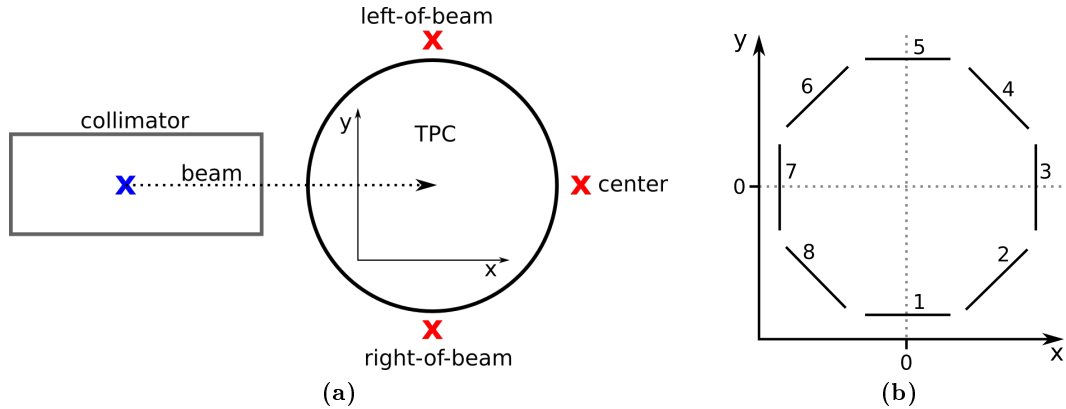


Figure 6.2: Sketch of the positioning of the ^{152}Eu source (marked red) around the MainzTPC for different measurements (a). In blue, the position for the ^{137}Cs used in Compton mode is drawn, along with the beam direction which applies for both Compton and neutron scattering. Inside the depicted TPC vessel seen from above, the coordinate system used for the position reconstruction in x - y is indicated. In (b), the relative positions of the individual APDs in x - y are illustrated.

positions “center” (in front of the TPC, but on the opposite side to the collimator), “left-of-beam” and “right-of-beam”. Left and right are relative to an observer looking from the collimator side, since at the HZDR both the gamma-rays and the neutrons for the scattering measurements were originated from the same direction.

The APD signals were analyzed using both the StepFinder and StepFitter routine mentioned in section 3.5.6. While the latter did not work for the APD calibration, the fitting of the APD waveforms from $S2$ signals works well and can therefore be employed for the signal analysis.

The reconstructed event distributions for each source position are shown in figure 6.3. The individual distributions are sorted such that figure 6.3b shows the events measured with the ^{152}Eu placed left-of-beam, figure 6.3a with the source positioned at the center position and figure 6.3c with the source right-of-beam.

The black straight lines indicate the APD positions in the x - y -plane. APD 1 is positioned at the bottom of the plot at the coordinates $(0, -35.2 \text{ mm})$, the numbering of the APDs seen from above is counter-clockwise. The brown circles mark the dimensions of the electric field mesh frames.

The general shape for all three plots is comparable, as are the clusters of events that can be observed. The distortion pattern has a shape similar to the expectation. The asymmetric shape of the pattern is presumably a consequence of not taking into account the difference in quantum efficiency for the APDs as well as the uncertainties considering the APD gain. Therefore the products $g_i \eta_i$ are not determined correctly and the pattern is distorted. The effect increases with the radial distance of the event from the TPC center.

All three distributions show two noticeable features. First, the reconstruction pattern has the least number of events in the region in front of APD 8. Simultaneously, there

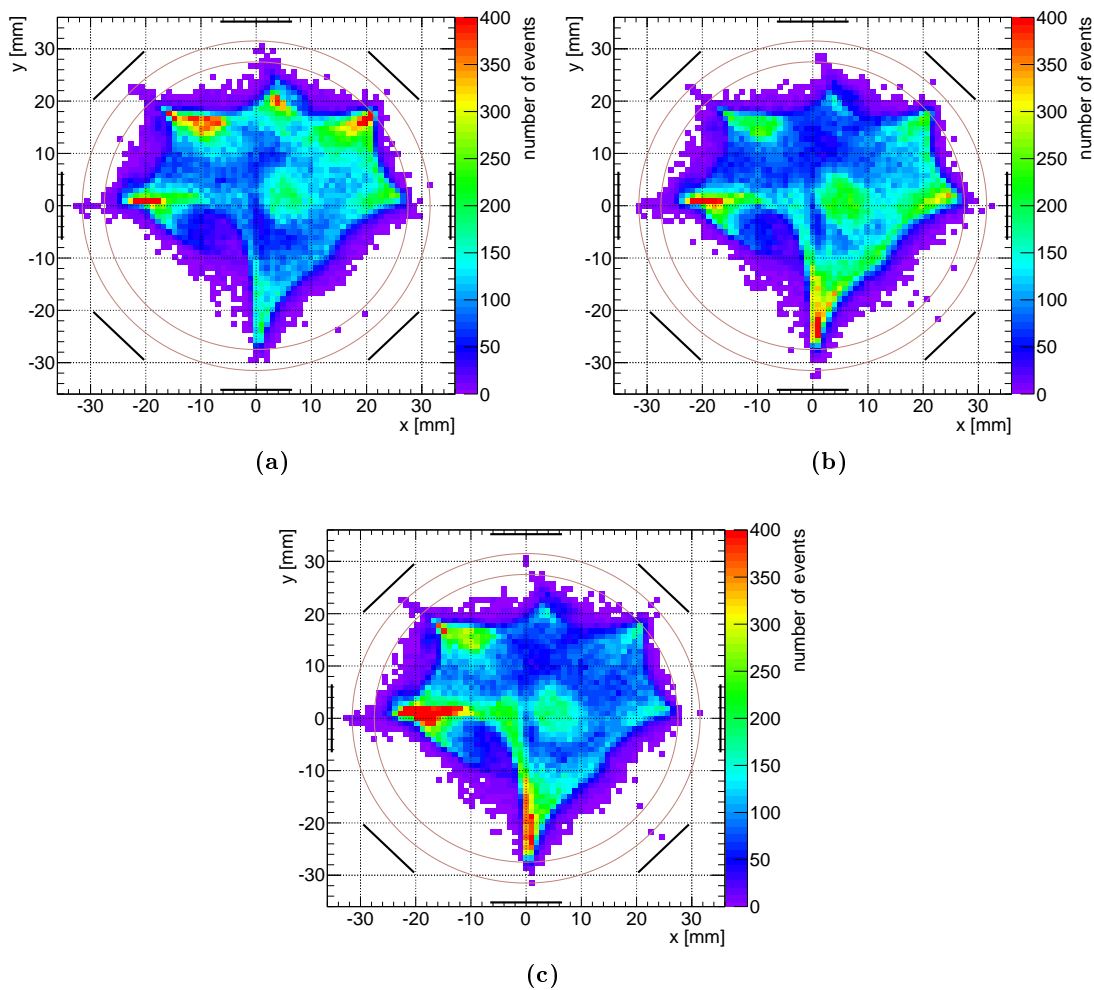


Figure 6.3: Position reconstruction in x - y with the APD gains from the APD calibration, for a ^{152}Eu source placed at the positions: (a) left-of-beam, (b) center and (c) right-of-beam. The plots show the TPC volume from above, with the collimator (or beam) position to the left (negative x -direction). The APDs are indicated as black straight lines, the brown circles mark the electric field mesh frames. The increase of the event numbers in different regions can be linked to the positioning of the ^{152}Eu source.

are distinct event clusters at $x \approx -20$ mm values and a y value of approximately zero, as well as at $y \approx -20$ mm values and a x value of approximately zero. They presumably emerge from events that were reconstructed further away from APD 8 than expected. Second, there is a circular-shaped event cluster visible at $x \approx 5$ mm and $y \approx 0$ mm of each event distribution, with a radius of roughly 5 mm. This also points to a non-perfect gain balance between the APDs.

For each of the event distributions, the events clusters are augmented in different regions. For the position left-of-beam, the source is expected to illuminate the TPC from

the positive y -direction. Figure 6.3a shows an increase in events reconstructed in the upper half of the x - y -plane, and further to the left compared to the measurement for the center position. For the center position in figure 6.3b, most events can be found on the right side, which fits the expectation. The right-of-beam measurement in figure 6.3c yields an event distribution with an increased number of events in the negative y -direction, where the source was placed.

The comparison of the three measurements and the differences in the event distributions indicate the source position for each measurement. It is difficult to determine the source position, but the placement of the ^{152}Eu source can be pinpointed from the increased number of events accumulated in specific regions of the individual distributions.

It is also possible that the named features have a different origin, but so far, no indication of a physical cause has been found. A correlation between the position reconstruction pattern and for example the liquid level tilt, in the TPC, as is described in chapter 7, could not be verified.

6.2.3 | Improvement of the Shape of the Reconstruction Pattern

To enhance the quality of the reconstruction result, the quantum efficiencies η_i could be adjusted relatively to each other. For this, the data from the three ^{152}Eu measurements at different positions was evaluated.

As a first step, the measurements left-of-beam and right-of-beam were examined considering the APD pair APD 1 and APD 5. The two APDs are positioned directly on the y -axis of the reconstruction plane and therefore do not carry any information about the position in x . Ideally, determining the position with these two APDs only for both source positions yields two position distributions in y with mirrored event distributions. The cutoffs for both distributions should remain at stable positions y_1 and y_2 and depend on the QE values η_i relative to each other. By adjusting one of the values the cutoff positions will supposedly reach the condition $y_1 = -y_2$, which means that the impact of the product $g_i \cdot \eta_i$ is cancelled out for this APD pair.

Figure 6.4 shows the distribution of the y -position determined only with the signals from APD 1 and 5 for the two source positions left-of-beam and right-of-beam. This result contradicts the expectation of a mirrored distribution for the source placed on the opposite side of the TPC. The comparison of both distributions does not allow a clear distinction of the two source positions. The histogram shapes are quite similar, as are the positions of the cutoff edges. The blue histogram - for the source placed left-of-beam (positive y) - is shifted slightly towards the positive y -direction but does not exhibit specific features that could be used as an alternative to the cutoff edges.

The most prominent feature of both distributions is a peak-like structure around $y \approx -16$ mm. The peak seems to be independent from the source position and might therefore have a different origin. By the time of writing this thesis, the nature of the peak was not resolved. It alters the distribution shape such that the adjustment of the QE values is not feasible with the data at hand.

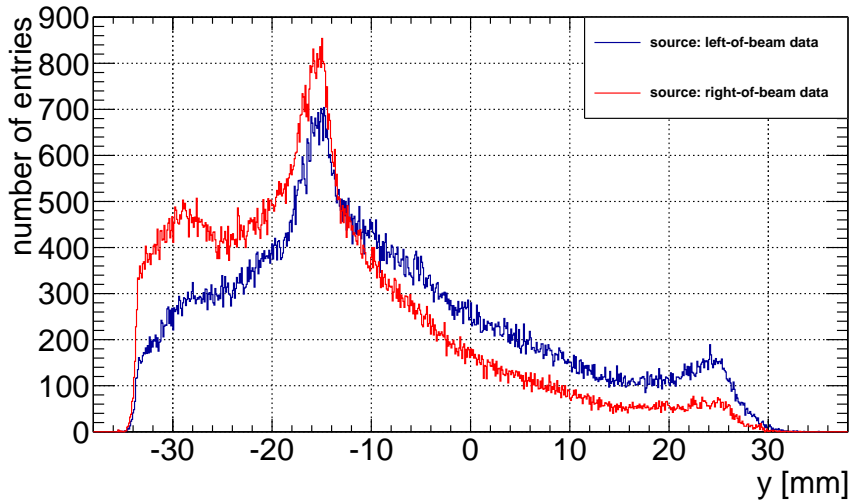


Figure 6.4: Distributions of the y -position determined with the signals from APD 1 and 5 for the two source positions left-of-beam and right-of-beam. Both distributions show the same shape and nearly identical cutoff edges.

6.2.4 Discrimination Ability

As seen in section 6.2.2, the centroid method allows a rough position reconstruction of the $S2$ signal with an array of APDs in the Mainz TPC. The reconstructed event positions are used to examine the ability to discriminate signals in different detector regions. As an example, the ^{152}Eu measurements discussed above are merged. Since all measurements were taken at the same drift field strength of 198 V/cm, the source position should not have any meaning for the signals measured in the TPC, except for their distribution in x - y . Using all three data sets, the event distribution should be more homogeneous than before.

Figure 6.5a shows the event distribution for the merged data sets. Except for three enhanced regions in the lower center, the left center and the upper left, there are no significant event clusters that could indicate a specific source position.

Figure 6.5b shows the corresponding spectrum for the $S1$ signal. This spectrum is employed in chapter 8 to determine the signal correction in $S1$, using the event position discrimination. Foremost, the smaller peak structure around 150 to 200 p.e. is interesting, as its peak position is studied for different interaction depths.

Using the position reconstruction mechanism as presented before, one can define a fiducial volume to find out whether certain signals originate from a specific part in the detector. This can be due to the source position, leading to more events in a certain region of x - y , or due to the energy of the incident gamma-rays which can penetrate the TPC to different lengths. Another application of the position reconstruction would be the identification and discrimination of signals from certain TPC regions that are background or noise events, for example if there was a sparking signal at a fixed position

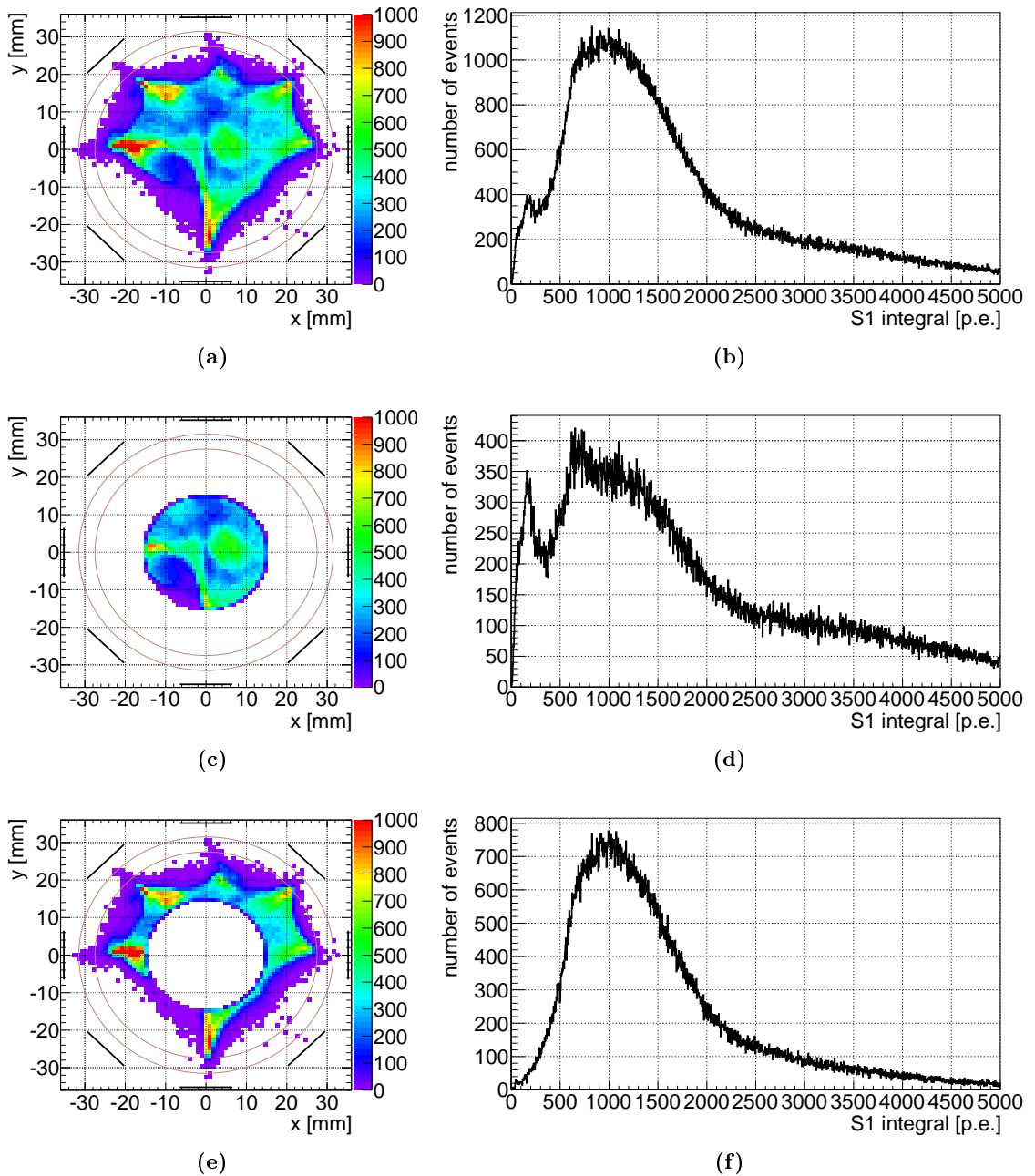


Figure 6.5: Event distribution and $S1$ spectrum of a ^{152}Eu measurement at a drift field of 198 V/cm . The event distribution reconstructed from the $S2$ signals (a) corresponds to the $S1$ spectrum in (b). Two peak structures are distinguishable in the spectrum, a narrow and small peak at about 150 to 200 p.e. , and a larger and broader peak structure probably arising as a superposition of different peaks around 1000 p.e. . The event distribution considering only events inside a radius of 15 mm around the center of the TPC (fiducial volume) is shown in (c), the fiducial cut leads to a reduction of the large peak structure in the $S1$ spectrum, as can be seen in (d). Compared to the complete spectrum, most of the events in the large peak are discriminated. The events outside the fiducial radius are plotted in (e). The corresponding $S1$ signals in (d) show one large peak structure, while the smaller peak at lower $S1$ has vanished from the spectrum. This suggests that the events contributing to the smaller peak structure primarily occur in the center of the TPC.

on one of the meshes or somewhere else in the active volume (which was not observed during our measurements).

Since the centroid method merely allows a rough position reconstruction, a circular fiducial volume in the center of the TPC was chosen. Considering the reconstruction mechanism, the position uncertainty should be smaller for events in the central region than for the TPC periphery. The fiducial volume defined here has a radius of 15 mm around the TPC center. This value was chosen after testing several radii and the outcome in the $S1$ spectrum.

The event distribution in the x - y -plane and the $S1$ spectrum obtained by only considering events reconstructed within 15 mm from the TPC center are shown in figures 6.5c and 6.5d. Compared to the complete $S1$ spectrum, one finds the large peak structure reduced by approximately a factor 3. The narrow peak on the other hand remains at roughly 80 % of its original height. This suggests that most of the events contributing to the small, narrow peak occur inside the central region of the TPC, while most of the events that account for the large peak structure are found in the outer regions.

As a cross-check, the complementary event distribution and its corresponding $S1$ spectrum are plotted in figures 6.5e and 6.5f. The $S1$ spectrum for the discriminated events contains the missing events from the large peak structure and shows now indication of a small narrow peak in the region between 150 and 200 p.e. This behaviour supports the conclusion about the different signals occurring in different TPC regions.

Choosing a smaller radius for the fiducial volume leads to a loss also for the events making up the small peak structure, while for larger radii, more events from the large peak structure prevail. The fiducial radius is set to 15 mm also in later chapters since for this value, the two peak populations in ^{152}Eu are separated most effectively.

6.3 | Status and Next Steps

As mentioned before, the centroid method provides a first-order reconstruction tool for the position in x - y . As demonstrated, using an optimized APD gain calibration, the reconstruction yields an event distribution which allows to find larger event clusters. Furthermore, the technique can be applied for event discrimination.

A first improvement considering the difficulties determining the APD gains is a recalibration of the APDs at the operating temperature for the respective data sets. The influence of the temperature on the APD performance suggests a recalibration of the APDs for each measurement at a different operating temperature. Using a more suitable pulse generator and repairing the broken optical fiber will improve on the calibration data and allow to also calibrate APD 8.

It is possible to roughly identify the gamma-ray source position relative to the MainzTPC, as shown in the previous section. Also, the x - y position reconstruction can already be used as a discrimination tool, which is employed in chapter 8 for the signal corrections. In other small dual-phase experiments like MIX or neriX, the structure of the metal meshes used to create the electric drift field had a visible impact on the distribution

of the reconstructed event positions. The granularity of the copper meshes used in the MainzTPC is very filigree and can therefore not be resolved in the distribution of the $S2$ light. To determine the spatial resolution in $x-y$ and the APD response to signals at different positions, a point-like gamma-ray source could be used to illuminate the TPC from the bottom. Alternatively, an internal source such as ^{37}Ar dissolved in the liquid xenon phase of the TPC can be used, as is investigated in [4].

To further improve the position reconstruction, a light response simulation of the MainzTPC is necessary. By creating signals in different positions in the $S2$ region, the response of the APDs is determined and listed in a so-called Light Collection Efficiency map (LCE or light map). This map assigns the $x-y$ position of the simulated event to the respective APD responses. As a consequence, the light distribution on the APDs in measurement data can then be compared to the simulated distributions using the method of least-squares or another type of fit mechanism. The event distribution reconstructed with a light map does not contain the distortions intrinsic to the centroid method and is being applied in large-scale experiments such as XENON1T. This method is currently under development for the MainzTPC data.

Overall, the findings prove that the APDs can be used for the position reconstruction and show the potential of these sensors already with first-order techniques.

Liquid Level Determination

Chapter 7

7.1 | Levelmeter Calibration

The height of the liquid level in the TPC has great influence on the detector performance, for example on the $S2$ signal generation, as described in 1.3.3. The knowledge about the liquid level and a possible tilt of the TPC is helpful for the understanding of the detector performance and for the event selection using the position reconstruction.

As described in section 3.2.4, the levelmeters are cylindrical capacitors which change their capacitance with respect to the liquid level inside. The calculation of the resulting capacitance is scaled with a reference capacitance C_{ref} according to equation (3.4). The calculated capacitance for the levelmeters can be erroneous if the connections between the different capacitors (reference capacitor or the levelmeters) and the UTI boards change between measurements. It was discovered that the capacitance values for the levelmeters were different after disconnecting and reconnecting the UTI boards to the setup, which led to measured capacitances with different offsets. Because of this, the calibration is carried out using only the raw data measured by the UTI and ignoring the value of the reference capacitor.

Therefore, equation (3.4) is slightly modified, to measure the relative capacitance R of the levelmeters:

$$R = \frac{T_x - T_{\text{off}}}{T_{\text{ref}} - T_{\text{off}}} = \frac{C_x}{C_{\text{ref}}} \quad (7.1)$$

As stated in section 3.2.4, the individual terms T_x , T_{ref} and T_{off} stand for the measured time constants of the unknown capacitance, which is equivalent with the levelmeter, the reference capacitance and the capacitive offset induced by the setup.

The calibration using this equation does not yield capacitance values for the levelmeters. Nevertheless, the change in capacitance is measured and can be translated into a height for the liquid level.

Note: The hardware of the UTI boards and their connections to the different capacitors were changed in July 2017, when the levelmeter readout showed strong instabilities. Therefore the levelmeter calibration had to be conducted twice to account for the data taken before (at the HZDR) and afterwards.

7.1.1 | Calibration of the Levelmeters with Data from July 2015

For the first calibration of the levelmeters it was convenient to use the monitored data of a test run on 7 July, 2015. During this test, the TPC was overfilled with liquid xenon, so that not only the capacitances in the empty state could be measured but also the capacitance of the completely immersed levelmeters.

Figure 7.1 shows the relative capacitances for all 4 levelmeters during the run of 7 July, 2015, for the time between 1:30 PM and 6 PM. On the very left, the values are flat and on a low level, which corresponds to the empty levelmeters. Shortly after 2 PM, the

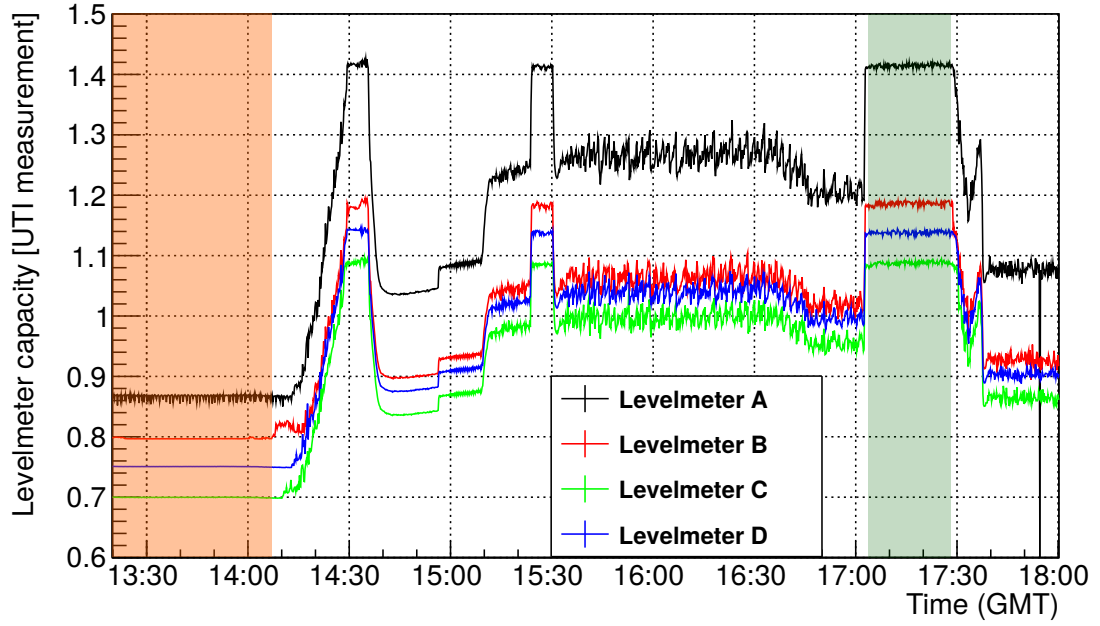


Figure 7.1: Relative levelmeter capacitance plotted versus the time of the measurement. This data was acquired on 07 July 2015 in a setup test for the levelling in the TPC. On the left, flat data lines with low values indicate the capacitance values for the empty levelmeters (orange area). The maximum values, as for example around 5:00-5:30 PM (greenish area), show the capacitance values for levelmeters completely filled with liquid xenon. Recuperation and other tests in between are responsible for the shape of the graphs. At several points the value of levelmeter A drops to zero, this is because of signal outliers in the acquisition data (which are set to zero by the Slow Control).

capacitances rise up to a maximum value, indicating the filling of the levelmeters with liquid xenon. As this was a test run, the level was changed several times, but it can be seen, that there is a maximum value that is reached three times during this run, once between 1:15 PM and 2:15 PM, then again \sim 3:20-3:30 PM and finally \sim 5:00-5:30 PM. To calibrate the levelmeters, both the relative minimum and the maximum capacitance of each levelmeter R_{\min} and R_{\max} are determined from the data. This is done by calculating the mean relative capacitance for a fixed time interval in the respective time region. For illustration, the time intervals are indicated with dashed vertical lines in figure 7.2. The capacitance values are listed in table 7.1.

Using the minimum and maximum relative capacitance values R_{\min} and R_{\max} , one can calculate a calibration slope m as follows:

$$m = \frac{R_{\max} - R_{\min}}{h}$$

$$\Delta m = \frac{1}{h} \sqrt{(\Delta R_{\max})^2 + (\Delta R_{\min})^2 + \left((R_{\max} - R_{\min}) \frac{\Delta h}{h} \right)^2} \quad (7.2)$$

The quantity h in the equation is the change in height between the different measurements which here corresponds to the complete height of the levelmeters of 10.0 mm. The uncertainty of the levelmeter height depends on the manufacturing precision and is estimated to be $\Delta h = 0.1$ mm. For the uncertainties for the capacitances the mean errors ΔR_{\min} and ΔR_{\max} of the found mean values are used. The obtained values for m are also listed in table 7.1.

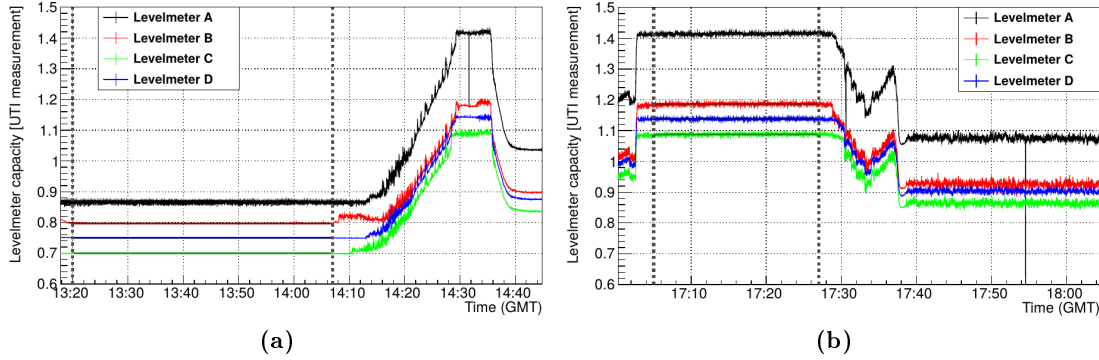


Figure 7.2: Levelmeter calibration 2015: To obtain (a) the relative capacitance R_{\min} for the empty levelmeters and (b) the relative capacitance R_{\max} in the time interval where the levelmeters were completely immersed in liquid xenon, the mean of the measured relative capacitance values was calculated in a fixed time window in the respective measurement interval. The time window limits are marked with dashed vertical lines.

Levelmeter	$R_{\min} [\times 10^{-3}]$	$\Delta R_{\min} [\times 10^{-3}]$	$R_{\max} [\times 10^{-3}]$	$\Delta R_{\max} [\times 10^{-3}]$	$m [\text{m}^{-1}]$	$\Delta m [\text{m}^{-1}]$
A	866.20	0.08	1414.53	0.09	54.83	0.06
B	797.96	0.08	1185.91	0.09	38.76	0.04
C	699.60	0.01	1087.75	0.07	38.81	0.04
D	750.56	0.01	1137.92	0.09	38.74	0.04

Table 7.1: Calibration slopes for the July 2015 data: Mean values for R_{\min} and R_{\max} of each levelmeter with the corresponding mean errors R_{\min} and R_{\max} and the calculated calibration slope using equation (7.2). The discrepancy between the m -values of levelmeters B, C and D compared to A is due to the fact that levelmeter A is read out by a different electronic board than the other three levelmeters. Apart from this, levelmeters B, C and D are very similar.

From table 7.1, one can directly see a discrepancy between the different calibration slopes m . For the levelmeters B, C and D, m has almost the same value, although they do not all agree within errors Δm . This indicates that there is an additional systematic error which is not taken into account yet. The value m for levelmeter A exceeds the other values by a factor of about 1.41. As described in section 3.2.4, the levelmeters are read out with two different UTI boards since each board can measure only three capacitances. While the levelmeters B, C and D are all connected to the same UTI board, levelmeter A is measured with the other one. Even small differences in the connections or the reference capacitance used to measure the actual levelmeter capacitance can account for the observed differences. Since each levelmeter is calibrated

independently, this should not affect the measurement of the liquid level.

7.1.2 Calibration of the Levelmeters with Data from July 2017

During the recommissioning of the MainzTPC in Mainz in summer 2017, the levelmeter readout hardware was modified. The change became necessary after testing the levelmeters with the realization, that disconnecting and reconnecting the UTI boards to the setup altered the levelmeter offset significantly.

After the modification, which included a renovation of all connections to the UTI boards and the replacement of one of the boards since it stopped working, it was clear that the previous calibration does not apply to the altered setup. Therefore, the MainzTPC was overfilled twice for calibration purposes on 10 and 11 July, 2017. Figure 7.3 shows both subsequent fillings.

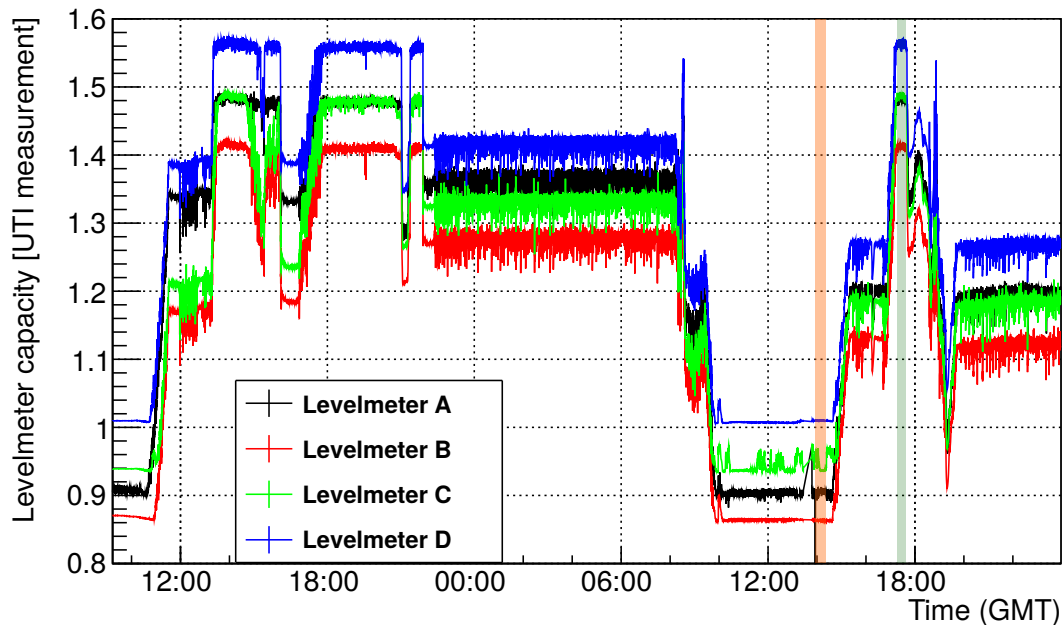


Figure 7.3: Relative levelmeter capacitance plotted versus the time of the measurement on 10 and 11 July, 2017, in a setup test for the levelling in the TPC before operation. During this time, the system was overfilled twice. The calibration time windows were chosen in the second filling period and are marked in orange (empty state) and greenish (full state).

It is noteworthy that the filling process includes a step, which is very clearly seen in the beginning of the measurement at 12 AM, before the level continues to rise to a maximum level. During the filling, the LXe ascends inside the TPC and starts to change the capacitance in the levelmeters, until it reaches the foreseen level defined by the weir. The LXe then starts spilling into the buffer volume, and the measured level stays

constant until the buffer is completely filled. After that, the level inside the TPC can rise further. The measured maximum value indicates the levelmeters being completely immersed.

Analogous to section 7.1.1, the minimum and maximum values for the relative capacitances of each levelmeter are determined by calculating the mean relative capacitance in the respective time interval of the measurement. Figure 7.4 shows the time windows chosen for the levelmeters in empty and overfilled condition. The mean values for R_{\min} and R_{\max} retrieved from this measurement are listed in table 7.2, along with the calibration values m for the modified setup from July 2017 which are calculated employing equation (7.2).

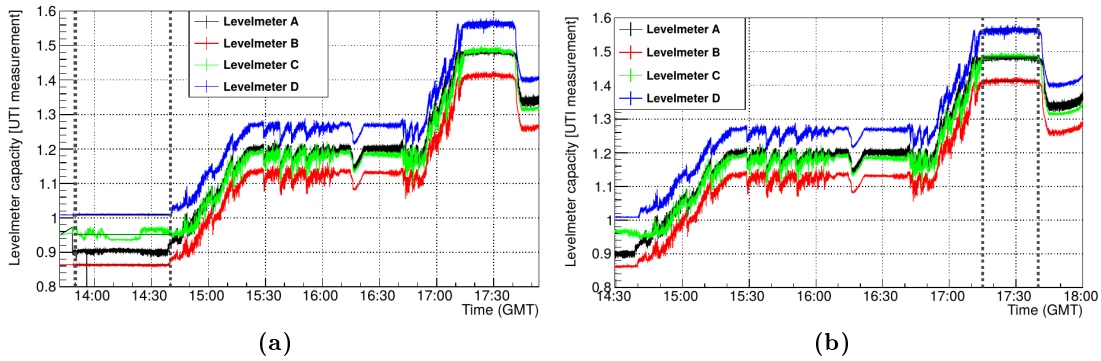


Figure 7.4: Levelmeter calibration 2017: To obtain (a) the relative capacitance R_{\min} for the empty levelmeters and (b) the relative capacitance R_{\max} in the time interval where the levelmeters were completely immersed in liquid xenon, the mean of the measured relative capacitance values was calculated in a fixed time window in the respective measurement interval. The time window limits are marked with dashed vertical lines.

Levelmeter	$R_{\min} [\times 10^{-3}]$	$\Delta R_{\min} [\times 10^{-3}]$	$R_{\max} [\times 10^{-3}]$	$\Delta R_{\max} [\times 10^{-3}]$	$m [\text{m}^{-1}]$	$\Delta m [\text{m}^{-1}]$
A	903.56	0.10	1480.61	0.09	57.70	0.06
B	863.89	0.02	1412.40	0.09	54.85	0.06
C	951.58	0.22	1484.63	0.09	53.30	0.06
D	1009.63	0.01	1563.11	0.12	55.35	0.06

Table 7.2: Calibration slopes for the July 2017 data: Mean values for R_{\min} and R_{\max} of each levelmeter with the corresponding mean errors ΔR_{\min} and ΔR_{\max} and the calculated calibration slope using equation (7.2). The slope m has similar values for the different levelmeters, although they do not agree within the errors Δm calculated from the mean values.

The resulting calibration factors m for the calibration data from July 2017 have very similar values. This is expected, since all levelmeters are identical in construction. The values m do not agree within their errors, which points to an additional systematic error.

7.1.3 | Capillarity

Considering the very small spacing between the inner and outer cylinder of the levelmeter, the effect of capillary action should be taken into account. The effect can be calculated using equation (7.3), which is derived in appendix A.2.

$$h_{\text{cap,theo}} = \frac{2\sigma_{\text{LXe}}}{\rho_{\text{LXe}}g(R-r)} = 2.2 \text{ mm} \quad (7.3)$$

Here, the surface tension is $\sigma_{\text{LXe}} = 15.19 \cdot 10^{-3} \frac{\text{N}}{\text{m}}$ (see appendix A.2) and the liquid xenon density is $\rho_{\text{LXe}} = 2.82 \frac{\text{kg}}{\text{cm}^3}$ for a temperature of 182.7 K (see section 2.1). The outer radius R is 5.5 mm and the inner radius r equals 5 mm.

The calculated value for $h_{\text{cap,theo}}$ accounts for more than 20 % of the complete levelmeter height of 10 mm. Therefore, a significant abrupt rise in the levelmeters at the beginning of the filling process is expected.

Figure 7.5 shows the time periods in the beginning of the levelmeter filling during the calibration measurements. The rising slopes show a lot of fluctuations, but small step-like structures in the beginning of each filling process can be found. Compared to the complete complete filling process (which can be found in the sections 7.1.1 and 7.1.2), these structures appear very small and not in the same order of magnitude as the theoretically expected effect.

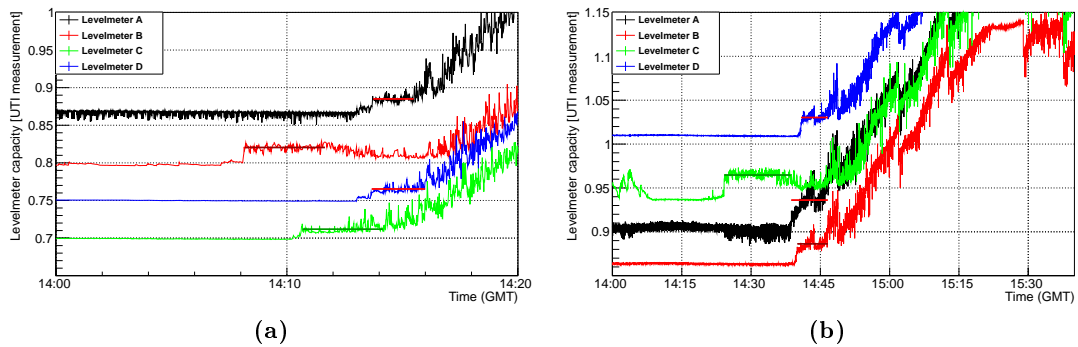


Figure 7.5: Effect of the capillary action in the levelmeters: For the calibrations in 2015 (a) and 2017 (b), in the beginning of the filling process one can find step-like structures where the level rises abruptly from the empty state value to a “non-zero” value. These structures are expected by the effect of capillary action, although the measured effect appears much smaller than the expectation.

Similar to the calibration process, the levelmeter values of these steps are measured by calculating the mean value of the measured relative capacitances. Table 7.3 holds the information of the mean values R_{cap} for each levelmeter. Using equation (7.4) and the minimum mean values R_{min} as well as the calibration values m from the respective calibration sections, the height difference h_{cap} between the empty levelmeter state and

the measurement value of the step-like structure is calculated.

$$h_{\text{cap}} = \frac{R_{\text{cap}} - R_{\text{min}}}{m} \quad (7.4)$$

$$\Delta h_{\text{cap}} = \frac{1}{m} \sqrt{(\Delta R_{\text{cap}})^2 + (\Delta R_{\text{min}})^2 + \left((R_{\text{cap}} - R_{\text{min}}) \frac{\Delta m}{m} \right)^2}$$

Levelmeter	$R_{\text{cap}} [\times 10^{-3}]$	$\Delta R_{\text{cap}} [\times 10^{-3}]$	$h_{\text{cap}} [\text{mm}]$	$\Delta h_{\text{cap}} [\text{mm}]$
2015				
A	885.10	0.01	0.34	< 0.01
B	820.44	0.01	0.58	< 0.01
C	711.70	0.01	0.31	< 0.01
D	765.27	0.01	0.38	< 0.01
2017				
A	936.14	0.05	0.56	< 0.01
B	886.32	0.02	0.41	< 0.01
C	964.73	0.01	0.25	< 0.01
D	1030.31	0.02	0.37	< 0.01

Table 7.3: Mean relative capacitance of each levelmeter for the structures associated with the effect of capillary action. The corresponding change in level height h_{cap} is calculated using equation (7.4).

The observed height differences range between 0.25 mm and 0.58 mm, which is much smaller than the expected theoretical value.

Since the outer cylinder of the levelmeter starts 1 mm below the inner cylinder, the levelmeter rise due to the capillary action for the outer cylinder only can be calculated. For this, the inner radius r in equation (7.3) is set to zero. The expected levelmeter rise is then $h_{\text{cap,theo},R} = 0.2 \text{ mm}$, which is much closer to the observed values.

The expected large rise of the level due to the effect of capillary can not be observed. Still, there seems to be an effect, which is much smaller. It exceeds the theoretical expectation for the capillary action when considering only the outer levelmeter cylinder. The reason for this can be connected to a possible combination of both effects resulting in an intermediate change of the liquid level. Also, the levelmeter tilt might have an influence on the observed effect.

The effect of capillarity should be investigated further to understand its impact on the levelmeter readout. For now, the mean value for each calibration will be used as an additional offset to the liquid level determination, since the effect of capillary leads to a determined liquid level which is higher than the actual level outside the levelmeters. As for all levelmeters the effect is expected to be equal in magnitude, the mean of h_{cap} is calculated. For both calibrations, the same value is obtained, with the uncertainty following from error propagation using the limits stated in table 7.3:

$$\bar{h}_{\text{cap}} = (0.40 \pm 0.02) \text{ mm}$$

7.1.4 | Comparison of the Calibration Results

The reference capacitance used for both calibrations is $C_{\text{ref}} = 10 \text{ pF}$. Multiplying this value with the derived values m should yield the change in capacitance for the levelmeters per millimeter. Table 7.4 shows the values m and the calculated calibration factors $m_C = m \cdot C_{\text{ref}}$. The uncertainty Δm_C evolves from error propagation assuming a capacitance uncertainty of $\Delta C_{\text{ref}} = 0.2 \text{ pF}$.

Levelmeter	$m \text{ [m}^{-1}\text{]}$	$\Delta m \text{ [m}^{-1}\text{]}$	$m_C \text{ [}\frac{\text{pF}}{\text{mm}}\text{]}$	$\Delta m_C \text{ [}\frac{\text{pF}}{\text{mm}}\text{]}$
2015				
A	54.83	0.06	0.5483	0.0110
B	38.76	0.04	0.3876	0.0078
C	38.81	0.04	0.3881	0.0078
D	38.74	0.04	0.3874	0.0078
2017				
A	57.70	0.06	0.5770	0.0116
B	54.85	0.06	0.5485	0.0110
C	53.30	0.06	0.5330	0.0107
D	55.35	0.06	0.5535	0.0111

Table 7.4: Calculated calibration factors in pF/mm for a reference capacitance of $C_{\text{ref}} = 10 \text{ pF}$.

The measured values of m_C can be compared to the value $m_{C,\text{theo}} = 0.560 \text{ pF/mm}$ from section 3.2.4 which is the theoretical expected change in capacity per change in liquid level.

The m_C values for the calibration of 2015 show large deviations from $m_{C,\text{theo}}$ for the levelmeters B, C and D which are all connected to the same UTI board. The values of approximately 0.388 pF/mm only account for about 75 % of the theoretical value. This indicates that there was a connectivity problem, introducing a systematic change in the measured capacitance value. Since the setup was not changed for the measurements at the HZDR, the calibration could be used for this experimental run. However, the absolute values for the levelmeter capacitances should not be trusted in this case.

For the calibration of 2017, the values of m_C are much closer to the theoretical $m_{C,\text{theo}}$, which indicates that also the levelmeters B, C and D are now connected better than before.

7.2 | Determination of the Liquid Level during Operation

For each experimental run, the liquid level has to be measured since it is not possible to exactly fill the same amount of xenon every time and restore the same thermodynamical conditions. Even changing the flux of the xenon recirculation affects the level. But once the setup is filled and the thermodynamical quantities of the system (temperatures, pressure, xenon recirculation speed) are stable, the level can be seen as a constant parameter for all measurements for the current conditions.

Contrary to the calibration measurements, the calibration slopes m for each levelmeter from section 7.1, together with the mean values for the empty and filled levelmeters, are now used to work out the actual liquid level. For this, equation (7.2) is solved for the height h :

$$h = \frac{R_{\max} - R_{\min}}{m}$$

$$\Delta h = \frac{1}{m} \sqrt{(\Delta R_{\max})^2 + (\Delta R_{\min})^2 + \left((R_{\max} - R_{\min}) \frac{\Delta m}{m} \right)^2} \quad (7.5)$$

The position of the levelmeters relative to the gap between anode and gate mesh introduces an offset. This is illustrated in figure 7.6.

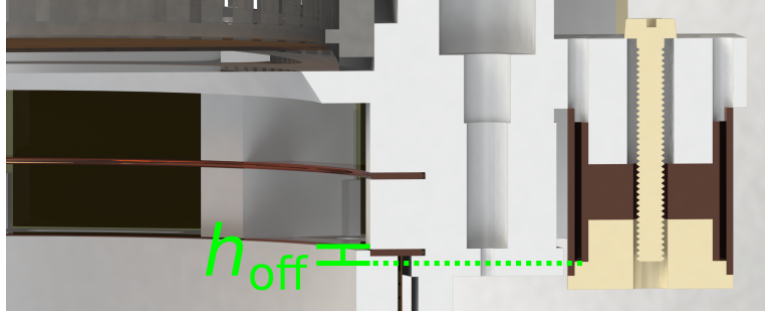


Figure 7.6: Relative position of the levelmeters with respect to the gate and anode mesh. The offset introduced by the lower edge of the levelmeters is marked in green.

The height which is determined using equation (7.5) provides the liquid level information with respect to the lower edge of the levelmeter inner cylinder. Since this lower edge is placed $1 \text{ mm} = h_{\text{off}}$ below the upper edge of the gate mesh, the liquid level inside the gate-anode gap is determined by equation (7.6), taking the levelmeter offset and the effect of capillary action into account:

$$h = \frac{R_{\max} - R_{\min}}{m} - h_{\text{off}} - h_{\text{cap}}$$

$$\Delta h = \sqrt{\frac{(\Delta R_{\max})^2 + (\Delta R_{\min})^2}{m^2} + \left((R_{\max} - R_{\min}) \frac{\Delta m}{m^2} \right)^2 + \Delta h_{\text{off}}^2 + \Delta h_{\text{cap}}^2} \quad (7.6)$$

The offset uncertainty is estimated to be $\Delta h_{\text{off}} = 0.1 \text{ mm}$ considering the precision of the positioning inside the TPC. The latter is dependent on the manufacturing precision and the different thermal expansion coefficients of the TPC structure materials.

7.2.1 Level during Run HZDR 2016 (Calibration July 2015)

For the run 18-28 April, 2016, the measured relative capacitances of the four TPC levelmeters are shown in figure 7.7. The plotted data ranges almost over the complete run time. This slow control system data set does not include the filling period since it had to be reconfigured in the very beginning. The relative capacitance values for the empty and filled levelmeters are obtained by calculating the mean value for the measured capacitance in the respective time windows (marked orange and greenish), pursuant the approach for the levelmeter calibration.

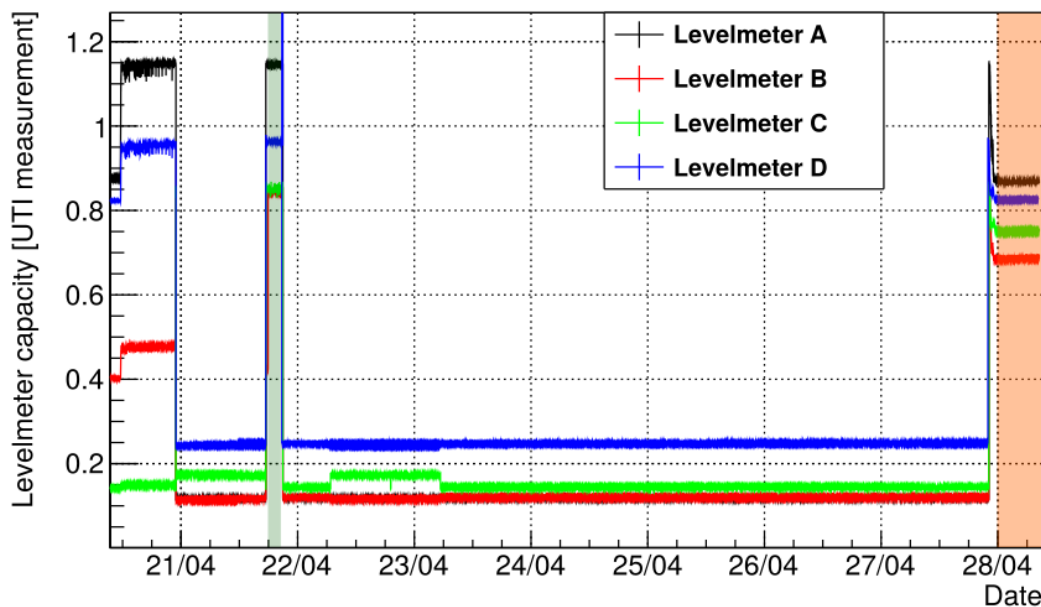


Figure 7.7: Levelmeter data from run 18-28 April 2016: The plot shows the relative capacitance values for the 4 TPC levelmeters. The filling process is not included in the data, that is why the values for the empty levelmeters have to be taken after the recuperation (flat part on 28 April). During the data taking with the other sensors in the TPC, the levelmeters are switched off. Therefore the only time period suitable for the liquid level determination during the run is in the evening of 21 April.

To get the capacitance values for the empty levelmeters the time interval after the recuperation is used, which is displayed in figure 7.8a along with the time window used to calculate the mean value. The recuperation took place on 28 April, so the empty levelmeter values are found at the very end of the total run.

As mentioned before, the readout of the levelmeters disturbs the APD signals, therefore

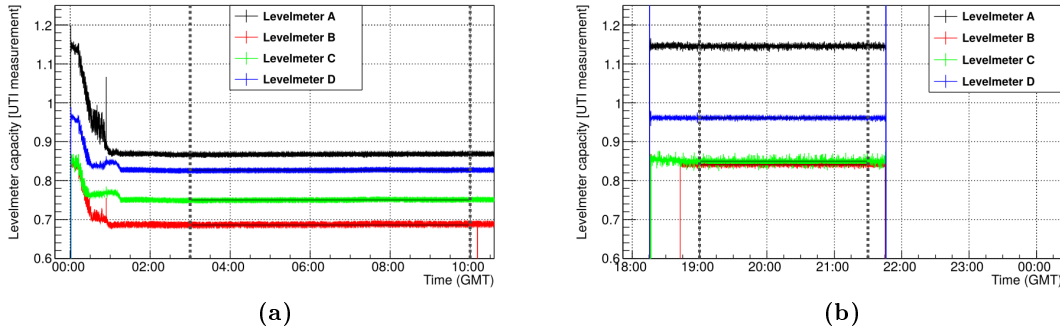


Figure 7.8: Levelmeter values during operation at HZDR in April 2016: Measurement of empty levelmeters (a) and at operation level (b). The dashed vertical lines indicate the limits of the time windows used to determine the mean relative capacitances.

most of the time the levelmeters were not active. Also, in the very beginning, some adjustments and tests were still made. Conclusively, the time interval which is used to determine the levelmeter values for the liquid level is on 21 April between 6 PM and 9:45 PM. This is a time period when everything was stable, so it was convenient to measure the liquid level with the stable conditions. A zoom to this time interval can be seen in figure 7.8b, with the time window limits for the mean value determination.

In table 7.5, the mean values for the minimum and maximum relative capacitances are listed along with the calculated heights for the four TPC levelmeters.

Levelmeter	$R_{\min} [\times 10^{-3}]$	$\Delta R_{\min} [\times 10^{-3}]$	$R_{\max} [\times 10^{-3}]$	$\Delta R_{\max} [\times 10^{-3}]$	h [mm]	Δh [mm]
A	868.44	0.01	1145.66	0.03	3.66	0.10
B	685.94	0.02	840.93	0.02	2.60	0.10
C	750.18	0.01	849.48	0.03	1.16	0.10
D	826.97	0.01	961.17	0.01	2.06	0.10

Table 7.5: Liquid level for the measurements at HZDR in April 2016 (with calibration values from 2015): Mean values for the relative capacitances in the empty state R_{\min} and with the liquid level at operation conditions R_{\max} of each levelmeter and calculated height h using equation (7.6).

The uncertainties for the heights Δh are dominated by the systematic error Δh_{off} .

As can be seen, the levelmeters show quite different levels, which indicates a tilt of the TPC. Determining the tilt of the MainzTPC using the calculated levels is the topic of section 7.3.

7.2.2 Level during Run July 2017 (Calibration July 2017)

To determine the level for the run in July 2017, the mean relative capacitances R_{\min} can be taken from table 7.2, since the calibration was conducted in the same run. The

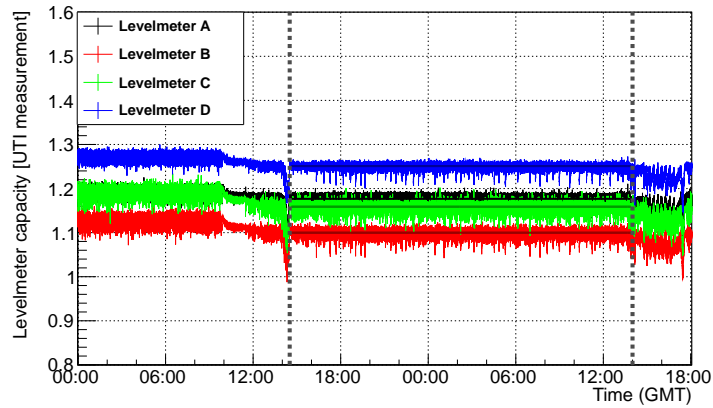


Figure 7.9: Relative levelmeter capacitance values at operation level on 12 July, 2017. The dashed vertical lines indicate the limits of the time window used to determine the mean relative capacitances. The value for the empty levelmeters is taken from table 7.2, since the calibration data was taken during the same experimental run. The slight “step”-like feature visible in the plot for some of the levelmeters was caused while minimizing the TPC tilt.

levelmeter values for the TPC during operation are extracted from a time window shown in figure 7.9. The SCS data for this is taken on 12 July, 2017, a day after the calibration.

Learning from the level determination for the measurements at the HZDR in 2016, the Mainz/TPC was adjusted to have a minimum tilt. This is evident in the heights h calculated for the retrieved mean relative capacitances in table 7.6. Although the heights do not agree within errors, they are much closer to each other than the levelmeter heights from the previous section. This is reflected in a smaller tilt angle, as is described in section 7.3.

Comparing the height values for the two runs, on average the heights in the levelmeters in July 2017 show higher values. This is not due to the adjusted liquid level, for which it is expected that the heights for the individual levelmeters is different than before. Apart from this, the level-defining weir was elevated by 1.26 mm, which explains the overall increase in liquid level.

Levelmeter	$R_{\min} [\times 10^{-3}]$	$\Delta R_{\min} [\times 10^{-3}]$	$R_{\max} [\times 10^{-3}]$	$\Delta R_{\max} [\times 10^{-3}]$	h [mm]	Δh [mm]
A	903.564	0.10	1176.67	0.03	3.33	0.10
B	863.887	0.02	1099.83	0.02	2.90	0.10
C	951.584	0.22	1158.82	0.02	2.49	0.10
D	1009.63	0.01	1251.00	0.02	2.96	0.10

Table 7.6: Liquid level for the measurements at Mainz in July 2017 (with calibration values from 2017): Mean values for the relative capacitances in the empty state R_{\min} and with the liquid level at operation conditions R_{\max} of each levelmeter and calculated height h using equation (7.6).

7.3 | Tilt in the Liquid Level

The determined level values for the respective levelmeters from section 7.2, especially for the measurements at the HZDR in April 2016, show quite large deviations. Despite the fact that many efforts were made to balance the TPC there obviously is a tilt, with a gradient roughly from levelmeter A with the highest value to levelmeter C.

The balancing of the TPC at the HZDR was done using an air level on the outer vessel flange. Since the TPC orientation inside the vessel is known and has been adjusted beforehand to match the outer vessel flange, this seemed reasonable. However, the balancing adjustment was carried out before filling the system. Three effects were not taken into account:

- Filling the MainzTPC with liquid xenon introduces an additional weight which has an impact on the tilt of the TPC, pulling it towards to ground.
- The change in temperature and the resulting negative thermal expansion of the materials also has an impact on the xenon cryostat. This can lead to a tilt of the TPC vessel unobservable from the outside, but invalidating the alignment of the inner vessel to the outer vessel horizontal level.
- The system itself is located inside an outer cryostat that is evacuated to minimize heat transfer. The insulation vacuum is strong enough to lift the TPC cryostat upwards.

For the determination of the liquid level in July 2017 these effects were considered. The balancing of the TPC was carried out after the filling process, using the raw levelmeter values obtained by the SCS system. As a result, the level tilt in July 2017 is much smaller.

To quantify the tilting effect, the four levelmeter positions can be fitted with a plane function described as follows:

$$h = p_0 + p_1 \cdot x + p_2 \cdot y$$

$$\Delta h = \sqrt{\Delta p_0^2 + (\Delta p_1 \cdot x)^2 + (\Delta p_2 \cdot y)^2 + (p_1 \cdot \Delta x)^2 + (p_2 \cdot \Delta y)^2} \quad (7.7)$$

The height of the liquid surface h is described here as a function of x and y , with an offset of p_0 and the respective slopes p_1 and p_2 . The fit was done in `python` using the method of least-squares `scipy.linalg.lstsq` from the linear algebra module. This method is used to solve a system of linear equations that is overestimated. Here, this system contains four equations:

$$h_1 = p_0 + x_{L1} \cdot p_1 + y_{L1} \cdot p_2$$

$$h_2 = p_0 + x_{L2} \cdot p_1 + y_{L2} \cdot p_2$$

$$h_3 = p_0 + x_{L3} \cdot p_1 + y_{L3} \cdot p_2$$

$$h_4 = p_0 + x_{L4} \cdot p_1 + y_{L4} \cdot p_2$$

The values h_k are the measured heights in each levelmeter and x_{Lk} and y_{Lk} are the levelmeter positions. These equations can be rewritten as:

$$\begin{pmatrix} h_1 \\ h_2 \\ h_3 \\ h_4 \end{pmatrix} = \begin{pmatrix} 1 & x_{L1} & y_{L1} \\ 1 & x_{L2} & y_{L2} \\ 1 & x_{L3} & y_{L3} \\ 1 & x_{L4} & y_{L4} \end{pmatrix} \cdot \begin{pmatrix} p_0 \\ p_1 \\ p_2 \end{pmatrix} \Leftrightarrow \vec{h} = A \cdot \vec{p} \quad (7.8)$$

This linear matrix equation is solved by the least-squares method, which means that the vector \vec{p} is varied so that the sum of the squares of the residuals for each single equation is minimized. Here, the `python`-method is applied and yields the fit plane parameters p_0 , p_1 and p_2 as well as the sum of the squared residuals.

Before applying the `scipy.linalg.lstsq` method, the vector \vec{h} as well as the matrix A are normalized using the weighting factors $w_k = \frac{1}{\Delta h_x}$. This is necessary to obtain the correct sum of the squared residuals which are then used to calculate the uncertainty of the fit parameter vector \vec{p} .

For this, one first has to find the eigenvalues of the matrix A by determining the eigenmatrix $A_\lambda = (A^T \cdot A)^{-1}$ with the eigenvalues $\lambda_k = \text{diag}(A_\lambda)$. The uncertainties Δp_k then are calculated according to equation (7.9), with NDF being the number of degrees of freedom, which here is $\text{NDF} = (4 - 3) = 1$ (number of measured heights - number of fit parameters).

$$\Delta p_k = \sqrt{\lambda_k \frac{p_k}{\text{NDF}}} \quad (7.9)$$

7.3.1 | Level Tilt at the HZDR in April 2016

For the levelmeter heights from table 7.5, the obtained values for the fit plane parameters are listed in table 7.7 with their respective uncertainties. Since for the fit, the MainzTPC center is at $(x, y) = (0, 0)$, the quantity p_0 equals the mean height of the liquid in the TPC, which here is 2.37 mm above the gate mesh.

	value k	Δp_k
p_0 [mm]	2.3685	0.0386
p_1	-0.0220	0.0011
p_2	-0.0151	0.0011

Table 7.7: Fit parameters from the least-squared plane fit to the levelmeter heights of the HZDR April 2016 measurement.

The fit parameters and their uncertainties can now be used to calculate the liquid level at any x - y -position in the MainzTPC with equation (7.7). To compare the fit to the measured heights, the plane function is evaluated at the levelmeter positions. The calculated heights, together with the measured heights, are listed in table 7.8, along with

Levelmeter	h [mm]	Δh [mm]	h_{fit} [mm]	Δh_{fit} [mm]
A	3.66	0.10	3.62	0.07
B	2.60	0.10	2.63	0.07
C	1.16	0.10	1.12	0.07
D	2.06	0.10	2.10	0.07

Table 7.8: Comparison of the measured heights of the run at the HZDR in April 2016 (with the calibration from 2015) h with the calculated heights h_{fit} for each levelmeter with the respective uncertainties. For each levelmeter, the measured and the calculated value are in good agreement within errors. For the calculation of the fit uncertainty, the spatial errors Δx and Δy were assumed to be 1.0 mm.

the respective uncertainties. The calculated as well as the measured heights in the levelmeters agree within their respective uncertainties.

Figure 7.10 shows the fit plane for the liquid level in the MainzTPC seen from above. There is a clear tilt visible with a falling gradient from the lower left to the upper right.

The radius of the colored plane corresponds to the active volume in the TPC. The maximum radius of the active volume is restricted by the copper frames of the gate and the

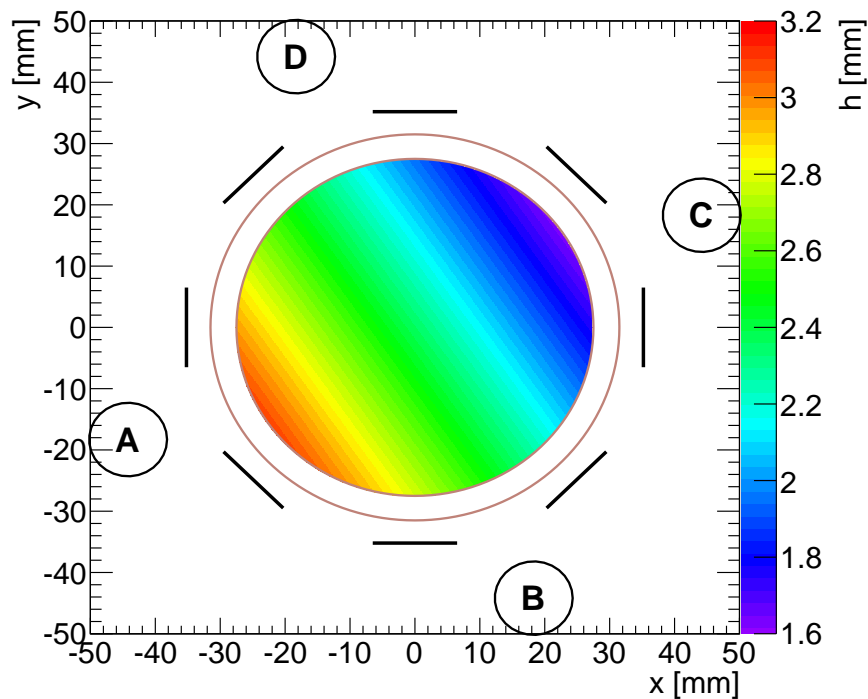


Figure 7.10: Fit plane function for the liquid level in the MainzTPC during the measurements at the HZDR in April 2016. The picture shows a tilt of the plane from the lower left to the upper right corner.

anode mesh, which have an inner radius of 27.5 mm. The inner and outer radii of the mesh frames are indicated as brown circles. Also the four levelmeters and the APDs are sketched at their respective positions.

For the inner mesh radius, the minimum and maximum heights in the TPC are calculated using equation 7.7:

$$\begin{aligned} h_{\text{active,min}} &= (1.63 \pm 0.06) \text{ mm} \quad \text{at}(x, y) = (22.80 \text{ mm}, 15.38 \text{ mm}) \\ h_{\text{active,max}} &= (3.10 \pm 0.06) \text{ mm} \quad \text{at}(x, y) = (-22.80 \text{ mm}, -15.38 \text{ mm}) \end{aligned}$$

Here, also a spatial error of $\Delta x = \Delta y = 1.0 \text{ mm}$ is assumed. The resulting difference in height inside the active volume is $\Delta h_{\text{active}} = (1.47 \pm 0.08) \text{ mm}$.

Besides the height difference in millimeters the tilt can also be expressed as an angle between the normal vector of the plane and the z -axis, that means the optimal normal vector. For the level plane at the HZDR in April 2016 one finds a tilt angle of

$$\alpha_{\text{tilt}} = (2.1615 \pm 0.0891)^\circ.$$

The calculation of the tilt angle is described in appendix A.3.

7.3.2 | Level Tilt in Mainz in July 2017

Since the level-defining weir was set to a higher level before the measurement in Mainz in July 2017, the mean level height is increased to $p_0 = 2.92 \text{ mm}$ above the gate mesh. The plane fit parameters for this data are listed in table 7.9. As expected the slopes p_1 and p_2 are smaller than for the HZDR level.

	value k	Δp_k
p_0 [mm]	2.9208	0.0105
p_1	-0.0084	0.0003
p_2	-0.0028	0.0003

Table 7.9: Fit parameters from the least-squared plane fit to the levelmeter heights of the July 2017 measurement in Mainz.

Comparing the measured values of the levelmeters with the calculated values from the plane fit, one finds that they agree within errors. The levelmeter values from measurement and fit are summarized in table 7.10.

Figure 7.11 shows the fit plane for the liquid level in the MainzTPC seen from above. Here also a tilt from the lower left to the upper right is visible, but it is less distinct and has a slightly different orientation.

For the inner mesh radius, the minimum and maximum heights in the TPC are calculated using equation 7.7, analogous to the previous subsection:

$$\begin{aligned} h_{\text{active,min}} &= (2.68 \pm 0.02) \text{ mm} \quad \text{at}(x, y) = (26.15 \text{ mm}, 8.50 \text{ mm}) \\ h_{\text{active,max}} &= (3.16 \pm 0.02) \text{ mm} \quad \text{at}(x, y) = (-26.15 \text{ mm}, -8.50 \text{ mm}) \end{aligned}$$

Levelmeter	h [mm]	Δh [mm]	h_{fit} [mm]	Δh_{fit} [mm]
A	3.33	0.10	3.34	0.02
B	2.90	0.10	2.89	0.02
C	2.49	0.10	2.50	0.02
D	2.96	0.10	2.95	0.02

Table 7.10: Comparison of the measured heights h of the run Mainz in July 2016 (with the calibration from 2017) with the calculated heights h_{fit} for each levelmeter with the respective uncertainties. For each levelmeter, the measured and the calculated value are in good agreement within errors. For the calculation of the fit uncertainty, the spatial errors Δx and Δy were assumed to be 1.0 mm.

The resulting difference in height inside the active volume is $\Delta h_{\text{active}} = (0.49 \pm 0.03)$ mm, which corresponds to a tilt angle of

$$\alpha_{\text{tilt}} = (0.7174 \pm 0.0243)^\circ$$

for the level in July 2017.

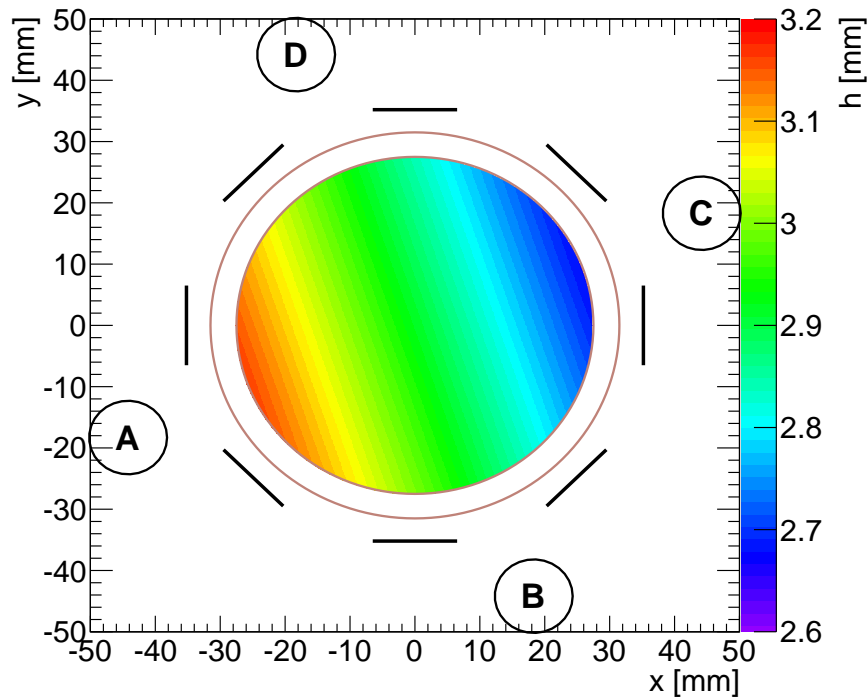


Figure 7.11: Fit plane function for the liquid level in the MainzTPC in Mainz in July 2017. The picture shows a tilt of the plane from the lower left to the upper right corner.

7.4 | Electric Field between Gate and Anode Mesh

In section 1.3.3 the impact of the liquid level on the electric field strength between the gate and the anode mesh is discussed. With the help of equation (1.2) it is possible to calculate the electric field strength in the gaseous phase as well as in the liquid phase depending on the level. The level, expressed by the fill factor f which varies between 0 for a complete gas phase to 1 for a gate-to-anode gap completely immersed in liquid xenon, has been determined and quantified in the form of a planar function such that it is possible to calculate the liquid level for every x - y -position between the gate and the anode mesh.

The electric fields $|\vec{E}_{\text{gas}}|$ and $|\vec{E}_{\text{liquid}}|$ are plotted in figure 7.12 for the level measured at the HZDR in 2016. The respective field strengths for the measurement carried out in Mainz in 2017 are found in figure 7.13.

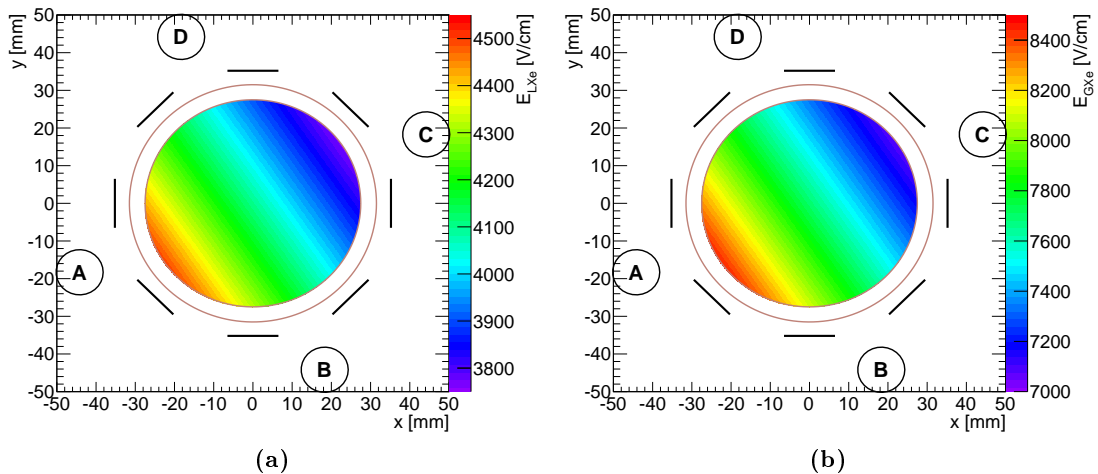


Figure 7.12: Electric field strength of the extraction field between the gate and the anode mesh in (a) the liquid phase and (b) the gaseous phase for the experimental run in April 2016 at the HZDR. Following the tilted liquid level, the field strengths decrease from the lower left of the graph to the upper right. The levelmeters are indicated with their respective positions as well as the APDs and the mesh frames.

The minimum and maximum electric field strengths for the gaseous and the liquid phase are summarized in table 7.11. Here, the field strengths are compared for the level measurements in April 2016 at the HZDR and in July 2017 in Mainz. Since the level was adjusted more accurately for the latter case and the tilt is significantly smaller, so are the differences for the minimum and maximum field strength values.

Table 7.11 also presents the extraction efficiencies for the respective field strengths in the liquid phase, as can be obtained from [40]. The extraction efficiency for the HZDR data from 2016 range between 83.5 % and 94.8 %. For the data taken in Mainz in 2017, the better balanced liquid level leads to an improvement of the extraction efficiency, achieving a range of 91.6 % up to 95.3 %. The slight enhancement of the efficiencies

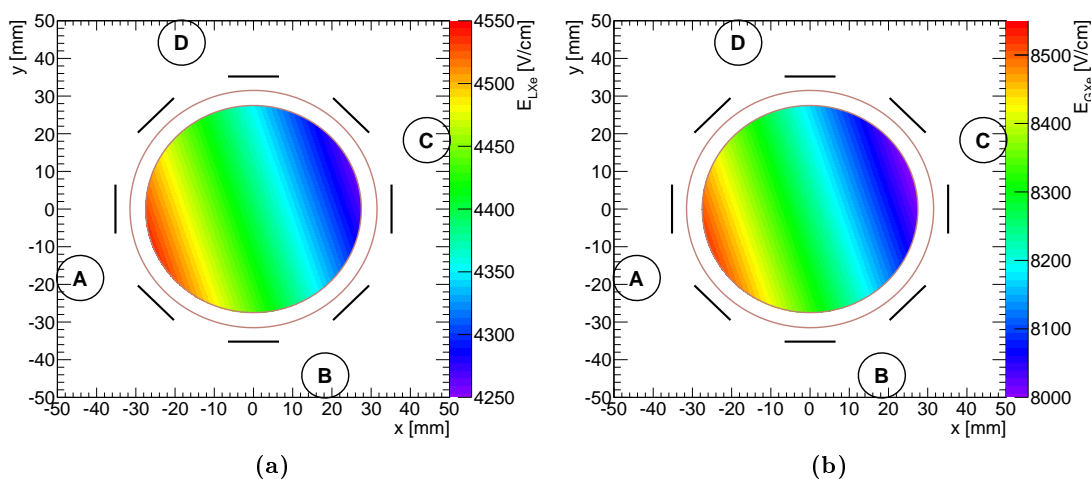


Figure 7.13: Electric field strength of the extraction field between the gate and the anode mesh in (a) the liquid phase and (b) the gaseous phase for the experimental run in July 2017 in Mainz. Following the tilted liquid level, the field strengths decrease from the lower left of the graph to the upper right. The levelmeters are indicated with their respective positions as well as the APDs and the mesh frames.

for the latter case can be explained with the increase in liquid level (by approximately 0.6 mm on average, done manually using the weir). This changes the fill parameter f and therefore also the electric field strengths $|\vec{E}_{\text{gas}}|$ and $|\vec{E}_{\text{liquid}}|$ to higher values.

Up to now, sparking limited the extraction field potential U_{ext} . For future operation, efforts should be made to increase the extraction field such that the extraction efficiency reaches 100 %. The necessary value for the external field strength $|\vec{E}_{\text{vac}}|$ using the liquid level determined for July 2017 is approximately 6.8 kV/cm ($U_{\text{ext}} = 3.4$ kV, which is 400 V higher than the voltage used before).

		$ \vec{E}_{\text{gas}} $ [V/cm]	$ \vec{E}_{\text{liquid}} $ [V/cm]	ϵ_{ext} [%]
2016	min	7082.45	3772.04	79.8
	max	8450.57	4500.69	91.6
	Δ	1368.12	728.65	
2017	min	8003.16	4262.41	88.5
	max	8520.16	4537.76	92.2
	Δ	517.00	275.35	

Table 7.11: Minimum and maximum values for the extraction field between the gate and the anode mesh in the liquid and gaseous phase and the respective extraction efficiencies for the data sets from the HZDR in 2016 and Mainz in 2017. Due to different TPC tilts, the data from 2016 shows larger field differences and a wider range for the extraction efficiency.

For the generation of the $S2$ signal, the electric field must exceed a value so that $\frac{E}{p} \sim 1.315 \text{ kV cm}^{-1} \text{ bar}^{-1}$ is fulfilled (see section 1.3.3). For the two data sets at hand, this condition is satisfied, with $\frac{E}{p} > 3.5 \text{ kV cm}^{-1} \text{ bar}^{-1}$.

7.5 | Examination of the measured $S2$ Width

The determination of the liquid level in the MainzTPC was done using the levelmeters, showing a tilt of the detector as described in the previous sections. A possibility to verify the liquid level tilt is the measurement of the $S2$ width in dependence of the x - y position. The gas gap between the liquid-gas interface and the anode mesh is the space where the $S2$ signal is produced by scintillation light caused by the extracted electrons. For a larger distance between liquid and anode, the extracted electrons can be accelerated more often before they lose their kinetic energy by exciting xenon atoms. Therefore the $S2$ width becomes larger for a larger gas gap or a lower liquid level.

Figure 7.14 shows the $S2$ width distribution in the x - y plane for Compton events at a drift field of 198 V/cm . The positions are reconstructed according to chapter 6. The value for the $S2$ width is taken from the Bottom PMT signal. In figure 7.14a, the $S2$ width is determined as the FWHM of the $S2$ peak, while figure 7.14b shows the $S2$ width measured at 10% of the peak height (“low width”). For each bin, covering an area of 1 mm^2 , the mean of the measured $S2$ widths is calculated.

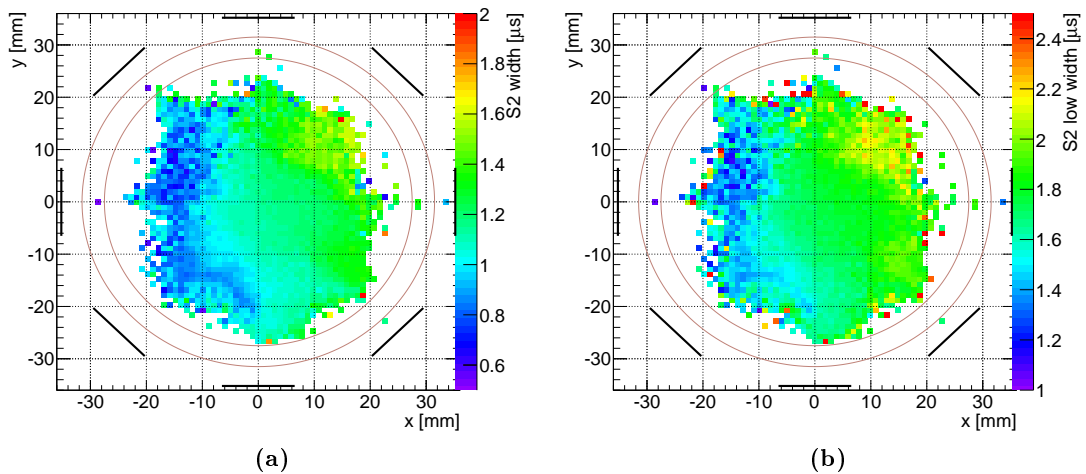


Figure 7.14: Mean $S2$ width distribution in x - y for a Compton measurement from April 2016 with a drift field of 198 V/cm , for the width determined at FWHM (a) and and 10% peak height (b). Both plots show the same behaviour as expected from the determined level tilt of the MainzTPC.

Compared to the level tilt determined for the April 2016 data, which is depicted in figure 7.10, the $S2$ width distribution shows a reverse picture in the x - y -plane. As expected, for a lower liquid level, the $S2$ width is larger and vice versa. This finding verifies

the level tilt determined with the levelmeters and is another confirmation that the position reconstruction with the APDs yields reasonable outcomes. Due to low statistics, a strong liquid level tilt and a saturation problem for large $S2$ signals (see section 8.5), the level tilt was not examined quantitatively using the $S2$ width distribution.

Since the extraction field was held constant for all measurements conducted so far and this field is responsible for the generation of the $S2$, the $S2$ distributions of measurements with higher drift fields show the same behaviour as depicted in figure 7.14. To demonstrate this, the $S2$ width for events measured at the largest drift field strength of 792 V/cm is plotted in figure 7.15. More precisely, while the $S2$ width is almost not affected by the change in drift field, the $S2$ integral increases due to the additional charge drifted upwards, as will be seen in chapters 8 and 9.

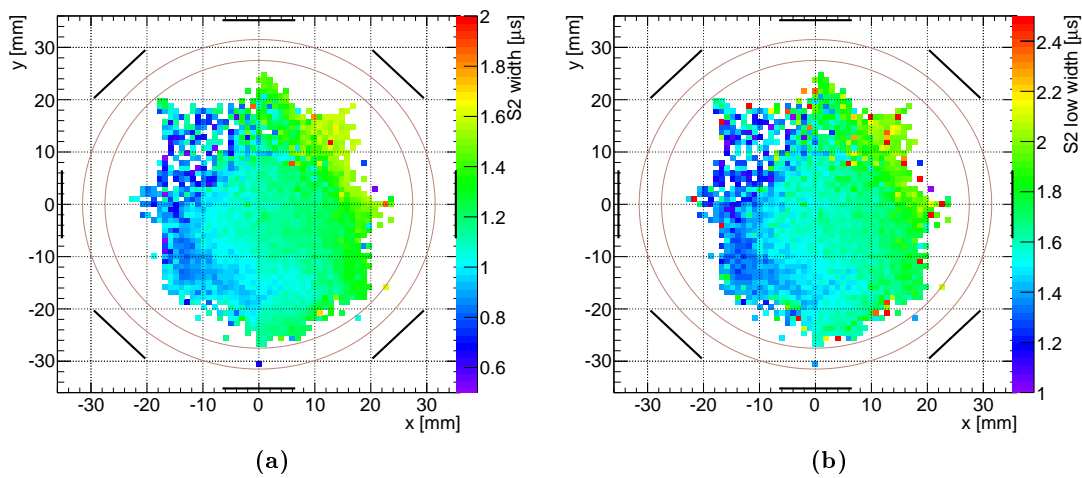


Figure 7.15: Mean $S2$ width distribution in x - y for a Compton measurement from April 2016 with a drift field of 792 V/cm, for the width determined at FWHM (a) and and 10% peak height (b). As expected, the change of the drift field strength does not affect the $S2$ width distribution, since the extraction field was held constant for all measurements.

Electron Drift and Signal Corrections

Chapter 8

8.1 | Electron Drift Velocity

The electron drift velocity can be determined by measuring the maximum drift time of the electrons in the TPC. For this, the time difference between the $S1$ and $S2$ signal is calculated for each event and the resulting time value is filled to a histogram, as for example shown in figure 8.1a. This histogram shows the drift time spectrum for a drift field strength of 198 V/cm. The gamma-ray source used here is a strong ^{137}Cs source which is collimated. The collimated beam hits the TPC mostly in the lower part, which explains the spectrum shape of the example histogram. The time difference was measured between the time position of the $S2$ signal and the time position of the $S1$ signal that generated the event trigger. Since the $S2$ signal has a certain width, the left edge of the signal was chosen as timing position. For the sharper $S1$ signal this is not necessary.

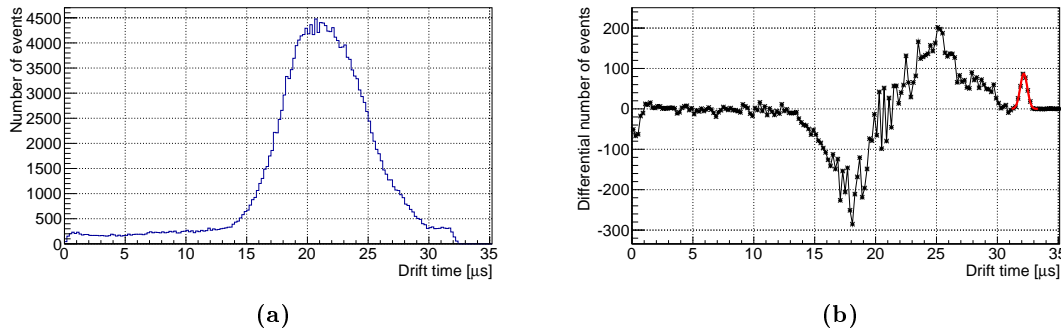


Figure 8.1: Electron drift time spectra for a drift field strength of 198 V/cm. Figure (a) shows the actual drift time spectrum. The maximum drift time t_{\max} can be obtained from the “step” at approximately 32 μs . The spectrum shape with the signal peaking between 15 and 30 μs shows the collimated beam from the ^{137}Cs source. In (b), a filter has been applied to the spectrum to enhance the effect of this “step”. As can be seen, it can be fitted by a Gaussian.

To determine the maximum drift time, one could simply take the value of the last filled bin, but since every measurement has some uncertainty, it is better to consider the last bin containing several counts. Indeed, as can be seen at approximately 32 μs , there is a step in the spectrum, which indicates the maximum drift time.

In order to obtain the maximum drift time t_{\max} with enhanced precision, a filter was applied to the spectrum:

$$\begin{aligned}
 \Sigma_0 &= n_N + n_{N-1} + n_{N-2} & \Delta_0 &= \Sigma_0 - \Sigma_0 \\
 \Sigma_1 &= n_{N-1} + n_{N-2} + n_{N-3} & \Delta_1 &= \Sigma_1 - \Sigma_0 \\
 \Sigma_2 &= n_{N-2} + n_{N-3} + n_{N-4} & \Delta_2 &= \Sigma_2 - \Sigma_1 \\
 & & & \vdots
 \end{aligned}$$

This filter starts at the last filled bin N of the histogram and summarizes the contents n_i of the three last bins (last, next-to-last, next-next-to-last). Then it summarizes the three bin contents starting with the next-to-last filled bin ($N - 1$) and so on. From each of these sums, the previous sum is subtracted (in case of the first sum, the subtracted value is the same and the difference is zero).

The resulting values Δ_i are plotted in a graph, which is displayed for 198 V/cm in figure 8.1b. The graph is some kind of differential spectrum of the drift time, which emphasizes the change in the drift time spectrum. Thus the step indicating the maximum drift time in the normal drift time spectrum appears in this graph as a peak which can be fitted with a Gaussian.

The corresponding plots for the drift field strengths of 396 V/cm, 594 V/cm and 792 V/cm can be found in Appendix B.3.

The maximum drift time determined from the drift time spectra corresponds to the electron drift time in both the drift field between cathode and gate mesh as well as the drift time in the extraction field between the gate mesh and the anode mesh, where the electrons drift from the gate to the liquid-gas interface and then create the $S2$ signal. To determine the correct drift velocity, only the electron drift in the drift field is taken into account, which means that the contribution of the extraction field has to be quantified and subtracted from the maximum drift time.

Figure 8.2 shows the $S1$ signal measured by the Bottom PMT in dependence of the drift

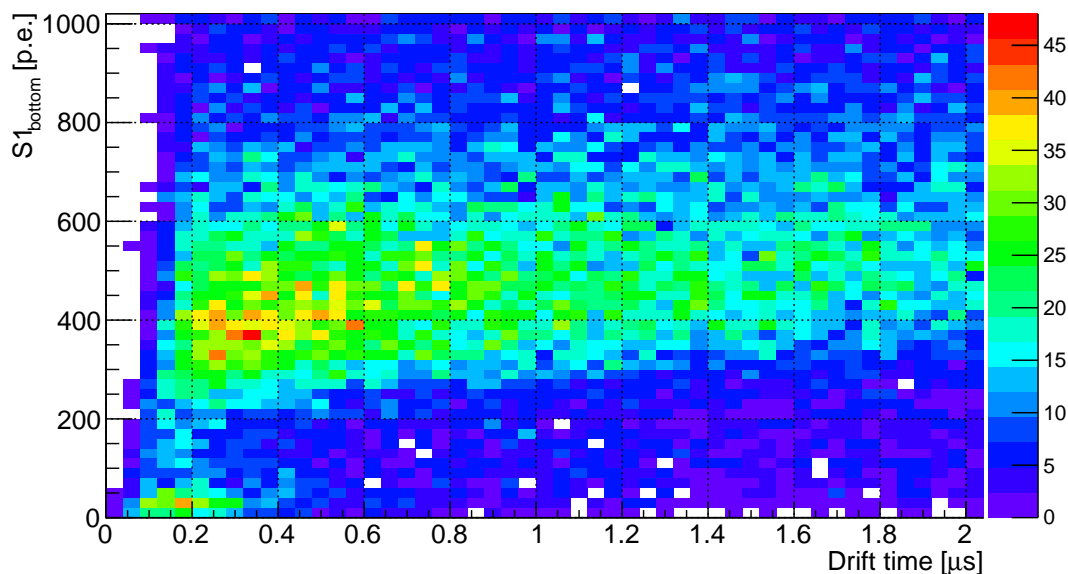


Figure 8.2: Determination of the gate time: The plot shows the $S1$ signal as measured by the Bottom PMT only in dependence of the drift time at a drift field of 198 V/cm. The dip in $S1$ at $\approx 0.2 \mu\text{s}$ indicates the gate mesh position.

time. The data was taken with a ^{152}Eu source at a drift field of 198 V/cm, illuminating the complete MainzTPC. At a drift time of $t_{\text{gate}} = (0.2 \pm 0.1) \mu\text{s}$, one can see a decrease in the $S1$ signal, which marks the gate position in terms of the drift time. The $S1$ light of events occurring above the gate mesh has to pass through the gate mesh first before being detected by the Bottom PMT, which leads to an attenuation of the signal. All measurements considered in this thesis were conducted with the same extraction field which means that the gate position in time can be applied to all measurements. The broad distribution of the gate position can be attributed to the tilt of the liquid level which has an impact on the $S2$ signal and therefore on the drift time measurement. The actual maximum drift time then is

$$t_{\text{drift,max}} = t_{\text{max}} - t_{\text{gate}} \quad \Delta t_{\text{drift,max}} = \sqrt{\Delta t_{\text{max}}^2 + \Delta t_{\text{gate}}^2} \quad (8.1)$$

The maximum drift length is $l_{\text{max}} = (50.5 \pm 0.2) \text{ mm}$, which is the distance between cathode mesh and gate mesh. The uncertainty is estimated considering the manufacturing process and the mounting precision in the TPC structure. The drift velocity then is calculated as follows, using the maximum drift time t_{max} reduced by the time position of the gate mesh t_{gate} :

$$v_{\text{drift}} = \frac{l_{\text{max}}}{t_{\text{drift,max}}} \quad \Delta v_{\text{drift}} = \frac{1}{t_{\text{drift,max}}} \sqrt{(\Delta l_{\text{max}})^2 + \left(\frac{l_{\text{max}}}{t_{\text{drift,max}}} \Delta t_{\text{drift,max}} \right)^2} \quad (8.2)$$

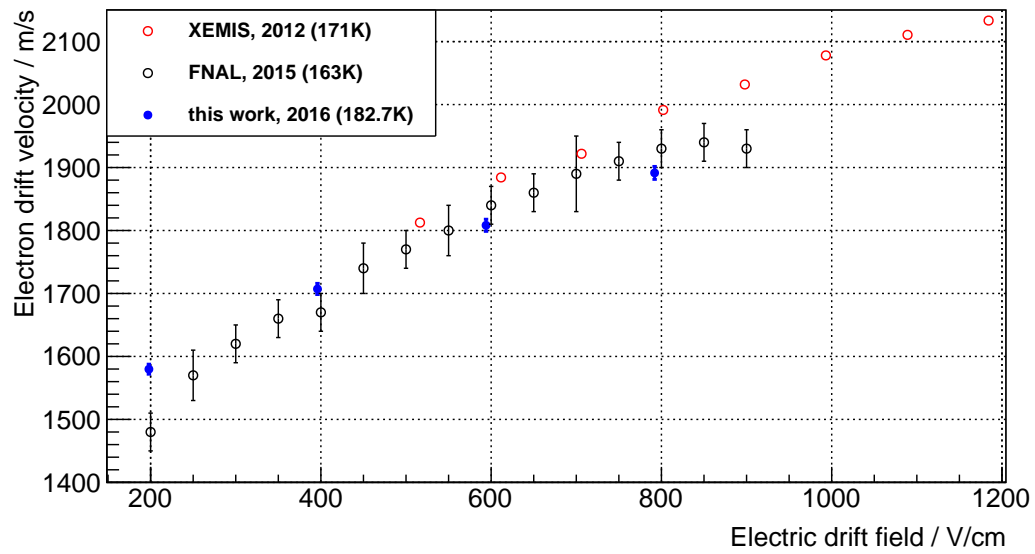
The uncertainty for the drift velocity is derived from error propagation. Table 8.1 lists the measured maximum drift times together with the calculated drift velocities for each applied drift field strength.

$E_{\text{drift}} \left(\frac{\text{V}}{\text{cm}} \right)$	$t_{\text{drift,max}} \left(\mu\text{s} \right)$	$\Delta t_{\text{drift,max}} \left(\mu\text{s} \right)$	$v_{\text{drift}} \left(\frac{\text{m}}{\text{s}} \right)$	$\Delta v_{\text{drift}} \left(\frac{\text{m}}{\text{s}} \right)$
198	31.9669	0.1001	1579.76	7.97
396	29.5813	0.1000	1707.16	8.89
594	27.9273	0.1000	1808.27	9.65
792	26.6988	0.1005	1891.47	10.31

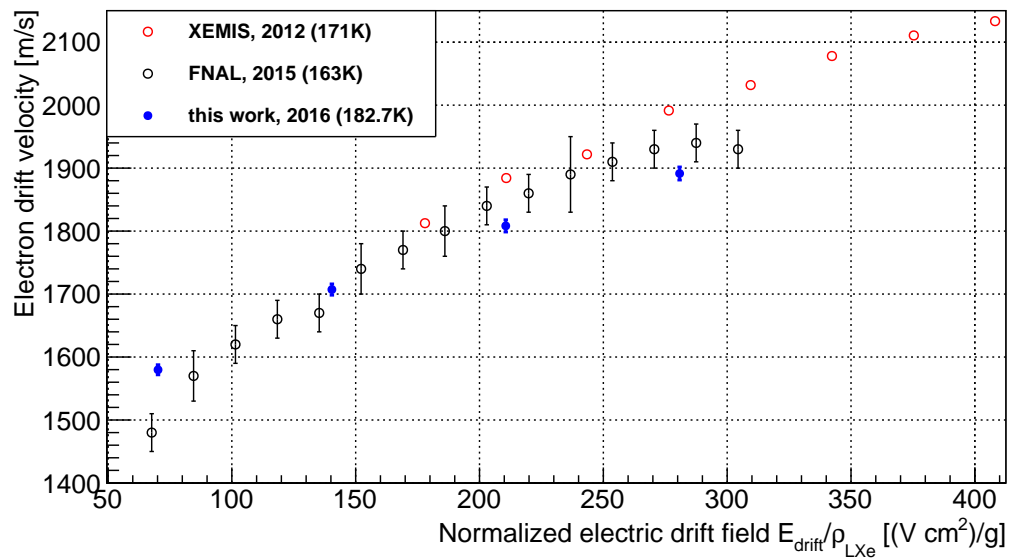
Table 8.1: Maximum drift times and the corresponding drift velocities for different electric drift field strengths. The maximum drift length is $(50.5 \pm 0.2) \text{ mm}$.

The determined drift velocities can be compared to previous measurements. This is displayed in figure 8.3a.

Each of these drift velocity measurements was taken for different fields, but they have an overlap so that they are comparable at least in part. Overall, the velocities measured with the MainzTPC are in agreement with the data points taken at the FNAL, except for the lowest drift field where a higher drift velocity was concluded from the MainzTPC. Unfortunately, the XEMIS data did not provide uncertainties for the data



(a)



(b)

Figure 8.3: Measured drift velocity in dependence of the electric drift field strength and comparable data from previous measurements ([103], [38]). In (a), the electric drift field values from each measurement are used, while in (b), the electric drift field is normalized to the liquid xenon temperature of the respective measurement. The normalization is done by dividing the electric field strength by the liquid xenon density for the corresponding temperature. In trend and magnitude, the measurements show similar values.

points so that it is not possible to definitely confirm whether the measurements agree within the errors. But in trend and magnitude all three measurements show similar values in the region of overlap.

The liquid xenon density is temperature-dependent. This affects the electron drift velocity. To account for this dependence, one can rescale the electric field strength with the xenon density for the respective measurement. The liquid xenon density for different temperatures is provided by NIST and plotted in figure 2.1a in section 2.1.

Figure 8.3b shows the drift velocity measurements conducted by different groups, with the electric drift field normalized to the respective liquid xenon density for each measurement, according to the liquid xenon temperatures.

While the overall shape of the measurement data is unchanged, the data sets are shifted with respect to each other, since each data set is normalized to a different temperature and hence different density.

8.2 | Drift Time and Interaction Depth

Analogous to equation 8.1 for the maximum drift time, the drift time for events at arbitrary depths in the MainzTPC can be determined. The drift time t_{drift} is calculated as the measured time difference between $S1$ and $S2$ signal subtracted by the gate time t_{gate} , which is defined in section 8.1:

$$t_{\text{drift}} = t_{S2-S1} - t_{\text{gate}} \quad \Delta t_{\text{drift}} = \sqrt{\Delta t_{S2-S1}^2 + \Delta t_{\text{gate}}^2} \quad (8.3)$$

The interaction depth is the translation of the drift time t_{drift} to the z -position of the interaction in the active volume of the MainzTPC. This translation not only gives a more intuitive measure of the event position but also normalizes the drift time distributions for different drift field strengths: Since the electron drift velocity increases with increasing drift field strength, the drift times of two events occurring at the same depth in the TPC but measured with different drift fields are unequal.

The conversion of drift time to interaction depth can be formulated as

$$z(t_{\text{drift}}) = \frac{t_{\text{drift}}}{t_{\text{drift,max}}} \cdot l_{\text{max}} = t_{\text{drift}} \cdot v_{\text{drift}} \quad (8.4)$$

$$\Delta z(t_{\text{drift}}) = \sqrt{(\Delta t_{\text{drift}} \cdot v_{\text{drift}})^2 + (t_{\text{drift}} \cdot \Delta v_{\text{drift}})^2}$$

In the following, the interaction depth of events in the TPC will be expressed either as t_{drift} or z , depending on convenience for the analysis. Note that the interaction depth is measured from the gate mesh downwards to the cathode mesh.

8.3 | S1 z -correction

The amount of $S1$ light detected by the two PMTs in the TPC depends on the event position. To quantify this dependency, the change of $S1$ with respect to the depth in the TPC is examined in this section.

The photons of the $S1$ signal do not illuminate Top PMT and Bottom PMT in the same way. In fact, the Bottom PMT detects a larger amount of light compared to the Top PMT. The reason for this is that the photons have to pass through the liquid-gas interface to reach the Top PMT. Only a fraction of the photons which are originally emitted to the upper part of the TPC hits the Top PMT photocathode, while another fraction undergoes total internal reflection. By this, the Bottom PMT which is completely immersed in the liquid xenon collects even more light. This effect has a varying impact for different depths of the TPC.

Figure 8.4 shows a sketch of the different signals from events with the same energy deposit in the TPC, but at different depths.

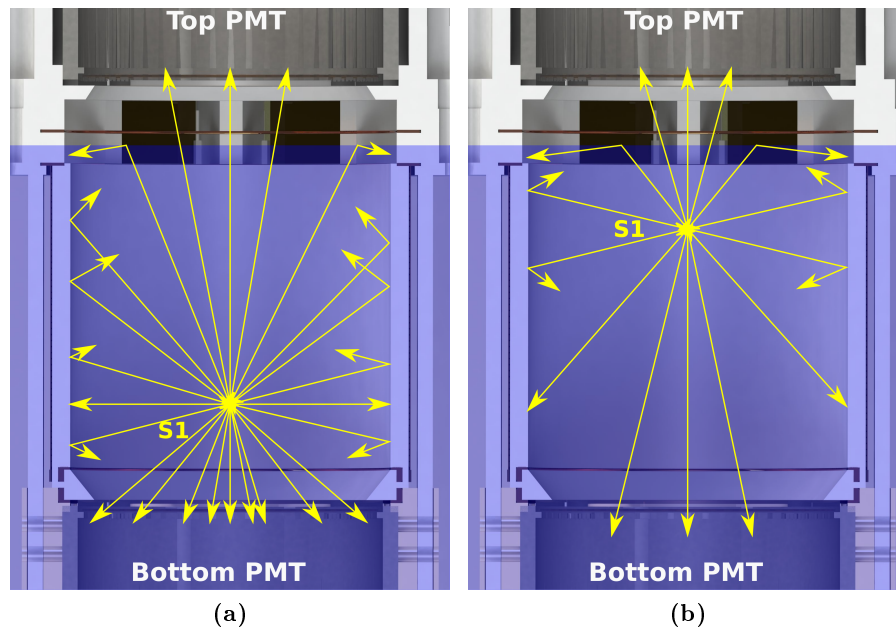


Figure 8.4: Illustration of the $S1$ signal variation with the interaction depth z : Signals with large interaction depths z as sketched in (a) lead to larger $S1$ signals, because most of the scintillation light is directly detected by the Bottom PMT. Also, the photons directed upwards have a small angle relative to the liquid surface normal, which leads to only a small amount of total internal reflection, while most upward photons are detected by the Top PMT. In (b), the $S1$ scintillation of the event at a low z leads to more internal reflection and the downward directed photons have a longer distance to overcome, on which they can be scattered and (in part) absorbed by the PTFE cylinder around the active volume. In total, both PMTs detect less light from events at low interaction depths z .

For events with the same energy deposit in different depths z in the TPC one expects the largest measured $S1$ close to the Bottom PMT, since most of the light is directly detected. The photons which are emitted upwards do not have large angles with respect to the liquid-gas interface normal and therefore the amount of total internal reflection is minimized. Events that occur further upwards in the TPC have a smaller fraction of photons that are directly detected by the Bottom PMT and more light is reflected on the liquid-gas interface so that the total $S1$ signal decreases for smaller depths in the TPC.

Vice versa, $S1$ signals for events with different energy deposits can have the same measured $S1$ values, depending on the interaction depth of the respective events.

To study this effect and find a correction function for the $S1$ signal at different z , data from gamma-ray source measurements are used. By examining an $S1$ peak in the spectrum at different interaction depths, one can measure the change in the position of the peak and hence in the $S1$ signal strength with varying z .

Figure 8.5 shows the $S1$ spectrum of a ^{152}Eu source for an applied drift field of 198 V/cm, measured with the DAQ Trigger set to a coincidence between the TPC PMTs. The quantity $S1$ integral on the horizontal axis is the sum of the signal integral from Top and Bottom PMT.

The spectrum does not show a distinctive source spectrum with the expected individual

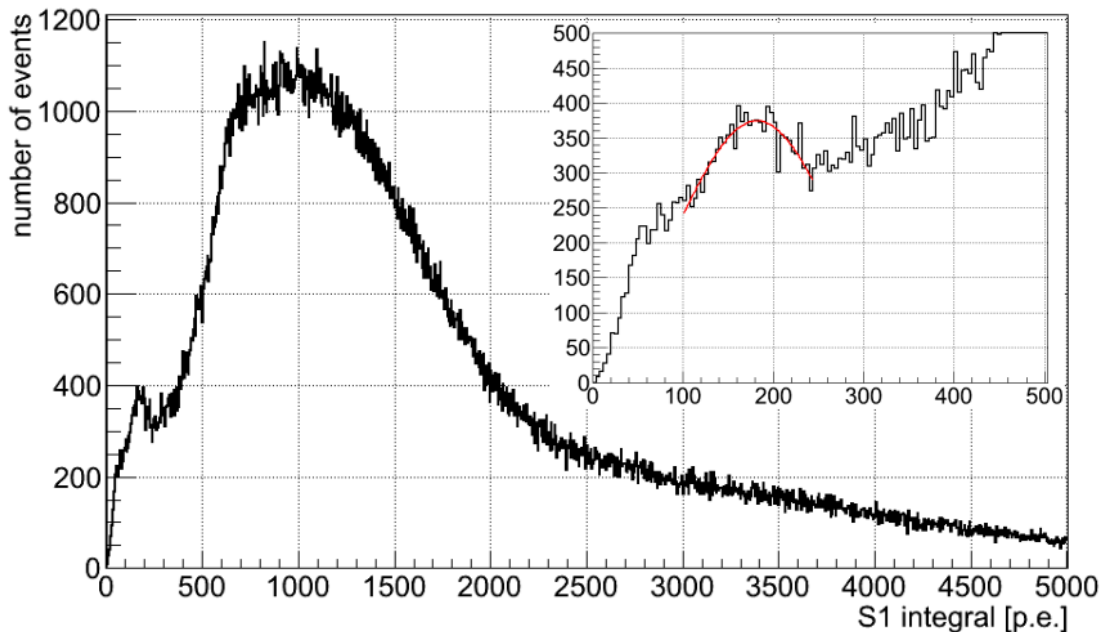


Figure 8.5: Measured $S1$ spectrum for an ^{152}Eu source with a drift field of 198 V/cm. Individual energy lines are not distinguishable, but the small, narrow peak feature in the region between 0 and 300 p.e. can be used for the analysis. To normalize the peak positions found for different interaction depths z , the narrow peak is fitted using a Gaussian as depicted in the zoomed in subplot, which has the same quantities on its axes as the main picture.

energy lines, which could be used for a TPC energy calibration. In the low $S1$ region between 0 and 300 p.e., a quite narrow peak is found which is suited for the analysis. An explanation for the small peak structure could be radiation from the atomic K-shell in xenon, which has an energy of 34.56 keV (see also section 2.2.1). Its emission lines are at 29.78 keV ($K_{\alpha 1}$), 29.46 keV ($K_{\alpha 2}$) and 33.62 keV ($K_{\beta 1}$) [60]. That means a part of the signal background might be caused by the de-excitation of the electron shells of xenon atoms after an interaction. The lower energies from the L-shells are not visible. For this analysis, the knowledge of the actual energy of an examined peak is not necessary since the z -correction is a relative correction.

Although the energy of the narrow peak is not needed, the mean value of the peak is used as a normalization value. When examining the peak position – which is the $S1$ integral – for different z , the change in position is compared to the mean $S1$ integral for the complete peak. Therefore a Gaussian fit according to equation (8.5) is carried out for the peak as shown in the subplot of figure 8.5.

$$f_{S1}(z) = \frac{A}{\sigma\sqrt{2\pi}} \cdot e^{-\frac{1}{2}\left(\frac{S1-\mu_{S1}}{\sigma}\right)^2} \quad (8.5)$$

For higher fields, the spectrum is shifted to lower values. Higher drift fields suppress electron recombination and lead to a lower $S1$ scintillation output. The spectra for 594 V/cm and 792 V/cm drift field strength can be found in appendix B.4.

The peak positions for the different fields determined using the fit from equation (8.5) are listed in table 8.2. The observed decrease in $S1$ integral at higher drift fields can be explained by the suppression of the electron recombination at the interaction point. With no applied drift field, the recombining electrons contribute to the $S1$ signal. By increasing the drift field, a growing fraction of the electrons released in the interaction are drifted away and thus the $S1$ signal is reduced.

In addition, table 8.2 includes the values for the same peaks examined with the applied $S1$ z -correction which is developed in this section. The change of the signal mean μ_{cS1}

E_{drift} [V/cm]	μ_{S1} [p.e.]	$\Delta\mu_{S1}$ [p.e.]	σ_{S1} [p.e.]	$\frac{\sigma_{S1}}{\mu_{S1}}$
198	177.61	2.23	100.53	0.566
594	162.38	2.89	88.66	0.546
792	147.99	5.21	74.67	0.504
	μ_{cS1} [p.e.]	$\Delta\mu_{cS1}$ [p.e.]	σ_{cS1} [p.e.]	$\frac{\sigma_{cS1}}{\mu_{cS1}}$
198	178.91	1.83	88.65	0.496
594	162.69	2.69	83.83	0.515
792	148.82	5.49	75.41	0.507

Table 8.2: $S1$ and $cS1$ integral values for the narrow peak structure in the ^{152}Eu spectrum, fitted with a Gaussian for different drift field strengths. As expected, the mean value for the peak decreases with increasing drift field due to the suppression of electron recombination. In comparison, the fraction $\frac{\sigma_{cS1}}{\mu_{cS1}}$ is smaller or equally large as its counterparts for the uncorrected signals.

is not very large, but the fraction $\frac{\sigma_{cS1}}{\mu_{cS1}}$ is smaller than for the uncorrected values for the field strengths 198 V/cm and 594 V/cm. For the highest drift field of 792 V/cm, the correction has no effect on the ratio between the signal width and its mean value. This means that the $S1$ z -correction has a measurable impact in the spectral shape of the $S1$ signal.

In anticipation of the Compton measurements discussed in section 9.6, the value for the corrected signal $cS1$ of the small peak structure can be linked to an energy deposit. Using the light yield values as specified in tables 9.13, B.13 and B.14, one can calculate a mean light yield value for the drift field strengths 198 V/cm, 594 V/cm and 792 V/cm. For this, the light yield values determined for the energies 20 – 40 keV were chosen. The resulting mean light yields LY_{mean} are listed in table 8.3, with $\Delta LY_{\text{mean}} = \sigma_{LY_{\text{mean}}}$. With these values the positions of the small peaks are converted to the energy deposit $E_{\text{TPC,calc}}$ employing equation (8.6). The calculated energy deposits are also found in table 8.3 and show values consistent with the K_{α} lines for xenon at 29.78 keV and 29.46 keV, respectively, within errors.

$$E_{\text{TPC,calc}} = \frac{\mu_{cS1}}{LY_{\text{mean}}} \quad \Delta E_{\text{TPC,calc}} = E_{\text{TPC,calc}} \cdot \sqrt{\left(\frac{\Delta\mu_{cS1}}{\mu_{cS1}}\right)^2 + \left(\frac{\Delta LY_{\text{mean}}}{LY_{\text{mean}}}\right)^2} \quad (8.6)$$

$E_{\text{drift}} \left[\frac{\text{V}}{\text{cm}}\right]$	$LY_{\text{mean}} \left[\frac{\text{p.e.}}{\text{keV}}\right]$	$\Delta LY_{\text{mean}} \left[\frac{\text{p.e.}}{\text{keV}}\right]$	$\mu_{cS1} \left[\text{p.e.}\right]$	$\Delta\mu_{cS1} \left[\text{p.e.}\right]$	$E_{\text{TPC,calc}} \left[\text{keV}\right]$	$\Delta E_{\text{TPC,calc}} \left[\text{keV}\right]$
198	6.21	0.18	178.91	1.83	28.81	0.89
594	5.27	0.17	162.69	2.69	30.87	1.12
792	5.15	0.27	148.82	5.49	28.90	1.85

Table 8.3: Correlation between scintillation light from the TPC calibration with ^{152}Eu and energy deposit for the corresponding scintillation signal in Compton measurements. Considering the change in $cS1$ for the different drift fields, the calculated energy deposits indicate similar values between 28.8 and 30.9 keV. The fit values for ^{152}Eu are taken from table 8.2.

As shown in section 6.2.4, the small, narrow peak of the ^{152}Eu spectrum can be associated with events occurring primarily in the central region of the TPC. The z -correction derived using these events will therefore be limited to this region inside a circle of 15 mm radius around the TPC center. Figure 8.6 summarizes the findings of section 6.2.4, by depicting the $S1$ spectra for the event distributions inside (red) and outside (blue) a radial fiducial volume of 15 mm to the complete $S1$ spectrum (black). The red spectrum is used for the analysis in this section.

The active volume of the MainzTPC, located between the gate mesh at the top and the cathode mesh at the bottom, is divided into slices of equal height. The number of these so-called z -slices was set to 20, leading to a slice thickness of 2.525 mm and a sufficient amount of statistics for each slice. For each measurement, the interaction depth z is calculated using the drift time between the $S1$ and $S2$ signal for each event and the $S1$ values are sorted to the respective z -slice. This yields 20 different $S1$ spectra per measurement, each for a different range in z .

Figure 8.7a shows an example of a z -slice at an interaction depth between 12.625 and

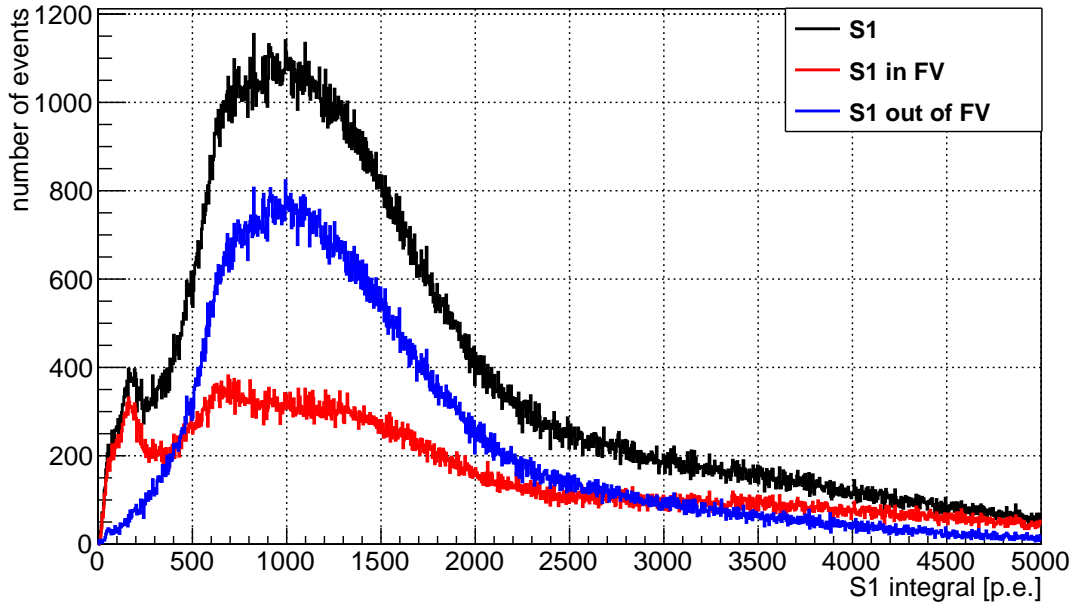


Figure 8.6: Contributions of the event distributions inside and outside a radial fiducial volume (FV) of 15 mm to the complete S_1 spectrum of ^{152}Eu at a drift field of 198 V/cm. The S_1 z -correction is carried out using the peak in the red spectrum, therefore the correction is limited to the central region of the TPC.

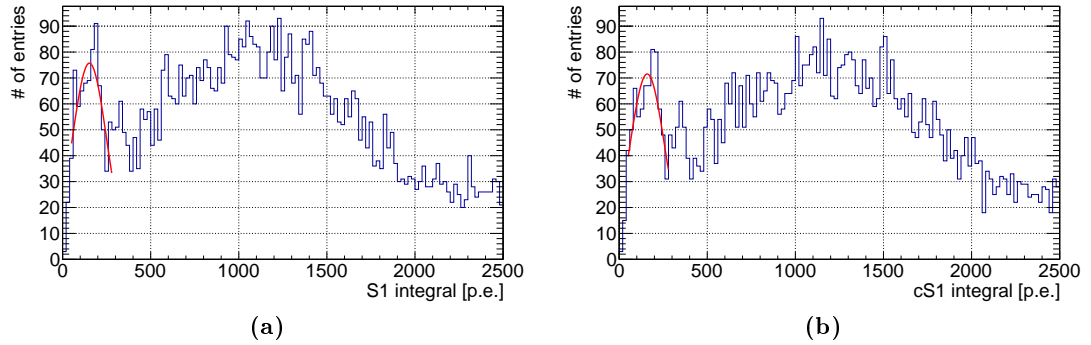


Figure 8.7: Example for a z -slice ($12.625 \text{ mm} \leq z < 15.15 \text{ mm}$) of the S_1 spectrum of ^{152}Eu , with the Gaussian fit between 50 and 250 p.e. to find the peak value for the respective interaction depth z . Figure (a) shows the slice for the measured S_1 data, in (b) the z -correction is applied for comparison.

15.15 mm. The peak position is not as clearly recognizable as in the complete spectrum in figure 8.5, still a fit is conducted between 50 and 250 p.e. to find the peak position $\mu_{S_1}(z)$ and to determine its uncertainty. For comparison, the same events are plotted in figure 8.7a with the applied z -correction. A small difference in shape is visible for the spectrum.

The $\mu_{S_1}(z)$ integral fit results for the peak values in all z -slices for three different drift

fields are summarized in table B.9 in appendix B.4. The peak values are plotted in figures 8.8a, 8.8b and 8.8c.

All three graphs show a similar shape. The found values for $\mu_{S1}(z)$ increase with increasing z , which confirms the expected behaviour of the $S1$ signal strength in dependence of the interaction depth. Furthermore, with increasing drift field strength the overall value of $S1$ integral decreases, which is related to the loss of electron recombination. The error in interaction depth corresponds to the range of the z -slices.

To account for the non-linear distribution of the data points, a second-order polynomial, as displayed in equation (8.7), is used as a fit function. The blue-grey area marks the 95% confidence band of the fit.

$$f_{S1z}(z) = p_0 + p_1 \cdot z + p_2 \cdot z^2 \quad (8.7)$$

The resulting fits are not normalized and therefore only valid for their respective drift field configuration. To generalize the findings, the data points are normalized using the mean $S1_{\text{peak,mean}}$ values from table 8.2. Since the normalized data points are independent of the drift field strength, the three data sets can be merged to obtain a mean $S1$ z -correction.

Each data point is determined with its specific uncertainty in $S1$, therefore the individual data points are weighted with their uncertainty. Equation (8.8) describes how the three datasets are merged: For each z -slice, the value $S1_{\text{peak},i}(z)$ is divided by a factor $f_i = S1_{\text{peak,mean},i}$ for the respective drift field strength. Then the data point is weighted with its uncertainty $\Delta S1_{\text{peak},i}(z)$. The sum of the three weighted values is then divided by the sum of all weights (the inverse of the uncertainties). The resulting graph is shown in figure 8.9.

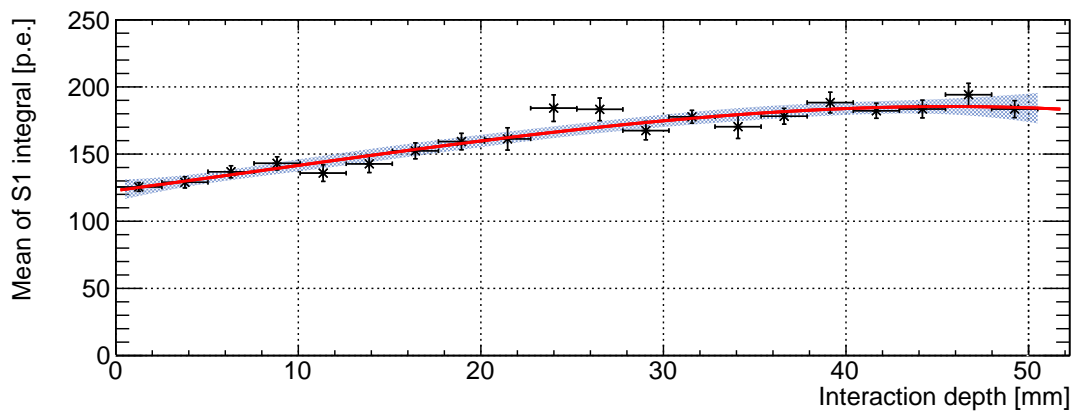
$$\overline{S1}_{\text{norm}}(z) = \frac{\sum \frac{S1_{\text{peak},i}(z)}{f_i} \cdot \frac{1}{\Delta S1_{\text{peak},i}(z)}}{\sum \frac{1}{\Delta S1_{\text{peak},i}(z)}} \quad (8.8)$$

The weighted mean method leads to smaller uncertainties, and compared to the non-normalized graphs the data points do not scatter much from the course of the overlaid second-order polynomial fit. The fit uncertainty, illustrated by the blue-grey area, is therefore smaller than before. Instead of an $S1$ integral value, the $S1$ z -correction factor is shown on the ordinate axis. The $S1$ z -correction factor is of the form of equation (8.7).

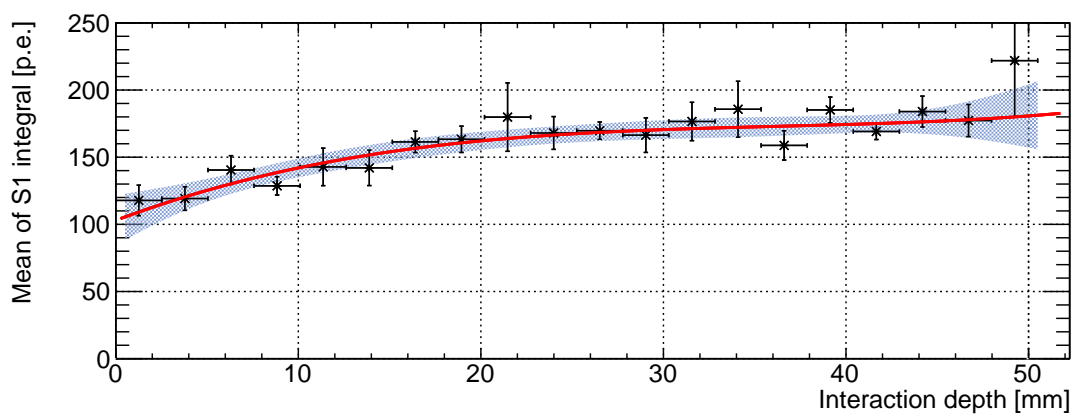
	value	uncertainty
p_0	$7.1080 \cdot 10^{-1}$	$0.2867 \cdot 10^{-1}$
p_1	$1.6674 \cdot 10^{-2}$	$0.5128 \cdot 10^{-2}$
p_2	$-2.2983 \cdot 10^{-4}$	$2.323 \cdot 10^{-4}$

Table 8.4: Parameters for the $S1$ z -correction function derived from second-order polynomial fit of the data points displayed in figure 8.9.

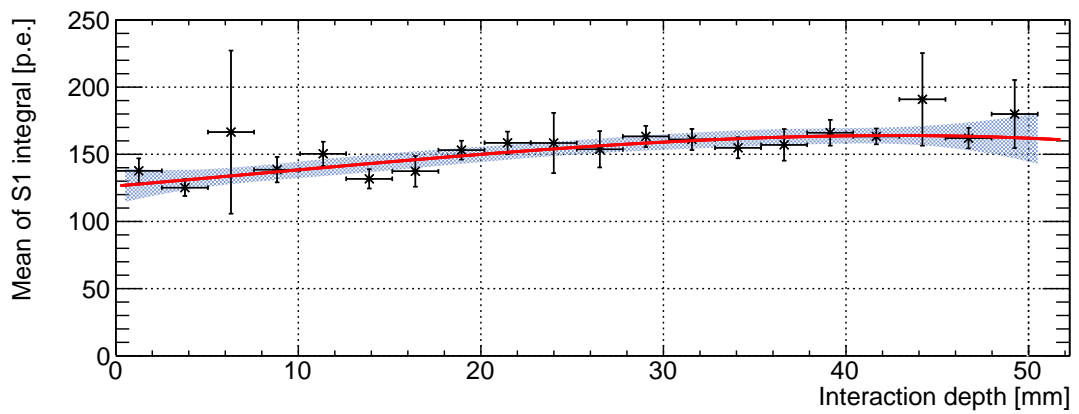
The fit parameters obtained from the data points in figure 8.9 are listed in table 8.4 and



(a) 198 V/cm



(b) 594 V/cm



(c) 792 V/cm

Figure 8.8: $\mu_{S1}(z)$ fit values at the peak position in dependence of the interaction depth z for the $S1$ spectrum of ^{152}Eu at a drift field strength of (a) 198 V/cm, (b) 594 V/cm and (c) 792 V/cm. The expected shape of an increasing value for higher z is observed for all drift fields. A second-order polynomial fit is drawn in red, the blue-grey overlay marks the 95% confidence band for the fit uncertainties.

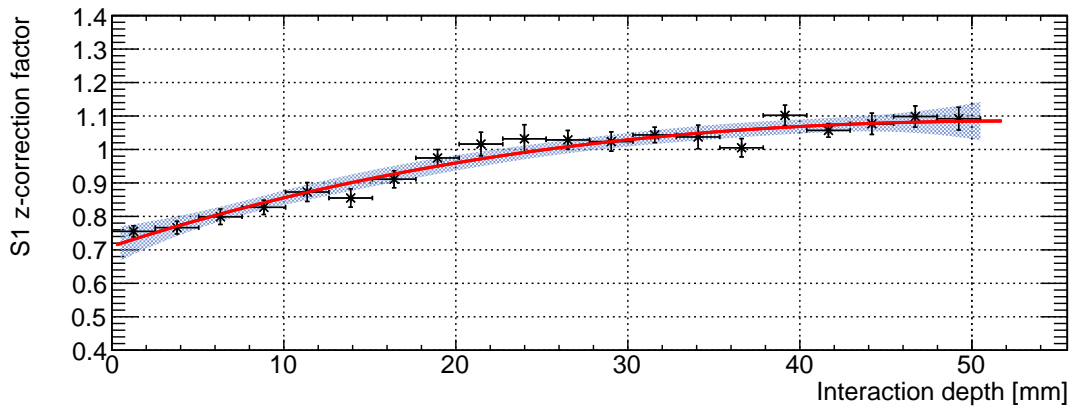


Figure 8.9: $S1$ z -correction factor in dependence of the interaction depth z . The data points of the data sets from three different drift field strengths are normalized and combined with a weighted mean. The second-order polynomial fit conducted on this graph represents the correction function used in the further analysis.

are used to correct the $S1$ signals in the further analysis of this thesis. As mentioned before, the ratios shown in table 8.2 document the viability of this signal correction. The application of the signal correction was done using equation (8.9). Dividing the measured signal $S1(z)$ by the factor $f_{S1z}(z)$ counters the depth-induced change of the measured amount of scintillation light.

$$cS1(z) = \frac{S1(z)}{f_{S1z}(z)} \quad (8.9)$$

8.4 | Electron Life Time and $S2$ z -correction

Electrons drifting through liquid xenon can be absorbed by electronegative impurities, because these do not have a noble gas electron configuration as the xenon atoms. The $S2$ signal of a specific event in the TPC changes for different amounts of impurities in the xenon such that a larger abundance of impurities leads to a smaller amount of drift electrons reaching the liquid-gas interface and creating the $S2$ signal. Due to the loss of electrons during the drift, the $S2$ signal is attenuated, so that a large energy deposit in the bottom region of the TPC and a smaller energy deposit in the upper part of the TPC can cause a comparable $S2$ signal. This is illustrated in figure 8.10.

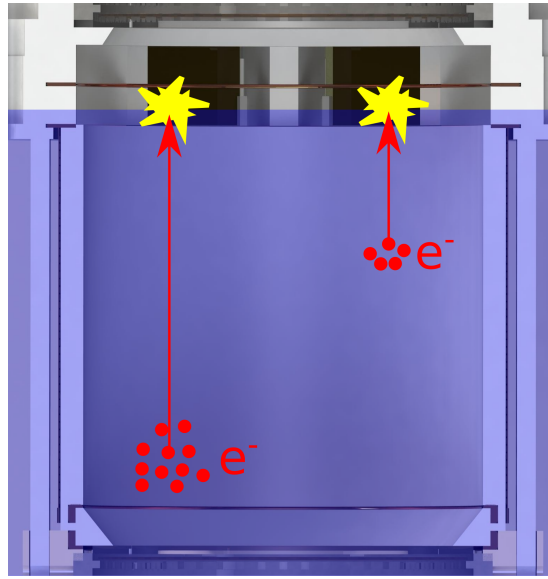


Figure 8.10: Illustration of the electron absorption by impurities in LXe: The sketch shows two interactions at different depths in the TPC. The interaction on the left, occurring at a large depth, releases a larger amount of electrons than the interaction drawn on the right at a higher altitude. Due to electron absorption during the drift process, the resulting $S2$ signal for both interactions is of equivalent strength.

The $S2$ signal is proportional to the electrons extracted to the gas phase and the electron number decreases with increasing drift length according to an absorption law (e.g. Beer-Lambert law), so that the $S2$ signal can be corrected as follows:

$$S2(t) = cS2 \cdot e^{-\frac{t}{\tau_e}} \Leftrightarrow cS2(t) = S2 \cdot e^{\frac{t}{\tau_e}} \quad (8.10)$$

Here, the $S2$ equals the integral value of the $S2$ signal peak in the waveform, $cS2$ is the corrected integral value. The signal attenuation is calculated depending on the drift time t with the electron lifetime τ_e as time constant.

Figure 8.11 shows the $S2$ spectrum for the ^{152}Eu source at an applied drift field of

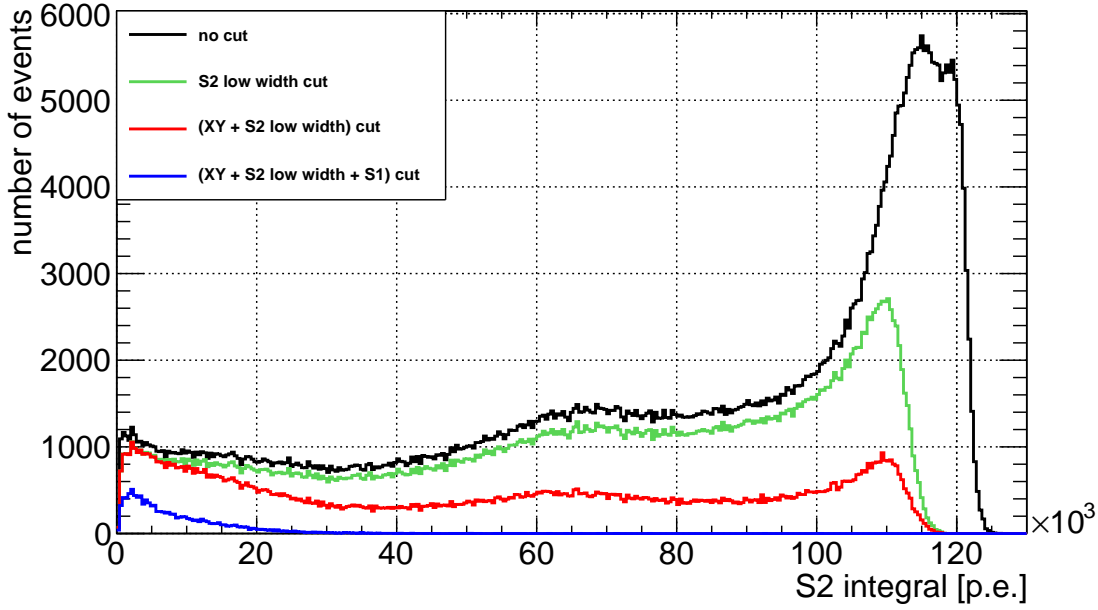


Figure 8.11: S_2 signal spectrum for a ^{152}Eu source at a drift field strength of 198 V/cm. In black, the complete spectrum is shown. The large peak structure on the right end of the spectrum is apparently an abrupt cut off due to saturation effects. The red spectrum consists of S_2 signals found within a radius of 15 mm in the x - y -plane. The blue spectrum are the S_2 signals from the red spectrum which are associated with the low-energy peak found in the S_1 spectrum.

198 V/cm. The complete spectrum (black) shows an event distribution without noteworthy signal features, except for large S_2 signals, where the spectrum reaches a maximum and ends in a sharp edge. This cutoff feature shows the signal saturation of the TPC PMTs, which is discussed in section 8.5. A first event selection is done using the S_2 low width as described in section 9.3.7. The remaining signals form the green spectrum. For the S_1 z-correction, the S_1 peak in the lower region of the spectra was used (see also figure 8.5). Analogously, the S_2 signals corresponding to the S_1 signals of this peak can be examined. The red spectrum in figure 8.11 consists of the S_2 signals from events with an x - y -position inside a 15 mm radius around the TPC center. The blue spectrum eventually shows the S_2 signals for an event selection in S_1 between 50 and 250 p.e. around the low energy S_1 peak. For smaller S_2 , a peak structure is found that is used to determine the electron lifetime.

$$\begin{aligned}
 g_{S_2}(z\text{-slice}) = & \frac{A}{\sigma_{S_2\text{mean}} \sqrt{2\pi}} \cdot \exp\left(-\frac{1}{2} \left(\frac{S_2 - S_{2\text{mean}}}{\sigma_{S_2\text{mean}}}\right)^2\right) \\
 & + \frac{B}{\sigma_{\text{bkg}} \sqrt{2\pi}} \cdot \exp\left(-\frac{1}{2} \left(\frac{S_2 - S_{2\text{bkg}}}{\sigma_{\text{bkg}}}\right)^2\right)
 \end{aligned} \tag{8.11}$$

The drift region is divided in several z -slices and the spectrum for the selected events is evaluated for each interval. The sum of two Gaussians as stated in equation (8.11) is used as a fit function to take into account the signal peak as well as the underlying background. The fit results for the peak positions $S2_{\text{mean}}$ are listed in table B.10 in appendix B.5.

Figure 8.12 gives an impression of one of the z -slices, here at a z between approximately 37.9 mm and 40.4 mm, with the Gaussian fit marked in red. The relatively coarse binning of 500 p.e. per bin is necessary to find the peak structure due to the wide range of the measured $S2$ signals.

The histograms are fitted with a sum of two Gaussians (red). The signal function is shown in green, a Gaussian modelling the background is overlaid in blue. For comparison, the same z -slice is also shown for the $cS2$ signal on the right, with the applied correction in z . Both signals have a similar position and shape.

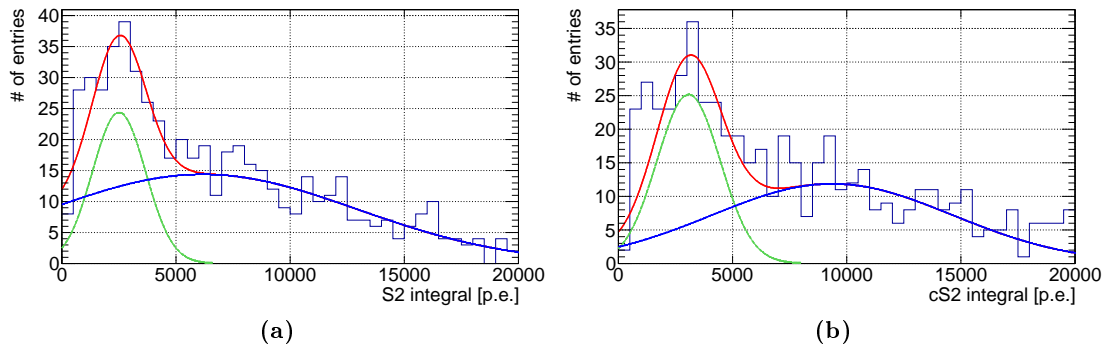


Figure 8.12: Example for a z -slice ($37.88 \text{ mm} \leq z < 40.40 \text{ mm}$) of the $S2$ spectrum of ^{152}Eu , with a double Gaussian fit according to equation (8.11) to find the peak value for the respective interaction depth z . Figure (a) shows the slice for the measured $S2$ data, in (b) the z -correction is applied for comparison. All other plots of the z -slices for $S2$ can be found in appendix B.5.

For a quantitative comparison, the $S2$ peak used for the determination of the z -correction is plotted in figure 8.13 in black. For the same signals the corrected $cS2$ (with the correction determined in this section) is also depicted in red. Both peaks are fitted with a Gaussian of the form of equation (8.5) (green, blue). The peak position of the $cS2$ distribution is shifted to larger signal values. This is expected since the correction of the $S2$ signal accounts for its attenuation. For the distributions at hand, a visible change in peak width is not identifiable by eye. Table 8.5 summarizes the fit values, showing a small decrease in peak width for the $cS2$ distribution and larger decrease for the fraction $\frac{\sigma_{cS2}}{\mu_{cS2}}$ compared to the uncorrected case.

In figure 8.14, the mean values $S2_{\text{mean}}$ are plotted in dependence of their respective drift time t . The decrease of $S2_{\text{mean}}$ with increasing z , as expected, is clearly visible in the graph.

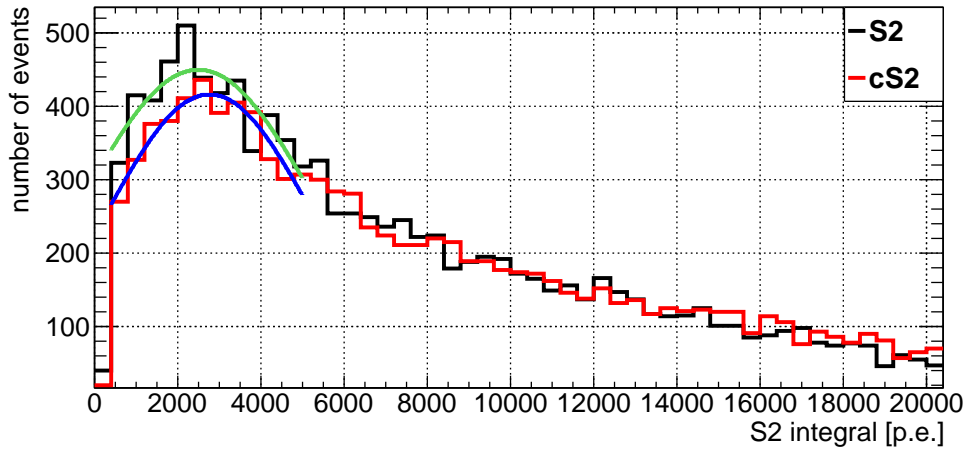


Figure 8.13: Comparison of the signal distribution for the $S2$ peak used to measure the electron lifetime for the measured and corrected signals.

E_{drift} [V/cm]	μ_{S2} [p.e.]	$\Delta\mu_{S2}$ [p.e.]	σ_{S2} [p.e.]	$\frac{\sigma_{S2}}{\mu_{S2}}$
198	2497	92	2804	1.12
	μ_{cS2} [p.e.]	$\Delta\mu_{cS2}$ [p.e.]	σ_{cS2} [p.e.]	$\frac{\sigma_{cS2}}{\mu_{cS2}}$
198	2766	73	2495	0.90

Table 8.5: $S2$ and $cS2$ integral values for the peak structure in the ^{152}Eu spectrum at 198 V/cm used to measure the electron lifetime, fitted with a Gaussian. The fraction $\frac{\sigma_{cS2}}{\mu_{cS2}}$ is smaller as its counterpart for the uncorrected signals.

An exponential fit corresponding to equation 8.10 yields an electron lifetime of

$$\tau_e = (131.41 \pm 38.18) \mu\text{s}.$$

This electron lifetime is very short compared to measurements conducted with other dual-phase xenon TPC which achieved electron lifetimes of the order of milliseconds [42]. This discrepancy arises probably due to experimental difficulties, as the MainzTPC was not able to measure clear energy lines in both $S1$ and $S2$ signals. Conducting the same analysis on identified energy lines instead of peak-like structures will improve the measurement accuracy. The lifetime found here has an uncertainty of the order of 29 % of the lifetime value.

With the available data only the lifetime for the measurements taken with a drift field strength of 198 V/cm could be evaluated. For the measurements with higher fields, the identification of a peak structure in the individual z -slices was not possible due to the broadly distributed $S2$ signals and the relatively low statistics.

Alternatively, the mean values $S2_{\text{mean}}$ can be examined with respect to the interaction depth to obtain the attenuation length for the $S2$ signal. The exponential fit to the

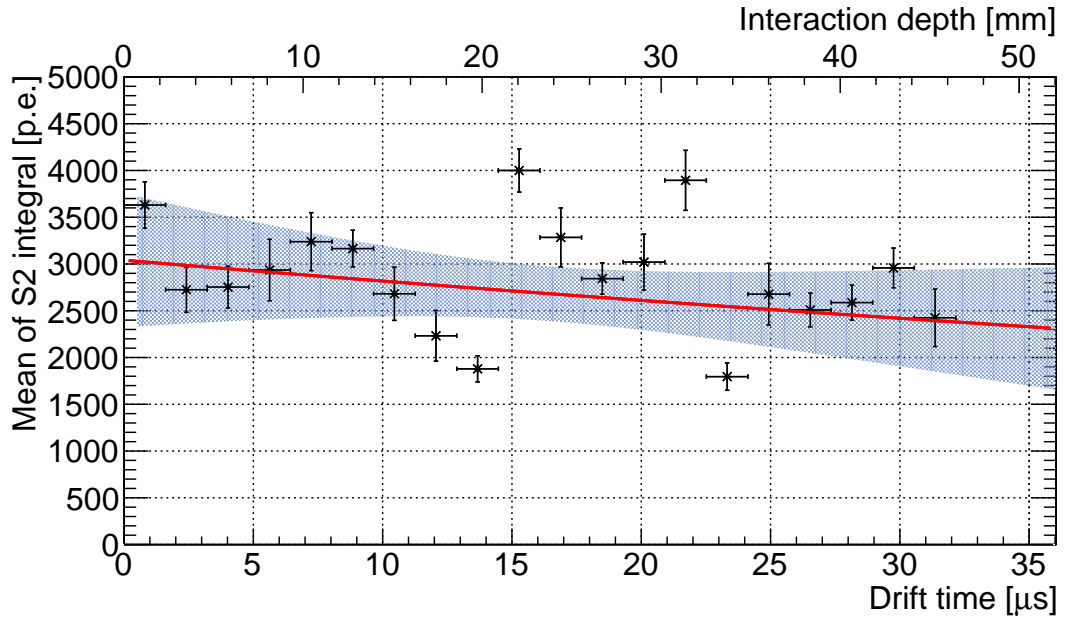


Figure 8.14: $S2$ signal peak mean values in dependence of the drift time and of the interaction depth for a ^{152}Eu source at a drift field strength of 198 V/cm. An exponential fit provides an electron lifetime of $\tau_e = (131.41 \pm 38.18) \mu\text{s}$ and an attenuation length of $l_e = (206.31 \pm 59.85) \text{mm}$, respectively, for the plotted data.

data is equivalent to equation (8.10):

$$cS2(z) = S2 \cdot e^{\frac{z}{l_e}} \quad l_e = (206.31 \pm 59.85) \text{mm} \quad (8.12)$$

With the electron lifetime the signal loss $a_{S2}(t)$ for $S2$ can be calculated according to equation (8.13) for different drift times.

$$\begin{aligned} \Delta S2(t) &= cS2 - S2 = S2 \left(e^{\frac{t}{\tau_e}} - 1 \right) \\ a_{S2}(t) &= \frac{\Delta S2}{S2}(t_{\max}) = \left(e^{\frac{t}{\tau_e}} - 1 \right) \\ \Delta a_{S2}(t) &= \sqrt{\left[\left(\frac{\Delta t}{\tau_e} \right)^2 + \left(\frac{-t \Delta \tau_e}{\tau_e^2} \right)^2 \right]} e^{2 \frac{t}{\tau_e}} \end{aligned} \quad (8.13)$$

For a drift field of 198 V/cm the maximum drift time is $(31.97 \pm 0.1) \mu\text{s}$ (see section 8.1), which leads to a maximum signal loss in $S2$ for events occurring at the very bottom of the active volume of $a_{S2}(t) = (26.9 \pm 8.8) \%$.

While the fraction $\frac{\sigma}{\mu}$ for the $S2$ signal improves using the corrected signals, the found value for the electron lifetime implies a large uncertainty. The impact of the $S2$ z -correction on the experimental data has to be checked and evaluated, whether it is even applicable at all.

8.5 | *S2* Signal Saturation

The TPC PMTs are responsible for the detection of *S1* and *S2* signals, which implies that the PMTs need to measure the light over a large dynamic range from a few photoelectrons for small *S1* signals up to tens of thousands of photoelectrons for large *S2* signals. As described in section 8.4 (figure 8.11), the *S2* signal spectrum shows an abrupt cutoff for large signals, which indicates a saturation of the measured signal. The measurement of the PMTs can be affected by different factors:

- Very large light signals can lead to a maximum charge depletion of the PMT photocathode. A saturation of the photocathode is unlikely, considering the amount of charge necessary for this effect. The resulting current which can be measured by the HV supply board would be easily identifiable, but large deviations from the PMT bias current required by the dynode resistor chain have not been observed.
- For the amplified PMT signals, the DetectorLab amplifier as well as the KPH amplifier constrain the maximum amplitude to 2 V and 1.5 V, respectively (see [3]). To cancel out the effects of the PMT amplifiers, the data examined here were collected by measuring the PMT signals directly on the SIS3316 without the amplifier electronics.
- The input range of the FADCs is limited to a 5 V range for the SIS3316 and a 1 V range for the SIS3305. Since the latter is only used to measure the *S1* signal, the input ranges should be sufficiently large.
- The charge signal in the PMT is amplified using 12 dynodes on different potentials. For the three last dynode stages, buffer (or reservoir) capacitances are connected in parallel to maintain the stability of the potentials on the dynode chain (see [82], [4]). If the signal current exceeds the current that can be provided by the charge stored on the capacitances, the potentials in the dynode chain will change as well as the PMT response.

To illustrate the impact of the buffer capacitances, figure 8.15 shows a sketch of the circuit for the dynode stages in question as well as the change of current when charging the capacitance.

In figure 8.15a, the dynodes are denoted as D11 and D12, an arbitrary dynode pair at the end of the dynode chain. The charge signal has already been passed on by the ten preceding dynodes and has therefore been amplified significantly. Without a charge signal, the potential between the two dynodes is set by the base current I_B to be $U_{11,12} = I_B R$. The PMT rise time (2.3 ns, according to [94]) is equivalent to the amount of time a signal needs to pass the dynode chain. After that the signal current is much larger than the base current: $i_{11,12} \gg I_B$. The current through the resistor R can therefore be neglected.

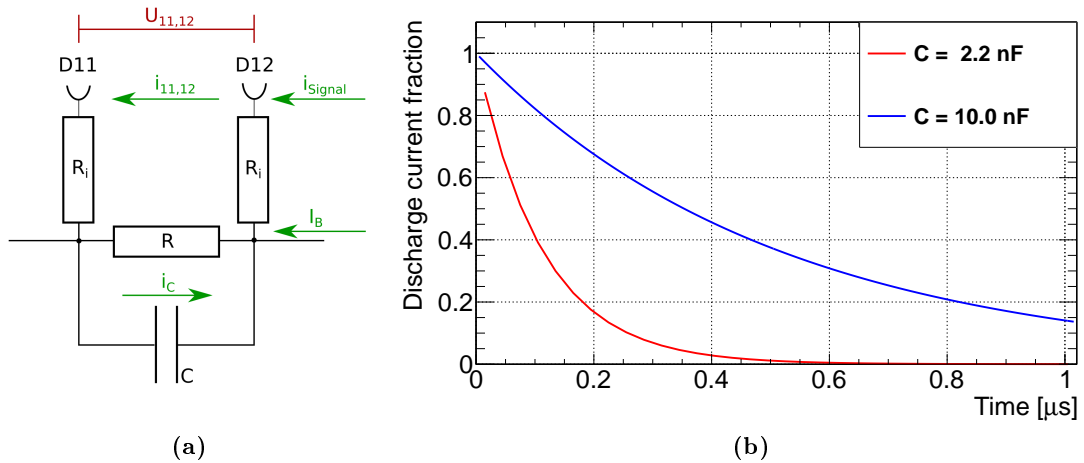


Figure 8.15: Impact of buffer capacitances to the dynode chain potentials: The sketch in (a) shows the a part of the dynode chain with a buffer capacitance as charge reservoir to maintain the potential between the dynodes when large signal currents occur. A complete schematic of the PMT base circuits used during the measurements can be found in appendix A.4. In (b), the current provided by the buffer capacitor with different capacitances is shown over time.

For large signals, the charge current $i_{11,12}$ would change the potential $U_{11,12}$. This leads to a change of the PMT gain and the response of the PMT becomes non-linear.

The potential between the two dynodes is supposed to remain stable, therefore the capacitance C installed in parallel to the charge flow between the dynodes is serving as a charge reservoir. Figure 8.15b shows the current during the discharging process (see equation (8.14)) of the capacitance for the two cases of a 2.2 nF capacitor, which was employed during the measurement discussed in this thesis, and for comparison a 10.0 nF capacitor over a 51Ω resistor (R_i). As can be seen, the 2.2 nF capacitor current drops more rapidly and falls below 1% of the initial current after $0.5 \mu\text{s}$. The current larger 10.0 nF capacitor decreases less steeply, reaching 1% after more than $2.3 \mu\text{s}$.

$$i_C(t) = i_{C,0} \left(1 - e^{-\frac{t}{\tau}} \right) \quad \text{with: } \tau = R_i C \quad (8.14)$$

For very large signals with short rising edges and large currents, the charge stored in the reservoir capacitances might not be sufficient to provide a stable potential.

To pinpoint the factor responsible for the saturation effect, the PMT performance is examined with respect to the different properties of the $S2$ signal. Figure 8.16 displays the $S2$ signal integral in dependence of the $S2$ amplitude for Top and Bottom PMT.

The graphs for both PMTs show a linear increase in both signal integral and amplitude for small amplitudes below 0.5 V on the Top PMT and around 0.7 V on the Bottom PMT. For higher amplitudes, the signal integral converges to a maximum value for both PMTs. Since the PMTs were operated at different bias voltages, the PMT gains are different which results in a saturation at unequal measurement values (see section 5.1). The maximum signal integral for the Top PMT is about $5 \cdot 10^4$ p.e., while the Bottom

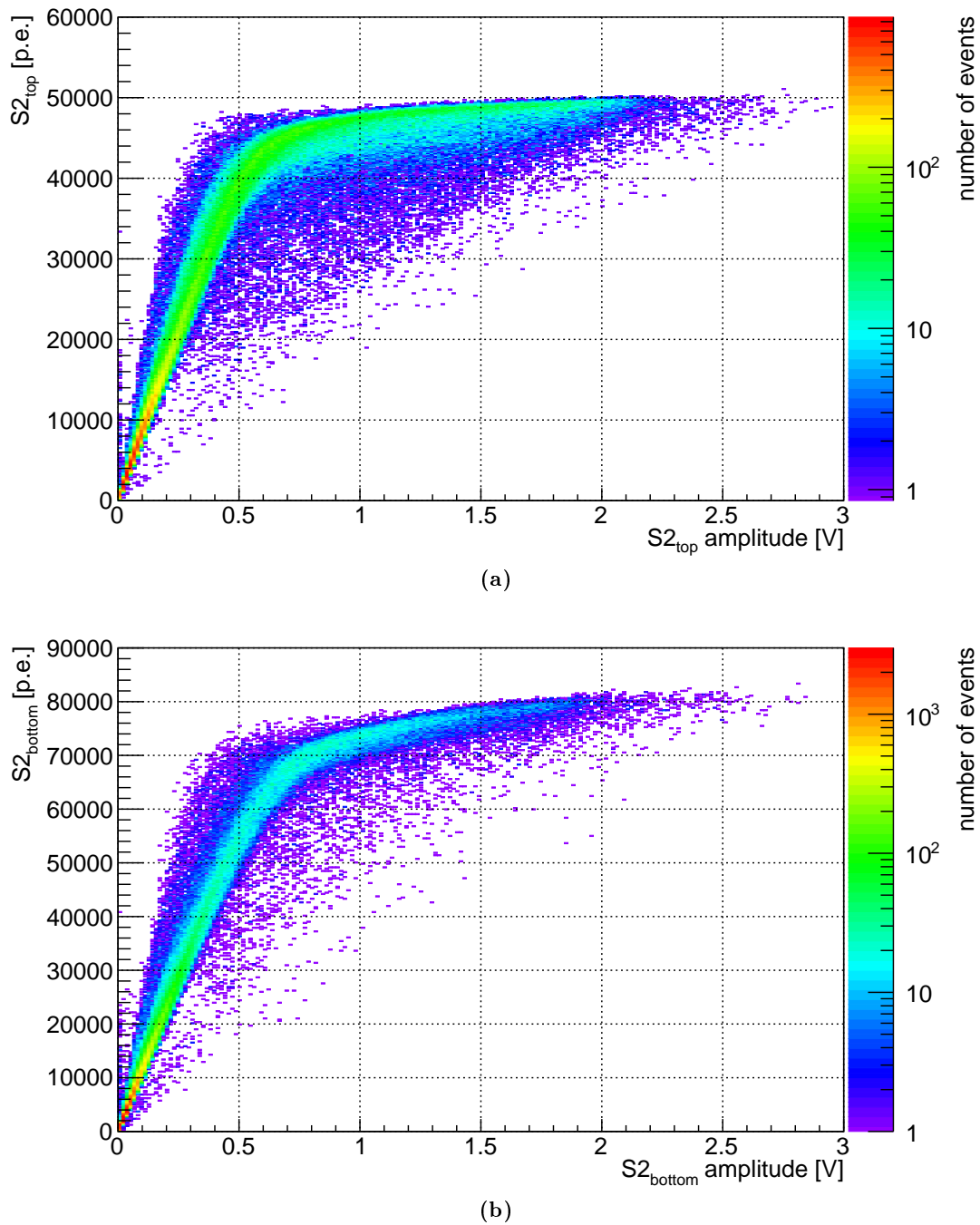


Figure 8.16: S_2 signal integral in dependence of the amplitude for a ^{137}Cs source measured with (a) Top PMT and (b) Bottom PMT for an applied drift field of 198 V/cm. The saturation in signal integral is clearly visible for both PMTs, the amplitude is not affected. Operated at different bias voltages of 1000 V for the Top PMT and 950 V for the Bottom PMT, the maximum measured signals are smaller for the Top PMT due to its higher gain.

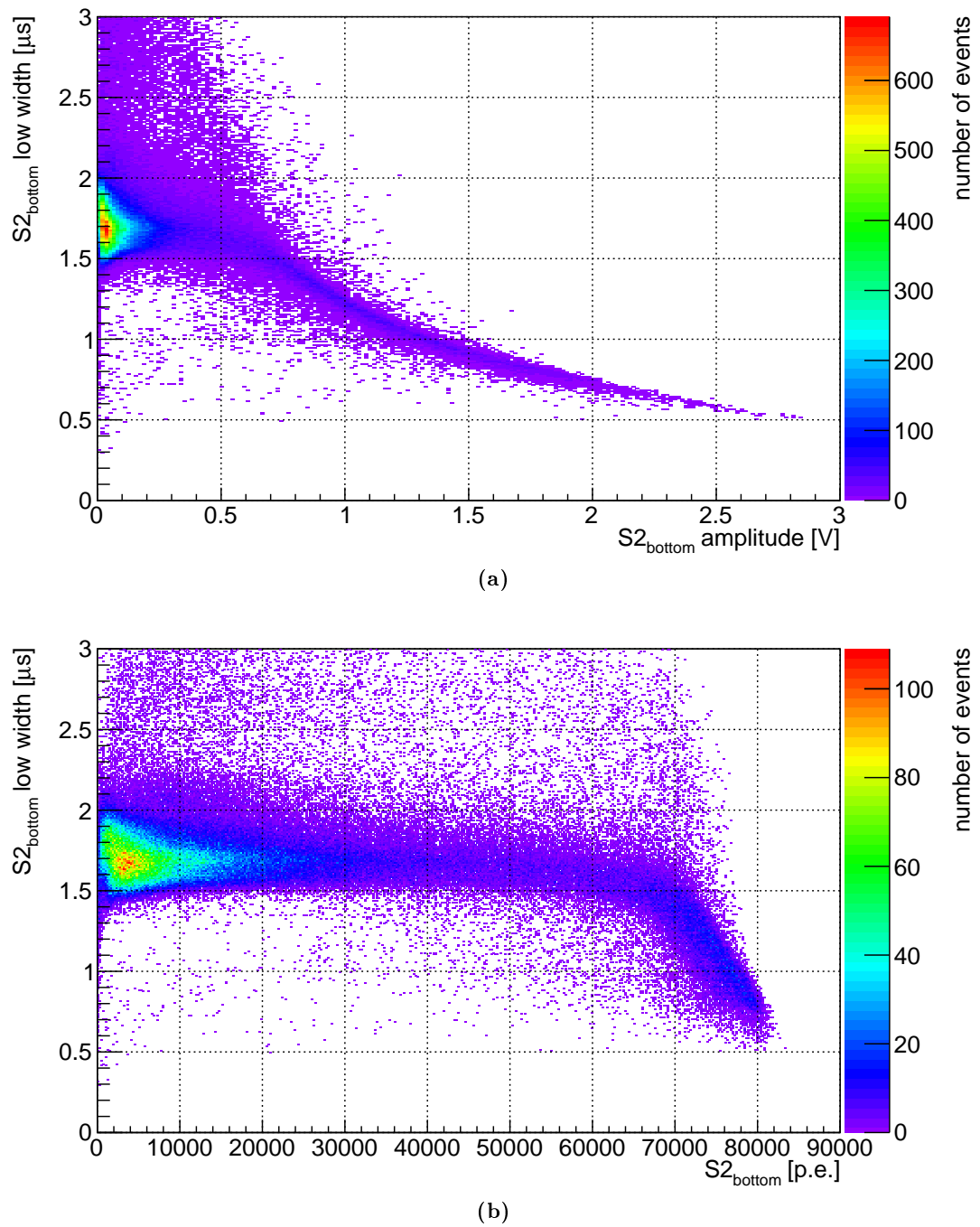


Figure 8.17: Correlation of the $S2$ low width with the $S2$ amplitude for the Bottom PMT (a): For a stable liquid level and hence a fixed gas gap between gate and anode mesh, the width is expected to be in a constant range. For larger amplitudes, a decrease in signal width is observed. The correlation of the $S2$ low width and the $S2$ integral depicted in (b) also shows a decrease of the signal width at high signal integrals.

PMT reaches a maximum integral of a little more than $8 \cdot 10^4$ p.e.

The PMT signal as such is independent of the applied drift field, therefore the data depicted in this section is only from measurements with 198 V/cm. Also, apart from the fact that the PMT gains are different, the signal response of the two PMTs is the same and hence the displayed plots for both PMTs only differ with respect to the maximum signal integral values. This is expected, since the PMTs as well as the PMT bases are identical in construction. For that reason, only the graphs for the Bottom PMT are presented in the following.

The $S2$ signal is limited with respect to the integral and not the amplitude. Also, since the plots shown in figure 8.16 are measured without PMT amplifiers on the SIS3316, which has a 5 V input range, the limited FADC input range as well as the maximum output limit of the amplifiers both do not contribute to the observed effect. The limitation of the integral, which corresponds to the measured charge signal, has to be caused either by photocathode depletion or an insufficient capacitance of the buffer capacitors in the dynode chain.

Figure 8.17 gives additional information to recognize the limiting effect. In figure 8.17a, the Bottom PMT $S2$ low width (measured at 10 % of the signal amplitude) is plotted versus the respective amplitude for the $S2$ signal. The event distribution has a particular shape. At small amplitudes, the signals have a width in the range of 1.6 to 1.8 μs . With increasing amplitude, the signal width shrinks down to a minimum value of approximately 0.5 μs . The change in width appears more distinct for amplitudes of circa 0.7 V or higher, which coincides with the kink in the integral-versus-amplitude plots above. Since the $S2$ width is proportional to the distance between the liquid-gas surface and the anode mesh, the $S2$ width is expected to be constant. Even taking into account a tilted liquid level (see chapter 7), the observed signal width may have a certain range but would not shrink as can be seen here.

In figure 8.17b, the correlation between the $S2$ width and the $S2$ integral is plotted. The width is constant over a large range of integrals but decreases for high signal integrals. The observed behaviour of the $S2$ integral, amplitude and width indicate that the saturation is caused by insufficient buffer capacitances in the dynode resistor chain. This conclusion is based on the fact, that the signal integral and therefore the measured charge has a maximum value, but not the signal amplitude. Furthermore, the decrease of the signal width for large signals can be explained by the fact that the buffer capacitors reach their maximum capacitance earlier for larger signals. The result is a smaller signal width paired with a large integral and amplitude.

At the time of the composition of this thesis, preliminary PMT tests have confirmed that replacing the buffer capacitances in the dynode resistor chain with higher capacitances improves the PMT performance and more detailed studies are planned to revise the PMT base design.

Compton Scattering

Chapter 9

9.1 | Introductory Remarks

The experimental setup of the MainzTPC, being the prototype version of this detector, was employed for test measurements already in 2015. The Compton data acquired at the HZDR in April 2016, after updating the DAQ system to version 2, represents the cleanest data set of the MainzTPC up-to-date, with respect to thermodynamic stability of the system. This holds especially true for the liquid level in the TPC between gate and anode mesh, which showed oscillations in measurements conducted before and after the science runs at the HZDR [3] and are still investigated in Mainz.

Also the analysis tools were still under development at the time of the experimental run, and most of the techniques presented in this thesis were not in an employable condition yet. Therefore, data cross-checks during the acquisition did not reveal the critical aspects that limit the informative value of the recorded data.

The findings discussed in this chapter present the current state of the MainzTPC detector performance and the corresponding analysis. Three factors which have a significant impact on the results are the following:

- The TPC calibration measurements do not show event distributions which can be linked to the energy lines of the respective gamma-ray sources. This is probably caused by an ineffective trigger setup for this measurement type. Without recognizable spectral lines the determination of a conversion of the energy deposit E_{TPC} to the respective amount of generated scintillation photons is prevented. This is discussed in more detail in section 9.4. Therefore the light yield discussed in section 9.6 can only be examined with regard to the amount of photoelectrons detected by the TPC PMTs.
- The TPC PMTs show saturation effects for large signals (see section 8.5). $S2$ signals in the range of $120 \cdot 10^3$ p.e. are the largest values obtained. At different drift fields, this amount of light for $S2$ can already be reached at low values for $S1$ below 1000 p.e., limiting the validity of the $S2$ signal information. This also has an impact on the viability of the TPC calibration measurements.
- Electronic noise limits the $S1$ signal detection in the low-energy regime, as discussed in section 9.5. This affects the light yield determination as it limits the data to values above a certain threshold. As a result, the expected behaviour of the light yield for small E_{TPC} can not be observed.

As these factors were not resolved by the time of the compilation of this thesis, most of the subsequently presented results can only be discussed qualitatively. A hardware update of the MainzTPC is necessary to deal with these difficulties.

9.2 | Conducted Measurements

9.2.1 | Overview of TPC Calibration Measurements

To calibrate the TPC in the range of the measured Compton energies, gamma-ray sources with energy lines in a similar range were used such as ^{133}Ba , which emits gamma-rays with for instance 81 keV and 356 keV, or ^{152}Eu with 122 keV. Apart from this, measurements with ^{60}Co and the ^{137}Cs source used for the Compton scattering were conducted. While the former has two gamma-ray lines at around 1.1 MeV and 1.3 MeV, the second has only one line at 661.6 keV. Since these energies exceed the energy range from the Compton measurements by far, they are not suitable for a calibration in this energy regime. Table 9.1 summarizes the measurements taken in TPC calibration mode (with the DAQ set to a TPC PMT coincidence trigger) and the number of events acquired for each source and drift field configuration. Note that the acquired events are stated before applying the event selection.

source	$E_{\text{drift}} \left[\frac{\text{V}}{\text{cm}} \right]$		
	198	594	792
^{60}Co	10^5	–	–
^{133}Ba	10^5	10^5	10^5
^{137}Cs	10^5	10^5	–
^{152}Eu	$12 \cdot 10^5$	$4 \cdot 10^5$	$4 \cdot 10^5$

Table 9.1: List of TPC calibration measurements with the respective number of events acquired. The high statistics for the ^{152}Eu are motivated by the suitable peak energy as well as the measurements at different source position for the test of the position reconstruction. Since the energy lines of ^{60}Co are very high-energetic, only one measurement with a field was conducted for potential comparisons.

Due to time limitations during the experimental run only three drift field strengths were applied in the calibration measurements, compared to four different configurations in the Compton measurements (see section 9.2.2). The ^{60}Co source, being identified as not directly suitable for calibration, was only measured for one field.

The higher statistics acquired for the ^{152}Eu are motivated by its main energy line being at around 122 keV, which should be energetic enough to reach the active volume inside the TPC and is also in the same order of magnitude as the energy deposits expected from the Compton scattering. The increased number of events should ensure sufficient statistics. Furthermore, this source was used to test the position reconstruction with the APDs (see chapter 6), and for this, three measurements of $4 \cdot 10^5$ events each were conducted with the ^{152}Eu placed on different sides of the MainzTPC cryostat at a drift field of 198 V/cm.

Table 9.2 lists the overall event rates for the individual calibration measurements. The event rates found for the three low-activity calibration sources ^{133}Ba , ^{152}Eu , and ^{60}Co range roughly between 100 and 320 Hz. The uncertainty for the calculated event rates

is of the order of only a few Hz. In case of ^{133}Ba and ^{152}Eu , which were measured with different drift fields, the rate remains almost constant for each source. The change of event rate with exchanged calibration sources indicates that the acquired data is caused by the gamma-rays from the respective source. Another sign that gamma-rays from the different sources are measured in the TPC is the spatial event distribution examined in chapter 6 about the position reconstruction.

For the experimental run, there was no background measurement which would allow to subtract the background spectrum from the different source spectra to obtain the actual gamma-ray source rates.

sources	E_γ [keV]	E_{drift} [$\frac{\text{V}}{\text{cm}}$]		
		198	594	792
^{60}Co	1173 (99.85 %), 1332 (99.98 %)	114.0	–	–
^{133}Ba	356 (62.05 %)	211.0	212.8	215.1
^{137}Cs	661.6 (85.10 %)	416.7	610.0	–
^{152}Eu	122 (28.53 %)	299.7	322.1	315.0

Table 9.2: Gamma-ray energies and event rates in the MainzTPC from the calibration measurements with different gamma-ray sources at different drift field strengths. The values for the gamma-ray energies and their branching ratios are taken from [60]. The ^{137}Cs source exceeds the other sources in terms of event rate due to its higher activity. The three other sources were small calibration sources with low, unknown activities. A comparison to the signal background could not be performed with the data at hand.

The ^{137}Cs source shows a different behaviour. Being the strongest source used for the calibration with nominal 37 MBq of activity, the event rates for ^{137}Cs measurements exceed the ones from the other sources significantly, with uncertainties up to 20 Hz. Furthermore, a change in event rate can be observed. This can be explained by the fact that for each drift field configuration, a measurement of all calibration sources was conducted, and therefore the ^{137}Cs had to be removed from the collimator to measure the other sources and reinstalled afterwards. Due to its high activity, even small deviations from its prior positioning inside the collimator can have an impact on the event rate in the TPC.

9.2.2 Overview of Compton Measurements

In the course of the MainzTPC Run in April 2016, a series of Compton scattering measurements was conducted. Table 9.3 summarizes the amount of acquired events for the measurements with regard to the drift field strength applied for the respective measurements at different nominal scattering angles. As described in section 3.5.2, the latter is a rough measure for the expected energy range depending on the positioning of the germanium detector. Note that the acquired events are stated before applying the event selection.

α_{nom} [°] \backslash $E_{\text{drift}}^{\text{nom}}$ [$\frac{\text{V}}{\text{cm}}$]	198	396	594	792
10 (0 – 40 keV)	$5 \cdot 10^4$	–	$2 \cdot 10^5$	–
15 (4 – 55 keV)	$1.5 \cdot 10^5$	$5 \cdot 10^4$	$1.9 \cdot 10^5$	$9.8 \cdot 10^4$
22.5 (9 – 90 keV)	10^5	–	–	–
30 (29 – 140 keV)	10^5	–	10^5	–
sum	$4 \cdot 10^5$	$4 \cdot 10^5$	$5 \cdot 10^4$	$9.8 \cdot 10^4$

Table 9.3: Compton measurement configurations with respect to nominal scattering angles (with the ranges for the expected energy deposit) and to the applied drift field strengths. Due to limited time for the measurements, the focus was set to two of the four drift field strengths.

The extraction field with an applied voltage of 3 kV for all measurements is not sufficiently strong to reach an extraction efficiency of 100 %, as is shown in section 7.4. The values for the electric fields were chosen to maintain a stable field configuration throughout the measurements, as tests with higher drift and extraction fields in previous runs (November/December 2015 and March 2016) led to tripping of the high voltage supply modules.

The distribution of the measurement time was chosen to have data for four different drift field strengths, but to also acquire sufficient statistics across various scattering angles for at least two field configurations, namely at 198 V/cm and 594 V/cm, with $4 \cdot 10^5$ and $4.9 \cdot 10^5$ recorded events, respectively. Because of their higher statistics, primarily the data sets of these two field configurations are used in case of example figures.

During the run, no zero-field Compton measurement was conducted. In retrospect, a zero-field measurement would have been desirable to get a normalization value for the determination of the light yield and the field quenching effect.

The observed mean event rate for Compton measurements (TPC and germanium coincidence) ranged between 5 and 10 Hz. This value changes in dependence of the precise source placement and orientation in the collimator, which can differ slightly. To make the source placement more reproducible, it could be mounted on a fixed holder that then is inserted to the collimator, constraining the positioning on the built-in cavity.

9.3 | Event Selection

9.3.1 | Fiducialization of the Active LXe Volume

The interaction point of a particle scattering in the TPC can be reconstructed in 3D using the centroid method on the $S2$ signal described in chapter 6 for x and y and the time difference between $S1$ and $S2$ signal together with the electron drift time determined in section 8.1 for the z -coordinate. This information is viable to define a fiducial volume inside the active LXe volume of the TPC.

Considering the determination of the z -correction function for $S1$ in section 8.3, the radius of the fiducial volume was chosen to be 15 mm around the TPC center.

The constraints of the interaction depth have to be distinguished for the individual measurement types: For the TPC calibration measurements the interaction depth can vary between the gate mesh and the cathode mesh, since the calibration is (mostly) carried out with uncollimated gamma-ray sources. The result is a largely uniform event distribution in z , as is shown in figure 9.1a. In case of the Compton measurements, the strong ^{137}Cs source is placed in the collimator and only illuminates a small fraction of the TPC height, as is shown in figure 9.1b. As only a part of the TPC height is illuminated by the source, the interaction depth can be constraint. For Compton measurements, the fiducial volume is limited to events in the interval $20\text{ mm} \leq z \leq 47.5\text{ mm}$.

The parameters for the fiducial volume are summarized in table 9.4.

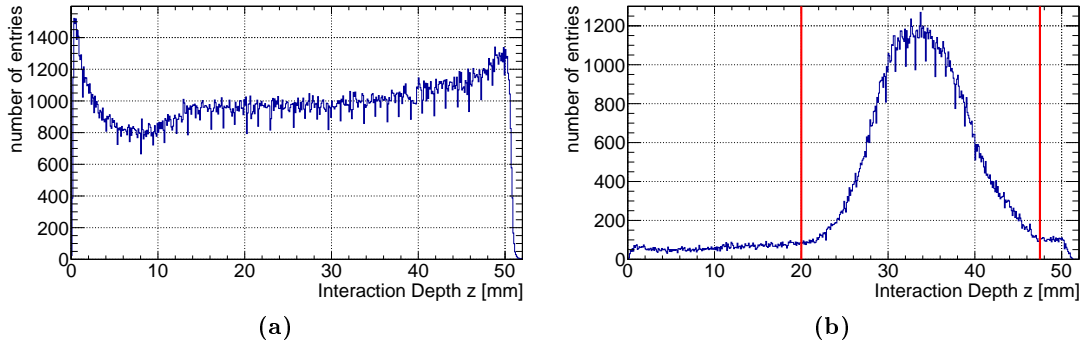


Figure 9.1: Comparison of the event distribution with respect to the interaction depth z in the TPC for (a) an uncollimated gamma-ray source as used in the TPC calibration measurements, here ^{152}Eu , and (b) a collimated ^{137}Cs source from the Compton measurements. The latter allows to define a smaller height interval for the fiducial volume, as indicated with the red vertical lines.

	radius [mm]	interaction depth [mm]
TPC Calibration	15	$0 \geq z \geq 50.5$
Compton	15	$20 \geq z \geq 47.5$

Table 9.4: Parameters for the fiducial volume.

9.3.2 | *S1* as Trigger Signal

The measured waveforms for the PMT signals can contain quite large numbers of *S1* signals, as small noise or background events are also identified as such by the Raw Data Analysis program. To determine the *S1* signal responsible for the DAQ trigger, the timing positions of all *S1* signals of all events for a specific measurement configuration are summed in a histogram as shown in figure 9.2.

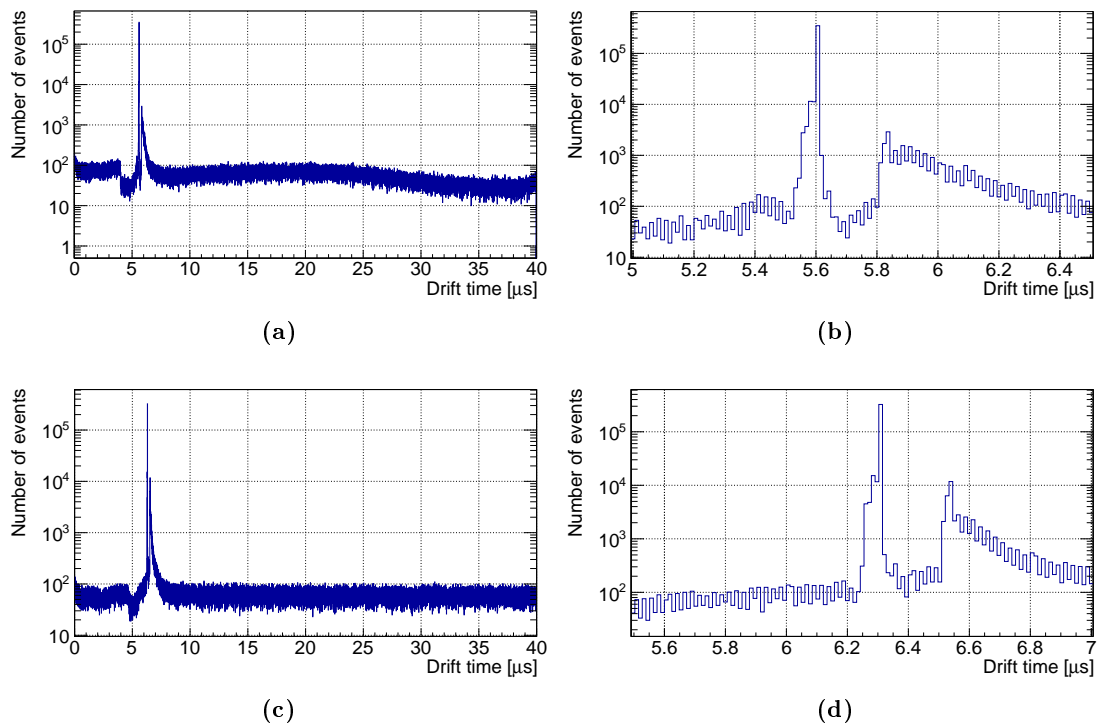


Figure 9.2: Timing position of the *S1* signal in the waveform for the Compton measurement in the upper row and a calibration measurement in the bottom row. As can be seen in figure (a), a significant peak can be found at 5.6 μs compared to the overall distribution. This particular position arises from the delayed *S1* signal in the Compton setup. The width of the signal peak, shown in a zoom-in in (b), motivates the length of the *S1* trigger window of 240 ns. For the calibration measurement below, the position distribution is similar but shifted to a higher value in time. This is due to the difference of the trigger configuration, which is set to TPC-only mode for the calibrations.

The upper row shows the $S1$ timing distribution for a Compton measurement, while the bottom row depicts the distribution for a calibration measurement. Dependent on the measurement type, a prominent peak in the number of $S1$ signals can be found at a specific time which corresponds to the pretrigger time defined in the DAQ system subtracted by the amount of time necessary for the signal processing. A time window of 240 ns is defined around this peak.

The decision to use the $S1$ signal as the trigger for the MainzTPC emerged from the fact that it is (almost) coincident with the signal in the germanium detector in the Compton scattering measurements. The DAQ system was developed with this specific measurement type as priority. Therefore, the $S1$ was used as the trigger signal also for the TPC calibration measurements. In retrospect, the $S2$ signal is more suitable to use as a trigger – at least for the TPC calibration measurements – considering the signal noise on the PMT channels which define the minimum detectable signal. Also, the larger $S2$ signals allow an easier setting for the signal thresholds.

9.3.3 | $S1$ in Dependence of E_{TPC} for the Compton Measurements

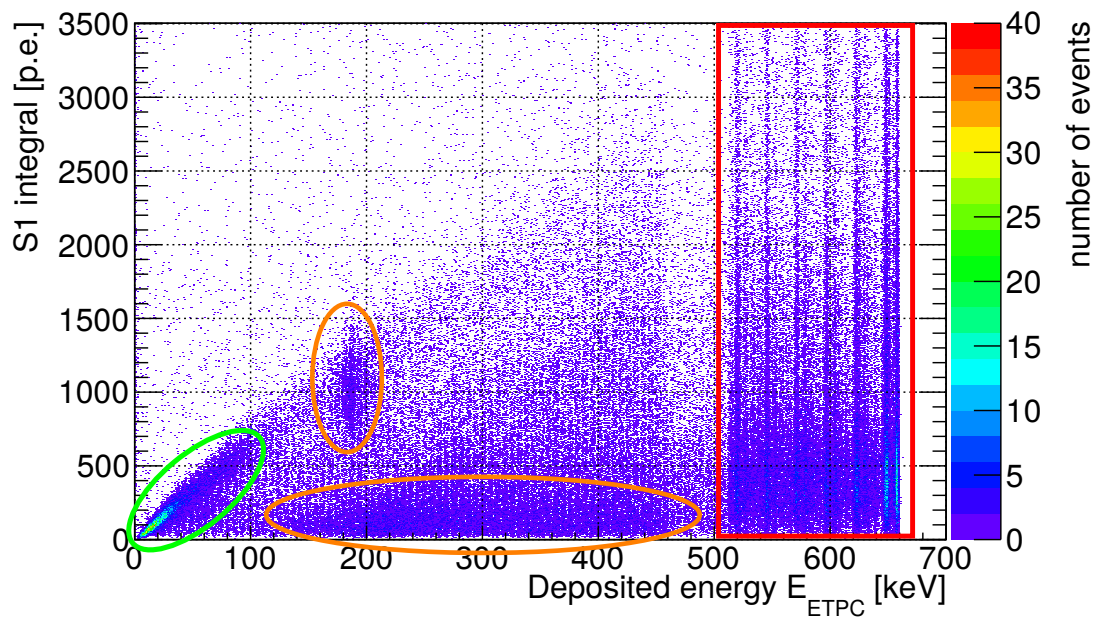
Table 9.3 in section 9.2.2 shows the number of all measured events for the different configurations. For the actual analysis, only a fraction of these events can be used. The event distribution of the $S1$ signals in dependence of the deposited energy E_{TPC} illustrates this in figure 9.3a. The data is taken from a Compton measurement at 198 V/cm. Since the gamma-ray source used for the Compton scattering is ^{137}Cs , the maximum value for E_{TPC} is found at 661.6 keV.

Four different event clusters can be distinguished, of which only one contains the sought-after events. The linear distribution in the lower left corner (green) marks the Compton scattering events. For these events there is a clear correlation between deposited energy and measured scintillation light. The majority is found for energies below around 50 keV. Due to statistics, only this lower regime could be analyzed.

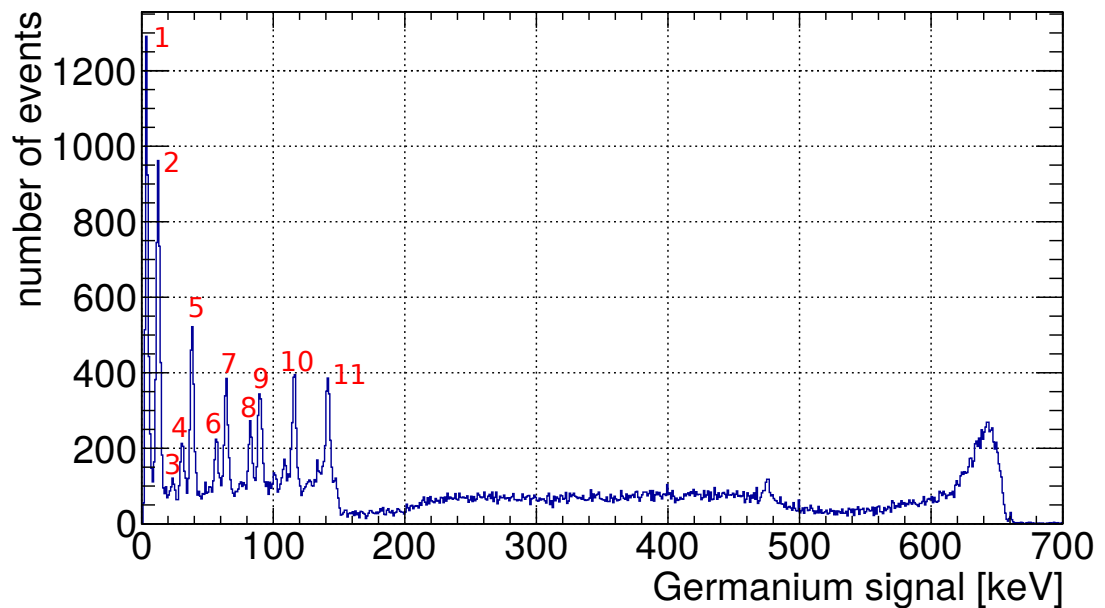
The upper orange ellipse points out the events that are caused by the gamma-rays scattering back in the germanium and then hitting the TPC. The observed energy deposit corresponds to 184 keV which is equivalent to the Compton edge for the 661.6 keV photon of the ^{137}Cs source. The lower orange ellipse marks the event cumulation of Compton events with the scattered photon not being fully absorbed in the germanium detector.

The origin of the vertical event clusters in the red-marked area at higher E_{TPC} (lower energies detected in the germanium detector) have not been identified. Since the plot represents the data from several measurements at the same drift field strength of 198 V/cm, the lines might be connected to different settings for the lower threshold for the germanium detector adjusted between the measurements. The fact that this leads to line structures for specific energies can not be accounted for, as there were no additional gamma-ray sources present.

Figure 9.3b shows the corresponding spectrum for the energy measured in the germanium detector for this Compton measurements. The unidentified signals at large E_{TPC}



(a)



(b)

Figure 9.3: $S1$ signals in dependence of the energy deposit E_{TPC} for a Compton measurement at 198 V/cm (a). The events marked in green are the Compton events. The upper orange region marks the back scatter events at the Compton edge while the lower orange region depicts Compton events with the scattered photon not being fully absorbed in the germanium. The events located in the red marked region on the right probably emerge from chance coincidences of the TPC with background in the germanium. The origin of these events could not be identified. In (b), the corresponding energy spectrum for the germanium detector used to determine the energy deposit is depicted. Besides the unknown peaks at low energies, the Compton edge is visible at roughly 480 keV and the events from the Compton measurement are found in the peak structure at the high-energy end of the spectrum.

are found at low values for the germanium signal. Using a Gaussian fit, eleven peaks in the low-energy range are fitted and listed in table 9.5. The table also lists possible candidates of gamma-ray sources emitting the observed energies. Some of these might be remains from previous measurements in the neutron facility nELBE where the data was acquired. Only isotopes with half-lives in the order of years were taken into account. Still, for some peaks no corresponding energy line can be found.

Besides this, a potential residual radioactivity in the facility is not expected to have such a predominant impact on the germanium spectrum and therefore does not conclusively explain the unknown energy peaks. In the background spectrum for this germanium detector as measured in [80], only peaks above 70 keV are present, and of these only one at 89.8 keV ($K_{\beta,1}$, Bi) has an energy corresponding to the peaks found here.

Peak	μ_{Peak} [keV]	σ_{Peak} [keV]	Isotope	Energy [keV]
1	4.01	1.07	–	–
2	12.54	1.73	^{228}Ra	13.52
3	23.22	3.50	^{172}Hf	23.93
4	30.98	2.24	^{93m}Nb	30.77
5	38.33	1.81	^{239}Pu	38.66
6	56.83	2.35	^{232}U , ^{252}Cf	57.78, 56.0
7	64.20	2.05	^{126}Sn	64.28
8	82.88	2.53	^{252}Cf	84.4
9	89.90	2.12	^{252}Cf , ^{248}Cm , ^{99}Tc	94.9, 94.9, 89.5
10	115.98	2.62	^{252}Cf	117.1, 117.7
11	141.47	2.83	^{248}Cm , ^{252}Cf	141.8, 141.1

Table 9.5: Fit values for the unknown energy peaks in the germanium spectrum for the Compton measurement at 198 V/cm. The Gaussian mean and standard deviation are stated for each distinctive peak in the low-energy region. For comparison, long-lived isotopes with similar gamma-ray energies are stated in the two right columns. The isotope data is taken from [60].

Limiting the region of interest to events with an energy deposit of $5 \text{ keV} \leq E_{\text{TPC}} \leq 100 \text{ keV}$ leads to significantly lower statistics. For the different measurement configurations, the event numbers used for analysis are summarized in table 9.6.

E_{drift} [$\frac{\text{V}}{\text{cm}}$]	198	396	594	792
number of events	20348	5155	26623	9644

Table 9.6: Number of events for different Compton measurement configurations with respect to the applied drift field strengths for an energy deposit E_{TPC} limited to the range between 5 and 100 keV.

Figure 9.4 shows the Compton data used for the subsequent analysis. Since the events are found mostly for lower energies and the statistics become lower at higher energies, the choices to limit the examinations to small energy intervals as described in later sections is comprehensible.

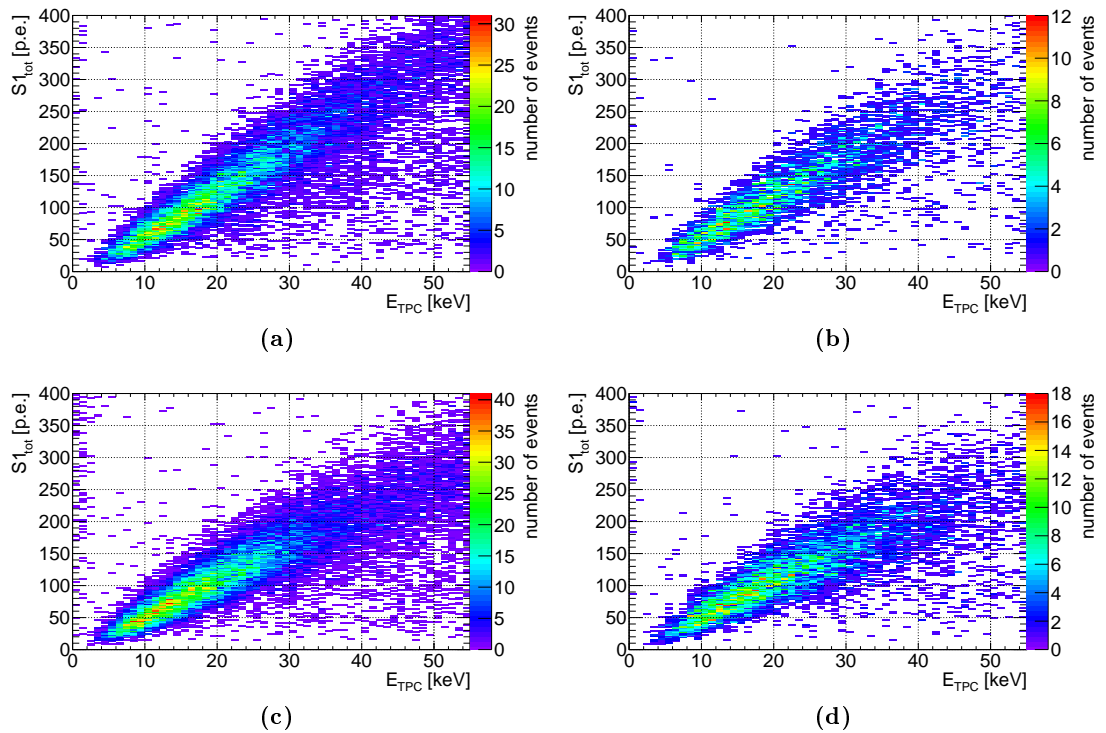


Figure 9.4: Primary scintillation signal $S1$ in dependence of the energy deposit E_{TPC} from a Compton measurement at drift field strengths of (a) 198 V/cm, (b) 396 V/cm, (c) 594 V/cm and (d) 792 V/cm.

To increase the fraction of actual Compton events in future measurements, several improvements could be applied. First, the trigger threshold for the germanium detector should be set to a much higher value, ensuring that only events with a large gamma-ray energy absorbed in the germanium are recorded. Choosing a value above 550 keV for the germanium trigger threshold would mean that only events with $E_{\text{TPC}} \leq 111.6$ keV were considered for the coincidence trigger condition. The events found in the orange and red regions would not be recorded at all. Second, using a larger germanium detector would increase the amount of fully absorbed gamma-rays and hence shift at least a fraction of events from the lower orange region to the green region of the Compton events, further increasing the statistics.

9.3.4 | $S1$ Top-Bottom Asymmetry in z

As mentioned in section 8.3 there is an asymmetry between $S1$ signals received on the Top and the Bottom PMT. It emerges on the one hand from the fact that the Top PMT is in the gaseous xenon phase and part of the scintillation directed upwards therefore will undergo internal reflection, which leads to a general reduction in $S1$ on the Top PMT.

On the other hand, the interaction depth z has a varying impact on the asymmetry between the Top and Bottom PMT.

The asymmetry can be expressed as the ratio of the two PMT signals, as stated in equation (9.1).

$$A_{S1} = \frac{S1_{\text{top}}}{S1_{\text{bottom}}} \quad (9.1)$$

Other definitions of the asymmetry such as the fraction of Top PMT signal to the summed signal are also possible.

Figure 9.5a shows the asymmetry A_{S1} for a calibration measurement at 198 V/cm with an uncollimated ^{152}Eu source. The TPC is illuminated over its complete height. The found asymmetry values form a bar-shaped distribution which decreases with increasing interaction depth. The figure shows both the asymmetry for the $S1$ signals (black) and the corrected $cS1$ signals. As expected, there is almost no deviation as the correction is cancelled out by the division in equation (9.1).

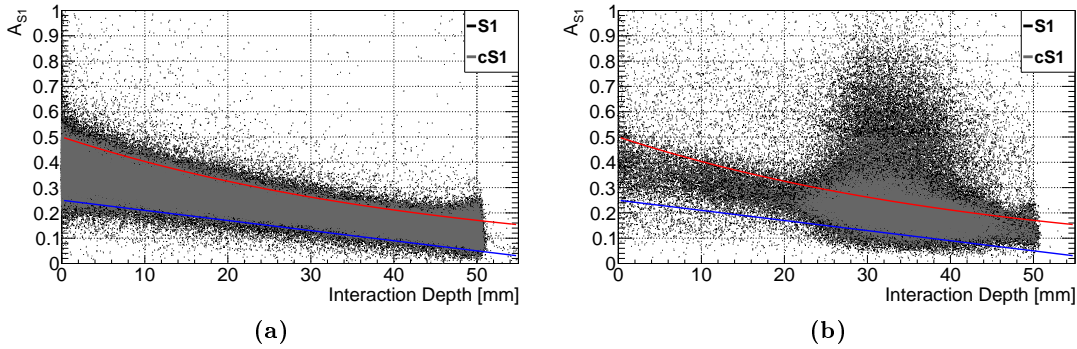


Figure 9.5: $S1$ asymmetry for a calibration (a) and a Compton measurement (b) at 198 V/cm. The asymmetry for $S1$ is shown in black, for corrected signals $cS1$ the ratio is overlaid in grey. Since the z -correction is applied to both Top and Bottom PMT signal, there are only small deviations in the event distribution and the limits depicted by the red and blue line are applicable for $S1$ and $cS1$.

The asymmetry distribution allows to define minimum and maximum limits for $A_{S1}(z)$, which then are valid for both corrected and uncorrected signals, using the functions from equation (9.2). For comparison, the same limits are applied to the asymmetry calculated for a Compton measurement at 198 V/cm in figure 9.5b. The collimation of the ^{137}Cs source leads to the observed event distribution localized in the lower central region of the TPC.

$$A_{S1,\text{max}}(z) = 0.5 \cdot \exp\left(-\frac{2.15 \cdot 10^{-2}}{\text{mm}} \cdot z\right) \quad (9.2)$$

$$A_{S1,\text{min}}(z) = 0.25 - \frac{4 \cdot 10^{-3}}{\text{mm}} \cdot z$$

The asymmetry, being a ratio of the two $S1$ signals from the PMTs, is not affected by the applied drift field. The asymmetry distributions for the higher drift fields at 396 V/cm,

594 V/cm and 792 V/cm were also plotted and overlaid with the functions defined in equation (9.2), showing the same behaviour as in figure B.20. The corresponding plots can be found in appendix B.6.

9.3.5 Multiple $S2$ Signals per Waveform

Ideally, the recorded waveforms should not contain more than one $S1$ peak, which also triggered the acquisition, and one $S2$ peak. In the data at hand, most waveforms contain more than one $S2$ signal (see table 9.7). Events with several large $S2$ signals are unusable for the analysis since it is not possible to tell which $S2$ signal belongs to the triggering $S1$. The disadvantage of restricting the event selection to only one $S1$ and $S2$ signal is the loss of statistics for the analysis. To demonstrate this, table 9.7 lists the fraction of events passing different event selection configurations.

	event selection configuration	%	E_{drift} [V/cm]			
			198	396	594	792
0	–	100.0	403186	50215	486139	98072
1	only one $S1$ & only one $S2$	11.9	47117	6739	47440	12473
2	one $S1$ in trigger window & only one $S2$	26.5	98147	14363	112740	29409
3	one $S1$ in trigger window & largest $S2$	54.2	222766	29305	215175	57779
4	configuration 3 with cuts on second $S2$	43.3	177826	23480	175012	45510

Table 9.7: Fraction and numbers of accepted events for different event selection configurations. The fractions are calculated as a mean of the fractions determined by analyzing different Compton data sets for a given selection configuration.

For the ideal case of only one $S1$ and one $S2$ signal per event waveform, the fraction of accepted events becomes 11.9 %. Most events contain noise peaks that are identified as $S1$ signals or even secondary $S2$ peaks. To study the effect of loosening the selection criteria, two additional selections were also examined.

The second configuration allows only one $S2$ signal and multiple $S1$ peaks. An additional condition is that only one $S1$ signal is found in the trigger window. The window is chosen to have a width of 30 samples, which corresponds to 240 ns. Not limiting the number of $S1$ signals increases the mean fraction of accepted events to 26.5 %.

In an attempt to include some additional data for the analysis, a third selection configuration was tested allowing one $S1$ signal in the trigger window and multiple $S2$ signals, leading to an acceptance of 54.2 % of the acquired events for the analysis. The remaining 45.8 % consist of events with more than one $S1$ signal in the trigger window. As an additional event selection criterion, the germanium signal – contributing to the coincidence trigger in the Compton measurement – is checked to only select events with exactly one signal occurring in the germanium detector. By this, multiple Compton scattering events, however unlikely, are sorted out. This is done to avoid signal pile-ups

in the germanium and therefore miscalculations of the energy deposit E_{TPC} due to the slow decrease of the step-like signal.

As described in section 2.2.2, the energy deposit of the scattered gamma-rays in the LXe is calculated according to equation (2.4):

$$E_{\text{TPC}} = \Delta E = E_0 - E'$$

All Compton measurements were conducted using a ^{137}Cs source with a gamma-ray energy of $E_0 = 661.6 \text{ keV}$. The energy E' measured with the germanium detector emerges from the measured voltage signal after applying the calibration function from section 5.2. In the following, instead of the germanium signal the deposited energy E_{TPC} is used for plots and analysis.

Figure 9.6 shows the summed $S1$ signal for both TPC PMTs plotted in dependence of

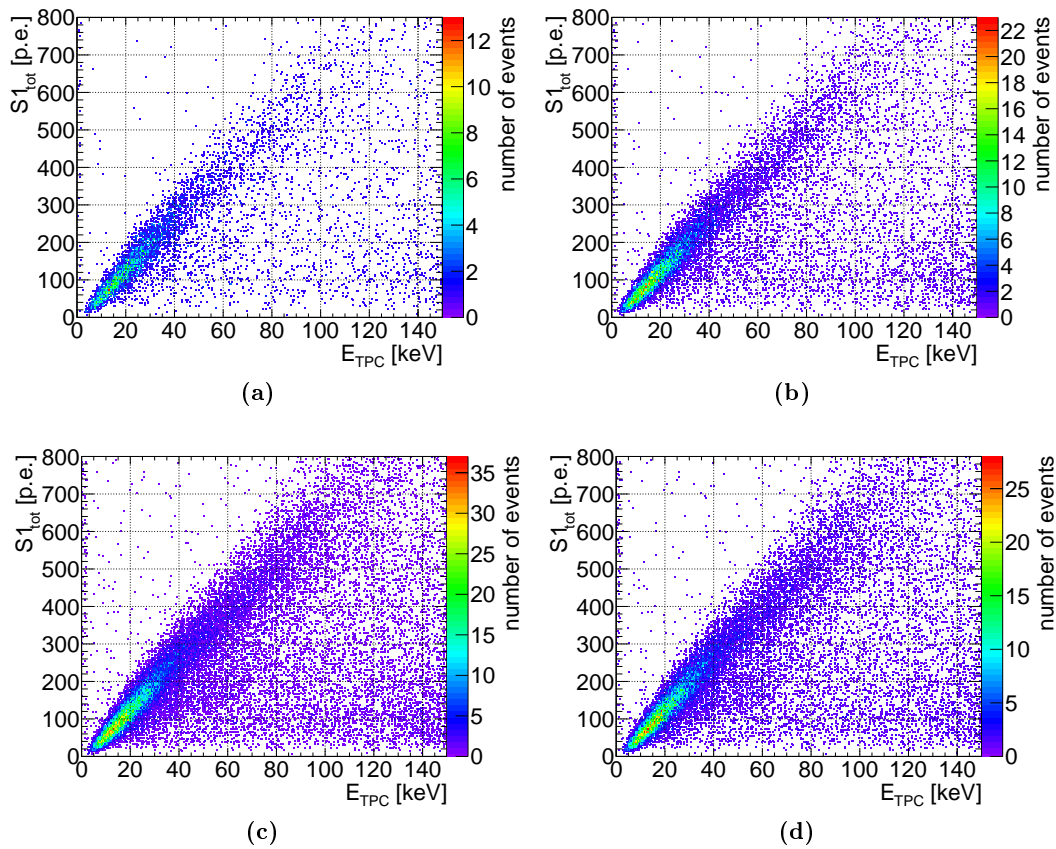


Figure 9.6: Comparison of different event selection configurations considering exemplarily the $S1$ signal in dependence of the energy deposit E_{TPC} . Configuration 1 is shown in (a), 2 in (b), 3 in (c) and 4 in (d), as stated in table 9.7. The shape of the signal distribution does not change significantly for the different configurations. For the less restrictive configurations, the distribution becomes broader and the statistics increase, as can be also seen from the range of the z -axis.

the energy deposit E_{TPC} .

As can be seen, the shape of the event distribution does not change for the different selection configurations, but the event statistics increases significantly by changing from the strictest configuration in figure 9.6a to the third and least restrictive in figure 9.6c. This led to the final event selection configuration for the analysis carried out in this thesis, which is shown in figure 9.6d and originates from configuration 3 by adding two additional selection conditions described below.

Besides the unchanged event distributions shown above, two further arguments support this decision:

1. In general, the largest $S2$ signal per event exceeds the second largest $S2$ signal by a factor of about 10 considering its peak integral. This can be seen in figure 9.7, which shows the second largest $S2$ versus the largest $S2$ signals on the left and their ratio in the plot on the right. Events with a ratio larger than 0.2 are excluded from the analysis. Note that figure 9.7a exhibits signal distributions that hint to different populations for the $S2$ signal. This effect is analyzed closer in section 9.7.3.
2. The majority of the largest $S2$ signals occur as the first $S2$ signals observed in the event waveforms and can therefore be associated with the triggering $S1$ signal. As is shown in section 9.3.6 (figure 9.8), only for a small fraction of less than 8 % of events the largest $S2$ signal is not the first occurring $S2$ in the waveform. For the analysis, only events with the largest $S2$ being the first $S2$ signal in the waveform are considered.

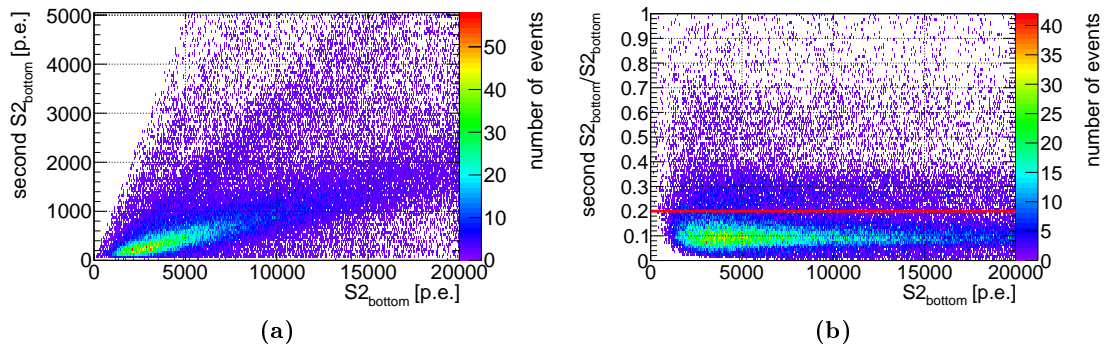


Figure 9.7: Examination of events containing more than one $S2$ signal: (a) shows the integral of the second largest $S2$ signal in dependence of the integral value of the largest $S2$ signal for each event in a Compton measurement with a drift field of 198 V/cm. The plot contains the signals from the Bottom PMT, which is chosen as representative for both TPC PMTs. In (b), the integral ratio of the second largest $S2$ and the largest $S2$ is plotted versus the largest $S2$ integral. The majority of events contains additional $S2$ signals which have an integral of about 10-20% of the largest $S2$ signal. The red line indicates the cut limit of 20% for events with more than one $S2$ signal.

9.3.6 Spatial Resolution of Double Scatters in z

The event selection does not allow multiple $S1$ signals in the trigger time window. The generation of more than one $S2$ signal could be due to multiple scatters or chance coincidences in the active LXe volume. The $S1$ signals of these interactions can not be separated with the timing resolution of the DAQ system, but the electron drift time for two events at different interaction depths z can be examined to find the minimum distance in z for two events to be distinguishable.

$$z_{\text{diff}} = z_{\text{second largest } S2} - z_{\text{largest } S2}$$

In figure 9.8a the difference in interaction depth z between the largest and the second largest $S2$ signal for each event with more than one $S2$ is plotted for a Compton measurement at 198 V/cm.

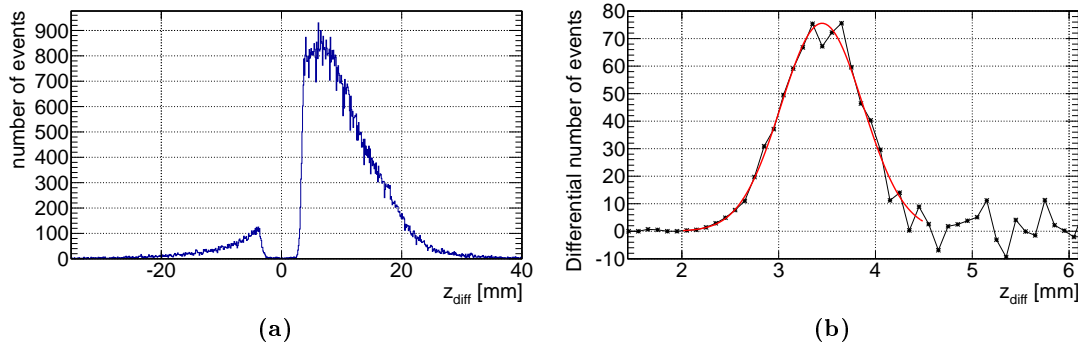


Figure 9.8: Difference z_{diff} between the interaction depths of the largest and second largest $S2$ signals in Compton events for a drift field of 198 V/cm. The distribution of z_{diff} in (a) shows that most of the largest $S2$ signals are the first charge signals occurring in the event waveforms. The gap around zero corresponds to minimum value of z_{diff} which is necessary to distinguish the $S2$ signals. The distribution is axis-symmetric, therefore a differential filter applied to either side (here positive) results in a peak at the rising edge of the distribution, shown in (b). The Gaussian fit of the peak position yields the minimum distance in d_z between to interactions in the active volume.

A distribution with values smaller and larger than zero is visible, with an imbalance in numbers of events for the negative and positive part of the distribution. Most of the observed second largest $S2$ signals are found at a later time position in the waveforms, which corresponds to larger z values¹. The distribution of the largest $S2$ in z is shown in figure 9.33 in section 9.6.3.

The distribution of z_{diff} has a particular gap around zero, with a sharp rising edge indicating the minimal distance d_z between to interaction points in z to be distinguishable.

¹The interaction depth z is defined as the absolute distance between the gate mesh and the interaction point. In cartesian coordinates, the positive direction of the z -vector points from the gate mesh downwards to the cathode mesh. See also section 8.2.

To find this minimum value d_z , a differential filter is applied to the distribution of z_{diff} in the same way as described in section 8.1 for finding the maximum drift time. The differentially filtered distribution is shown in figure 9.8b and yields a peak where z_{diff} is changing substantially. Using a Gaussian fit, the peak position d_z as well as its standard deviation σ_{d_z} and their uncertainties are obtained.

Table 9.8 lists the Gaussian fit values for the z_{diff} distributions from the Compton measurements with drift field strengths of 198 V/cm (as depicted in figure 9.8), 396 V/cm, 594 V/cm and 792 V/cm. The fit value for d_z is similar for all drift fields, which is expected since the determination of the interaction depth z acts as a normalization. For comparison, the drift time differences t_d between the considered $S2$ signals for the individual drift fields are listed in the last two columns.

$E_{\text{drift}} \left[\frac{\text{V}}{\text{cm}} \right]$	d_z [mm]	Δd_z [mm]	σ_{d_z} [mm]	$\Delta \sigma_{d_z}$ [mm]	t_d [μs]	Δt_d [μs]
198	3.45	0.01	0.42	0.01	2.18	0.27
396	3.53	0.02	0.46	0.02	2.07	0.27
594	3.52	0.02	0.41	0.02	1.95	0.23
792	3.58	0.02	0.45	0.02	1.89	0.24

Table 9.8: Results for the minimum vertical distance d_z between two interactions in the MainzTPC, obtained from the filtered z_{diff} distributions from measurements with different drift field strengths using a Gaussian fit.

The mean value for d_z can be calculated to be $\bar{d}_z = (3.52 \pm 0.04)$ mm. The uncertainty is determined from the Δd_z values using error propagation. Since the peak position marks the center of the rising edge in the z_{diff} distribution in figure 9.8a, the standard deviation offers a more suitable measure for the uncertainty of the minimum distance between interaction points than the fit uncertainty of the peak position. Calculating the mean standard deviation yields (0.44 ± 0.04) mm.

The minimum distance in z for which two interactions can be distinguished is therefore determined to

$$d_z = (3.52 \pm 0.44) \text{ mm.}$$

9.3.7 Width of the $S2$ Signal as Selection Tool

The $S2$ signal width depends on the electric field in the gaseous phase of the TPC and the gap between liquid-gas interface and anode mesh. The electric field accelerates the electrons extracted from the LXe until their kinetic energy is sufficient to cause scintillation. Afterwards, the electrons are accelerated again, until they reach the anode mesh. The $S2$ width can therefore be estimated for a given TPC configuration. The $S2$ width is also dependent on the interaction depth z due to the diffusion of the electron cloud released in the interaction in the LXe.

The $S2$ width is defined in two different ways in the MainzTPC analysis: The standard

$S2$ width is equivalent to the FWHM (width at 50% of the signal amplitude). In addition, an $S2$ low width at 10% of the signal amplitude is measured.

Figure 9.9 shows the dependence of the interaction depth z for both types of $S2$ widths (top row: FWHM, bottom row: $S2$ low width) for ^{152}Eu calibration data on the left and Compton data on the right at a drift field strength of 198 V/cm.

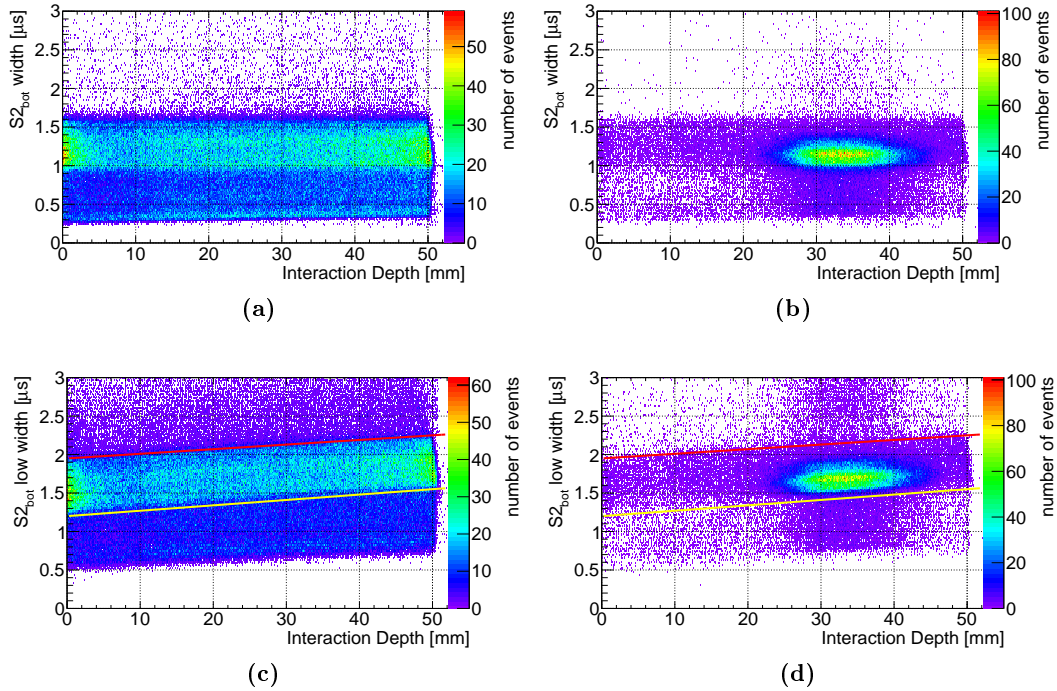


Figure 9.9: $S2$ width in dependence of the interaction depth z : For the $S2$ width at FWHM, a change with interaction depth can not be observed for either the ^{152}Eu data (a) or the Compton data (b). In contrast, the z -dependence is visible for the $S2$ low width for both ^{152}Eu data (c) and Compton data (d). For both Compton and calibration data (at the same drift field strength of 198 V/cm), the measured widths are found within the same limits. In red and yellow, an upper and lower limit on the band-shaped distribution for the $S2$ low width can be used to select events.

For the Compton data on the right, most of the events are found in an interval between 20 and 47.5 mm of interaction depth, as mentioned in section 9.3.1. The $S2$ width at FWHM shows values approximately between 1 and 1.4 μs , while the $S2$ low width values are higher with about 1.2 to 2.2 μs . This behaviour is expected from the signal shapes. In contours, an event band is visible for the Compton data in both plots, showing how the signal width changes with z . For the $S2$ width at FWHM no explicit change is visible over the complete range for the interaction depth. The $S2$ low width shows a decrease in width for lower z . Since this is equivalent with a shorter drift length, the effect of the charge diffusion in the LXe can be observed here.

The event distributions for the non-collimated calibration data from ^{152}Eu on the left

show broad bands of events which are equivalent to the bands only visible as contours on the right. In case of the calibration data, the change of $S2$ width is also only visible for the $S2$ low width.

In red and yellow, linear graphs are added to the plots for the $S2$ low width as upper ($w_{S2\text{width,max}}$) and lower ($w_{S2\text{width,min}}$) limits for the observed band-shaped structure. Their analytical functions are stated in equation (9.3) and can be used to constrain the event selection.

$$\begin{aligned} w_{S2\text{width,max}}(z) &= 0.006 \frac{\mu\text{s}}{\text{mm}} \cdot z + 1.95 \mu\text{s} \\ w_{S2\text{width,min}}(z) &= 0.007 \frac{\mu\text{s}}{\text{mm}} \cdot z + 1.20 \mu\text{s} \end{aligned} \quad (9.3)$$

Using the Compton data, a mean value for both types of $S2$ widths can be determined using a Gaussian fit. The fit results are stated in table 9.9 for all drift field configurations, with the uncertainty being the Gaussian standard deviation. The fitted distributions of the $S2$ widths are depicted in figure 9.10 for 198 V/cm, the corresponding plots for the other drift fields can be found in appendix B.7.

Regarding the $S2$ FWHM width, the obtained mean value is constant for all fields, except for a minor reduction for the highest field. A change in width can be observed

$E_{\text{drift}} \left[\frac{\text{V}}{\text{cm}} \right]$	$S2_{\text{FWHM,mean}} [\mu\text{s}]$	$\Delta S2_{\text{FWHM,mean}} [\mu\text{s}]$	$S2_{\text{low,mean}} [\mu\text{s}]$	$\Delta S2_{\text{low,mean}} [\mu\text{s}]$
198	1.15	0.13	1.71	0.13
396	1.15	0.13	1.63	0.12
594	1.15	0.13	1.60	0.13
792	1.14	0.13	1.57	0.13

Table 9.9: Results for the Gaussian fits of the $S2$ FWHM width and low width distributions. The FWHM width remains almost constant while the low width decreases with increasing drift field strength. The uncertainty is given by the Gaussian standard deviation.

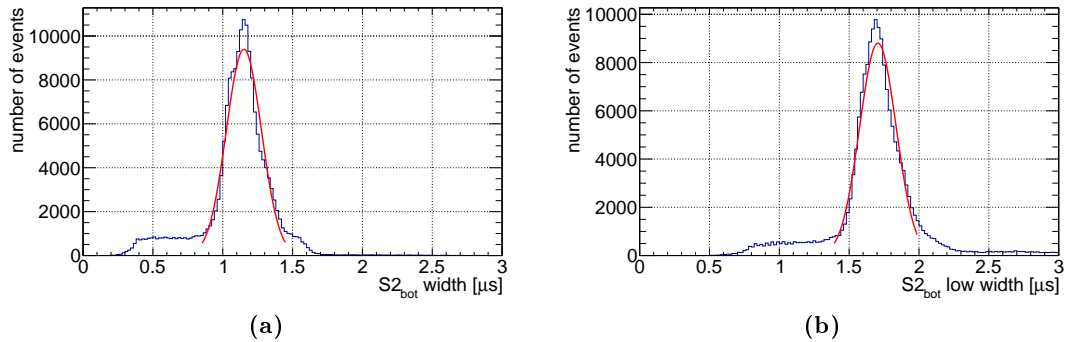


Figure 9.10: $S2$ width for the Compton data at a drift field of 198 V/cm for (a) FWHM and (b) low width at 10% height of the signal amplitude.

for the $S2$ low width, which is reduced by around 8% considering the highest value for 198 V/cm and the lowest value for 792 V/cm. With increasing drift field strength the diffusion of the electron cloud in the LXe and hence the $S2$ width is reduced since the electrons are drifting faster to the gas phase and have less time to diffuse.

To compare the measured $S2$ widths with the expectancy for the TPC configuration, the findings from chapter 7 can be employed. Using the minimum and maximum electric field strengths for the extraction field in the gaseous phase as stated in table 7.11 in section 7.4 and the GXe pressure of $p_{\text{GXe}} = 2.379$ bar, the reduced electric field strengths can be calculated to

$$E_{\text{red},x} = \frac{E_x}{p} \quad \text{with } x = \text{min, max} \quad (9.4)$$

$$E_{\text{red},\text{min}} = 2977.33 \frac{\text{V}}{\text{cm bar}} \quad E_{\text{red},\text{max}} = 3552.47 \frac{\text{V}}{\text{cm bar}}$$

The uncertainty for the gas pressure is negligible with less than 4 mbar.

The relation between reduced electric field and electron drift velocity was measured in [104]. Extrapolating the data for the calculated field strengths yields the drift velocities

$$v_{\text{min}} = 6000 \frac{\text{m}}{\text{s}} \quad v_{\text{max}} = 7200 \frac{\text{m}}{\text{s}} \quad (9.5)$$

From section 7.3.1 the gap length l_x between the liquid-gas interface and the anode mesh can be extracted from the minimum and maximum liquid height and the total distance between gate and anode mesh of 5 mm. Labeling the distances according to the minimum and maximum electric field values as in equation (9.4) yields:

$$l_{\text{min}} = 3.37 \text{ mm} \quad l_{\text{max}} = 1.90 \text{ mm} \quad \Delta l_x = 0.06 \text{ mm} \quad (9.6)$$

By dividing the gap lengths by the corresponding electron drift velocities one finds the drift times of the electrons between the LXe and the anode mesh, which constitutes the time range available for the $S2$ generation.

$$t_x = \frac{l_x}{v_x} \quad \text{with } x = \text{min, max} \quad (9.7)$$

$$t_{\text{min}} = (0.56 \pm 0.01) \mu\text{s} \quad t_{\text{max}} = (0.26 \pm 0.01) \mu\text{s}$$

These values are valid for all drift field strengths, since the extraction field strength and therefore the electric field in the gaseous phase was held constant for all measurements in this experimental run.

The theoretical $S2$ width only accounts for half (t_{min}) to less than a quarter (t_{max}) of the measured $S2$ FWHM width. An explanation for this discrepancy was not found yet.

The performance of the Raw Data Analysis tool could be checked, although browsing the signal waveforms of the studied data confirmed the values obtained for the signal widths.

A more probable cause of the large signal width could be the motion of the electron cloud before its extraction to the gaseous phase. Diffusion processes as discussed in [39] would distort the cloud in longitudinal and transversal direction. The non-optimal extraction efficiency (see section 7.4) could have an impact as electrons might be captured in the liquid-gas interface region and extracted with a time delay.

In addition, the electric field lines in the gas phase could be examined further, using simulations, to understand the electron paths and time scales better. Possible variations in the path lengths of the electrons could contribute to a broader signal width.

9.4 | TPC Calibration

The calibration of a xenon TPC with gamma-ray sources to have a direct link between the measured signals and the energy deposit (without relying on a secondary detector such as a germanium detector as in the Compton scattering mode) is crucial to determine the conversion factor from the PMT signals measured in photoelectrons to the actual number of photons and electrons released in the interaction in the LXe, as described in section 2.3.2. This section shows the result of the calibration measurements and the difficulties and limits that were encountered.

9.4.1 | Observed Calibration Data

As a comparison² to the example plot from [75] in section 2.3.2, figure 9.11 shows the $cS2$ signal in dependence of the corresponding $cS1$ signal for a calibration measurement using a ^{133}Ba source with an applied drift field strength of 198 V/cm, 594 V/cm and 792 V/cm, respectively.

For the data plots on the left, only the fiducialization, the condition that only one $S1$ signal may be present in the trigger window and the selection of the largest $S2$ signal are applied. On the right, the complete set of event selections as presented in section 9.3 impacts the plots.

With less restrictions considering the event selection, the plots on the left exhibit event structures which are not present on the right. The event distribution in the $cS2$ - $cS1$ plane is shaped as a broad diagonal band that reaches a maximum at around $140 \cdot 10^3$ p.e. in $cS2$. This maximum can be found for all three field configurations and represents the limit of the PMTs due to the saturation effect discussed in section 8.5. Besides a small conglomeration of events in the low $cS1$ and low $cS2$ region, only one distinct large structure is visible for all drift field strengths. The structure is an event distribution with $cS2$ signals between roughly $120 \cdot 10^3$ and $140 \cdot 10^3$ p.e. and it becomes even more distinct at higher drift fields. This effect emerges from the increase of charge signal at the expense of the scintillation signal, which causes the events found at high $cS1$ and low to medium $cS2$ to shift to lower $cS1$ and higher $cS2$ values (field quenching, see also section 9.6.2).

The shift from higher $cS1$ to lower $cS1$ values is evident considering how the mean $cS1$ value of the large event distribution changes with increasing drift field, as the large distribution is shifted to lower $cS1$. The accompanying increase in $cS2$ can not be observed due to the PMT saturation.

The diagonal “band” of events, which broadens with increasing $cS1$ and $cS2$, is an independent event structure for the lowest drift field of 198 V/cm. With increasing drift field, this distribution merges with the large distribution, as can be expected. Distinctive

²A direct comparison considering the amount of measured photoelectrons for the $cS1$ and $cS2$ signals can not be drawn due to the differences in detector design.

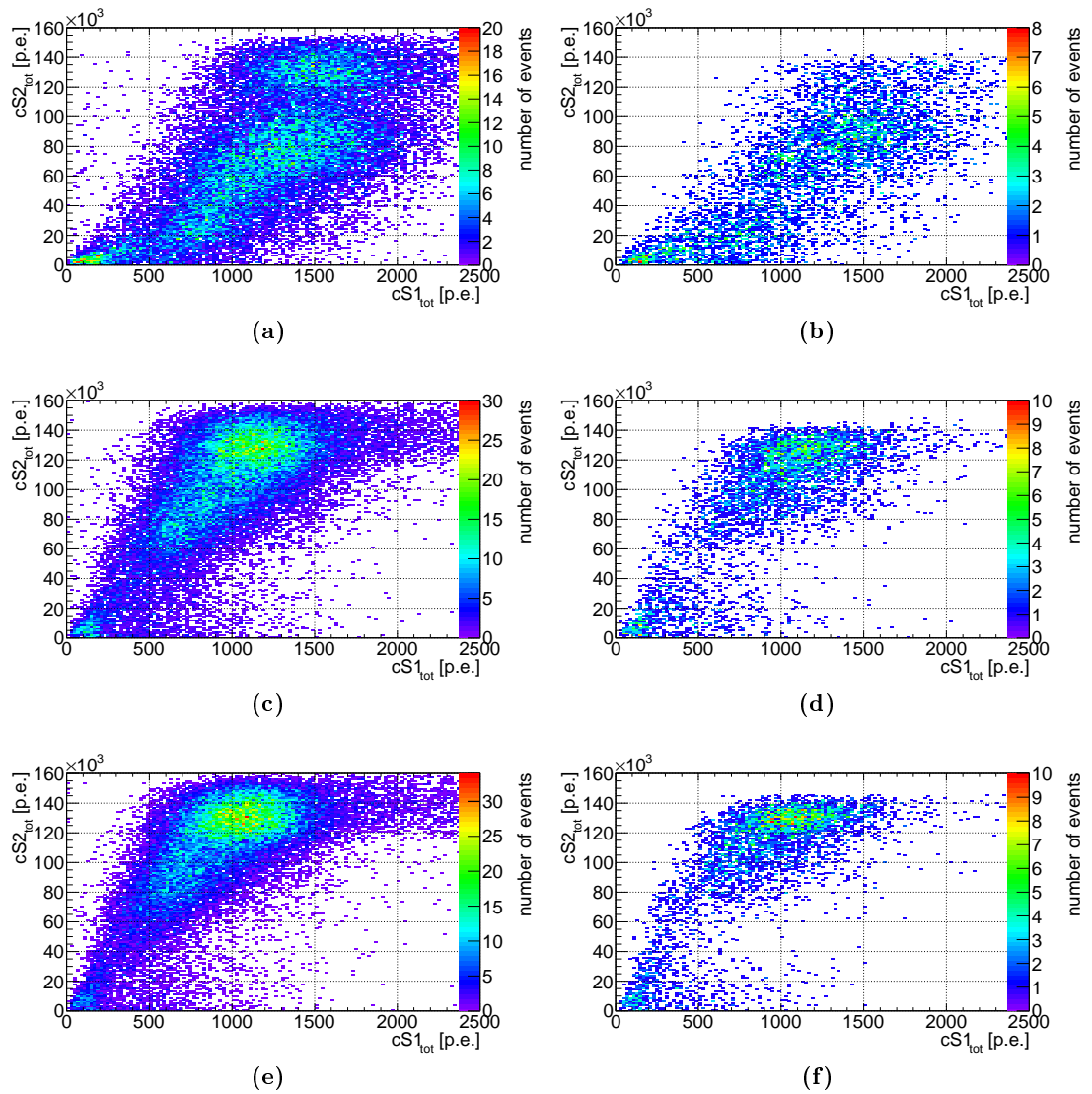


Figure 9.11: Event distributions in $cS2$ versus $cS1$ for the ^{133}Ba calibration measurements at drift fields of 198 V/cm (top row), 594 V/cm (center row) and 792 V/cm (bottom row), with different event selections on the left and on the right, as described in the text. The expected anti-correlated event distributions corresponding to the gamma-ray energy lines are not visible in the plots. The change in $cS1$ due to the increased drift field can be observed. The saturation of the TPC PMTs limits the informative value of the $cS2$ signal.

event structures corresponding to the energy lines of ^{133}Ba , with the most prominent being 356 keV line, are not visible in the calibration data. A distinction between different event distributions is prevented by the PMT saturation.

Taking all the event selections into account, the distributions on the right side look different. For all plots the event conglomerations at low $cS1$ and $cS2$ are also present, but comparing the plots for 198 V/cm, the large distribution at maximum $cS2$ seems to have vanished. A slightly visible structure around $cS1 = 150$ p.e. and $cS2 = 100 \cdot 10^3$ p.e. suggests that a part of the diagonal event structure constitutes the remaining event distribution. Considering the shift to lower $cS1$ and larger $cS2$ with increasing drift field, the brighter distributions visible for the 594 V/cm and 792 V/cm measurements might be the shifted signals from the diagonal structure instead of relics of the large event structure mentioned above. Despite all event selections, there is no clear indication of the expected energy lines of the ^{133}Ba source.

The calibration measurements with the ^{152}Eu source, which has an energy line at the intermediate energy of 122 keV, are depicted in figure 9.12. Analogous to the plots for ^{133}Ba , the left column shows the plots with the less restrictive event selection and the right one the event distribution with the complete selection set applied. For ^{152}Eu , a higher amount of data was acquired. The structures found in the event distributions for drift field strengths of 198 V/cm, 594 V/cm and 792 V/cm are therefore more clearly visible than for the ^{133}Ba measurements. In comparison, the distributions for both sources show similar structures at the positions in the $cS2$ - $cS1$ plane, without displaying any distinct source-specific features.

The largest amount of events considering the calibration measurements was collected for the ^{152}Eu source at a drift field strength of 198 V/cm. A zoom to the low $cS1$ and $cS2$ region of figure 9.12b is depicted in figure 9.13. The small event structure, which is visible in both ^{152}Eu and ^{133}Ba event distributions, exhibits zones in the range of $0 \text{ keV} \leq cS1 \leq 1000 \text{ keV}$ similar to the event distributions that is theoretically expected in the $cS2$ - $cS1$ plane. Still there are no recognizable event conglomerations that can be associated to energy lines in the respective gamma-ray source spectrum.

The reason why no clear event structures associated with the expected gamma-ray lines can be observed might be linked to the trigger mode for the calibration measurements. The DAQ trigger for recording the signal is set to a coincidence between the two TPC PMTs. A distinction between $S1$ and $S2$ signal is not possible with the trigger setup. Also, signals from afterpulses or other background events may contribute to the observed spectra.

Since the event distributions in figures 9.11 and 9.12 show little difference and the validity of the measured $S2$ signal is compromised due to the saturation effect, a closer examination of the event rate conducted.

As described in section 9.2.1, the event rates for the calibration measurements with different gamma-ray sources vary from each other which indicates that the measured events are caused by the individual source instead of some background noise. Table 9.2 lists the individual event rates supporting this assumption. Figure 9.14 shows the event rate in dependence of the $cS1$ signal for the four calibration sources ^{133}Ba , ^{152}Eu , ^{137}Cs

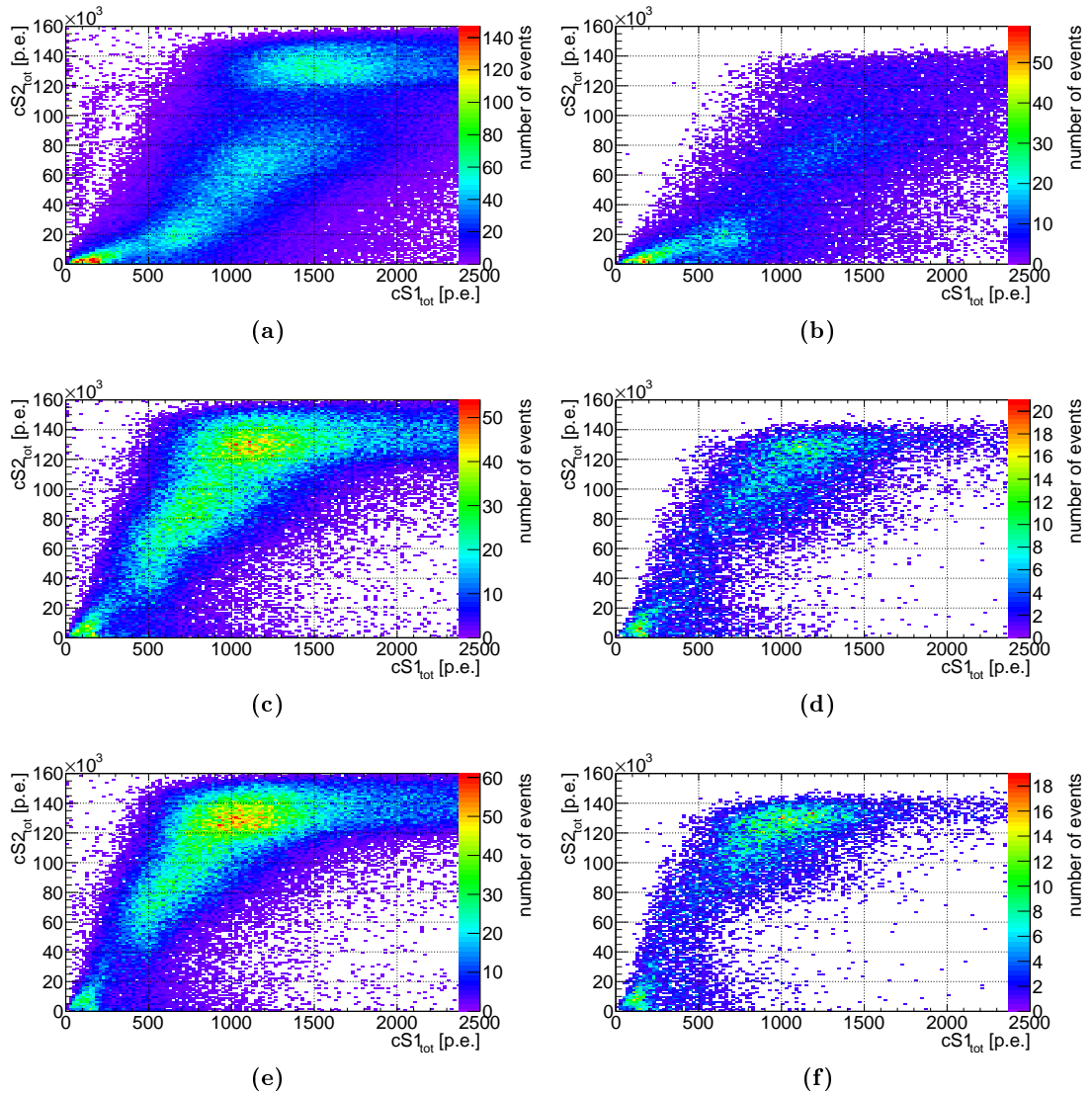


Figure 9.12: Event distributions in $cS2$ versus $cS1$ for the ^{152}Eu calibration measurements at drift fields of 198 V/cm (top row), 594 V/cm (center row) and 792 V/cm (bottom row), with different event selections on the left and on the right, as described in the text.. Despite higher measurement statistics, it is not possible to identify source-specific event structures that can be associated to gamma-ray lines. The observed event distributions resemble the ones found for ^{133}Ba .

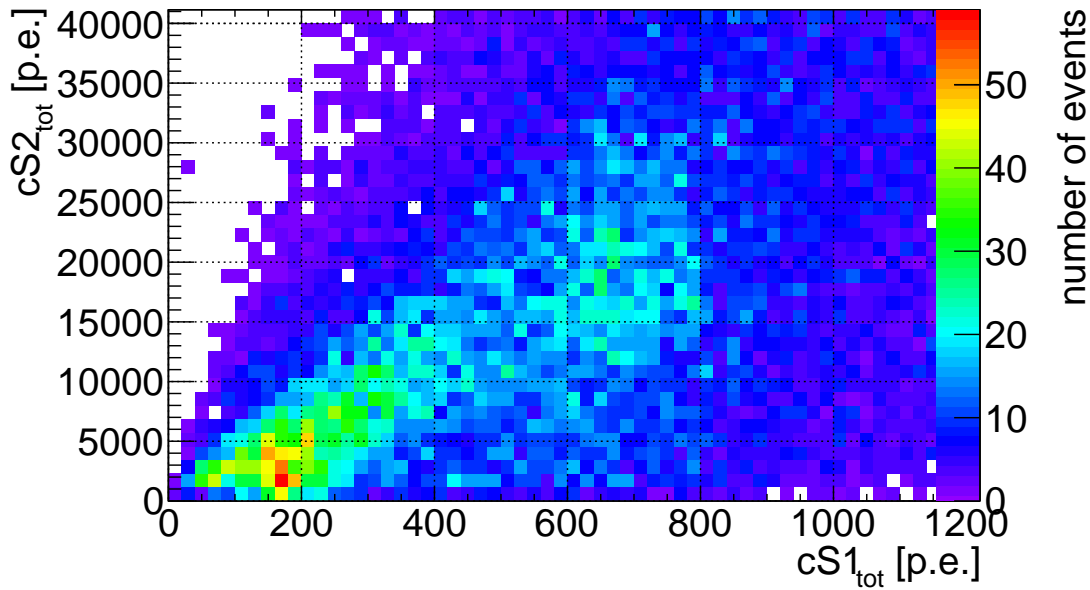


Figure 9.13: Event distribution (zoom) in $cS2$ versus $cS1$ for the ^{152}Eu calibration measurement at a drift field strength of 198 V/cm. The events show a similar distribution as expected but do not exhibit structures that can explicitly be linked to energy lines of the gamma-ray spectrum.

and ^{60}Co at a drift field strength of 198 V/cm, for the less restricted event selection on the left and the complete selection set on the right. The event rate for the different spectra is calculated by dividing the $cS1$ spectrum of each source measurement by the acquisition livetime.

On the left, the histograms of ^{133}Ba , ^{152}Eu , and ^{60}Co all exhibit the same shape of the event rate spectra. A small peak-shaped structure can be found around 200 p.e. (probably X-ray radiation from the K-shell, see section 8.3), followed by a broad, large peak structure stretching from roughly 500 to 1500 p.e. in case of ^{60}Co and from 500 up to 2000 p.e. for the other two sources.

The event rate spectrum of the ^{137}Cs shows a different distribution: The small peak structure is shifted to values between 200 and 400 p.e., the large broad peak structure corresponds to the one found for ^{133}Ba or ^{152}Eu , and a third peak structure is visible between 2000 and 4000 p.e.

After applying all event selections in figure 9.14b the spectra are suppressed significantly and the ^{137}Cs peak is almost not visible. The second peak of ^{137}Cs is shifted to lower $cS1$ compared also to the large peak structures of the other sources. The spectral shapes are more similar than before.

The slightly different shapes show the impact of the individual sources on the measurement data. The resemblance of the spectra might indicate the presence of an underlying signal background, which has more impact on the low-activity sources than on the high-

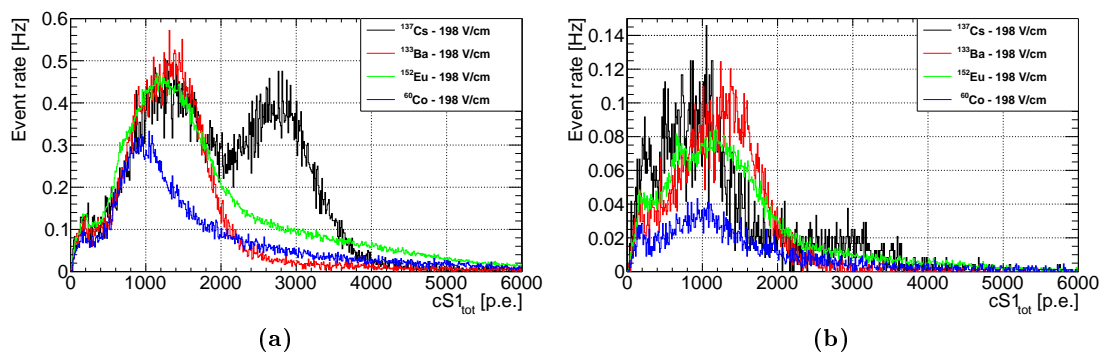


Figure 9.14: Event rates in dependence of the $cS1$ signal for calibration measurements with different gamma-ray sources at a drift field strength of 198 V/cm for (a) an event selection including only fiducialization, one $S1$ in the trigger time window and the selection of the largest $S2$ and (b) the complete event selection set applied. In case of the low-activity sources ^{133}Ba , ^{152}Eu , and ^{60}Co , the spectral shapes are quite similar, even though the event rate for the latter source is significantly smaller than for the other two. The strongest source ^{137}Cs shows the same spectral behaviour as the other three and an additional peak at higher $cS1$, between 2000 and 4000 p.e. This last peak can be associated with the 661.6 keV line of the ^{137}Cs source. With all selections applied, the third peak of ^{137}Cs is suppressed and the spectral distributions of all sources become more similar.

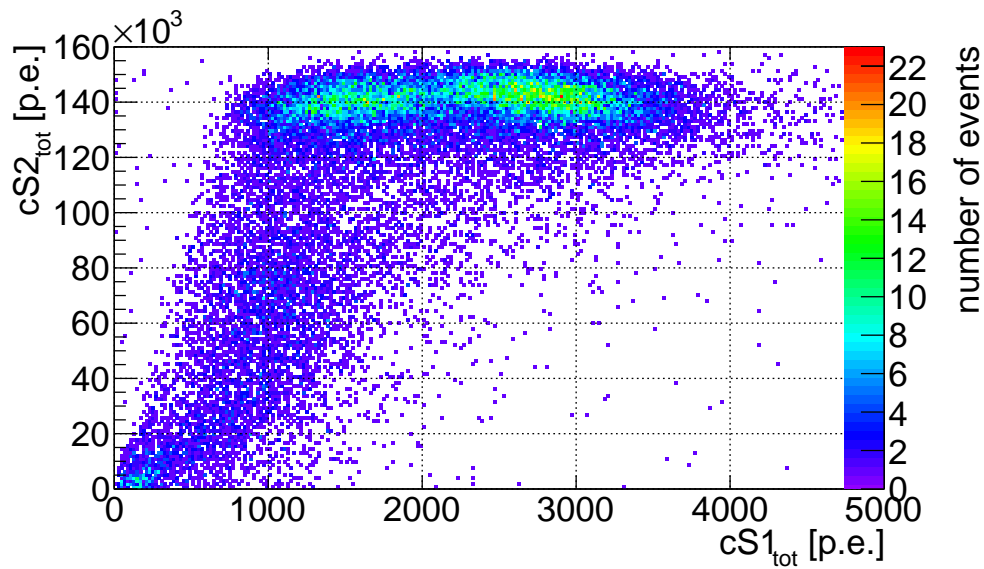
activity ^{137}Cs source. The impact of background noise is not quantifiable, because the activities of the ^{133}Ba , ^{152}Eu , and ^{60}Co are unknown and the background was not measured separately in the experimental run of April 2016.

Another explanation for the non-visible spectral lines could be the trigger configuration. As mentioned above, the TPC coincidence in its current form does not seem suitable for the TPC calibration measurements. The trigger setup used for the calibration measurement is susceptible for signal background, since compared to the Compton mode, the TPC PMT coincidence trigger condition is much less restricted. The triple coincidence for the Compton measurement between both TPC PMTs and the germanium detector ensures a very clean data set in comparison, while TPC PMT coincidences alone are much more likely to occur, even by background events. These seem to dominate the calibration spectra and have to be studied in more detail to find their origin.

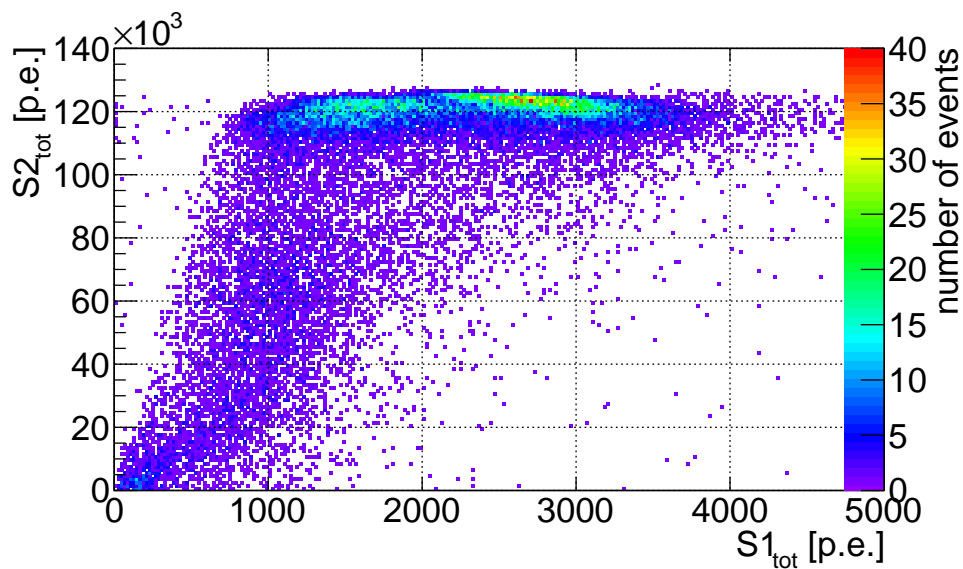
9.4.2 Estimation of the Energy Resolution in $S1$

The third peak found in the ^{137}Cs spectrum for the $cS1$ can also be identified in the $cS2$ - $cS1$ plane, as can be seen in figure 9.15a, also for a drift field of 198 V/cm. Besides the event distribution found for the ^{133}Ba and ^{152}Eu source, a second broad structure is located at $cS1$ signals between 2000 and 4000 p.e. and $cS2$ signals at the saturation limit. An energy calibration using the combination of $cS1$ and $cS2$ signals is therefore not possible as the considered event cluster might be distorted.

Figure 9.15b depicts the same data set without the signal correction for $S1$ and $S2$.



(a)



(b)

Figure 9.15: Event distribution in (a) $cS2$ versus $cS1$ and (b) $S2$ versus $S1$ for the ^{137}Cs calibration measurement at a drift field of 198 V/cm. Compared to the other calibration sources, ^{137}Cs exhibits an additional event structure in the $cS1$ region between 2000 and 3500 p.e., which can be associated with the 661.6 keV gamma-ray line. The PMT saturation distorts this distribution on the $cS2$ scale, preventing the energy measurement using the combined signals. The saturation effect is even more explicitly visible for the uncorrected signals in (b), where the events are piling up at the maximum $S2$.

While there is only a slight change regarding the $S1$ signal distribution, the change in $S2$ is significant. Without the correction, the saturation effect becomes more evident as the events are stacked at the maximum of $S2$. Given the fact that these are the original signal values before correction, the $S2$ signal is not usable for the energy calibration. Fitting the 661.6 keV line in the $cS1$ spectra leads to the energy resolution presented in table 9.10. The fit is a Gaussian similar to equation (8.5). The fitted spectra can be found in appendix B.8. The uncertainty of the peak position determining the amount of scintillation light measured for the $E_\gamma = 661.6$ keV line of ^{137}Cs is given by the standard deviation σ_{S1} .

The light yield value arising from the photopeak is calculated following equation (9.8). The energy resolution with approximately 20.5–21 % for the drift fields of 198 V/cm and 594 V/cm is worse compared to the resolution achieved for the combined signal in [76] for ^{137}Cs at a drift field strength of 1 kV/cm, which is 1.7%. For the $cS1$ signal alone, they found a resolution of 10.3 %, which also is better than the resolution found with the MainzTPC so far. Taking the underlying signal background into account in future measurements will increase the energy resolution significantly.

E_{drift} [$\frac{\text{V}}{\text{cm}}$]	198	594
$cS1(661.6 \text{ keV})$ [p.e.]	2669	2145
$\sigma_{S1}(661.6 \text{ keV})$ [p.e.]	559	441
$LY_{\text{calib}}(661.6 \text{ keV})$ [p.e./keV]	4.03	3.24
$\Delta LY_{\text{calib}}(661.6 \text{ keV})$ [p.e./keV]	0.84	0.67
energy resolution ($\sigma_{S1}/cS1$)(661.6 keV) [%]	20.94	20.56

Table 9.10: Determination of the scintillation response for the 661.6 keV gamma-ray line of ^{137}Cs at different drift field strengths. From the fit results for the $cS1$ signal the light yield and its uncertainty at this energy are calculated.

$$LY_{\text{calib}}(E_\gamma) = \frac{cS1(E_\gamma)}{E_\gamma} \quad \Delta LY_{\text{calib}}(E_\gamma) = \frac{\sigma_{S1}(E_\gamma)}{E_\gamma} \quad (9.8)$$

The energy calibration with the ^{137}Cs is not sufficient to cross-check the findings for the light yield from the Compton measurements in section 9.6, since the light yield depends non-linearly on the energy deposit in the LXe and the deposit from the Compton scattering is far below the 661.6 keV line. However the low light yield value agrees with the expected trend of the light yield to decrease with increasing energy deposit.

9.4.3 Examining the $S2$ Signal using the APDs

The $S2$ signals measured with the TPC PMTs can not be used for the calibration because of the saturation effect discussed in section 8.5. The APDs primarily used for the

position reconstruction also detect the large $S2$ signal and therefore provide an alternative measured signal for the analysis.

Since the APDs have not been calibrated to an absolute value, a relative value is examined with the $S2$ signal as the sum of the APD signal amplitudes according to equation (9.9) (corrected by their gain as for the position reconstruction in chapter 6).

$$S2_{\Sigma\text{APD}} = \sum_{i=1}^N \frac{A_i}{g_i \eta_i} \quad N = 8, \quad \eta_i = 1 \quad (9.9)$$

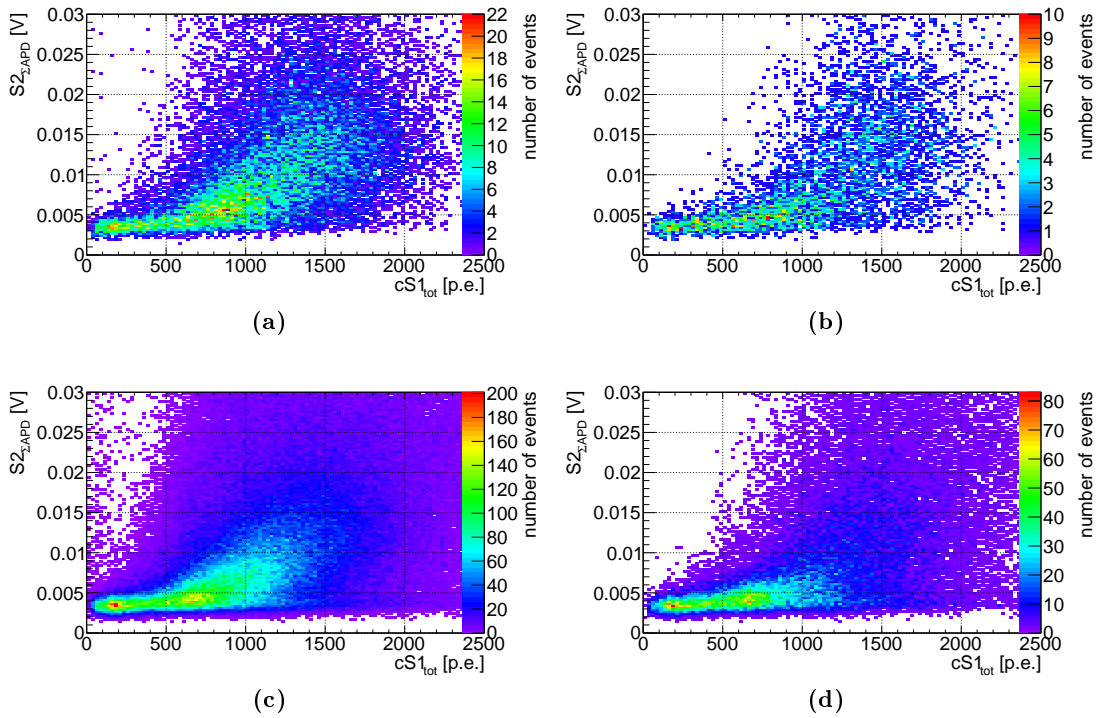


Figure 9.16: Event distributions in $S2$ from the summed APD amplitudes versus $cS1$ for ^{133}Ba (top row) and ^{152}Eu (bottom row) at 198 V/cm. On the left, only the fiducialization, the condition that one $S1$ is present in the trigger time window and the selection of the largest $S2$ are used as event selections, on the right the complete set of event selections is applied. The shape of the event distributions is similar to the one observed in figure 9.13 and also similar to the theoretical expectation. Still the plots show no specific event clusters that could be associated with energy lines from gamma-ray sources.

The $S2_{\Sigma\text{APD}}-cS1$ plane shown in figure 9.16 gives an impression of the event distribution. The left column shows the event distribution with the less restricted event selection as described in the previous subsections, in the right column the complete event selection set from section 9.3 is applied. The top row shows the event distribution for ^{133}Ba and the bottom row for ^{152}Eu . In both cases the drift field strength was 198 V/cm.

Compared to the event distributions obtained with the $cS2$ signal from the TPC PMTs, the plots here do not contain the large event distribution at high $S2$. The events form a cone-shaped, diagonal band which is arched upwards for higher $cS1$, and the small structure at low $cS1$ and low $cS2$ found in the previous plots seems to be included in this band.

In figure 9.16b, event clusters seem to be present at the upper end of the diagonal cluster for the ^{133}Ba source. For a proper analysis, the statistics are not sufficient.

The field quenching effect is observed for higher drift field strengths. The event distributions for the drift fields of 594 V/cm and 792 V/cm are shown in appendix B.8.

As for the analysis of the signals being measured with the TPC PMTs alone, the event distributions suggest that an improvement of the calibration measurement setup is necessary and inevitable to obtain reasonable results with the MainzTPC. Using the APDs as an alternative mean to measure the $S2$ signal seems to be a valid technique once the trigger setup and noise conditions are optimized for the event recording.

9.4.4 | Improvements of the TPC Calibration

With the data at hand, it is not possible to conduct a TPC calibration fulfilling the requirements of the precision aimed for with the MainzTPC. In the current state of the detector, an energy calibration using the combined signal of scintillation and charge is prevented by the saturation of the TPC PMTs for large signals.

Three key aspects have to be improved in order to calibrate the MainzTPC and achieve a sufficient energy resolution:

1. On the hardware side, the update of the TPC PMT bases to avoid the saturation effect is indispensable. The previous subsections show that even the 661.6 keV line from the ^{137}Cs is distorted and for optimal energy resolution, both $S1$ and $S2$ have to be taken into account.
2. Understanding and eliminating the signal background is a crucial aspect for the calibration. By studying the signal background both in measurement and simulation its sources might be identified and neutralized. The background can also be measured separately and then subtracted from the calibration spectrum obtained with the same experimental settings. In addition, the employment of calibration sources with significantly higher activities ensures faster data acquisition and less impact of the signal background.
3. Since the measurement is triggered event-by-event, adjusting the trigger setup to eliminate the signal background from the acquired data is even more preferable. Instead of using the TPC trigger as described in this thesis with a coincidence on the TPC PMTs on signals which are of the size of $S1$, the trigger setup could be configured to recognize $S2$ signals. The application of a $S2$ trigger setup is also studied in [4].

9.5 | Trigger Efficiency

9.5.1 | Effect and Measurement of the *S1* Trigger Efficiency

Ideally all signals that have the correct characteristics to account for an event should be recorded by the MainzTPC DAQ. Various factors influence the trigger generation: The position of the event in the active volume of the TPC has an impact on the amount of light detected for the *S1* signal, which constitutes at least part of the trigger signal. The transparency of the mesh electrodes as well as the quantum efficiency (QE) of the PMTs also reduce *S1*.

For clean measurements, the signal threshold has to be chosen above the noise level. The threshold substantially prevents the detection of signals below the chosen value and the trigger efficiency provides the means to account for these signals.

Small *S1* signals may still be found in the FADC waveforms but are too small to cause a triggering signal for the DAQ system. The trigger efficiency and hence the energy threshold for the MainzTPC with DAQ version 2 and the setup at the HZDR is examined here.

Figure 9.17a shows schematically the impact of the trigger efficiency on a Gaussian signal distribution. For all energy deposits, the number of detected photons varies, mostly according to Poisson statistics and due to anti-correlation of charge and light production. In addition, there is a dependency of the light collection efficiency on the interaction location in the TPC. Measuring the *S1* signals for a fixed energy deposit therefore leads to an event distribution in *S1* which approaches a Gaussian shape for sufficiently bright signals. The distribution shown as a dashed blue line is influenced by the trigger efficiency, which is assumed here to have the shape of a Fermi-Dirac distribution (red). Within the rising threshold of the trigger efficiency, the resulting measured distribution (solid blue) shows the loss in number of events as well as a shift of the mean of the signal distribution to higher values. This shifting effect becomes more distinct for smaller energy deposits. As a result, the spectrum will be distorted according to the trigger efficiency.

The trigger efficiency of the MainzTPC setup has been measured with an external trigger based on the coincident emission of two gamma-rays (at 1.17 MeV and 1.33 MeV) of a ^{60}Co source embedded in a NaI(Tl) well detector, placed next to the cryostat. Figure 9.17b shows the setup. ^{60}Co emits two gamma-rays simultaneously at arbitrary angles. Most of the gamma-rays will hit the surrounding scintillator, while a fraction will hit the TPC active volume. The DAQ Trigger is generated by the NaI(Tl) scintillator at an energy threshold of roughly 850-900 keV³.

The measurement was carried out for only one orientation and location of the well-detector next to the cryostat, at the center position defined in section 6.2.2.

³The energy threshold was estimated using the NaI(Tl) signal from a ^{137}Cs source peaking at ~ 150 mV (661.6 keV) on the CFD and from a ^{60}Co source with a signal peak (corresponding to 1.33 MeV at ~ 300 mV). The set CFD threshold was 203 mV.

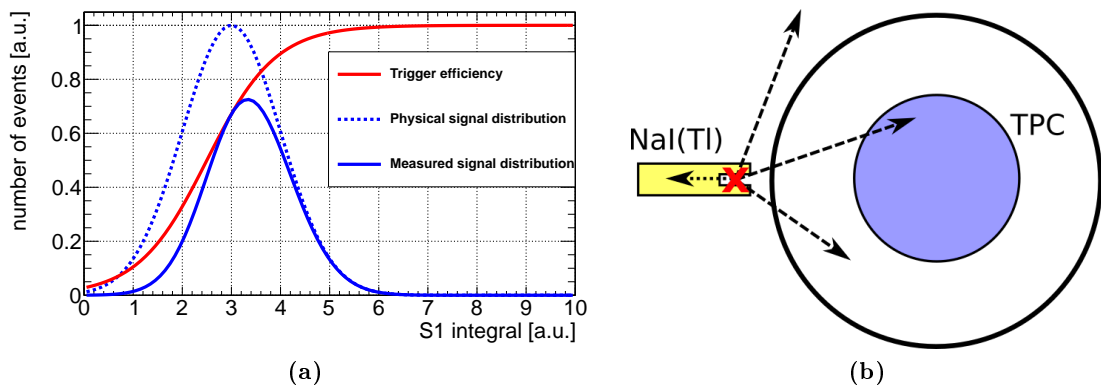


Figure 9.17: The effect of the trigger efficiency is illustrated in (a), showing the expected signal distribution (dashed blue line) and the measured distribution (solid blue) for small S_1 signals. The latter emerges from the influence of the trigger efficiency, here chosen to be of the form of a Fermi-Dirac distribution (red). The units are arbitrary. The setup is sketched in (b): A ^{60}Co source (red X) is placed inside a NaI(Tl) well scintillator (yellow). An event is recorded for a gamma-ray hit in the scintillator (dotted arrow). The simultaneously emitted second gamma-ray has an arbitrary direction. For a fraction of the measured events, a coincidence with the TPC active volume (blue) occurs.

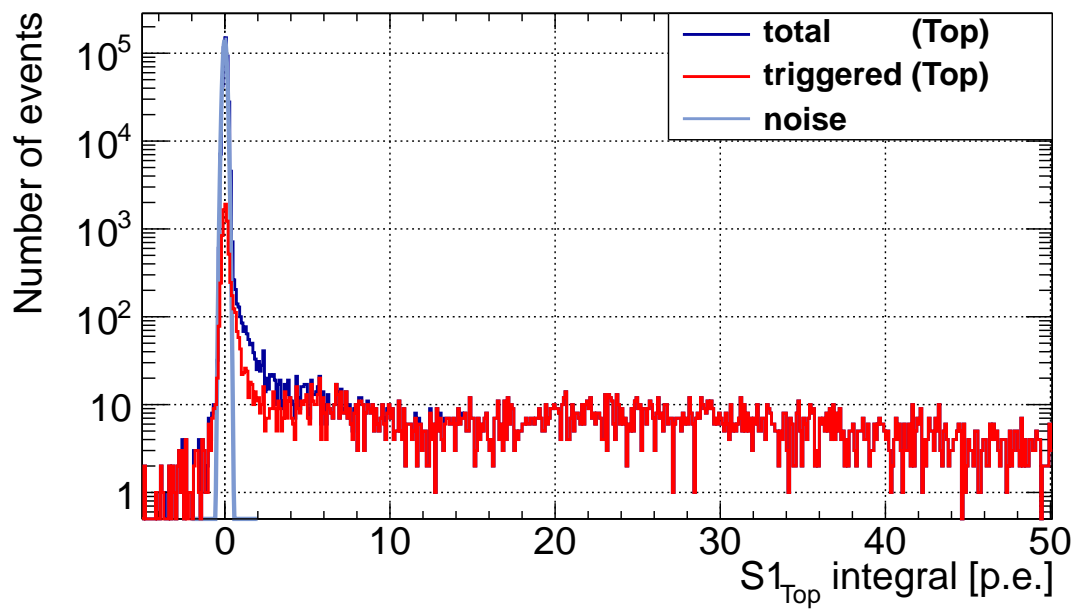
The DAQ version 2 setup records the PMT signal waveforms as well as the CFD signals on the TDC board. The TDC data includes the individual CFD signals from each PMT, which correspond to a trigger signal by each single PMT, and also the digital signals from the logic board, especially the TPC coincidence trigger signal.

By triggering the DAQ with the scintillator, the waveforms of the TPC PMTs are recorded regardless of their content. Since the time of flight for the gamma-rays is known, the waveforms can be analyzed using a Fixed Window Integral (see section 3.5.6) around the signal position in the waveforms. This approach ensures that even small signals that might be overseen by the PeakFinder algorithm are taken into account. The found signals are then compared to the respective TDC data, which shows whether the individual PMTs surpassed the trigger threshold for the particular signal or not.

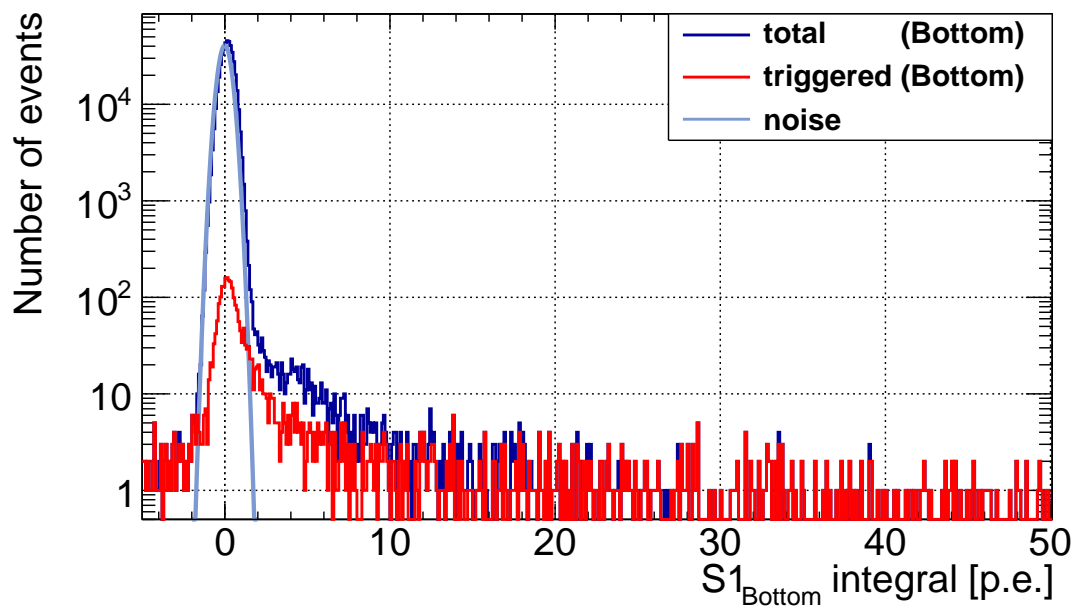
9.5.2 Determination of the Trigger Efficiency

The setup allows to compare different trigger settings using only one measurement: The trigger efficiency can be measured by comparing the TDC and FADC data for the Top and Bottom PMT individually, but also for the coincidence of both TPC PMTs. The trigger efficiency measurement was conducted at a drift field strength of 198 V/cm and 594 V/cm, respectively.

The waveforms for a given PMT are analyzed with the Fixed Window Integral, and the integral S_1 values are collected in a histogram shown in figure 9.18 for the Top PMT and the Bottom PMT, respectively. For the same events, the data from the TDC board is



(a)



(b)

Figure 9.18: Spectra of the signal obtained with the Fixed Window Integral Method for the individual TPC PMTs at a drift field strength of 198 V/cm. The blue spectrum contains all signals in the fixed window. The red spectrum shows all signals with an additional TDC signal for the respective PMT at the trigger time. The ratio of the two spectra yields the trigger efficiency. The light blue line is a Gaussian fit to the noise peak around zero. The panels show the signals found on the Top PMT channel (a) and the Bottom PMT channel (b). The binning is 0.1 p.e. for the $S1$ integral.

checked whether the CFD threshold was exceeded within a 75 ns, resulting in the second histogram for events that would have caused a trigger.

Both histograms are plotted in figure 9.18 for the individual PMTs for a trigger efficiency measurement with a drift field strength of 198 V/cm. The events counted as triggered events need to have coincident CFD signals on the respective PMT channel on the TDC board. As expected, for low signals the amount of triggered events is much less than the amount of signals found in the waveforms. With increasing signal integral, the amount of triggered signals approaches the total number of found signals.

The integral value for $S1$ is labeled $S1_{\text{Top}}$ and $S1_{\text{Bottom}}$ in the histograms in figure 9.18. This nomenclature was chosen to emphasize that the $S1$ integral is determined for each channel separately. For the combined signal, the $S1$ integrals of both channels are summed as:

$$S1_{\text{Total}} = S1_{\text{Top}} + S1_{\text{Bottom}} \quad (9.10)$$

Around zero, a peak structure can be found for both the triggered and all found signals, representing noise. Using a Gaussian function (equation (9.11)), shown in light blue, centered at $\mu_{S1} = 0$, a fit is carried out to get a rough estimation of the noise peak width. The fit results are listed in table 9.11.

$$f_{\text{noise}}(S1_X) = N \cdot e^{-\frac{1}{2} \left(\frac{S1_X - \mu_{S1}}{\sigma} \right)^2} \quad S1_X = S1_{\text{Top}}/S1_{\text{Bottom}}/S1_{\text{Total}} \quad (9.11)$$

From the fits shown in figure 9.18 one can see that the peak structure itself has the expected Gaussian form and that noise can be expected in the range of up to 0.6 p.e. for the Top PMT and 1.8 p.e. for the Bottom PMT.

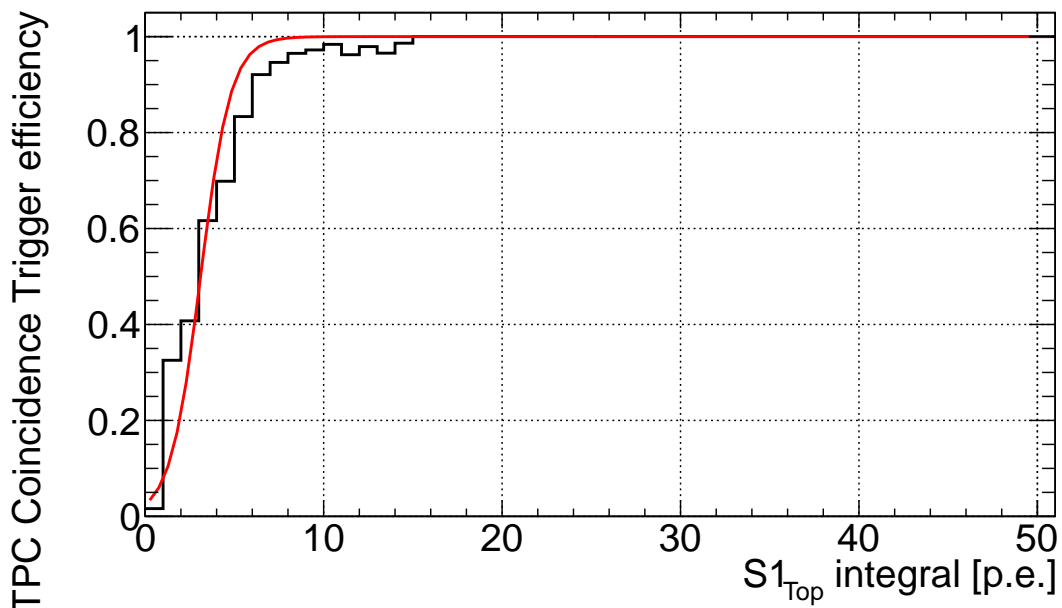
PMT(Trigger)	198 $\frac{\text{V}}{\text{cm}}$		594 $\frac{\text{V}}{\text{cm}}$	
	$N [\times 10^4]$	$\sigma_{S1} [\text{p.e.}]$	$N [\times 10^5]$	$\sigma_{S1} [\text{p.e.}]$
Top (Top)	14.447 ± 0.028	$0.1111 \pm (1 \cdot 10^{-4})$	16.384 ± 0.030	$0.1103 \pm (1 \cdot 10^{-4})$
Bottom (Bottom)	4.075 ± 0.008	$0.3747 \pm (5 \cdot 10^{-4})$	5.020 ± 0.009	$0.3592 \pm (4 \cdot 10^{-4})$
Total (Coincidence)	3.904 ± 0.008	$0.3651 \pm (4 \cdot 10^{-4})$	4.947 ± 0.009	$0.3581 \pm (4 \cdot 10^{-4})$

Table 9.11: Gaussian fit parameters of the noise peak in the $S1$ integrals obtained for the trigger efficiency measurements. The mean of the Gaussians was set to $\mu_{S1} = 0$.

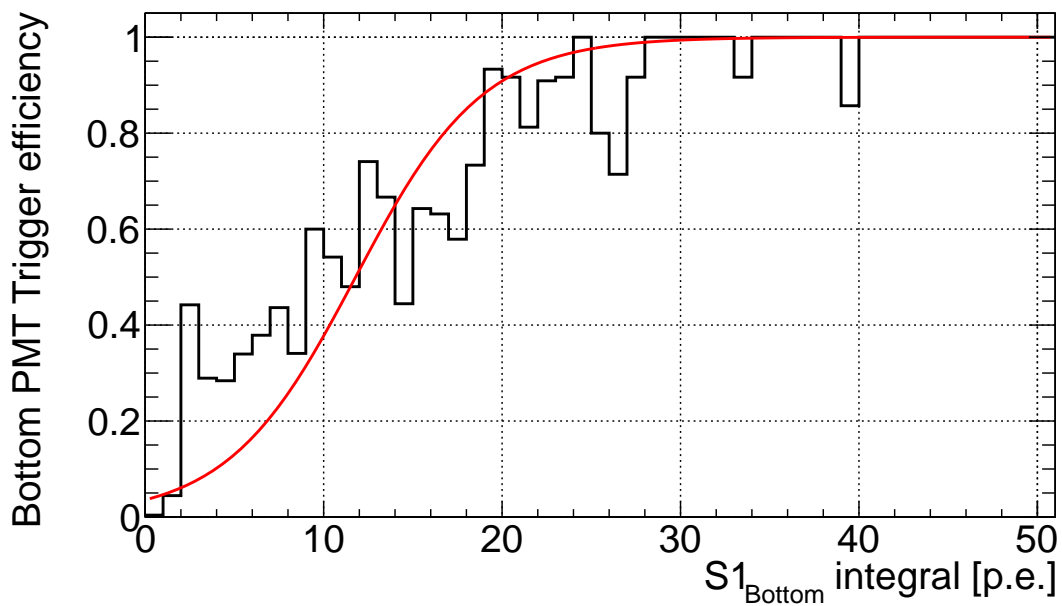
Figure 9.19 shows the trigger efficiency for each PMT. It is created by dividing the number of the triggered events by the total number of events for each bin in $S1$, with a bin width of 1 p.e.⁴. The trigger efficiency rises from zero to 100 %, reaching 90 % at ~ 6 p.e. for the Top PMT and ~ 20 p.e. for the Bottom PMT. The limited statistics for higher values of $S1$ leads to the observed fluctuations in trigger efficiency. Its slow rise in figure B.26a results from the low gain of the Bottom PMT at the chosen operating voltage of 950 V⁵.

⁴The larger binning for the trigger efficiency compared to the $S1$ integral histograms is motivated by the low statistics of the triggered signals.

⁵See section 5.1.

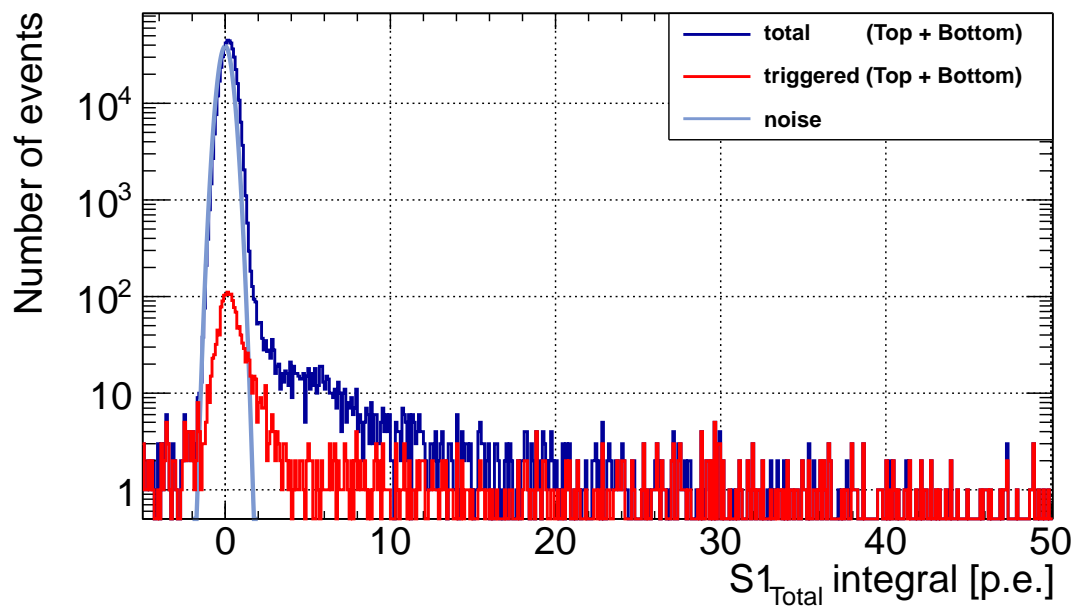


(a)

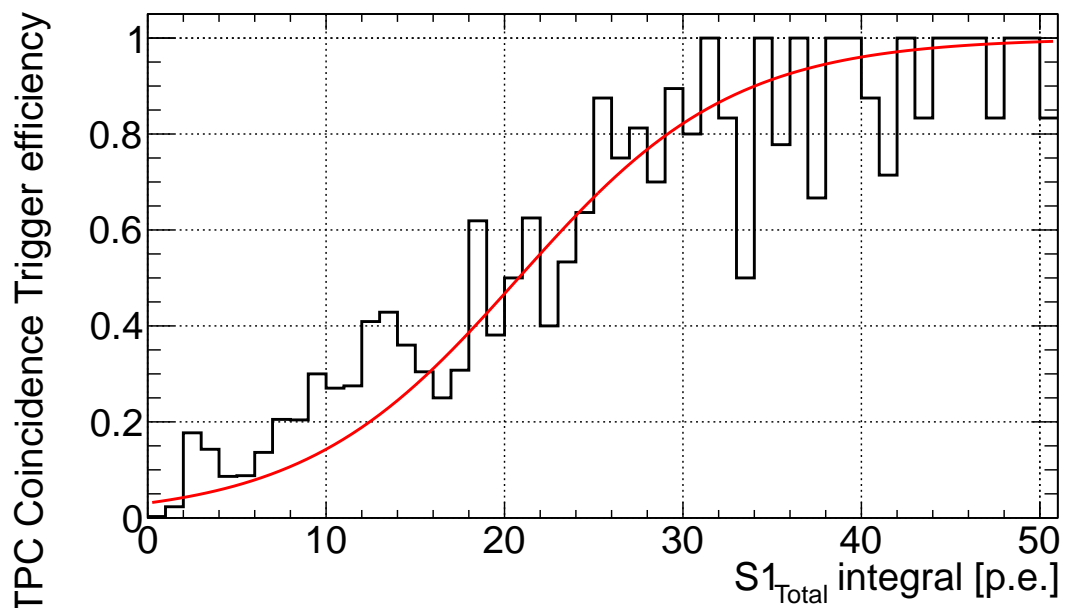


(b)

Figure 9.19: Trigger efficiency for the individual TPC PMTs at a drift field strength of 198 V/cm. A value of 90% is reached first for signals around 6 p.e. for the Top PMT in (a) and ~ 20 p.e. for the Bottom PMT in (b). The shape of the trigger efficiency is approximated with a fit using a Fermi-Dirac distribution as described in the text.



(a)



(b)

Figure 9.20: Spectra of the signal obtained with the Fixed Window Integral Method for the TPC PMT coincidence (a). The blue spectrum contains all signals in the fixed window. The red spectrum shows all signals with an additional TDC signal for the Bottom PMT at the trigger time. The ratio of the two spectra yields the trigger efficiency, shown in (b). A value of 100% is reached first for signals above 30 p.e. The shape of the trigger efficiency is approximated with a fit using a Fermi-Dirac distribution as described in the text. The trigger efficiency measurement was conducted at a drift field strength of 198 V/cm.

The trigger efficiency of the TPC coincidence mode requires a CFD signal in both Top and Bottom PMT channel. Using the summed signal $S1_{\text{Total}}$, the histograms for triggered and all found signals are shown in figure 9.20a. The shape of the two histograms have a strong resemblance to the corresponding figure B.26a, considering the width of the noise peak and the height ratio between the peaks for total and triggered signals. Figure 9.20b shows the trigger efficiency for the measurement at a drift field strength of 198 V/cm for the coincidence mode. The trigger efficiency reaches about 90 % at ~ 30 p.e. As stated on the x-axis, the $S1$ integral value is the sum of both Top and Bottom PMT. The slow rise of the trigger efficiency can be explained by this fact, since each PMT has a contribution to $S1_{\text{Total}}$. Also, the low gain of the Bottom PMT influences the trigger efficiency in the coincidence mode.

The trigger efficiencies for Top PMT, Bottom PMT and their coincidence are overlaid in figure 9.21 for the different trigger settings. Each histogram depicts the trigger efficiency for the $S1$ measured by either one PMT or the sum, with the trigger setting noted in parentheses. This allows to compare the trigger efficiency for the signals measured on a single PMT $S1_X$ for the two trigger settings “Top”/“Bottom” (single mode) and “Coinc” (coincidence). As expected, the choice of the coincidence trigger leads to

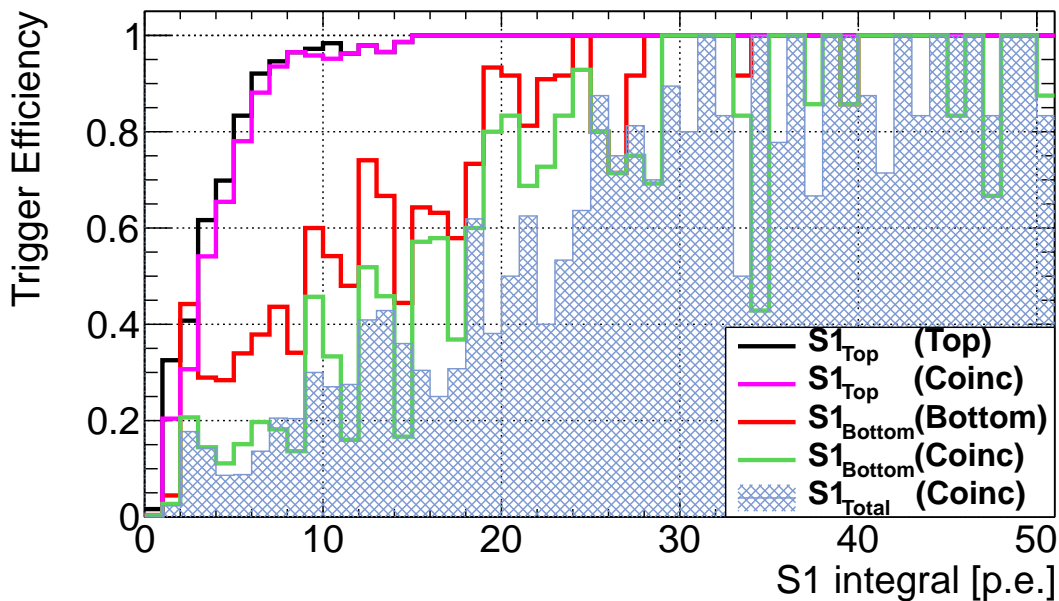


Figure 9.21: Comparison of the trigger efficiencies determined for the Top PMT, Bottom PMT and summed signal for single and coincidence trigger mode. The Top PMT with the higher gain yields a better trigger efficiency than the Bottom PMT. The labels name the signal channel X as well as the trigger mode in parentheses. For the two PMTs, the change from single trigger mode to coincidence trigger mode leads to a shift of the trigger efficiency curve to larger $S1$ integral values. Labeled $S1_{\text{Total}}$, the summed signal for the coincidence mode is depicted for comparison. The Bottom PMT has a strong impact on the coincidence trigger performance. The applied drift field strength is 198 V/cm.

slightly less signals and a shift of the trigger efficiency curves to larger $S1$ values. This effect is more prominent for the Bottom PMT, which is the limiting sensor here for the coincident trigger.

For a direct comparison, the efficiency of the summed signal is shown as hatchures. Although it gives the impression of a much worse trigger efficiency, it has to be noted that it can not be directly compared to the efficiencies for the single PMTs due to its integral $S1_{\text{Total}}$.

The Bottom PMT trigger efficiency surpassing the Top PMT trigger efficiency at low $S1$ of 2 – 3 p.e. might emerge from the broader noise distribution for the Bottom PMT, as shown in figure B.26a.

To quantify the step-like behaviour of the trigger efficiency, a fit function of the form of a Fermi-Dirac distribution was chosen. Although this distribution has no physical connection to the trigger efficiency, it has the appropriate shape to describe the efficiency distribution mathematically. Its fit parameters A_{FD} and B_{FD} are defined in equation (9.12), marking the center point and the width of the distribution.

$$f_{\text{FD}}(S1) = 1 - \frac{1}{1 + \exp\left(\frac{S1 - A_{\text{FD}}}{B_{\text{FD}}}\right)} \quad (9.12)$$

The function $f_{\text{FD}}(S1)$ was used to examine the trigger efficiencies of Top PMT, Bottom PMT and their coincidence mode for the drift field strengths of 198 V/cm and 594 V/cm. The corresponding figures, beside the ones presented above, can be found in appendix B.9. The resulting fit parameters A_{FD} and B_{FD} are listed in table 9.12.

$E_{\text{drift}} \left[\frac{\text{V}}{\text{cm}} \right]$	198			
	PMT(Trigger)	A_{FD} [p.e.]	B_{FD} [p.e.]	χ^2
Top (Top)		3.10 ± 1.92	0.85 ± 0.85	0.235
Bottom (Bottom)		11.79 ± 4.09	3.57 ± 1.79	1.933
Top (Coincidence)		3.51 ± 1.91	0.75 ± 0.70	0.272
Bottom (Coincidence)		17.37 ± 4.09	4.81 ± 2.17	2.556
Total (Coincidence)		20.80 ± 4.58	6.02 ± 2.28	1.994
$E_{\text{drift}} \left[\frac{\text{V}}{\text{cm}} \right]$	594			
	PMT(Trigger)	A_{FD} [p.e.]	B_{FD} [p.e.]	χ^2
Top (Top)		3.02 ± 1.88	0.82 ± 0.87	0.171
Bottom (Bottom)		12.82 ± 3.90	3.99 ± 1.79	2.079
Top (Coincidence)		3.38 ± 1.98	0.71 ± 0.73	0.249
Bottom (Coincidence)		20.71 ± 4.19	5.90 ± 2.41	3.981
Total (Coincidence)		21.30 ± 4.49	6.09 ± 2.31	2.106

Table 9.12: Fit parameters of the trigger efficiency for five different sensor(trigger) settings, determined using a Fermi-Dirac distribution at two different drift field strengths. For the fit, a number of degrees of freedom of 49 was found.

The large uncertainties, especially for the parameter B_{FD} , can be explained by the impact of the noise to the $S1$ integral spectrum. For the Top PMT, the center position at approximately 3 p.e. with an uncertainty of almost 2 p.e. places the rising flank of the trigger efficiency close to the noise region. Also, the low statistics for higher $S1$ which lead to the large fluctuations that are visible in figure 9.20b can have an influence on the fit quality. Furthermore, the fit parameters for both drift field configurations are in agreement for each measurement. This is expected since the change in drift field strength only leads to smaller $S1$ signals overall, but the trigger thresholds of the PMTs and therefore the trigger efficiency should not be affected.

The trigger efficiency valid for the Compton data - the coincidence mode for the summed signal - in this thesis is marked bold. Since the measurements for both drift field strengths yield the same fit values, the mean of the found parameter values is chosen for further analysis:

$$A_{\text{FD}} = (21.05 \pm 3.21) \text{ p.e.} \quad B_{\text{FD}} = (6.06 \pm 1.62) \text{ p.e.} \quad (9.13)$$

9.5.3 | Further Steps to improve the Trigger Efficiency

Considering the goals of the MainzTPC, a trigger efficiency which reaches 100 % first for the summed $S1$ of around 40 p.e. is not sufficient.

One aspect that has a large impact on the trigger efficiency is the choice of signal threshold in the DAQ system, namely at the stage of the CFDs. The CFD threshold of the PMTs had to be set to quite high values due to electronic noise. The PTR (see section 3.3.2) introduces a noise signal which could not be eliminated by grounding and shielding the amplifiers and cables involved and which has to be dealt with to improve the data quality in future measurements.

For the data at hand, the APDs were not recorded and the x - y -position of events can therefore not be evaluated. In subsequent experimental runs, the trigger efficiency measurements will include the APD data to examine the influence of the event position.

The trigger efficiency has a great influence on the measurements, mainly with respect to the low-energy signal region, and therefore has an impact on the results of the data from Compton scattering as well as neutron scattering measurements (which have not been examined in this thesis). Enhancing the trigger efficiency for the coincidence of the TPC PMTs will be a necessary step to accurately measure Compton events in the range of only a few keV.

9.6 | Primary Scintillation $cS1$

9.6.1 | Light Yield for $cS1$

Studying the $S1$ signal using the Compton scattering setup allows to directly link the amount of generated direct scintillation light to the energy deposit E_{TPC} . Figure 9.22 shows the $cS1$ signal (corrected for z) for a measurement with a drift field strength of 198 V/cm plotted against the corresponding deposited energy.

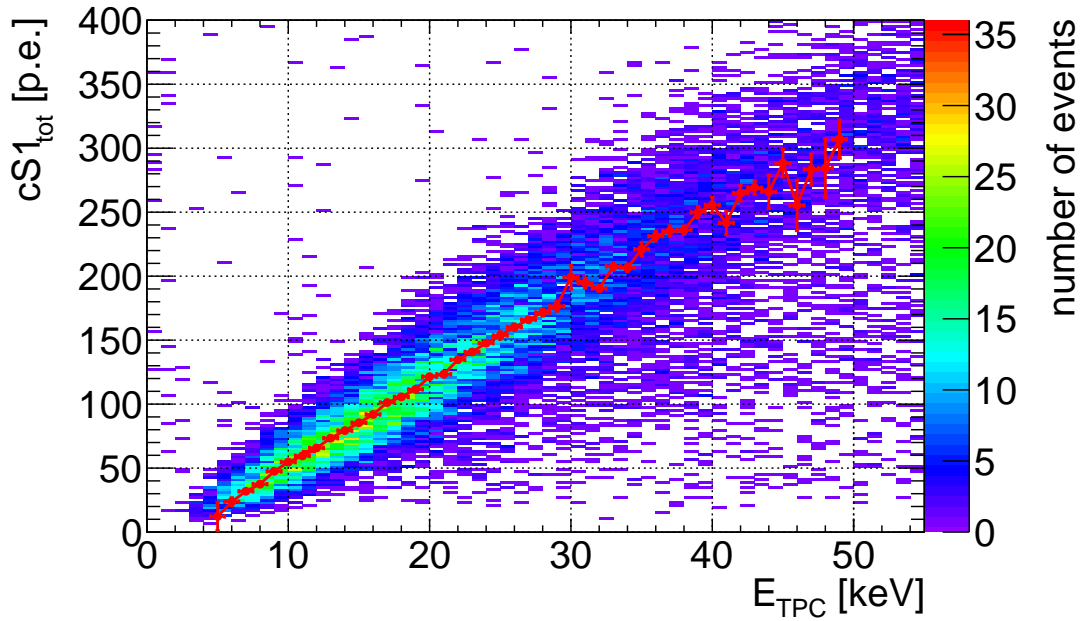


Figure 9.22: Detected $cS1$ signal in dependence of the energy deposit E_{TPC} for Compton scattering with an applied drift field of 198 V/cm. In red, the fit values for the Gaussian mean per energy slice are overlaid. The error bars indicate the uncertainty from equation (9.15) calculated from the fit. The graph suggests a linear relation between deposited energy and generated scintillation light.

The data distribution shows a roughly linear correlation between $cS1$ and energy. The energy range covers values between ~ 5 and 50 keV, which can be accounted to the angular position of the germanium detector. For higher energies, the statistics become very small. Lower signals are not detected in the data sets at hand, which can be linked to the $S1$ trigger efficiency and the sensor thresholds necessary to suppress electronic noise (see section 9.5).

To determine the light yield, the graph shown in figure 9.22 is sliced with respect to the deposited energy E_{TPC} , with a slice width of $dE_{\text{TPC}} = 1$ keV. Some examples for energy slices are presented in figure 9.23. The shape of the signal distribution suggests the use of a Gaussian fit function. To account for the $S1$ trigger efficiency which distorts the

signal distribution especially for small signals, the Gaussian fit function with amplitude A , mean μ_{cS1} and standard deviation σ_{cS1} is multiplied by the trigger efficiency function found in section 9.5, as stated in equation (9.14), where the values for A_{FD} and B_{FD} are taken from equation (9.13) for the combined $S1$ signal.

$$f_{LY,cS1}(cS1) = f_{FD}(cS1, A_{FD}, B_{FD}) \cdot f_{Gaussian}(\mu_{cS1}, \sigma_{cS1})$$

$$= \left(1 - \frac{1}{1 + \exp\left(\frac{cS1 - A_{FD}}{B_{FD}}\right)} \right) \cdot \frac{A}{\sigma_{cS1} \sqrt{2\pi}} \cdot e^{-\frac{1}{2} \left(\frac{cS1 - \mu_{cS1}}{\sigma_{cS1}} \right)^2} \quad (9.14)$$

The fit parameters for the $cS1$ -slices are listed in table 9.13.

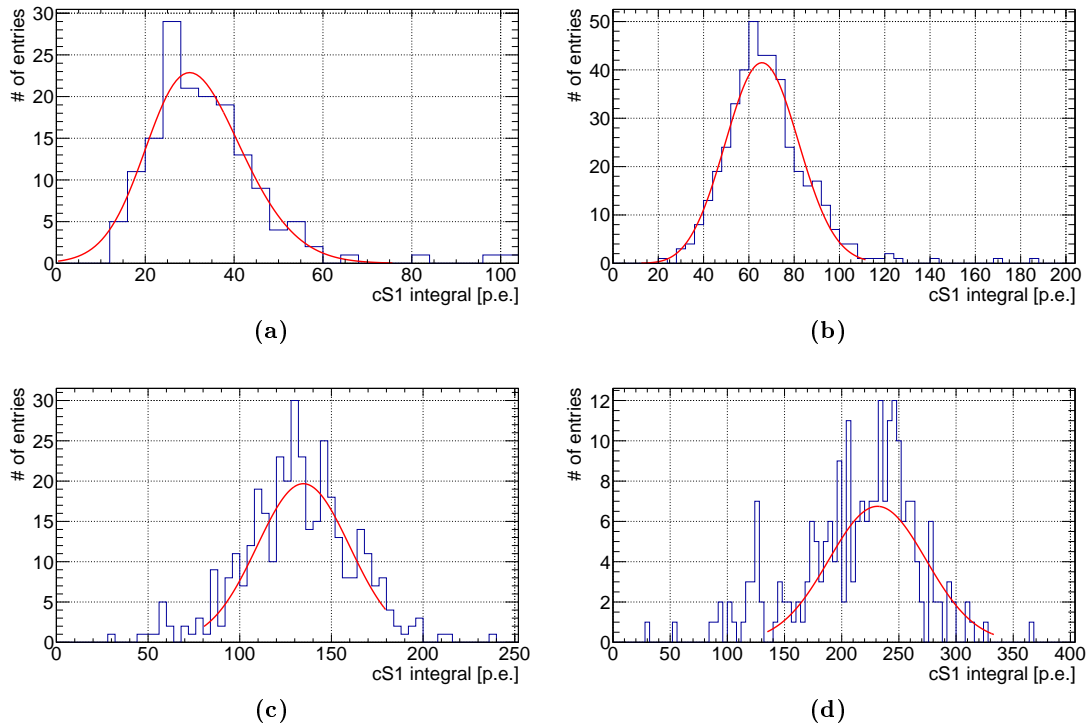


Figure 9.23: Examples of the $cS1$ signal distribution for nearly monoenergetic ranges in deposited energy: (a) $5.5 \text{ keV} < E_{TPC} < 6.5 \text{ keV}$, (b) $11.5 \text{ keV} < E_{TPC} < 12.5 \text{ keV}$, (c) $21.5 \text{ keV} < E_{TPC} < 22.5 \text{ keV}$ and (d) $35.5 \text{ keV} < E_{TPC} < 36.5 \text{ keV}$. With increasing energy deposit, the $cS1$ signal distributions become broader.

E_{TPC} [keV]	μ_{cS1} [p.e.]	$\Delta\mu_{cS1}$ [p.e.]	σ_{cS1} [p.e.]	$\Delta\sigma_{cS1}$ [p.e.]	χ^2_{red}	LY [$\frac{\text{p.e.}}{\text{keV}}$]	ΔLY [$\frac{\text{p.e.}}{\text{keV}}$]
5	12.24	11.19	15.16	4.96	0.81	2.45	2.29
6	23.75	3.10	14.27	2.02	0.45	3.96	0.84
7	31.89	1.32	13.58	1.00	0.53	4.56	0.68
8	37.46	1.31	15.51	1.29	0.96	4.68	0.61
9	47.47	0.93	15.13	0.79	0.53	5.27	0.60
10	54.70	0.90	15.44	0.76	1.11	5.47	0.55
11	59.52	0.94	16.77	0.79	0.75	5.41	0.50
12	65.74	0.84	16.12	0.75	0.58	5.48	0.46
13	73.37	0.88	16.24	0.68	1.11	5.64	0.44
14	79.29	0.88	17.46	0.78	0.39	5.66	0.41
15	85.45	1.12	20.10	0.88	1.33	5.70	0.39
16	91.92	0.91	18.88	0.81	0.97	5.74	0.36
17	101.26	0.95	19.14	0.73	1.38	5.96	0.35
18	105.64	1.39	22.90	1.35	1.32	5.87	0.34
19	111.51	1.05	20.37	1.02	0.96	5.87	0.31
20	121.46	1.38	23.03	1.19	1.43	6.07	0.31
21	123.30	1.63	25.66	1.58	0.95	5.87	0.29
22	134.69	1.87	25.24	1.71	1.67	6.12	0.29
23	140.72	1.60	25.67	1.49	0.82	6.12	0.27
24	147.66	1.72	23.57	1.89	1.57	6.15	0.27
25	153.72	2.92	33.09	3.35	0.50	6.15	0.27
26	160.23	2.41	30.31	2.54	1.13	6.16	0.25
27	165.98	1.91	25.95	2.04	0.86	6.15	0.24
28	171.62	2.87	29.13	3.03	0.70	6.13	0.24
29	176.45	3.85	28.02	3.38	1.21	6.08	0.25
30	199.24	9.33	38.10	7.74	1.40	6.64	0.38
31	194.64	4.02	36.37	5.57	0.67	6.28	0.24
32	190.39	2.31	26.21	2.53	1.17	5.95	0.20
33	207.68	3.01	28.56	3.24	1.40	6.29	0.21
34	206.61	2.97	34.77	3.16	1.30	6.08	0.20
35	221.10	5.39	54.86	6.66	0.95	6.32	0.24
36	231.26	3.87	42.54	4.17	0.93	6.42	0.21
37	235.33	3.94	42.99	4.62	0.70	6.36	0.20
38	235.97	3.34	39.69	3.33	0.68	6.21	0.19
39	249.92	4.57	42.82	6.71	1.17	6.41	0.20
40	255.69	6.13	52.66	7.79	0.88	6.39	0.22
41	241.70	9.33	67.59	13.83	0.95	5.90	0.27
42	265.00	6.28	50.54	7.92	1.12	6.31	0.21
43	269.17	5.22	40.73	6.59	0.89	6.26	0.19
44	265.89	13.12	85.09	18.26	0.67	6.04	0.33
45	288.30	10.86	78.70	16.04	0.56	6.41	0.28
46	255.33	19.80	113.37	31.44	0.60	5.55	0.45
47	283.38	12.05	82.63	18.29	0.66	6.03	0.29
48	284.37	23.20	120.47	40.22	0.41	5.92	0.50
49	307.06	14.81	86.08	22.35	0.56	6.27	0.33

Table 9.13: Parameters of the $cS1$ slices for the determination of the light yield for a drift field strength of 198 V/cm. The values for the mean signal μ_{cS1} and its standard deviation σ_{cS1} as well as their uncertainties are obtained by fitting the individual energy slices, as well as the reduced χ^2 . The light yield LY and its error are calculated using equation (9.15).

The mean values μ_{cS1} with their errors are divided by the value of E_{TPC} for the respective energy slice, as stated in equation (9.15).

$$LY_{cS1}(E_{\text{TPC}}) = \frac{\mu_{cS1}(E_{\text{TPC}})}{E_{\text{TPC}}} \quad (9.15)$$

$$\Delta LY_{cS1}(E_{\text{TPC}}) = LY_{cS1}(E_{\text{TPC}}) \cdot \sqrt{\left(\frac{\Delta\mu_{cS1}(E_{\text{TPC}})}{\mu_{cS1}(E_{\text{TPC}})}\right)^2 + \left(\frac{dE_{\text{TPC}}}{E_{\text{TPC}}}\right)^2}$$

The standard deviation σ_{cS1} allows to quantify the energy resolution for the MainzTPC with respect to the scintillation signal. For the four different drift field strengths, the values for σ_{cS1} from the Compton measurements are plotted against the energy deposit E_{TPC} in figure 9.24. The signal distributions become broader for increasing energy deposit, which results in an increasing standard deviation. In the region below ~ 30 keV, the graphs for all drift field configurations show overlapping values. Above 30 keV, the measured standard deviations deviate from each other, which is most likely caused by the lower statistics in the respective energy slices.

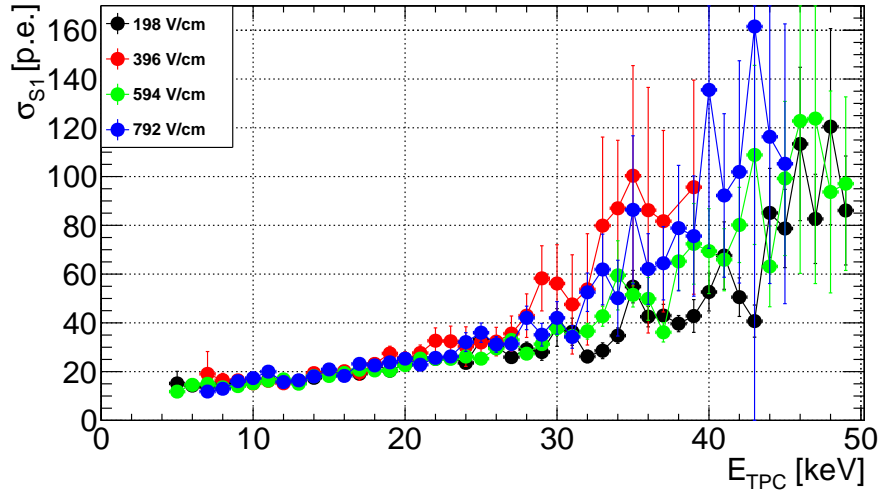


Figure 9.24: Energy resolution in the MainzTPC: The standard deviation σ_{cS1} in dependence of the energy E_{TPC} for the different drift field strengths. The measured standard deviations show similar values for low energy deposits. For $E_{\text{TPC}} > 30$ keV, the values start to deviate, with larger uncertainties due to lower statistics.

The energy resolution in $cS1$ is independent of the applied drift field. Therefore the values obtained from the four different configurations are combined and the weighted mean value is calculated for each energy. This leads to the graph shown in figure 9.25a. The graph is fitted using a function stated in equation (9.16), which also contains the found fit parameters. The fit function is drawn in red. The blue dashed area marks the 95 % confidence level for the fit.

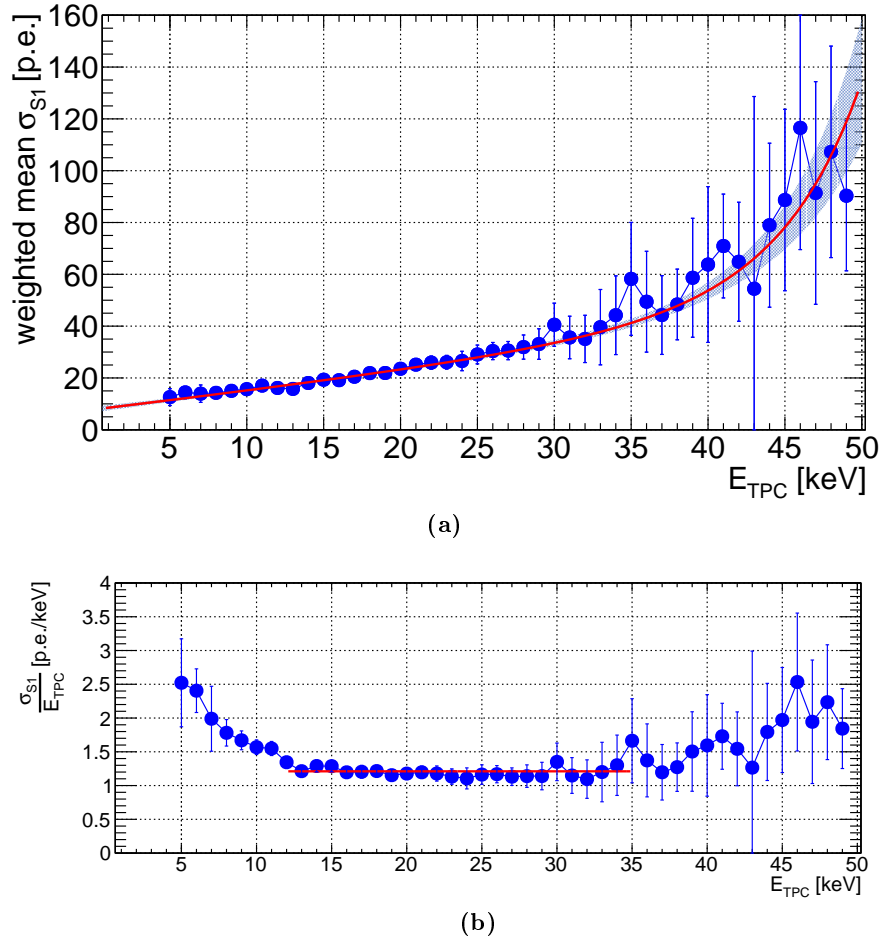


Figure 9.25: Energy resolution in the MainzTPC: (a) The weighted mean of σ_{cS1} for the measurements from all drift fields in dependence of the energy E_{TPC} . In red, a fit according to equation (9.16) is shown, with the blue area being the 95 % confidence level for the fit. (b) shows the relative energy resolution, with σ_{cS1} being divided by the respective energy deposit. The relative energy resolution remains constant for the energy range between 12 and 35 keV at a value of 1.21 p.e./keV.

$$\sigma_{S1}(E_{TPC}) = a_{\sigma} + b_{\sigma} \cdot E_{TPC} + \exp\left(\frac{(E_{TPC})^2}{c_{\sigma}^2}\right) \quad (9.16)$$

with: $a_{\sigma} = 6.79$ p.e. $b_{\sigma} = 0.72 \frac{\text{p.e.}}{\text{keV}}$ $c_{\sigma} = 23.52$ keV

The observable overall increase in σ_{cS1} with increasing energy can be associated to the increase in scintillation light. This means, with more scintillation light, the spread of the signal distribution can vary over a larger range of measured photoelectrons.

Figure 9.25b depicts the relative energy resolution, with the weighted mean of σ_{cS1} divided by the respective energy deposit. As can be seen, the resolution has a mean of (1.21 ± 0.02) p.e./keV in the energy region between 12 and 35 keV, as was determined

using a constant fit shown in red. Below this energy range, the resolution shows values up to 2.5 p.e./keV, above 35 keV the values fluctuate around 2 p.e./keV. In the outer regions this might also be linked to the smaller statistics of the considered energy slices. Overall, the relative energy resolution appears to be quite stable.

Figure 9.26 shows the light yield calculated from table 9.13 for the drift field of 198 V/cm. It ranges between 2.45 p.e./keV for $E_{\text{TPC}} = 6$ keV and 6.64 p.e./keV for 30 keV. The considered energy range between 6 and 49 keV was chosen to provide sufficient statistics in each energy slice for the data fit.

For low energies, the light yield shows a steep increase from 2.45 p.e./keV up to roughly 5.5 p.e./keV at 10 keV. After that, the light yield rises smoothly to its maximum at around 30 keV. In the energy range between 20 and 40 keV, there is only a slight change in light yield. For energies above 30 keV, its value becomes constant and shows even tendencies to decreases for the highest energy values.

The steep rise of the light yield at small E_{TPC} is directly connected to the trigger efficiency and could not be observed when the energy slices first were only fitted using a simple Gaussian. This emphasizes the influence of the trigger efficiency measurement.

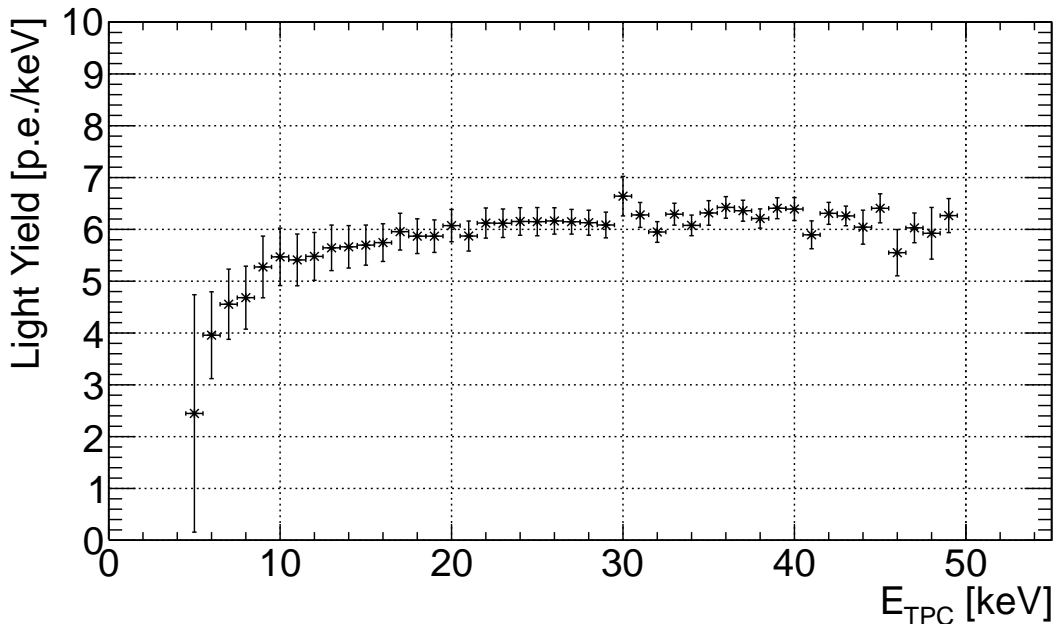


Figure 9.26: Light yield for a Compton scattering measurement with an applied drift field of 198 V/cm. It is the mean $cS1$ signal determined from energy slices with a Gaussian fit multiplied with the trigger efficiency, divided by the corresponding energy deposit E_{TPC} . For low energies, the light yield increases up to a maximum value at around 30 keV. The light yield value remains approximately constant or even decreases slightly for higher E_{TPC} above 30 keV.

The light yields for the other field configurations were determined analogously. The corresponding plots showing the $cS1$ signal in dependence of E_{TPC} as well as the individual light yield graphs and the parameter tables can be found in appendix B.10.

Figure 9.27 depicts the light yield graphs for the four different drift field strengths. The light yield curve for the lowest drift field at 198 V/cm reaches the highest values and with increasing drift field strength, the observed light yields become smaller. This behaviour is expected since the increasing drift field strength leads to a suppression in electron recombination as more electrons are drifted away from the point of interaction, and is discussed in more detail in section 9.6.2.

The shapes of the light yield curves appear similar and all of them display the steep rise for the light yield in the low-energy range up to about 10 keV. The light yield for 198 V/cm rises moderately up to its maximum at around 30 keV and remains constant. For 396 V/cm, the light yield shows a similar curve with slightly lower values and a decreasing tendency above 30 keV. For the two highest field strengths at 596 V/cm and 792 V/cm, the light yield reaches a maximum value already after the steep rise at low E_{TPC} , remains constant at approximately 5.3–5.4 p.e./keV in the range between 15 and 25 keV and then starts to decrease notably.

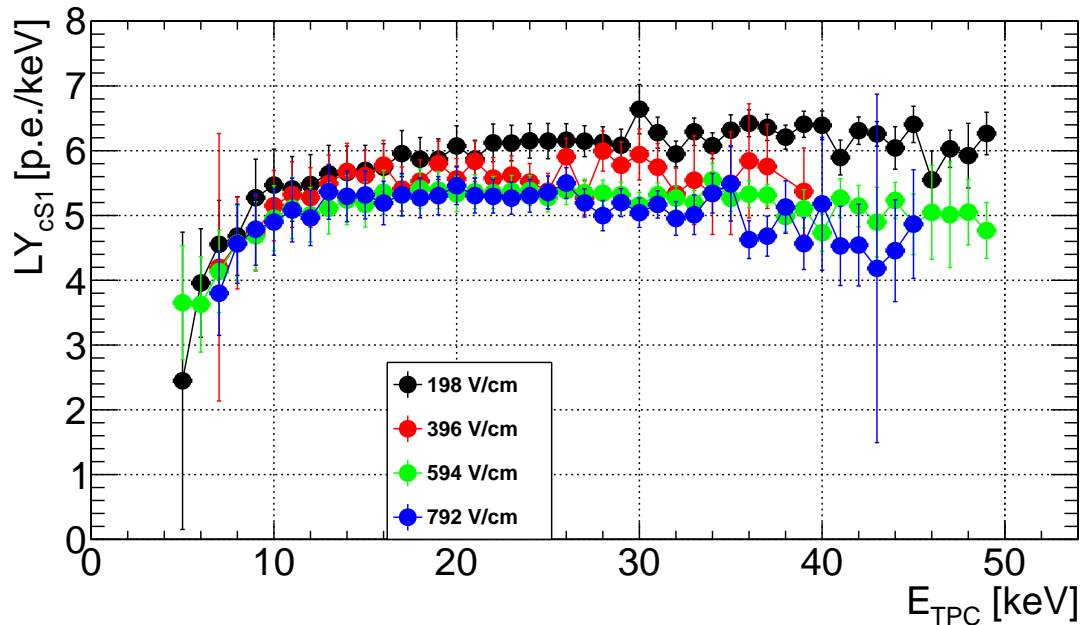


Figure 9.27: Light yield LY_{cS1} in dependence of E_{TPC} for different drift field strengths. For increasing drift field, the measured light yield generally exhibits lower values. For all field strengths, the observed light yield shows a steep rise for the light yield at low E_{TPC} , followed by a more moderate increase with increasing energy and a stagnation or even a decrease in light yield for higher energy deposit values. This trend is evident for the two highest drift fields. In the low-energy region, the graphs seem to overlap. The data points for the individual measurements cover different ranges of E_{TPC} : Due to the different amount of available data for each drift field configuration, energy slices with too low statistics were not considered.

As mentioned in section 9.1, the conversion factor between the measured photoelectrons and the actual number of photons produced by the event could not be determined.

A quantitative comparison to simulations by NEST [1] or measurements conducted by Goetzke et al. with a similar TPC called neriX [2] as presented in section 2.5 is not possible. Therefore, the observed light yield is discussed qualitatively. For comparison, the mentioned simulation and measurement results are shown in figure 2.7.

The general shape of the light yield curves obtained with the MainzTPC is similar to the expectation given by NEST and neriX. The steep rise for low energy deposits can be observed for E_{TPC} between 0 and roughly 10 keV. At these low energies, the light yield graphs for all drift fields seem to overlap, which is also observed in both the NEST simulation and the neriX measurement. Below 5 keV, a comparison of the light yield determined with the MainzTPC is not possible due to low statistics in the $S1$ data from the Compton measurements.

Except for the lowest drift field of 198 V/cm, the light yield curves for all drift fields have their maximum values between 20 and 30 keV, as expected, and show a decrease in light yield for higher energies. For the lowest drift field, the light yield remains at a roughly constant level. Regarding the measured light yield in figure 2.7b, the maximum light yield there is found between 30 and 40 keV. This suggests that the limited energy range of the MainzTPC light yield leads to the observed constant value for the low drift field.

The energy range of the MainzTPC light yield is more limited than the NEST model and neriX data, but the tendency of the light yield to decline above 30 keV is apparent at least for the two highest fields. For the two lower fields, the declining tendency is only subtly developed. This also suggests that the stronger decline observed in NEST and neriX with increasing drift field is present in the MainzTPC data at hand.

It has to be noted that for the light yield determined in this section only a part of the event selection tools were applied. The limits of the fiducial volume along with a single $S1$ in the trigger time window and the choice of the largest $S2$ signals all contribute to the event distribution shown in figure 9.22. When adding the $S1$ asymmetry and $S2$ width cuts, the remaining statistics become very low and the observed light yield curves take on a flat shape. This result is shown in figure 9.28 but is not examined further, as the low statistics deny the possibility for a meaningful analysis.

9.6.2 | Field Quenching

It can be observed that the light yield generally decreases with increasing drift field strength. This effect is called “field quenching” and is expected because, at higher drift field, a larger fraction of the electrons released in the Compton interaction is separated from the Xe_2^+ ionized dimers (see section 2.3) and recombination being suppressed to a higher extent. A reduction of the $S1$ signal is the result. Table 9.14 lists the light yield values with respect to different energy ranges in E_{TPC} and different drift field strengths. For the respective energy intervals, the mean of the measured light yield values is stated.

From the previous section it is known that the light yield is not constant or even linear

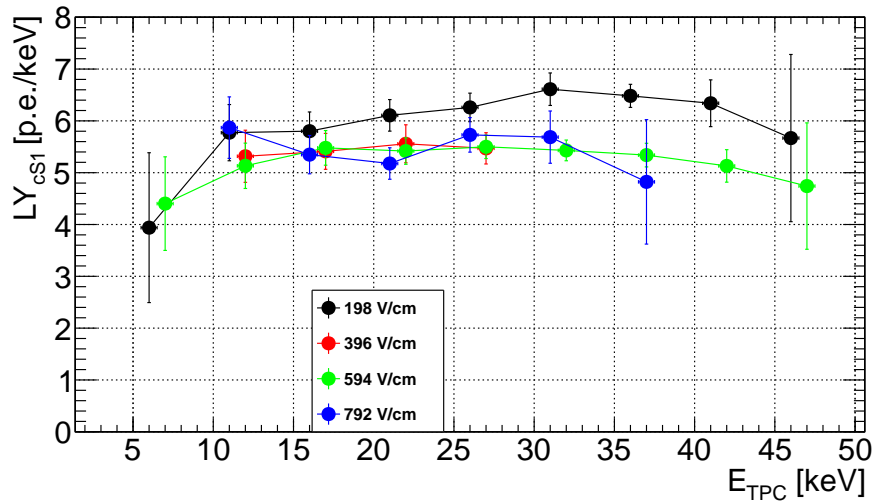


Figure 9.28: Light yield LY_{cS1} in dependence of E_{TPC} for different drift field strengths with all cuts from the event selection. The light yield curves for the drift fields of 198 and 594 V/cm follow the same trend as observed for the less constricted event sample, but due to lower statistics fewer data points are available for analysis. For the fields at 396 and 792 V/cm, the shape of the light yield curve is not recognizable anymore.

E_{TPC} [keV]	198 [$\frac{V}{cm}$]		396 [$\frac{V}{cm}$]		594 [$\frac{V}{cm}$]		792 [$\frac{V}{cm}$]	
	LY_{cS1}	ΔLY_{cS1}	LY_{cS1}	ΔLY_{cS1}	LY_{cS1}	ΔLY_{cS1}	LY_{cS1}	ΔLY_{cS1}
1 – 10	4.40	0.18	4.66	0.10	4.27	0.09	4.51	0.12
11 – 20	5.74	0.02	5.55	0.02	5.25	0.01	5.26	0.01
21 – 30	6.16	0.02	5.68	0.02	5.33	0.01	5.25	0.01
31 – 40	6.27	0.02	5.55	0.03	5.21	0.02	5.02	0.03
41 – 50	6.08	0.03	–	–	5.03	0.02	4.41	0.04

LY_{cS1} [$\frac{p.e.}{keV}$] and ΔLY_{cS1} [$\frac{p.e.}{keV}$]

Table 9.14: Light yield values of $cS1$ from Compton measurements with different drift field strengths for different energy ranges in E_{TPC} . For each energy interval, the mean light yield is determined. With increasing drift field strength the amount of primary scintillation light decreases. For 1–10 keV, the low statistics for the measurements at 394 V/cm and 792 V/cm lead to a deviation from the expected trend. For 41 – 50 keV, no data points are available for 394 V/cm.

with energy deposit. The choice of narrow energy intervals allows to examine the light yield for a specific range in energy deposit at different drift fields. By this the change of the light yield with increasing energy deposit is taken into consideration.

Figure 9.31 shows the field quenching for the energy intervals specified above. The decrease in light yield with increasing drift field is visible for all energy intervals except for the lowest one. There the obtained light yield is shifted to higher values for measurements at 394 V/cm and 792 V/cm due to lower statistics.

The available data sets do not contain a Compton measurement without an applied drift

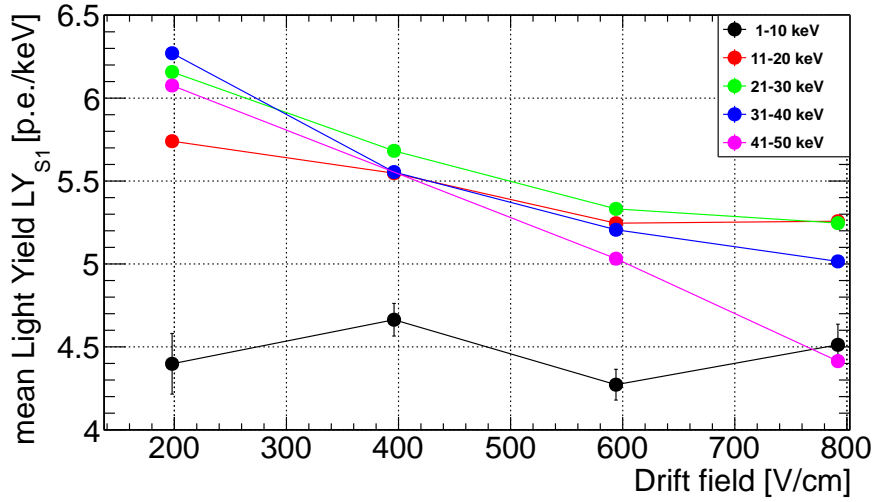


Figure 9.29: Field quenching: Change of the light yield LY_{S1} in dependence of the drift field strength and the energy deposit E_{TPC} . Except for the lowest energy interval the quenching effect with increasing drift field is observable for different energy deposits.

field. A normalization of the light yield to the unquenched zero-field value is therefore not directly possible. In the following, the data at hand is used to estimate a zero-field light yield value.

Aprile et al. examined the field quenching effect in [105] for an energy deposit of 122 keV and found the black data points presented in figure 9.30. The scintillation response is normalized to the zero-field light yield, as shown on the ordinate axis as $LY_{CS1}(E_{drift})/LY_{CS1}(0)$. Using an exponential function depending on the drift field strength E_{drift} , as stated in equation (9.17), allows to fit the black data points. Table 9.15 summarizes the found fit parameters.

$$f_{FQ}(E_{drift}) = a_{FQ} + \exp(b_{FQ} + c_{FQ} \cdot E_{drift}) \quad (9.17)$$

	value	error
a_{FQ} [p.e./keV]	0.514	0.014
b_{FQ} [(V/cm) $^{-1}$ · p.e./keV]	-0.783	0.030
c_{FQ}	$-4.4 \cdot 10^{-3}$	$0.4 \cdot 10^{-3}$

Table 9.15: Fit parameters for the exponential fit from equation (9.17) of the field quenching.

The fit function is then used to assign a relative light yield value to each of the light yields determined for the MainzTPC. The resulting values f_{FQ} for the individual light yield values are listed in table 9.16, along with the corresponding theoretical maximum light

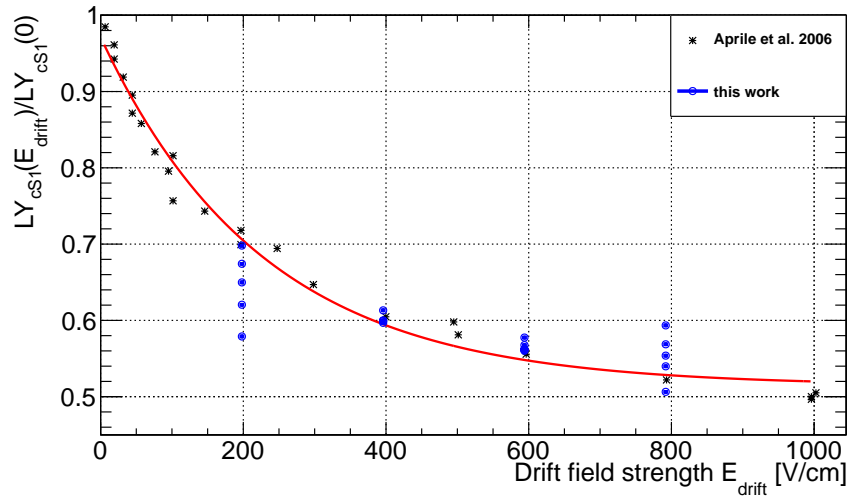


Figure 9.30: Relative light yields in dependence of the drift field strength: The relative light yields corresponding to a maximum measured without an applied drift field (black data points, from [105]) are fitted with a function according to equation (9.17). The fit function is used to normalize the light yields measured with the MainzTPC to the theoretical zero-field light yield $\overline{LY}_{0,\text{calc}}$ (see equation (9.18)). These relative light yields are overlaid in the plot as blue circles.

yield $\overline{LY}_{\text{calc}}$ at zero drift field, which is calculated following equation (9.18). Note that the uncertainty $\Delta\overline{LY}_{\text{calc}}$ is the standard deviation of the four values used to determine the mean.

The individual light yields from table 9.14 are then normalized using the respective zero-field light yield value from table 9.16 and overlaid in figure 9.30. For the lowest drift field, the data points are found below the curve of the fit function. For the two middle fields, the data points follow the shape of the overall distribution. At 792 V/cm, the data points are spread out but distributed around the fit curve. The deviations to the data from [105] can be explained by the fact that the energy deposit and hence the light yields compared here are not in the same range, which could lead to differences in the quenching behaviour. Low statistics in the MainzTPC data also has an impact on the data quality.

$$LY_{0,\text{calc}}(E_{\text{drift}}) = \frac{LY_{\text{range}}(E_{\text{drift}})}{f_{FQ}(E_{\text{drift}})} \quad \Delta LY_{0,\text{calc}}(E_{\text{drift}}) = \sigma_{LY_{0,\text{calc}}} \quad (9.18)$$

Figure 9.31 depicts the absolute values for the light yields in dependence of the drift field strength. The zero-field light yield is added as a dotted marker and the curve between 0 and 198 V/cm is indicated with a dotted line. Together with this theoretically estimated value the data points show a similar exponential shape as the relative data points in figure 9.30.

The drift field strengths applied in the MainzTPC measurements are all in the range below 1 kV/cm. The field quenching effect increases exponentially in the low field range be-

$E_{\text{drift}} \left[\frac{\text{V}}{\text{cm}} \right]$	$f_{FQ}(E_{\text{drift}})$	$E_{\text{TPC}} \text{ [keV]}$				
		1 – 10	11 – 20	21 – 30	31 – 40	41 – 50
		$LY_{0,\text{calc}}(E_{\text{drift}}) \left[\frac{\text{p.e.}}{\text{keV}} \right]$				
198	0.706	6.23	8.13	8.72	8.88	8.61
396	0.595	7.83	9.33	9.55	9.33	–
594	0.548	7.79	9.58	9.72	9.51	9.18
792	0.528	8.53	9.95	9.93	9.50	8.35
$\overline{LY_{0,\text{calc}}} \left[\frac{\text{p.e.}}{\text{keV}} \right]$		7.60	9.25	9.48	9.30	8.71
$\sigma_{LY_{0,\text{calc}}} \left[\frac{\text{p.e.}}{\text{keV}} \right]$		0.97	0.79	0.53	0.30	0.43

Table 9.16: For different ranges in E_{TPC} and for the individual drift field configurations, the estimated maximum light yields $LY_{0,\text{calc}}(E_{\text{drift}})$ are calculated according to equation (9.18). The value $\overline{LY_{0,\text{calc}}}$ is the average of the light yields for one energy range, not taking into account the drift fields. Using equation (9.18), the zero-field value for the energy-dependent light yield is calculated.

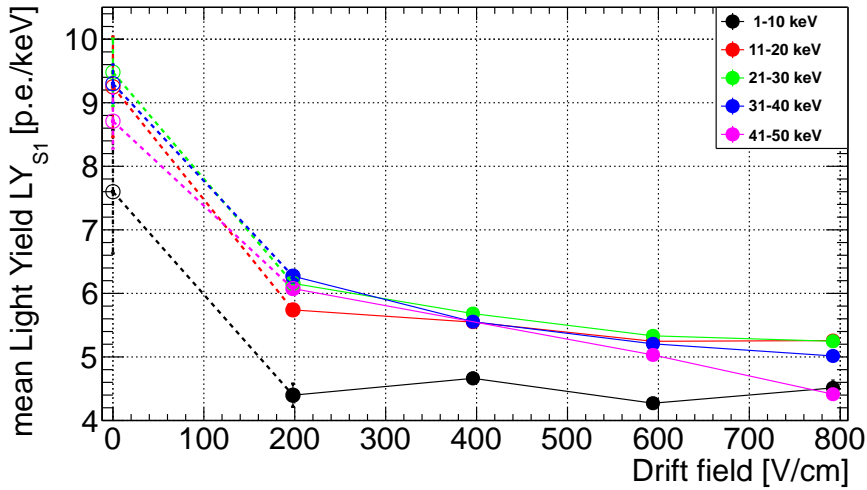


Figure 9.31: Field quenching with estimated zero-field value in dependence of the drift field strength. The exponential distribution of the data points can be perceived in a rudimentary form.

fore asymptotically flattening out between 1 kV and 3 kV, according to the measurements in [105]. The flattening of the field quenching is already visible in figures 9.30 and 9.31, but saturation is not reached yet for the applied fields.

The quenching effect in $cS1$ leads to an increased signal for the charge signal $S2$ (or $cS2$, respectively), since the electrons that would have recombined now contribute to the $S2$ signal. This “inverse quenching” effect is present in the examination of the charge signal in section 9.7.3.

9.6.3 Impact of the $S1$ z -correction

The effect of the z -correction for the $S1$ signals from the Compton data is examined here to get an impression of the magnitude of change in the signal values. Exemplarily, the Compton data for the drift field strength of 594 V/cm is used for illustration.

Figure 9.32a shows the dependency of the $S1$ signal and its z -corrected equivalent $cS1$ in figure 9.32b of the deposited energy E_{TPC} . A difference is almost not visible between the two graphs. The event distribution for $cS1$ appears to be slightly narrower than for the uncorrected $S1$.

Both distributions are divided into energy slices with a width of 1 keV and for each slice, the signal distribution is fitted. The results are depicted in figure 9.32c, using the standard deviation of the Gaussian fit as a measure for the distribution spread. It can be seen that the mean values for $cS1$ are found to be slightly below the mean of their

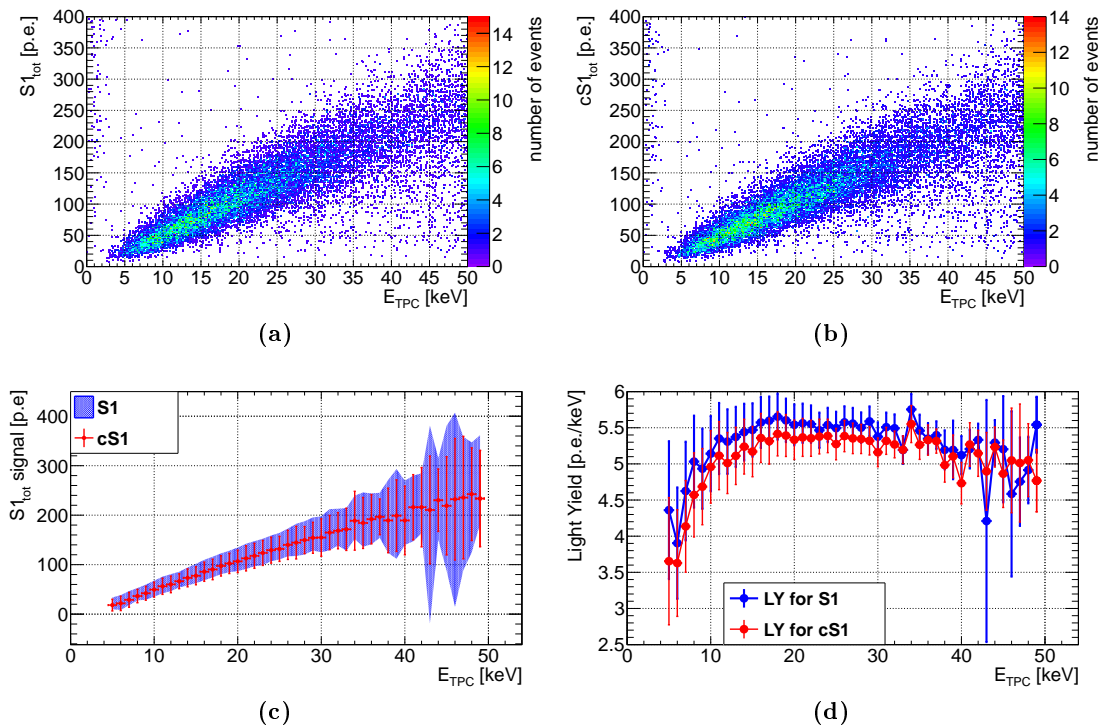


Figure 9.32: Comparison of the scintillation signals with and without z -correction for the Compton data acquired at a drift field strength of 594 V/cm. The signal distribution in dependence of the energy deposit E_{TPC} , measured with the germanium detector, is shown for $S1$ in (a) and for $cS1$ in (b). The distributions do not differ significantly, for $cS1$, the distribution is slightly narrower than for $S1$. Both distributions are divided into signal slices of 1 keV width and the respective results from the Gaussian fits are overlaid in (c). The mean value for $cS1$ is always slightly higher than for $S1$. In (d), the light yield in dependence of E_{TPC} are shown, with the light yield for $cS1$ generally exceeding the one for $S1$.

counterparts for $S1$. The reason for this is explained below.

This leads to a generally lower light yield for $cS1$, which can be seen in figure 9.32d. The light yields determined for both $S1$ and $cS1$ are plotted in dependence of the energy deposit E_{TPC} . Within errors, their mean values are in agreement for most energies.

The comparison of $S1$ and $cS1$ yields similar results for all examined drift fields.

The $S1$ z -correction seems to have very small influence on the Compton data. This can be explained by the event distribution regarding the interaction depth z . The Compton measurements were conducted using the strong ^{137}Cs source which was placed inside a lead collimator. The collimated gamma-ray beam only illuminated a fraction of the active volume in the MainzTPC. Figure 9.33a shows the event distribution in z for the Compton measurements at all drift fields. Since the position of the lead collimator was unchanged for all measurements, the illumination of the TPC is the same for all measurements and is limited to an interaction depth of roughly $22\text{ mm} < z < 48\text{ mm}$. The corresponding distributions for the correction factor $f_{S1}(z)$, which was introduced in section 8.3, show that for most signals, the correction factor ranges between roughly 1 and 1.1, as depicted in figure 9.33b. This explains that there is almost no change between the event distributions of $S1$ and $cS1$, apart from a slight decrease for the corrected signal due to the form of equation (8.9).

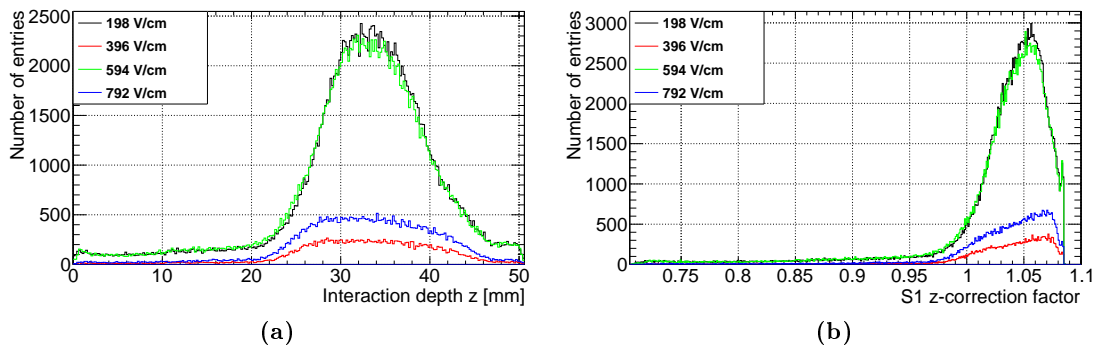


Figure 9.33: Event distribution in z for the Compton measurements and corresponding $S1$ z -correction factors for all drift fields. The collimation of the gamma-ray beam leads to a narrow distribution for the correction factor between values of roughly 1 and 1.1, explaining the small influence of the $S1$ z -correction.

9.7 | Secondary Scintillation $cS2$

9.7.1 | Event distribution for $cS2$

For the $cS2$ signal a similar, roughly linear dependence of the energy deposit E_{TPC} as found for the $cS1$ signal is expected. Figure 9.34 shows the event distribution in the $cS2$ - E_{TPC} plane for the drift field strengths of 198 V/cm, 396 V/cm, 594 V/cm and 792 V/cm. The applied event selection consists of the complete set from section 9.3: Fiducialization, only one $S1$ in the trigger time window, choice of the largest $S2$, $S2$ width cut and $S1$ asymmetry cut.

Especially for the two lower field configurations the plots depict two clearly separated event clusters or populations. A second population is neither expected for $cS2$ nor observed in the complementary $cS1$ - E_{TPC} graphs. The upper population is more promi-

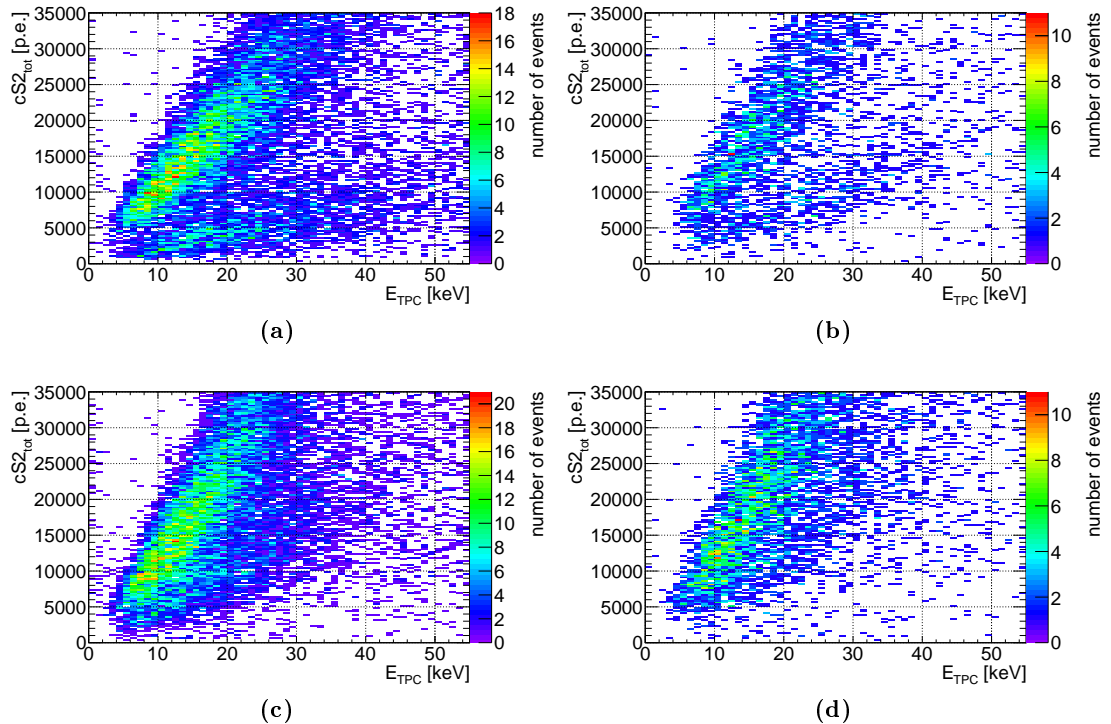


Figure 9.34: Event distributions of $cS2$ in dependence of E_{TPC} for the applied drift field strengths of (a) 198 V/cm, (b) 396 V/cm, (c) 594 V/cm and (d) 792 V/cm. The graphs exhibit two different populations, which are most prominent for the lowest drift field of 198 V/cm. With increasing drift field strength, the lower population seems to approach the upper population until the two event distributions merge for the highest field of 792 V/cm. Independently, the increase of the amount of measured $cS2$ signal for increasing drift field can be observed. For the plots, the event selection set “d” from table 9.17 is applied.

ment and does only change slightly with increasing drift field, shifting to larger $cS2$ values at lower energy deposits. The lower event population presumably experiences more effect from the applied drift field as it seems to merge with the upper population at higher drift fields.

Figure 9.35 shows the event distribution for the Compton measurement at 198 V/cm with different event selection sets applied to the data. A red line of the form

$$cS2 = 4 \cdot 10^2 \cdot E_{\text{TPC}}$$

divides the two populations on the event plane. The gradient of the line is chosen by eye and allows to compare the numbers of events for the populations and the impact of the individual selection sets. The resulting values are listed in table 9.17.

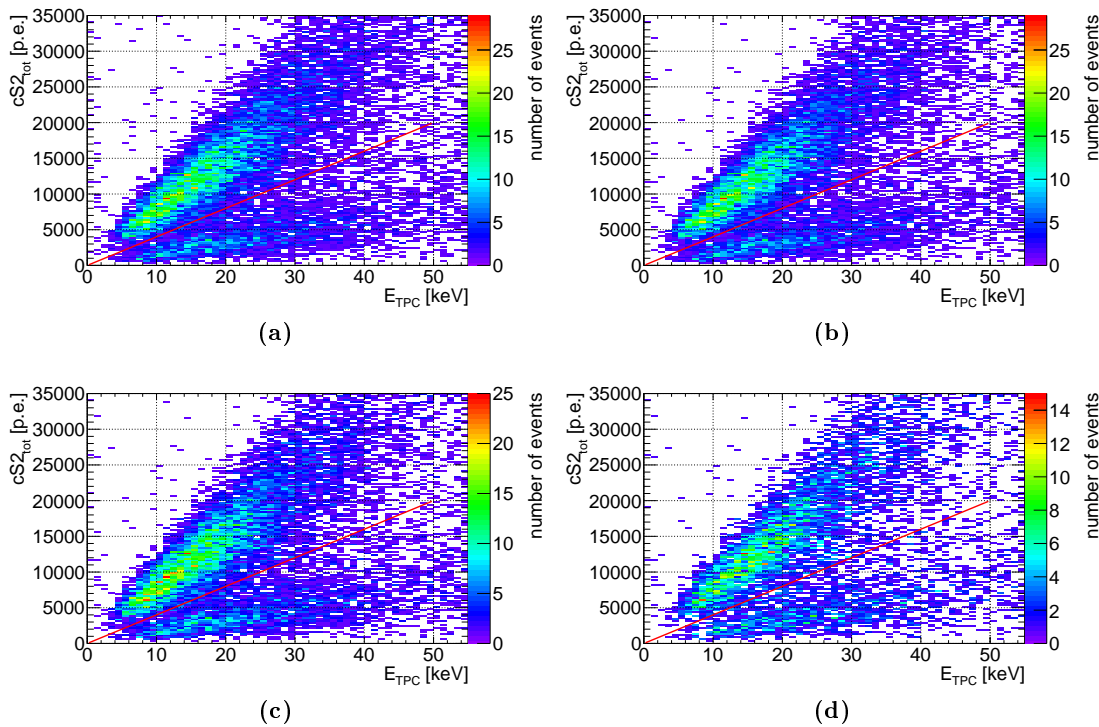


Figure 9.35: Event distributions of $cS2$ in dependence of E_{TPC} at 198 V/cm, with different applied event selection sets. The event selection for each subfigure is stated in table 9.17. As can be seen, the selections decrease the number of events for each population, but no population is explicitly impacted by a specific selection or cut.

Applying the different selection sets decreases the number of events passing the selection process, but in each case both populations are impacted in the same order of magnitude. The ratio of both populations becomes smaller with increasing number of selections, but the upper population exceeds the lower by at least a factor of 3.2–3.5.

The behaviour of the two populations was also examined with respect to different event

$E_{\text{drift}} \left[\frac{\text{V}}{\text{cm}} \right]$	Selection	up	down	ratio (up/down)
198	a	15082	3503	4.30545
198	b	11397	3420	3.33246
198	c	10627	3278	3.24192
198	d	6060	1880	3.2234
396	a	4308	879	4.90102
396	b	3232	841	3.84304
396	c	2969	820	3.62073
396	d	1728	492	3.5122

Selection	Description
a	basic selection (configuration 4 from table 9.7): only one $S1$ in trigger time window, selection of largest $S2$
b	basic + fiducialization
c	basic + fiducialization + $S2$ width cut
d	basic + fiducialization + $S2$ width cut + $S1$ asymmetry

Table 9.17: Statistics and ratio of the upper and lower population for the drift field strengths 198 V/cm and 396 V/cm with different applied event selections.

quantities, as shown in figure 9.36. The four plots each contain histograms for the upper (red) and lower population (blue) as well as the sum of all events (black) from Compton measurements at 198 V/cm. The lowest drift field configuration was chosen since it exhibits the largest discrepancy between the two populations. All event selections are applied.

Figure 9.36a depicts the spectra of the $cS1$ signal. The spectra are similar in position and shape, without any deviating features, and only in statistics a difference is visible. For the event distribution in z in figure 9.36b, the same statement holds true. Here, a slight shift of the lower population to smaller z is indicated, but it is not a prominent feature and was not examined further.

Figure 9.36c and 9.36d show the $S2$ signal width of the Bottom PMT at FWHM and at 10% of the signal amplitude, respectively. In both cases, the signals of the lower population show a slight shift to larger widths. Since the spectra for the lower population are almost completely covered by the distribution of the upper population, the examination of the differing events does not seem promising.

Even for the strict condition allowing only one $cS1$ and one $cS2$ signal per waveform (configuration 1 in table 9.7), the two populations emerge for the $cS2$ signal. However, allowing a second $S2$ and choosing the largest one to be the signal $S2$ leads to an increase for the upper population.

In summary, the origin of the double population event distribution remains unknown.

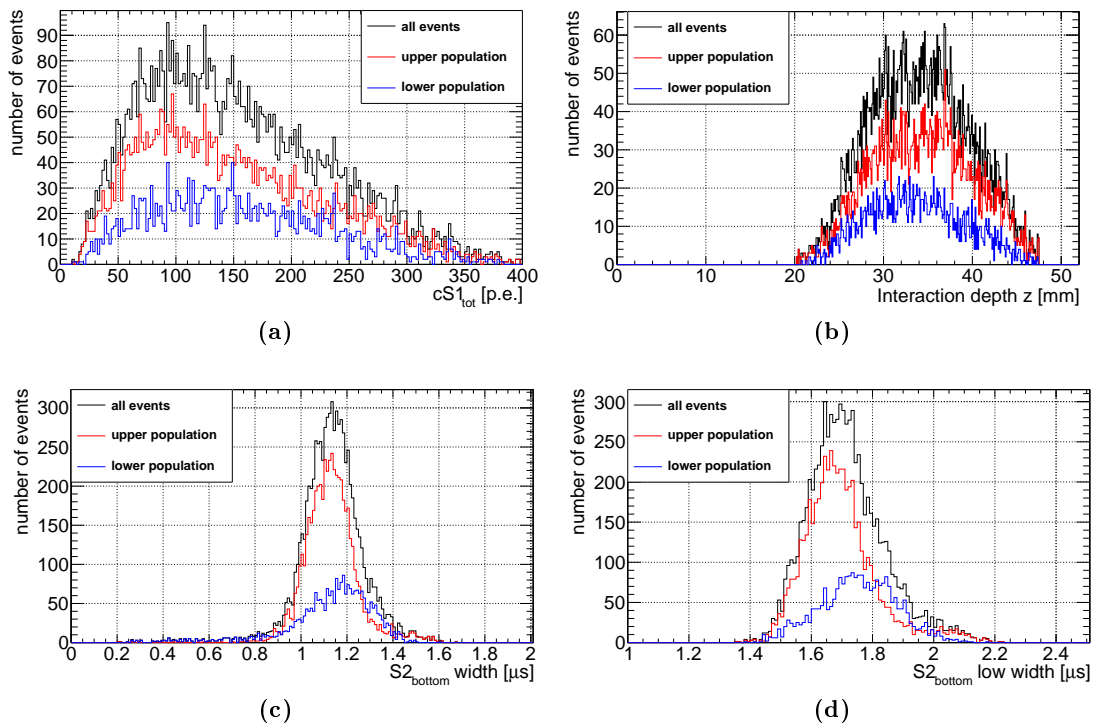


Figure 9.36: Spectra of (a) the $cS1$ signal, (b) the interaction depth z , (c) the $S2$ signal width (FWHM) of the Bottom PMT and (d) the $S2$ signal width (at 10% of the signal height) of the Bottom PMT for the two event populations from the Compton data at a drift field of 198 V/cm. No distinct features that are significant only for one event population are visible.

Neither of the quantities or selections mentioned above show a distinct connection to one specific population which would hint to the physical cause. Even while browsing waveforms of events for the two populations, there was no difference visible in shapes of either $S1$ or $S2$. This phenomenon has to be investigated further in future science runs.

The effect of two emerging populations is also visible in the $cS2$ - $cS1$ plane, as can be seen in section 9.8.

Since the upper population is the most prominent of the two event distributions and considering the fact that the lower population seems to be merged completely with the upper one for the highest field, the upper population is used for the subsequent analysis of the $cS2$ signal. The expected shift of the $cS2$ event distributions to higher values with increasing drift field strength, which can be observed in figure 9.34 is evidence of the influence of the drift field on the amount of charge generating the $S2$.

9.7.2 | Charge Yield Calibration using Single *S2* signals

The *S2* signal is proportional to the charge released in the interaction and drifted to the GXe phase. Analogous to the light yield, which ideally should quantify the *S1* scintillation in photons per keV, the *S2* carries the information on the amount of electrons released in the interaction. The charge yield *QY* is stated in electrons per keV. To get to this quantity, a conversion factor is needed to find the amount of photoelectrons created by one electron. A technique already used in other experiments such as XENON1T is the examination of single electron *S2* signals.

Single electron *S2* signals can be characterized as signals with small amplitudes but relatively long widths. The typical width of these signals is in the order of about 1 μ s, in contrast to the small widths of a few tens to roughly 100 ns for *S1* signals.

For the measurements examined in the course of this thesis, the single electron *S2* signals could not be identified. The Raw Data Analysis tool used to find the signal peaks and to quantify their properties can not resolve signals which are very small and very broad in time. Therefore a direct calibration with the data used in this thesis is not available.

In July 2018, data for single electron *S2* signals was acquired and the respective analysis, now based on the tool *PAX*⁶, showed values of

$$\begin{aligned} S2_{1e^-} &= 18.32 \pm 0.12 \frac{\text{p.e.}}{e} & \sigma_{1e^-} &= 6.66 \pm 0.10 \frac{\text{p.e.}}{e} & \text{for } ^{133}\text{Ba} & \text{and} \\ S2_{1e^-} &= 18.18 \pm 0.20 \frac{\text{p.e.}}{e} & \sigma_{1e^-} &= 6.77 \pm 0.16 \frac{\text{p.e.}}{e} & \text{for } ^{137}\text{Cs}. \\ \overline{S2_{1e^-}} &= 18.25 \pm 0.16 \frac{\text{p.e.}}{e} \end{aligned}$$

These values are taken from [5]. In the same bachelor thesis, smaller values have been found in a later measurement. Since there was a change in the TPC setup between the measurements, the latter values will be ignored.

The calibration value $\overline{S2_{1e^-}}$ is the mean value for the examined single electron *S2* distributions, therefore it should be stressed that converting the measured scintillation signals to charge values will give an impression of the charge yield of the MainzTPC. For future measurements this calibration should be done with the data of the respective experimental run.

9.7.3 | Charge Yield *QY* for *cS2*

Analogously to section 9.6.1 the *cS2*- E_{TPC} -plane is sliced in energy with a slice width of $dE_{\text{TPC}} = 1$ keV and the signal distributions for *cS2* for each slice are fitted with a Gaussian. The *cS2*- E_{TPC} -plane is shown in figure 9.37 for the drift field at 198 V/cm. In red, the mean values from the Gaussian fits with their respective errors are overlaid.

⁶Analysis tool written in *Python* for the XENON1T experiment.

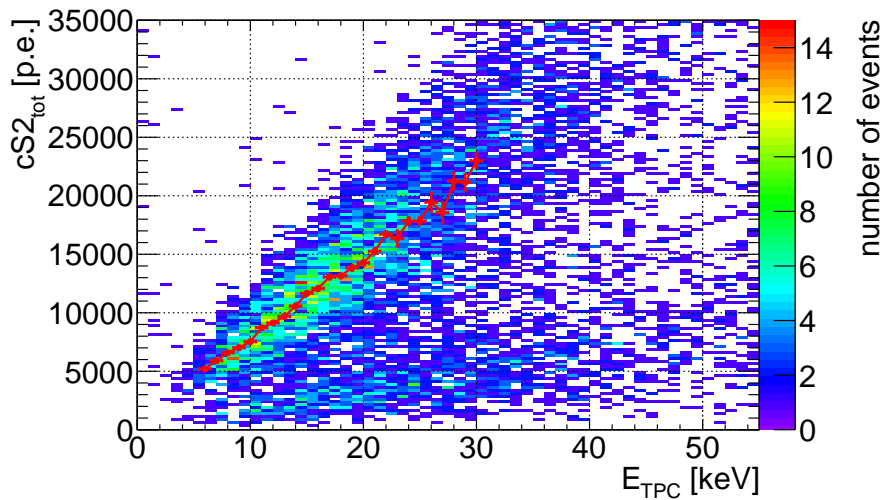


Figure 9.37: Detected $cS2$ signal in dependence of the energy deposit E_{TPC} for Compton scattering with an applied drift field of 198 V/cm. In red, the fit values for the Gaussian mean per energy slice are overlaid. The uncertainty shown here is the Gaussian mean error from the fit. The graphical appearance suggests a linear relation between deposited energy and generated secondary scintillation light and therefore between E_{TPC} and the number of electrons released in the scattering interaction.

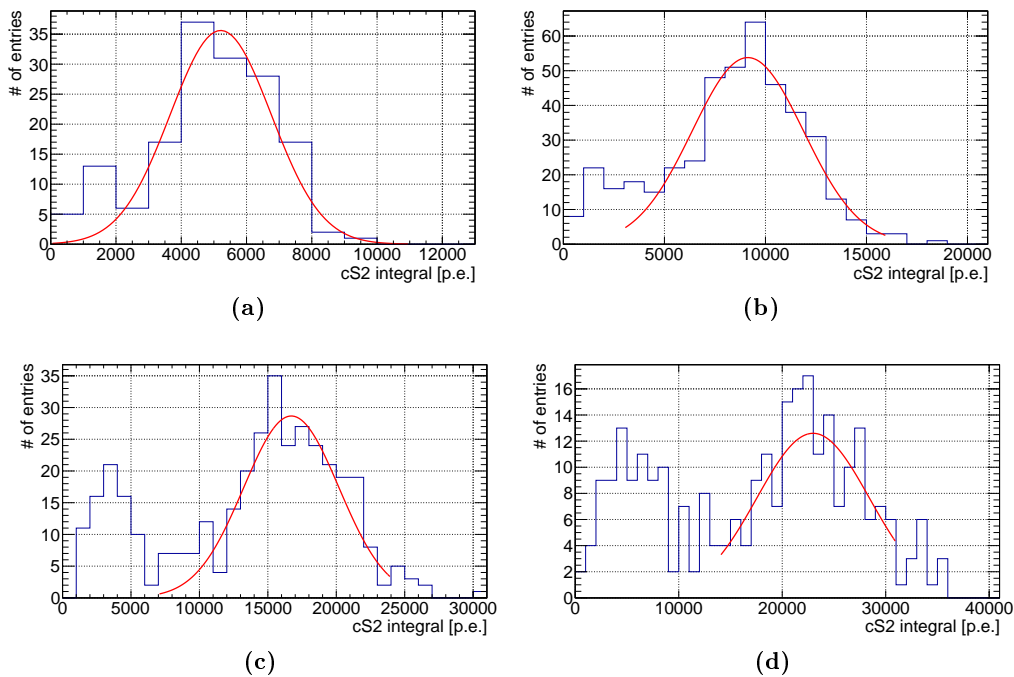


Figure 9.38: Examples of the $cS2$ signal distribution for nearly monoenergetic ranges in deposited energy: (a) $5.5 \text{ keV} < E_{TPC} < 6.5 \text{ keV}$, (b) $11.5 \text{ keV} < E_{TPC} < 12.5 \text{ keV}$, (c) $21.5 \text{ keV} < E_{TPC} < 22.5 \text{ keV}$ and (d) $29.5 \text{ keV} < E_{TPC} < .5 \text{ keV}$. With increasing energy deposit, the $cS2$ signal distributions become broader. Even for low E_{TPC} a coarse binning is necessary to obtain a peak-like structure in the signal distribution because of the wide range for the signal values. At low $cS2$, the lower signal population is visible as a smaller peak structure.

In a range between 6 and 30 keV, the $cS2$ signal provides sufficient statistics to conduct a Gaussian fit. Some energy slices are shown exemplarily in figure 9.38 for this measurement. Compared to the signal distributions in $cS1$, the Gaussian fits yield much higher mean values and much larger standard deviations due to the broader distributions of the $cS2$ signals.

In addition, the lower event population described in section 9.7.1 is visible at smaller $cS2$ signal integrals. For the fit – as for the subsequent analysis – the lower population was not considered.

The fit results for the measurement at 198 V/cm are found in table 9.18, for the other fields the tables are listed in appendix B.10.

E_{TPC} [keV]	μ_{cS2} [p.e.]	$\Delta\mu_{cS2}$ [p.e.]	σ_{cS2} [p.e.]	$\Delta\sigma_{cS2}$ [p.e.]	χ^2_{red}	QY [$\frac{e^-}{\text{keV}}$]	ΔQY [$\frac{e^-}{\text{keV}}$]
6	5209	142	1548	115	13.47	47.57	8.05
7	5906	131	1816	164	11.05	46.23	6.70
8	6584	114	1768	115	15.31	45.10	5.70
9	7015	145	2310	142	16.21	42.71	4.84
10	7535	143	2214	115	19.20	41.29	4.22
11	8721	113	1987	83	23.86	43.44	4.01
12	9129	166	2755	150	18.39	41.68	3.57
13	9681	157	2791	160	17.43	40.81	3.23
14	10574	171	2798	175	15.97	41.39	3.05
15	11658	168	2828	145	19.47	42.59	2.93
16	12078	199	3292	194	16.96	41.36	2.70
17	13059	201	3078	174	17.66	42.09	2.59
18	13159	212	3445	236	14.60	40.06	2.34
19	13842	255	3800	282	13.47	39.92	2.25
20	14262	229	3654	215	17.02	39.07	2.08
21	15254	258	3973	256	15.51	39.80	2.04
22	16715	241	3478	228	15.26	41.63	2.02
23	16358	673	6401	924	6.93	38.97	2.36
24	17837	329	4346	347	12.54	40.72	1.89
25	17845	322	4792	271	17.67	39.11	1.75
26	19453	799	5516	687	8.03	41.00	2.33
27	18561	919	6488	1111	5.84	37.67	2.35
28	21240	721	5765	820	7.03	41.57	2.08
29	21158	699	6088	1073	5.67	39.98	1.94
30	22985	601	5441	768	7.08	41.98	1.82

Table 9.18: Parameters of the $cS2$ slices for the determination of the charge yield for a drift field strength of 198 V/cm. The values for the mean signal μ_{cS2} and its standard deviation σ_{cS2} as well as their uncertainties are obtained by fitting the individual energy slices, as well as the reduced χ^2 . The charge yield QY and its error are calculated using equation (9.19).

The charge yield QY_{cS2} is calculated using equation (9.19). Similar to the light yield calculation, the mean value for the signal integral $\mu_{cS2}(E_{\text{TPC}})$ in a given energy interval is divided by the mean energy deposit E_{TPC} for this interval. Dividing by the calibration value $\overline{S2}_{1e^-}$ converts the number of measured photoelectrons to the number of

electrons.

$$QY_{cS2}(E_{\text{TPC}}) = \frac{1}{S_{21e^-}} \frac{\mu_{cS2}(E_{\text{TPC}})}{E_{\text{TPC}}} \quad (9.19)$$

$$\Delta QY_{cS2}(E_{\text{TPC}}) = QY_{cS2} \cdot \sqrt{\left(\frac{\Delta\mu_{cS2}(E_{\text{TPC}})}{\mu_{cS2}(E_{\text{TPC}})}\right)^2 + \left(\frac{dE_{\text{TPC}}}{E_{\text{TPC}}}\right)^2 + \left(\frac{\Delta S_{21e^-}}{S_{21e^-}}\right)^2}$$

The charge yield is determined for all four drift field configurations and is presented in figure 9.39.

The charge yields QY_{cS2} determined with the MainzTPC decrease in the low-energy region between 5 and about 20 keV for the lowest drift field of 198 V/cm and between 5 and about 10 keV in case of the 594 V/cm. Below 5 keV, no data points are available. This can be explained with the trigger settings and the related trigger efficiency in $S1$ which only accepts signals above a certain energy deposit.

For the measurement at 396 V/cm, the curve starts at 9 keV. Its increase for larger E_{TPC} is indicated but with large uncertainties on the data. For the highest field of 792 V/cm

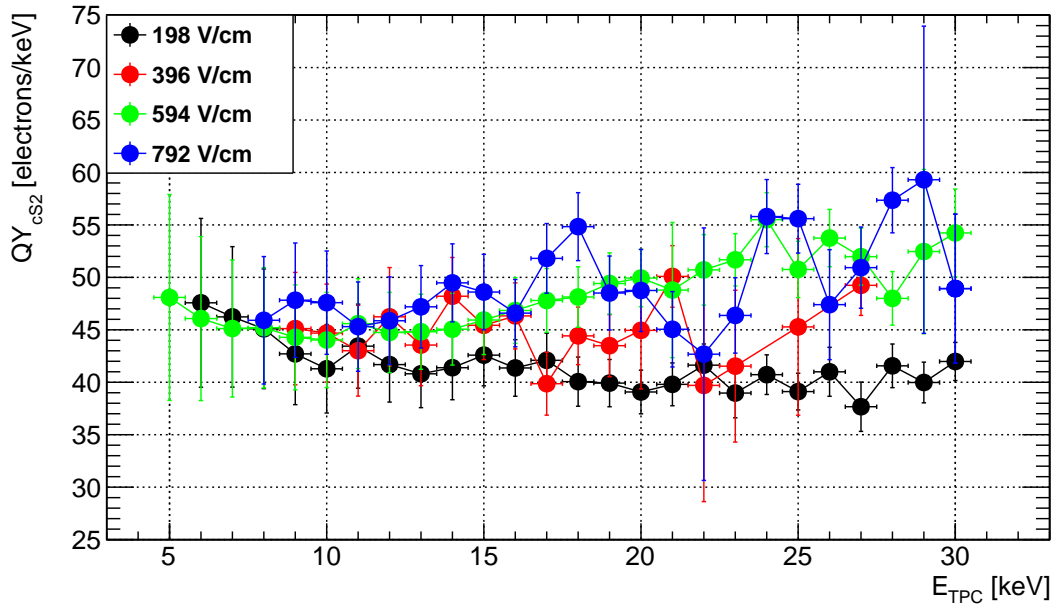


Figure 9.39: Charge yield QY_{cS2} in dependence of E_{TPC} for different drift field strengths. For all field strengths, the observed charge yield shows a slight decrease at low E_{TPC} . The charge yield for 198 V/cm seems to reach a constant value, while the charge yields for the two highest fields increase to higher values for $E_{\text{TPC}} > 10$ keV. For the drift field strength of 396 V/cm, the determined charge yield values also seem to increase for increasing drift deposit, although the charge yield values show large uncertainties due to the low statistics of this configuration. In the low-energy region, the graphs overlap. The data points for the individual measurements cover different ranges of E_{TPC} : Due to the different amount of available data for each drift field configuration, energy slices with too low statistics were not considered.

also large uncertainties are observed but the increasing tendency of the charge yield is clearly visible.

In the low-energy region the light yield curves for the different drift field strengths overlap. In comparison with previous simulations and measurements as discussed in section 2.5 (see figure 2.8), in general the charge yield shows a similar shape as expected. It does not show the same features that can be found for the NEST simulation in figure 2.8a, such as the steep decrease at low energies and the double-minimum structure between roughly 20 and 100 keV. The decrease is indicated, but as can be seen from the neriX measurements in figure 2.8b, the steep decrease is observed at energies ≤ 5 keV which is the lower limit of the data in this analysis. The overlap of the charge yield curves can also be observed in both the NEST simulations and the neriX measurements, where these trends are even more distinctive.

The shapes of the QY_{cS2} curves measured with the MainzTPC in figure 9.39 are similar to the ones measured by the neriX experiment. The double-minimum structure is not found in the charge yield from neriX either. The decrease in the low-energy region is comparable with regard to the energy deposit E_{TPC} . With the exception of the QY_{cS2} curve at 198 V/cm, the other curves show an increase for increasing energy deposit. For the curve at 198 V/cm, this can be compared to the 1.9 kV curve from the neriX measurement (blue points in figure 2.8b), which does not increase below roughly 40 keV. This increase can not be observed for the QY_{cS2} curve at 198 V/cm since the data statistics from the MainzTPC measurements are not sufficient in this energy region.

The comparison of the absolute charge yield values is of interest only with respect to the experimental data. The NEST simulation does not take any detector properties into account. In direct comparison to the neriX charge yield, the MainzTPC shows generally higher values. For example, the minimum of the charge yield at 190 V/cm is below 30 keV for neriX, while the charge yield measured with the MainzTPC at 198 V/cm shows values of around 40 keV. This discrepancy can be caused by several aspects, such as a different amount of electrons being absorbed while drifting through the liquid phase (due to different detector scales or xenon purity). The calibration value $S2_{1e^-}$ presumably plays a keyrole here. The presented charge yield should be seen as an estimation which has to be verified or adjusted by future measurements.

The estimated value for the charge yield and its behaviour in dependence of E_{TPC} show that the MainzTPC is able to meet its design goals once the technical issues mentioned earlier in the chapter have been dealt with.

9.7.4 | Impact of the $S2$ z -correction

As shown in section 9.6.3 the z -positions of the Compton events were determined to be mostly in a limited range in the lower part of the TPC volume due to the collimation of the ^{137}Cs source. In $S1$, the correction does not have a significant impact due to the form of its correction function. In $S2$, the correction factor e^{z/l_e} becomes larger for larger z . The impact of the $S2$ z -correction is therefore larger than for $S1$.

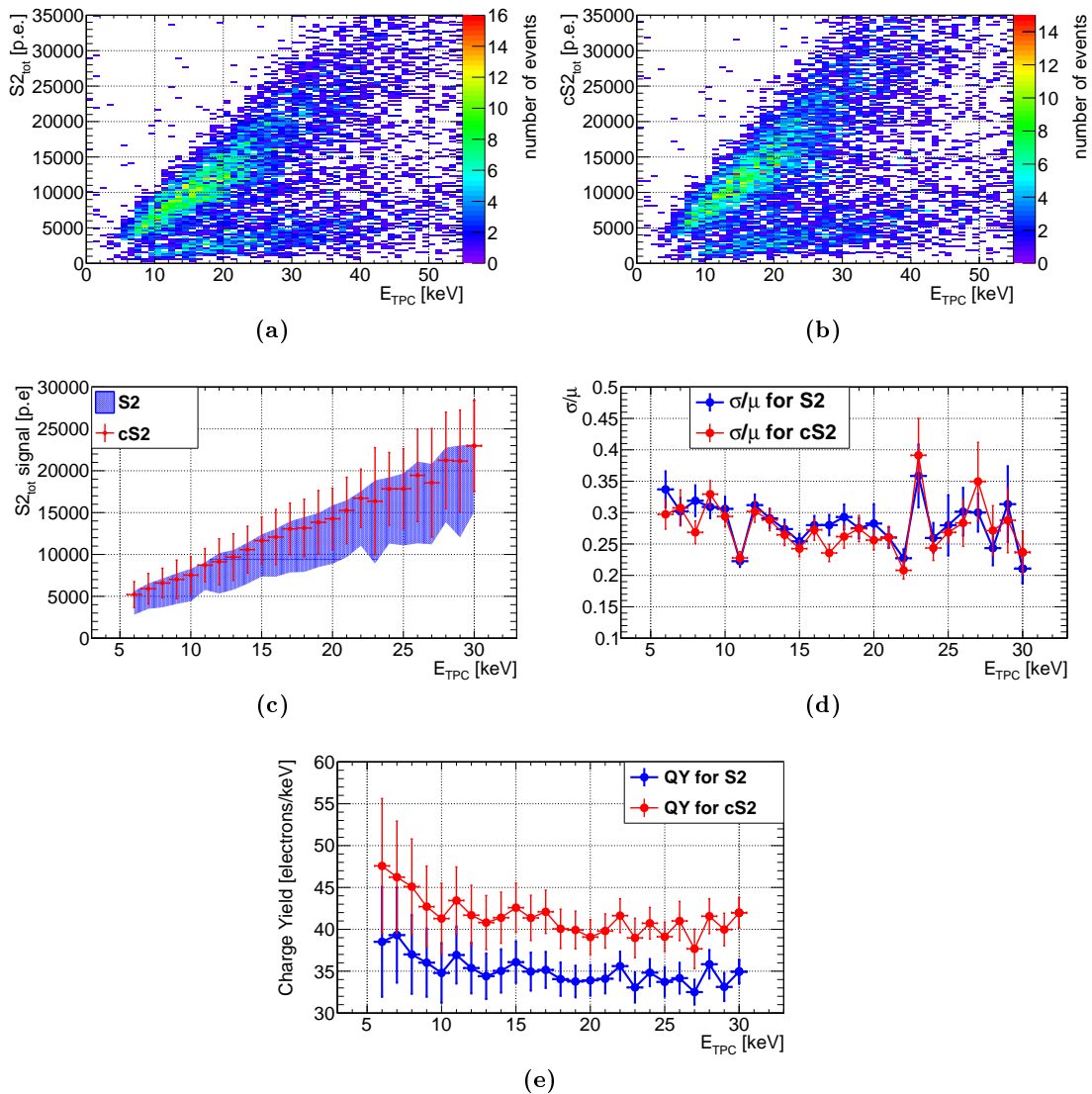


Figure 9.40: Event distribution for (a) the uncorrected $S2$ and (b) the corrected $cS2$ in dependence of E_{TPC} for a drift field strength of 198 V/cm. The $S2$ z -correction has a visible effect on the shape of the distribution as well as on the signal values. The Gaussian fits for both the uncorrected and corrected signals are overlaid in (c) (with the standard deviation as a measure of the distribution spread). The general shift to larger values as a consequence of the z -correction can be observed. The distribution width is slightly increased for the increased value of the corrected signals, as can be seen from the comparable values for the ratio $\frac{\sigma}{\mu}$ depicted in (d). A direct comparison of the charge yields determined with uncorrected and corrected signals is shown in (e). For $cS2$ the charge yield exceeds its uncorrected counterpart by 15–23%.

This can already be seen in the TPC calibration section in figure 9.15. The corrected signal $cS2$ becomes more broadly distributed than its measured counterpart $S2$ and is shifted to larger values. The same effect can be observed for the Compton data, as shown in figure 9.40.

The corrected event distribution in figure 9.40b has a similar shape as the uncorrected distribution in figure 9.40a, but the $cS2$ signals are shifted to higher values – as expected, since they are corrected for the loss of the $S2$ signal with increasing depth – and the overall distribution appears slightly broader for the corrected signals.

The mean values from the Gaussian fits from the energy slices for both the uncorrected and corrected signal are overlaid in figure 9.40c. For the uncertainty the standard deviation from the fits is used to illustrate the distribution spread. The shift to higher values for the corrected signal can be observed. Figure 9.40d shows the signal resolution $\frac{\sigma}{\mu}$ for both cases. The signal resolution does not change significantly for the two cases which means that the distribution is broader for the corrected signals.

The impact of the $S2$ z -correction leads to a significant difference between the uncorrected and corrected signal. The charge yield for $cS2$ is between 15–23 % higher than for its counterpart, as can be seen in figure 9.40e.

All values for the uncorrected signal from the measurement at 198 V/cm are listed in table B.18 in appendix B.10.

For future measurements, it is recommended to increase the electron lifetime in the MainzTPC to reduce the impact of the $S2$ z -correction on the measured signal strength. Considering the difficulties in deriving the electron lifetime (see section 8.4), it can be used effectively to correct the signal loss without worsening the signal resolution.

9.8 | Compton $cS2$ and $cS1$ as Calibration Signals

The calibration of the MainzTPC using the energy lines from different low-energy gamma-ray sources was unsuccessful, as described in section 9.4. Since the Compton measurements include an energy measurement in form of the detection of the scattered gamma-ray with the germanium detector, both $cS1$ and $cS2$ signal can be linked to the energy deposit E_{TPC} . The combined information of both TPC signals and the deposited energy can be employed for a TPC calibration.

In the energy range studied in the Compton measurements, the $S2$ signals should not be affected by the PMT saturation. The event distribution in the $S2$ - $S1$ -plane for the uncorrected signals is shown in figure 9.41a, the corresponding distribution for the corrected signals $cS1$ and $cS2$ can be found in figure 9.41b. The applied drift field strength is 198 V/cm, and the plots do not show evidence for signal saturation. The effect of the $S2$ z -correction is visible, as the event distribution in figure 9.41b is shifted to larger values in $cS2$ and exhibits a slightly broader spread of the events in the signal distributions.

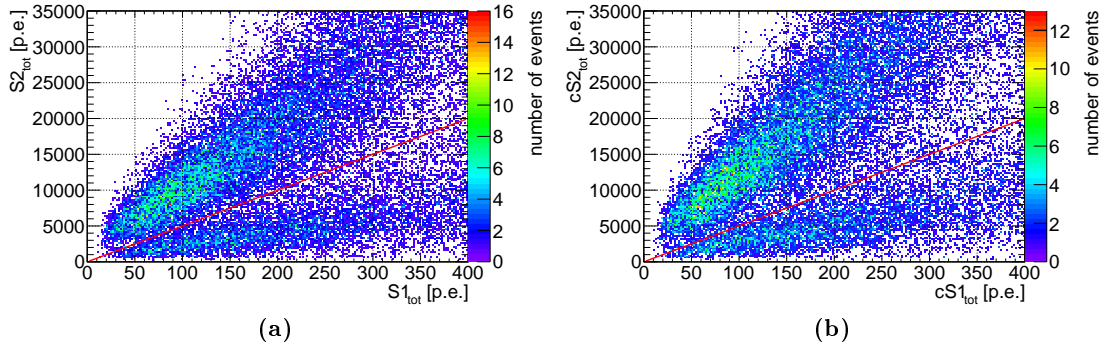


Figure 9.41: Event distribution for the Compton measurements at a drift field of 198 V/cm in the $S2$ - $S1$ -plane on the left and in the $cS2$ - $cS1$ -plane for the corrected signals on the right. While the impact of the $S2$ z -correction is visible, the correction for $S1$ is too small to be noticed here. As for the $S2$ - E_{TPC} -plane, two event populations can be observed. For the analysis, only the upper population is of interest and therefore a rough cut (red line) is applied.

As described in section 9.7.1, only the upper population is of interest for the analysis. Therefore, the lower population is cut from the event distributions according to equation (9.20). The slope of the relation is based on observation and is chosen to be simple and to keep the upper population as complete as possible. It is applied for both the uncorrected and corrected signal distributions.

$$S2(S1) = 50 \cdot S1 \quad \text{or} \quad cS2(cS1) = 50 \cdot cS1 \quad (9.20)$$

The information about the energy deposit for each event in the $cS2$ - $cS1$ -plane allows to

select the events for a given energy interval. The resulting event distribution in $cS2$ - $cS1$ is expected to show the anti-correlation between the scintillation and the charge signal from the interaction, as described in section 2.3.2. Using a small interval for E_{TPC} , the distributions should be equivalent to the energy lines expected from calibration gamma-ray sources.

Figure 9.42 depicts the event distributions for three energy ranges for the uncorrected signals on the left and the corrected signals on the right.

The three energies with (a) $(6 - 8)$ keV, (b) $(16 - 18)$ keV and (c) $(24 - 26)$ keV in figures 9.42a, 9.42b and 9.42c were chosen exemplarily to show the change of the distributions in the range between 5 and 30 keV. The expected increase for both TPC signals for increasing E_{TPC} is visible. For the corrected signals on the right, the slightly wider spread and the shift to larger values in $cS2$ due to the z -correction can be observed. For increasing E_{TPC} , the event distributions become more and more distorted, without exhibiting a recognizable and distinct anti-correlation between the two TPC signals.

Selecting events by energy deposit in intervals as small as applied here leads to a crucial loss in statistics for the individual energy ranges. The amount of data points for each interval is not sufficient for a data fit. Here, the interval width is chosen to be $dE_{\text{TPC}} = 2$ keV and therefore broader than in the preceding sections, taking into account the germanium energy resolution of roughly 2.6 keV for ^{137}Cs as found in section 5.2.2. Even extending the interval does not lead to more suitable distributions, as this also means a wider spread in both signal ranges. Furthermore, choosing a larger interval in energy is equivalent with the reduction of the energy resolution.

For the drift field strengths of 396 V/cm, 594 V/cm and 792 V/cm, the calibration using the Compton measurements is also not possible for the same reasons as described for the case of 198 V/cm.

This approach for a TPC calibration has the advantage to examine the energy resolution in a continuous manner and is therefore an eligible alternative or at least a supplement to the TPC calibration with the photo-peaks of gamma-ray sources. For the data at hand the statistics are not sufficiently high to perform the calibration. In future experimental runs, longer data acquisition periods for Compton measurements should be part of the measurement plan.

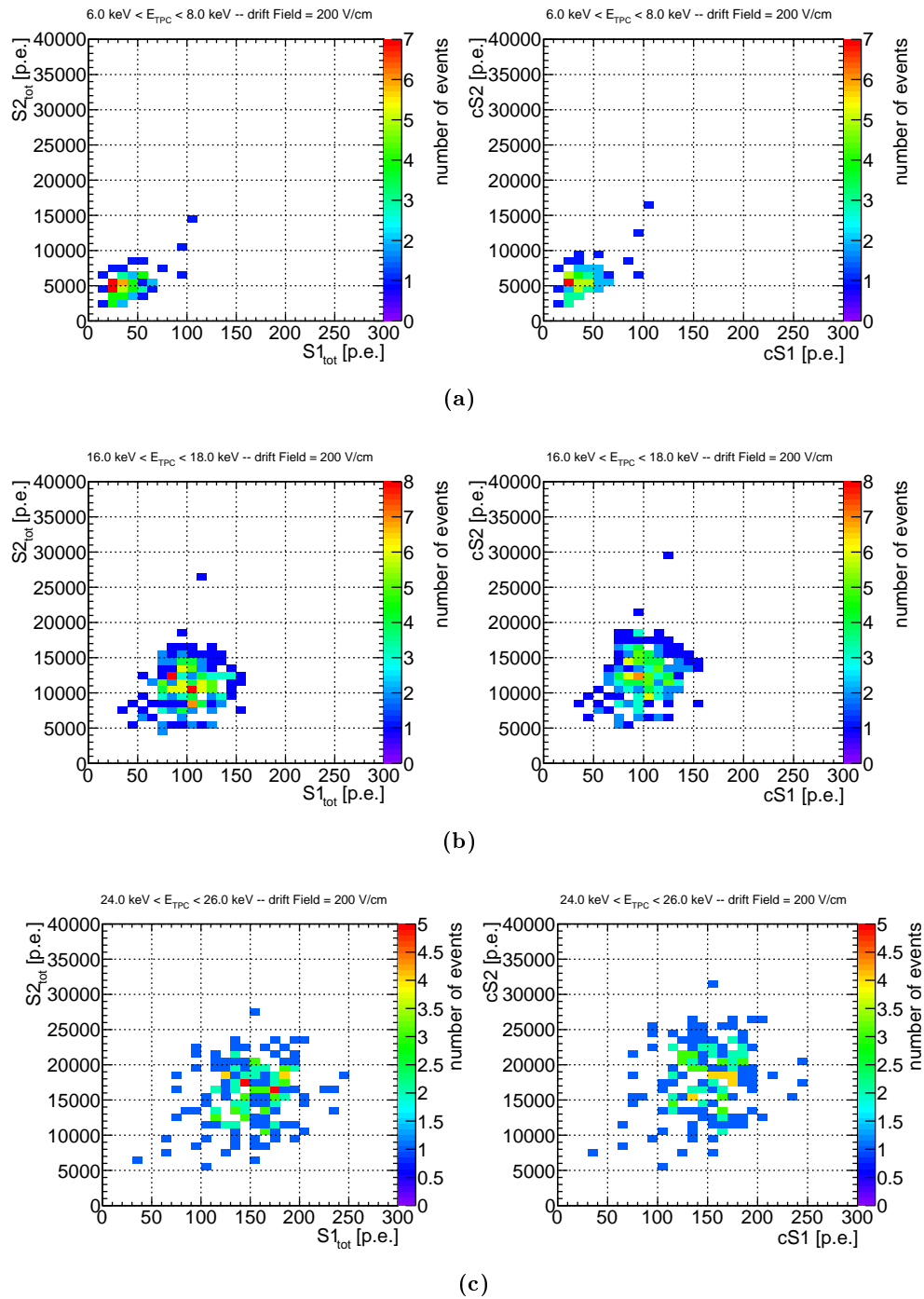


Figure 9.42: Combined MainzTPC signal for Compton measurements with a drift field of 198 V/cm, for events in three different intervals for the energy deposit E_{TPC} . The left column shows the events in the uncorrected $S2$ - $S1$ -plane, while the right columns depicts the corrected $cS2$ - $cS1$ -plane. The three energy intervals are (a) (6 – 8) keV, (b) (16 – 18) keV and (c) (24 – 26) keV. These values were chosen exemplarily. The increase in both signals for increasing E_{TPC} is observed as well as the influence of the $S2$ z -correction. The low statistics prevents the quantitative evaluation of the event distributions for a TPC calibration.

Summary & Outlook

Chapter 10

10.1 | Summary

The MainzTPC, a working prototype of a dual-phase xenon time projection chamber, was co-developed and constructed as part of this work. It is designed for both Compton and neutron scattering to measure the response of liquid xenon as a detection material to electronic and nuclear recoils in the low-energy regime. Both Compton and neutron scattering measurements were conducted at the HZDR in 2015 and 2016.

During the development of the MainzTPC detector, the surrounding support systems such as gas system, cryogenic system with liquefaction stage and the monitoring slow control system were implemented to the experimental setup, tested and adjusted.

The MainzTPC is optimized for Compton scattering and allows for a 3D position reconstruction employing an array of APDs around the liquid-gas interface. The utilization of APDs for the x - y position reconstruction is a novelty for this sort of experiment.

In the course of this thesis, the Data Acquisition system (DAQ) was developed and used to acquire data in both Compton and neutron scattering measurements. The DAQ system plays a crucial role in the experimental setup because it is responsible for the recognition of events in the MainzTPC and triggering the acquisition stage. The system controls the data consistency while recording events on two different FADCs and even a TDC, storing the data in a customary data format with a variety of selectable parameters defining the data properties. It was built to be extendable and versatile for different requirements, such that the trigger conditions and acquisition channel parameters can be adjusted according to the needs of the current measurement.

Two different DAQ versions concerning hardware and software were developed. DAQ version 2 was applied during test measurements and the experimental runs for both Compton and neutron scattering at the HZDR for this dissertation and the thesis by Bastian Beskers [3], examining the $S1$ scintillation pulse shape, while DAQ version 1 was employed in Mainz for further theses [4, 5].

To examine the low-energy response of LXe for electronic recoils, the gamma-ray measurements conducted at the HZDR were examined in this thesis. For this, the measured data was processed using the Raw Data Analysis framework from [3]. Tools were developed to analyze the processed data using the *ROOT* framework and the performance of the MainzTPC detector was evaluated concerning basic properties:

A rudimentary position reconstruction in x - y utilizing the APD data was tested applying the centroid method. The results show that – apart from calibration difficulties – the APDs can be used for the position reconstruction in a first-order approach and a fiducialization of the active volume is possible. Complementing the reconstruction of the x - y position, the interaction depth z can also be determined, documenting the ability of the MainzTPC for 3D position reconstruction.

The measurement of the liquid level inside the MainzTPC with the capacitive levelmeters was conducted for the setup at two different experimentation sites. For both measurement periods, the level as well as the tilt could be determined, along with the electric field in the gaseous xenon phase and the change for the $S2$ width with varying

liquid level.

The electron drift velocities determined with the MainzTPC are in good agreement with previous measurements.

For the two main signals occurring in the MainzTPC detector, the $S1$ and $S2$, the dependence on the interaction depth z was examined and corresponding correction functions were introduced.

The fact that the MainzTPC is a prototype leads to limits of the observed detector performance, for example concerning the PMT saturation for large signals. The examination of the TPC calibration data with gamma-ray sources led to the conclusion that a direct calibration was not feasible with the data from the conducted measurements. Also the trigger efficiency showed that background noise has a non-negligible impact on the acquired data.

The study of the $S1$ light yield LY from Compton measurements was conducted and qualitatively compared to simulations and previous measurements from other experiments [1, 2], showing similar curve progressions. For the charge yield QY , a calibration from [5] was used to get an estimation of the measured $S2$ signal in terms of number of electrons. The comparison to [1] and [2] indicates a conformable behaviour of the determined charge yield.

In addition, the field quenching effect on both $S1$ and $S2$ were investigated as well as the impact of the respective signal corrections.

The procedures and tools developed as part of this thesis provide useful information about the detector performance and possible sources of error for specific functionalities. In future experimental runs, the presented tools and methods will be helpful to ensure an improved operation of the MainzTPC.

Disregarding the detector-intrinsic aspects affecting the measurement data, it can be concluded that the results from the Compton measurements are promising and will lead to reasonable results once the mentioned detector issues were resolved and its performance meets the initial requirements. The ability of the MainzTPC to study the low-energy response for electronic recoils is evident and the results presented in this thesis for the uncalibrated TPC show comparable behaviours for the light and charge response as found in similar experiments.

10.2 | Outlook

As presented in this thesis, the MainzTPC as a prototype detector has not yet reached its full potential. The findings from [3] about the scintillation pulse shape as well as the results of this thesis about the behaviour of the light and charge yield signals in the MainzTPC show that further improvements of the detector will lead to the expected detector performance.

Most of the changes or improvements concerning the experimental setup are related to the MainzTPC hardware.

A first improvement on the DAQ system should be the implementation of an $S2$ trigger mode. Triggering on the $S2$ signal for the calibration measurements could lead to an enhanced event data quality since noise signals should not contribute to the recorded events as the threshold is set much higher than the PMT noise levels. In addition, background measurements of the MainzTPC will be carried out to understand underlying background and to get a cleaner data set.

Furthermore, a reduced electronic noise level on the PMT signal channels is crucial to enable the measurement of energy deposits below the 5 keV limit. This is also necessary to improve the $S1$ trigger efficiency since the $S1$ in coincidence with the germanium signal remains the essential trigger signal in Compton measurements. Together with a smarter threshold on the germanium detector, the amount of acquired data suitable for the analysis is expected to increase substantially.

An update of the PMT base design to deal with the saturation effects is also one of the major changes to be done for future measurements. The necessary modifications should ensure that both low-energy $S1$ signals and very large $S2$ signals are detectable with the dynamic range of the PMTs without signal distortions.

Optimizing the setup concerning the liquid level height and the strength of both electric drift field and extraction field is also an important step to maximize the charge collection and therefore the energy resolution of the MainzTPC. Up to now, higher fields could not be maintained stable for a longer measurement period, which should be dealt with in upcoming hardware modifications. A simultaneous minimization of the level tilt will also improve the $S2$ signal uniformity throughout the gaseous volume.

For the DAQ system, an update of the setup at Mainz currently laid out in the DAQ version 1 to the setup used at the HZDR (DAQ version 2), is strongly recommended. Controlling the trigger generation with the logic board as well as handling the individual analog trigger pulses provided by the CFDs are two major advantages of the DAQ version 2. Further advancements for the DAQ depend on possible hardware improvements of the DAQ system.

The very short electron lifetime determined in this thesis has a large impact on the measured $S2$ signal. It indicates a poor xenon purity but is probably caused by the non-optimal event signal selection for the $S2$ z -correction (since no distinct peak could be identified in the $S2$ spectrum). Without the PMT saturation effect the measurement of the electron lifetime is expected to yield larger values.

Apart from the experimental sector, detector simulations should be carried out for background studies, expected signals from calibration, NEST predictions for the MainzTPC and improvement of tools such as the x - y -position reconstruction using the APDs.

Part IV

APPENDICES

Formula derivations and Schematics

Appendix A

A.1 | Derivation of the electric fields in the $S2$ region

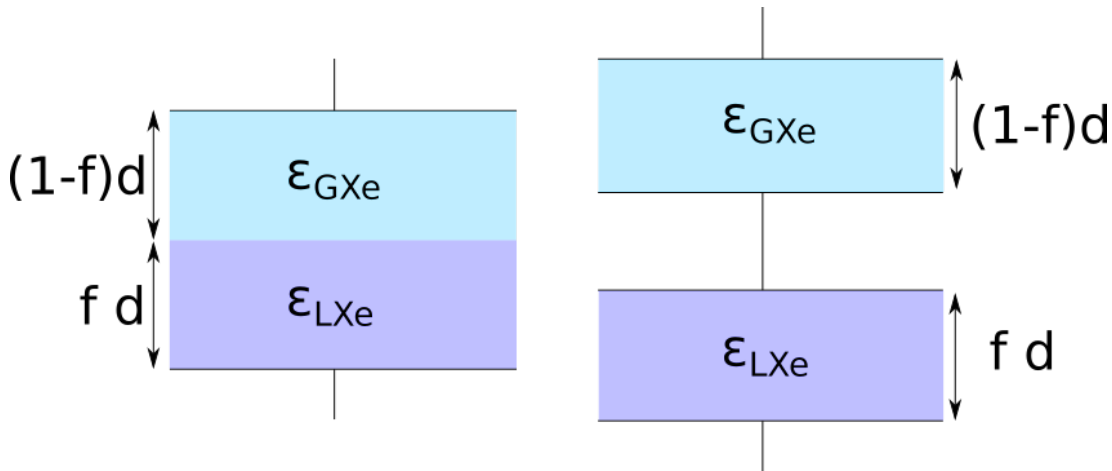


Figure A.1: The gate and the anode mesh resemble a capacitor, which is sketched on the left. The electric field is dependent on the applied bias voltage and the distance d between the meshes or “capacitor plates”. As shown in the sketch, d has to be divided between the liquid and the gaseous xenon phase, which are indicated by the relative permittivities. To calculate the capacitance for this capacitor, the sketch can be replaced by the one on the right, which shows a serial connection between two capacitors. Each of them corresponds to one of the xenon phases on the left. Therefore they have different gaps between the capacitor plates and also different permittivities. This sort of connection scheme also is called a capacitive voltage divider.

The anode and the gate mesh can be considered to be a capacitor. Under operation conditions, the gap between the meshes is partly filled with liquid xenon, the upper part with xenon gas. In this situation, one can treat the anode-to-gate region as a serial connection of two capacitors with different dielectrical mediums inside.

The formulae needed here are the capacitance of a condensator with two plates and the relation between charge and voltage. In case of a serial connection of capacitors, the charge is equal for all capacitors.

$$C = \varepsilon_0 \varepsilon_x \frac{A}{d} \quad Q = C \cdot U \quad Q_{\text{tot}} = Q_l = Q_g \quad (\text{A.1})$$

In the formula of the capacitance C , ε_0 is the permittivity in vacuum, ε_x is the relative permittivity of the medium, A is the plate area and d the distance between the capacitor plates. Further, Q depicts the charge and U the voltage on the capacitor. The subscripts g and l refer to the gaseous and the liquid phase, respectively.

This system is also called a capacitive voltage divider. Similar to a voltage divider with resistors, the total capacitance can be calculated as shown below.

$$\frac{1}{C_{\text{tot}}} = \frac{1}{C_g} + \frac{1}{C_l} \Leftrightarrow C_{\text{tot}} = \frac{C_g \cdot C_l}{C_g + C_l}$$

Since the charge is equal for all capacitors, one can express the voltage on one capacitor by the total voltage applied to the system. For this, we replace the capacitances C_r by their constituents from equation (A.1). To account for the fractions of liquid and gas phase between the gate and the anode mesh, a fill factor f is introduced, which can vary between 0 and 1 and refers to the liquid fraction.

$$\begin{aligned}
 U_l \cdot C_l &= U_{\text{tot}} \cdot C_{\text{tot}} \\
 U_l &= U_{\text{tot}} \frac{C_{\text{tot}}}{C_l} = U_{\text{tot}} \frac{C_g}{C_g + C_l} \\
 &= U_{\text{tot}} \frac{\varepsilon_0 \varepsilon_{\text{GXe}} \frac{A}{d(1-f)}}{\varepsilon_0 \varepsilon_{\text{GXe}} \frac{A}{d(1-f)} + \varepsilon_0 \varepsilon_{\text{LXe}} \frac{A}{df}} \\
 &= U_{\text{tot}} \frac{\varepsilon_{\text{GXe}}(1-f)^{(-1)}}{\varepsilon_{\text{GXe}}(1-f)^{(-1)} + \varepsilon_{\text{LXe}}f^{(-1)}} \\
 &= U_{\text{tot}} \frac{\varepsilon_{\text{GXe}} \cdot f}{\varepsilon_{\text{GXe}} \cdot f + \varepsilon_{\text{LXe}} \cdot (1-f)}
 \end{aligned}$$

The voltage in the liquid part of the anode-gate region, U_l , is now expressed in dependence of the applied voltage U_{tot} and the contributions of the permittivities according to the fill factor.

The corresponding electric field in the liquid region is then calculated to be:

$$E_l = \frac{U_l}{d \cdot f} = U_{\text{tot}} \frac{\varepsilon_{\text{GXe}}}{\varepsilon_{\text{GXe}} \cdot f + \varepsilon_{\text{LXe}} \cdot (1-f)}$$

Analogously, one can derive the relation for the the electric field in the gas phase:

$$E_g = \frac{U_g}{d \cdot (1-f)} = U_{\text{tot}} \frac{\varepsilon_{\text{LXe}}}{\varepsilon_{\text{GXe}} \cdot f + \varepsilon_{\text{LXe}} \cdot (1-f)}$$

A.2 | Derivation of the capillarity effect

To calculate the height of the liquid due to the capillary action, one has to consider the force which is caused by the adhesion between the liquid and the solid of the capillary. This force F_c can be expressed by length L of the liquid-solid contact line, the surface tension σ of the liquid and the contact angle θ between solid surface and liquid surface. The latter can be thought of as a parameter of the wettability of a solid surface by a liquid and is zero for liquid xenon at temperatures above 164 K [106].

$$F_c = L\sigma \cos \theta$$

For the levelmeters the liquid between the cylinders has two contact lines, which leads to an overall value for the length $L = 2\pi(R + r)$ with R being the inner radius of the

outer cylinder and r being the outer radius of the inner cylinder. The capillary force is in equilibrium with the gravitational force acting on the liquid:

$$F_c = F_g = mg = \rho\pi(R-r)^2g$$

Solving for the height leads to the following expression

$$h = \frac{2\sigma(R+r)}{\rho g(R-r)^2} = \frac{2\sigma}{\rho g(R-r)}$$

The value for the surface tension σ is temperature-dependent. Using the data from [107] plotted in figure A.2, one finds a linear fit function in the temperature region of interest:

$$\sigma(T) = -1.834 \cdot 10^{-3} \frac{\text{N}}{\text{m K}} + 48.700 \cdot 10^{-3} \frac{\text{N}}{\text{m}}$$

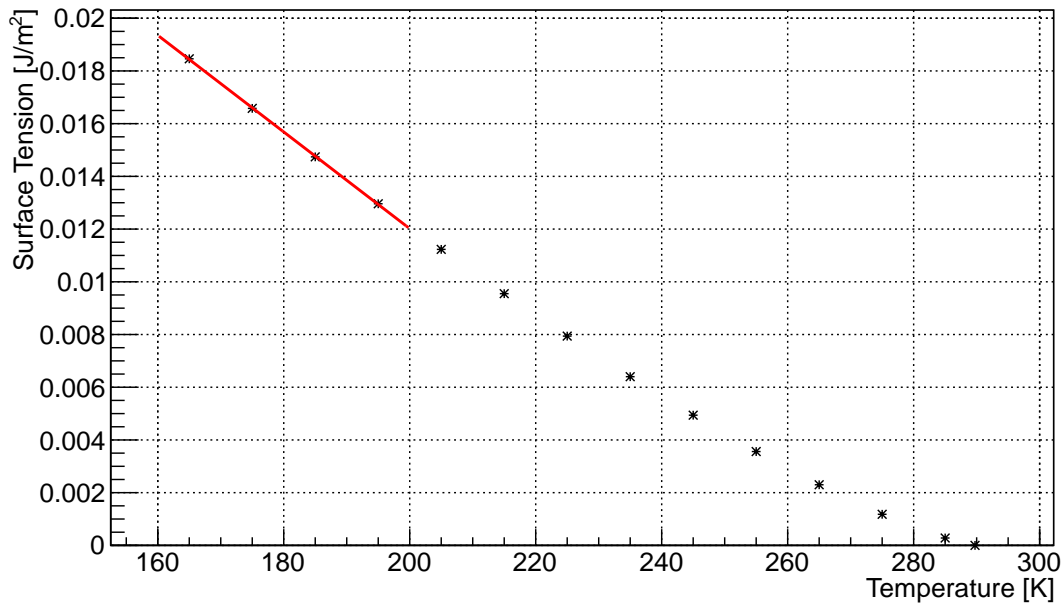


Figure A.2: Fit of the LXe surface tension in dependence of the temperature. Data found in [107].

A.3 | Tilt angle for the liquid level fit plane

To determine the tilt angle between a tilted plane and the optimal normal vector $\vec{n}_z = (0, 0, 1)^T$, first the normal vector of the plane from equation (7.7)

$$h = p_0 + p_1 \cdot x + p_2 \cdot y$$

has to be calculated. The normal vector \vec{n}_{plane} is

$$\vec{n}_{\text{plane}} = \begin{pmatrix} n_1 \\ n_2 \\ n_3 \end{pmatrix} = \frac{1}{\sqrt{1^2 + (-p_1)^2 + (-p_2)^2}} \cdot \begin{pmatrix} -p_1 \\ -p_2 \\ 1 \end{pmatrix}$$

The scalar product of the two vectors \vec{n}_{plane} and \vec{n}_z can be used to find the tilt angle:

$$\alpha_{\text{tilt}} = \arccos \frac{\vec{n}_{\text{plane}} \cdot \vec{n}_z}{|\vec{n}_{\text{plane}}| \cdot |\vec{n}_z|} = \arccos \frac{n_{pz} n_{zz}}{|\vec{n}_{\text{plane}}| \cdot |\vec{n}_z|} \quad (\text{A.2})$$

Since \vec{n}_z only has a non-zero value for the z -component, a lot of terms vanish from the equation. Of course, this angle is in radiant and has to be multiplied by $\frac{180^\circ}{\pi}$ to be expressed in degrees.

The uncertainty of α_{tilt} can be calculated using error propagation. For this, the errors of the individual quantities have to be taken into account. It can be seen that $n_{zz} = |\vec{n}_z| = 1$ and $\Delta n_{zz} = \Delta |\vec{n}_z| = 0$ by definition.

The remaining quantities and errors are

$$\begin{aligned} |\vec{n}_{\text{plane}}| &= \sqrt{1 + (-p_1)^2 + (-p_2)^2} & \Delta |\vec{n}_{\text{plane}}| &= \frac{\sqrt{(-p_1 \cdot \Delta p_1)^2 + (-p_2 \cdot \Delta p_2)^2}}{|\vec{n}_{\text{plane}}|} \\ n_{pz} &= \frac{1}{\sqrt{1 + (-p_1)^2 + (-p_2)^2}} & \Delta n_{pz} &= n_{pz}^3 \sqrt{(p_1 \Delta p_1)^2 + (p_2 \Delta p_2)^2} \end{aligned}$$

This leads to the resulting formula for the tilt angle:

$$\alpha_{\text{tilt}} = \arccos \frac{1}{1 + p_1^2 + p_2^2} \quad (\text{A.3})$$

The corresponding uncertainty for the angle is calculated as:

$$\Delta \alpha_{\text{tilt}} = \frac{2}{\sqrt{1 - \left(\frac{1}{1+p_1^2+p_2^2}\right)^2}} \frac{\sqrt{(p_1 \Delta p_1)^2 + (p_2 \Delta p_2)^2}}{(1 + p_1^2 + p_2^2)^2} \quad (\text{A.4})$$

A.4 | TPC PMT base circuit - Schematic

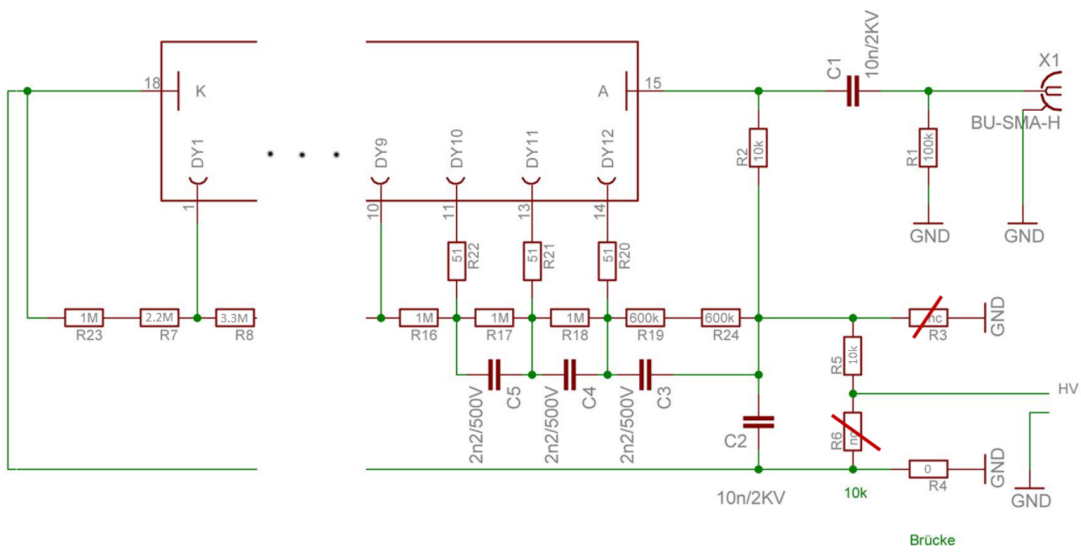


Figure A.3: Schematic of the TPC PMT base circuit board: The circuit board can be used with positive (as shown here) or negative bias voltage. The configuration of the connections in the lower left is decisive. The scheme also shows the dynode chain and its reservoir (or buffer) capacitors. Image from [4].

Tables and Graphs

Appendix B

B.1 | Germanium calibration

	E_{γ} (keV)	A	ΔA	σ (μ V)	$\Delta\sigma$ (μ V)	μ_{peak} (V)	$\Delta\mu_{\text{peak}}$ (μ V)
^{137}Cs	661.6	1.77804	0.00063	675.20	0.30	0.406547	0.26
^{22}Na	511	1.68219	0.00064	754.36	0.34	0.314125	0.33
^{22}Na	1274	0.31466	0.00062	673.35	1.64	0.783892	1.50
^{133}Ba	356	1.33194	0.00050	461.68	0.20	0.218703	0.18

Table B.1: Gaussian fit values for the gamma-ray source photon peaks of ^{137}Cs , ^{22}Na and ^{133}Ba

	E_{γ} (keV)	A_L	ΔA_L	s	Δs	t (V)	Δt (μ V)
^{137}Cs	661.6	$1.46201 \cdot 10^{-3}$	$1.22070 \cdot 10^{-6}$	$6.33883 \cdot 10^{-4}$	$3.3336 \cdot 10^{-7}$	0.406576	0.26
^{22}Na	511	$1.50814 \cdot 10^{-3}$	$1.35607 \cdot 10^{-6}$	$7.02140 \cdot 10^{-4}$	$3.9528 \cdot 10^{-7}$	0.314128	0.32
^{22}Na	1274	$2.75228 \cdot 10^{-3}$	$1.33951 \cdot 10^{-6}$	$6.57951 \cdot 10^{-4}$	$1.85924 \cdot 10^{-6}$	0.783915	1.46
^{133}Ba	356	$7.66657 \cdot 10^{-4}$	$7.05922 \cdot 10^{-7}$	$4.40656 \cdot 10^{-4}$	$2.54279 \cdot 10^{-7}$	0.218706	0.20

Table B.2: Lorentzian fit values for the gamma-ray source photon peaks of ^{137}Cs , ^{22}Na and ^{133}Ba

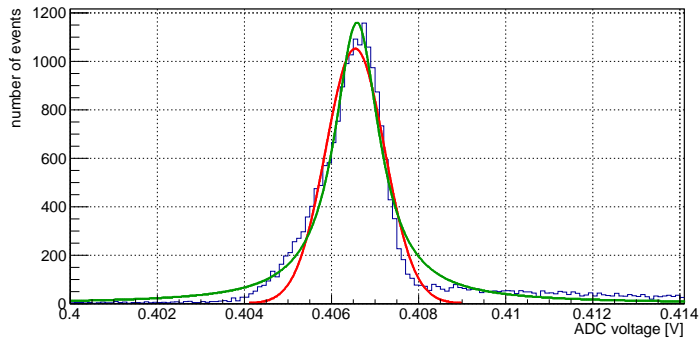


Figure B.1: Germanium detector calibration: 661.6 keV peak from ^{137}Cs . Fit with a Gaussian (red) and a Lorentzian (green) function. The fit results are listed in the tables B.1 and B.2.

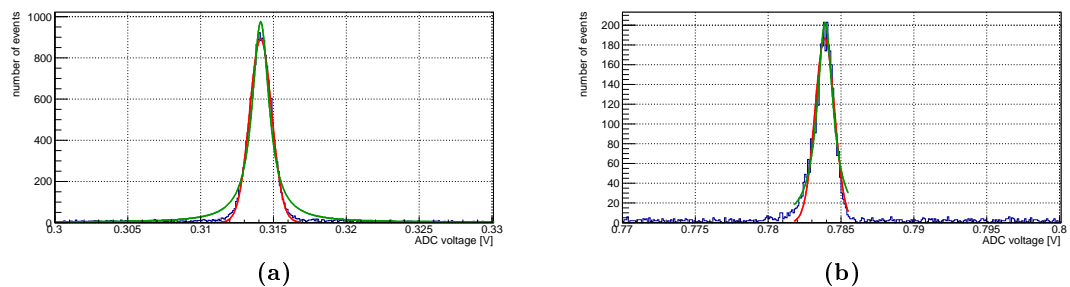


Figure B.2: Germanium detector calibration: (a) 511 keV peak and (b) 1274 keV peak from ^{22}Na . Fit with a Gaussian (red) and a Lorentzian (green) function. The fit results are listed in the tables B.1 and B.2.

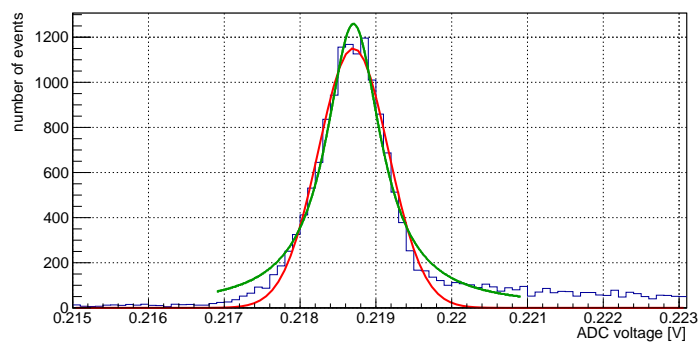


Figure B.3: Germanium detector calibration: 356 keV peak from ^{133}Ba . Fit with a Gaussian (red) and a Lorentzian (green) function. The fit results are listed in the tables B.1 and B.2.

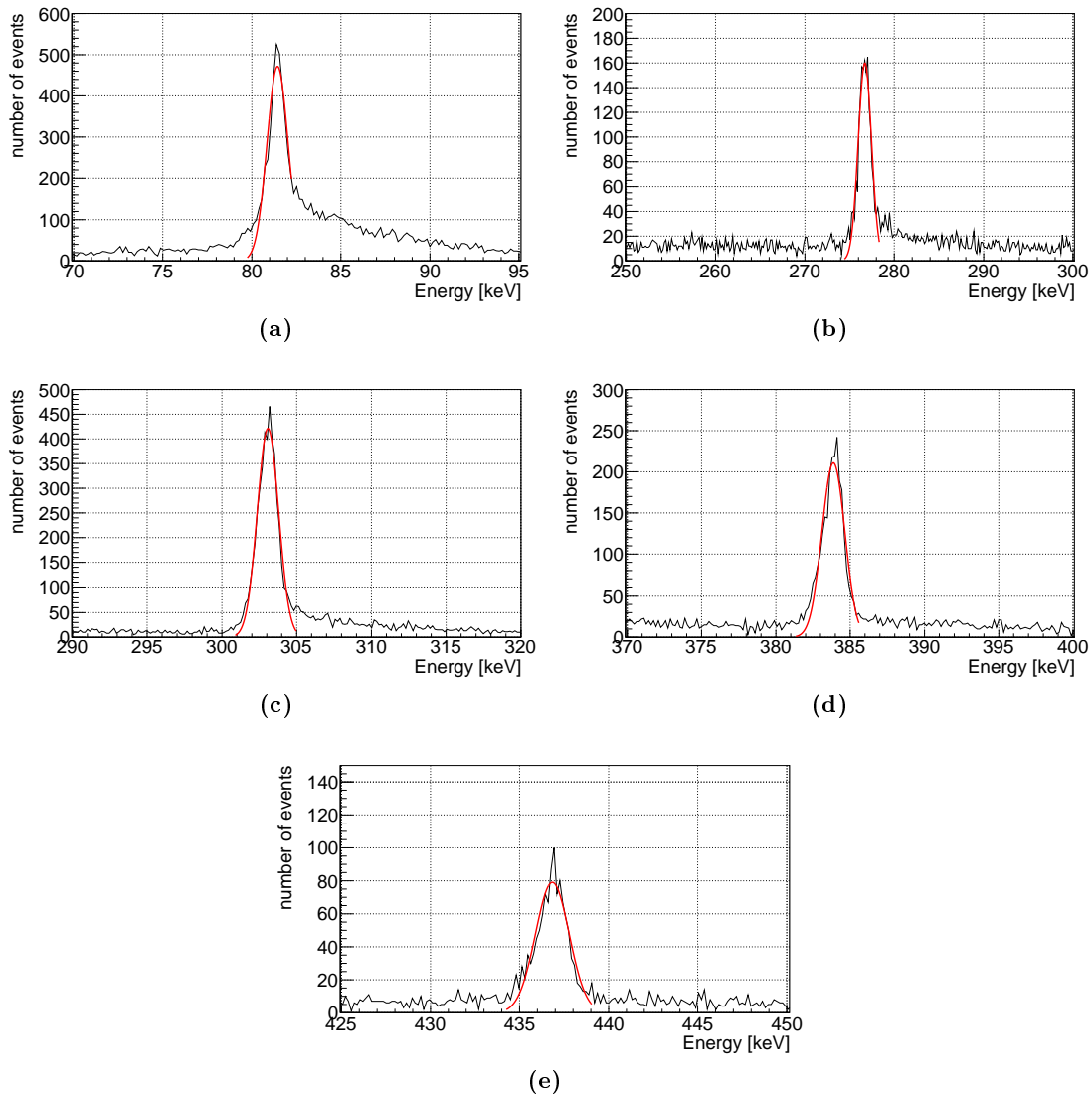


Figure B.4: ^{133}Ba energy peaks fitted with a Gaussian. The plots show the peaks at (a) 80.8 keV, (b) 276.7 keV, (c) 302.8 keV, (d) 381.6 keV and (e) 436 keV.

B.2 | APD calibration

U_{bias} [V]	LED [%]	APD 8		
		μ_{APD} [V]	σ_{APD} [V]	$\Delta\mu_{\text{APD}}$ [V]
1540	70	0.678339	0.014552	0.000066
1550	70	0.854912	0.017654	0.000080
1550	60	0.032054	0.007769	0.000035
1555	60	0.036258	0.007875	0.000036
1555	70	0.963106	0.019527	0.000089
1560	70	1.081038	0.022199	0.000102
1560	60	0.040512	0.008000	0.000036
1565	60	0.045426	0.008374	0.000038
1565	70	1.218784	0.022979	0.000104

Table B.3: APD calibration fit parameters from Gaussian fits of the APD height distributions of APD 8. For this APD only signals at high bias voltages could be detected, which is not sufficient to conduct a complete calibration.

APD	U_{bias}	$m_g [\times 10^{-3} \text{ V}^{-1}]$	$\Delta m_g [\times 10^{-7} \text{ V}^{-1}]$	U_0 [V]	ΔU_0 [V]	g_0	$\Delta g_0 [\times 10^{-5}]$	g	Δg
1	1500	13.11	10.0	1147.11	0.02	2.17654	101.2	104.25	0.38
2	1500	13.60	10.0	1147.18	0.02	2.33551	107.9	123.74	0.47
3	1500	13.07	10.2	1142.29	0.02	1.86688	91.9	109.21	0.36
4	1500	14.24	4.3	1178.42	0.01	3.87553	30.7	101.24	0.10
5	1500	15.08	3.7	1138.59	0.01	3.65954	47.5	236.73	0.41
6	1500	16.58	1.0	1208.27	0.01	4.75269	9.2	130.71	0.04
7	1500	16.00	1.7	1212.84	0.02	5.23991	9.5	104.10	0.28
8	1540	-	-	-	-	-	-	-	-

Table B.4: Gain curve fit parameters and errors employing equation (5.12) for each APD at its bias voltage U_{bias} during operation in the MainzTPC experiment.

U_{bias} [V]	LED [%]	APD 1			APD 2		
		μ_{APD} [V]	σ_{APD} [V]	$\Delta\mu_{\text{APD}}$ [V]	μ_{APD} [V]	σ_{APD} [V]	$\Delta\mu_{\text{APD}}$ [V]
100	100	0.047588	0.010735	0.000049	0.040883	0.011263	0.000051
150	100	0.049267	0.010506	0.000048	0.042168	0.010847	0.000049
200	100	0.050389	0.010252	0.000046	0.043190	0.010495	0.000048
250	100	0.051327	0.010261	0.000046	0.043918	0.010366	0.000047
300	100	0.052352	0.010205	0.000046	0.044785	0.010275	0.000047
350	100	0.052963	0.010033	0.000045	0.045280	0.010042	0.000046
400	100	0.053306	0.010063	0.000046	0.045585	0.010014	0.000045
450	100	0.053838	0.010008	0.000045	0.046003	0.009930	0.000045
425	100	0.053734	0.010057	0.000046	0.045967	0.010018	0.000045
475	100	0.054176	0.009978	0.000045	0.046298	0.009956	0.000045
500	100	0.054792	0.010011	0.000045	0.046726	0.009899	0.000045
550	100	0.055727	0.009981	0.000045	0.047619	0.009876	0.000045
600	100	0.056546	0.009951	0.000045	0.048266	0.009773	0.000044
650	100	0.057750	0.009975	0.000045	0.049365	0.009811	0.000044
700	100	0.059195	0.010030	0.000045	0.050584	0.009817	0.000044
750	100	0.061515	0.009976	0.000045	0.052656	0.009739	0.000044
800	100	0.064579	0.010091	0.000046	0.055307	0.009807	0.000044
850	100	0.068876	0.009976	0.000045	0.059062	0.009699	0.000044
900	100	0.074355	0.009997	0.000045	0.063801	0.009727	0.000044
950	100	0.082491	0.010131	0.000046	0.071021	0.009746	0.000044
1000	100	0.094418	0.010099	0.000046	0.081648	0.009704	0.000044
1050	100	0.110742	0.010272	0.000047	0.096225	0.009855	0.000045
1100	100	0.136990	0.010324	0.000047	0.119743	0.009921	0.000045
1150	100	0.177412	0.010360	0.000047	0.156650	0.009895	0.000045
1200	100	0.243164	0.010580	0.000048	0.217256	0.010125	0.000046
1250	100	0.355881	0.010833	0.000049	0.321683	0.010317	0.000047
1300	100	0.552000	0.011478	0.000052	0.506709	0.010997	0.000050
1350	100	0.894924	0.012701	0.000058	0.843832	0.012187	0.000055
1250	90	0.255510	0.010693	0.000048	0.231553	0.010214	0.000046
1250	80	0.154442	0.010404	0.000047	0.139826	0.010043	0.000045
1250	70	0.056900	0.010206	0.000046	0.051717	0.009705	0.000044
1300	70	0.084157	0.010313	0.000047	0.077504	0.009816	0.000044
1300	80	0.237689	0.010617	0.000048	0.218502	0.010186	0.000046
1350	70	0.136436	0.010504	0.000048	0.127665	0.010030	0.000045
1350	80	0.398854	0.011357	0.000051	0.373408	0.010818	0.000049
1400	70	0.245874	0.011110	0.000050	0.235405	0.010699	0.000048
1400	80	0.711866	0.013133	0.000060	0.684301	0.012873	0.000058
1400	60	0.018449	0.010441	0.000057	0.017596	0.009997	0.000055
1425	60	0.021819	0.010447	0.000051	0.021016	0.009985	0.000049
1425	70	0.337565	0.011733	0.000053	0.326792	0.011234	0.000051
1425	80	0.967808	0.013880	0.000063	0.948209	0.013500	0.000061
1450	60	0.027118	0.010524	0.000049	0.026300	0.010022	0.000046
1450	70	0.486353	0.012888	0.000058	0.478751	0.012698	0.000058
1475	60	0.035818	0.010569	0.000048	0.035353	0.010056	0.000046
1475	70	0.706704	0.014721	0.000067	0.712232	0.014914	0.000068
1500	60	0.050046	0.010795	0.000049	0.050447	0.010382	0.000047
1500	70	1.070598	0.018639	0.000085	1.114976	0.019479	0.000088
1510	60	0.059061	0.011042	0.000050	0.060521	0.010651	0.000048
1510	70	1.295162	0.020873	0.000095	1.377285	0.022689	0.000103
1520	60	0.070249	0.011317	0.000051	0.073233	0.011104	0.000050
1520	70	1.554299	0.024271	0.000110	1.686047	0.026877	0.000122
1530	60	0.084318	0.011757	0.000053	0.089657	0.011725	0.000053
1530	70	1.922505	0.030948	0.000141	2.140804	0.036137	0.000165
1540	60	0.103952	0.012449	0.000056	0.113961	0.012875	0.000058
1550	60	0.131032	0.013638	0.000062	0.149487	0.014919	0.000068
1555	60	0.149223	0.014466	0.000066	0.175947	0.016740	0.000076
1560	60	0.172036	0.015693	0.000071	0.209711	0.019342	0.000088
1450	70	0.495814	0.012829	0.000058	0.487415	0.012599	0.000057
1450	70	0.496215	0.012989	0.000059	0.486744	0.012748	0.000058
1450	60	0.027377	0.010427	0.000048	0.026600	0.009903	0.000046
1450	60	0.027527	0.010543	0.000049	0.026573	0.009973	0.000046
1450	70	0.495657	0.013014	0.000059	0.485728	0.012746	0.000058
1450	70	0.494877	0.013335	0.000060	0.484540	0.013148	0.000060
1450	60	0.027533	0.010532	0.000049	0.026698	0.010066	0.000047
1450	60	0.027521	0.010431	0.000048	0.026599	0.009942	0.000046
1450	70	0.494241	0.012906	0.000058	0.483363	0.012677	0.000057

Table B.5: APD calibration fit parameters from Gaussian fits of the APD height distributions of APD 1 and 2.

U_{bias} [V]	LED [%]	APD 3			APD 4		
		μ_{APD} [V]	σ_{APD} [V]	$\Delta\mu_{\text{APD}}$ [V]	μ_{APD} [V]	σ_{APD} [V]	$\Delta\mu_{\text{APD}}$ [V]
100	100	0.019500	0.008680	0.000041	0.231843	0.011315	0.000051
150	100	0.019591	0.008221	0.000039	0.240268	0.011139	0.000051
200	100	0.019699	0.007688	0.000036	0.247388	0.010935	0.000050
250	100	0.019818	0.007558	0.000035	0.254955	0.011075	0.000050
300	100	0.019884	0.007401	0.000034	0.267778	0.010897	0.000049
350	100	0.019997	0.007133	0.000033	0.271019	0.011077	0.000050
400	100	0.020131	0.007082	0.000033	0.265642	0.010852	0.000049
450	100	0.020299	0.006918	0.000032	0.268468	0.010755	0.000049
425	100	0.020274	0.007022	0.000032	0.272353	0.011574	0.000052
475	100	0.020352	0.006878	0.000031	0.272587	0.011056	0.000050
500	100	0.020512	0.006864	0.000031	0.274481	0.011023	0.000050
550	100	0.020809	0.006770	0.000031	0.285481	0.011222	0.000051
600	100	0.021060	0.006744	0.000031	0.287777	0.011680	0.000053
650	100	0.021464	0.006619	0.000030	0.296657	0.011762	0.000053
700	100	0.022030	0.006584	0.000030	0.302051	0.011618	0.000053
750	100	0.022819	0.006589	0.000030	0.315326	0.011277	0.000051
800	100	0.023853	0.006488	0.000029	0.338055	0.011260	0.000051
850	100	0.025355	0.006431	0.000029	0.364435	0.010893	0.000049
900	100	0.027305	0.006348	0.000029	0.388949	0.012681	0.000058
950	100	0.030358	0.006345	0.000029	0.434294	0.012543	0.000057
1000	100	0.034586	0.006297	0.000029	0.508267	0.014295	0.000065
1050	100	0.040361	0.006379	0.000029	0.590636	0.011664	0.000053
1100	100	0.050175	0.006396	0.000012	0.742612	0.012614	0.000057
1150	100	0.064969	0.006225	0.000010	0.978262	0.016409	0.000077
1200	100	0.089061	0.006372	0.000013	1.356770	0.018690	0.000090
1250	100	0.130322	0.006505	0.000014	1.982361	0.017616	0.000117
1300	100	0.203354	0.006846	0.000011	3.080619	0.018629	0.000093
1350	100	0.324995	0.008123	0.000037	4.725501	0.017583	0.000100
1250	90	0.094167	0.006494	0.000013	1.412137	0.015495	0.000071
1250	80	0.057355	0.006344	0.000011	0.840700	0.018775	0.000111
1250	70	0.021872	0.006309	0.000029	0.278549	0.011208	0.000051
1300	70	0.031855	0.006246	0.000028	0.431009	0.011916	0.000054
1300	80	0.088298	0.006429	0.000010	1.311442	0.019179	0.000097
1350	70	0.051555	0.006339	0.000014	0.726066	0.013476	0.000061
1350	80	0.148197	0.006749	0.000016	2.249501	0.035714	0.000197
1400	70	0.092209	0.006694	0.000017	1.382817	0.015505	0.000071
1400	80	0.260973	0.007599	0.000034	4.179120	0.020032	0.000131
1400	60	0.008209	0.006399	0.000052	0.057361	0.010617	0.000048
1425	60	0.009421	0.006281	0.000042	0.076297	0.010810	0.000049
1425	70	0.127332	0.006993	0.000032	1.845364	0.016994	0.000078
1425	80	0.358443	0.008648	0.000039	4.660421	0.005302	0.000005
1450	60	0.011352	0.006316	0.000035	0.106898	0.011155	0.000051
1450	70	0.183766	0.007672	0.000035	2.684859	0.025103	0.000118
1475	60	0.014578	0.006274	0.000030	0.156407	0.011774	0.000053
1475	70	0.263606	0.008977	0.000041	3.968675	0.034849	0.000177
1500	60	0.019962	0.006393	0.000029	0.232087	0.012792	0.000058
1500	70	0.407451	0.011701	0.000053	4.679584	0.005368	0.000004
1510	60	0.023399	0.006474	0.000029	0.285119	0.014002	0.000063
1510	70	0.496936	0.013196	0.000060	4.873130	0.009607	0.000047
1520	60	0.027651	0.006709	0.000030	0.351618	0.015607	0.000071
1520	70	0.602252	0.015538	0.000070	4.954869	0.006040	0.000027
1530	60	0.033235	0.007036	0.000032	0.421314	0.017125	0.000078
1530	70	0.755196	0.019513	0.000089	4.951502	0.001813	0.163832
1540	60	0.040909	0.007455	0.000034	0.531431	0.020453	0.000093
1550	60	0.051732	0.008250	0.000037	0.669475	0.022147	0.000101
1555	60	0.059150	0.008929	0.000040	0.779174	0.026816	0.000122
1560	60	0.068042	0.009798	0.000044	0.899655	0.030646	0.000140
1450	70	0.187458	0.007561	0.000034	2.798593	0.021678	0.000099
1450	70	0.188343	0.007594	0.000034	2.750373	0.043879	0.000255
1450	60	0.011468	0.006230	0.000034	0.107091	0.011069	0.000050
1450	60	0.011530	0.006212	0.000033	0.107083	0.011217	0.000051
1450	70	0.188169	0.007596	0.000034	2.747358	0.046366	0.000245
1450	70	0.188556	0.007758	0.000035	2.685965	0.022715	0.000127
1450	60	0.011622	0.006286	0.000034	0.108771	0.011405	0.000052
1450	60	0.011481	0.006129	0.000033	0.106489	0.010994	0.000050
1450	70	0.188240	0.007617	0.000035	2.677886	0.022544	0.000105

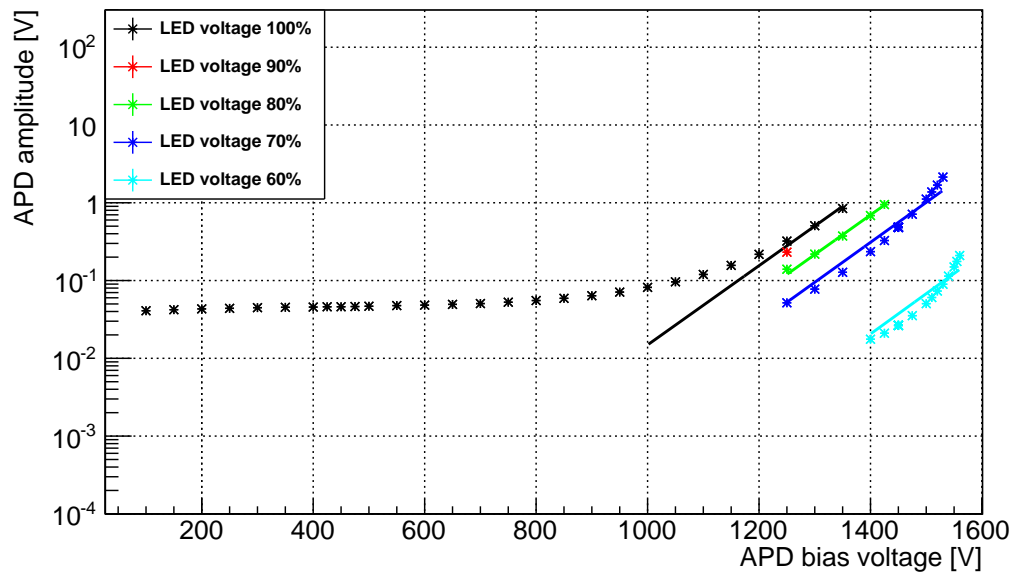
Table B.6: APD calibration fit parameters from Gaussian fits of the APD height distributions of APD3 and 4.

U_{bias} [V]	LED [%]	APD 5			APD 6		
		μ_{APD} [V]	σ_{APD} [V]	$\Delta\mu_{\text{APD}}$ [V]	μ_{APD} [V]	σ_{APD} [V]	$\Delta\mu_{\text{APD}}$ [V]
100	100	0.089962	0.013829	0.000063	0.266820	0.012390	0.000056
150	100	0.095424	0.012888	0.000059	0.281305	0.011595	0.000053
200	100	0.101550	0.012366	0.000056	0.292047	0.011137	0.000051
250	100	0.108682	0.011595	0.000053	0.300586	0.010582	0.000048
300	100	0.117261	0.011251	0.000051	0.308222	0.010362	0.000047
350	100	0.122024	0.010932	0.000050	0.314551	0.010080	0.000046
400	100	0.123060	0.010622	0.000048	0.319386	0.009797	0.000045
450	100	0.125545	0.010559	0.000048	0.324809	0.009641	0.000044
425	100	0.126602	0.010642	0.000048	0.322433	0.009663	0.000044
475	100	0.128887	0.010567	0.000048	0.327567	0.009581	0.000044
500	100	0.133836	0.010355	0.000047	0.330718	0.009455	0.000043
550	100	0.141020	0.010145	0.000046	0.337438	0.009374	0.000043
600	100	0.146102	0.009982	0.000045	0.344548	0.009216	0.000042
650	100	0.153575	0.010034	0.000046	0.354251	0.009159	0.000041
700	100	0.158757	0.009952	0.000045	0.366035	0.009073	0.000041
750	100	0.172000	0.009600	0.000044	0.382481	0.008814	0.000040
800	100	0.186214	0.009558	0.000043	0.404577	0.008830	0.000040
850	100	0.204732	0.009537	0.000043	0.435078	0.008820	0.000040
900	100	0.225997	0.009717	0.000044	0.477273	0.008865	0.000040
950	100	0.255872	0.009827	0.000045	0.536479	0.008773	0.000040
1000	100	0.306682	0.009943	0.000045	0.622538	0.008758	0.000040
1050	100	0.361948	0.010153	0.000046	0.746469	0.008683	0.000040
1100	100	0.467542	0.009515	0.000043	0.934792	0.008748	0.000040
1150	100	0.622714	0.013612	0.000064	1.227561	0.009090	0.000041
1200	100	0.887425	0.011558	0.000054	1.700560	0.009224	0.000042
1250	100	1.341591	0.016024	0.000073	2.501908	0.009904	0.000045
1300	100	2.071173	0.023621	0.000118	3.928036	0.011314	0.000052
1350	100	3.705592	0.022751	0.000106	4.705097	0.004722	0.000021
1250	90	0.939941	0.011474	0.000056	1.784161	0.009300	0.000042
1250	80	0.556970	0.012394	0.000059	1.048497	0.008882	0.000040
1250	70	0.178506	0.009351	0.000042	0.342408	0.008541	0.000039
1300	70	0.283448	0.009658	0.000044	0.539217	0.008863	0.000040
1300	80	0.887294	0.014056	0.000064	1.648370	0.009505	0.000043
1350	70	0.497349	0.010141	0.000046	0.913131	0.009584	0.000043
1350	80	1.552751	0.017942	0.000087	2.791695	0.011642	0.000053
1400	70	0.958755	0.011353	0.000051	1.680818	0.011924	0.000054
1400	80	2.857973	0.0101309	0.001770	4.629462	0.004780	0.000022
1400	60	0.034394	0.009652	0.000044	0.060505	0.008950	0.000040
1425	60	0.047310	0.009772	0.000044	0.084914	0.009128	0.000041
1425	70	1.296856	0.014761	0.000067	2.348212	0.014128	0.000064
1425	80	4.039306	0.028506	0.000158	4.739534	0.004807	0.000022
1450	60	0.069556	0.009996	0.000045	0.122584	0.009457	0.000043
1450	70	1.915829	0.017002	0.000077	3.395869	0.018578	0.000084
1475	60	0.105527	0.010488	0.000048	0.183989	0.010247	0.000046
1475	70	2.889409	0.024277	0.000110	4.627779	0.005262	0.000024
1500	60	0.160914	0.011559	0.000052	0.286048	0.011743	0.000053
1500	70	4.641641	0.032159	0.000149	4.838857	0.008074	0.000037
1510	60	0.203735	0.012237	0.000055	0.347154	0.012681	0.000057
1510	70	4.641586	0.005985	0.000013	4.983472	0.001054	0.000005
1520	60	0.249933	0.013421	0.000061	0.425258	0.014004	0.000063
1520	70	4.698724	0.006574	0.000030	4.998182	0.000891	0.000004
1530	60	0.301494	0.015969	0.000072	0.525533	0.016228	0.000074
1530	70	4.913591	0.021582	0.000199	4.999728	0.000103	0.000235
1540	60	0.386056	0.017844	0.000081	0.663138	0.019126	0.000087
1550	60	0.491164	0.020197	0.000092	0.855873	0.023839	0.000108
1555	60	0.576672	0.023552	0.000107	0.981759	0.027070	0.000123
1560	60	0.677184	0.026576	0.000121	1.132650	0.030934	0.000141
1450	70	1.964422	0.015800	0.000072	3.400622	0.018239	0.000083
1450	70	1.949558	0.019845	0.000090	3.393868	0.018425	0.000084
1450	60	0.069559	0.010094	0.000046	0.122749	0.009532	0.000043
1450	60	0.069675	0.009997	0.000045	0.123396	0.009531	0.000043
1450	70	1.927041	0.025882	0.000130	3.390495	0.018081	0.000082
1450	70	1.873285	0.022298	0.000120	3.387326	0.019172	0.000087
1450	60	0.069725	0.009985	0.000045	0.122405	0.009511	0.000043
1450	60	0.068083	0.010127	0.000046	0.122491	0.009537	0.000043
1450	70	1.873323	0.021589	0.000098	3.379055	0.018428	0.000084

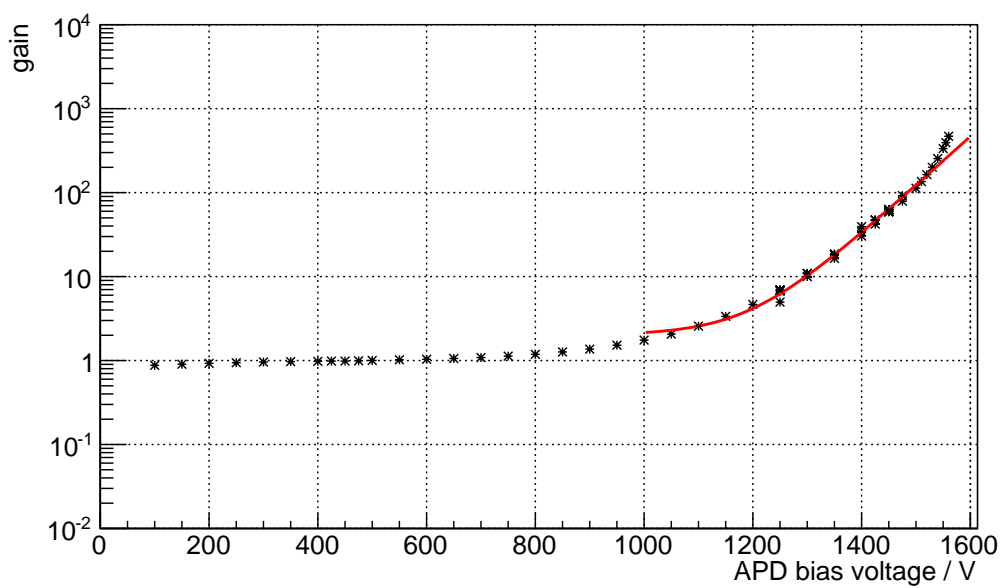
Table B.7: APD calibration fit parameters from Gaussian fits of the APD height distributions of APD5 and 6.

U_{bias} [V]	LED [%]	APD 7		
		μ_{APD} [V]	σ_{APD} [V]	$\Delta\mu_{\text{APD}}$ [V]
100	100	0.339397	0.012210	0.000055
150	100	0.356201	0.011422	0.000052
200	100	0.368455	0.011030	0.000050
250	100	0.378231	0.010452	0.000047
300	100	0.386860	0.010155	0.000046
350	100	0.394108	0.009933	0.000045
400	100	0.399684	0.009608	0.000044
450	100	0.405993	0.009530	0.000043
425	100	0.403090	0.009529	0.000043
475	100	0.409186	0.009487	0.000043
500	100	0.412660	0.009322	0.000042
550	100	0.420476	0.009221	0.000042
600	100	0.428928	0.009024	0.000041
650	100	0.440504	0.009029	0.000041
700	100	0.454840	0.008974	0.000041
750	100	0.475172	0.008757	0.000040
800	100	0.502428	0.008760	0.000040
850	100	0.540342	0.008739	0.000039
900	100	0.592693	0.008761	0.000040
950	100	0.666118	0.008654	0.000039
1000	100	0.772585	0.008662	0.000039
1050	100	0.926795	0.008690	0.000039
1100	100	1.160412	0.008743	0.000040
1150	100	1.522545	0.009027	0.000041
1200	100	2.104688	0.009392	0.000043
1250	100	3.087858	0.010161	0.000046
1300	100	4.727606	0.007500	0.000034
1350	100	4.814866	0.009635	0.000044
1250	90	2.204720	0.009556	0.000043
1250	80	1.296234	0.009018	0.000041
1250	70	0.424043	0.008604	0.000039
1300	70	0.666115	0.009073	0.000041
1300	80	2.032435	0.009924	0.000045
1350	70	1.121982	0.010117	0.000046
1350	80	3.425954	0.012648	0.000057
1400	70	2.054416	0.013267	0.000060
1400	80	4.643865	0.011074	0.000051
1400	60	0.074337	0.009579	0.000043
1425	60	0.103777	0.010074	0.000046
1425	70	2.860060	0.015810	0.000072
1425	80	4.893502	0.011561	0.000053
1450	60	0.149328	0.010610	0.000048
1450	70	4.120577	0.021002	0.000095
1475	60	0.222730	0.011393	0.000052
1475	70	4.633425	0.014013	0.000064
1500	60	0.344270	0.013473	0.000061
1500	70	4.938716	0.012477	0.000072
1510	60	0.416672	0.014335	0.000065
1510	70	4.973604	0.000862	0.000004
1520	60	0.508700	0.015833	0.000072
1520	70	4.978947	0.000894	0.000005
1530	60	0.625962	0.018082	0.000082
1530	70	4.981080	0.000925	0.000006
1540	60	0.785542	0.021270	0.000096
1550	60	1.003076	0.026130	0.000119
1555	60	1.144819	0.029103	0.000132
1560	60	1.312783	0.032535	0.000148
1450	70	4.132412	0.020008	0.000091
1450	70	4.124136	0.020323	0.000092
1450	60	0.149912	0.010117	0.000046
1450	60	0.150556	0.010064	0.000046
1450	70	4.120115	0.020019	0.000091
1450	70	4.116690	0.021255	0.000097
1450	60	0.149333	0.010095	0.000046
1450	60	0.149463	0.010221	0.000046
1450	70	4.107142	0.020609	0.000093

Table B.8: APD calibration fit parameters from Gaussian fits of the APD height distributions of APD 7.

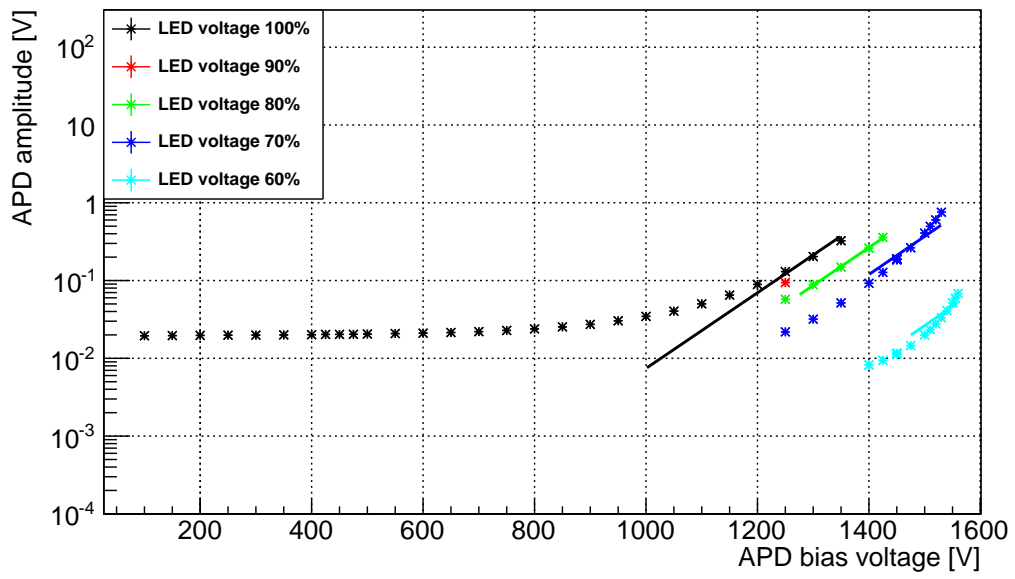


(a)

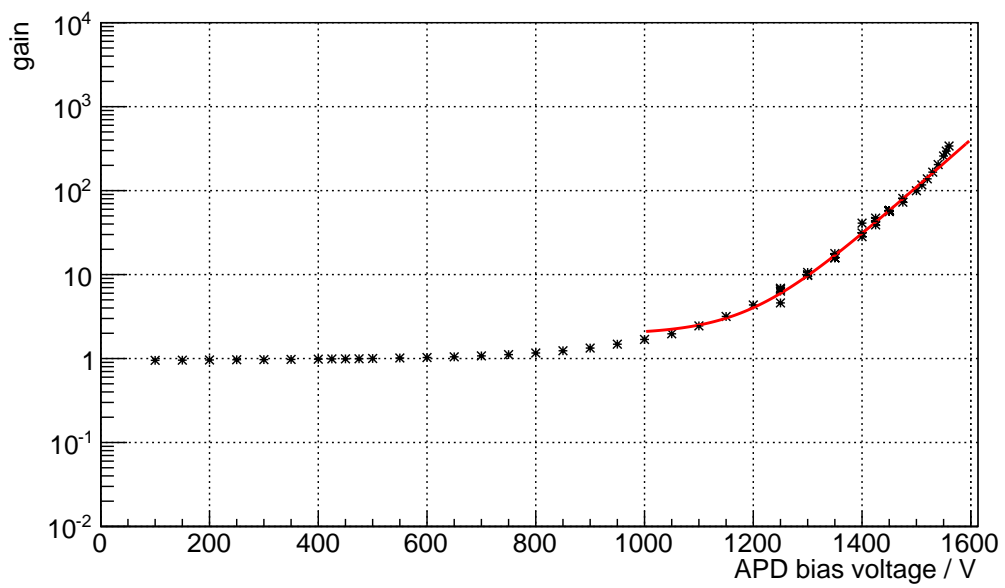


(b)

Figure B.5: APD calibration signal amplitudes for different LED pulse voltages in dependency of the APD bias voltage (APD2). Figure (a) shows the raw data points with the exponential fits to determine the offsets for the adjustment of the data points with respect to the LED voltage percentage. Figure (b) depicts the resulting gain curve with an exponential fit.

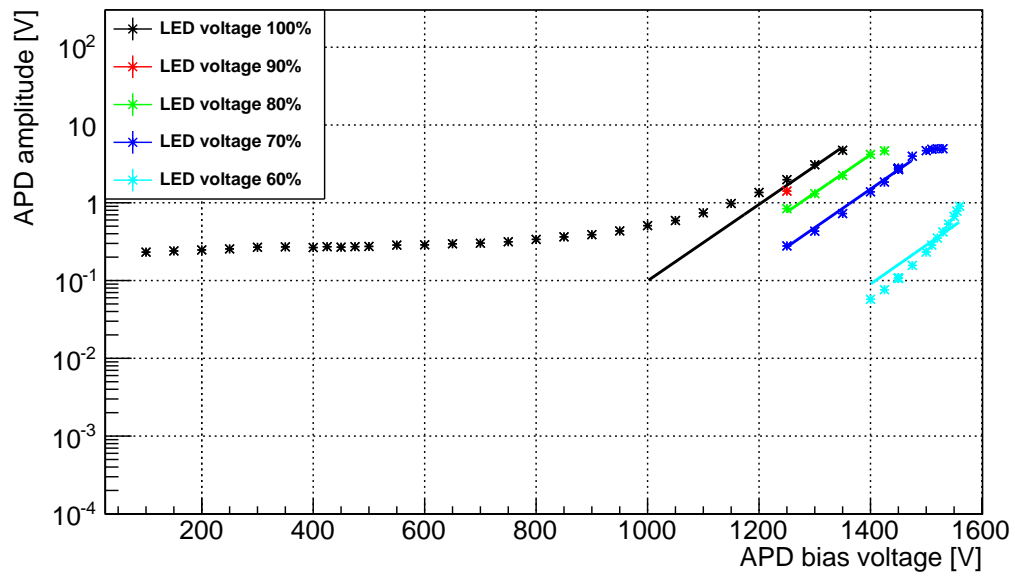


(a)

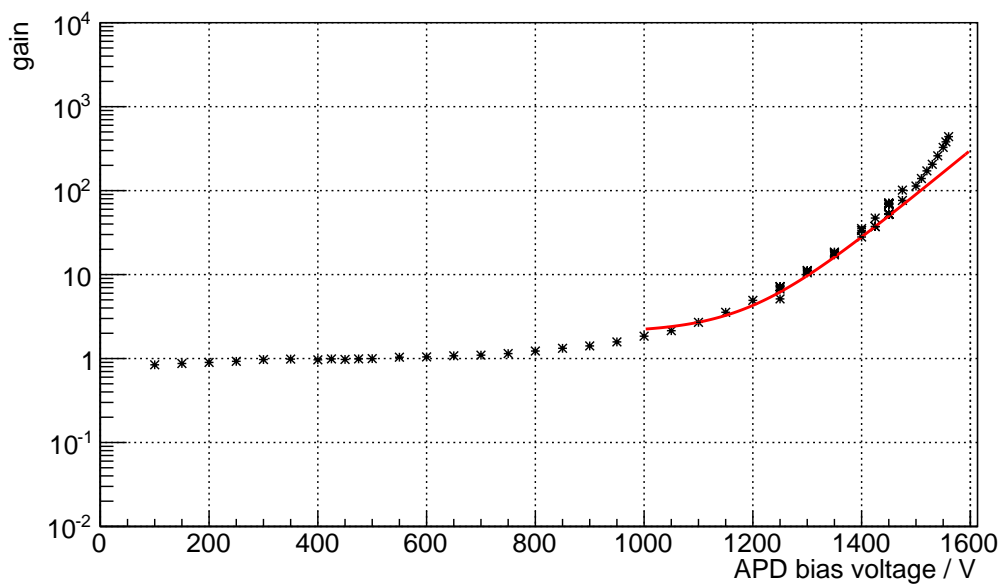


(b)

Figure B.6: APD calibration signal amplitudes for different LED pulse voltages in dependency of the APD bias voltage (APD3). Figure (a) shows the raw data points with the exponential fits to determine the offsets for the adjustment of the data points with respect to the LED voltage percentage. Figure (b) depicts the resulting gain curve with an exponential fit.

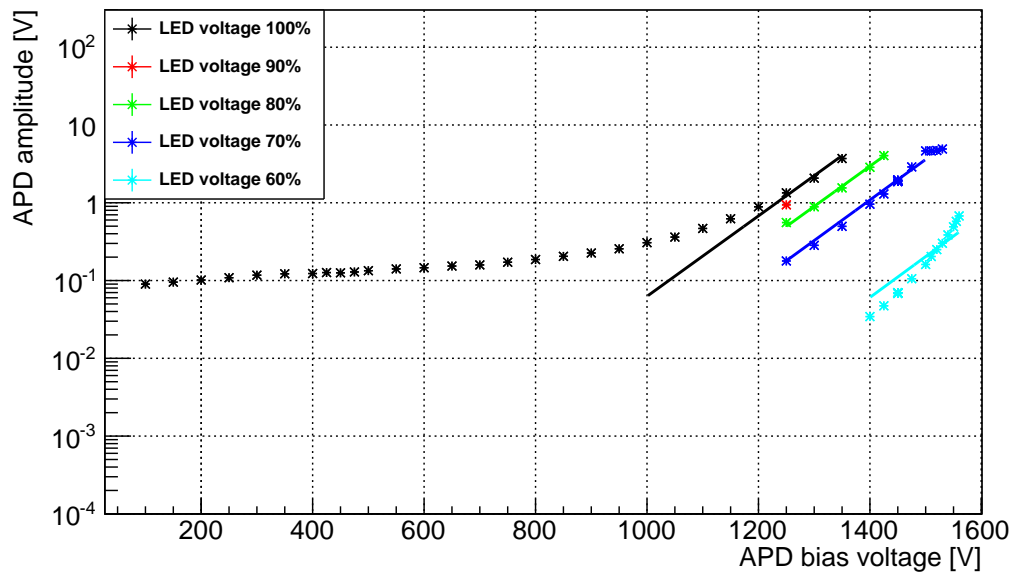


(a)

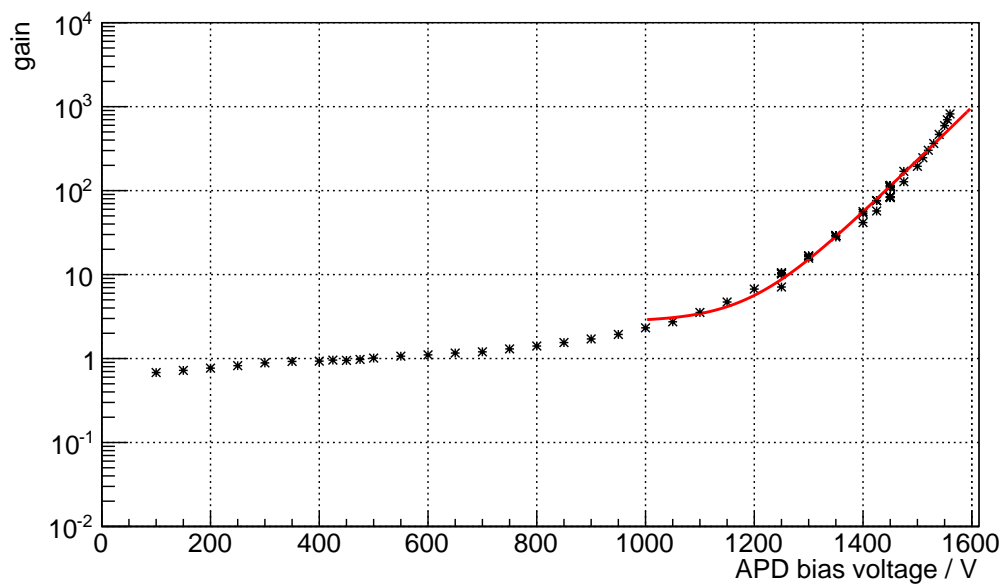


(b)

Figure B.7: APD calibration signal amplitudes for different LED pulse voltages in dependency of the APD bias voltage (APD4). Figure (a) shows the raw data points with the exponential fits to determine the offsets for the adjustment of the data points with respect to the LED voltage percentage. Figure (b) depicts the resulting gain curve with an exponential fit.

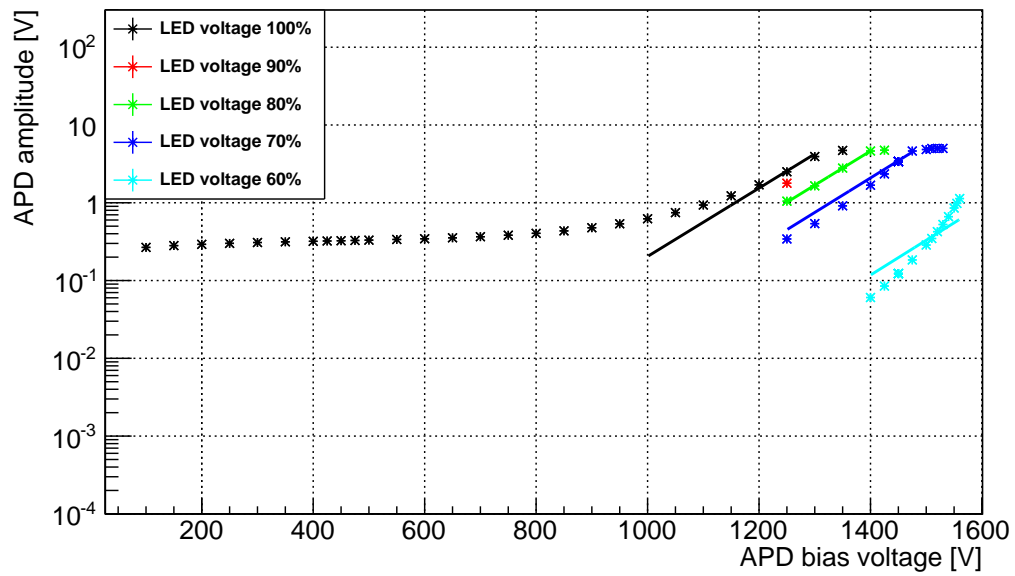


(a)

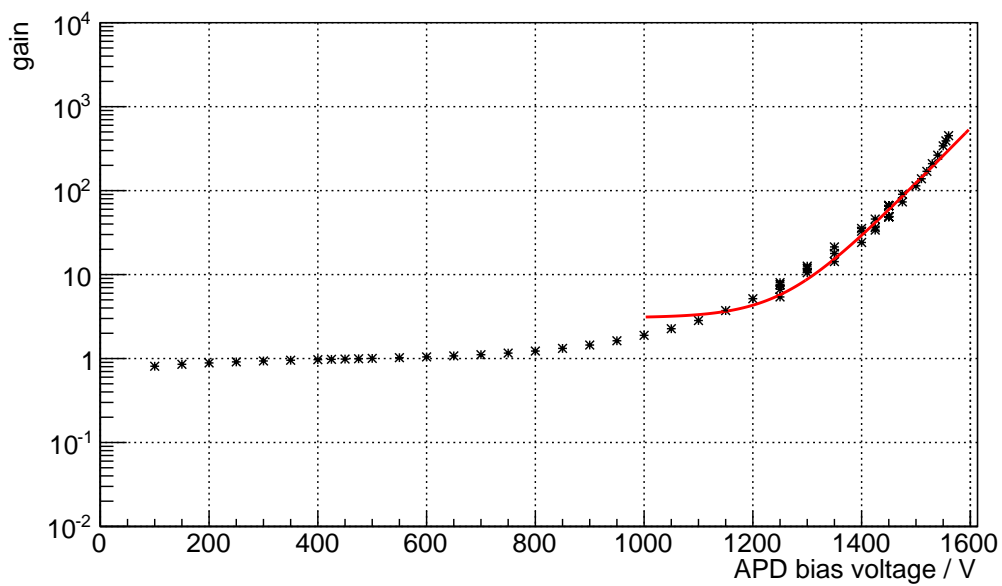


(b)

Figure B.8: APD calibration signal amplitudes for different LED pulse voltages in dependency of the APD bias voltage (APD5). Figure (a) shows the raw data points with the exponential fits to determine the offsets for the adjustment of the data points with respect to the LED voltage percentage. Figure (b) depicts the resulting gain curve with an exponential fit.

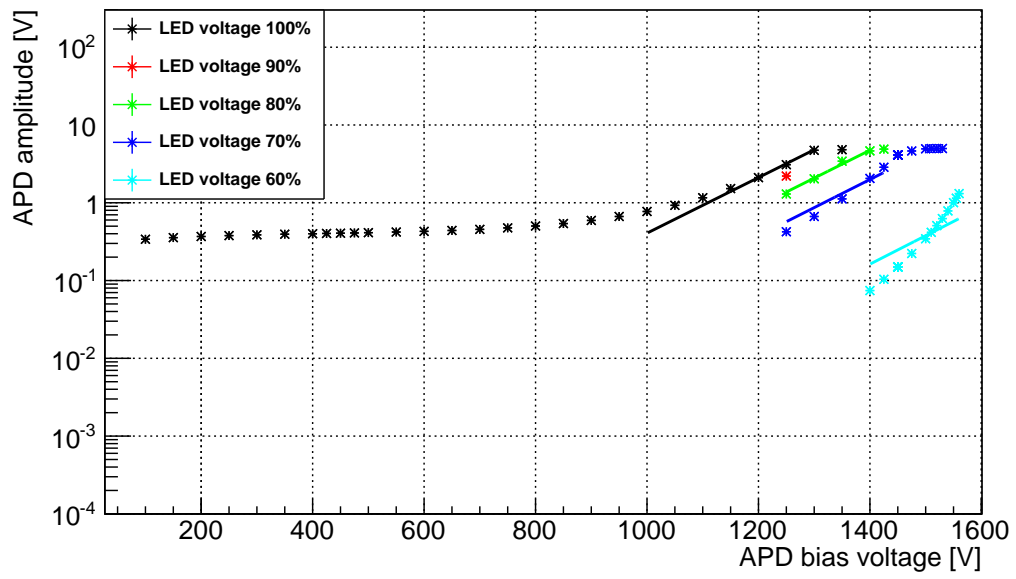


(a)

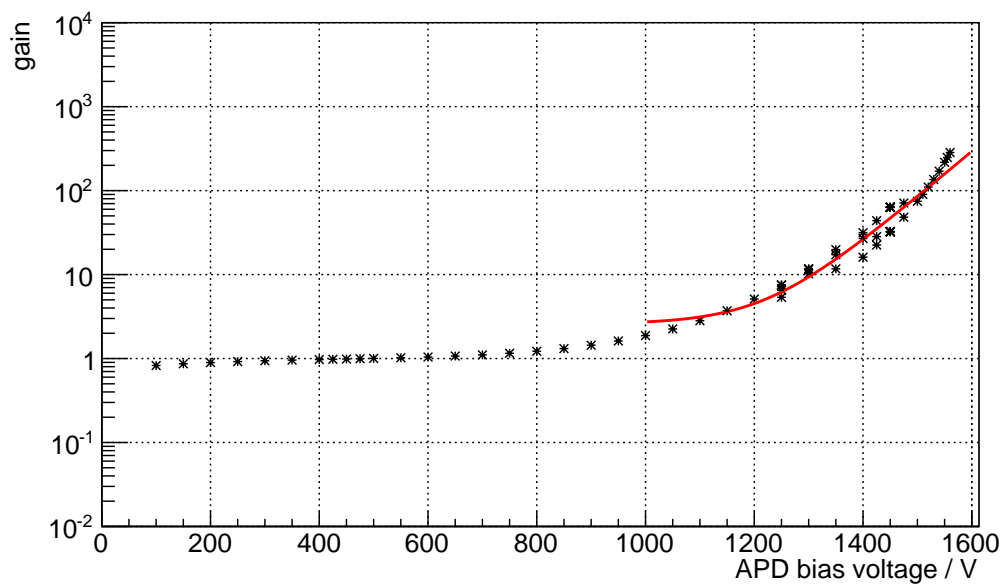


(b)

Figure B.9: APD calibration signal amplitudes for different LED pulse voltages in dependency of the APD bias voltage (APD6). Figure (a) shows the raw data points with the exponential fits to determine the offsets for the adjustment of the data points with respect to the LED voltage percentage. Figure (b) depicts the resulting gain curve with an exponential fit.



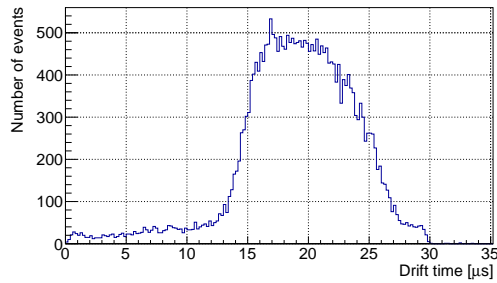
(a)



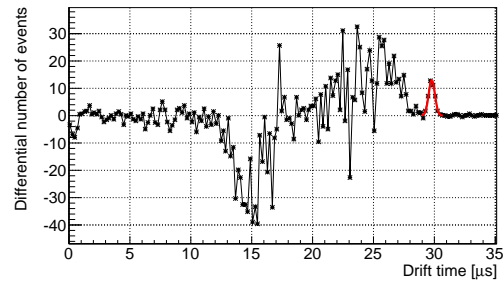
(b)

Figure B.10: APD calibration signal amplitudes for different LED pulse voltages in dependency of the APD bias voltage (APD7). Figure (a) shows the raw data points with the exponential fits to determine the offsets for the adjustment of the data points with respect to the LED voltage percentage. Figure (b) depicts the resulting gain curve with an exponential fit.

B.3 | Determination of maximum drift time

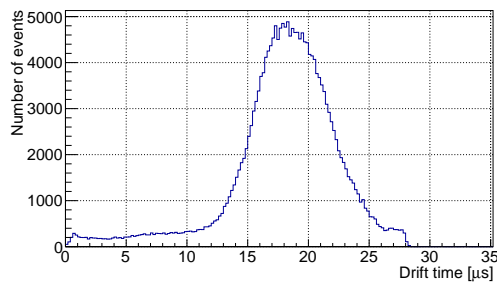


(a)

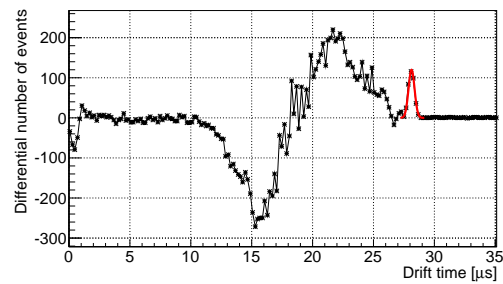


(b)

Figure B.11: Electron drift time spectra for a drift field strength of 396 V/cm. Figure (a) shows the actual drift time spectrum. The maximum drift time t_{\max} can be obtained from the “step” at approximately 30 μs . In (b), a filter has been applied to the spectrum to enhance the effect of this “step”. As can be seen, it can be fitted by a Gaussian.



(a)



(b)

Figure B.12: Electron drift time spectra for a drift field strength of 594 V/cm. Figure (a) shows the actual drift time spectrum. The maximum drift time t_{\max} can be obtained from the “step” at approximately 28 μs . In (b), a filter has been applied to the spectrum to enhance the effect of this “step”. As can be seen, it can be fitted by a Gaussian.

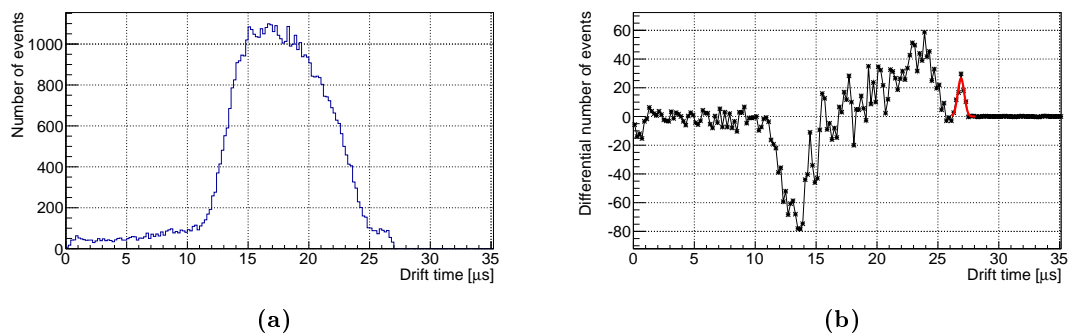


Figure B.13: Electron drift time spectra for a drift field strength of 792 V/cm. Figure (a) shows the actual drift time spectrum. The maximum drift time t_{max} can be obtained from the “step” at approximately 27 μs. In (b), a filter has been applied to the spectrum to enhance the effect of this “step”. As can be seen, it can be fitted by a Gaussian.

B.4 | $S1$ z -correction

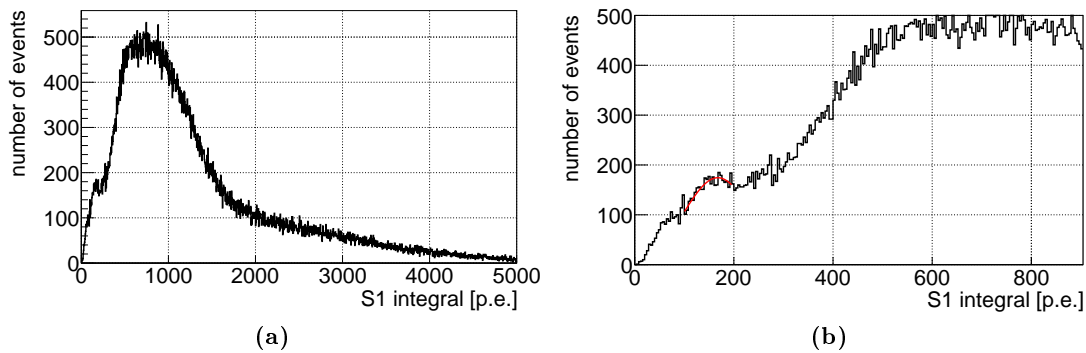


Figure B.14: Measured $S1$ spectrum for an ^{152}Eu source with a drift field of 594 V/cm. The spectrum shape is shifted to lower $S1$ integral values compared to the spectrum for a drift field of 198 V/cm. For the normalization the peak used in the $S1$ z -correction analysis is fitted with a Gaussian.

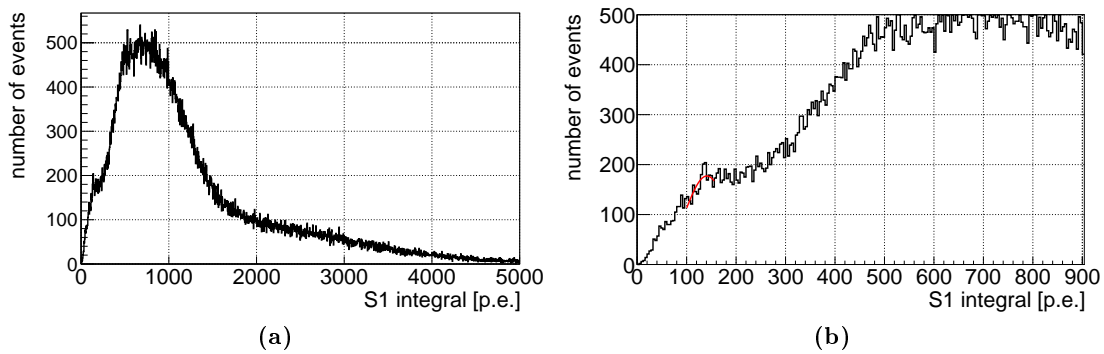


Figure B.15: Measured $S1$ spectrum for an ^{152}Eu source with a drift field of 792 V/cm. The spectrum shape is shifted to lower $S1$ integral values compared to the spectra at lower drift fields. For the normalization the peak used in the $S1$ z -correction analysis is fitted with a Gaussian.

z [mm]	198 V/cm		594 V/cm		792 V/cm	
	$S1_{\text{peak}}$	$\Delta S1_{\text{peak}}$	$S1_{\text{peak}}$	$\Delta S1_{\text{peak}}$	$S1_{\text{peak}}$	$\Delta S1_{\text{peak}}$
1.2625	125	3	118	11	138	9
3.7875	129	4	119	9	125	6
6.3125	137	5	140	11	167	61
8.8375	143	5	129	7	139	9
11.3625	136	6	143	14	150	9
13.8875	143	6	142	13	132	7
16.4125	152	6	161	8	137	11
18.9375	159	6	163	10	153	7
21.4625	161	8	180	25	159	8
23.9875	184	10	168	12	158	22
26.5125	183	8	170	6	154	13
29.0375	168	7	166	13	163	8
31.5625	178	5	177	14	161	8
34.0875	170	9	186	21	155	8
36.6125	178	6	159	11	157	12
39.1375	188	8	185	10	166	10
41.6625	182	6	169	6	163	6
44.1875	184	7	184	11	191	34
46.7125	194	8	177	12	162	8
49.2375	183	6	222	42	180	25

Table B.9: Fit results from the Gaussian fits in the z -slices of the $S1$ spectrum of ^{152}Eu for different drift field strengths. z denotes the center of the z -slice interval. $S1_{\text{peak}}$ is the Gaussian mean, the uncertainty $\Delta S1_{\text{peak}}$ is the mean error.

B.5 | $S2$ z -correction

z -slice	z [mm]	t_{drift} [μs]	$S2_{\text{mean}}$ [p.e.]	$\Delta S2_{\text{mean}}$ [p.e.]	$\sigma S2_{\text{mean}}$ [p.e.]	$\Delta\sigma S2_{\text{mean}}$ [p.e.]
1	1.26	0.80	3630	248	1944	281
2	3.79	2.41	2725	242	1416	502
3	6.31	4.02	2753	223	1241	219
4	8.84	5.63	2935	328	1553	429
5	11.36	7.24	3238	309	1665	393
6	13.89	8.85	3164	196	1602	292
7	16.41	10.45	2681	284	1365	359
8	18.94	12.06	2232	271	1217	272
9	21.46	13.67	1878	140	654	91
10	23.99	15.28	3999	231	2625	312
11	26.51	16.89	3284	314	2441	503
12	29.04	18.50	2843	167	1432	170
13	31.56	20.10	3019	298	2779	554
14	34.09	21.71	3894	320	2628	280
15	36.61	23.32	1795	146	638	113
16	39.14	24.93	2677	329	1483	506
17	41.66	26.54	2508	180	1165	220
18	44.19	28.15	2587	187	1093	188
19	46.71	29.75	2958	212	1981	359
20	49.24	31.36	2424	307	2202	1008

Table B.10: Double Gaussian fit results for the $S2$ peak positions for different interaction depths, stated in depth z and drift time t_{drift} , respectively. The examined peak is found in the $S2$ spectrum of events with a selection in $S1$. The (rounded) uncertainties for the z -slices are $\Delta z = 1.26$ mm and $\Delta t_{\text{drift}} = 0.804$ μs .

z -slice	A	ΔA	$S2_{\text{bkg}}$ [p.e.]	$\Delta S2_{\text{bkg}}$ [p.e.]	σ_{bkg} [p.e.]	$\Delta\sigma_{\text{bkg}}$ [p.e.]	B	ΔB
1	124275	24847	10490	1292	5819	859	156105	30232
2	69527	33147	7842	2683	6599	1560	180285	63367
3	54181	14910	7433	1032	5749	770	172453	27122
4	56940	21818	7045	1782	6584	1168	161676	40811
5	64614	25369	7460	1509	6058	938	182749	41901
6	93920	23436	7821	2518	7760	1629	167662	50194
7	55330	22276	6206	1532	6543	908	238501	50099
8	51650	15618	8381	1198	6766	960	209618	32762
9	43611	8056	6849	508	5385	446	203521	16873
10	141089	26827	11135	2147	6184	1376	95120	29516
11	123009	41940	10948	2702	6658	1875	139327	52132
12	96776	17697	8629	1044	5546	853	156509	26179
13	165095	57820	8912	5729	8243	3257	124332	83164
14	162550	22826	13007	1271	4289	1225	82741	22594
15	42842	8943	5909	631	5567	560	226487	22631
16	73154	31271	6332	2190	6714	1179	198656	61259
17	71052	18652	6159	1502	6774	973	243537	48064
18	77338	13731	8237	930	6240	721	182118	24107
19	135363	39349	8986	2107	6001	1191	168974	51448
20	106910	87961	8462	6290	7937	3709	195806	148298

Table B.11: Additional double Gaussian fit parameters for the $S2$ peak positions for different interaction depths.

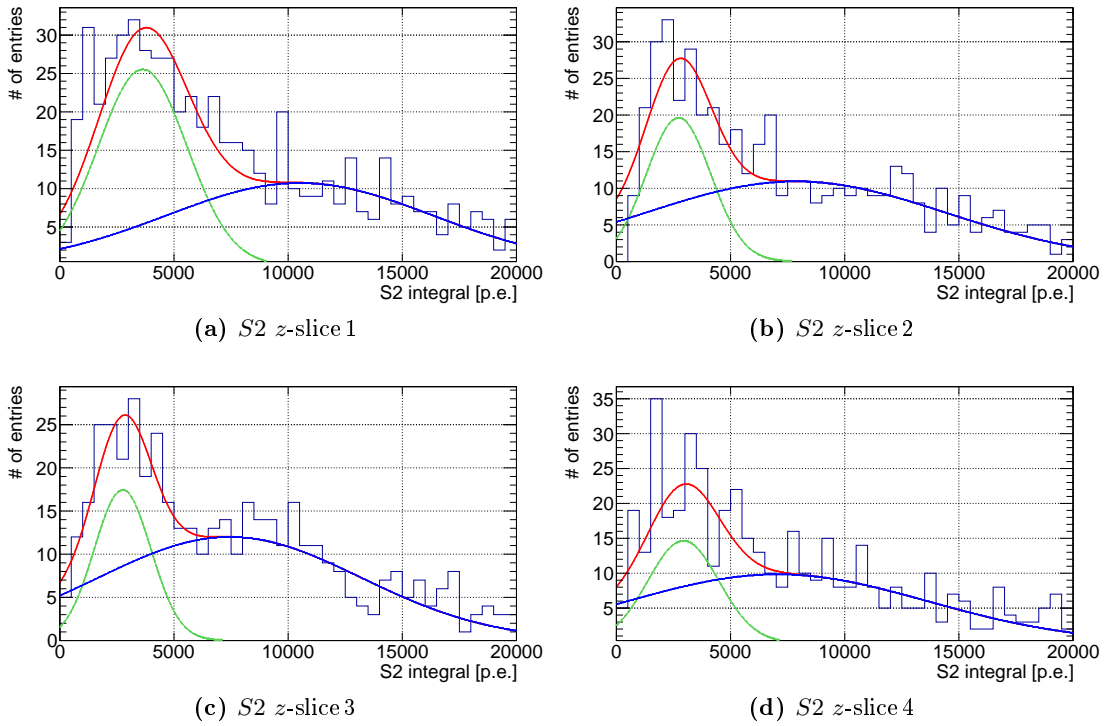


Figure B.16: z -slices 1-4 with double-Gaussian fit function.

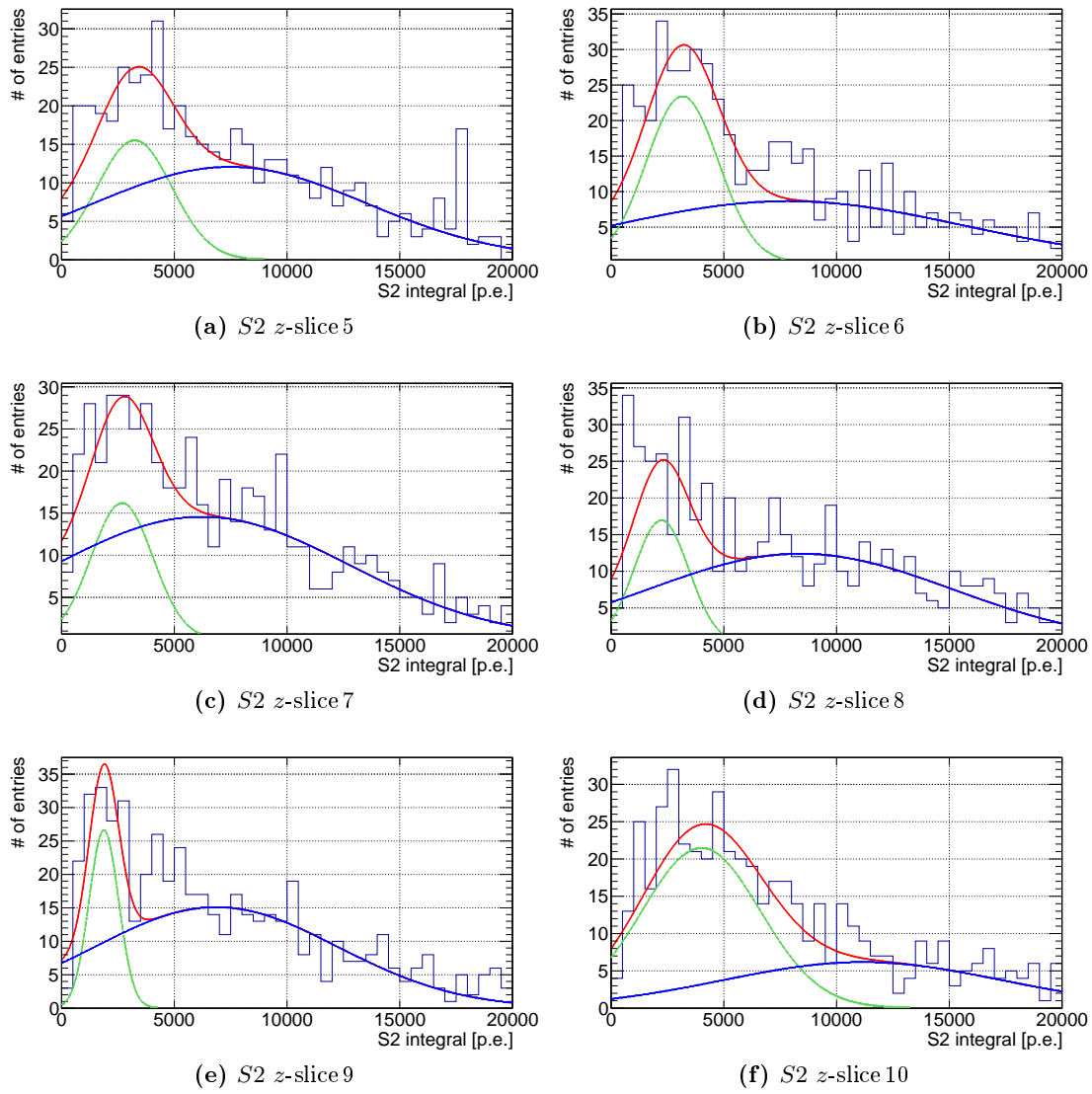
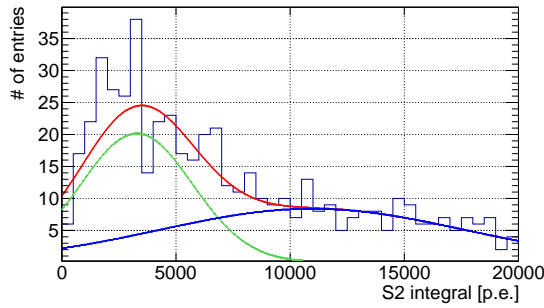
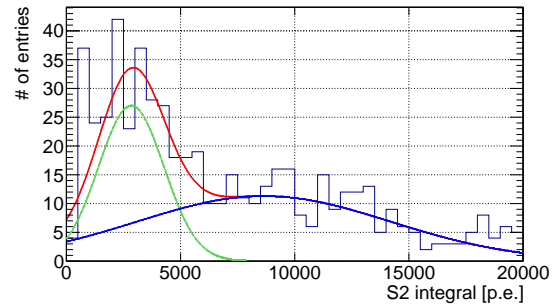


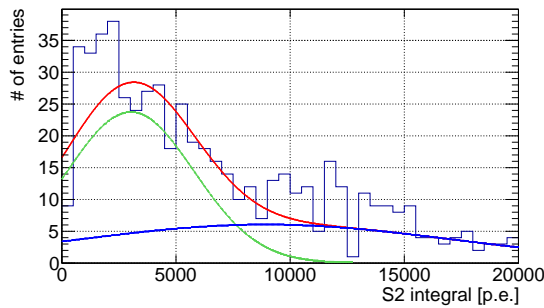
Figure B.17: z -slices 5-10 with double-Gaussian fit function.



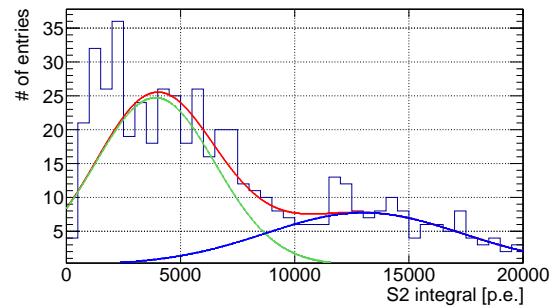
(a) S_2 z -slice 11



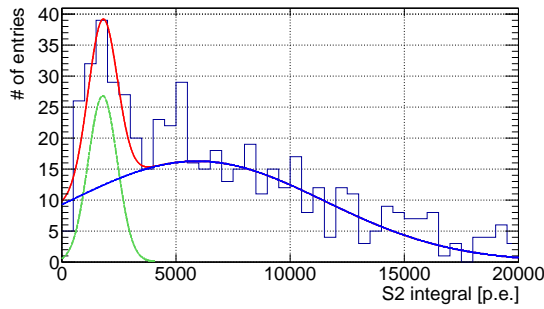
(b) S_2 z -slice 12



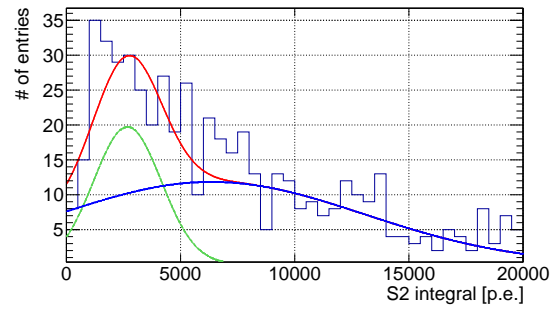
(c) S_2 z -slice 13



(d) S_2 z -slice 14

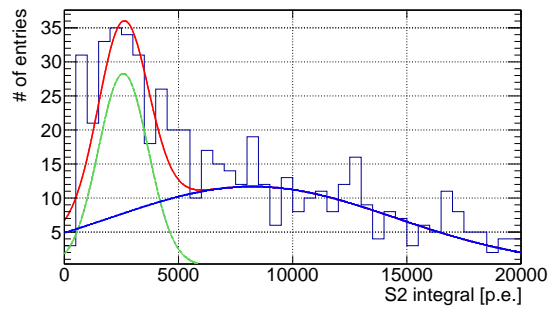
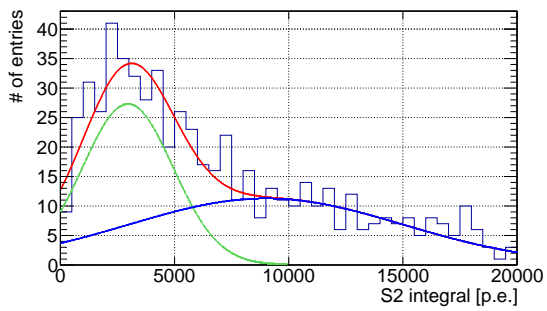
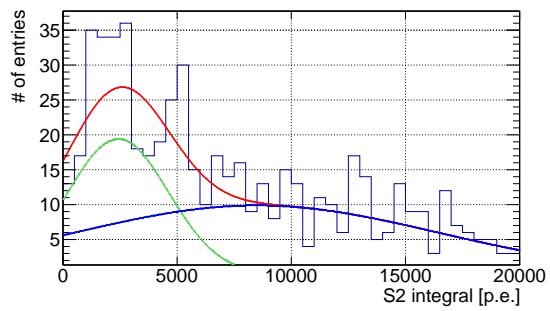


(e) S_2 z -slice 15



(f) S_2 z -slice 16

Figure B.18: z -slices 11-16 with double-Gaussian fit function.

(a) S_2 z -slice 17(b) S_2 z -slice 19(c) S_2 z -slice 20**Figure B.19:** z -slices 17, 19 & 20 with double-Gaussian fit function.

B.6 | S1 Asymmetry

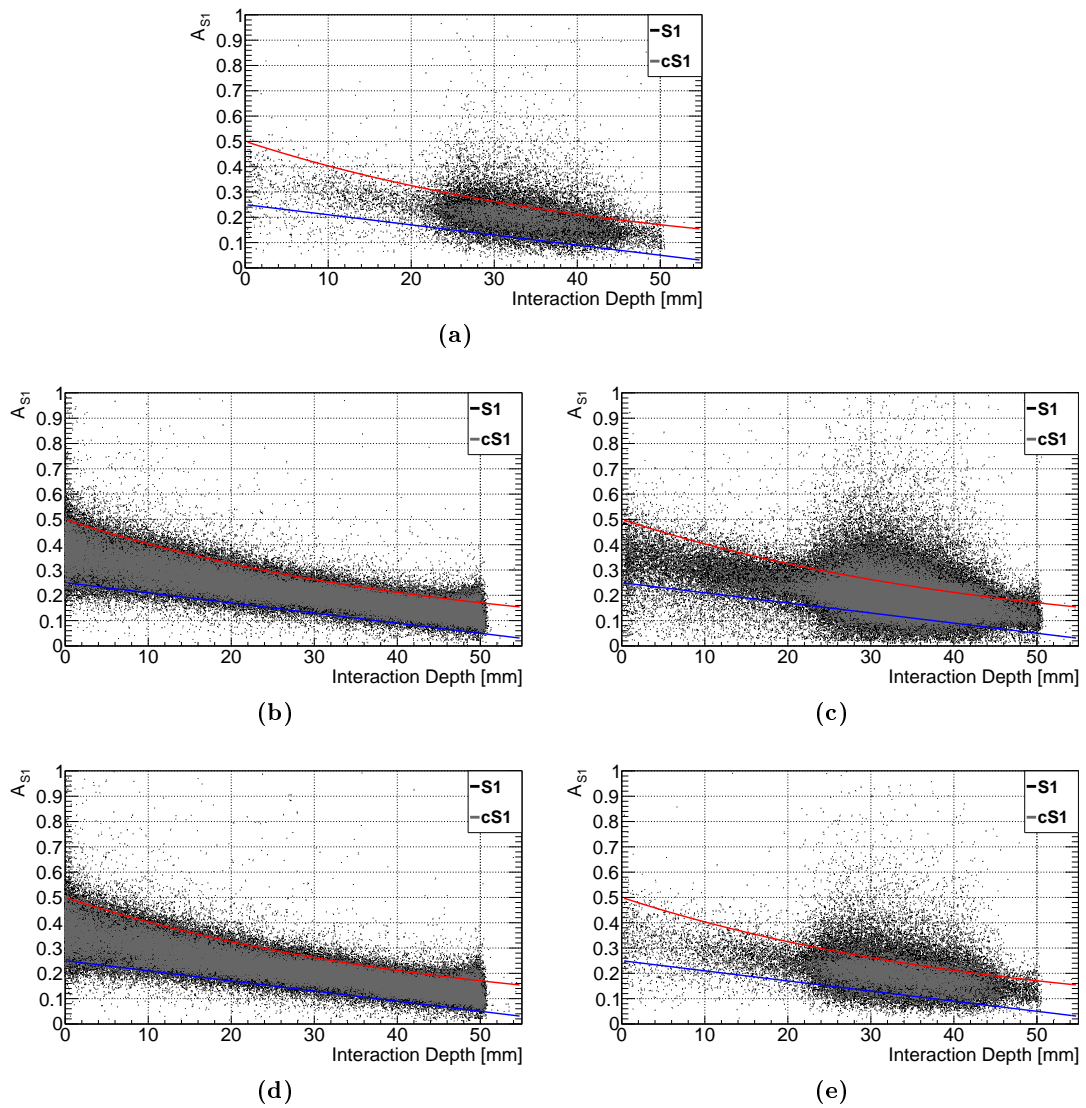


Figure B.20: $S1$ asymmetry for a calibration (left) and a Compton measurement (right) at at 396 V/cm (top row), 594 V/cm (center row) and 792 V/cm (bottom row). The blue and red lines mark the minimum and maximum limits for the accepted asymmetry values, as described in section 9.3.4. Note that for the drift field of 396 V/cm, no calibration data was taken.

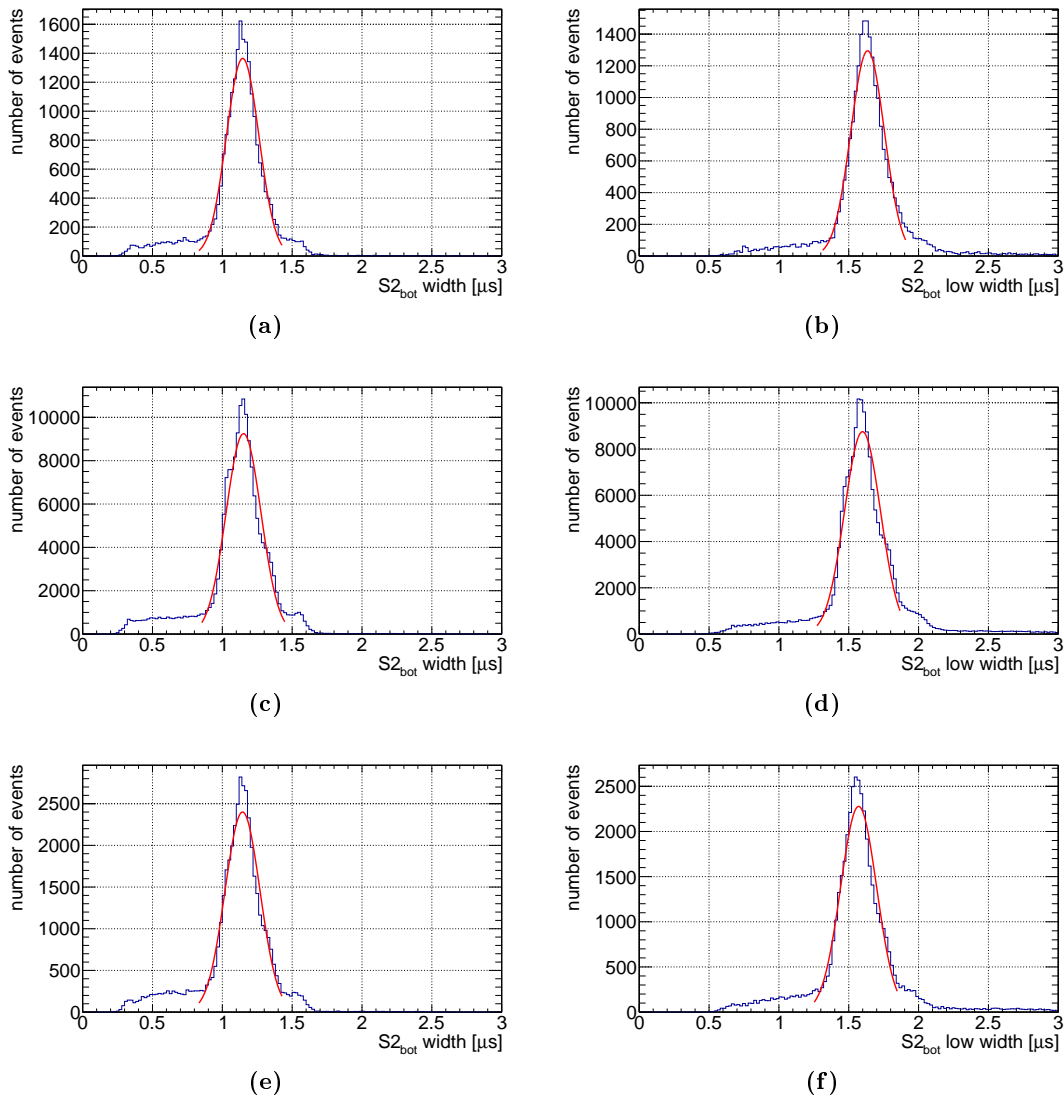
B.7 | S_2 Width

Figure B.21: S_2 width for the Compton data at drift fields of 396 V/cm (top row), 594 V/cm (center row) and 792 V/cm (bottom row) for FWHM (left) and low width at 10% height of the signal amplitude (right).

B.8 | TPC Calibration

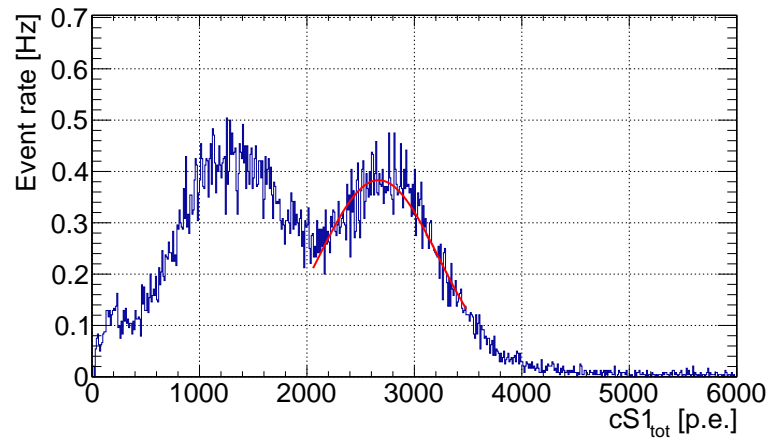


Figure B.22: Event rate in dependence of $cS1$ for ^{137}Cs at 198 V/cm, with Gaussian fit of the 661.6 keV gamma-ray line.

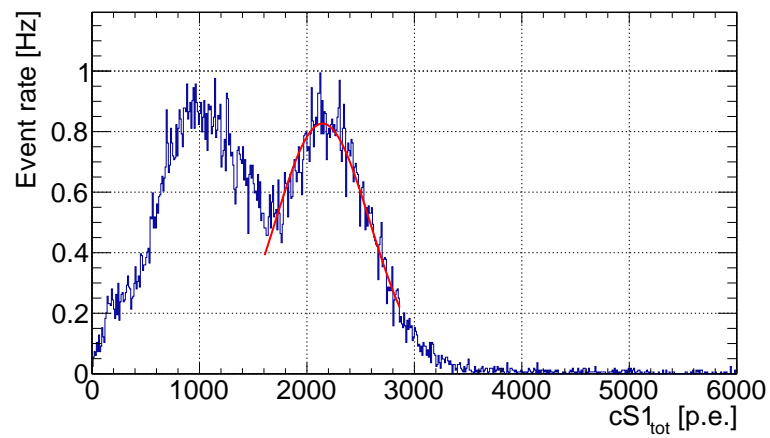


Figure B.23: Event rate in dependence of $S1$ for ^{137}Cs at 594 V/cm, with Gaussian fit of the 661.6 keV gamma-ray line.

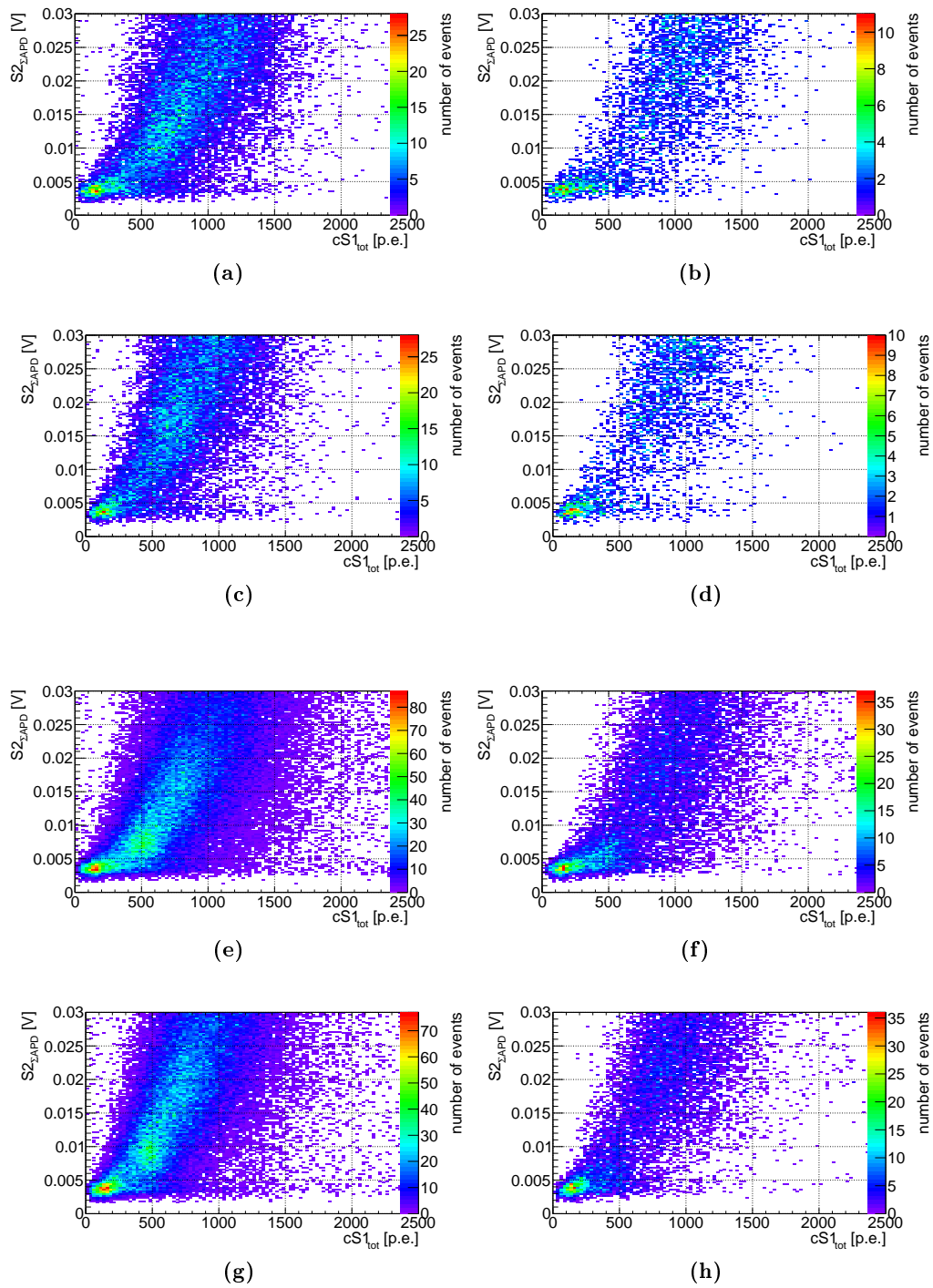


Figure B.24: Event distributions in S_2 from the summed APD amplitudes versus cS_1 for ^{133}Ba at 594 V/cm (top row) and 792 V/cm (second row) and ^{152}Eu at 594 V/cm (third row) and 792 V/cm (bottom row). On the left, only the fiducialization, the condition that one S_1 is present in the trigger time window and the selection of the largest S_2 are used as event selections, on the right the complete set of event selections is applied. The shape of the event distributions is similar to the one observed in figure 9.13 and also similar to the theoretical expectation. Still the plots show no specific event clusters that could be associated with energy lines from gamma-ray sources.

B.9 | Trigger Efficiency

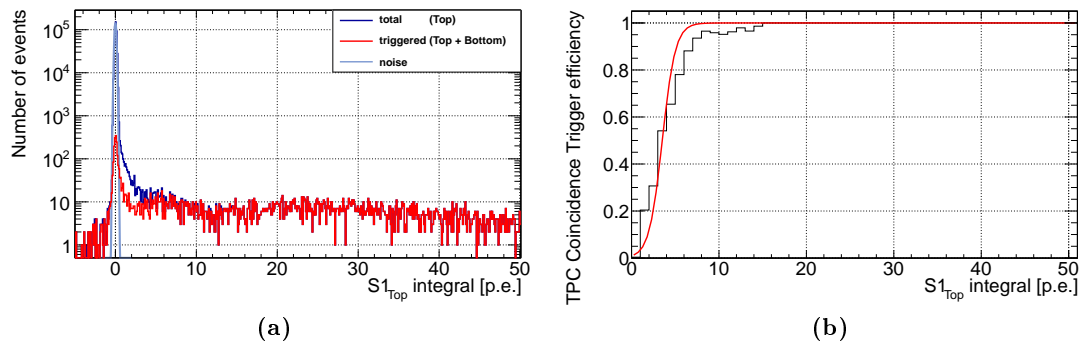


Figure B.25: Spectra of the signal obtained with the Fixed Window Integral Method for the Top PMT for signals obtained in coincidence trigger mode (a). The blue spectrum contains all signals in the fixed window. The red spectrum shows all signals with an additional TDC signal for both PMTs at the trigger time. The ratio of the two spectra yields the trigger efficiency, shown in (b). A value of 100 % is reached first for signals above 6 p.e. The shape of the trigger efficiency is approximated with a fit using a Fermi-Dirac distribution. The trigger efficiency measurement was conducted at a drift field strength of 198 V/cm.

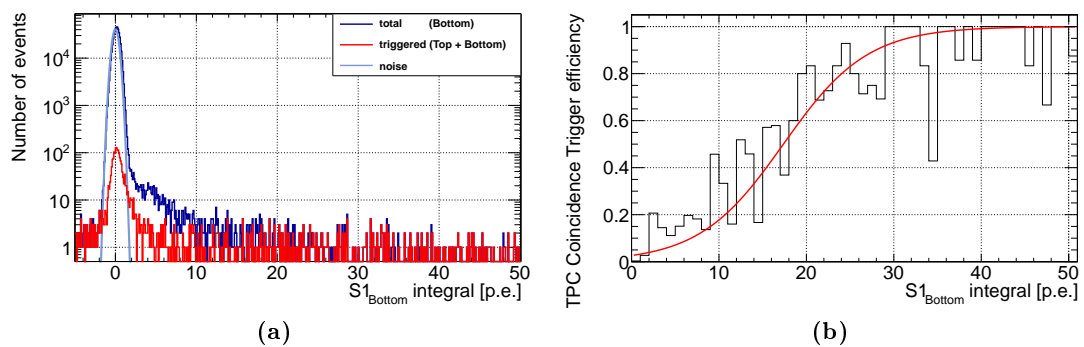


Figure B.26: Spectra of the signal obtained with the Fixed Window Integral Method for the Bottom PMT for signals obtained in coincidence trigger mode (a). The blue spectrum contains all signals in the fixed window. The red spectrum shows all signals with an additional TDC signal for both PMTs at the trigger time. The ratio of the two spectra yields the trigger efficiency, shown in (b). A value of 100 % is reached first for signals above 20 p.e. The shape of the trigger efficiency is approximated with a fit using a Fermi-Dirac distribution. The trigger efficiency measurement was conducted at a drift field strength of 198 V/cm.

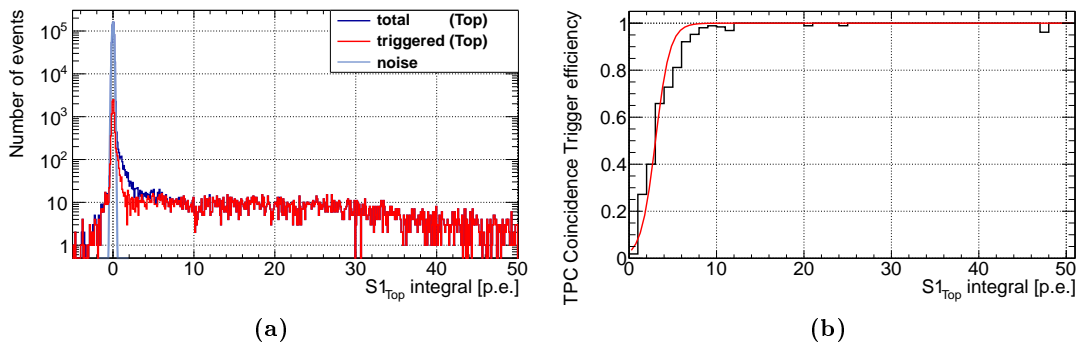


Figure B.27: Spectra of the signal obtained with the Fixed Window Integral Method for the Top PMT (a). The blue spectrum contains all signals in the fixed window. The red spectrum shows all signals with an additional TDC signal for the Bottom PMT at the trigger time. The ratio of the two spectra yields the trigger efficiency, shown in (b). A value of 100% is reached first for signals above 6 p.e. The shape of the trigger efficiency is approximated with a fit using a Fermi-Dirac distribution. The trigger efficiency measurement was conducted at a drift field strength of 594 V/cm.

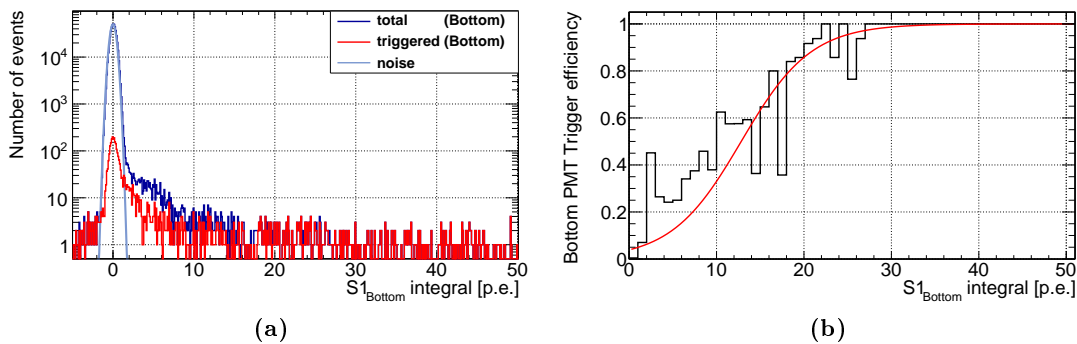


Figure B.28: Spectra of the signal obtained with the Fixed Window Integral Method for the Bottom PMT (a). The blue spectrum contains all signals in the fixed window. The red spectrum shows all signals with an additional TDC signal for the Bottom PMT at the trigger time. The ratio of the two spectra yields the trigger efficiency, shown in (b). A value of 100% is reached first for signals above 20 p.e. The shape of the trigger efficiency is approximated with a fit using a Fermi-Dirac distribution. The trigger efficiency measurement was conducted at a drift field strength of 594 V/cm.

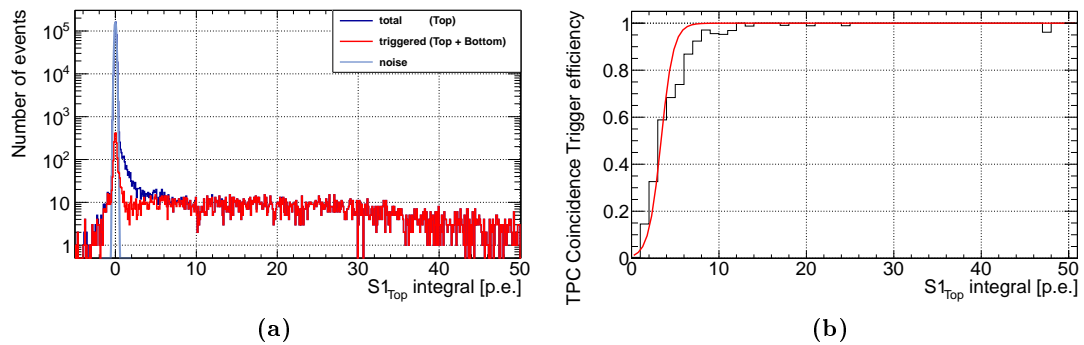


Figure B.29: Spectra of the signal obtained with the Fixed Window Integral Method for the Top PMT for signals obtained in coincidence trigger mode (a). The blue spectrum contains all signals in the fixed window. The red spectrum shows all signals with an additional TDC signal for both PMTs at the trigger time. The ratio of the two spectra yields the trigger efficiency, shown in (b). A value of 100 % is reached first for signals above 6 p.e. The shape of the trigger efficiency is approximated with a fit using a Fermi-Dirac distribution. The trigger efficiency measurement was conducted at a drift field strength of 594 V/cm.

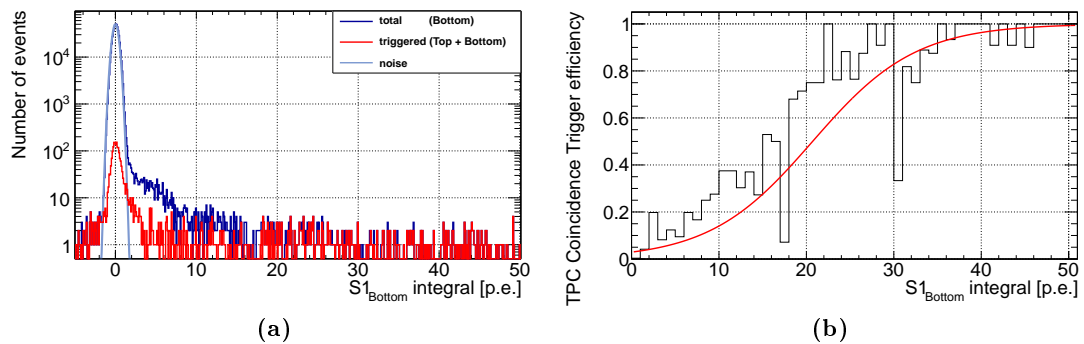


Figure B.30: Spectra of the signal obtained with the Fixed Window Integral Method for the Bottom PMT for signals obtained in coincidence trigger mode (a). The blue spectrum contains all signals in the fixed window. The red spectrum shows all signals with an additional TDC signal for both PMTs at the trigger time. The ratio of the two spectra yields the trigger efficiency, shown in (b). A value of 100 % is reached first for signals above 20 p.e. The shape of the trigger efficiency is approximated with a fit using a Fermi-Dirac distribution. The trigger efficiency measurement was conducted at a drift field strength of 594 V/cm.

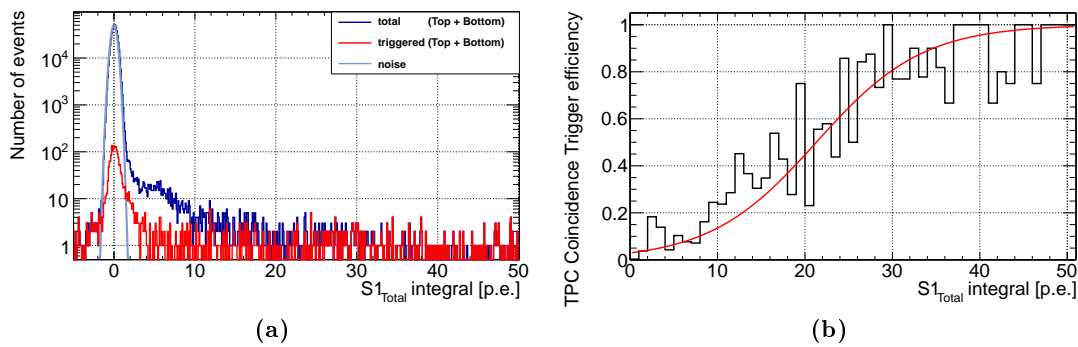


Figure B.31: Spectra of the signal obtained with the Fixed Window Integral Method for the TPC PMT coincidence (a). The blue spectrum contains all signals in the fixed window. The red spectrum shows all signals with an additional TDC signal for both PMTs at the trigger time. The ratio of the two spectra yields the trigger efficiency, shown in (b). A value of 100% is reached first for signals above 30 p.e. The shape of the trigger efficiency is approximated with a fit using a Fermi-Dirac distribution as described in the text. The trigger efficiency measurement was conducted at a drift field strength of 594 V/cm.

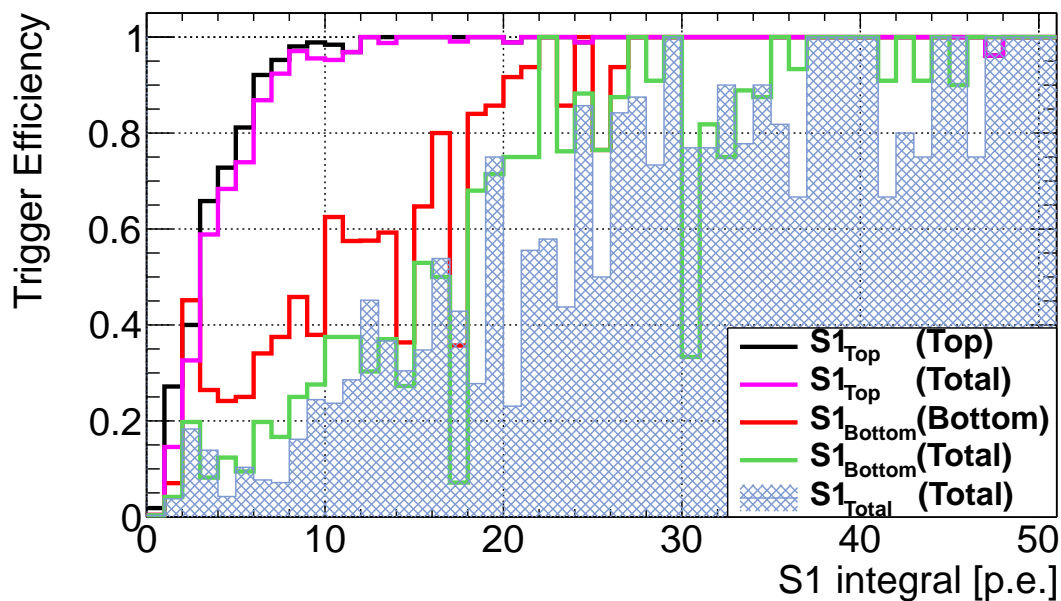


Figure B.32: Comparison of the trigger efficiencies determined for the Top PMT, Bottom PMT and summed signal for single and coincidence trigger mode. The Top PMT with the higher gain yields a better trigger efficiency than the Bottom PMT. The labels name the signal channel X as well as the trigger mode in parentheses. For the two PMTs, the change from single trigger mode to coincidence trigger leads to a shift of the trigger efficiency curve to larger $S1$ integral values. Labeled $S1_{Total}$, the summed signal for the coincidence mode is depicted for comparison. The Bottom PMT has a strong impact on the coincidence trigger performance. The applied drift field strength is 594 V/cm.

B.10 | Light Yield

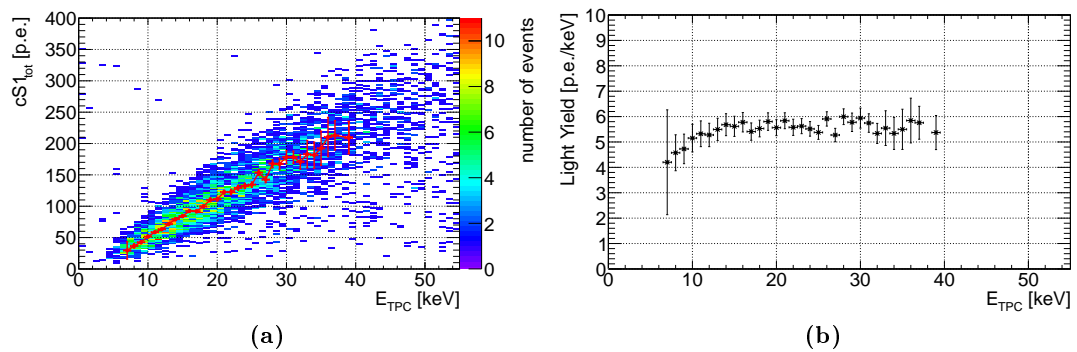


Figure B.33: Detected $cS1$ signal in dependence of the energy deposit E_{TPC} for Compton scattering with an applied drift field of 396 V/cm (a). The graph suggests a linear relation between deposited energy and generated scintillation light. The light yield shown in (b) is the mean $cS1$ signal determined with a Gaussian fit from energy slices, divided by the corresponding energy deposit E_{TPC} . The light yield slightly increases with deposited energy for energies below ≈ 15 keV and does not change significantly for the deposited energies above this value.

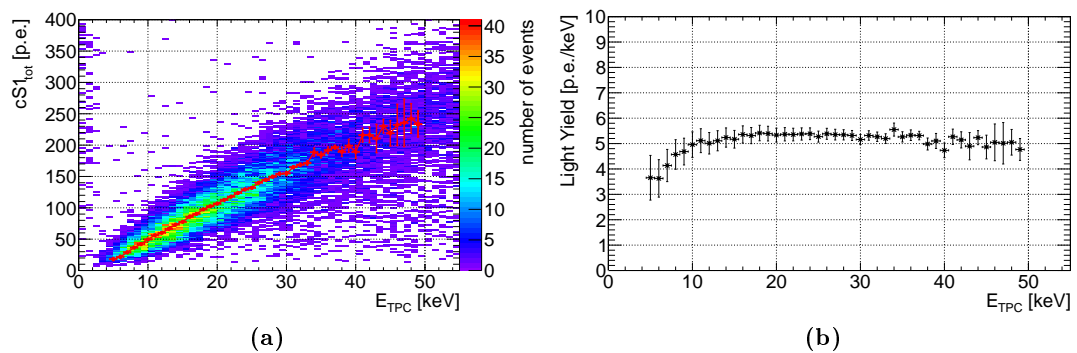


Figure B.34: Detected $cS1$ signal in dependence of the energy deposit E_{TPC} for Compton scattering with an applied drift field of 594 V/cm (a). The graph suggests a linear relation between deposited energy and generated scintillation light. The light yield shown in (b) is the mean $cS1$ signal determined with a Gaussian fit from energy slices, divided by the corresponding energy deposit E_{TPC} . For low energies, the light yield increases up to a maximum value at around 20 keV. The light yield value remains constant or even decreases slightly for higher E_{TPC} above 30–40 keV.

E_{TPC} [keV]	μ_{cS1} [p.e.]	$\Delta\mu_{cS1}$ [p.e.]	σ_{cS1} [p.e.]	$\Delta\sigma_{cS1}$ [p.e.]	χ_{red}^2	LY [$\frac{\text{p.e.}}{\text{keV}}$]	ΔLY [$\frac{\text{p.e.}}{\text{keV}}$]
7	29.41	13.83	19.08	9.17	2.31	4.20	2.06
8	36.60	3.34	16.51	2.79	0.93	4.57	0.71
9	42.54	2.26	16.42	1.94	0.42	4.73	0.58
10	51.52	1.72	15.16	1.60	0.63	5.15	0.54
11	58.55	1.66	16.23	1.52	0.69	5.32	0.51
12	63.32	1.64	15.21	1.51	1.13	5.28	0.46
13	71.42	1.57	16.02	1.33	0.95	5.49	0.44
14	79.53	2.10	19.40	2.17	1.07	5.68	0.43
15	84.24	1.96	19.34	1.84	0.63	5.62	0.40
16	92.43	1.98	20.18	2.03	0.65	5.78	0.38
17	91.95	2.10	19.66	3.23	1.13	5.41	0.34
18	99.54	2.11	23.17	2.14	0.68	5.53	0.33
19	110.26	3.03	27.46	2.97	0.79	5.80	0.34
20	111.28	2.96	25.20	2.99	0.91	5.56	0.32
21	122.56	3.04	27.64	3.28	0.88	5.84	0.31
22	122.71	4.26	32.67	5.27	0.74	5.58	0.32
23	129.35	3.88	32.45	6.21	1.00	5.62	0.30
24	132.38	4.13	30.27	8.11	0.88	5.52	0.29
25	134.43	4.23	31.96	6.07	0.79	5.38	0.27
26	153.59	4.36	32.32	5.85	0.70	5.91	0.28
27	142.38	4.78	35.58	7.23	1.11	5.27	0.26
28	167.86	6.28	42.95	8.93	0.71	5.99	0.31
29	167.49	8.81	58.26	13.36	0.70	5.78	0.36
30	178.24	10.22	56.15	15.90	0.50	5.94	0.39
31	178.11	9.73	47.56	20.35	0.73	5.75	0.36
32	170.76	11.46	53.73	22.83	0.67	5.34	0.40
33	182.99	21.89	79.88	36.32	0.41	5.55	0.68
34	181.49	20.79	86.98	27.89	0.54	5.34	0.63
35	192.43	27.17	100.34	45.17	0.38	5.50	0.79
36	210.38	31.17	86.20	50.36	0.29	5.84	0.88
37	212.99	23.26	81.68	37.21	0.34	5.76	0.65
39	209.49	25.63	95.64	43.90	0.23	5.37	0.67

Table B.12: Parameters of the $cS1$ slices for the determination of the light yield for a drift field strength of 396 V/cm. The values for the mean signal μ_{cS1} and its standard deviation σ_{cS1} as well as their uncertainties are obtained by fitting the individual energy slices, as well as the reduced χ^2 . The light yield LY and its error are calculated using equation (9.15).

E_{TPC} [keV]	μ_{cS1} [p.e.]	$\Delta\mu_{cS1}$ [p.e.]	σ_{cS1} [p.e.]	$\Delta\sigma_{cS1}$ [p.e.]	χ_{red}^2	LY [$\frac{\text{p.e.}}{\text{keV}}$]	ΔLY [$\frac{\text{p.e.}}{\text{keV}}$]
5	18.27	2.45	11.81	1.56	0.92	3.65	0.88
6	21.77	2.53	14.58	1.85	0.76	3.63	0.74
7	28.95	1.62	15.00	1.30	1.11	4.14	0.63
8	36.57	0.88	13.55	0.80	1.26	4.57	0.58
9	42.16	0.73	14.06	0.65	1.28	4.68	0.53
10	49.58	0.76	15.20	0.72	1.05	4.96	0.50
11	56.25	0.79	16.33	0.71	1.40	5.11	0.47
12	60.14	0.74	16.83	0.69	1.27	5.01	0.42
13	66.44	0.64	15.04	0.48	1.01	5.11	0.40
14	73.33	0.82	18.15	0.65	1.26	5.24	0.38
15	77.56	0.75	18.22	0.54	1.24	5.17	0.35
16	85.73	0.83	19.43	0.64	1.18	5.36	0.34
17	90.35	0.93	20.77	0.82	1.28	5.31	0.32
18	97.47	0.90	20.49	0.73	1.29	5.42	0.30
19	102.45	1.08	20.41	0.93	1.50	5.39	0.29
20	106.68	1.05	22.66	0.84	0.86	5.33	0.27
21	112.69	1.26	25.34	1.05	0.66	5.37	0.26
22	117.81	1.21	25.22	0.96	0.68	5.35	0.25
23	123.70	1.28	25.23	0.98	1.24	5.38	0.24
24	129.28	1.36	26.19	1.09	1.03	5.39	0.23
25	131.85	1.30	25.31	1.10	0.98	5.27	0.22
26	140.01	1.64	29.49	1.64	0.95	5.38	0.22
27	144.53	1.94	33.01	1.91	0.72	5.35	0.21
28	149.66	1.83	27.36	1.89	1.56	5.34	0.20
29	154.26	2.04	31.26	2.20	1.02	5.32	0.20
30	154.79	3.00	37.82	3.02	1.23	5.16	0.20
31	164.88	2.29	34.66	2.27	1.14	5.32	0.19
32	168.60	2.71	36.57	3.23	0.77	5.27	0.19
33	171.45	3.59	42.71	4.10	0.80	5.20	0.19
34	188.74	6.72	59.48	14.19	1.39	5.55	0.26
35	184.24	4.71	51.49	4.98	0.58	5.26	0.20
36	191.86	5.29	49.84	8.79	1.27	5.33	0.21
37	196.68	3.19	36.12	3.96	0.86	5.32	0.17
38	189.36	7.45	65.22	11.86	0.60	4.98	0.24
39	199.03	10.33	72.40	16.55	0.72	5.10	0.30
40	189.32	10.45	69.42	17.43	0.86	4.73	0.29
41	215.99	11.18	65.90	12.74	0.57	5.27	0.30
42	216.13	12.34	80.16	15.42	0.73	5.15	0.32
43	210.55	22.59	108.88	36.73	0.44	4.90	0.54
44	230.26	10.99	63.13	16.52	0.83	5.23	0.28
45	218.87	20.44	99.21	31.61	0.56	4.86	0.47
46	232.22	32.93	122.80	62.51	0.49	5.05	0.72
47	235.56	38.02	123.78	67.66	0.46	5.01	0.82
48	242.47	23.70	93.69	41.40	0.63	5.05	0.50
49	233.62	20.54	97.09	35.59	0.38	4.77	0.43

Table B.13: Parameters of the $cS1$ slices for the determination of the light yield for a drift field strength of 594 V/cm. The values for the mean signal μ_{cS1} and its standard deviation σ_{cS1} as well as their uncertainties are obtained by fitting the individual energy slices, as well as the reduced χ^2 . The light yield LY and its error are calculated using equation (9.15).

E_{TPC} [keV]	μ_{cS1} [p.e.]	$\Delta\mu_{cS1}$ [p.e.]	σ_{cS1} [p.e.]	$\Delta\sigma_{cS1}$ [p.e.]	χ^2_{red}	LY [$\frac{\text{p.e.}}{\text{keV}}$]	ΔLY [$\frac{\text{p.e.}}{\text{keV}}$]
7	26.59	2.50	11.84	2.00	0.95	3.80	0.65
8	36.51	1.74	12.97	1.40	0.87	4.56	0.61
9	43.09	1.43	16.08	1.64	0.86	4.79	0.56
10	49.00	1.53	17.35	1.27	1.10	4.90	0.51
11	55.92	1.85	19.99	1.58	1.04	5.08	0.49
12	59.55	1.24	15.73	1.18	0.93	4.96	0.43
13	69.75	1.20	16.42	1.02	1.06	5.37	0.42
14	74.15	1.38	18.03	1.09	0.86	5.30	0.39
15	79.76	1.54	20.90	1.39	0.53	5.32	0.37
16	83.09	1.34	18.24	1.38	1.34	5.19	0.34
17	90.47	1.64	23.19	1.60	0.60	5.32	0.33
18	94.90	1.64	22.55	1.34	1.10	5.27	0.31
19	100.81	1.74	23.81	1.48	0.78	5.31	0.29
20	109.18	2.00	25.34	1.91	1.09	5.46	0.29
21	111.45	1.90	22.84	1.75	0.97	5.31	0.27
22	116.51	2.07	25.64	1.96	0.94	5.30	0.26
23	121.16	2.18	26.23	1.85	0.57	5.27	0.25
24	127.31	2.93	32.11	3.86	0.94	5.30	0.25
25	133.88	3.41	35.97	3.97	1.49	5.36	0.25
26	143.00	2.82	31.15	3.20	1.01	5.50	0.24
27	140.25	2.76	31.38	2.86	0.66	5.19	0.22
28	139.94	4.21	42.03	4.82	0.58	5.00	0.23
29	150.77	3.50	35.14	4.67	0.91	5.20	0.22
30	151.30	4.61	42.04	6.70	0.98	5.04	0.23
31	160.31	3.98	34.22	4.64	0.59	5.17	0.21
32	158.53	6.68	52.55	7.89	0.83	4.95	0.26
33	165.39	8.77	61.90	14.49	0.90	5.01	0.31
34	181.66	8.88	50.13	15.54	0.88	5.34	0.30
35	192.07	19.32	86.36	30.37	0.69	5.49	0.57
36	166.60	9.47	62.08	14.50	0.49	4.63	0.29
37	173.21	10.46	64.46	15.05	0.43	4.68	0.31
38	194.97	14.50	78.86	25.73	0.67	5.13	0.40
39	178.06	14.89	75.59	24.66	0.46	4.57	0.40
40	207.19	40.68	135.55	64.99	0.33	5.18	1.03
41	185.74	24.65	92.25	33.54	0.40	4.53	0.61
42	190.83	26.10	101.92	45.58	0.22	4.54	0.63
43	179.89	115.60	161.54	179.29	0.31	4.18	2.69
44	196.11	34.34	116.32	60.18	0.30	4.46	0.79
45	219.07	37.44	105.25	57.37	0.49	4.87	0.84
46	191.22	133.68	200.00	193.86	0.38	4.16	2.91

Table B.14: Parameters of the $cS1$ slices for the determination of the light yield for a drift field strength of 792 V/cm. The values for the mean signal μ_{cS1} and its standard deviation σ_{cS1} as well as their uncertainties are obtained by fitting the individual energy slices, as well as the reduced χ^2 . The light yield LY and its error are calculated using equation (9.15).

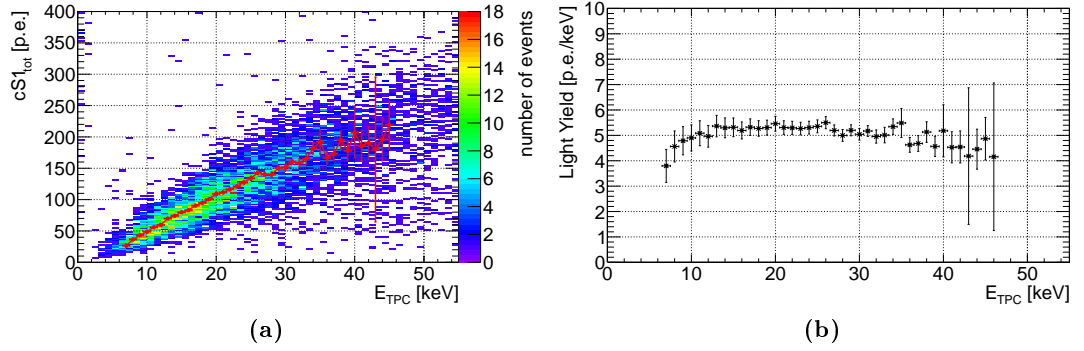


Figure B.35: Detected $cS1$ signal in dependence of the energy deposit E_{TPC} for Compton scattering with an applied drift field of 792 V/cm (a). The graph suggests a linear relation between deposited energy and generated scintillation light. The light yield shown in (b) is the mean $cS1$ signal determined with a Gaussian fit from energy slices, divided by the corresponding energy deposit E_{TPC} . For low energies, the light yield increases up to a maximum value between 10–20 keV. The light yield value remains constant or even decreases slightly for higher E_{TPC} above 30–40 keV.

E_{TPC} [keV]	μ_{cS2} [p.e.]	$\Delta\mu_{cS2}$ [p.e.]	σ_{cS2} [p.e.]	$\Delta\sigma_{cS2}$ [p.e.]	χ^2_{red}	QY [$\frac{e^-}{keV}$]	ΔQY [$\frac{e^-}{keV}$]
9	7410	303	2452	342	7.17	45.12	5.36
10	8155	235	1653	215	7.67	44.69	4.67
11	8634	364	3479	340	10.22	43.01	4.33
12	10126	581	4351	573	7.59	46.24	4.70
13	10332	454	4091	620	6.60	43.55	3.88
14	12316	325	2777	312	8.91	48.20	3.69
15	12436	320	2979	371	8.03	45.43	3.27
16	13528	342	3182	291	10.94	46.33	3.15
17	12367	569	4999	604	8.27	39.86	3.00
18	14593	373	3787	351	10.78	44.42	2.74
19	15079	637	5331	985	5.41	43.49	2.96
20	16407	1861	4678	1542	3.03	44.95	5.59
21	19197	634	4008	714	5.61	50.09	2.94
22	15940	4385	6040	2774	2.18	39.70	11.08
23	17434	2938	7212	2252	3.20	41.53	7.24
25	20658	3746	8856	5809	1.52	45.28	8.42
27	24264	1069	6581	1355	4.86	49.24	2.87
28	31158	5761	11573	6074	1.91	60.98	11.50
29	25564	2459	9749	3477	2.80	48.30	4.95

Table B.15: Parameters of the $cS2$ slices for the determination of the charge yield for a drift field strength of 396 V/cm. The values for the mean signal μ_{cS2} and its standard deviation σ_{cS2} as well as their uncertainties are obtained by fitting the individual energy slices, as well as the reduced χ^2 . The charge yield QY and its error are calculated using equation (9.19).

E_{TPC} [keV]	μ_{cS2} [p.e.]	$\Delta\mu_{cS2}$ [p.e.]	σ_{cS2} [p.e.]	$\Delta\sigma_{cS2}$ [p.e.]	χ^2_{red}	QY [$\frac{e^-}{\text{keV}}$]	ΔQY [$\frac{e^-}{\text{keV}}$]
5	4388	174	1641	155	10.56	48.09	9.81
6	5045	154	1769	120	14.75	46.07	7.82
7	5764	120	1962	98	20.06	45.12	6.53
8	6599	137	2424	102	23.87	45.20	5.74
9	7274	135	2615	110	23.75	44.28	5.00
10	8035	188	3191	179	17.85	44.03	4.54
11	9152	202	3174	170	18.69	45.59	4.28
12	9799	166	3237	158	20.52	44.74	3.82
13	10632	206	3567	195	18.25	44.81	3.58
14	11512	278	4493	389	11.55	45.06	3.42
15	12575	313	4729	455	10.40	45.93	3.29
16	13677	305	4375	365	11.99	46.84	3.14
17	14829	333	4560	463	9.85	47.80	3.04
18	15810	320	4673	467	10.00	48.13	2.88
19	17134	439	5248	682	7.70	49.41	2.92
20	18226	370	4347	384	11.31	49.93	2.73
21	18697	2299	8353	2991	2.79	48.79	6.45
22	20362	966	6270	1214	5.16	50.72	3.36
23	21691	412	4619	519	8.89	51.68	2.49
24	24310	447	4095	439	9.33	55.50	2.57
25	23157	777	7691	761	10.11	50.76	2.69
26	25502	819	7929	1058	7.50	53.75	2.73
27	25610	920	8772	1117	7.85	51.97	2.72
28	24527	943	7952	914	8.70	48.00	2.55
29	27766	4022	10195	3689	2.76	52.46	7.82
30	29694	2051	7660	2122	3.61	54.24	4.19

Table B.16: Parameters of the $cS2$ slices for the determination of the charge yield for a drift field strength of 594 V/cm. The values for the mean signal μ_{cS2} and its standard deviation σ_{cS2} as well as their uncertainties are obtained by fitting the individual energy slices, as well as the reduced χ^2 . The charge yield QY and its error are calculated using equation (9.19).

E_{TPC} [keV]	μ_{cS2} [p.e.]	$\Delta\mu_{cS2}$ [p.e.]	σ_{cS2} [p.e.]	$\Delta\sigma_{cS2}$ [p.e.]	χ^2_{red}	QY [$\frac{e^-}{\text{keV}}$]	ΔQY [$\frac{e^-}{\text{keV}}$]
8	6703	285	2417	260	9.29	45.91	6.08
9	7855	188	2449	143	17.18	47.82	5.45
10	8685	218	2887	168	17.13	47.59	4.92
11	9095	201	2705	188	14.41	45.30	4.26
12	10044	360	3714	307	12.10	45.86	4.18
13	11196	344	3874	277	14.00	47.19	3.93
14	12641	277	3642	223	16.30	49.48	3.72
15	13304	411	4695	389	12.05	48.60	3.60
16	13604	375	4137	314	13.18	46.59	3.21
17	16074	384	4812	394	12.23	51.81	3.32
18	18013	325	4144	310	13.37	54.83	3.24
19	16820	831	7011	982	7.14	48.51	3.53
20	17794	1106	6632	972	6.82	48.75	3.91
21	17265	1093	7218	1443	5.00	45.05	3.59
22	17135	4767	10264	3778	2.72	42.68	12.04
23	19464	1237	7947	2065	3.85	46.37	3.59
24	24439	1142	8387	1262	6.65	55.80	3.53
25	25366	1077	8514	1033	8.24	55.60	3.28
26	22491	2323	11642	3100	3.76	47.40	5.24
27	25095	1652	10327	2072	4.98	50.93	3.87
28	29308	1168	9055	1364	6.64	57.35	3.11
29	31387	7671	24579	26519	0.93	59.31	14.65
30	26788	3774	14486	6261	2.31	48.93	7.10

Table B.17: Parameters of the $cS2$ slices for the determination of the charge yield for a drift field strength of 792 V/cm. The values for the mean signal μ_{cS2} and its standard deviation σ_{cS2} as well as their uncertainties are obtained by fitting the individual energy slices, as well as the reduced χ^2 . The charge yield QY and its error are calculated using equation (9.19).

E_{TPC} [keV]	μ_{S2} [p.e.]	$\Delta\mu_{S2}$ [p.e.]	σ_{S2} [p.e.]	$\Delta\sigma_{S2}$ [p.e.]	χ_{red}^2	QY [$\frac{e^-}{\text{keV}}$]	ΔQY [$\frac{e^-}{\text{keV}}$]
6	4217	152	1421	110	12.90	38.51	6.57
7	5022	106	1517	104	14.55	39.31	5.69
8	5402	122	1723	127	13.61	37.00	4.71
9	5916	121	1828	99	18.47	36.02	4.08
10	6349	137	1943	115	16.86	34.79	3.57
11	7414	94	1651	65	25.39	36.93	3.41
12	7748	147	2417	123	19.67	35.38	3.04
13	8161	139	2374	119	19.92	34.40	2.73
14	8951	153	2450	127	19.26	35.03	2.59
15	9877	148	2511	114	21.95	36.08	2.49
16	10206	164	2858	144	19.89	34.95	2.28
17	10906	170	3055	171	17.82	35.15	2.16
18	11186	191	3277	217	15.08	34.05	2.00
19	11709	200	3222	183	17.62	33.77	1.89
20	12374	227	3497	373	9.37	33.90	1.83
21	13068	225	3402	210	16.21	34.10	1.75
22	14297	216	3250	199	16.31	35.61	1.73
23	13876	442	4973	678	7.33	33.06	1.80
24	15254	289	3959	359	11.03	34.83	1.62
25	15384	505	4305	725	5.94	33.72	1.77
26	16212	593	4886	592	8.25	34.17	1.84
27	16015	410	4806	473	10.15	32.50	1.49
28	18310	554	4457	485	9.19	35.83	1.71
29	17528	638	5495	1039	5.29	33.12	1.69
30	19133	388	4032	442	9.11	34.95	1.40

Table B.18: Parameters of the $S2$ slices for the determination of the charge yield for a drift field strength of 198 V/cm. The values for the mean signal μ_{S2} and its standard deviation σ_{S2} as well as their uncertainties are obtained by fitting the individual energy slices, as well as the reduced χ^2 . The charge yield QY and its error are calculated using equation (9.19).

Data sheets

Appendix C

HAMAMATSU

PHOTOMULTIPLIER TUBE

PRELIMINARY DATA SHEET

Aug.2011

R6041-406

**For Low Temperature Operation especialy for Liq.Xe application,
Bialkali Photocathode Low profile
57mm(2Inch)Diameter,12stage,Head-on Type, Synthetic Silica**

General

Parameter		Description	Unit
Spectral response range		160 to 650	nm
Window material		Synthetic silica glass	-
Photocathode	Material	Bialkali	-
	Minimum Effective Area	45	mm dia
Dynode structure		Metal channel Dynode	-
Number of stages		12	-
Weight		Approx 110	g
Operating Ambient Temperature		-110 to +50	deg C
Storage Temperature		-110 to +50	deg C

Maximum Ratings (Absolute Maximum Values)

Parameter	Value	Unit
Supply voltage Between Anode and Cathode	1000	V dc
Average anode current	0.1	mA

Characteristics at 25 deg C

Parameter		Min.	Typ.	Max.	Unit
Cathode Sensitivity	Luminous (2856K)	-	100	-	uA/lm
	QE at 175 nm	20	30	-	%
Anode Sensitivity	Luminous (2856K)	-	100	-	A/lm
Gain (Current Amplification)		-	1x10 ⁶	-	-
Anode Dark Current (after 30min. storage in darkness)		-	5	50	nA
Time Response	Anode Pulse Rise Time	-	2.3	-	ns
	Electron Transit time	-	16	-	ns
	Transit Time Spread	-	0.75	-	ns
Pulse Linearity at ±2 % Deviation		-	40	-	mA

NOTE: Anode characteristics are measured with a voltage distribution ratio shown below

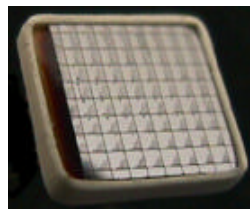
Voltage Distribution Ratio and Supply Voltage

K	Dy1	Dy2	Dy3	Dy4	Dy5	Dy6	Dy7	Dy8	Dy9	Dy10	Dy11	Dy12	P
2	2	2	1	1	1	1	1	1	1	1	1	1	1.2

Supply Voltage : 800 V K : Cathode Dy : Dynode P : Anode

Figure C.1: Hamamatsu Photomultiplier tube R6041-406 data sheet [94].

Silicon Avalanche Photodiode

64 mm² active area of **S0814**Array with 64 pixels. **A6403**

Features

- Gain above 1,000 at operating condition of best signal-to-noise ratio. (Maximum gain of 10,000.)
- Large active area
- High quantum efficiency (QE) extends beyond visible spectrum
- High speed at 1064 nanometer wavelength of YAG lasers
- Pulse counting mode is the most-frequent style of use.
- Optical Photon Counting (2-3 photons) when cooled

Devices

Type No.	Description
S0223	2 mm x 2 mm active area detector
S0814	8 mm x 8 mm active area detector
S1315	13 mm x 13 mm active area detector
A1604	Array of 16 detector pixels. Pixels are in a 4 x 4 pattern. Each pixel: 2 mm x 2 mm area, 2.48 mm pitch
A6403	Array of 64 detector pixels. Pixels are in an 8 x 8 pattern. Each pixel: 1 mm x 1 mm area, 1.27 mm pitch.

Specifications

Parameter	Typical Value at 22°C
gain (at optimal signal-to-noise ratio)	300 to 2000
capacitance	0.7 pf/mm ²
bias voltage (device is typically operated at optimal signal to noise ratio)	1650 to 1750 volts
QE at 400 nm	50 %
QE at 532 nm	65 %
QE at 830 to 905 nm	75 %
QE at 1064 nm	20 %

Type No.	S0223	S0814	S1315	A1604	A6403
nominal Active Area (if array, of pixel) mm ²	4	64	169	4	1
Rise Time for a charged particle, ns	≤ 1	≤ 1	≤ 1	≤ 1	≤ 1
Rise Time at 532 nm, ns	5	8	10	5	5
Rise Time at 1064 nm, ns	< 2	< 2	< 2	< 2	< 2
Noise Equivalent Power, rms f W/(Hz) ^{1/2}	19	42	85	19	10
Noise, FWHM eV	200	450	900	200	100

Applications

- LIDAR, LADAR
- Medical Imaging. PET sensor provides both timing and energy information.
- High Energy Physics. Read-out of optical fibers
- Bio Sensors
- Telecommunications

RMD, Inc.
 44 Hunt Street Watertown, MA 02472 USA
 e-mail pwaer@rmdinc.com
 telephone 617 668 6907 facsimile 617 926 9743
 copyright © RMD, Inc. June 2003 document: siapd009

Figure C.2: RMD Avalanche Photodiode S1315 data sheet [108].

QUALITY ASSURANCE DATA SHEET

GEM Series HPGe (High-Purity Germanium) Coaxial Detector System

Model and Serial Numbers

Detector Model No. GEM-F5930-S
 Cryostat Configuration CFG-SH-70 Ship Date 25-Mar-13
 Dewar Model DWR-30 Serial No. 53-P42580A
 Preamplifier Model A257P When calling Customer Service, always
 reference the Detector Serial No.
 Preamplifier Serial No. 13011099 Sales Order No. 15012583
 H. V. Filter Model 138EMI
 H. V. Filter Serial No. 13063368
 SMART-1-P Serial No. _____

Cryogenic Information

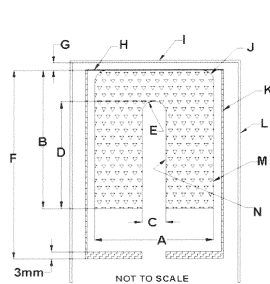
Dewar Capacity 30 liters Static Holding Time 14 days
 Detector Cool-Down Time 8 hours

High Voltage Bias

Recommended Operating Bias POSITIVE 1500 Volts

Performance Specifications*

	Warranted	Measured	Amp Shape Time
Resolution (FWHM) at 1.33 MeV, ⁶⁰ Co	<u>1.8 keV</u>	<u>1.7 keV</u>	<u>6</u> μ s
Peak-to-Compton Ratio, ⁶⁰ Co	<u>50:1</u>	<u>61:1</u>	<u>6</u> μ s
Relative Efficiency at 1.33 MeV, ⁶⁰ Co	<u>Nom 24 %</u>	<u>27 %</u>	<u>6</u> μ s
Peak Shape (FWTM/FWHM), ⁶⁰ Co	<u>1.90</u>	<u>1.87</u>	<u>6</u> μ s
*Peak Shape (FWFM/FWHM), ⁶⁰ Co	<u>2.65</u>	<u>2.61</u>	<u>6</u> μ s
* FWFM/FWHM is typical not warranted			
Resolution (FWHM) at 122 KeV, ⁵⁷ Co	<u>725 eV</u>	<u>626 eV</u>	<u>6</u> μ s



E: NOMINAL 5-mm RADIUS

F: 94-mm CUP LENGTH

G: 3-mm SPACE

H: 0.03-mm/0.03-mm Al/Mylar

I: 1-mm Al

J: NOMINAL 8-mm RADIUS

K: 0.8-mm Al

L: 1-mm Al

M: 0.7-mm Ge/Li DEAD LAYER

N: 0.3-micron Ge/B DEAD LAYER

A= 58.8 mm
Crystal Diameter

B= 42.2 mm
Crystal Length

C= 9.2 mm
Hole Diameter

D= 21.8 mm
Hole Depth

OTHER Cryo: SH # 15818

Data Certified By: Thomas Jennings

Form no. 0308BK vers. 1

DATE 3-25-13

Figure C.3: Ortec GEM-F5930-S HPGe detector data sheet [90].

List of Tables

2.1	Xenon isotopes, natural abundance and half-life decay times.	24
2.2	Atomic binding energies for electrons in ^{54}Xe	29
3.1	Electric drift field voltages applied in the measurements at the HZDR. . .	47
3.2	Nominal scatter angles for the Compton measurements conducted at the HZDR in April 2016 and actual measured intervals for the energy deposit.	63
4.1	Typical signal ratios $\frac{S_2}{S_1}$ with respect to the integral and amplitude of the signals.	74
4.2	Control register for the logic board configuration.	88
4.3	Input and output assignments for the CAEN V1495 logic board.	89
4.4	Input signal assignment to the SIS3820 VME scaler.	114
5.1	Germanium calibration: Fit values for gamma-ray peaks in calibration source spectra.	128
5.2	Calculated residuals showing the relative deviation of the germanium calibration function from the measured data for each data point.	129
5.3	Germanium detector energy resolution measured as the gamma-ray peak standard deviation and FWHM.	131
5.4	APD calibration: Parameters of the exponential fits to the raw data points in the respective LED voltage ranges.	135

5.5	Fit parameters for the APD gain curve for each APD at its bias voltage during operation.	138
6.1	APD gain values from calibration.	142
7.1	Calibration slopes for the July 2015 data: Mean values for R_{\min} and R_{\max} of each levelmeter and calculated calibration slope.	154
7.2	Calibration slopes for the July 2017 data: Mean values for R_{\min} and R_{\max} of each levelmeter and calculated calibration slope.	156
7.3	Effect of capillary: Measured mean capacitances and calculated change in level height.	158
7.4	Calculated calibration factors in pF/mm for a reference capacitance of $C_{\text{ref}} = 10$ pF.	159
7.5	Determined liquid level for the measurements at HZDR in April 2016 (with calibration values from 2015).	162
7.6	Determined liquid level for the measurements at Mainz in July 2017 (with calibration values from 2017).	163
7.7	Fit parameters from the least-squared plane fit to the levelmeter heights of the HZDR April 2016 measurement.	165
7.8	Comparison of the measured heights of the run at the HZDR in April 2016 (with the calibration from 2015) with the values calculated using the plane fit.	166
7.9	Fit parameters from the least-squared plane fit to the levelmeter heights of the July 2017 measurement in Mainz.	167
7.10	Comparison of the measured heights of the run Mainz in July 2016 (with the calibration from 2017) with the values calculated using the plane fit.	168
7.11	Extraction field in liquid and gaseous phase in dependence of the liquid level and respective extraction efficiencies for the data sets from the HZDR in 2016 and Mainz in 2017.	170
8.1	Maximum drift times and corresponding drift velocities for different drift field strengths.	176
8.2	$S1$ and $cS1$ integral values for the narrow peak structure in the ^{152}Eu spectrum, fitted with a Gaussian for different drift field strengths.	181

8.3	Correlation between scintillation light from the TPC calibration with ^{152}Eu and energy deposit for the corresponding scintillation signal in Compton measurements.	182
8.4	Parameters for the $S1$ z -correction function	184
8.5	$S2$ and $cS2$ integral values for the peak structure in the ^{152}Eu spectrum at 198 V/cm used to measure the electron lifetime, fitted with a Gaussian. 190	
9.1	List of TPC calibration measurements with the respective number of events acquired.	199
9.2	Gamma-ray energies and event rates in the MainzTPC from the calibration measurements with different gamma-ray sources at different drift field strengths.	200
9.3	List of Compton measurement configurations with respect to nominal scattering angles and to the applied drift field strengths.	201
9.4	Parameters for the fiducial volume.	203
9.5	Fit values for the unknown energy peaks in the germanium spectrum for the Compton measurement at 198 V/cm.	206
9.6	Number of good events for different Compton measurement configurations with respect to the applied drift field strengths.	206
9.7	Accepted events for different event selection configurations.	209
9.8	Fit results for the minimum vertical distance d_z between two interactions in the MainzTPC for different drift field strengths.	213
9.9	Results for the Gaussian fits of the $S2$ FWHM width and low width distributions.	215
9.10	Determination of the scintillation response for the 661.6 keV gamma-ray line of ^{137}Cs at different drift field strengths.	225
9.11	Gaussian fit parameters of the noise peak in the $S1$ integrals obtained for the trigger efficiency measurements.	231
9.12	Fit parameters of the trigger efficiency for five different sensor(trigger) settings, determined using a Fermi-Dirac distribution at two different drift field strengths.	235
9.13	Parameters of the $cS1$ slices for the determination of the light yield for a drift field strength of 198 V/cm.	239

9.14	Light yield values of $cS1$ from Compton measurements with different drift field strengths for different energy ranges in E_{TPC}	245
9.15	Fit parameters for the exponential fit of the field quenching.	246
9.16	Estimated maximum and zero-field light yield values.	248
9.17	Statistics and ratio of the upper and lower population for the drift field strengths 198 V/cm and 396 V/cm with different applied event selections.	253
9.18	Parameters of the $cS2$ slices for the determination of the charge yield for a drift field strength of 198 V/cm.	257
B.1	Gaussian fit values for the gamma-ray source photon peaks of ^{137}Cs , ^{22}Na and ^{133}Ba	278
B.2	Lorentzian fit values for the gamma-ray source photon peaks of ^{137}Cs , ^{22}Na and ^{133}Ba	278
B.3	APD calibration fit parameters from Gaussian fits of the APD height distributions of APD 8.	281
B.4	Gain curve fit parameters and errors for each APD at its bias voltage during operation.	281
B.5	APD calibration fit parameters from Gaussian fits of the APD height distributions of APD 1 and 2.	282
B.6	APD calibration fit parameters from Gaussian fits of the APD height distributions of APD 3 and 4.	283
B.7	APD calibration fit parameters from Gaussian fits of the APD height distributions of APD 5 and 6.	284
B.8	APD calibration fit parameters from Gaussian fits of the APD height distributions of APD 7.	285
B.9	Fit results from the Gaussian fits in the z-slices of the $S1$ spectrum of ^{152}Eu for different drift field strengths.	295
B.10	Double Gaussian fit results for the $S2$ peak positions for different interaction depths.	296
B.11	Additional double Gaussian fit parameters for the $S2$ peak positions for different interaction depths.	297
B.12	Parameters of the $cS1$ slices for the determination of the light yield for a drift field strength of 396 V/cm.	310

B.13 Parameters of the <i>cS1</i> slices for the determination of the light yield for a drift field strength of 594 V/cm.	311
B.14 Parameters of the <i>cS1</i> slices for the determination of the light yield for a drift field strength of 792 V/cm.	312
B.15 Parameters of the <i>cS2</i> slices for the determination of the charge yield for a drift field strength of 396 V/cm.	313
B.16 Parameters of the <i>cS2</i> slices for the determination of the charge yield for a drift field strength of 594 V/cm.	314
B.17 Parameters of the <i>cS2</i> slices for the determination of the charge yield for a drift field strength of 792 V/cm.	315
B.18 Parameters of the <i>S2</i> slices for the determination of the charge yield for a drift field strength of 198 V/cm.	316

List of Figures

1.1	Rotation curve - star velocities in a spiral galaxy depending on their distance to the galactic center.	8
1.2	Cluster dynamics - “Bullet Cluster”.	10
1.3	Cosmic Microwave Background – Left: Sky map of temperature differences. Right: Power spectrum in dependence of the multipole moment. . .	11
1.4	Left: WIMP miracle. Right: Dark Matter detection modes.	13
1.5	Overview on different experiments for direct Dark Matter detection. . .	15
1.6	TPC principle.	17
1.7	Particle discrimination using the ratio $S2/S1$: Sketch of ER and NR signals and XENON1T data of ER and NR.	19
1.8	Electric field between gate and anode mesh: Sketch of the region between the meshes and plot of the relative electric field strength in liquid and gaseous phase.	20
1.9	Exclusion curves: Experimental sensitivity to spin-independent WIMP-nucleon interaction for different Dark Matter experiments.	21
2.1	Left: Liquid xenon density in dependence of the xenon temperature. Right: Expected WIMP rates in different mediums.	25
2.2	Cross-sections for different photon interactions with xenon: Photoabsorption, Compton scattering and pair production.	26
2.3	Particle scattering with xenon, sketch for derivation of the Compton and neutron scattering formula.	27

2.4	Scheme of the scintillation and ionization processes in LXe after an energy deposit by a scattering particle.	32
2.5	Example plot for the energy calibration of a dual-phase xenon TPC and sketch of the combination of scintillation and charge signal.	34
2.6	<i>S1</i> pulse shape: Measured photon signal of the deexcitation of liquid xenon. Plots taken from [77] and [78].	35
2.7	Comparison with literature: Light yield from simulations with NEST and measurements with neriX.	36
2.8	Comparison with literature: Charge yield from simulations with NEST and measurements with neriX.	37
3.1	The MainzTPC detector – Left: Photograph of the TPC during assembly in the clean room. Right: CAD view.	44
3.2	The MainzTPC - rendered cut view of a CAD model.	45
3.3	Meshes for the generation of the electric field in the MainzTPC.	48
3.4	Electric field cage.	49
3.5	MainzTPC levelmeters: Photograph and CAD cut view.	49
3.6	MainzTPC in the xenon cryostat – Left: Photograph of cryostat with buffer volume. Middle: CAD drawing illustrating the TPC position inside the cryostat. Right: CAD drawing highlighting the levelling weir.	52
3.7	Cooling system – Left: Funnel-shaped vessel containing the PTR cold finger. Right: Cooling system in cryostat, connected to the MainzTPC.	54
3.8	Sketch of the cryocooling system.	55
3.9	Gas system.	56
3.10	Light sensors in the MainzTPC – Left: Hamamatsu R6041 PMT. Right: RMD S1315 APD	59
3.11	The MainzTPC setup for both Compton and neutron scattering at the HZDR.	61
3.12	Sketch of the nominal angle in the Compton scattering setup.	63
3.13	Distributions of the energy deposit in the TPC for the Compton scattering, measured with the germanium detector.	64

4.1	<i>S1</i> and <i>S2</i> signals measured on the Top PMT during a Compton measurement.	73
4.2	Comparison of the <i>S1</i> signal recorded on the SIS3316 and SIS3305 FADC board.	74
4.3	Measured APD and germanium signals as examples for “step”-like signal shapes.	75
4.4	VME crate with DAQ and HV boards.	76
4.5	Baselines on SIS3316 and SIS3305, exemplarily for a measurement with a PMT.	77
4.6	Constant Fraction Discriminator – Left: Front panel photograph. Right: Sketch of the CFD principle.	78
4.7	DAQ version 1: Connections between the electronic modules.	83
4.8	DAQ version 2: Connections between the electronic modules.	85
4.9	Logic scheme for the trigger generation with CAEN V1495	86
4.10	Occurrence time of <i>S1</i> signal and germanium signal from Compton scattering measurements.	90
4.11	Compton event trigger generation with DAQ version 2 - oscilloscope measurement.	91
4.12	Neutron event trigger generation with DAQ version 2 - oscilloscope measurement.	93
4.13	Trigger logic for DAQ version 2 including gated logic signals.	94
4.14	Measured time difference between external trigger signal and start of data sampling on the SIS3305 board, using the internal TDC feature.	99
4.15	Correction of the peak position of a test pulse measured with the SIS3305.100	
4.16	MainzTPC DAQ version 1 acquisition scheme: Overview of the acquisition cycles.	105
4.17	MainzTPC DAQ version 2 acquisition scheme: Refined program structure involving the DAQ Trigger generation with the CAEN V1495.	107
4.18	Illustration of the data acquisition and readout procedure for the HF and the non-HF mode.	109

4.19	Measurement of test events with the SIS3316 for different event rates with non-HF mode and HF mode – Left: Total measurement time. Right: Measured live-times.	110
4.20	Three-level file hierarchy of the MainzTPC data format.	111
4.21	Overview of all headers for the MainzTPC data format.	113
5.1	SPE spectra of Top and Bottom PMT for different bias voltages.	123
5.2	Germanium calibration spectra of ^{137}Cs , ^{22}Na and ^{133}Ba	127
5.3	Germanium calibration: Linear fit of the photon peak voltage values from the gamma-ray source spectra.	128
5.4	^{137}Cs spectra plotted versus energy to measure the germanium energy resolution.	129
5.5	^{22}Na spectra plotted versus energy to measure the germanium energy resolution.	130
5.6	^{133}Ba spectra plotted versus energy to measure the germanium energy resolution.	130
5.7	FWHM for the germanium detector plotted in dependence of the measured energy and energy resolution fit.	132
5.8	APD calibration signals for a bias voltage of 1000 V. (Screenshot of the DataViewer program.)	134
5.9	APD signal height distributions for APD 4 at a bias voltage of 1000 V, obtained with the raw data processing routines StepFitter and StepFinder.	135
5.10	APD calibration signal amplitudes for different LED pulse voltages in dependency of the APD bias voltage (APD 1).	136
5.11	APD gain curve for APD 1.	137
6.1	Illustration of the centroid method: $S2$ light distribution and distorted position reconstruction in the x - y -plane	141
6.2	Sketch of the positioning of the ^{152}Eu source around the MainzTPC to measure the impact onto the $S2$ position reconstruction. The relative APD positions in the plots are illustrated.	143
6.3	Position reconstruction in x - y with the APD gains from the APD calibration, for a ^{152}Eu source placed at three positions.	144

6.4	Distributions of the y -position determined with the signals from APD 1 and 5 for two different source positions.	146
6.5	Event distribution and $S1$ spectrum of a ^{152}Eu measurement at a drift field of 198 V/cm, complete event set and applied fiducialization.	147
7.1	Relative levelmeter capacitance plotted versus the time of the measurement (calibration data from July 2015).	153
7.2	Levelmeter calibration 2015: Zoom to measurement periods for levelmeters in empty and completely filled state.	154
7.3	Relative levelmeter capacitance plotted versus the time of the measurement (calibration data from July 2017).	155
7.4	Levelmeter calibration 2017: Zoom to measurement periods for levelmeters in empty and completely filled state.	156
7.5	Effect of the capillary action in the levelmeters.	157
7.6	Relative position of the levelmeters with respect to the gate and anode mesh.	160
7.7	Levelmeter measurement of the run in April 2016.	161
7.8	Level determination April 2016: Levelmeter values for empty state and at operation conditions.	162
7.9	Level determination July 2017: Plot of the levelmeter values at operation conditions.	163
7.10	Fit plane function for the liquid level in the MainzTPC during the measurements at the HZDR in April 2016.	166
7.11	Fit plane function for the liquid level in the MainzTPC during the measurements in Mainz in July 2017.	168
7.12	Electric extraction field strengths in liquid and gaseous phase for April 2016 at the HZDR.	169
7.13	Electric extraction field strengths in liquid and gaseous phase for July 2017 in Mainz.	170
7.14	Mean $S2$ width distribution in x - y for a Compton measurement at 198 V/cm drift field, verifying the determined level tilt of the MainzTPC.	171
7.15	Mean $S2$ width distribution in x - y for a Compton measurement at 198 V/cm drift field. For a constant extraction field, the change of the drift field strength does not affect the $S2$ width distribution.	172

8.1	Electron drift time spectra for a drift field strength of 198 V/cm: Measured drift time spectrum and filtered spectrum.	174
8.2	Determination of the gate time.	175
8.3	Measured drift velocity in dependence of the electric drift field strength and comparable data from previous measurements.	177
8.4	Illustration of the $S1$ signal variation with the interaction depth z	179
8.5	Measured $S1$ spectrum for an ^{152}Eu source with a drift field of 198 V/cm. The peak used for the $S1$ z -correction is identified and fitted using a Gaussian.	180
8.6	Contributions of the event distributions inside and outside a radial fiducial volume of 15 mm to the complete $S1$ spectrum of ^{152}Eu at a drift field of 198 V/cm.	183
8.7	Example for a z -slice with Gaussian fit for the $S1$ z -correction.	183
8.8	$S1$ integral fit values at the peak position in dependence of the interaction depth z for the $S1$ spectrum of ^{152}Eu at a drift field strength of (a) 198 V/cm, (b) 594 V/cm and (c) 792 V/cm.	185
8.9	Combined function for the $S1$ z -correction factor in dependence of the interaction depth z	186
8.10	Illustration of the electron absorption by impurities in LXe.	187
8.11	$S2$ signal spectrum for a ^{152}Eu source at a drift field strength of 198 V/cm.	188
8.12	Example for a z -slice with a double Gaussian fit for the $S2$ z -correction.	189
8.13	Comparison of $S2$ and $cS2$ signal distribution.	190
8.14	$S2$ z -correction fits: $S2$ signal peak mean values in dependence of the drift time and of the interaction depth.	191
8.15	Impact of buffer capacitances to the dynode chain potentials.	193
8.16	PMT saturation: $S2$ signal integral in dependence of the amplitude for a ^{137}Cs source measured with Top PMT and Bottom PMT.	194
8.17	PMT saturation: Correlations of the $S2$ low width with the signal amplitude and integral.	195
9.1	Comparison of the event distribution with respect to the interaction depth z in the TPC for uncollimated and collimated gamma-ray sources.	202

9.2	Timing position of the $S1$ signal in the waveform for the Compton and calibration measurement.	203
9.3	$S1$ signals in dependence of the energy deposit E_{TPC} for a Compton measurement at 198 V/cm.	205
9.4	$S1$ in dependence of E_{TPC} from Compton measurements at different drift field strengths.	207
9.5	$S1$ asymmetry for a calibration and a Compton measurement at 198 V/cm.	208
9.6	Comparison of different event selection configurations considering exemplarily the $S1$ signal in dependence of the energy deposit E_{TPC}	210
9.7	Comparison of the largest $S2$ and the second largest $S2$ signal in Compton data for the Bottom PMT.	211
9.8	Difference z_{diff} between the interaction depths of the largest and second largest $S2$ signals in Compton events for a drift field of 198 V/cm.	212
9.9	$S2$ width in dependence of the interaction depth z	214
9.10	$S2$ width for the Compton data at a drift field of 198 V/cm (FWHM and low width).	215
9.11	Event distributions in $cS2$ versus $cS1$ for the ^{133}Ba calibration measurements at different drift field strengths.	219
9.12	Event distributions in $cS2$ versus $cS1$ for the ^{152}Eu calibration measurements at different drift field strengths.	221
9.13	Event distribution (zoom) in $cS2$ versus $cS1$ for the ^{152}Eu calibration measurement at a drift field strength of 198 V/cm.	222
9.14	Event rates in dependence of the $cS1$ signal for calibration measurements with different gamma-ray sources at a drift field strength of 198 V/cm.	223
9.15	Event distribution in $cS2$ versus $cS1$ for the ^{137}Cs calibration measurement at a drift field of 198 V/cm.	224
9.16	Event distributions in $S2$ from the summed APD amplitudes versus $cS1$ for ^{133}Ba and ^{152}Eu at 198 V/cm.	226
9.17	Sketches of the influence of the trigger efficiency on a signal distribution in $S1$ (a) and trigger efficiency setup (b)	229
9.18	Spectra of the signal obtained with the Fixed Window Integral Method for the individual TPC PMTs at a drift field strength of 198 V/cm.	230

9.19	Trigger efficiency for the individual TPC PMTs at 198 V/cm.	232
9.20	Trigger Efficiency: $S1$ integral spectra and efficiency plot for the TPC PMT coincidence at 198 V/cm.	233
9.21	Comparison of the trigger efficiencies determined for the Top PMT, Bottom PMT and summed signal for single and coincidence trigger mode at 198 V/cm.	234
9.22	Detected $cS1$ signal in dependence of the energy deposit E_{TPC} for Compton scattering with an applied drift field of 198 V/cm.	237
9.23	Examples of the $cS1$ signal distribution for nearly monoenergetic ranges in deposited energy.	238
9.24	Energy resolution in the MainzTPC in dependence of the energy deposit for the different drift field strengths.	240
9.25	Energy resolution (weighted mean) in the MainzTPC in dependence of the energy.	241
9.26	Light yield for a Compton scattering measurement with an applied drift field of 198 V/cm.	242
9.27	Light yield LY_{cS1} in dependence of E_{TPC} for different drift field strengths.	243
9.28	Light yield LY_{cS1} in dependence of E_{TPC} for different drift field strengths with all applied cuts.	245
9.29	Field quenching: Change of the light yield LY_{cS1} in dependence of the drift field strength and the energy deposit E_{TPC}	246
9.30	Relative light yields in dependence of the drift field strength.	247
9.31	Field quenching with estimated zero-field value in dependence of the drift field strength.	248
9.32	Comparison of the scintillation signals with and without z -correction for the Compton data acquired at a drift field strength of 594 V/cm.	249
9.33	Event distribution in z for the Compton measurements and corresponding $S1$ z -correction factors for all drift fields.	250
9.34	Event distributions of $cS2$ in dependence of E_{TPC} for different applied drift field strengths, exhibiting two event populations.	251
9.35	Event distributions of $cS2$ in dependence of E_{TPC} at 198 V/cm, with different applied event selection sets.	252

9.36	Spectra of various quantities for the two event populations from the Compton data at a drift field of 198 V/cm.	254
9.37	Detected $cS2$ signal in dependence of the energy deposit E_{TPC} for Compton scattering with an applied drift field of 198 V/cm.	256
9.38	Examples of the $cS2$ signal distribution for nearly monoenergetic ranges in deposited energy.	256
9.39	Charge yield QY_{cS2} in dependence of E_{TPC} for different drift field strengths.	258
9.40	Event distribution for the corrected and uncorrected $S2$ in dependence of E_{TPC} for a drift field strength of 198 V/cm.	260
9.41	Event distribution in $S2$ vs $S1$ and $cS2$ vs $cS1$ for the Compton measurements at a drift field of 198 V/cm.	262
9.42	Combined MainzTPC signal for Compton measurements with a drift field of 198 V/cm, for events in three different intervals for the energy deposit E_{TPC}	264
A.1	Sketch of the gate-anode-mesh region for the derivation of the extraction field strength in the liquid and gaseous phase.	272
A.2	Fit of the LXe surface tension in dependence of the temperature, data from literature.	274
A.3	Schematic of the TPC PMT base circuit board.	276
B.1	Germanium detector calibration spectrum from ^{137}Cs with Gaussian and Lorentzian fit functions.	278
B.2	Germanium detector calibration spectrum from ^{22}Na with Gaussian and Lorentzian fit functions.	279
B.3	Germanium detector calibration spectrum from ^{133}Ba with Gaussian and Lorentzian fit functions.	279
B.4	Additional ^{133}Ba peak fits for the the germanium energy resolution.	280
B.5	APD calibration signal amplitudes for different LED pulse voltages in dependency of the APD bias voltage (APD 2).	286
B.6	APD calibration signal amplitudes for different LED pulse voltages in dependency of the APD bias voltage (APD 3).	287
B.7	APD calibration signal amplitudes for different LED pulse voltages in dependency of the APD bias voltage (APD 4).	288

B.8	APD calibration signal amplitudes for different LED pulse voltages in dependency of the APD bias voltage (APD 5).	289
B.9	APD calibration signal amplitudes for different LED pulse voltages in dependency of the APD bias voltage (APD 6).	290
B.10	APD calibration signal amplitudes for different LED pulse voltages in dependency of the APD bias voltage (APD 7).	291
B.11	Electron drift time spectra for a drift field strength of 396 V/cm: Measured drift time spectrum and filtered spectrum.	292
B.12	Electron drift time spectra for a drift field strength of 594 V/cm: Measured drift time spectrum and filtered spectrum.	292
B.13	Electron drift time spectra for a drift field strength of 792 V/cm: Measured drift time spectrum and filtered spectrum.	293
B.14	Measured spectrum for an ^{152}Eu source with a drift field of 594 V/cm and Gaussian fit of the peak used for the $S1$ z -correction	294
B.15	Measured spectrum for an ^{152}Eu source with a drift field of 792 V/cm and Gaussian fit of the peak used for the $S1$ z -correction	294
B.16	z -slices 1-4 with a double Gaussian fit for the $S2$ z -correction.	297
B.17	z -slices 5-10 with a double Gaussian fit for the $S2$ z -correction.	298
B.18	z -slices 11-16 with a double Gaussian fit for the $S2$ z -correction.	299
B.19	z -slices 17, 19 & 20 with a double Gaussian fit for the $S2$ z -correction.	300
B.20	$S1$ asymmetry for a calibration and a Compton measurement at 396 V/cm, 594 V/cm and 792 V/cm.	301
B.21	$S2$ width for the Compton data at drift fields of 396 V/cm, 594 V/cm and 792 V/cm (FWHM and low width).	302
B.22	Event rate in dependence of $cS1$ for ^{137}Cs at 198 V/cm, with Gaussian fit of the 661.6 keV gamma-ray line.	303
B.23	Event rate in dependence of $S1$ for ^{137}Cs at 594 V/cm, with Gaussian fit of the 661.6 keV gamma-ray line.	303
B.24	Event distributions in $S2$ from the summed APD amplitudes versus $cS1$ for ^{133}Ba and ^{152}Eu at 594 V/cm and 792 V/cm.	304
B.25	Trigger Efficiency: $S1$ integral spectra and efficiency plot for the Top PMT in coincidence mode at 198 V/cm.	305

B.26 Trigger Efficiency: $S1$ integral spectra and efficiency plot for the Bottom PMT in coincidence mode at 198 V/cm.	305
B.27 Trigger Efficiency: $S1$ integral spectra and efficiency plot for the $\bar{A}\%$ PMT at 594 V/cm.	306
B.28 Trigger Efficiency: $S1$ integral spectra and efficiency plot for the Bottom PMT at 594 V/cm.	306
B.29 Trigger Efficiency: $S1$ integral spectra and efficiency plot for the Top PMT in coincidence mode at 594 V/cm.	307
B.30 Trigger Efficiency: $S1$ integral spectra and efficiency plot for the Bottom PMT in coincidence mode at 594 V/cm.	307
B.31 Trigger Efficiency: $S1$ integral spectra and efficiency plot for the TPC PMT coincidence at 594 V/cm.	308
B.32 Comparison of the trigger efficiencies determined for the Top PMT, Bottom PMT and summed signal for single and coincidence trigger mode at 594 V/cm.	308
B.33 Detected $cS1$ signal in dependence of the energy deposit E_{TPC} for Compton scattering with an applied drift field of 396 V/cm and corresponding light yield.	309
B.34 Detected $cS1$ signal in dependence of the energy deposit E_{TPC} for Compton scattering with an applied drift field of 594 V/cm and corresponding light yield.	309
B.35 Detected $cS1$ signal in dependence of the energy deposit E_{TPC} for Compton scattering with an applied drift field of 792 V/cm and corresponding light yield.	313
C.1 Hamamatsu Photomultiplier tube R6041-406 data sheet.	318
C.2 RMD Avalanche Photodiode S1315 data sheet.	319
C.3 Ortec GEM-F5930-S HPGe detector data sheet.	320

Bibliography

- [1] Szydakis, M. *et al.*, “Enhancement of NEST capabilities for simulating low-energy recoils in liquid xenon,” *JINST*, vol. 8 C10003, 2013.
- [2] Goetzke, L. W. *et al.*, “Measurement of light and charge yield of low-energy electronic recoils in liquid xenon.” arXiv:1611.10322v1 [astro-ph.IM], November 2016.
- [3] Beskers, B., ‘*MainzTPC*’ - *Design and commissioning of a dual-phase xenon time-projection-chamber for studies of the scintillation pulse shape*. PhD thesis, Johannes Gutenberg-Universität Mainz, 2017.
- [4] Wenz, D., “Improving the calibration of MainzTPC using the isotope ^{37}Ar ,” Master thesis, Johannes Gutenberg-Universität Mainz, 2018.
- [5] Backens, J., “Gitterinduzierte Einzelelektronenereignisse in der MainzTPC,” Bachelor thesis, Johannes Gutenberg-Universität Mainz, 2018.
- [6] Griest, K. and Kamionkowski, M., “Supersymmetric dark matter,” *Elsevier Physics Reports*, vol. 333-334, pp. 167–182, 2000.
- [7] Babcock, H. W., “The Rotation of the Andromeda Nebula,” *Lick Observatory Bulletin*, vol. 19, pp. 41–51, 1939. Provided by the SAO/NASA Astrophysics Data System.
- [8] Rubin, V. C. and Ford, Jr., W. K., “Rotation of the Andromeda Nebula from a Spectroscopic Survey of Emission Regions,” *The Astrophysical Journal*, vol. 159, p. 379, February 1970. Provided by the SAO/NASA Astrophysics Data System.
- [9] Colless, M., “Encyclopedia of Astronomy & Astrophysics.” <http://www.astro.caltech.edu/~george/ay21/eea/eea-comacluster.pdf>, 2006.
- [10] Zwicky, F., “Die Rotverschiebung von extragalaktischen Nebeln,” *Helvetica Physica Acta*, vol. 6, pp. 110–127, 1933.

- [11] Clowe, D. *et al.*, “A direct empirical proof of the existence of Dark Matter,” *The Astrophysical Journal*, vol. 648, pp. L109–L113, 2006.
- [12] Mather, J. C. and Fixsen, D. J. and Shafer, R. A. and Mosier, C. and Wilkinson, D. T., “Calibrator Design for the COBE Far-Infrared Absolute Spectrophotometer (FIRAS),” *The Astrophysical Journal*, vol. 512, pp. 511–520, February 1999.
- [13] Planck Collaboration, “Planck 2015 results - XI. CMB power spectra, likelihoods, and robustness of parameters,” *Astronomy & Astrophysics*, vol. 594, p. 99, October 2016.
- [14] Bekenstein, J. D., “Tensor-vector-scalar-modified gravity: from small scale to cosmology.” arXiv:1201.2759 [astro-ph.CO], January 2012.
- [15] Perkins, D. H., *Particle Astrophysics*. Oxford Master Series in Particle Physics, Astrophysics, and Cosmology, Oxford University Press, 2nd ed., 2009.
- [16] Mei, D.-M. and Hime, A., “Muon-Induced Background Study for Underground Laboratories.” arXiv:astro-ph/0512125, December 2005.
- [17] Bernabei, R. *et al.*, “DAMA/LIBRA results and perspectives.” arXiv:1612.01387 [hep-ex], December 2016.
- [18] KIMS Collaboration, “New Limits on Interactions between Weakly Interacting Massive Particles and Nucleons Obtained with CsI(Tl) Crystal Detectors,” *Physical Review Letters*, vol. 108, p. 181301, April 2012.
- [19] CoGeNT Collaboration, “Search for an Annual Modulation in a P-type Point Contact Germanium Dark Matter Detector.” arXiv:1106.0650 [astro-ph.CO], October 2012.
- [20] SuperCDMS Collaboration, “Low-Mass Dark Matter Search with CDMSlite.” arXiv:1707.01632 [astro-ph.CO], July 2017.
- [21] EDELWEISS Collaboration, “Performance of the EDELWEISS-III experiment for direct dark matter searches.” arXiv:1706.01070 [physics.ins-det], June 2017.
- [22] Schieck, J. *et al.*, “Direct Dark Matter Search with the CRESST II Experiment.” arXiv:1706.01070 [physics.ins-det], November 2016.
- [23] Coron, N. *et al.*, “2010 update on the ROSEBUD project,” in *Identification of Dark Matter 2010*, PoS(IDM2010)054, 2010.
- [24] Felizardo, M. *et al.*, “The SIMPLE Phase II Dark Matter Search.” arXiv:1404.4309 [hep-ph], April 2014.
- [25] Behnke, E. *et al.*, “Final results of the PICASSO dark matter search experiment,” *Astroparticle Physics*, vol. 90, pp. 85–92, 2017.

- [26] Bolte, W. J. *et al.*, “A bubble chamber for dark matter detection (the COUPP project status),” in *Journal of Physics Conference Series*, vol. 39 of *Journal of Physics Conference Series*, pp. 126–128, May 2006.
- [27] PICO Collaboration, “Dark Matter Search Results from the PICO-60 C₃F₈ Bubble Chamber.” arXiv:1702.07666 [astro-ph.CO], August 2017.
- [28] Battat, J.B.R. *et al.*, “DMTPC: A dark matter detector with directional sensitivity.” arXiv:0907.0675 [astro-ph.CO], July 2009.
- [29] Daw, E. *et al.*, “The DRIFT Directional Dark Matter Experiments.” arXiv:1110.0222 [physics.ins-det], October 2011.
- [30] NEWS Collaboration, “NEWS: Nuclear Emulsions for WIMP Search.” arXiv:1604.04199 [astro-ph.IM], April 2016.
- [31] ArDM Collaboration, “The ArDM Liquid Argon Time Projection Chamber at the Canfranc Underground Laboratory: a ton-scale detector for Dark Matter Searches.” arXiv:1612.06375 [physics.ins-det], December 2016.
- [32] DarkSide Collaboration, “Results from the first use of low radioactivity argon in a dark matter search.” arXiv:1510.00702 [astro-ph.CO], October 2015.
- [33] Uchida, H. *et al.*, “Search for inelastic WIMP nucleus scattering on ¹²⁹Xe in data from the XMASS-I experiment.” arXiv:1401.4737v4 [astro-ph.CO], April 2014.
- [34] Akimov, D. Y. *et al.*, “WIMP-nucleon cross-section results from the second science run of ZEPLIN-III.” arXiv:1110.4769 [astro-ph.CO], October 2011.
- [35] LUX Collaboration, “Results from a search for dark matter in the complete LUX exposure.” arXiv:1608.07648 [astro-ph.CO], August 2016.
- [36] PandaX-II Collaboration, “Dark Matter Results From 54-Ton-Day Exposure of PandaX-II Experiment.” arXiv:1708.06917 [astro-ph.CO], August 2017.
- [37] XENON Collaboration, “First Dark Matter Search Results from the XENON1T Experiment.” arXiv:1705.06655 [astro-ph.CO], May 2017.
- [38] Yoo, J. and Jaskierny, W.F., “Electron drift in a large scale solid xenon,” *JINST*, vol. 10, 2015.
- [39] Chepel, V. and Araujo, H., “Liquid noble gas detectors for low energy particle physics.” arXiv:1207.2292 [physics.ins-det], July 2012.
- [40] Policarpo, A. J. P. L. *et al.*, “Electron multiplication and secondary scintillation in liquid xenon: New prospects,” *ICFA Instrum. Bull.*, vol. 15, no. SLAC-PUB-16092, p. 4, 1997.

-
- [41] Haynes, W. M., *Handbook of Chemistry and Physics*, ch. 6, p. 209. CRC Press, 93 ed., 2012.
- [42] Aprile, E. and Doke, T., “Liquid Xenon Detectors for Particle Physics and Astrophysics.” arXiv:0910.4956v1 [hep-ex], October 2009.
- [43] XENON Collaboration, “Blessed plots - internal communication,” November 2017.
- [44] Billard, J. *et al.*, “Implication of neutrino backgrounds on the reach of next generation dark matter direct detection experiments.” arXiv:1307.5458 [hep-ph], July 2013.
- [45] XENON Collaboration, “Dark Matter Search Results from a One Tonne×Year Exposure of XENON1T.” arxiv:1805.12562v1 [astro-ph.CO], May 2017.
- [46] Particle Astrophysics Group - Brown University, “DMTools - Dark Matter Limit Plot Generator.” <http://dmttools.brown.edu>, accessed November 2016.
- [47] LZ Collaboration, “LUX-ZEPLIN (LZ) Technical Design Report.” arXiv:1703.09144 [physics.ins-det], March 2017.
- [48] XENON Collaboration, “Physics reach of the XENON1T dark matter experiment.” arXiv:1512.07501 [physics.ins-det], December 2015.
- [49] DARWIN Collaboration, “DARWIN: towards the ultimate dark matter detector.” arXiv:1606.07001 [astro-ph.IM], June 2016.
- [50] Coarasa, I. *et al.*, “Annual modulation of dark matter: The ANAIS-112 case.” arXiv:1704.06861 [astro-ph.IM], April 2017.
- [51] SABRE Collaboration, “SABRE: WIMP modulation detection in the northern and southern hemisphere.” arXiv:1601.05307 [physics.ins-det], April 2017.
- [52] Adhikari, G. *et al.*, “Initial performance of the COSINE-100 experiment,” *The European Physical Journal*, vol. C78, p. 107, February 2018.
- [53] KIMS Collaboration, “The status of KIMS-NaI experiment,” *Nucl. Part. Phys. Proc.*, vol. 273-275, pp. 295–301, 2016.
- [54] DM-Ice Collaboration, “First search for a dark matter annual modulation signal with NaI(Tl) in the Southern Hemisphere by DM-Ice17.” arXiv:1602.05939 [physics.ins-det], February 2016.
- [55] DarkSide Collaboration, “DarkSide-20k: A 20 Tonne Two-Phase LAr TPC for Direct Dark Matter Detection at LNGS.” arXiv:1707.08145 [physics.ins-det], July 2017.
- [56] Aprile, E. *et al.*, “Conceptual design and simulation of a water Cherenkov muon veto for the XENON1T experiment.” arXiv:1406.2374 [astro-ph.IM], June 2014.

- [57] Commission on Isotopic Abundances And Atomic Weights, “Standard atomic weights 2015.” <http://www.ciaaw.org/atomic-weights.htm>, accessed October 2016.
- [58] Royal Society of Chemistry, “Periodic table - xenon.” <http://www.rsc.org/periodic-table/element/54/xenon>, accessed October 2016.
- [59] National Institute of Standards and Technology (NIST), “Atomic weights and Isotopic Compositions of Xenon.” <https://www.nist.gov/pml/atomic-weights-and-isotopic-compositions-relative-atomic-masses>, accessed October 2016.
- [60] National Nuclear Data Center, “NuDat2 - Nuclear Database.” <http://www.nndc.bnl.gov/nudat2/>, accessed November 2016.
- [61] XENON Collaboration, “Removing krypton from xenon by cryogenic distillation to the ppq level.” arXiv:1612.04284 [physics.ins-det], December 2016.
- [62] L’AIR LIQUIDE S.A., “Gas Encyclopedia Air Liquide,” accessed September 2017.
- [63] National Institute of Standards and Technology (NIST), “Thermophysical Properties of Fluid Systems.” <http://webbook.nist.gov/chemistry/fluid/>, accessed October 2016.
- [64] Cerdeno, D. and Green, M., *Direct detection of WIMPs*, vol. Particle Dark Matter: Observations, Models and Searches, ch. 17, pp. 347–369. Cambridge University Press, February 2010.
- [65] National Institute of Standards and Technology (NIST), “XCOM Photon Cross-Section Database.” <http://physics.nist.gov/PhysRefData/Xcom/html/xcom1.html>, accessed July 2017.
- [66] Thompson, A. C. *et al.*, *X-ray Data Booklet*. University of California: Lawrence Berkeley National Laboratory, 3 ed., October 2009.
- [67] Zavattini, G. *et al.*, “Linearity discontinuities in Xe-filled X-ray microstrip detectors,” *Nuclear Instruments & Methods in Physics Research, Section A: Accelerators, Spectrometers, Detectors, and Associated Equipment*, vol. 401, pp. 206–2016, December 1997.
- [68] Demtröder, W., *Experimentalphysik 3: Atome, Moleküle und Festkörper*. Springer-Verlag Berlin Heidelberg, 2005.
- [69] Sissol, P., “Monte-Carlo-Simulationen eines Compton-Streuexperimentes zur Messung der Szintillations- und Ionisationseigenschaften von flüssigem Xenon mit einer Zwei-Phasen-Xenon-Zeitprojektionskammer,” Diploma thesis, Johannes Gutenberg-Universität Mainz, 2012.

- [70] East, L. V. and Lewis, E. R., “Compton Scattering By Bound Electrons,” *Physica*, vol. 44, pp. 595–613, 1969.
- [71] Acharya, V. B., Singh, B. and Ghumman, B. S., “Compton Scattering of 145 keV Gamma Rays by K-Shell Electrons of Silver,” *Physica Scripta*, vol. 23, pp. 21–23, 1981.
- [72] Ordonez, C. E. *et al.*, “Doppler broadening of energy spectra in Compton cameras,” in *Proc. IEEE Nuclear Science Symp*, no. 2, pp. 1361–1365, 1997.
- [73] Mei Y., *Direct Dark Matter Search with the XENON100 Experiment*. PhD thesis, Rice University, 2011.
- [74] Szydagis, M. *et al.*, “NEST: a comprehensive model for scintillation yield in liquid xenon,” *JINST*, vol. 6 P10002, 2011.
- [75] Stephenson, S. *et al.*, “MiX: A Position Sensitive Dual-Phase Liquid Xenon Detector.” arXiv:1507.01310v2 [physics.ins-det], July 2015.
- [76] Aprile, E. *et al.*, “Observation of anticorrelation between scintillation and ionization for MeV gamma rays in liquid xenon,” *Physical Review B*, vol. 76, July 2007.
- [77] Kubota, S. *et al.*, “Dynamical behavior of free electrons in the recombination process in liquid argon, krypton, and xenon,” *Physical Review B*, vol. 20, no. 8, pp. 3486–3496, 1979.
- [78] Hitachi, A. *et al.*, “Dynamical behavior of free electrons in the recombination process in liquid argon, krypton, and xenon,” *Physical Review B*, vol. 27, no. 9, pp. 5279–5285, 1983.
- [79] Hils, C., “Studie von internen Kalibrationsmethoden für Flüssig-Xenon-TPCs zur direkten Suche nach Dunkler Materie,” Diploma thesis, Johannes Gutenberg-Universität Mainz, 2013.
- [80] Scheibelhut, M., “Aufbau und Simulation eines Comptonstreuexperimentes mit einem Xenon- und einem Germaniumdetektor,” Diploma thesis, Johannes Gutenberg-Universität Mainz, 2013.
- [81] Morbitzer, M., “Aufbau einer Testkammer zur Charakterisierung von Avalanche-Photodioden für eine Flüssig-Xenon-TPC,” Bachelor thesis, Johannes Gutenberg-Universität Mainz, 2012.
- [82] Jennewein, T., “Charakterisierung von Photomultiplier Tubes hinsichtlich deren Verwendung in Flüssig-Xenon Zeitprojektionskammern,” Bachelor thesis, Johannes Gutenberg-Universität Mainz, 2012.
- [83] Kjartansson, E., “Realization of a System to Control and Monitor the Operation of a Liquid Xenon Time Projection Chamber,” Bachelor thesis, Johannes Gutenberg-Universität Mainz, 2012.

- [84] DuPont, “Kapton® Polyimide Film.” <http://www.dupont.com/products-and-services/membranes-films/polyimide-films/brands/kapton-polyimide-film.html>, accessed October 2017.
- [85] Precision Eforming, LLC, “Electroformed Micro Mesh Prdouct Catalog.” <http://www.precisionforming.com/electroformed-micro-mesh-product-catalog/>, 2017.
- [86] Smartec BV, “Datasheet: Universal Transducer Interface (UTI).” <http://www.smartec-sensors.com>, November 2010.
- [87] Smartec BV, “Measuring accurately small sensor signals via long wires with a microcontroller.” <http://www.smartec-sensors.com>, March 2011.
- [88] Shagin, P. *et al.*, “Avalanche Photodiode for Liquid Xenon Scintillation: Quantum Efficiency and Gain,” *JINST*, vol. 4, no. 1, 2009.
- [89] CAEN Tools for Discovery, “A1422 Low Noise Fast Rise Time CSP.” <http://caen.it/csite/CaenProd.jsp?parent=13&idmod=604>, 2014.
- [90] Ortec, “Quality Assurance Data Sheet,” March 2013.
- [91] Beyer, R. *et al.*, “Inelastic sscattering of fast neutron from excited states in ^{56}Fe ,” *Nuclear Physics A*, vol. 927, pp. 41–52, March 2014.
- [92] Junghans, A. R. *et al.*, “nELBE: Neutron time-of-flight experiments at ELBE.” <https://www.hzdr.de/db/Cms?pNid=317>, October 2017.
- [93] Scheibelhut, M., *PhD thesis in preparation*. PhD thesis, Johannes Gutenberg-Universität Mainz, 2020.
- [94] Hamamatsu Photonics, “Photomultiplier tube Data sheet,” 2011.
- [95] Struck Documentation, *SIS1100/3100 LINUX Driver - Programmers Manual*. SIS GmbH, v148 ed., October 2010.
- [96] Struck Documentation, *SIS3316 16 Channel VME Digitizer - User Manual*. SIS GmbH, v110 ed., February 2015.
- [97] Struck Documentation, *SIS3305 5 GS/s, 2.5 GS/s, 1.25 GS/s 10-bit VME Digitizer - User Manual*. SIS GmbH, v202 ed., February 2017.
- [98] CAEN Tools for Discovery, *CAEN V1290 A/N / VX1290 A/N - 32/16 Channel Multihit TDCs*. CAEN S.p.A., 7 ed., May 2006.
- [99] CAEN Tools for Discovery, *CAEN V1495 General Purpose VME Board*. CAEN S.p.A., 16 ed., June 2015.
- [100] Struck Documentation, *SIS3820 VME Scaler - User Manual*. SIS GmbH, v186 ed., February 2009.

-
- [101] CAEN Tools for Discovery, *CAEN V6533 - 6 Ch. Programmable HV Power Supply*. CAEN S.p.A., 6 ed., March 2014.
- [102] iseg Spezialelektronik, *iseg High Voltage Power Supply - VME HIGH PRECISION series - Operators Manual*. iseg Spezialelektronik GmbH, 1.05 ed., March 2012.
- [103] Oger, T. et al., “A liquid xenon TPC for a medical imaging Compton telescope,” *Nuclear Instruments and Methods in Physics Research A*, vol. 695, pp. 125–128, 2012.
- [104] Bowe, J.C., “Drift Velocity of Electrons in Nitrogen, Helium, Neon, Argon, Krypton, and Xenon,” *Phys. Rev.*, vol. 117, pp. 1411–1415, March 1960.
- [105] Aprile, E. et al., “Simultaneous Measurement of Ionization and Scintillation from Nuclear Recoils in Liquid Xenon as Target for a Dark Matter Experiment.” arXiv:astro-ph/0601552, January 2006.
- [106] Machin, W. D., “Hysteresis and Irreversible Phase Transitions: Xenon adsorbed on a Mesoporous Silica Gel,” *J. Chem. Soc. Faraday Trans.*, vol. 88, pp. 729–735, 1992.
- [107] Smith, B. L. et al., “Surface Tension and Energy in Liquid Xenon,” *The Journal of Chemical Physics*, vol. 47, pp. 1148–1152, 1967.
- [108] RMD Inc., “Avalanche Photodiodes Data sheet,” 2012.